FINAL REPORT

Accelerated Dynamic Corrosion Test Method Development

SERDP Project WP-1673

NOVEMBER 2017

James Dante
Southwest Research Institute

SERDP
DOD ▪ EPA ▪ DOE

Page Intentionally Left Blank

Page Intentionally Left Blank

REPORT DOCUMENTATION PAGE

Form Approved
OMB No. 0704-0188

1. REPORT DATE *(DD-MM-YYYY)*
11/03/2017

2. REPORT TYPE
SERDP Final Report

3. DATES COVERED *(From - To)*
5/11/2009 - 12/31/2016

4. TITLE AND SUBTITLE
Accelerated Dynamic Corrosion Test Method Development

5a. CONTRACT NUMBER
Contract: 09-C-0033

5b. GRANT NUMBER

5c. PROGRAM ELEMENT NUMBER

6. AUTHOR(S)
James Dante

5d. PROJECT NUMBER
WP-1673

5e. TASK NUMBER

5f. WORK UNIT NUMBER

7. PERFORMING ORGANIZATION NAME(S) AND ADDRESS(ES)
Southwest Research Institute
6220 Culebra Road
Division 18 / Bldg. 128
San Antonio, TX 78238

8. PERFORMING ORGANIZATION REPORT NUMBER
WP-1673

9. SPONSORING/MONITORING AGENCY NAME(S) AND ADDRESS(ES)
Strategic Environmental Research and Development Program
4800 Mark Center Drive, Suite 17D03
Alexandria, VA 22350-3605

10. SPONSOR/MONITOR'S ACRONYM(S)
SERDP

11. SPONSOR/MONITOR'S REPORT NUMBER(S)
WP-1673

12. DISTRIBUTION/AVAILABILITY STATEMENT
Distribution A; unlimited public release

13. SUPPLEMENTARY NOTES

14. ABSTRACT
Perhaps the most widely recognized accelerated corrosion test is the ASTM B117 salt fog test. However, numerous studies have demonstrated that this test method has poor correlation to outdoor exposures, particularly for non-chromate primers. As a result, more realistic cyclic environmental exposures have been developed to more closely resemble actual atmospheric corrosion damage. Several existing tests correlate well with the outdoor performance of some materials and assemblies of interest, but not all. The risk, then, is that promising new environmentally friendly technologies may be incorrectly rejected based on corrosion processes observed in flawed laboratory tests.

15. SUBJECT TERMS
Accelerated Dynamic Corrosion, Test Method Development

16. SECURITY CLASSIFICATION OF:			**17. LIMITATION OF ABSTRACT**	**18. NUMBER OF PAGES**	**19a. NAME OF RESPONSIBLE PERSON**
a. REPORT	**b. ABSTRACT**	**c. THIS PAGE**			James Dante
					19b. TELEPHONE NUMBER *(Include area code)*
UNCLASS	UNCLASS	UNCLASS	UNCLASS	307	210-522-5458

Page Intentionally Left Blank

ABSTRACT SUMMARY

Perhaps the most widely recognized accelerated corrosion test is the ASTM B117 salt fog test. However, numerous studies have demonstrated that this test method has poor correlation to outdoor exposures, particularly for non-chromate primers. As a result, more realistic cyclic environmental exposures have been developed to more closely resemble actual atmospheric corrosion damage. Several existing tests correlate well with the outdoor performance of some materials and assemblies of interest, but not all. The risk, then, is that promising new environmentally friendly technologies may be incorrectly rejected based on corrosion processes observed in flawed laboratory tests.

The development of accurate laboratory corrosion tests requires a basic understanding of the relationship between specific environmental variables and specific modes of corrosion failure. This requires fundamental studies to relate simple environmental parameters to actual conditions at the surface of a material and how those conditions specifically effect corrosion and protection. The overall goal of this project was to develop an improved dynamic accelerated corrosion test environment that more accurately predicts material system corrosion behavior in operational environments. Throughout this program, the research team assessed the relationship between environmental parameters and the resulting corrosion modes of various material systems. The corrosion of metals (boldly exposed, in occluded sites, and in galvanic couples), coating adhesion, and mechanical properties of metals as a function of environmental parameters (including humidity cycling, chemistry, and temperature) were assessed. These findings were then used to identify controlling factors for different damage modes. The relationships between exposure parameters and the resulting corrosion damage were then used to develop an accelerated test method that results in corrosion damage more similar to that observed in outdoor exposures than previous tests.

The single most relevant factor in governing atmospheric corrosion is the relative humidity (RH). Significant effort has been expended throughout the course of this work to define how RH and cyclic variations in RH affect corrosion rates and corrosion modes. On bare carbon steel surfaces, it was shown that corrosion can continue at RH values as low as 10% for some deposited salt chemistries. However, it should be noted that below 50% RH the corrosion rate is "very low" according to the ISO standard 9223. Multi-Electrode Array (MEA) studies of steel and aluminum under cyclic RH conditions were also performed. Real time MEA data revealed that under cyclic RH conditions, spikes in corrosion rate occurred during wetting and drying cycles. These spikes were also observed for aluminum systems indicating the importance of cyclic RH.

The effect of cyclic RH conditions on a creviced steel surface and galvanic couples were also examined. Under conditions of high RH, the surface outside of the crevice became totally cathodic such that all anodic currents were within the occluded crevice. Upon drying, the internal and external portions of the crevice decoupled and corrosion current was observed external to the crevice mouth. This coupling and decoupling effect was also observed for galvanic couples between steel and aluminum. Specifically, coupling was seen above the deliquescence relative humidity (DRH), the point at which deposited salt absorbs sufficient water from the atmosphere to dissolve. Metallographic analysis of galvanic assemblies showed that intergranular corrosion, pitting, and fissure formation within the bolt hole of a galvanic fastener occurred only under conditions where RH was cycled. These findings suggest that for values of RH above 50%, there are at least two regions of RH that are important. The regions are divided at the DRH. Above the DRH, thick electrolyte layers are present, allowing long-range electrochemical interactions such as coupling of galvanic materials and crevice regions. Below the DRH, it is likely that as drying begins, the thin electrolyte film begins to break into smaller islands. While corrosion can still occur under these isolated electrolyte islands, long range electrochemical coupling forces can no longer effect corrosion.

As with bare metal and metal assemblies, cyclic variation in RH plays a key role in driving degradation of coated samples. In an attempt to better understand the role of the number of cycles and time of wetness on adhesion, further testing was performed using RH cycles of varying lengths and proportions of high RH to low RH periods. Sensor data as well as image analysis suggest that coating delamination is a strong function of the time of wetness within a given cycle. Therefore, adhesion loss is less a function of the number of cycles than of corrosion rate. A drying step is required to solidify corrosion product and lift the coating from the surface. Additionally, extended periods in the intermediate RH range resulted in the appearance of exfoliation corrosion. The duty cycle for accelerating delamination would include relatively long exposure in the wet portion of a cycle. For accelerating corrosion after delamination, a short drying cycle would be appropriate.

RH duty cycle plays a strong role in both coating adhesion and corrosion rate at a coating defect. MEA data were used to demonstrate the effect of coating inhibitors on the corrosion current distribution. The addition of Class C or Class N primer resulted in the localization of galvanic attack to the vicinity of the galvanic interface at high RH

values. Aluminum attack was more distributed at RH values below DRH. As with the uncoated samples, decoupling of a galvanic couple occurs below the DRH.

Similar to coating delamination and galvanic decoupling, cracking is enhanced under conditions of cyclic RH. However, an increase in crack growth is only observed under conditions where the RH is falling. Test solution chemistry was found to be an important factor in determining crack growth rates. Specifically, the presence of sulfate species in the test solution was found to drastically increase observed crack growth rates. The degree of coating delamination and cracking can be controlled by the amount of time in the RH range between 50% RH and the DRH of the deposited salt.

Atmospheric chemistry is another major factor in governing corrosion rates. Salt speciation will determine the value of DRH and salt composition will have an effect on specific corrosion and cracking rates. Likewise, salt loading density will directly affect electrolyte formation geometry and overall material coverage. Based on work in this effort it was observed that the composition of salts that are found on sample assemblies (both in laboratory environments and outdoors) mimic the exposure conditions. In other words, in coastal environments, deposit composition closely resembles that of seawater while in accelerated lab tests, the composition closely resembles that of the spray solution.

Nevertheless, slight differences in composition are observed. For example, samples exposed at Pt. Judith and Daytona Beach had slightly reduced amounts of chloride, sulfate and nitrate indicating their reactiveness to the exposed surfaces. Thus, these ionic constituents are important in the corrosion reactions observed. After three weeks of exposure to laboratory environments, the maximum amount of salt loading is fairly similar for ASTM B117, ASTM G85-A5 and ASTM G85-A4. In contrast, loading levels for the GM9540P test are nearly a factor of 10 or more lower. This dilution is consistent with the observed reduction in corrosion rate.

Measurements were also made on samples exposed to outdoor environments for a period of one year. It was observed that Pt. Judith had the highest salt content. Examination of in-situ corrosion rate data, short term mass loss data, and visual observations reveal that the highest damage rates were observed at Pt. Judith. Further examination of sensor data reveals that an increase in cumulative corrosion coincides with increases in time of wetness and conductance. Conductance data relates directly to the salt loading observed, revealing that the chemical environment at Pt. Judith is more aggressive than the other ambient locations. Of particular interest is that the salt load loads for LAX are high, but the damage observed after long term exposure is mild. Examination of the data reveals, however, that the cumulative time of wetness is relatively low at LAX. Thus despite the relatively high salt loading, the conductance of the electrolyte layer remains low, resulting in a lower corrosion rate and demonstrating the importance of RH.

Due to the importance of RH levels and cycling, sensors and software programs were used to define appropriate time intervals within each RH range. Sensors were used to continuously measure RH at the outdoor exposure sites for several months. The RH levels were binned in four categories: (RH < 50%, rising RH with 50% < RH < DRH, falling RH with 50% < RH < DRH, and RH > DRH. In this case, it was assumed that NaCl dominated chemistry and so 76% RH was used as the DRH value. From this data, the percentage of time spent in each bin was calculated and normalized to the total exposure time. Results of this binning indicate that the severity of attack is not simply a function of percentage of time in each RH range but also the absolute amount of time in each range in each cycle.

Using the findings described above, an accelerated test protocol was developed and written. The test protocol provides detailed information regarding the testing apparatus, sample preparation, solution preparation, testing procedure, as well as post-test inspections and reporting. It was written in the format of the standard ASTM tests to facilitate easy discussion and adoption. Initial testing revealed that the resulting exposure environments were more mild than anticipated and limited corrosion was observed. Based on RH values achieved during testing and the percentage of time in each RH range, it was expected that exposure conditions would result in damage similar to what is observed at LAX. Photographs of the panels after testing revealed this to be the case. The mild exposures were primarily a function of test chambers performing in an unexpected manner. Differences in chamber performance between team member laboratories have been noted throughout this effort. Differences in high and low RH values as well as ramp rates varied significantly between labs despite efforts to reconcile differences. In order to achieve desired exposure conditions, rigorous control of relative humidity is required and must be called out in test specifications. This will require the use of more sophisticated test equipment but will ensure lab to lab reproducibility and the creation of damage states observed in the field.

Table of Contents

List of Figures

List of Figures (Continued)

List of Figures (Continued)

List of Figures (Continued)

List of Figures (Continued)

List of Figures (Continued)

List of Figures (Continued)

List of Figures (Continued)

List of Figures (Continued)

List of Figures (Continued)

List of Figures (Continued)

List of Figures (Continued)

List of Figures (Continued)

List of Figures (Continued)

List of Tables

CHAPTER 1
BACKGROUNG AND OBJECTIVE

Perhaps the most widely recognized accelerated corrosion test is the ASTM B117 salt fog test (ASTM, 2011a). Numerous studies have demonstrated that this test method has poor correlation to outdoor exposures (Cleveland Society for Coatings Technology, 1994; Davidson, et al., 2003; Howard, Lyon, & Scantlebury, 1999a; Howard, Lyon, & Scantlebury, 1999b; Leard & Dante, 2003; Lyon, Thompson, & Johnson, 1992). As a result, more realistic cyclic environmental exposures have been developed to emulate actual atmospheric corrosion conditions (Bovard et al., 2007; GM, 1997; Goldie, 1996; Repp, 2002; SAE, 2003). While most cyclic tests were initially developed for coated steel, they have been widely used for evaluation of other alloys in the automotive and aerospace industries. Testing according to these cyclic protocols has improved the ability to correlate laboratory tests with operational environment exposures (Price, Dante, & Buckingham, 2007). These correlations, however, are limited to specific performance metrics and generalizations can often not be made. For example, a cyclic laboratory test may rank the performance of a temporary coating system high, but exposure to UV radiation during real world service may degrade the performance to less than that of a UV resistant system. On the other hand, while “permanent” coatings chalk due to UV exposure, there is little effect on the ability of a coating system to inhibit corrosion at a defect. In this case, a simple cyclic test environment may accurately reflect corrosion within a defect, but not chalking of the coating.

There are numerous current examples of the failure of current corrosion test methodologies to accurately predict real world failure. As one example, silver filled gap sealants and paints in contact with aluminum structure were approved for use on new weapon systems based on acceptable ASTM B117 corrosion test performance. Even so, critical failures were observed in the field in very short time periods. As a second example, many programs have focused on the development of new corrosion prevention technologies to replace chromate based systems. Some of these systems have promising outdoor exposure results, but fail to meet laboratory corrosion test requirements of military coating specifications. It is apparent that promising new environmentally friendly technologies may be rejected based on corrosion processes observed in flawed laboratory tests that do not reflect operational environment failure modes.

Often in the development of new laboratory techniques, statistical analyses are used to compare the relative rankings of various corrosion protection technologies in lab tests to rankings of the same technologies found in “real world” exposures. The result of such methods is the formulation of tests specific to the materials and outdoor exposure sites used to develop the empirical relationships. In this approach the laboratory testing is not useful for other service environments or modes of failure associated with galvanic couples, crevice environments, and mechanical loads. The study by Davidson clearly demonstrated the ability of the SAE J2334 (and to a slightly lesser degree GM9540P and Ford APGE) test to rank the performance of coated steel coupons relative to a severe outdoor environment (Davidson et al., 2003). Subsequently, it has been found that the SAE J2334 and GM9540P tests do not provide a reasonable relative ranking of aluminum corrosion (Bovard, et al., 2006; Sheetz, 2000).

Current predictive models of atmospheric corrosion consist of simple correlations among easily measured atmospheric variables (e.g., relative humidity, temperature, salt deposition, pollutant gas concentration) and observed corrosion rates. Unfortunately, regression analyses for corrosion rates that consider these "obvious" variables have been uniform failures, with correlation coefficients consistently near or below 0.5 (Feliu, Morcillo, & Feliu, 1993; Knotkova, Boshek, & Kreisloca,1995). This strongly suggests that several key factors that influence corrosion have not been considered and accelerated corrosion tests based on simple relationships between these traditional environmental variables cannot replicate service performance. Regardless, this approach has been the basis for the current generation of test methods.

The development of accurate laboratory corrosion tests requires a basic understanding of the relationship between specific environmental variables and specific modes of corrosion failure. This will require fundamental studies to relate simple environmental parameters to actual conditions at the surface of a material and how those conditions specifically effect corrosion and protection. As an example, De la Fuente et al. varied chloride and SO_2 concentration applied during laboratory exposures in an attempt to develop corrosion products that mimic outdoor exposures (De La Fuente, Chico, & Morcillo, 2006). While chlorides and sulfate levels in the corrosion product changed as a function of input levels, the authors were not able to fully reproduce the nature of corrosion products found in the field. In a separate study, Howard et al. varied both chemistry, time of wetness, and the number of cycles in an accelerated test chamber to "dial in" expected corrosion damage found in galvanized steel roofing components (Howard, Lyon, Scantlebury, 1990; Howard, Lyon, Scantlebury, 1999). They demonstrated that damage observed during actual service could be replicated, but only under a limited set of input conditions. Further, Zhu suggested attention be given to the ratio of wet/dry time in cyclic chamber tests since his results indicated that the wetness and corrosion rate within a crevice increased very rapidly with the number of cycles resulting in a region that never dried during the dry cycle (Zhu, Thierry, & Kucera, 1997). This phenomenon was also observed by Cooper, and in a separate study by Dante during exposures in a GM9540P environment (Cooper, Ma, Wikswo, & Kelly, 2004; Dante, Price, Sabata, & Sabata, 2007).

This effort was based upon the concept that a more comprehensive understanding of the relationship between environmental variables and corrosion failure modes requires the consideration of additional variables including mechanical loading and surface environments that develop on materials exposed to natural atmospheres (Figure 1).

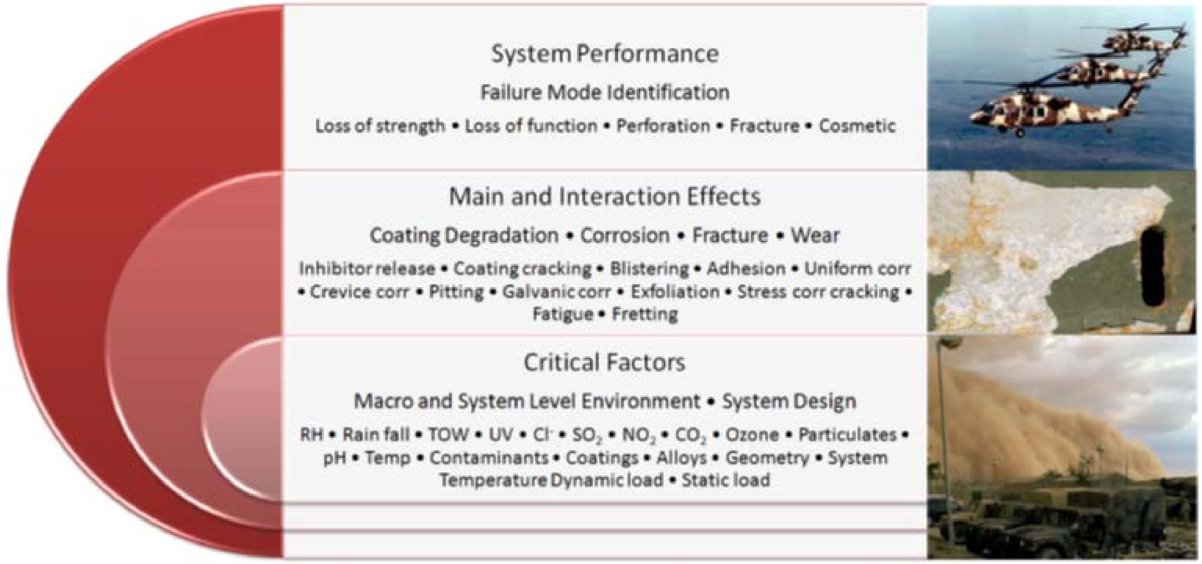

Figure 1. Dependence of failure mode on the critical environmental, mechanical and design variables.

Actual surface environments are a strong function of salt deposits, atmospheric gasses, and time of wetness as well as interactions among these variables. While some work has been done to identify corrosion sample designs for the automotive industry, little work has been done to identify sample geometries appropriate for airframes. No work has been reported where load is applied during accelerated corrosion chamber testing. Time of wetness is achieved by varying spray, humidity, and drying conditions/times, but little is understood regarding wetting and drying at the surface of a sample particularly in occluded areas. There has also been no explicit account for the speciation, spatial variability, and associated deposition fluxes of chemical species such as chlorine and bromine containing compounds that are introduced into the lower atmosphere from both natural and anthropogenic sources. These reactive halogen gasses can be subsequently transformed by reactions involving oxidants (ozone and hydroxyl radical) in the presence of UV light and water.

Throughout this program, the research team was seeking to critically assess the relationship between environmental parameters and the resulting corrosion modes of various material systems. The corrosion of metals (boldly exposed, in occluded sites, and in galvanic couples), coating conductivity and diffusivity, and the mechanical properties of metals and coatings as a function of environmental parameters (including humidity cycling, UV exposure, chemistry, and temperature) were being assessed. The ultimate goal of this effort was to develop a more comprehensive laboratory exposure method (Dynamic Accelerated Corrosion Test Method – DACTM) that addresses appropriate failure modes for a given environment (Figure 2).

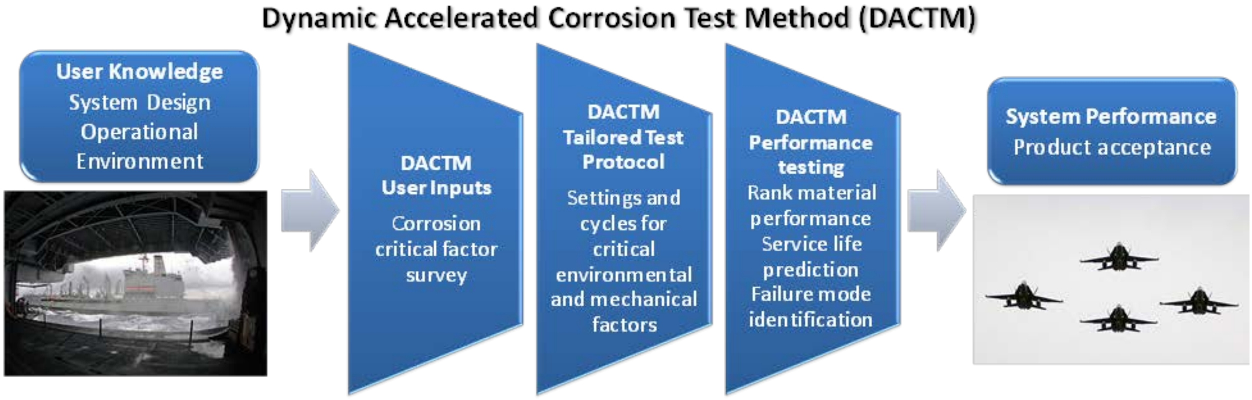

Figure 2. Rapid transition of new corrosion prevention technologies.

This report is divided into 10 Chapters. Chapter 2 – Chapter 8 are meant to be self inclusive and therefore include separate materials handling and results and discussion section within each Chapter. Chapter 2 – Chapter 6 specifically describe the results of laboratory studies that elucidate how environmental parameters (relative humidity (RH) in particular) affect corrosion. In Chapter 2, the relationship between RH and corrosion rate is shown. The relationships between RH and crevice and galvanic corrosion are shown in Chapter 3. Coating performance as a function of cyclic RH is shown in Chapter 4 and the effects of cyclic RH on corrosion protection within a coating defect is shown in Chapter 5. Finally, the effects of cyclic RH and solution chemistry on corrosion cracking is shown in Chapter 6.

In Chapter 7, a comparison of corrosion morphology between accelerated laboratory tests and outdoor exposures is described. Further, a comparison of corrosion performance between laboratory and outdoor exposures using in-situ corrosion sensors is provided to help explain observed differences in corrosion behavior in differing environments. Chemical analysis of ionic species found on the surfaces of samples exposed to laboratory and outdoor exposures is provided in Chapter 8. Comparisons are made in order to provide information needed in the development of an improved accelerated laboratory corrosion test.

Chapter 9 serves four purposes. The primary intent is to summarize the findings from Chapter 2 – Chapter 8 and describe the specific implications each environmental effect has on the development of an improved accelerated corrosion test method. Then, an initial recommendation for a proposed test method is provided in the form of an ASTM specification. Finally, chemical and morphology of panels exposed to the new tests are described to assess the successfulness of the initial recommended test protocols. Several recommendations for improvements are provided in Chapter 10, a description of possible future efforts are defined based from the results of this project.

CHAPTER 2
EFFECT OF RELATIVE HUMIDITY ON SINGLE ALLOY BARE SURFACES

In atmospheric environments, corrosion is often approximated as a discontinuous process reliant on the availability of electrolyte to provide ionic conduction between cathodic and anodic sites for damage to develop at a considerable rate. A critical question in atmospheric corrosion is when can a surface be considered wet enough for corrosion to occur at a considerable rate? Great advances have been made in understanding the relationship between the state of the electrolyte on a surface and the corrosion response under the cases of thin films and macroscopic drops at high humidity levels. Relatively little information is available regarding this relationship under aerosol-size deposits and at lower humidity levels that could be expected on outdoor surfaces.

In this section, we test the contention that the deliquescence point of a single salt contaminant serves as the delineation between a wet and a dry surface as well as the boundary between significant and insignificant corrosion attack. We do so for NaCl, $MgCl_2$, and artificial seawater (ASW) microparticles on mild steel at the initial stages of corrosion under isohumidity conditions. An understanding of the contributions of these phenomena to the atmospheric corrosion of steel should have an impact on the design of accelerated test regimes as well as the interpretation of field exposure data.

In addition, the relative humidity values required for corrosion and the measure of drying time are investigated under iso-static RH conditions and during humidity cycling using multielectrode arrays (MEA). It has been demonstrated, for example, that while corrosion of carbon steel coated with KCl starts at 67% RH, it does not stop even at humidity values as low as 25% RH. An increase in corrosion rate is often observed during drying. Understanding the significance of the ratio of wet-to-dry time at the corrosion interface is critical be able to develop an RH duty cycle capable of inducing appropriate forms of corrosion attack.

2.1 Materials and Methods

2.1.1 *2.1.1 Effect of RH and salt deposition on the corrosion morphology of steel*

Details of the experimental procedures are given in the following sections, but an overview of the approach is warranted. The surfaces of polished mild steel coupons were loaded with NaCl, $MgCl_2$ or artificial seawater microparticles in the form of droplets or crystals and were subjected to isohumidity conditions for up to 300 days. After exposure, surfaces of select sample sets were cleaned, and surface profilometry was used to characterize attack morphology and quantify volume loss.

2.1.1.1 Samples for NaCl, $MgCl_2$, and artificial seawater examination

Coupons of AISI 1010 plain carbon steel measuring 25 × 25 mm were polished to a 0.01 μm colloidal silica finish. After polishing, samples were rinsed with ultrapure (UP) water (18.2 MOhm cm, <5 ppb TOC) and absolute ethanol (>99.5%), then dried in a stream of zero grade compressed air.

2.1.1.2 Samples for drop size investigation

Both low carbon steel and high purity iron substrates were used in this experiment. Coupons of AISI 1010 plain carbon steel (Alabama Specialty Products, Munford, Alabama) measuring 25 × 25 mm were polished to a 0.01 µm colloidal silica mirror finish. A 13 mm diameter 6N (99.9999%) purity iron rod (ESPI Metals, Ashland, Oregon) was vacuum annealed at 680°C for seven weeks and then cut into 3 mm thick samples. Three surface finishes were prepared on the iron to test the effect of substrate roughness on the corrosion behavior. One set of samples was polished to a mirror finish using 0.01 µm colloidal silica, another was ground to 600 grit with silicon carbide (SiC) grinding paper, and the last was ground with 1200 grit paper. All grinding was done in the presence of ultrapure water. After preparation, surfaces were rinsed with ultrapure (UP) water (18.2 Mohm·cm, <5 p.p.b. total organic carbon), cleaned with acetone (>99.5%) and ethanol (>99.5%), and then dried in a stream of zero grade compressed air.

Samples were stored in a desiccator (<10%RH) for two days before salt printing. Another set of prepared samples were stored in a desiccator for ten days to see if increased storage time affected the corrosion behavior. Surface roughness was quantified by the roughness average before exposure, Ra (ISO 4287), as measured with a white light interferometer (Zygo Corp., U.S.). The z-resolution and lateral resolution of the white light interferometer in the configuration utilized were 1 nm and 0.55 µm, respectively. The profilometry scans were analyzed in MountainsMap software (Digital Surf, France) to determine the surface roughness. Surface profilometry scans were also used after exposure to quantify the volume loss and total attack area with respect to the plane of the original surface.

2.1.1.3 Salt loading for NaCl, $MgCl_2$, and artificial seawater examination

Prior to exposure, salt was deposited onto the coupons using a custom inkjet printer inside a humidity-controlled chamber pictured in Figure 3. Specifically, a near saturated aqueous solution of NaCl (99.999% purity, metals basis), $MgCl_2$ (>99.99% purity), or ASTM D1141 artificial seawater (ASW) was dispensed onto each coupon in a 10 × 10 mm square array pattern of 126 × 126 droplets. The in-air diameter of the droplets dispensed was ~14 µm for NaCl, 35 µm for ASW and 15 µm for $MgCl_2$, which is representative of the larger size fraction of natural sea salt aerosols. The resulting salt loading density was measured after printing to be $8.6 \pm 0.1\ \mu g \cdot cm^{-2}$ for NaCl, $15.7 \pm 0.1\ \mu g \cdot cm^{-2}$ for ASW, and $7.9 \pm 0.1\ \mu g \cdot cm^{-2}$ for $MgCl_2$. These loadings, in terms of chloride content, are within the range of those reported (1 to 20 $\mu g \cdot cm^{-2}$) for chloride measured on surfaces of boldly exposed zinc plates in coastal marine environments.

For one set of NaCl-loaded samples, here termed the droplet-loaded samples, printing was carried out at 78% RH and 21°C so that the deposits were in the form of droplets at the start of the exposure. On another set, referred to as the crystal-loaded samples, the pattern was printed in the same manner, but onto samples heated on a stage at 60°C. Heating resulted in near instantaneous (<1 s) crystallization of the droplets when they hit the surface with no detectable signs of corrosion resulting from this process.

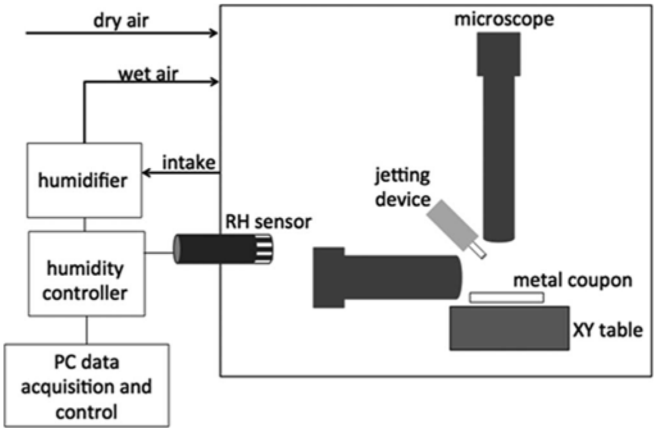

Figure 3. Schematic of inkjet printing system and surrounding humidity chamber.

2.1.1.4 Droplet deposition for drop size investigation

The equipment and general process described in section 2.1.1.3 and pictured in Figure 3 was used to deposit salt droplets. For these experiments, solutions of NaCl (99% purity) in ultra-pure water and in absolute ethanol (>99.5%) were prepared and passed through a 0.2 μm particulate filter. Drops of each solution were deposited randomly on steel and iron substrates at ambient laboratory temperature (21 ± 2°C). Saturated aqueous sodium chloride solution (5.43 M) was used to generate droplets 100–1,000 μm in diameter and was deposited at 75% RH. The ethanol solution (8.76 mM) was used to create smaller drops. This was done by first depositing the ethanol salt drops onto the substrate, and then evaporating the ethanol away at 40% RH. The resulting NaCl particles were then rehydrated to 75% RH, the deliquescence relative humidity (DRH) of NaCl. The DRH is the relative humidity at which a soluble salt spontaneously absorbs water from the air to form a saturated salt solution. All drops deposited at 75% RH therefore had a concentration of 5.43 M NaCl. Due to the reduced NaCl solubility, the ethanol solution deposited less salt and thus produced smaller droplets when hydrated (20–100 μm in diameter). Drop diameters on steel and iron varied up to 14% and 7% from the calculated average, respectively. For a given sample, each drop size was repeated at least 8 times; some drop sizes had as many as 18 drops printed. The number of drops printed depended on the required droplet spacing and the droplet spacing was chosen as to avoid contact of neighboring secondary salt spreading regions.

2.1.1.5 Isohumidity exposures

Immediately after printing, the samples were placed in glass containers that contained saturated salt solutions or desiccant to maintain a particular RH. In order to ensure the deposits on the droplet-loaded coupons stayed wet (deliquesced) at the start of the isohumidity exposures, the containers were pre-filled with humidified zero air to achieve 77–80% RH. Likewise, chambers holding the crystal-loaded coupons were pre-filled with dry (<5% RH) zero air. Afterwards, the air ports on the chambers were closed and they were left to equilibrate to their RH set point (controlled by the salt solution or desiccant) at 21 ± 2°C. In-situ measurements using a calibrated RH sensor (Vaisala, HMP110) indicated that the atmospheres within the chambers equilibrated to within 1.5% of the expected RH in one hour or less and remained there during the duration of the exposures. Coupons were exposed to these conditions for up to 30 days.

Throughout the exposure period, coupons were removed at intervals from the chambers to assess the corrosion response.

For the drop size investigations, droplet-loaded samples were left in the inkjet humidity chamber at 75 ±2% RH and 21±2°C for 24 hours. In-situ drop geometry was characterized by measuring the contact angle and the drop diameter on the surface of the coupon with optical microscopes in the inkjet chamber. The contact angle and drop geometry were measured based on the line of symmetry with the drop reflection on the substrate in ImageJ software.

2.1.1.6 Post-exposure analysis for NaCl, $MgCl_2$, and ASW

Upon removal from the exposure chambers, samples were either immediately stripped of rust for profilometry measurements or left with the corrosion product intact. Samples with the corrosion product left intact were stored in a vacuum desiccator prior to analysis. For the samples for which rust was removed, this was achieved by immersing the samples in an aqueous solution of 1M dibasic ammonium citrate heated to 40°C for 1–5 min (dependent on rust amount). This immersion was followed by rinsing with UP water and drying with compressed air. The cleaned coupons were then scanned using a NewView 7300 white light interferometer (Zygo Corp., US). The manufacturer-stated height resolution of the instrument in the configuration utilized was ~1 nm with a lateral resolution of ~500 nm. At least three areas within the printed regions of each coupon were scanned, with each area measuring 1 × 1 mm. An additional scan was carried out in the unprinted (uncorroded) region of each coupon to serve as a reference. Each scan was then analyzed to determine total volume loss and maximum pit depth with respect to the original polished plane of the coupon. The dataset resulting from this analysis consisted of 2–4 coupons of each type (i.e., droplet or crystal-loaded) per isohumidity set point and exposure period.

2.1.1.7 Post-exposure analysis for drop size examination

Following the 24-hour exposure, the samples were immediately moved to a desiccator (<1% RH) until further analysis. Micrographs of the corroded area were taken with a reflected light optical microscope. A Quanta 650 emission field SEM-EDS (FEI, Oregon) was used to examine the corrosion morphology and to determine the composition of the corrosion product and salt spreading region. The SEM was operated in high vacuum, backscattered electron mode using a 15 kV accelerating voltage and a 10 mm working distance. The corrosion product was removed by immersion in a 0.9 M diammonium citrate solution heated to 65°C for 1–2 minutes (modified ASTM G-1). Subsequent damage evaluations and profilometery of the surface were conducted using a white light interferometer (Zygo Corp., U.S.).

2.1.2 *Corrosion currents under isostatic and cyclic RH conditions*

A schematic representation of the MEA technique is shown in Figure 4. A corroding metal surface consists of anodic (corroding) and cathodic sites. The number of electrons removed at the anodic site must equal the number of electrons consumed at the cathodic sites. By dividing a surface into discrete elements, it can be assumed that some of these sites become primarily anodes while others become primarily cathodes. Electrically isolating these discrete elements at the surface and connecting them to a common electrode forces the flow of electrons through a controlled path. Current flowing through each discrete electrode can then be measured by placing a zero resistant ammeter (ZRA) on each electrode.

A MEA probe was fabricated with 100 Carbon Steel 1018 electrodes, each measuring 250 microns in diameter (Figure 5a). The MEA was coated with either NaCl or sea salt prior to exposure. Approximately 2.7 mg of salt was applied onto the MEA within an o-ring to limit the exposed area to the region of the electrodes. The resultant salt load was approximately 10mg/cm^2 which is 10 to 100 times greater than outdoor salt loads. The MEA was then placed in an environmental chamber (Figure 5b) and exposed to various levels of relative humidity (RH). Note that the applied salt remained fixed on the MEA surface due to electrostatic forces even when the electrode was inverted.

For cyclic RH testing, the MEA probe was placed in an Auto Technology accelerated environmental chamber where RH was cycled between 100% RH and less than 20% RH. The RH was controlled using wet-bottom humidity (i.e. no fog). As described previously, NaCl was deposited directly onto the probes. In addition to the MEA probe, a wetness sensor (Aginova) was placed in the chamber to record RH, temperature, and surface wetness.

Current was measured from each electrode during the course of the experiment at 2 minute or 5 minute intervals (Figure 6). The total anodic current was calculated by adding all of the current greater than 0 A at each time. The cumulative charge passed was then calculated by integrating the total anodic current over the life of the experiment. The cumulative charge is related to mass loss through the Faraday equation. Note that the total mass loss expected during the testing would be higher than that what is calculated since measurements are made at intervals rather than continuously.

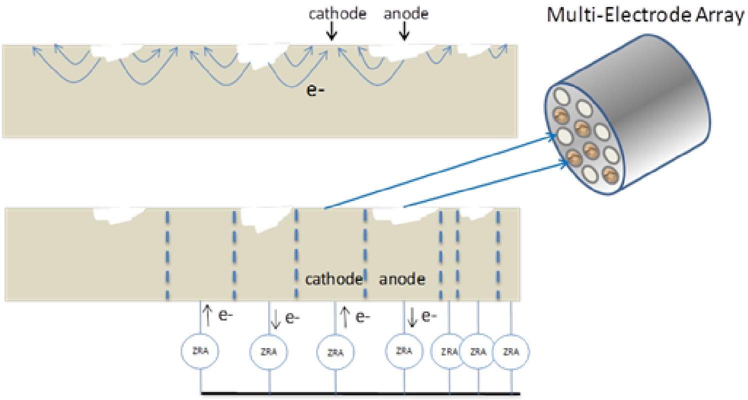

Figure 4. Schematic representation of the theory behind the MEA measurement technique.

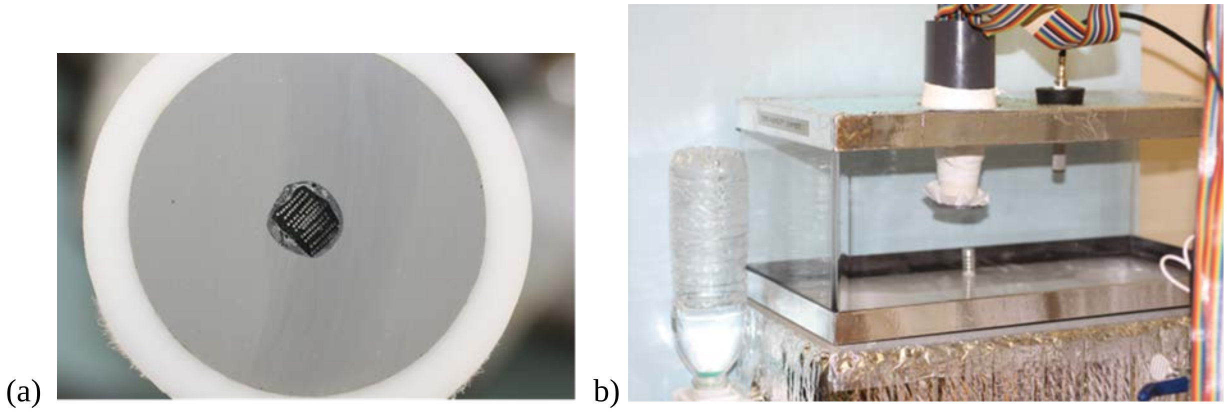

Figure 5. (a) Close up image of a 100 electrode carbon steel electrode. (b) Placement of the carbon steel electrode within an environmental exposure chamber.

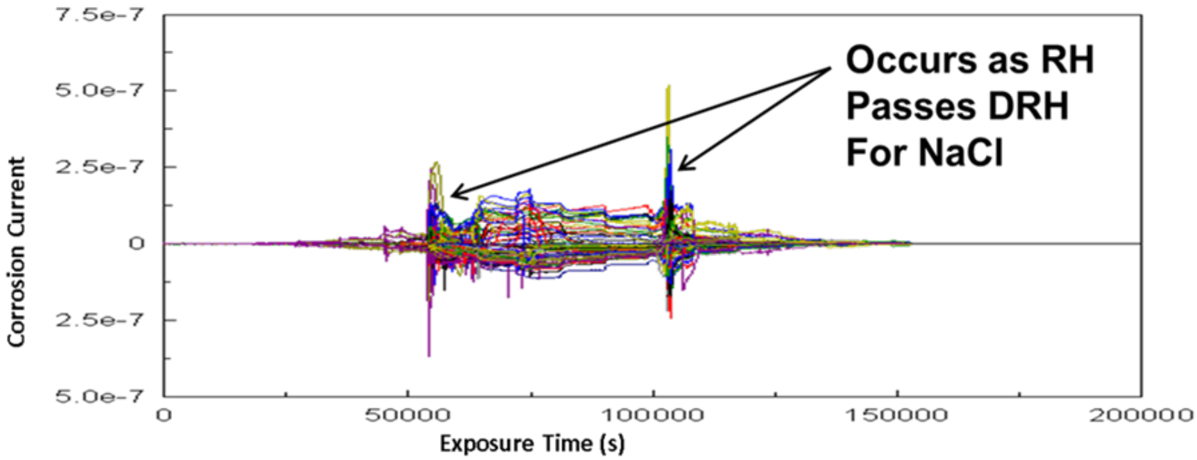

Figure 6. Plot of currents from all 100 electrodes from the MEA assembly. In this test, RH was ramped from 50% RH to 90% RH followed by a ramp back down to 50% RH. Each isohumidity step was 2.5 hours.

2.2 Results and Discussion

2.2.1 Effect of RH and salt deposition on the corrosion morphology of steel

2.2.1.1 Effect of RH on attack morphology and volume loss in the presence of NaCl

Figure 7 shows a series of scan profiles and images of surfaces of NaCl droplet-loaded coupons after seven days of isohumidity exposure. The surface profiles and images were taken of the same areas of the samples. These images and the following descriptions are generally representative of the disparities in attack morphology witnessed with respect to relative humidity, regardless of the exposure times examined or of the original state of the salt deposits (droplet or crystal). In general, corrosion at 33% RH was found to progress radially from a subset of the salt deposits in a fern-like pattern reminiscent of salt creep. Corrosion at 53% RH also clearly emanated from certain salt deposits, but the damage was more filamentary which resulted in discrete pitting. Additionally, needle-like crystals formed in areas around the rust formations and between the original NaCl deposits, and can be seen as thin, irregular lines in the 53% optical image. Coupons exposed at 64% RH exhibited the most uniform corrosion attack in that the greatest amount of area was corroded. Above 64% RH, the number density of pits was found to decrease and their size increased substantially with increasing relative humidity. No sign of sustained corrosion attack was detected at 0% and 23% RH for the maximum time tested here (30 days).

As a means of quantitatively comparing attack morphology across the RH range and between droplet-loaded and crystal-loaded samples, the average maximum pit depth was determined for each sample type and humidity level, Figure 8. These values were computed by averaging the maximum pit depth found in each of the scans for all samples of a certain type (droplet or crystal) exposed at the same relative humidity. It is notable here that the dispersion reflected by the error bars at 85% and 90% RH at 30 days is due to the low number density of pits compared to the field of view of the profilometry scans, as represented by the 90% profile in Figure 7. Figure 8b demonstrates the fact that crystal-loaded coupons generally witnessed the similar attack trends to the droplet-loaded coupons.

The average nominal corrosion depth observed on the samples is given in Figure 9. These values were calculated by dividing the volume loss for each scan by the area of the scan (field of view). Independent t-tests indicated that data points that fall above the noise threshold (dashed line) in these plots were significantly different ($p < 0.04$) from measurements taken in the unprinted regions of the coupons. Independent t-tests were also carried out to compare corrosion depth values given in Figure 9b between the droplet-loaded and crystal-loaded samples after 30 days exposure. There was no significant difference in average depth ($p \geq 0.09$) for all of the humidity levels with the exception of those exposed at 71%RH ($p = 0.03$). The sample size used for each comparative group in these analyses was between 7 and 9 scan measurements.

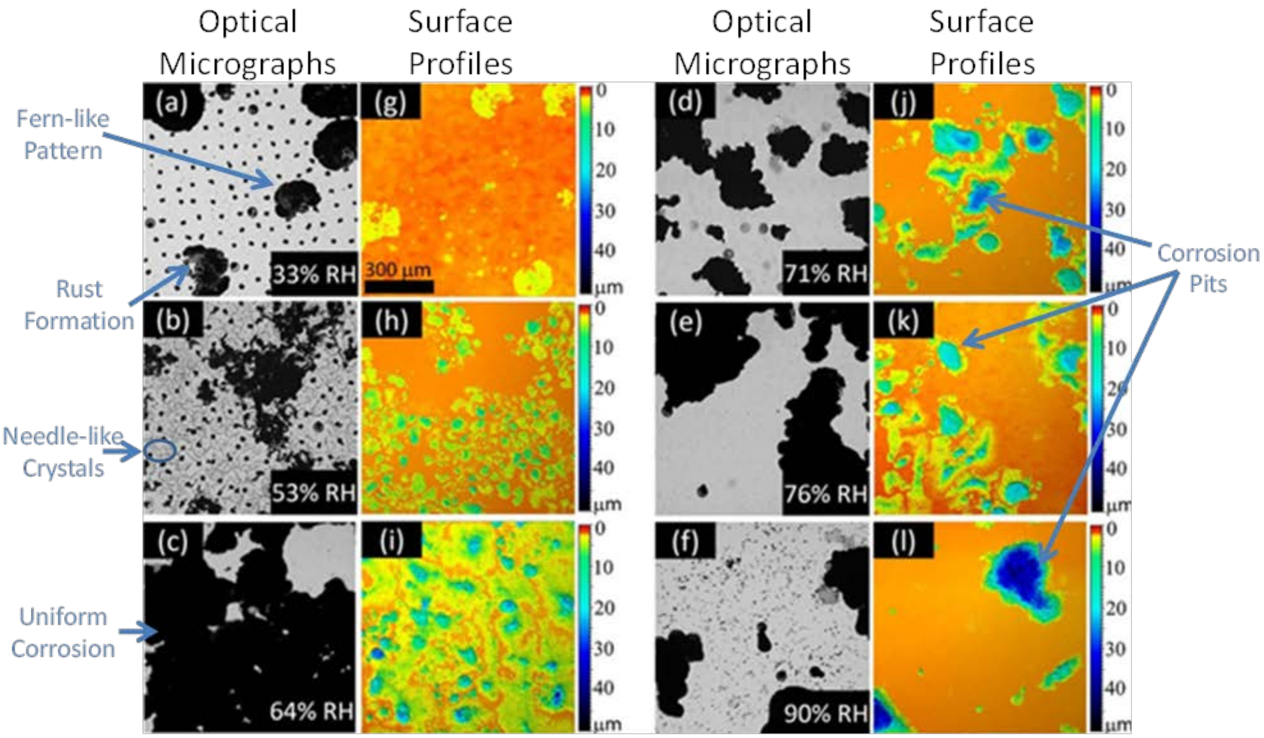

Figure 7. Optical micrographs of NaCl droplet-loaded coupons after 7 d exposure and before rust removal (a-f); measured surface profiles after rust removal for the same exposure period (g-l). All images are of the same scale and of the same areas. The black regions in (a-f) are areas of rust formation.

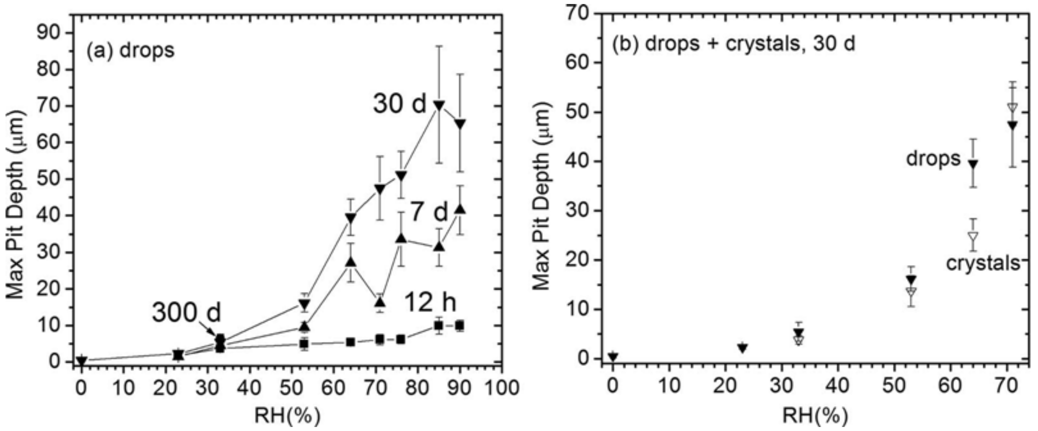

Figure 8. Average maximum pit depth vs. RH for (a) NaCl droplet-loaded samples across entire RH range examined and (b) NaCl droplet and NaCl crystal-loaded samples below the DRH of NaCl. The bars represent standard deviation.

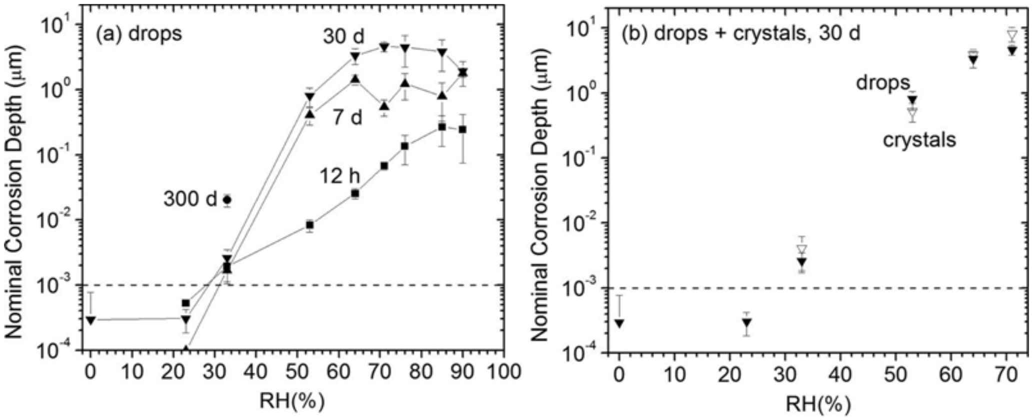

Figure 9. Average volume loss divided by scan area (nominal depth) vs. RH for (a) NaCl droplet-loaded samples across entire RH range examined and (b) NaCl droplet and NaCl crystal-loaded samples below the DRH of NaCl. The dashed line represents the upper bound of the 95% confidence interval of volume loss measured on clean areas outside the printed salt pattern. The bars represent standard deviation.

2.2.1.2 The effect of drop size on the attack morphology in the presence of NaCl

The previous section examined similar initial drops in different exposure environments. However, as the concentration of a salt solution is fixed for a certain relative humidity, the same amount of deposited salt will have a different solution volume — and therefore drop size — at different relative humidities. To isolate the effect of drop size, experiments in this section deposited drops of different sizes, but all drops were held at the same RH, therefore producing the same concentration in the deposited drops.

During the exposure period, the drop diameters increased slightly (<5%) and contact angles decreased as much as 5 degrees, but remained between 55 and 70 degrees for all substrates. There were no observable trends between drop size and contact angle. At 75% RH, corrosion was observed under most deposited droplets. For each substrate, there was a drop size below which corrosion initiation was not observed on every sample – referred to as “fractional corrosion”. Furthermore, for drops that initiated corrosion, a distinct region formed around the corroded region that was comprised of salt – herein referred to as the “secondary spreading region”. Finally, both attack morphology and volume loss varied with deposited drop diameter, indicating a strong dependency on drop geometry.

The attack morphology and surface location of attack was a function of deposited drop size, with attack primarily outside the original drop perimeter (filiform-type) prevalent in smaller drop sizes (<150 μm). In larger drop sizes, attack was confined to within the perimeter of the original drop. Examples of these two types of attack are shown in Figure 10 and Figure 11. The progression of the filiform-type corrosion and resulting damage is exemplified in Figure 10. This type of attack initiated at the edge of the drops as indicated by the formation of small pools (Figure 10a). The filament head (i) then traveled away from the original droplet (ii) and secondary salt (iii) spread radially from the drop (Figure 10b-c). Profilometry of the areas after removal of the corrosion product showed that attack occurred outside of the original droplet area (Figure 10d).

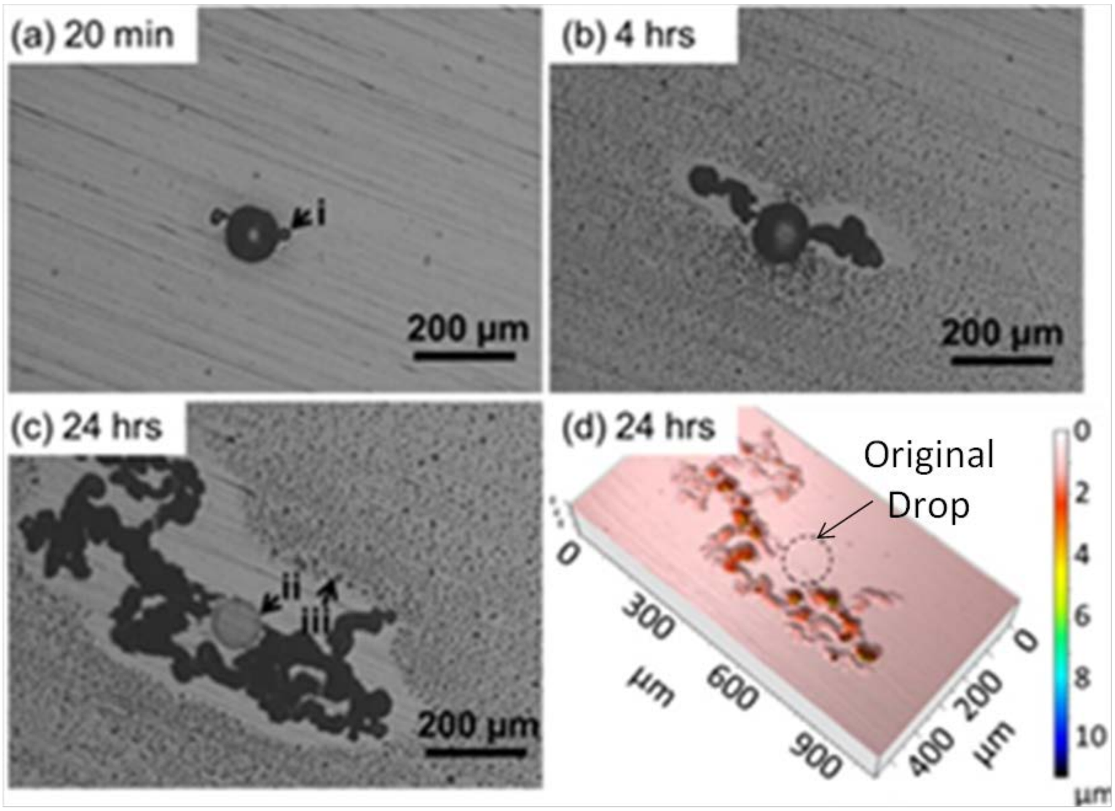

Figure 10. Filiform corrosion under a 100 µm drop on 1200 grit iron after: (a) 20 min, (b) 4 hours and (c) 24 hours (d) 3D topography of corrosion attack. Important features: (i) initiation of the filament head, (ii) original drop, and (iii) secondary salt deposit.

As the drop diameter increased, a smaller fraction of corrosion attack was filiform-type and pitting became more Evans-like (attack confined under original drop) for both iron and steel substrates (Figure 12). This type of corrosion attack initiates and grows within the original droplet area (Figure 11). In some cases, these large drops also formed small solution pools outside the perimeter (Figure 11a), yet corrosion still initiated within the drop (Figure 11c).

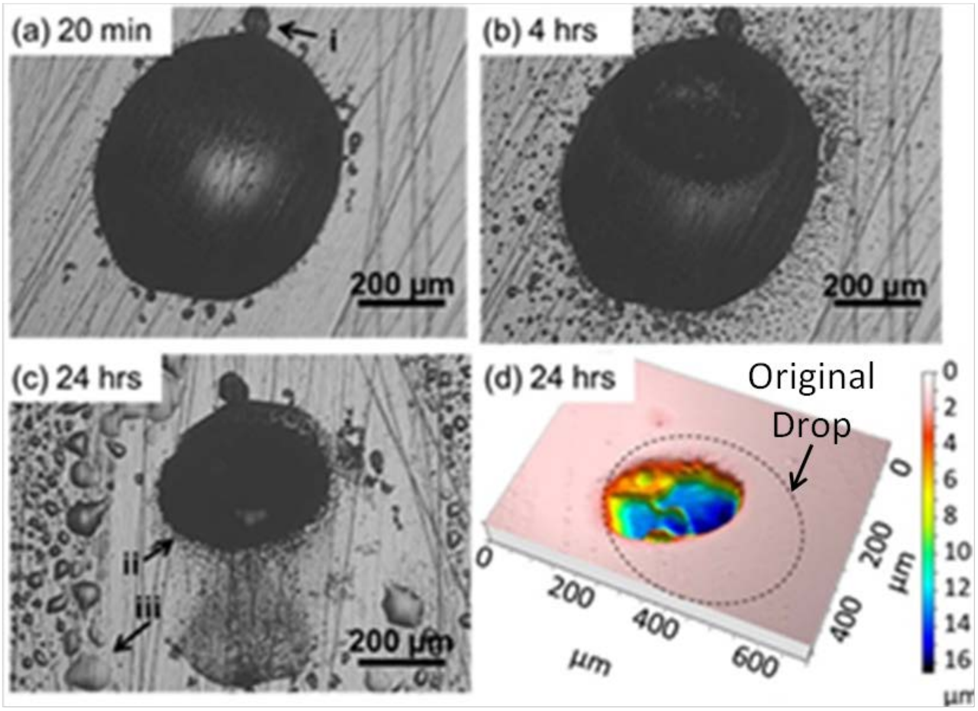

Figure 11. Evans type corrosion under a 600 µm drop on 1200 grit iron after: (a) 20 min, (b) 4 hours and (c) 24 hours (d) 3D topography of corrosion attack. Pitting occurs within initial drop area, as denoted by the dashed perimeter in (d). Important features: (i) filament head, (ii) original drop, and (iii) secondary salt deposition.

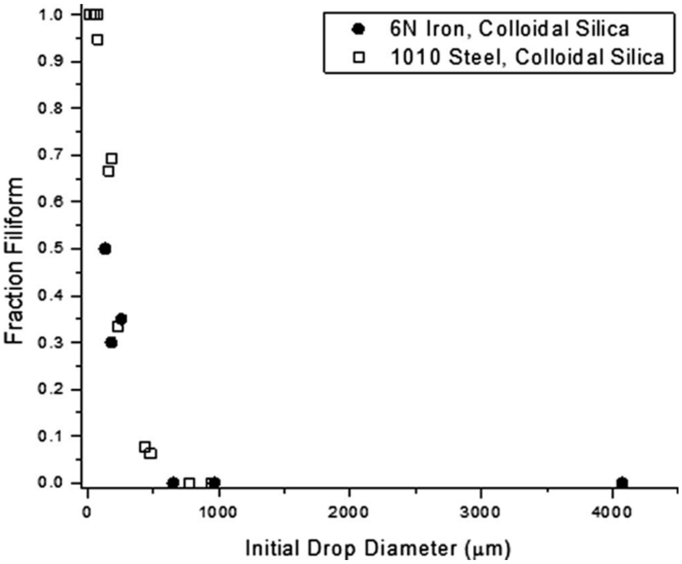

Figure 12. Fraction of corrosion attack that was filiform ($N_{filiform}$ /N_{total}) as a function of initial drop diameter for drops under which detectable corrosion occurred.

The results of this study show that Evans' drop corrosion behavior is not applicable to all drop geometries on bare metal substrates. The smallest drops for both the 1010 steel and iron experiments exhibited filiform corrosion (Figure 10) instead of radial, Evans-type pitting (Figure 11). Filiform-type corrosion has been previously observed on 1018 steel and pure iron. Weissenrieder and Leygraf (2004) found that filiform corrosion occurs at the perimeter of NaCl-containing droplets on bare iron, which agrees with Li and Hihara's observation that filiform corrosion starts at solution pools leaked at the perimeter of the original droplet (Li & Hihara, 2010). Weissenrieder and Leygraf (2004) contend that the initiation is due to local weaknesses in the iron oxide film and do not mention these solution pools.

For those drops under which detectable corrosion occurred, there was no statistical difference in volume loss between the four types of prepared substrates (Figure 13). This lack of a difference may be due to the similarities in composition between the 6N iron and 1010 steel or the large variance in volume loss for each drop size. For some drop sizes, the standard deviation of volume loss was as large as the average, which is most likely because of the mixed (from drop to drop) pitting morphologies (filiform vs. Evans) observed in this size range, Figure 12. Finally, there was no statistical difference in volume loss between samples stored in the desiccator for two days and those stored for ten days. Work by Li and Hihara (2010) suggested that an increase in storage time affects the thickness and stability of the oxide layer, however, this effect was not observed in this work.

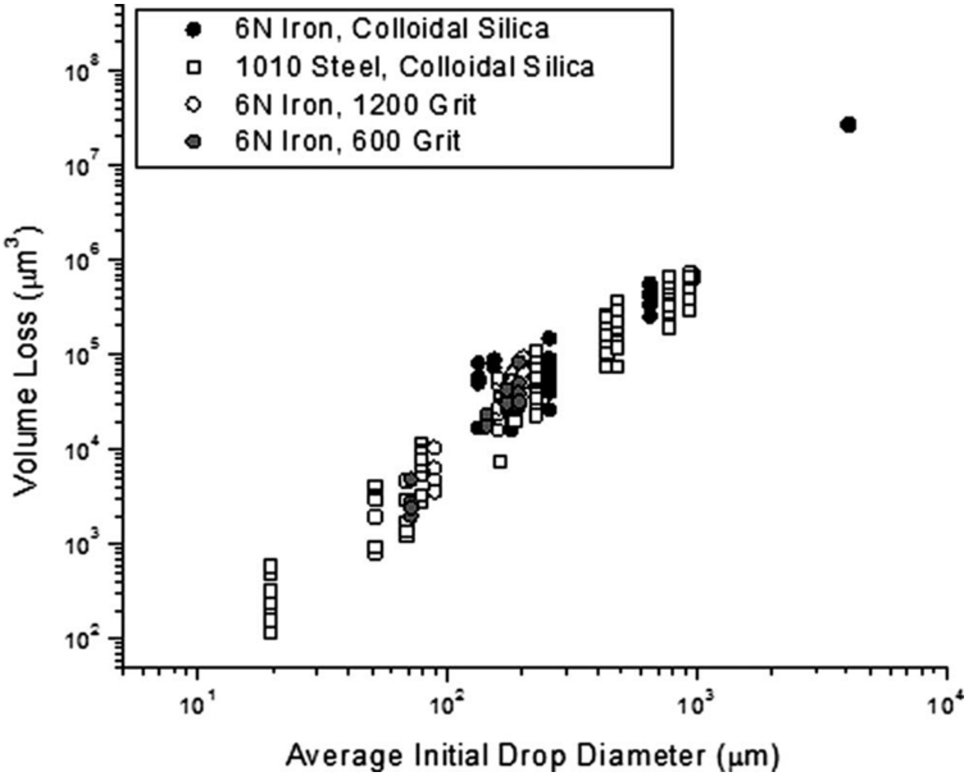

Figure 13. Volume loss versus initial drop diameter for drops under which detectable corrosion occurred.

2.2.1.3 MgCl$_2$-induced corrosion of steel

Isohumidity exposures of MgCl$_2$ on steel indicated that sustained corrosion occurred down to at least 11% RH while attack became more severe with increasing RH and time. Figure 14 shows a series of surface profiles and optical micrographs of the coupons after the 7 d exposure. Corrosion at 11% RH and 23% RH was generally confined to areas directly underneath a subset of the MgCl$_2$ deposits. At 33% RH, coupons exhibited radial spreading of shallow attack from circular pits under a fraction of the original droplets. At 53% RH, pitting was less confined to original droplet area and more uniform in nature (numerous pits covering more area). Attack at 75% and 90% RH was similar in appearance to that at 53%, but relatively deeper and sparser. These morphology trends held across all exposure durations.

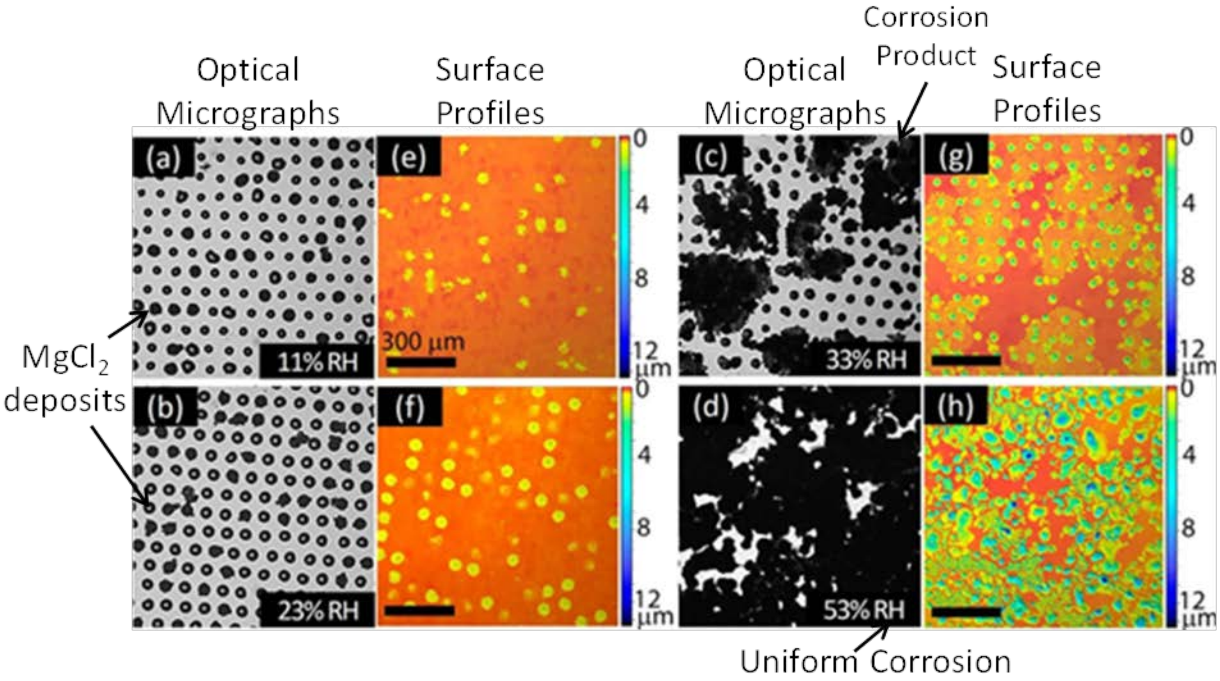

Figure 14. Optical micrographs of MgCl$_2$ -loaded coupons (8 µg · cm^{-2}) after 7 d of exposure at the humidity indicated and before rust removal (a-d). Measured surface profiles after rust removal for the same exposure period are also shown (e-h). All images are the same scale.

The average maximum pit depth, shown in Figure 15, generally increased monotonically with time and RH, with the exception of 75% and 90% RH exposures at longer times. These values were computed by averaging the maximum pit depth found in each of the scans for all samples exposed at the same relative humidity. A similar trend is seen in the overall volume loss, given in Figure 16 as the nominal corrosion depth. These values were calculated by dividing the volume loss for each scan by the area of the scan (field of view).

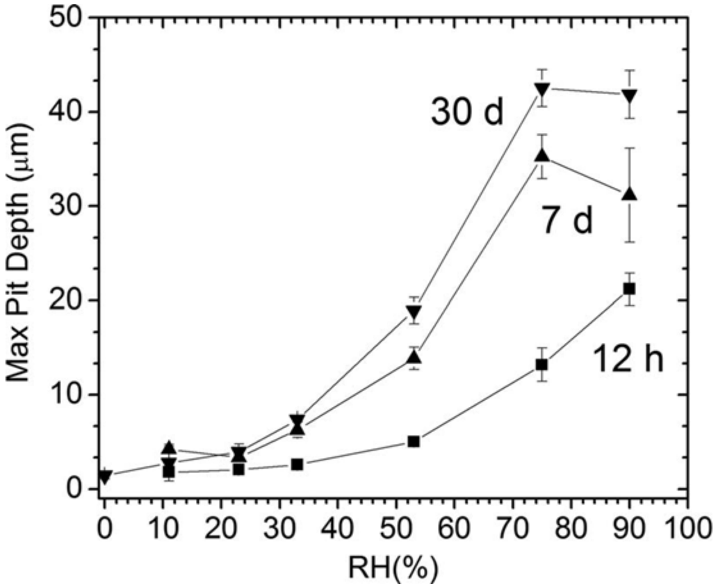

Figure 15. Average maximum pit depth vs. RH for MgCl2 -loaded steel coupons (8 μg cm^{-2}). The bars represent standard deviation.

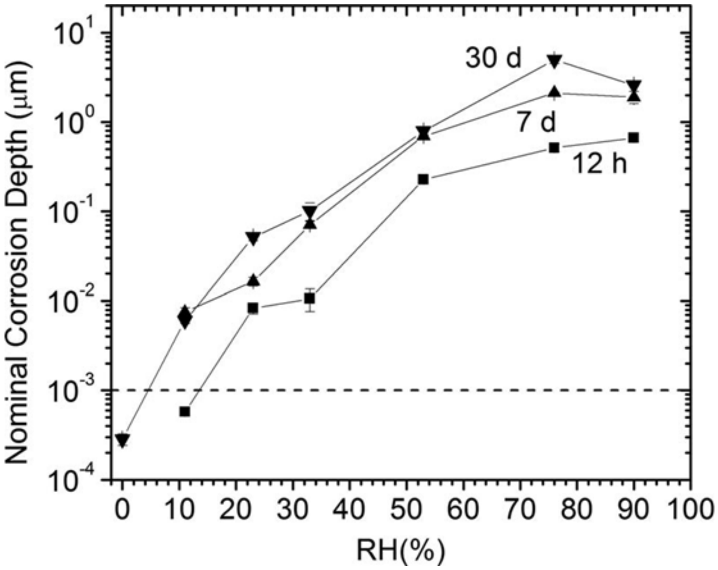

Figure 16. Average volume loss divided by scan area (nominal depth) vs. RH for MgCl2 -loaded steel coupons (8 μg · cm^{-2}). The bars represent standard deviation. The dashed line represents the upper bound of the 95% confidence interval of volume loss measured on clean areas outside the printed salt pattern.

2.2.1.4 Corrosion of steel in the presence of ASW under isohumidity conditions

Isohumidity exposure of steel coupons loaded with 16 μg/cm^2 ASW exhibited sustained corrosion detectable down to 33% RH. The observed trends in attack morphology also shared traits with those coupons loaded with $MgCl_2$ and NaCl. Figure 17 shows a series of surface profiles and optical micrographs of the ASW coupons after the 7 d exposure. Corrosion at 33% RH was shallow and confined to areas under the original deposits or was in the form of radial attack reminiscent of that which occurred under the $MgCl_2$ deposits at the same humidity level, Figure 14. Attack at 53% RH and above exhibited similar trends as those seen for the NaCl-loaded coupons in Section 2.2.1.1.

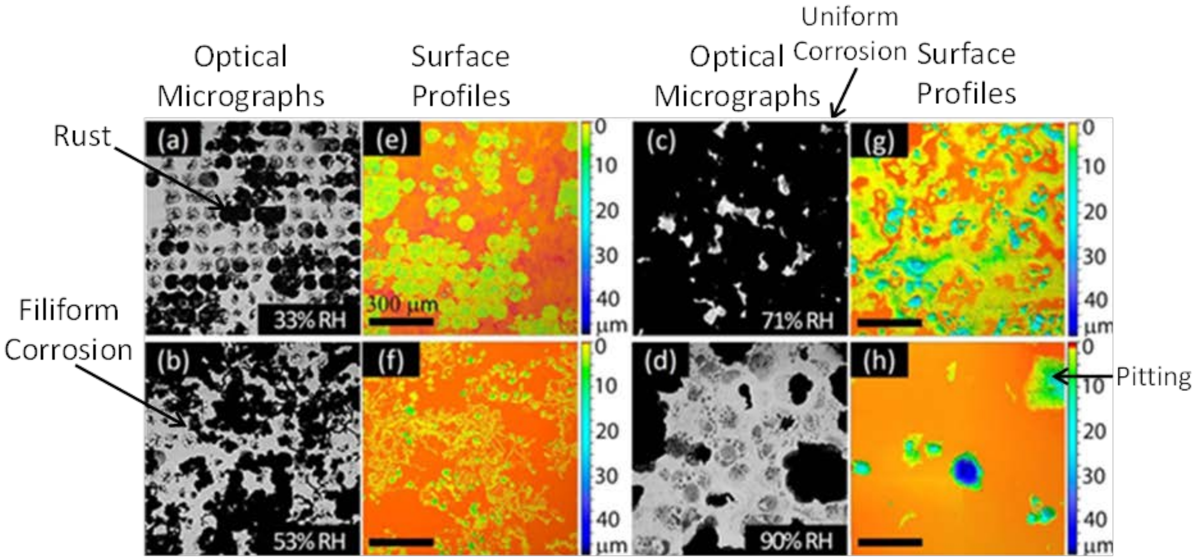

Figure 17. Optical micrographs of ASW-loaded coupons (16 μg · cm−2) after 7 d of exposure at the humidity indicated and before rust removal (a-d). Measured surface profiles after rust removal for the same exposure period are also shown (e-h). All images are the same scale.

As with $MgCl_2$ and NaCl, the ASW maximum pit depth generally increased monotonically with RH with a drop-off in slope occurring at >76% RH at longer times (Figure 18). A similar trend is seen in the overall volume loss, given in Figure 19 as the nominal corrosion depth.

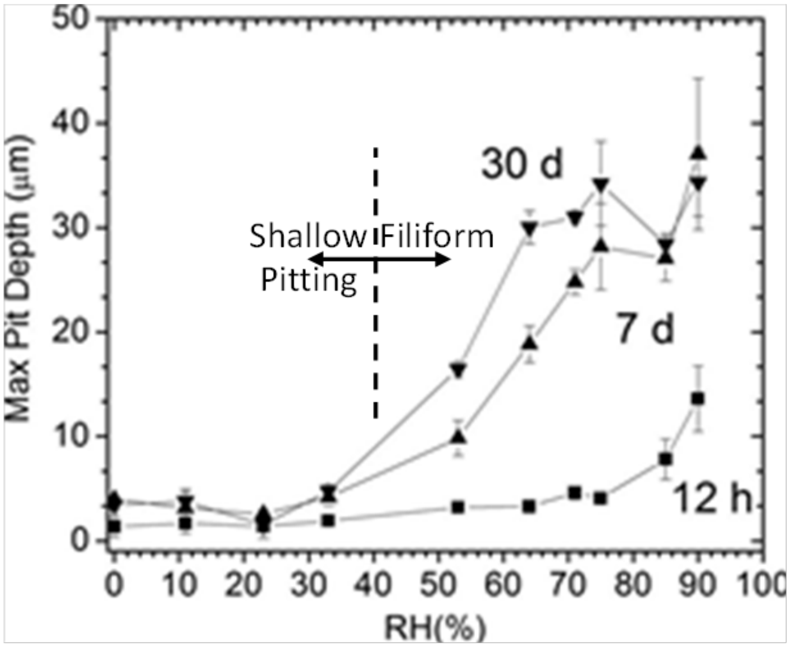

Figure 18. Average maximum pit depth vs. RH for ASW-loaded steel coupons (16 µg cm^{-2}). The bars represent standard deviation.

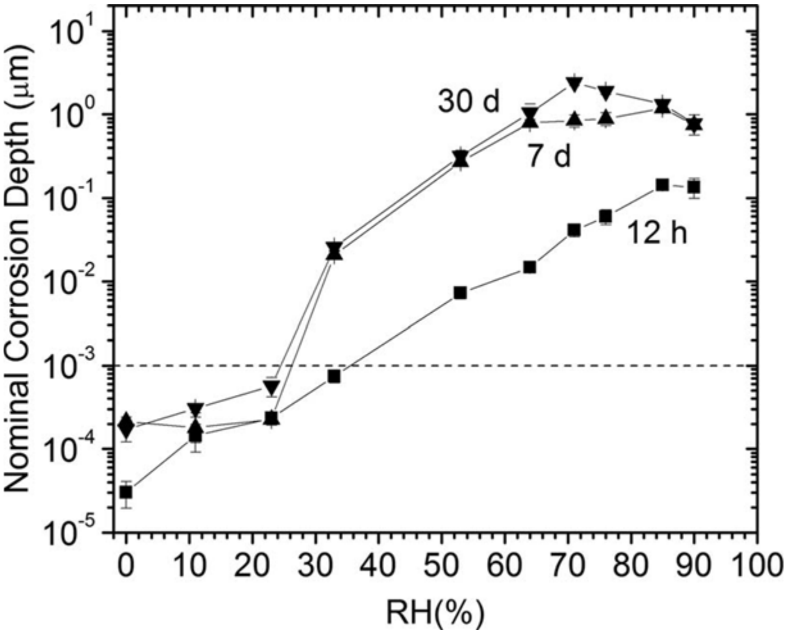

Figure 19. Average volume loss divided by scan area (nominal depth) vs. RH for ASW-loaded steel coupons (16 µg · cm^{-2}). The bars represent standard deviation. The dashed line represents the upper bound of the 95% confidence interval of volume loss measured on clean areas outside the printed salt pattern.

Distinct differences in attack morphology and surface state of the ASW contaminated steel are also apparent between 33% and 53% RH. An inflection of maximum pit depth as a function of RH occurs in this range, Figure 18. This sharp change reflects the transition from shallow pitting radiating from deposits at 33% RH to more discrete pits and filiform-type corrosion at 53%. These trends are similar to those reported for NaCl alone.

2.2.1.5 Effect of RH on corrosion response

The results presented here show that the deliquescence point of NaCl (roughly 76% RH) does not represent a critical RH threshold below which corrosion cannot initiate nor be sustained at a considerable rate for mild steel. To illustrate this, the 30 day volume loss data presented in Figure 9, Figure 16, and Figure 19 were converted to per annum penetration rates and compared to the ISO 9223 corrosivity categories for mild steel in Figure 20.

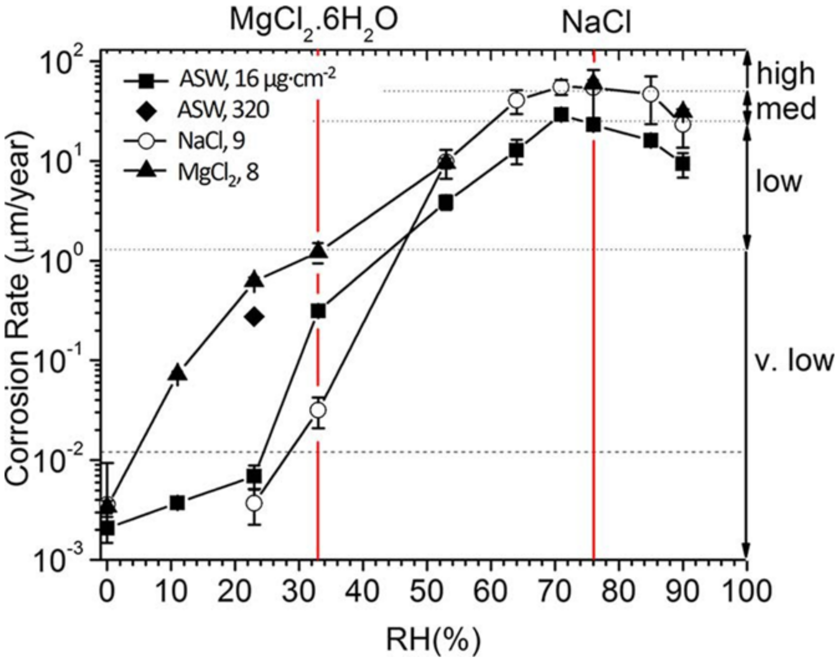

Figure 20. 30 d volume loss data from all isohumidity exposures normalized to a per annum corrosion rate and compared to the DRH of NaCl (76%) and $MgCl2.6H_2O$ (33%) along with the ISO 9223 atmospheric corrosivity classifications for steel. The loading density of salt associated with each of these exposures is given in the legend. The lowest dashed line represents the upper bound of the 95% confidence interval of volume loss measured on clean areas outside the printed salt pattern. The bars represent standard deviation.

The minimum RH at which sustained corrosion was detectable under NaCl deposits was 33% RH in these experiments, regardless of the initial state of the deposits, i.e., drops or crystals, (Figure 8). This finding is not unique in the sense that mild steel has been reported to corrode in the presence of NaCl below its DRH (76%) in both the case of drying of droplets and by initiation under crystalline deposits of this salt down to at least 50% RH. Our findings, however, lower the observed threshold for initiation and sustainment by 20% RH since corrosion was observed at relative humidities as low as 33% RH.

From examining Figure 20, it is clear that, although corrosion loss was detectable at 33% RH on NaCl printed samples, the rate of corrosion was negligible at 0.03 µm/year. At ≥53% RH, however, corrosion rates averaged over 300 to 2500 times higher (10 to 75 µm/year). In fact, the corrosion rate at the DRH was comparable to that at 64% RH. It is also important to point out that no significant difference in volume loss, and hence corrosion rate, at 30 d was observed between the crystal and the drop samples.

The minimum RH at which sustained corrosion was detectable under ASW deposits was 23%, but some of the results suggest that corrosion may be sustained at even lower humidity levels. The fact that a higher salt loading density (314 $\mu g \cdot cm^{-2}$) was required to detect corrosion down to this level, as opposed to the lower loading density (16 $\mu g \cdot cm^{-2}$) where the minimum was 33% RH, indicates that corrosion rate is dependent on the loading level and detection limits of the examination methodology. This result is reasonable given the comparatively minute amount of electrolyte available at these low humidity levels. If the presence of Mg-Cl rich electrolyte is what is largely enabling corrosion at these low levels, then the results for the $MgCl_2$ experiments, where this electrolyte is in relative excess, support this and suggest that corrosion is possible down to 11% RH, and likely even lower.

2.2.2 *Corrosion currents under isostatic and cyclic RH conditions*

2.2.2.1 Corrosion currents under isostatic RH conditions

In a first set of experiments, exposures were performed by increasing the RH from 50% to 90% followed by lowering the RH back to 50% in 5% RH increments. Each step was held for 2.5 hours. The cumulative charge passed at each RH values is shown in Figure 21a.

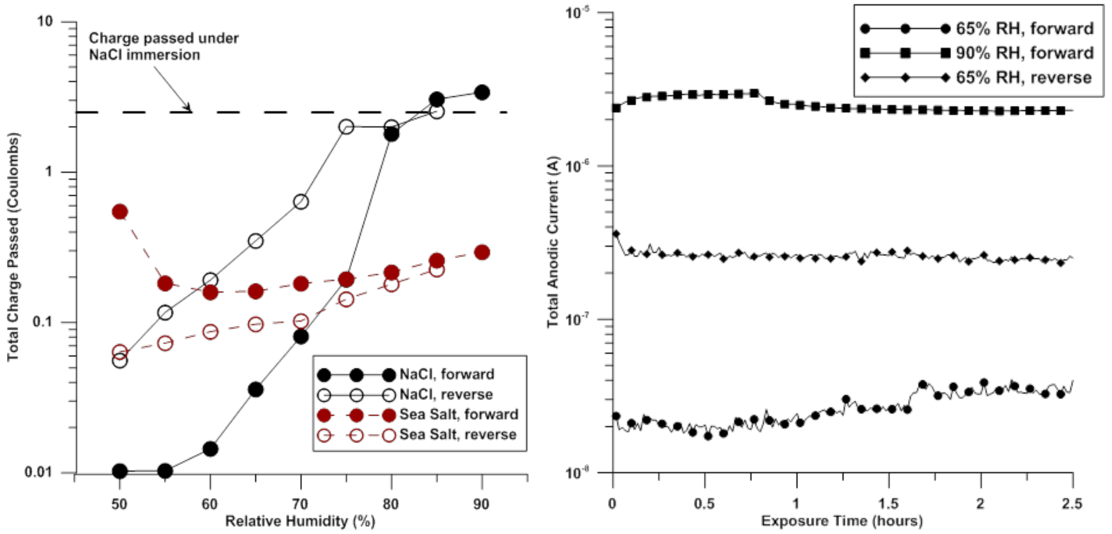

(a) (b)

Figure 21. (a) Total charge passed at various values of RH under a 2.7 mg deposit of NaCl or Sea Salt. Each RH values was held for 2.5 hours. Open circles represent stepping from higher RH values down. (b) Total anodic current passed under a NaCl deposit at select values of RH during the stepped RH experiment.

Under a NaCl deposit, corrosion begins at values of RH as low as 60% RH. Above the DRH of NaCl (76% RH), the total charge passed increases by a factor of 10 followed by a more modest increase at high RH values. As RH increases above the deliquescence point, values in corrosion rate increase as a result of increasing oxygen activity with decreasing chloride concentration. Interestingly, as the RH stepped from higher to lower values, the total charge passed is a factor of 10 higher than what was passed at the equivalent RH prior to wetting.

As was shown previously using an Au electrode, a surface remains wet below the DRH for a finite time as a result of efflorescence. Thus, corrosion processes continue below the DRH as a result of the presence of water. The decrease in the total charge passed cannot be a function of chloride concentration since below the DRH, a saturated solution exists. Therefore, the decreasing corrosion rate is likely the result of a shrinking water volume. As the droplet dries, it covers less of the corroding substrate. Examination of the current passed during select RH steps (Figure 21b) indicates that this drying rate would be slow (i.e. there is very little change in the total current at 65% RH during the downward stepping RH levels). Also note that above the DRH, the total charge passed is in the range of that which observed in a bulk 3.5w% NaCl solution.

The total charge passed when sea salt is deposited on the MEA is not a strong function of RH as is observed for the MEA under a NaCl deposit. Sea Salt contains $MgCl_2$ and, to a lesser extent, $CaCl_2$. The DRH for these two salts is 33% and 12% respectively. Thus, at 50% RH, the surface of the MEA remains wet compared with the relatively dry surface of the MEA under the NaCl deposit (Figure 22). Contrary to results under NaCl, stepping the RH down from 90% results in lower total charge passed compared with the equivalent RH values on the forward scan.

Interestingly, there is not a large increase in total charge passed as the MEA increase above 76% RH under sea salt deposits. Finally, the total charge passed under sea salt deposits is a factor of 10 lower than that observed for steel under NaCl at high humidity values. This is likely the result of the pH of seawater (in the range of 8.0 to 8.4) relative to that of NaCl (<7). Higher pH promotes passivation of the steel and thus slows corrosion. This finding is consistent with observations of corrosion product on the MEA surfaces after testing (Figure 22).

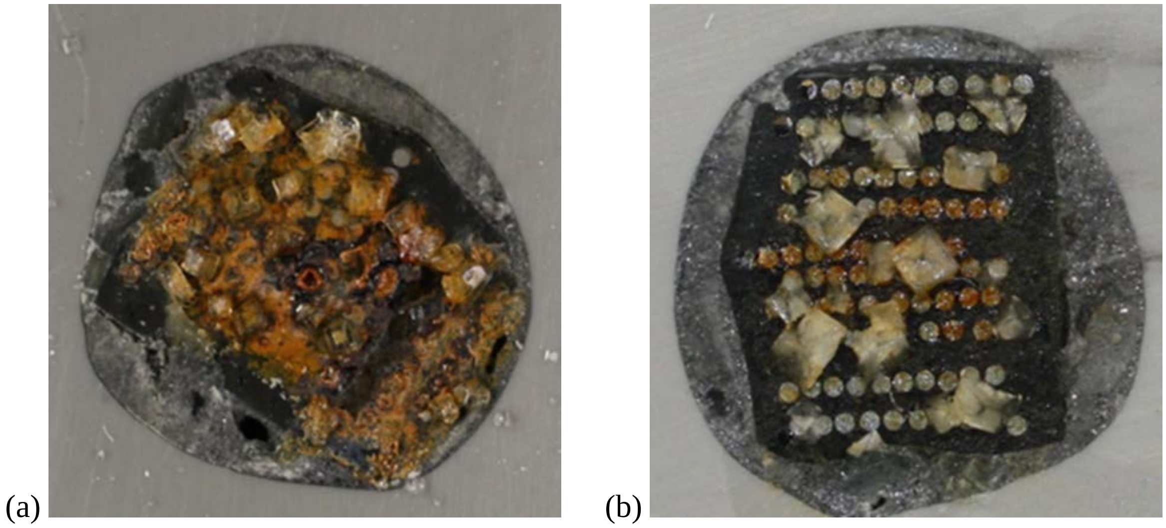

Figure 22. Images taken of the MEA electrode after completion of the exposure (a) under a NaCl deposit and (b) under a sea salt deposit. The shiny spots in (b) are reflections of lighting from condensed water in the partially deliquesced salt. The large solid crystals in (b) are NaCl.

2.2.2.2 Effect of drying conditions on corrosion

The MEA electrode was exposed to controlled RH steps. Initially, conditions were held at 90% RH at 30ºC for 2.5 hours. The RH was then stepped down to an RH < DRH for an additional 8 hours. The total anodic current as a function of time is shown in Figure 23a for RH of 70% and 50%. A peak can be seen when stepping from 90% RH to lower values of humidity while under a NaCl deposit. Interestingly, this peak is not observed for the MEA exposed to sea salt. Thus, it is likely that the peak is associated with passing through the deliquescence point of the surface deposit. This is consistent with Figure 21 where a peak is observed when the RH is stepped from 75% to 80% RH and again when stepping down between 80% and 75%. The width of this peak decreases when stepping to progressively lower RH values which suggests that for progressively larger decreases in the RH below the deliquescence point, the MEA surface dries faster. The time for the current to pass below a corrosion current density of 10^{-5} A/cm^2 as a function of the low RH value (shown in Figure 23b) is in agreement with this finding.

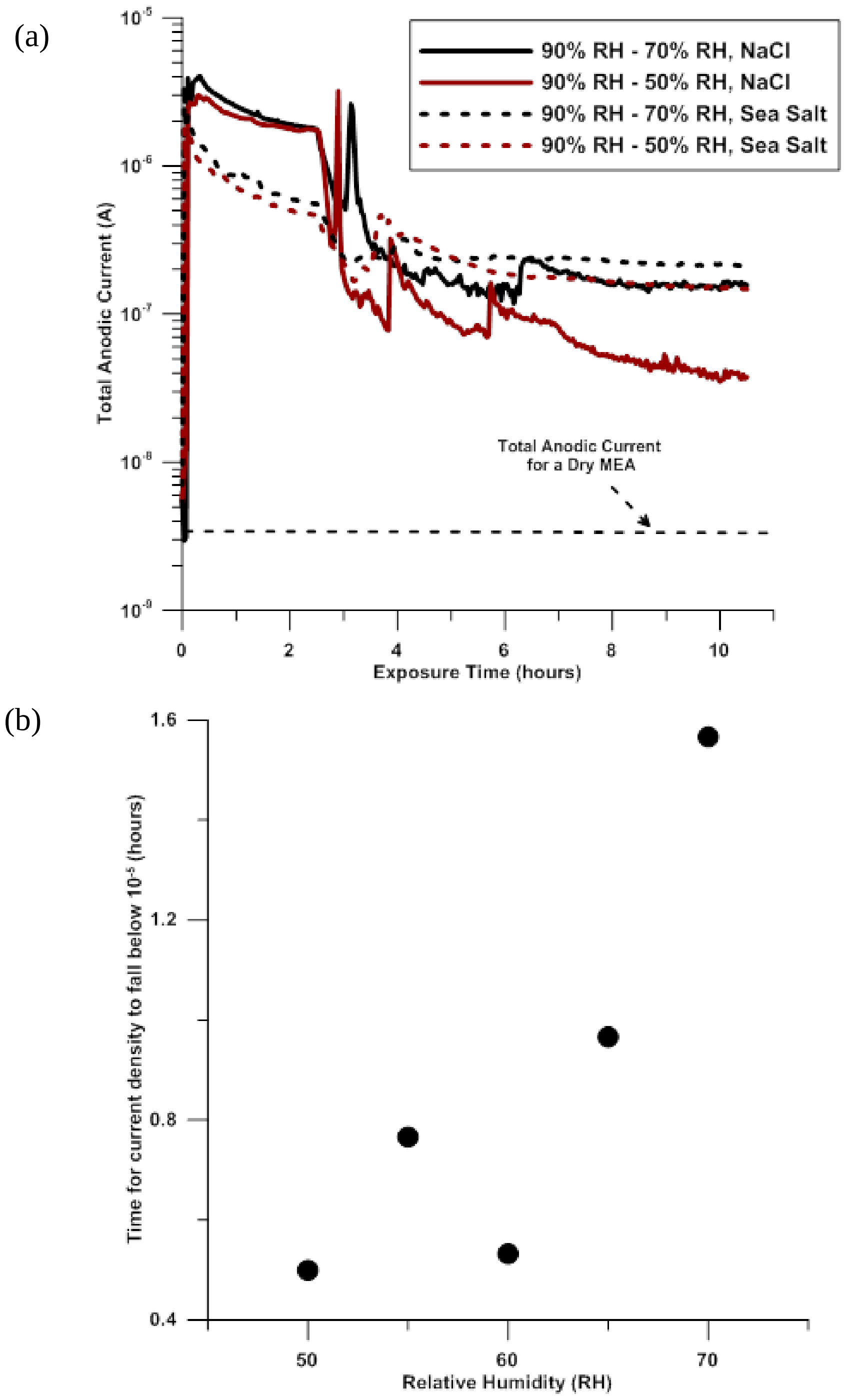

Figure 23. (a) Total anodic charge passed when RH is stepped from 90% RH to 70% or 50% for the MEA electrode exposed to either a NaCl or sea salt deposit. (b) Time required for the corrosion current density to fall below 10^{-5} A/cm^2. Cumulative charge during 8 hours of exposure to the indicated RH values after exposure to the 90% RH for 2.5 hours.

Examination of Figure 23a reveals that as the RH is stepped to 50% RH, the corrosion current is decreasing slowly with time for the MEA exposed to NaCl. In contrast, the electrode exposed to sea salt shows no decrease in corrosion current over time after the relative humidity step. This observation is consistent with wetness sensor data where surfaces exposed to coastal environments in Australia can remain wet to RH values less than 20% and suggests that corrosion can occur for sustained times at RH values well below the DRH.

Even at a low RH value of 50%, the corrosion current is well above the corrosion current observed for a dry MEA electrode.

The total charge passed at RH values below the DRH after 2.5 hours of wetting at 90% RH is shown in Figure 24 for NaCl and sea salt covered surfaces. Note that despite the higher corrosion current under NaCl deposits at RH greater than DRH, more charge is passed as the RH is stepped to values less than the DRH for sea salt covered surfaces. This is in agreement with the fact that the surface remains wet and that corrosion rate of steel under sea salt is not a strong function of RH (Figure 24) because at least partial wetting occurs at very low RH values for surfaces under sea salt. It should also be noted that the differences observed for the charge passed at a given RH values should increase with time as the corrosion current slowly decays for a NaCl coated sample relative to that of the sea salt-coated sample.

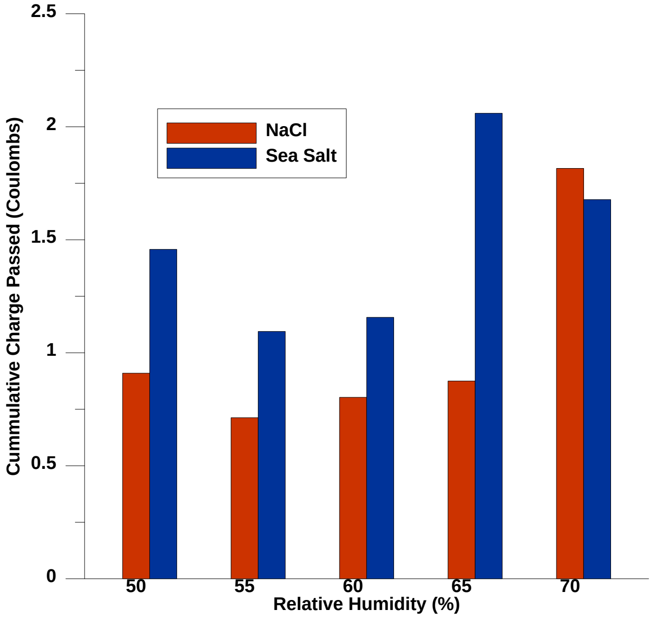

Figure 24. Total charge passed during an 8 hour exposure period at the indicated RH values after a 2.5 hour hold at 90% RH.

2.2.2.3 Effect of cyclic RH on corrosion

To this point, we have described the corrosion of steel under isostatic or stepped RH conditions. Under actual environmental conditions, however, RH typically varies in cyclic manner. In this section, testing under cyclic RH conditions is described.

In this test, a single RH cycle included a 3 hour wetting period at 30°C followed by a 5 hour dry off period at 40°C. The temperature was raised to 40°C during the dry off period in order to achieve lower RH values. The total anodic current passed during a 24 exposure is compared with the chamber RH in Figure 25a. Note that the current reached values similar to those observed under iso-static RH conditions. Also note that the peaks associated with passing through the surface DRH point can still be seen. As expected, the corrosion current increases above the DRH for NaCl. While the corrosion current increases with RH, there is a lag between a decrease in RH and a decrease in anodic current. Corrosion is observed at values of RH reaching well below 40%. Unlike under the iso-static RH conditions, the current density decreased to levels observed for a dry surface (5×10^{-9} A). This occurred since the RH value dropped to very low values reducing drying time significantly.

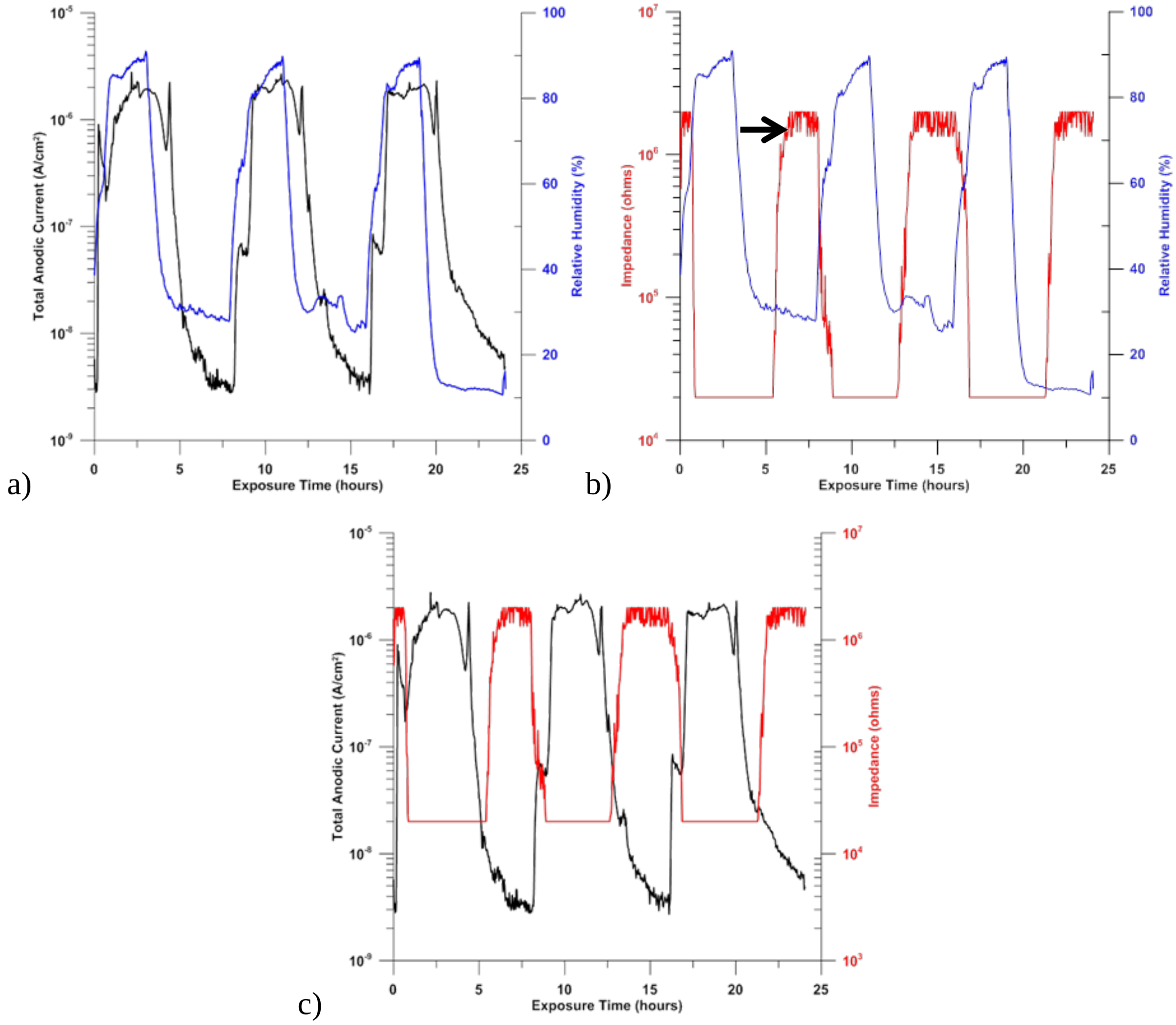

Figure 25. (a) Total anodic current and RH plotted vs. time. (b) Impedance values measured from the TOW sensor and RH plotted vs. time. (c) Total anodic current and impedance plotted vs. time. Each cycle consists of 3 hours at high RH and 30°C followed by 5 hours at low RH and 40°C.

A comparison between the anodic current, RH, and impedance values from the TOW sensor (Figure 25a and b) reveals a lag between the RH and the surface wetting. Low values of impedance indicate that electrolyte is bridging the gap between the wetness sensor electrodes. Examination of Figure 25c reveals that corrosion is occurring only when the TOW sensor indicates the surface is wet and hysteresis in drying is a result of efflorescence effects as described earlier.

A variable of considerable interest within this program was the relationship between TOW and corrosion. While we have shown that corrosion occurs under conditions where a surface electrolyte exists, a question remains as to how the total TOW relates to corrosion. A set of experiments were run with varying durations of TOW over a 24 hour period. The results (shown in Figure 26a) depict the total anodic current for three different cycling conditions: 24 hours at high RH, 1 hour at high humidity followed by 1 hour dry repeated for 12 cycles, and 3 hours at high RH followed by 3 hours dry for 4 cycles. If it is assumed that total TOW governs the corrosion rate, then it must hold that for TOW values that are a fraction of the 24 hour high RH conditions, the total charge passed during those cyclic exposures would be an equal fraction of the total charge passed during the 24 hour high RH test. Data in Figure 26b indicate that this is not the case. The line drawn in the figure suggests the predicted value if total TOW governed the corrosion loss. Note that for TOW values of 12 hours, the data lie well below the predicted line. Further, the total charge passed during the two different cycles where the TOW was 12 hours are not equivalent.

The discrepancy between the predicted ideal behavior and that observed can be explained based on the data shown in Figure 26a. The initial slope of the total anodic current is similar for the three cycles. Note that while the corrosion occurs (high total anodic currents) are at the expected intervals, the magnitude of the corrosion current is a function of exposure time under high RH conditions. For longer periods of high RH, it may be that TOW governs corrosion rate. This will be the subject of longer term testing. The effect of long term exposures on drying will also be the subject of continued study.

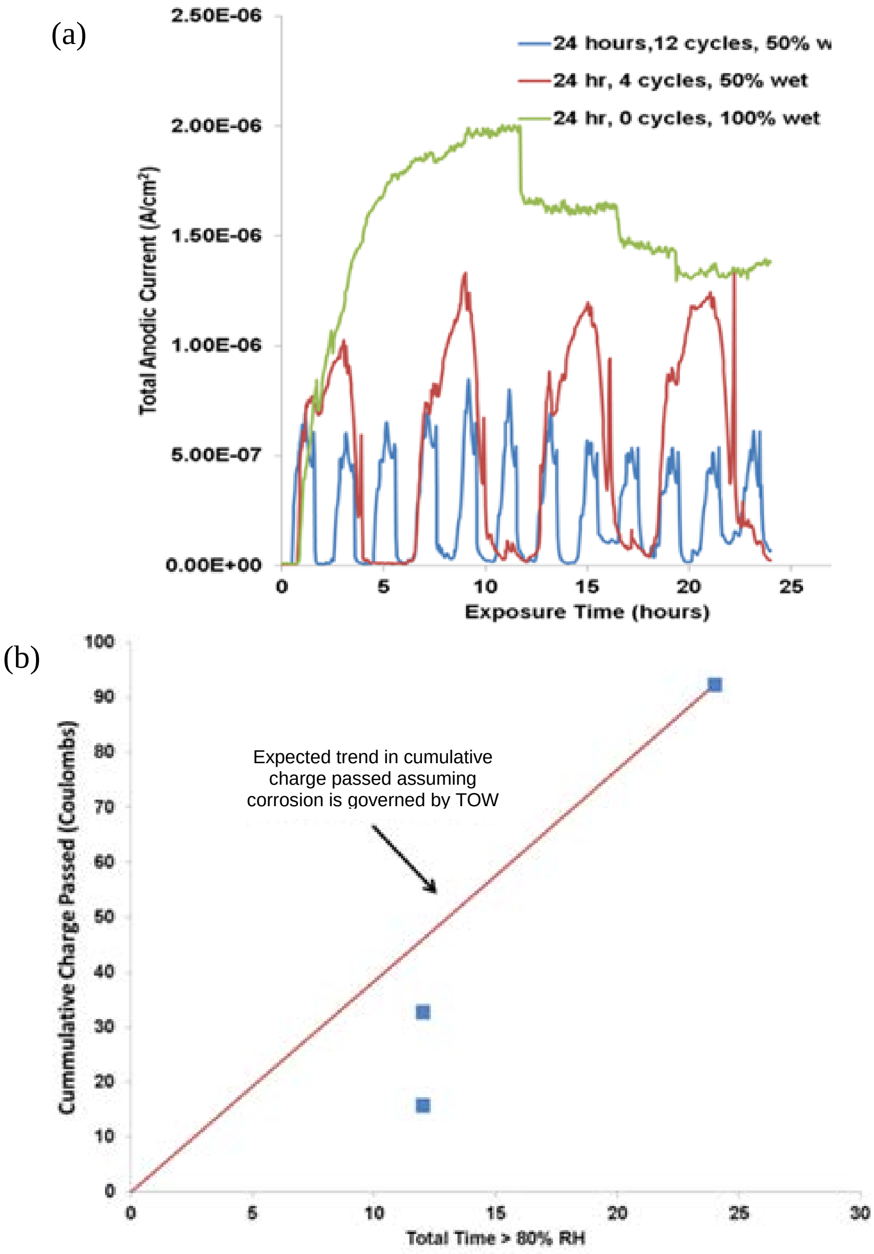

Figure 26. (a) Total anodic current as a function of exposure time for three different exposure cycles. (b) Total anodic charge passed as a function of time of wetness.

CHAPTER 3
EFFECT OF RH ON CREVICE AND GALVANIC CORROSION

During accelerated exposure testing, testing of complex geometries are often ignored despite the evidence of enhanced corrosion attack in occluded regions and at galvanic sites. Based on the results demonstrated in Chapter 2, it is clear that significant corrosion can occur at RH values below DRH for bare, single component coupons. Very limited information exists regarding the effect of RH on crevice and galvanic couples at this RH values under static or cyclic conditions. In this chapter, multielectreode array experiments are described that were designed to understand the effect of RH on crevice and galvanic corrosion under atmospheric conditions.

3.1 Materials and Methods

3.1.1 *Effect of cyclic RH on corrosion in a crevice*

The effect of cyclic RH on corrosion in a crevice was investigated using a multi-electrode array (MEA). The 100 electrode array was made out of 1018 carbon steel wires embedded in epoxy. In order to mimic the presence of a tight crevice on the surface of the MEA probe, a glass cover slip was placed over 50 electrodes and fastened to the electrode body using electroplaters tape. This allowed the measurement of currents associated with corrosion both within and outside of the crevice region.

After the application of 2.7 mg of NaCl, the MEA was exposed to cyclic RH conditions. The exposure consisted of 3 hours at high RH under wet bottom RH conditions followed by 5 hours of drying. This cycle was repeated for 96 hours. Throughout the RH cycles, the anodic and cathodic currents passed through the individual electrodes were measured using a Scribner MMA system. Cumulative anodic and cathodic currents were then calculated from the measured current values.

3.1.2 *Effect of cyclic RH on galvanic corrosion*

3.1.2.1 Multielectrode arrays

The experimental techniques described in this section were used to examine galvanic behavior of aluminum/copper/steel multi-electrode array in a variety of environments, including relative humidity cycles and existing accelerated corrosion tests. Currents passed by the array were measured throughout the exposure and subsequently analyzed.

For the galvanic studies, two MEA probes were used with 100 electrodes, each measuring 250 µm in diameter. One MEA consisted of one hundred 1018 carbon steel wires arranged in a 10 by 10 grid. For the second MEA, AA2024-T0 wire was used for 80 of the pins. The T0 anneal allowed the wire to be drawn to a suitable diameter. Four copper wires were included to replicate the effect of copper-rich intermetallic particles found in heat-treated aluminum and known to strongly influence the corrosion of the matrix material. Sixteen 1018 carbon steel wires were used to simulate a steel fastener in an aluminum matrix. The layout of these electrodes is shown in Figure 27.

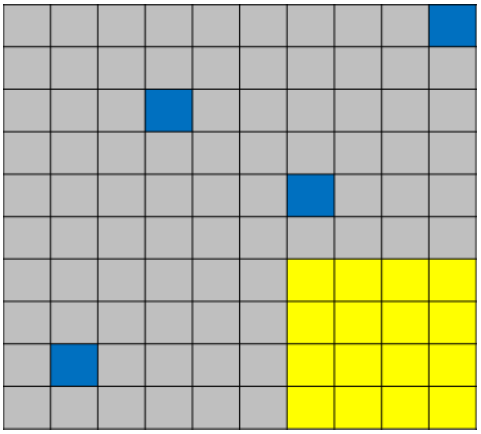

Figure 27. Diagram of the aluminum/steel array used in this study. Aluminum pins are shown in grey, copper in blue, and steel in yellow. Only 50 electrodes were used at a time. To mimic an all-aluminum surface, the bottom five rows were masked. To explore galvanic interactions between steel, aluminum and copper, the top five rows were masked.

The current on each electrode was measured and recorded using a Scribner MMA multi-electrode array system. These currents were analyzed independently or summed. These two MEAs were used to create three MEA arrays. By masking the top five rows of the aluminum and steel electrode pictured in Figure 27, an array of 50 aluminum, copper, and steel electrodes was exposed. This arrangement was used to investigate galvanic interactions between the dissimilar metals. By masking the bottom five rows, only aluminum and copper electrodes were exposed. This configuration was used to examine aluminum behavior. The all-steel array was used to examine the behavior of the steel without galvanic coupling.

3.1.2.2 Relative humidity exposures

The environment for the relative humidity exposure was controlled by a Thunder Scientific relative humidity chamber. Chamber relative humidity was verified using a calibrated humidity probe. Relative humidity was ramped from 40% to 90% in 5% steps. After reaching 90% RH and holding for 2.5 hrs, the relative humidity was stepped down in 5% steps. Each step lasted 2.5 hours. This cycle is illustrated in Figure 28. The temperature was held constant at 30°C. The MEA was supported face-down in this environment during testing. Immediately prior to introduction to the humidity chamber, NaCl was placed on the surface of the electrodes at a loading density of approximately 10 mg/cm^2.

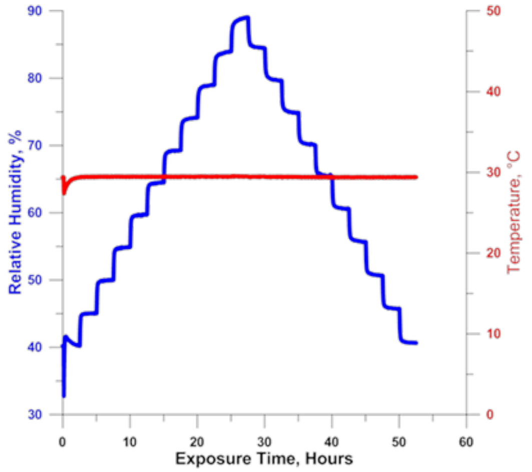

Figure 28. Relative humidity and temperature conditions for exposure of the MEA.

3.1.2.3 Accelerated testing

The aluminum/steel multi-electrode array was also introduced to three common accelerated tests: ASTM B117, GM9540, and ASTM G85A5. Test profiles and solution chemistries are given below in Figure 29. Tests were performed in an AutoTech (Model CCT-NC-40) chamber. For these tests, the top five rows of the aluminum/steel/copper MEA were masked to retain conformity with the humidity ramp testing.

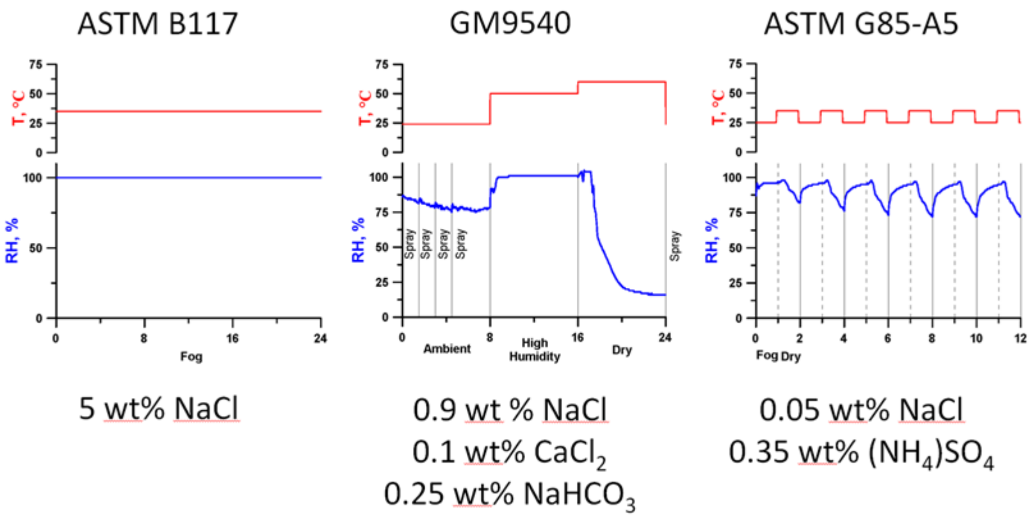

Figure 29. Test profiles for ASTM B117 (Left), GM9540P (Center), and ASTM G85 A5 (Right).

3.2 Results and Discussion

3.2.1 *Effect of cyclic RH on corrosion in a crevice*

The total anodic and cathodic currents for the electrodes outside of the crevice and inside of the crevice are shown in Figure 30a and b respectively. Initially, corrosion occurred on both the inside and outside of the crevice. Interestingly corrosion current spikes were higher inside of the crevice compared with outside of it but in both locations, corrosion current cycled with RH. After 30 hours, however, a distinct shift to higher anodic and cathodic currents can be seen within the crevice. While the cyclic nature of the corrosion current continued, the variation in current with each incremental cycle diminished, resulting in continuous corrosion within the crevice. It is observed that similar to the anodic current fluctuations, cathodic current fluctuations within the crevice diminish.

Outside of the crevice, on the other hand, the anodic current decreased significantly while the cathodic current increased. This suggests a coupling between electrodes outside of the crevice with those inside of the crevice (i.e. cathodic nature of the electrodes outside of the crevice influence corrosion within the crevice). Close examination of the data reveals that while cathodic current inside of the crevice can sustain corrosion even under drying conditions, fluctuations in the cathodic currents outside of the crevice have a strong influence on the anodic currents in the crevice (Figure 30c and d).

Electrode maps from the MEA probe are shown at 43.5 hours and 49 hours in Figure 30e and 30f respectively. In the figure, blue squares represent locations of cathodic currents while red squares indicate locations of anodic current (corrosion). The top five rows in the figures represent electrodes outside of the crevice while the bottom five rows represent electrodes inside of the crevice. The 43.5 hours occurs just after stepping the RH to lower values while 49 hours occurs just after switching the RH to wet bottom RH control.

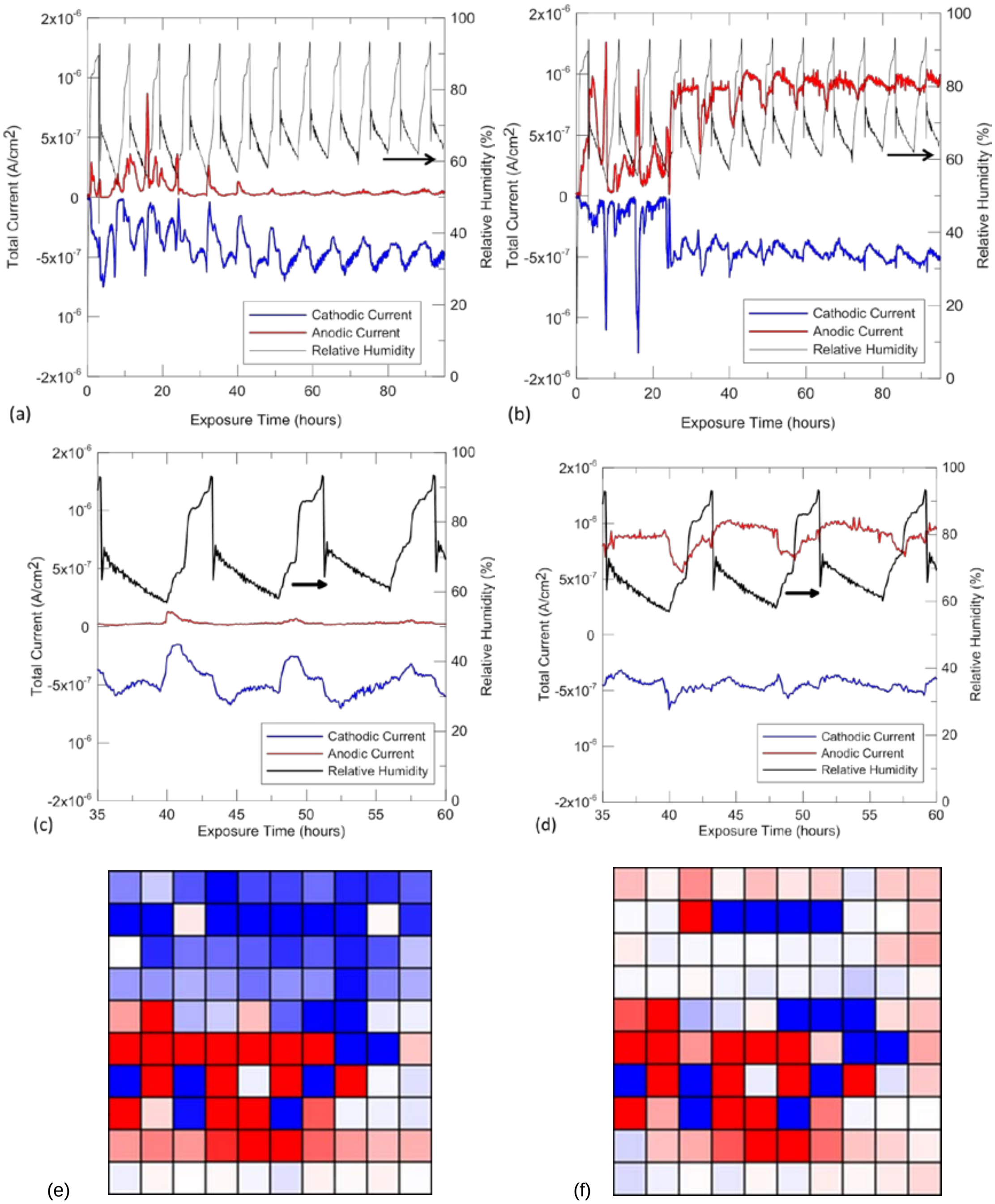

Figure 30. Anodic and cathodic currents and RH for MEA electrodes (a) outside of the crevice and (b) inside of the crevice. Anodic and cathodic currents and RH for MEA electrodes (c) outside of the crevice and (d) inside of the crevice looking at the time between 35 and 60 hours. Screen capture of the MEA current map at (e) 43.5 hours and (f) at 49 hours. Red boxes and curves represent anodic currents while blue boxes and curves represent cathodic currents.

It can be seen in Figure 30e that the electrodes outside of the crevice are predominantly cathodic at the end of the high RH cycle. As the RH is switched to higher values (Figure 30f), a small increase in anodic current occurs outside of the crevice. This increase in current reverses as the surface wets, coupling the outside and inside of the crevice region and driving the outside in the cathodic direction since stable anodes already exist inside of the crevice.

3.2.2 *Effect of cyclic RH on galvanic corrosion*

The effects of relative humidity on galvanic interactions between steel and aluminum are examined in this section. Given the prevalence of mixed metal assemblies within DoD systems, the behavior of these galvanic assemblies with relative humidity is important to understand. Testing under accelerated corrosion conditions should replicate the galvanic interaction seen in the exposure environment.

3.2.2.1 Validation of MEA under isohumidity exposures

Using the all-steel multi-electrode array (MEA), similar behavior to the steel static exposures described above was observed (compare Figure 20 with Figure 31). Corrosion increased with increasing humidity when humidities were below the DRH of the salt. Above the DRH, corrosion rate stabilized and even decreased. These findings demonstrated that trends observed using the MEA are similar to metal surfaces and thus provide confidence that the MEA can be used in these types of exposures as a surrogate surface.

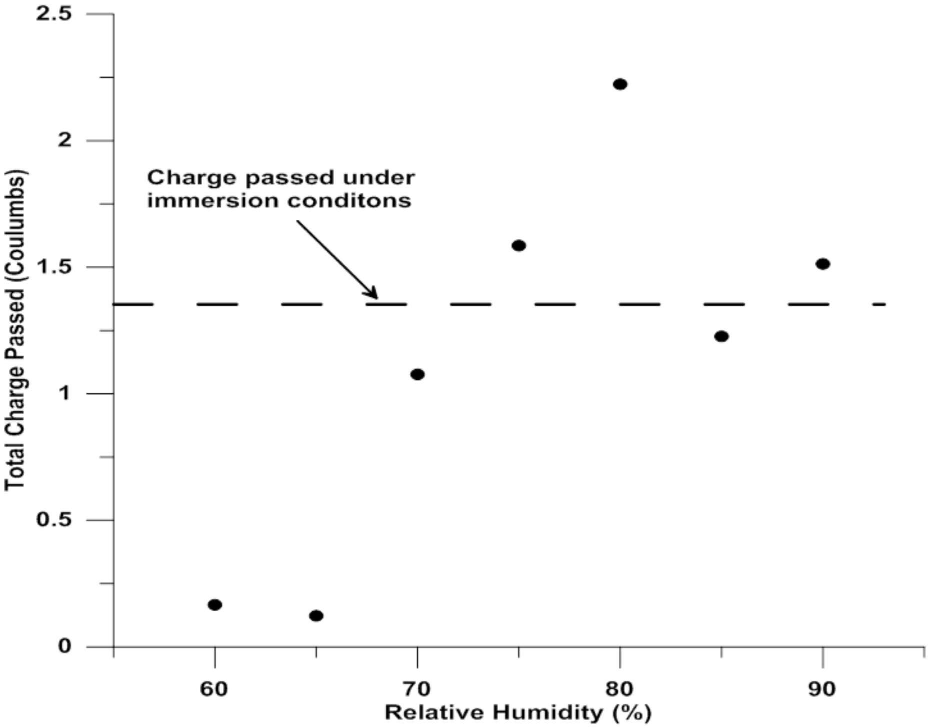

Figure 31. Total charge passed on a steel multi electrode array exposed to a series of iso-humidity conditions. Each humidity step was 2.5 hrs long.

3.2.2.2 Galvanic MEA in RH ramps

Interesting interactions between the steel and aluminum electrodes were observed when the top five rows of the aluminum/steel MEA were masked, leaving steel, aluminum, and copper electrodes exposed. Currents from electrodes of each material were analyzed to determine if they were anodic or cathodic, and anodic currents for each material were summed. Total anodic currents of the steel and of the uninhibited aluminum electrodes are shown in Figure 32a.

Bursts of anodic current are observed on both the aluminum and steel electrodes during the RH ramps in both directions (up and down). The steel is largely inactive during the period when the aluminum passes anodic current. As the aluminum becomes more anodic, the steel becomes cathodic. For the high-humidity portion of the ramp, the steel is entirely cathodic.

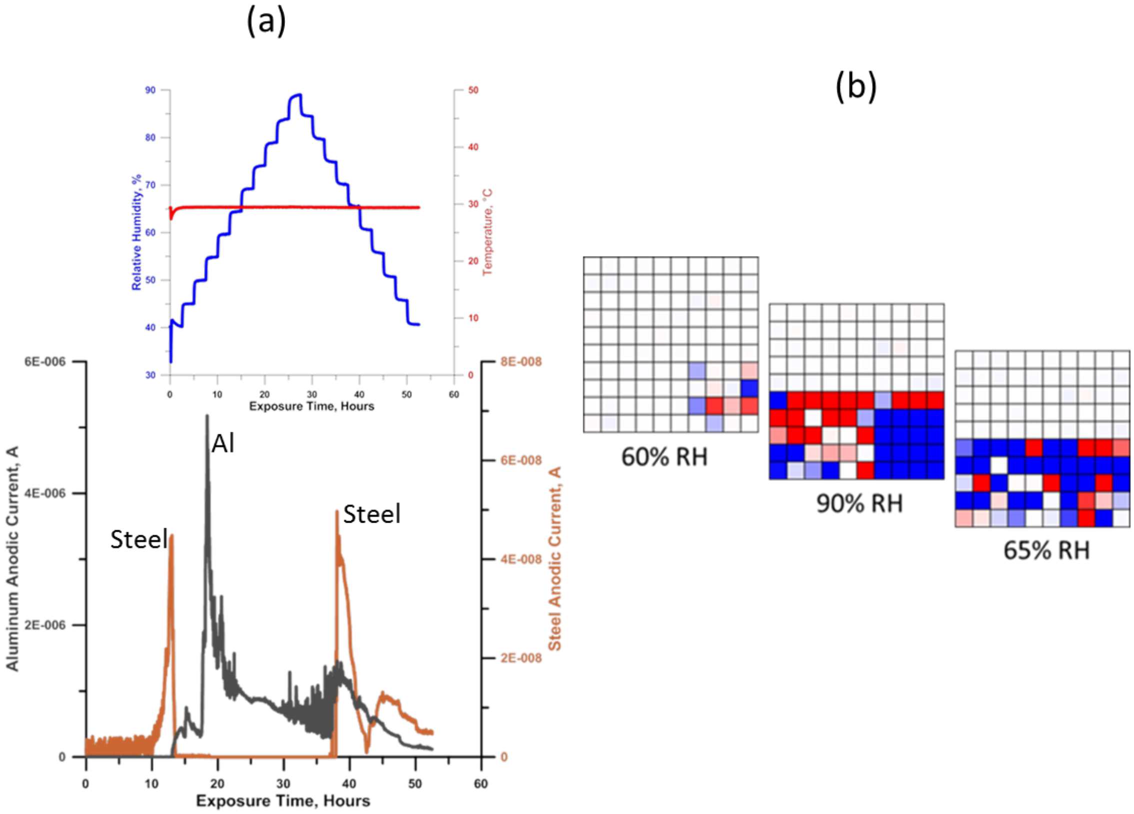

Figure 32. (a) Anodic currents of the steel and aluminum electrodes in the un-inhibited galvanic MEA. The RH ramp profile is also shown for reference (Figure 28). b) Diagrams of the multi-electrode array. Electrodes acting as anodes are red, and cathodes are shown in blue. The sixteen steel electrodes are in the lower right corner. The top 50 electrodes were masked.

Diagrams of the MEA (Figure 32b) demonstrate even more clearly that the steel electrodes act almost exclusively as cathodes during the period of highest anodic current on the aluminum electrodes. In these diagrams, electrodes acting as anodes are red, and cathodes are shown in blue. The steel electrodes, located in the lower right, include cathodic sites at lower humidities, but at the high humidities, all steel electrodes are cathodic.

The presence of steel anodes at low relative humidities indicates the lack of galvanic coupling between the steel and the aluminum. The galvanic interaction between the steel and aluminum is likely not strong at low relative humidities because there is not a continuous electrolyte layer across the surface to provide electrolytic conductivity between the two dissimilar metals. As the relative humidity increases, the volume of the solution on the surface also increases, covering a larger area on the electrode surface and thereby forming a conductive path between the steel and the aluminum. Without this electrolyte bridging, however, the steel electrodes may act independently from the aluminum electrodes, resulting in steel corrosion.

3.2.2.3 Accelerated testing

Testing of the MEA in the accelerated test chamber reveals complex galvanic behavior between the steel and aluminum similar to that observed during the RH ramps. Total currents (summing both the anodic and cathodic currents) for each metal are shown in Figure 33. Current passed on the copper electrode is small as there is only one copper electrode exposed in this configuration. As it is expected due to its relative nobility, the total current is cathodic for copper. Aluminum electrodes act primarily as anodes, and steel electrodes act primarily as cathodes.

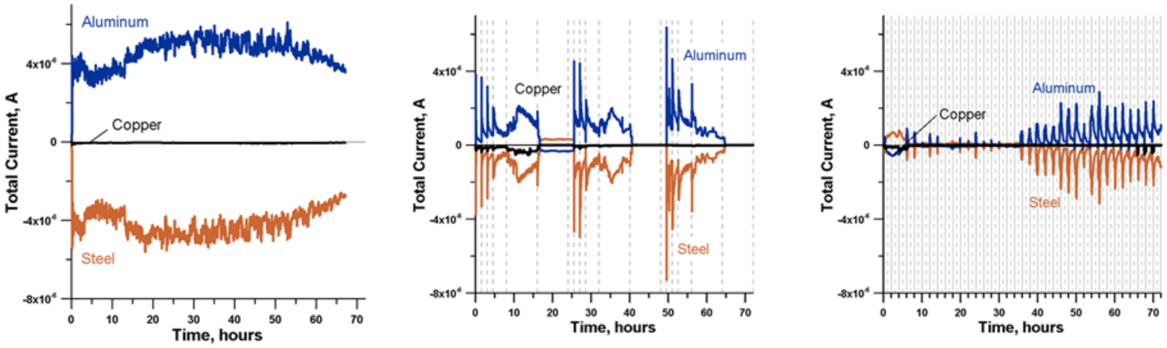

ASTM B117 GM 9540P ASTM G85-A5

Figure 33. Total currents for each metal in the accelerated test environments. The aluminum/copper/steel MEA was used with the top five rows masked.

Given that the steel is primarily cathodic, times when steel electrodes act as anodes are of particular interest. To examine these occurrences, the summed anodic currents on each electrode material were examined. As can be seen in Figure 34, the steel is cathodic (i.e. its anodic current is 0) for the entire duration of the ASTM B117 test, a steady-state salt fog test. The MEA diagrams confirm these results, showing the steel to be blue (cathodic) throughout the exposure. Given the high volume of fog produced during this test, it is reasonable to assume that a continuous, highly-conductive electrolyte film was present on the surface of the MEA during testing.

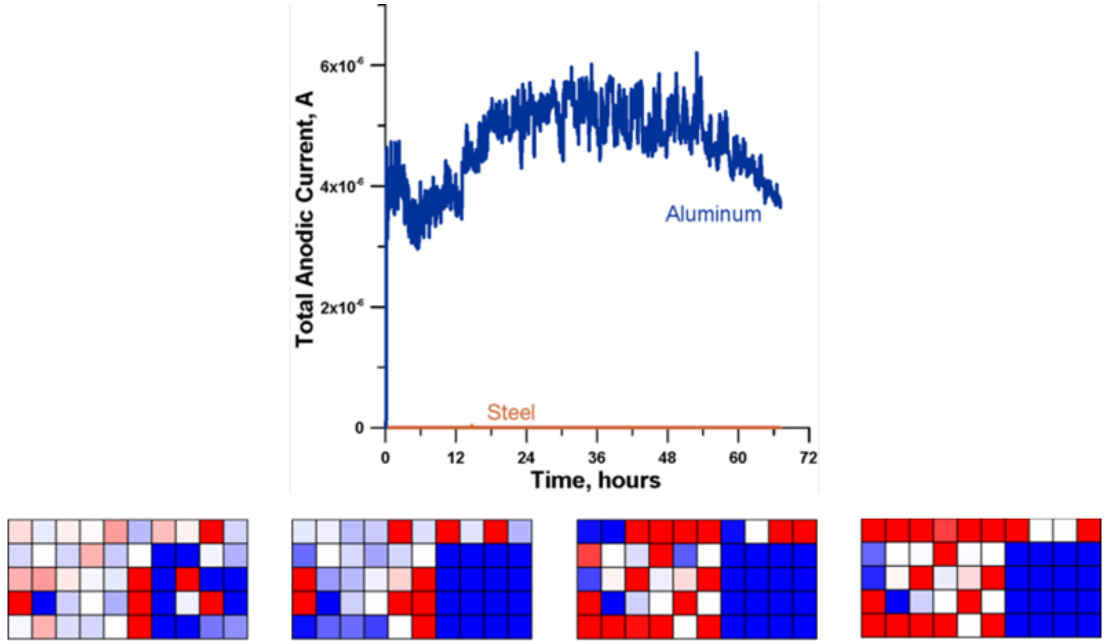

8 min 12 min 2.5 hr 40 hr

Figure 34. Results from an ASTM B117 exposure. Total anodic currents for aluminum and steel electrodes on the MEA (top). Diagram of the MEA (bottom). Anodes are shown in red, cathodes in blue. The sixteen steel electrodes are in the bottom right of the array.

Partial decoupling between the steel and aluminum is observed in the two cyclic tests: GM9540P and ASTM G85 A5 as can be seen in Figure 35. As observed in the relative humidity ramp exposures, current increases during transitions from wet to dry. While the overall steel current is cathodic, some anodic behavior is observed, particularly during transitions. Of particular interest are the peaks in steel current in the ASTM G85 A5 test. Close examination of the detailed chart shows that the increases in the steel current occur during the drying phase, not during fogging. This supports the idea that anodic currents are primarily found on steel when continuous electrolyte films are not present. The idea of a discontinuous film below DRH is consistent with observations in Figure 7. Above the DRH, localized corrosion sites are observed as a result of the large cathodic area under the continuous film. Below the DRH, many surface sites are activated with cathodic regions in the vicinity of each site. This is also consistent with the spike in anodic currents observed on steel electrodes when passing through the DRH.

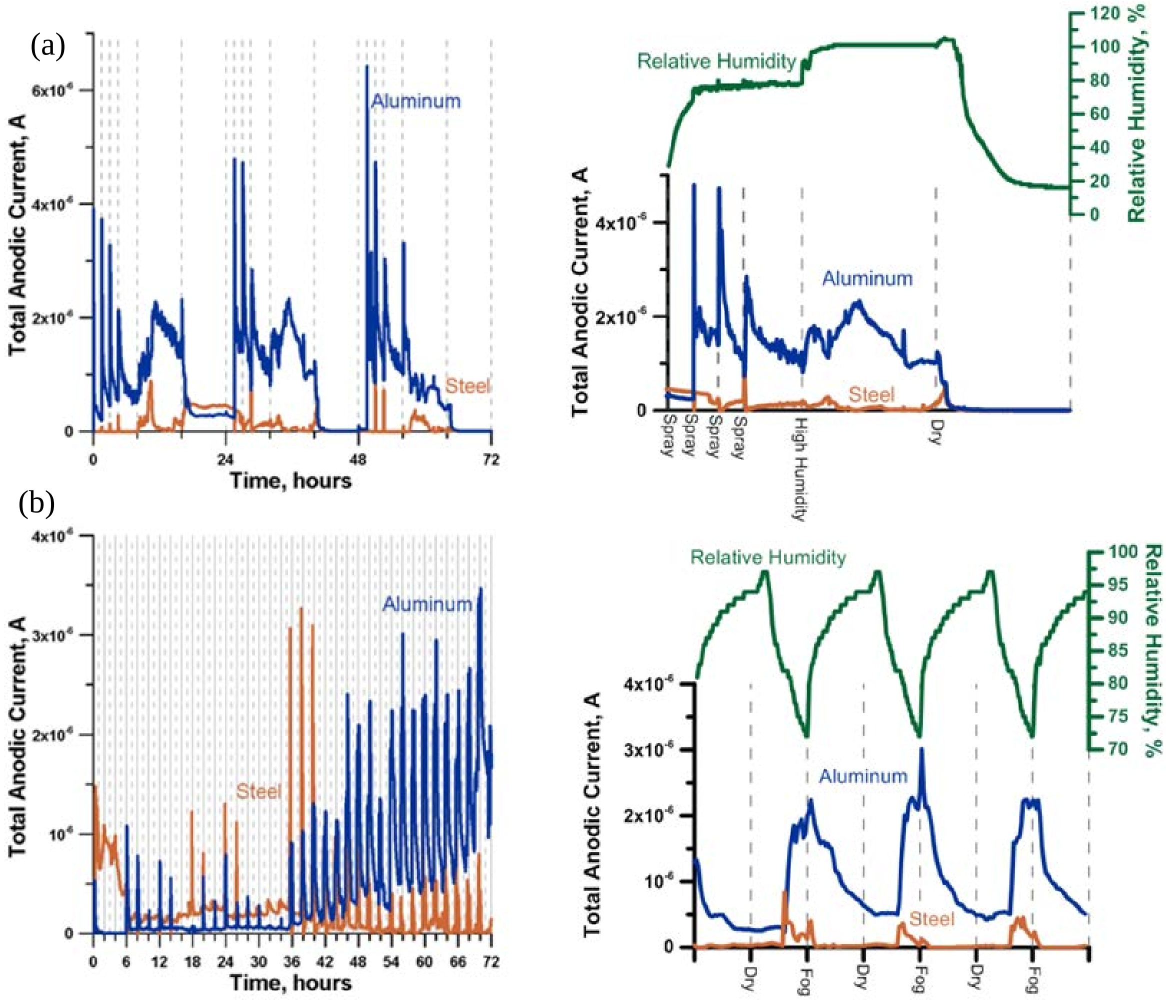

Figure 35. Total anodic current for (a) GM 9540P and (b) ASTM G85A5 tests. Graphs on the left depict total anodic current for the duration of the test. Graphs on the right show details from those exposures for clarity.

3.2.2.4 Current thresholds and RH ranges

Current thresholds were used to categorize the MEA behavior into three modes: a) aluminum and steel anodic currents both below the threshold, b) aluminum and steel anodic current both above the threshold, and c) aluminum current above the threshold but steel below the threshold. The first situation corresponds to low relative humidity environments where an electrolyte is not present in large volumes on the MEA surface. The second case corresponds to middle RHs and transitional periods where sufficient solution volumes are present on the surfaces of the MEA to enable each material's self-corrosion, but a continuous film is not yet present to provide galvanic coupling of the steel and aluminum. The final case corresponds to the equilibrium reached at an RH value above deliquescence where a strong galvanic interaction between the aluminum and the steel is present. A current threshold of 1.7×10^{-7} Amps was chosen for the steel electrodes. This threshold was selected by choosing a current that was sufficiently above baseline currents to represent active corrosion, but was still low enough to capture low corrosion currents.

The threshold for aluminum was scaled to be proportional to the number of exposed electrodes. The threshold values provided a means to clearly distinguish transitional currents associated with large RH changes from the baseline current observed during these exposures.

Relative humidity ranges were suggested for each of these three modes. This approach was suggested by the work outlined above in Section 2.2.1.5. This work demonstrated that corrosion rate does not increase linearly with RH and that corrosion behavior fell into three categories of relative humidity. Using this approach, low RH is categorized as below 50%, intermittent RH is between 50% and the expected deliquescence point of the salt, and high RHs are above the deliquescence point of the salt.

As sodium chloride is the primary salt in the ASTM B117 and GM9540P electrolyte, liquid films are expected to form above 76% RH due to the deliquescence of sodium chloride. The ASTM G85A5 test electrolyte salt is primarily ammonium sulfate which has a deliquescence relative humidity of approximately 81%, so this was assumed to be the deliquescence relative humidity for the ASTM G85A5 test. Humidity data obtained during each test was analyzed to determine the amount of time the test humidity fell into each RH range. Tabulated comparisons of the time spent in each corrosion mode and the time spent in each RH category are shown in Table 1.

As observed in the table, there is reasonable agreement between the time spent in each relative humidity ranges and the corresponding corrosion behavior. These comparisons are strongest for the ASTM B117 and GM 9540P tests. This agreement indicates the validity of the RH range approach. By demonstrating the connection between different galvanic corrosion modes and the RH ranges of the test, this comparison provides a confirmation of the importance of selecting appropriate RH ranges for testing.

Table 1. Current Thresholds and Relative Humidity Ranges.

GM 9540P	RH <50%	50%<RH<76%	RH>76%
	25.4%	18.3%	56.3%
	Al Off, Steel Off	Al On, Steel On	Al On, Steel Off
	23.5%	19.9%	52.8%
ASTM G85 A5	RH <50%	50%<RH<81%	RH>81%
	0%	21.2%	78.8%
	Al Off, Steel Off	Al On, Steel On	Al On, Steel Off
	7.4%	23.0%	69.4%
ASTM B117	RH <50%	50%<RH<76%	RH>76%
	0%	0%	100%
	Al Off, Steel Off	Al On, Steel On	Al On, Steel Off
	0%	0%	100%

CHAPTER 4
EFFECT OF RH ON COATING ADHESION

Coating Adhesion is a primary metric for performance. It is known that cyclic RH plays a key role in adhesion. However, this data is based on post test examination of samples for a limited number of tests. In this Chapter, numerous cycle exposure tests were performed. New methods to quantify corrosion damage are presented that facilitate a comparison of the loss of coating adhesion with each method. Based on these comparisons, criteria for specific RH ranges that control coating adhesion will be developed and used in the development of an improved accelerated corrosion exposure test.

4.1 Materials and Methods

4.1.1 *Test coupons for coating adhesion investigations*

Test coupons were fabricated at the U.S. Navy Naval Air Systems Command (NAVAIR) and were subsequently exposed to either accelerated laboratory testing or outdoor exposure at one of four different sites. These coupons consisted of two dissimilar substrates joined with six fasteners made out of different materials and finished with either chromated or non-chromated coating systems. A schematic of the lap coupon design is shown in Figure 36, and the material systems are detailed in Table 2. The objective of testing was to evaluate galvanic coupling between the dissimilar substrates, as well as galvanic interactions between the fasteners and substrate materials. The effect of exposure environment on occluded areas was evaluated through characterization of the lap area between the top and bottom plates. The samples were coated to mimic currently used dissimilar metal assemblies in the DoD systems. The top and bottom plate surfaces were not sanded prior to assembly and coating.

Prior to exposure, the coatings were scribed around the fastener area to introduce mechanical damage into the coating and generate conditions under which galvanic corrosion could occur.

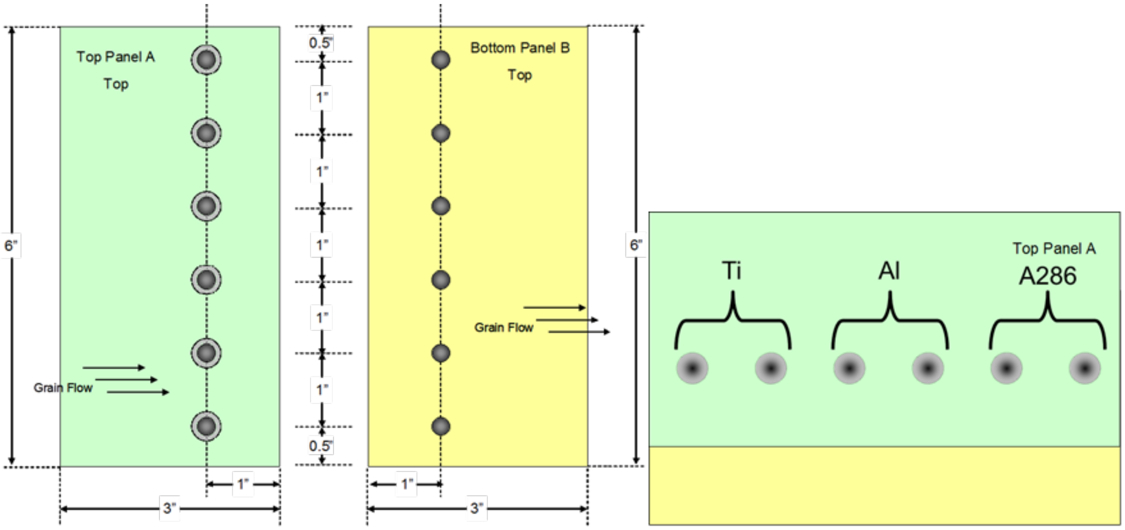

Figure 36. Schematic of lap coupon configuration. Dimensions of both top and bottom panels (left) and final assembled configuration with labels indicating placement of different fastener types: Ti, Al, A286 (CRES) (right).

Table 2. Materials Used in the Outdoor and Laboratory Lap Coupons.

Assembly Designator	Base Plate	Top Plate	Coating System	Fasteners
A	Inert metal (C-22)	Inert metal (C-22)	None	Ti, CRES, Al
B	AA2024	AA7075-T6	1200S+PPG CA7233+PPG CA8201	Ti, CRES, Al
C	AA2024	carbon fiber composite	TCP+Deft02GN084+PPG CA8201	Ti, CRES, Al
D	AA2139	high hard steel	TCP+23377-N(Deft)+53039-Type 4	Grad 8, Rc = 35, Zn plated
E	AA5083	high hard steel	TCP+53022-Type 3+53039-Type 4	Grad 8, Rc = 35, Zn plated
F	AA2024	AA7075-T6	TCP+Deft02GN084+PPG CA8201	Ti, CRES, Al
G	AA2024	AA7075-T6	TCP+PPG EWAE118A+PPG CA8201	Ti, CRES, Al

4.1.2 *Visual observations of galvanic corrosion*

After outdoor exposure or accelerated laboratory testing, lap coupons were photographed to document visual evidence of corrosion. Both the top and bottom plates were photographed before and after disassembly.

4.1.3 *Coating removal procedure*

Characterization of the coupon surface and measurements of the corroded area around the scribe was achieved with high-resolution optical microscopy or surface profilometry. However, this required removal of coatings and corrosion products to reveal the underlying corroded metal surface. Coatings and corrosion products were removed from a subset of the Al alloy panels (specifically, assembly types B and G) by immersing the panels in heated, concentrated nitric acid for 15 minutes. The bath solution contained 50–78% nitric acid by weight, and the bath temperature was maintained at 110 ± 10° F. After removal from the acid solution, panels were thoroughly rinsed with DI water and lightly abraded to remove any residual corrosion products. Manual abrasion was minimized to preserve surface morphology of the corroded areas. Figure 37 shows a representative top plate after coating removal.

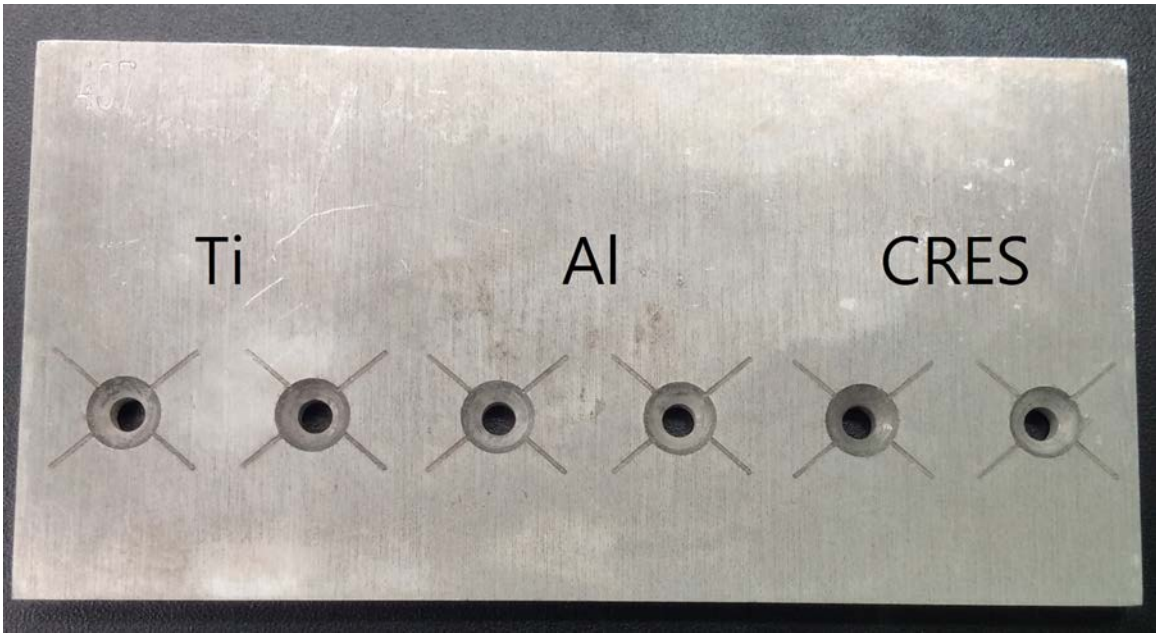

Figure 37. Photograph of a representative top plate of the galvanic assembly after coating removal.

4.1.4 *Fastener scribe characterization*

The corrosion damage at the fastener scribes was evaluated after coating removal using a Bruker NPFLEX optical profilometer with a 10x objective. This microscope uses white light interferometry (WLI) to obtain 3D profiles of the surface. The Bruker system requires several stitching operations to cover a reasonably large surface area and is sensitive to tilt and dynamic range chosen. For this reason, each scribe around the empty fastener holes was imaged separately to obtain 2D and 3D surface profiles of corrosion morphology in and around the scribes.

Some coupons were also imaged using a Bruker ContourGT-K optical microscope, and a subset were sent to Southwest Research Institute (SwRI) to be imaged using a Keyence VR-3100 macroscope that is capable of rapidly scanning large areas. The images taken by the Bruker system were analyzed using the Bruker Vision 64 program. The surface parameters calculated during the analysis of the measured depth profiles are listed in Table 3.

Table 3. Relevant Surface Parameters Used to Quantify Corrosion Around Fastener Scribes.

Parameter	Definition from Vision64 software	Significance
Maximum scribe depth	Minimum value of dataset.	Shows maximum depth of scribe.
Average scribe depth	Averaged values across dataset.	Can be used to correlate surface corrosion and scribe corrosion.
Scribe volume	The amount of liquid that it would take to submerge the dataset to its highest point.	Gives an amount of material lost due to corrosion.
Lateral surface area	The surface being measured in the lateral direction.	2D surface area that corresponds to scribe widening; an effective "area corroded."
Contour surface area	The total exposed three-dimensional surface area being analyzed, including peaks and valleys.	3D surface area that corresponds to scribe widening and/or roughening.
Surface area index	Relative flatness of a surface. Contour over Lateral.	Relative flatness of the surface.
Surface Roughness	Arithmetic average of absolute values.	Mathematical average of surface roughness.

The panels were also analyzed using a Keyence VR-3100 series macroscope. The top plate with the scribe and the bottom plate were both analyzed as shown in Figure 38. For the analysis, each rivet location was cropped for individual analysis. The size of the analyzed area was 25 mm in width and 27 mm in height for each rivet location of each panel.

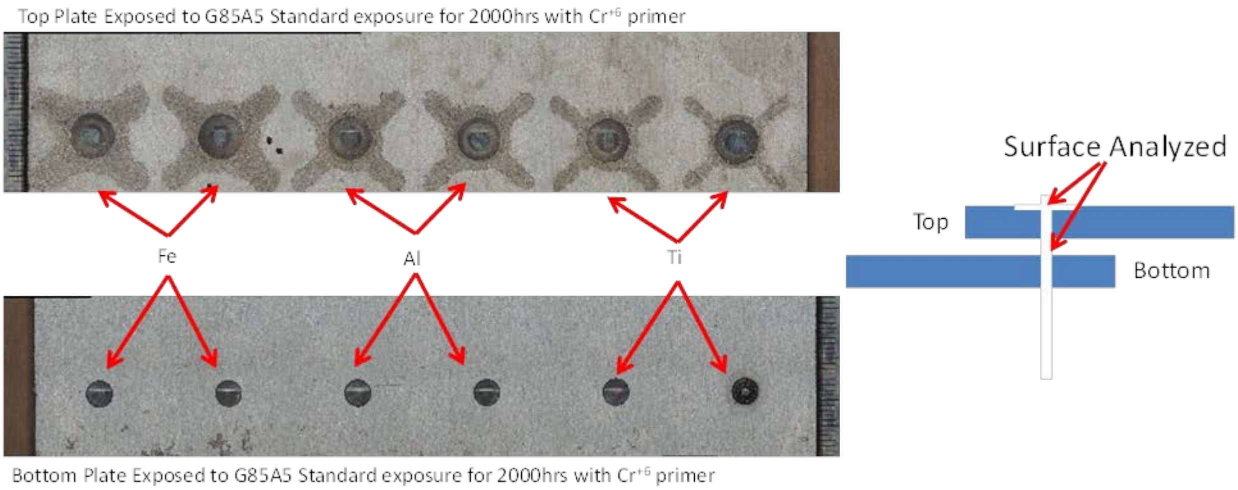

Figure 38. Surfaces analyzed using the Keyence VR-3100 series macroscope.

The analysis examined four parameters: maximum damage depth, average damage depth, total volume loss and percent surface area corroded. The effect of different rivet types, exposure conditions and primers was examined.

4.1.5 *RH controlled coatings evaluations using witness coupons and corrosion sensors*

The witness coupons provide ground truth evaluation of corrosion damage using mass loss measurements while the corrosion sensors quantify the corrosion rate to characterize the aggressiveness of specific environmental conditions.

4.1.5.1 Accelerated test conditions

A test matrix composed of three environmental exposure cycles was developed to quantify the effects of two environmental factors - drying and drying event frequency - on coating performance and corrosion damage (Table 4). The comparison between Cycle A and Cycle B evaluates how the degree of drying affects coating performance. The comparison between Cycle A and Cycle C evaluates how the frequency of cycles affects corrosion damage while the total time of wetness is held constant. The three test cycles all have a 67% time of wetness (percent time with RH > 76%). The testing was performed in a Thermotron SM environmental chamber with programmable temperature and humidity control. For all test cycles, the temperature was held at constant at 49.0 ± 0.1 °C. The RH changes were controlled as step functions to avoid experimental complexities associated with RH ramp times and rates (Figure 39). The samples were dipped once a week in the ASTM G85-A2 salt solution of 5 wt% NaCl, pH adjusted to 2.8 – 3.0 with acetic acid.

Table 4. Accelerated test cycle conditions with a constant temperature of 49 ^{o}C.

	Cycle A	Cycle B	Cycle C
Max RH	90%	90%	90%
Min RH	40%	65%	40%
Max RH Time (hr)	2	2	8
Min RH Time (hr)	1	1	4
Salt Dip Frequency (per wk)	1	1	1

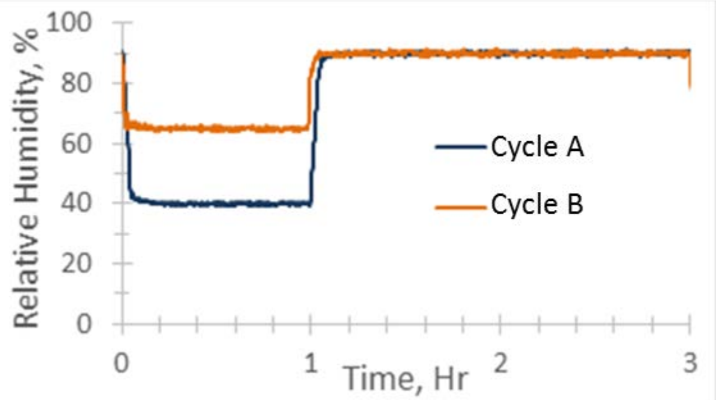

Figure 39. Chamber RH as a function of time for Cycles A and B at 49 °C.

4.1.5.2 Materials for testing

This cyclic RH testing included standard test panels, mass loss coupons with fasteners, and multi-sensor panels (Figure 40). The standard test panels were used to obtain visual scribe creep ratings according to ASTM D1654. Each mass loss panel contained six mass loss coupons. Half of these mass loss coupons were used by SwRI to obtain quantitative measurement of material loss and scribe creep. Luna performed mass loss measurements on the other half of the mass loss coupons according to ASTM G1. Finally, the multi-sensor panels contain gold (Au), aluminum (Al), and aluminum/stainless steel (Al/SS) interdigitated electrode (IDE) sensors. These sensors were used to generate corrosion rate measurements in real time and to determine timing for removal of samples from testing. Coated Au IDE sensors are used to characterize the ionic conductivity and barrier properties of the coating while uncoated Au IDE are used to characterize the solution resistance of the thin film electrolytes that form on the panel surface in response to salt contaminant loading and relative humidity.

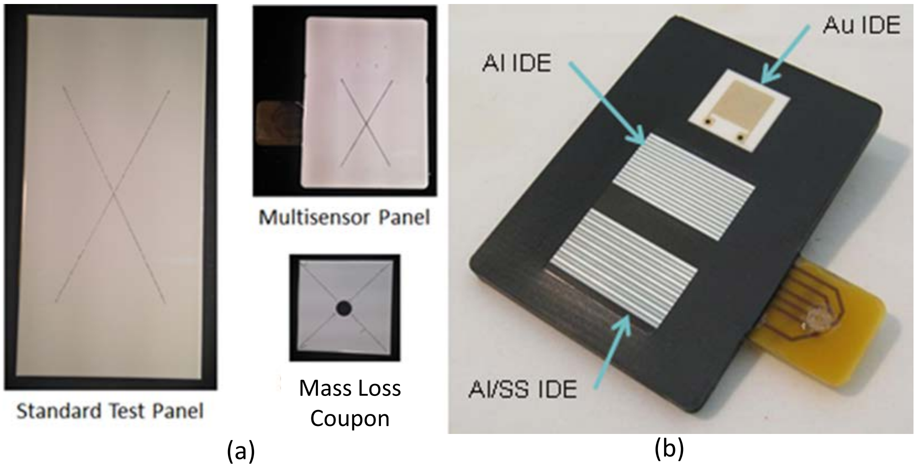

(a) (b)

Figure 40. (a) Coated and scribed materials for cyclic RH testing. (b) Uncoated multisensor panel (MSP) with interdigitated electrode (IDE) sensors. Two coating systems were used for the cyclic RH testing (Table 5).

The Al IDE sensor measures the free corrosion of the AA7075-T6 alloy. The Al/SS IDE measures the galvanic corrosion between the AA7075-T6 and 316 stainless steel. The Au IDE was tested in the fully painted condition with no scribe while the Al and Al/SS IDE sensors were scribed.

The coatings were applied by NAVAIR and all samples had the same pretreatment and topcoat. The difference between the two coating systems was the use of solvent borne (Deft 02GN084) and water borne (PPG EWAE118A) chrome-free primers. For each coating system in a given cycle, there were two multisensor panels (MSP), nine standard test panels, and 18 mass loss coupons (Figure 40). Three standard test panels and six mass loss coupon were pulled at three time intervals of 350, 905, and 1,320 hours during each cycle.

Table 5. Coating Systems Used for Cyclic RH Testing.

Pretreatment	Primer	Topcoat
TCP	Deft 02GN084 (23377K, TY I, CL N)	PPG CA8201
TCP	PPG EWAE118A (85582D, TY II, CL N)	PPG CA8201

4.1.5.3 Corrosion sensor measurements

The data collection was automated for the Au, Al, and Al/SS IDE sensors of the multi-sensor panel. The Au IDE and Al IDE sensors for coating property and AA7075-T6 free corrosion measurements, respectively, were monitored using electrochemical impedance spectroscopy (EIS). EIS measurements were performed with a Gamry Interface 1000 multiplexed with a Pickering card to sequentially characterize each of the impedance-based sensors. Each impedance-based sensor was scanned from 1 MHz to 0.16 Hz at 5 points per decade frequency with a 10 mV RMS amplitude AC signal and a bias of zero volts versus open circuit potential. The corrosion rates are estimated as currents for the Al IDE sensors, where the excitation voltage (ΔE) is divided by the impedance modulus (Z) to obtain current (Scully, 2000). Each scan took approximate three minutes, so each impedance sensor was measured every 24 minutes. The Al/SS IDE sensor for measuring galvanic corrosion was monitored using a zero resistance ammeter (ZRA). The multi-channel ZRA circuit was used to acquire the Al/SS galvanic corrosion rate every 30 seconds.

4.1.5.4 Effect of the frequency of test cycles on galvanic interactions of coated surfaces

Half of the mass loss coupons were used to obtain quantitative measurement of material loss and scribe creep utilizing a Keyence VR-3100 series macroscope as described in Section 4.1.4. Prior to the analysis of the scribe corrosion, the samples were cleaned in nitric acid according to ASTM G1. The size of the analyzed area was 25 mm in width and 27 mm in height centered at the rivet location for each panel.

The analysis examined four parameters: maximum damage depth, average damage depth, total volume loss and percent surface area corroded.

4.2 Results and Discussion

4.2.1 *Comparison of accelerated laboratory tests*

The effect of environmental chemistry and RH cycling was investigated using a set of the scribed chromate-coated (with chromate primer) test coupons. These coupons were exposed to (i) neutral salt fog (ASTM B117), (ii) cyclic, acidic salt fog (ASTM G85A2) and (iii) continuous acidic salt fog (ASTM G85 A1). Images of these coupons after exposure are shown in Figure 41 The depth profiles of the scribes measured with white light interferometry are also included. Significant differences were found between the different exposure environments. Very little attack was seen in the case of the neutral salt fog exposure. The test coupons exposed to cyclic acidic salt fog showed the most corrosion damage at the scribe. The continuous acidified salt fog, on the other hand, did not cause damage to the scribed areas, but initiated widely distributed corrosion under the primer away from the scribes.

Coupon	Panel Image	Depainted	Profile of scribe
#1 Neutral salt fog			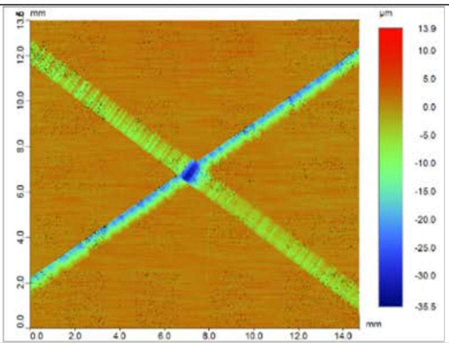
#3 cyclic acidic salt fog			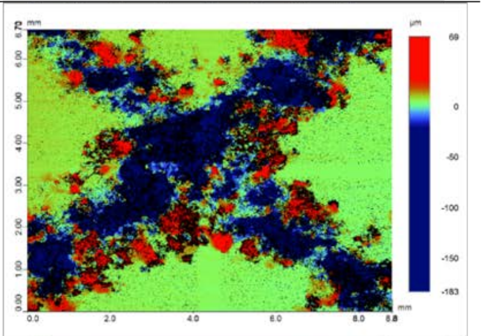
#6 continuous acidic salt fog			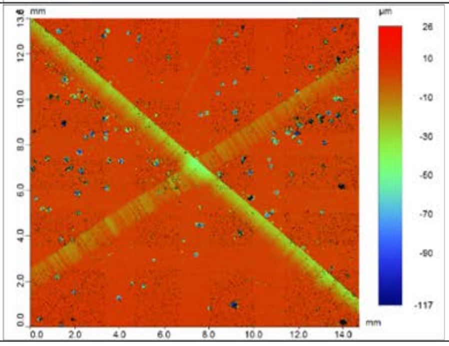

Figure 41. Images of chromate-coated test coupons exposed to different accelerated laboratory environments.

4.2.2 *Coating degradation in accelerated laboratory tests*

A subset of indoor exposure coupons were stripped, imaged, and analyzed using the same procedure defined in Section 4.1. The objective was to quantify the extent of coating degradation and subsequent corrosion damage caused by different accelerated testing protocols and to enable a comparison between coating performance on coupons exposed outdoors and those exposed to accelerated chamber tests. Figure 42 shows photographic images of the selected accelerated test coupons before and after disassembly, but prior to coating removal.

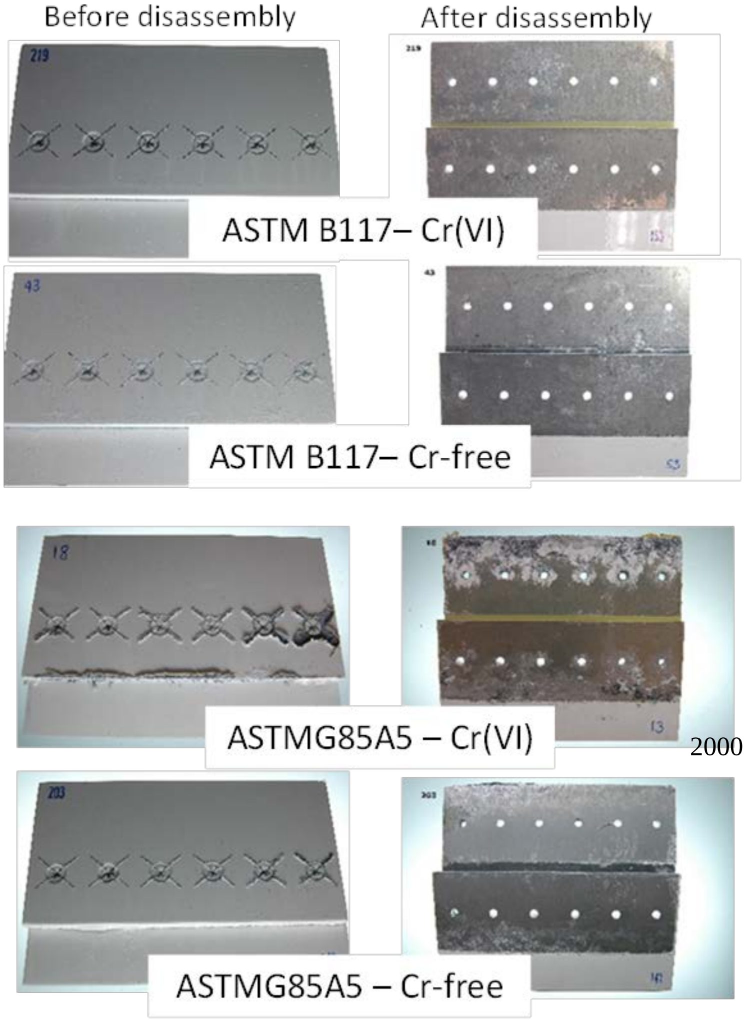

2000 hr-test

Figure 42. Photographic images of the selected accelerated test coupons before and after disassembly. The tests were run for 1500 hrs except for the ASTM G85A5 with the Cr(VI) coating, which was run for 2000 hrs.

In the case of the chromated coating tested in the ASTM B117 environment, all scribes were 5-15% bright with no undercutting. The non-chromated coating showed similar damage across the entire panel; the upper areas of the scribes were dark, while the lower areas were filled with white corrosion products, and the characteristic filaments of filiform corrosion were protruding from several scribe apexes. One such filament was visible in the 2D profilometry image of the scribe shown in Figure 43.

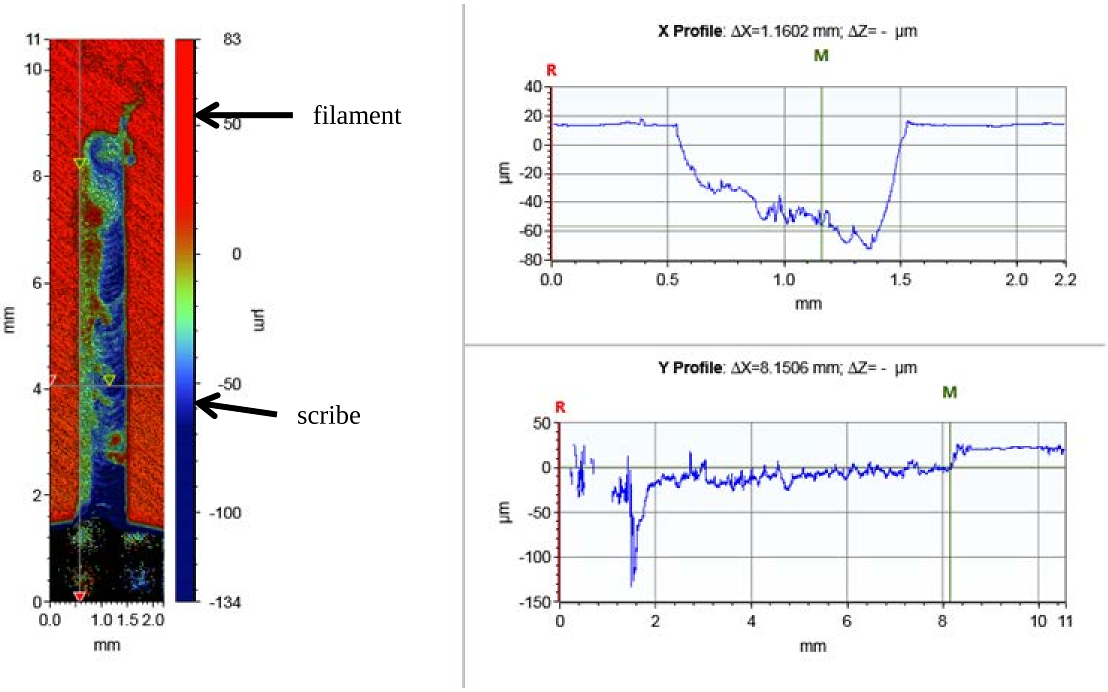

Figure 43. 2D surface profile of scribe on coupon 43 showing metal loss due to filiform-type filaments.

In contrast to the ASTM B117 environment, the coupons exposed to the ASTM G85 A5 test have significantly more visible coating degradation and scribe creep, especially around the CRES fasteners. After 2000 hours of exposure in the ASTM G85 A5 environment, there was excessive recession in the scribes, delamination of the top panel at the lap edge, and heavy corrosion in the faying area. Figure 44 shows the 2D surface profile of a scribe adjacent to a Ti fastener on a test panel exposed to ASTM G85 A5 for 2000 hrs. The coating was removed from the panel prior to imaging. This image shows that the scribe widened considerably, and the scribe boundary became jagged as metal loss propagated non-uniformly away from the scribe. In the regions around the Al and CRES fasteners, scribe creep was so extensive, that it became difficult to define a clear boundary between the individual scribes.

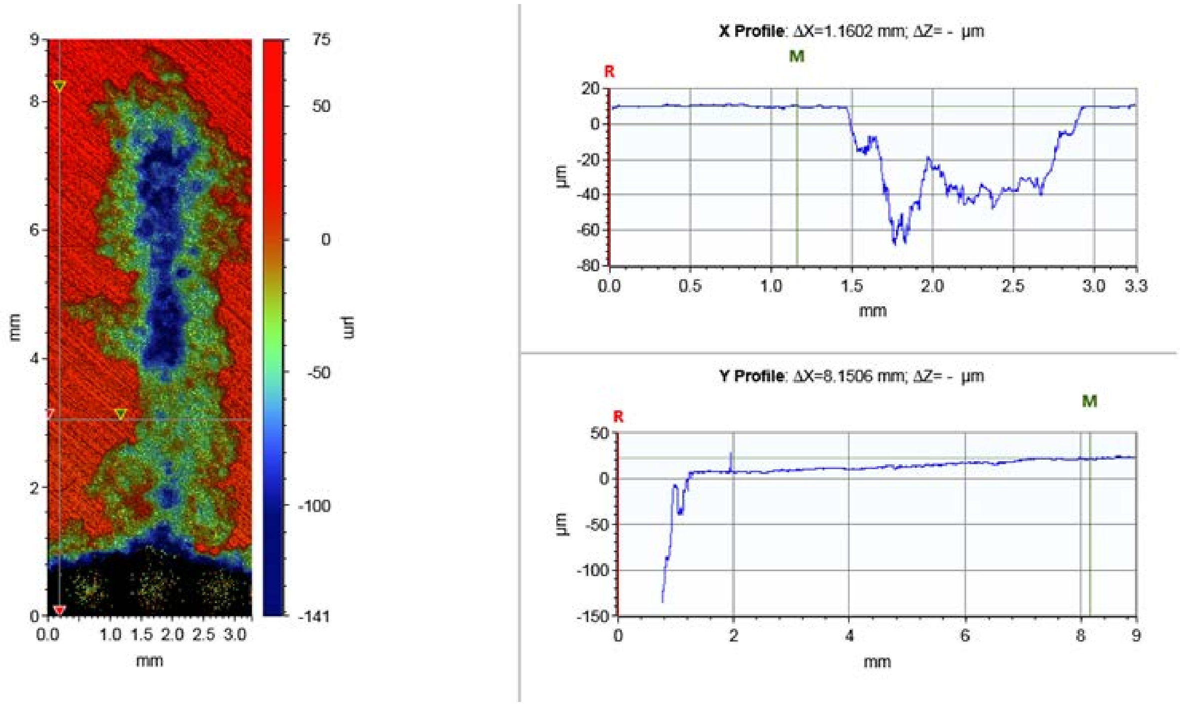

Figure 44. 2D surface profile of a scribe adjacent to a Ti fastener on a test panel exposed to ASTM G85 A5 for 2000 hrs.

A series of photographs documenting the extent of corrosion in lap coupons exposed to different accelerated tests—both before and after disassembly—is shown in Figure 45 and Figure 46. Several general observations were made from visual inspection of the test coupons:

- ASTM G85 A5 was the most aggressive accelerated test for assemblies containing Al panels, while not as aggressive for the steel/Al galvanic assemblies.
- GM9540P caused the most galvanic attack, with corrosion at the A286 CRES fasteners being greater than at the Ti fasteners.
- CRES and Ti fasteners tended to seize in Al coupons after 2000 hours of testing in either GM9540P or ASTM G85 A5. Al fasteners seized in ASTM G85 A4 testing for the non-chromate primers.
- Except for ASTM G85 A5, the panels coated with chromate primer showed little corrosion at scribes or in laps.
- ASTM B117 was the least aggressive of the exposures with slight galvanic corrosion at CRES fasteners.
- The graphite composite over Al panels showed corrosion in the lap and on Al fasteners.
- In general, GM9540P and ASTM G85 A5 were more aggressive on steel/Al coupons than either ASTM G85 A4 or ASTM B117.

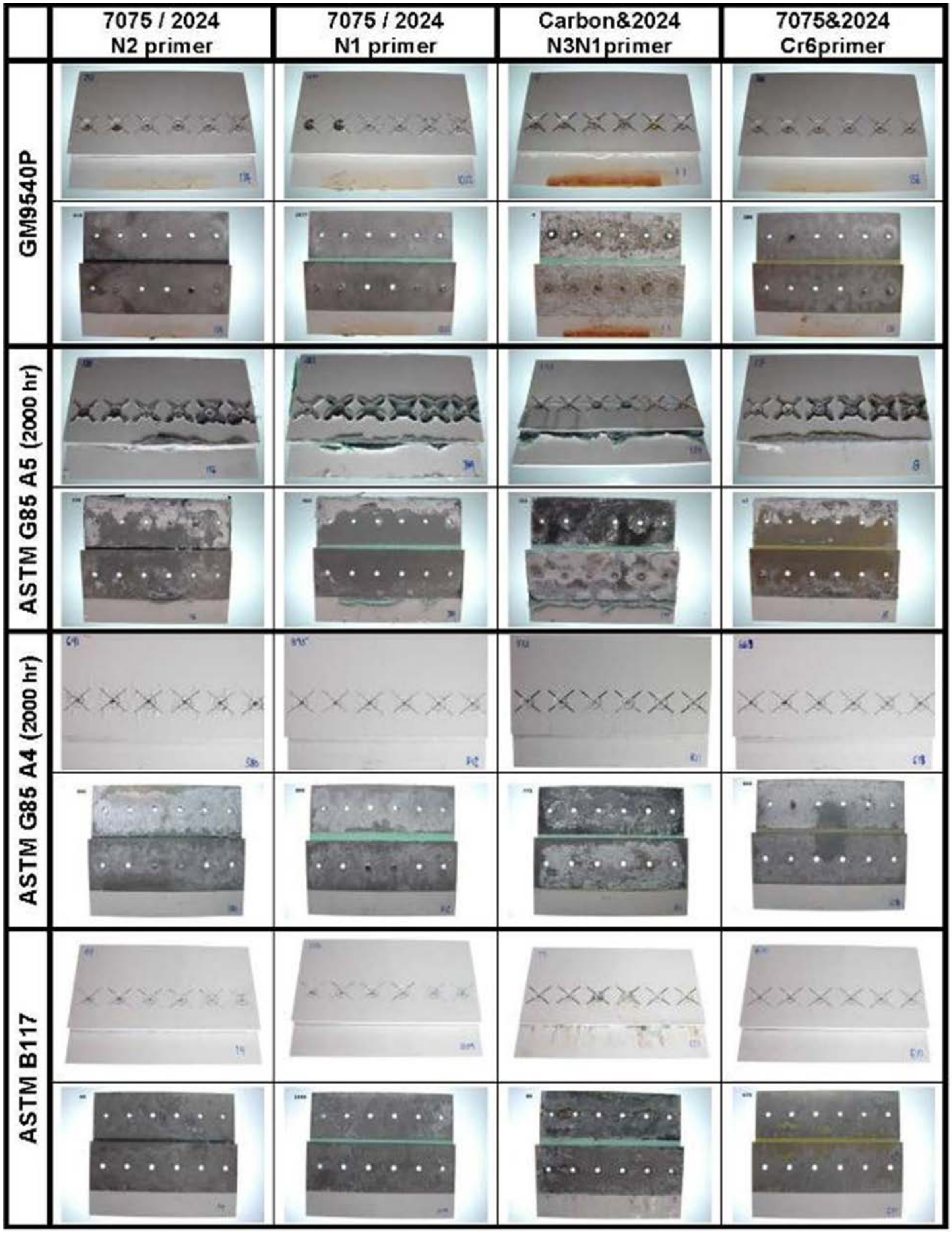

Figure 45. Lap coupons consisting of primarily Al alloy panels after 2000 hours of accelerated laboratory testing.

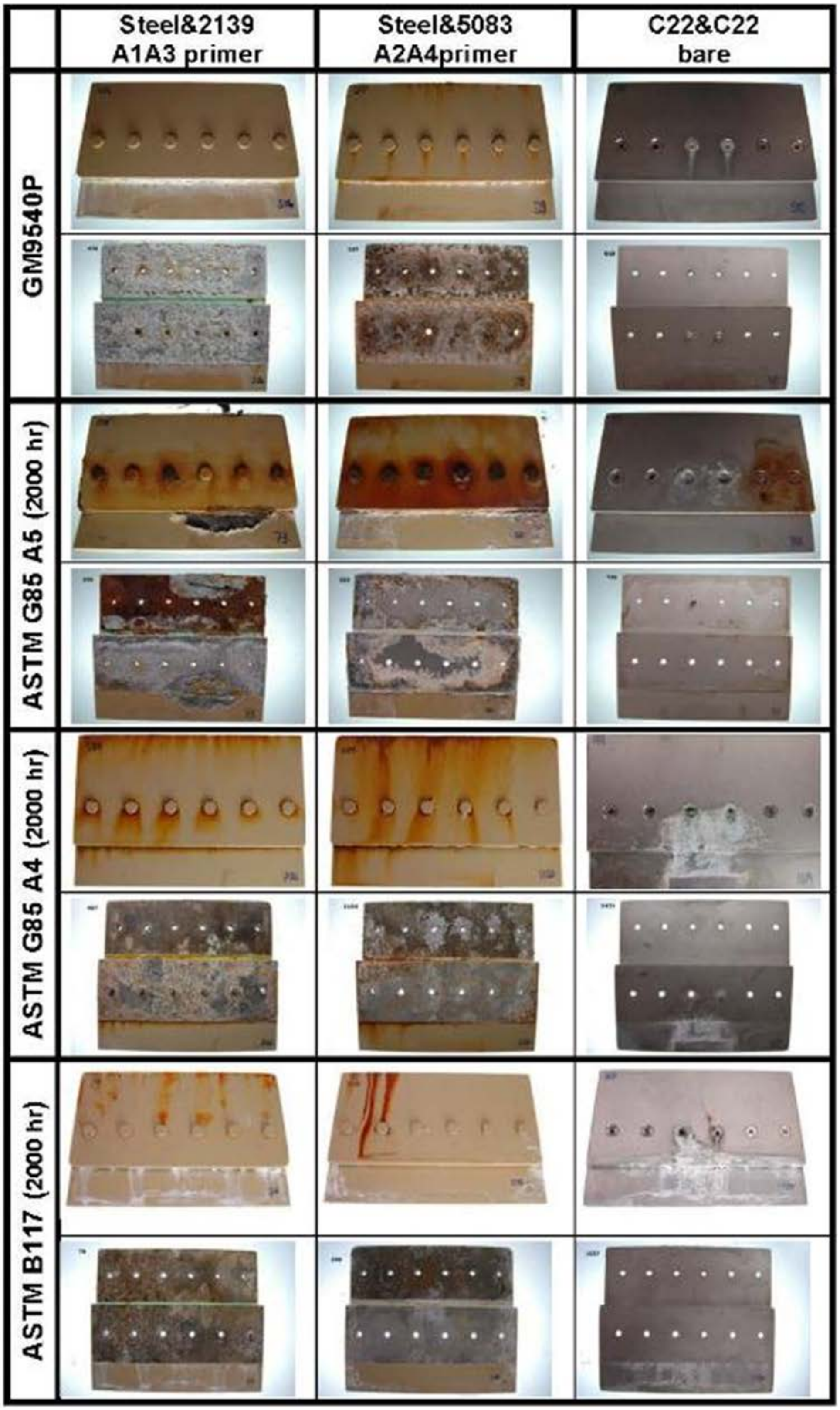

Figure 46. Lap coupons consisting of either steel or C22 panels after 2000 hours of accelerated laboratory testing.

4.2.3 *Fastener scribe characterization*

To evaluate the impact of fastener type on the extent of galvanic corrosion, the area around the fastener scribes was imaged using white light interferometry (WLI), and the 2D and 3D surface profiles were analyzed. Examples of corroded areas around the scribe are shown in Figure 47. The galvanic assembly type F (AA2024-T3 base plate, AA7075-T6 top plate and non-chrome coating system) was used in these tests. The panels were exposed for 1500 hrs in ASTM G85A5 environment. Coupon 635 shows more general corrosion along the scribe line with some undercutting of the paint film. Coupon 582 shows more pitting-like morphology. Figure 48 - Figure 50 show images of the scribes at the aluminum and A286 CRES fasteners on assembly type F coupons that were exposed to GM9540P (coupon 1080) and ASTM G85 A5 (coupon 635). The fastener hole and scribe are marked in the figures. Very little corrosion is seen in case of the GM9540P exposure. In contrast, extensive corrosion is seen in the ASTM G85 A5 exposure with the scribe line becoming both deeper and wider. White lines mark the original scribe. The blue and green colors outside the white lines indicate corrosion outside the scribe.

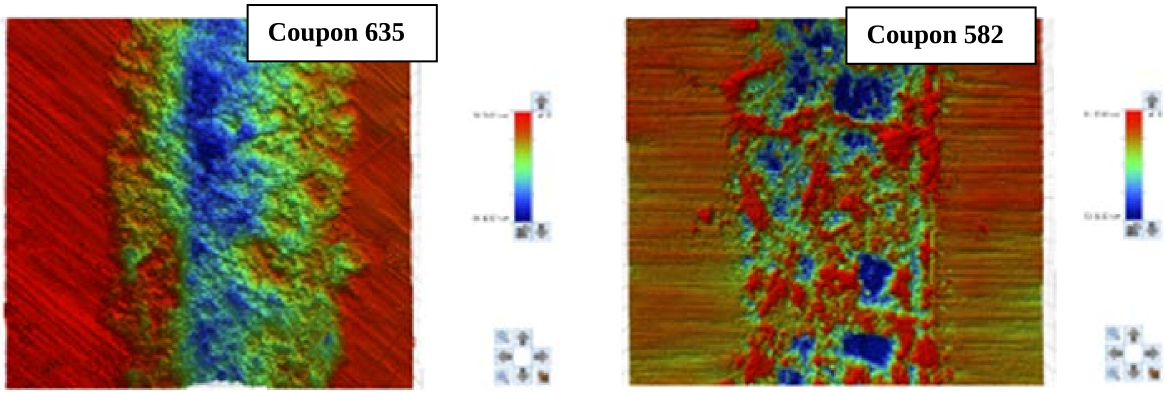

Figure 47. WLI images of a 5mm x 5mm corroded area around a fastener scribe.

	ASTM G85 A5 (Coupon 635)	GM9540P (Coupon 1080)
CRES fastener	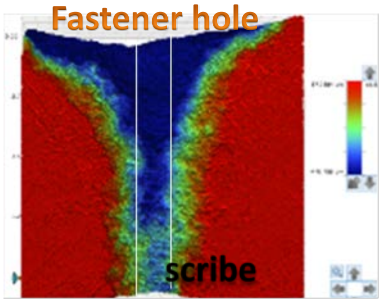	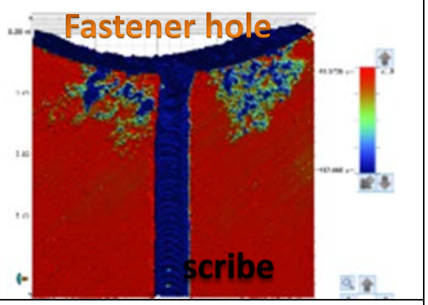
Aluminum fastener	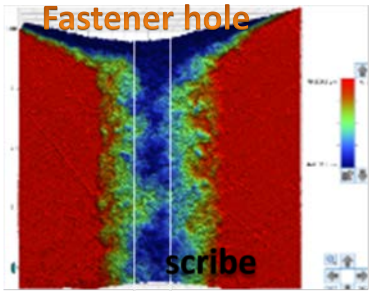	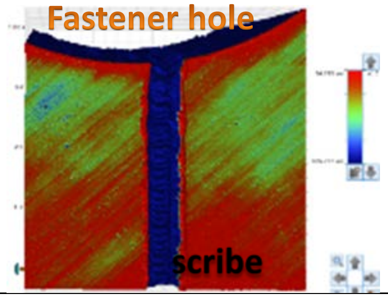

Figure 48. Corrosion at fastener/panel interface in assembly type F (AA7075, N1 primer) after 2000 hrs of exposure.

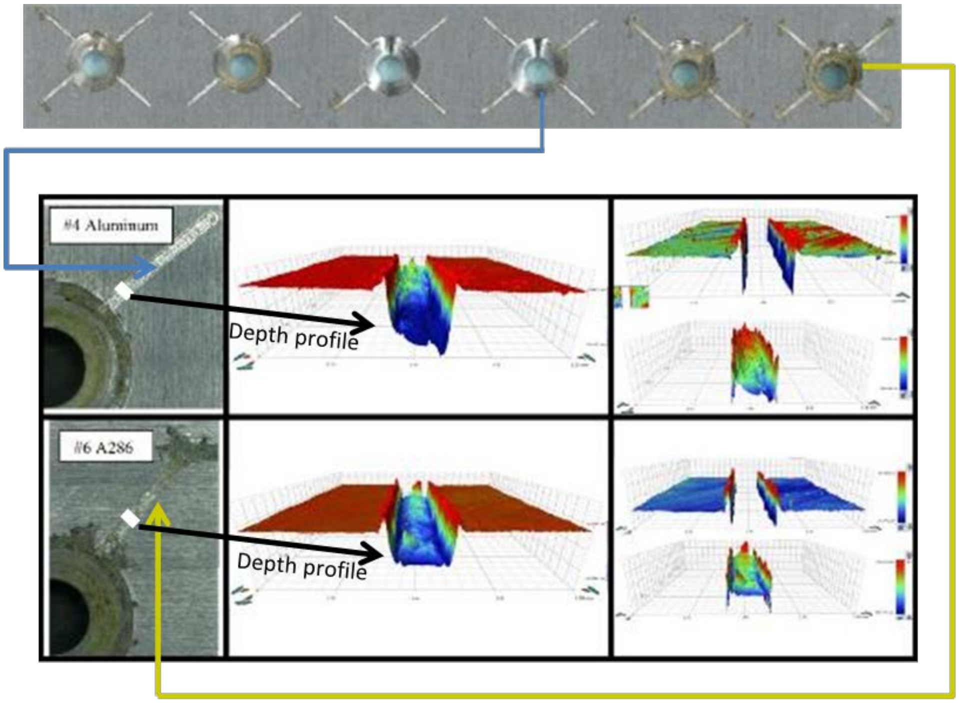

Figure 49. Photographs and WLI images of fastener scribes on coupon 1080 after 2000 hours of GM9540P testing.

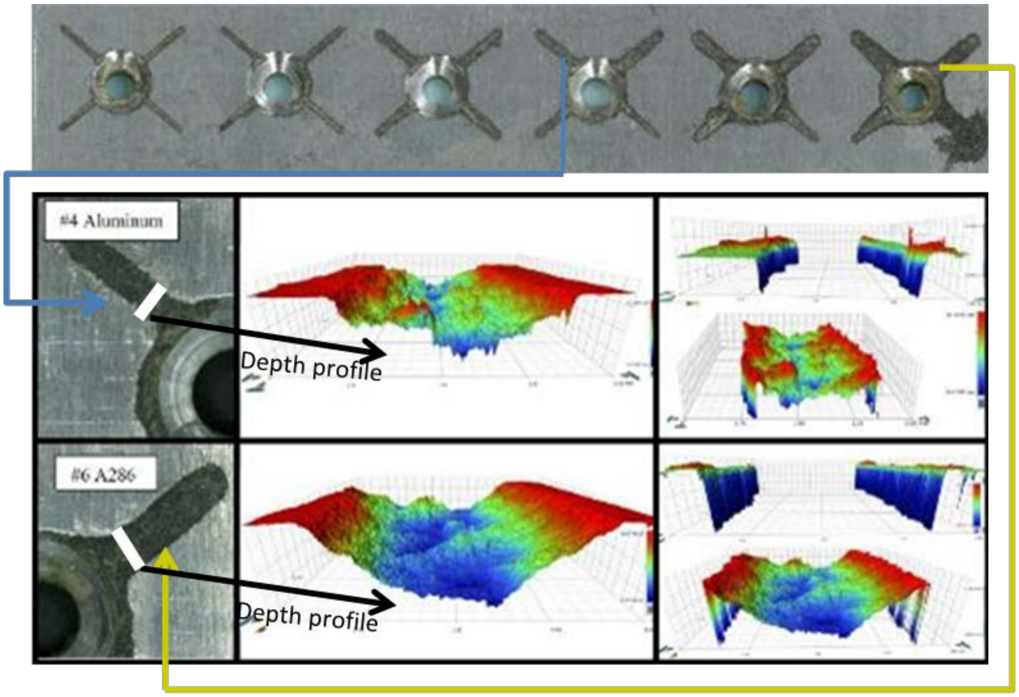

Figure 50. Photographs and WLI images of fastener scribes on coupon 635 after 2000 hours of ASTM G85 A5 testing.

4.2.4 *Analysis of the corrosion features of the lap joints*

The corrosion features around the scribe were examined using the Keyence VR-3100 series macroscope as a function of exposure time for different rivet materials, coatings and laboratory exposure techniques in the case of assemblies B, F and G (Figure 36, Table 2). As shown in Figure 51, there appears to be an incubation time prior to the spreading of corrosion around the rivet hole and along the scribe. Corrosion damage is not significant up to approximately 1500 hrs, after which there is a marked increase in the affected area, and the depth of the damage, as well.

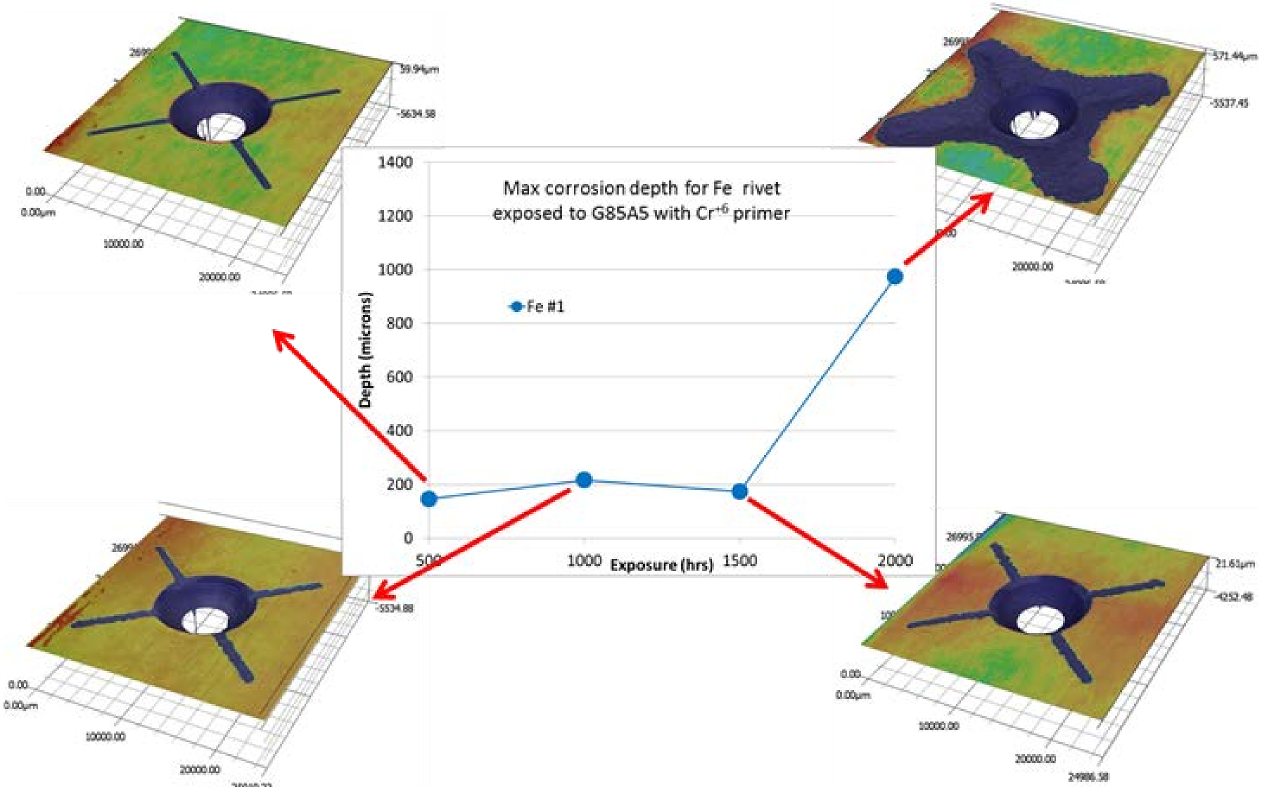

Figure 51. Change in corrosion features with time on assembly B (Table 2).

When comparing the behavior of the different rivet materials under different test conditions, the steel rivet showed the largest maximum corrosion depth in the ASTM G85A5 tests regardless of the primer chemistry. At the same time, the GM9540P and ASTM B117 tests did not indicate a difference in galvanic performance for the different rivet materials. The results are summarized in Figure 52.

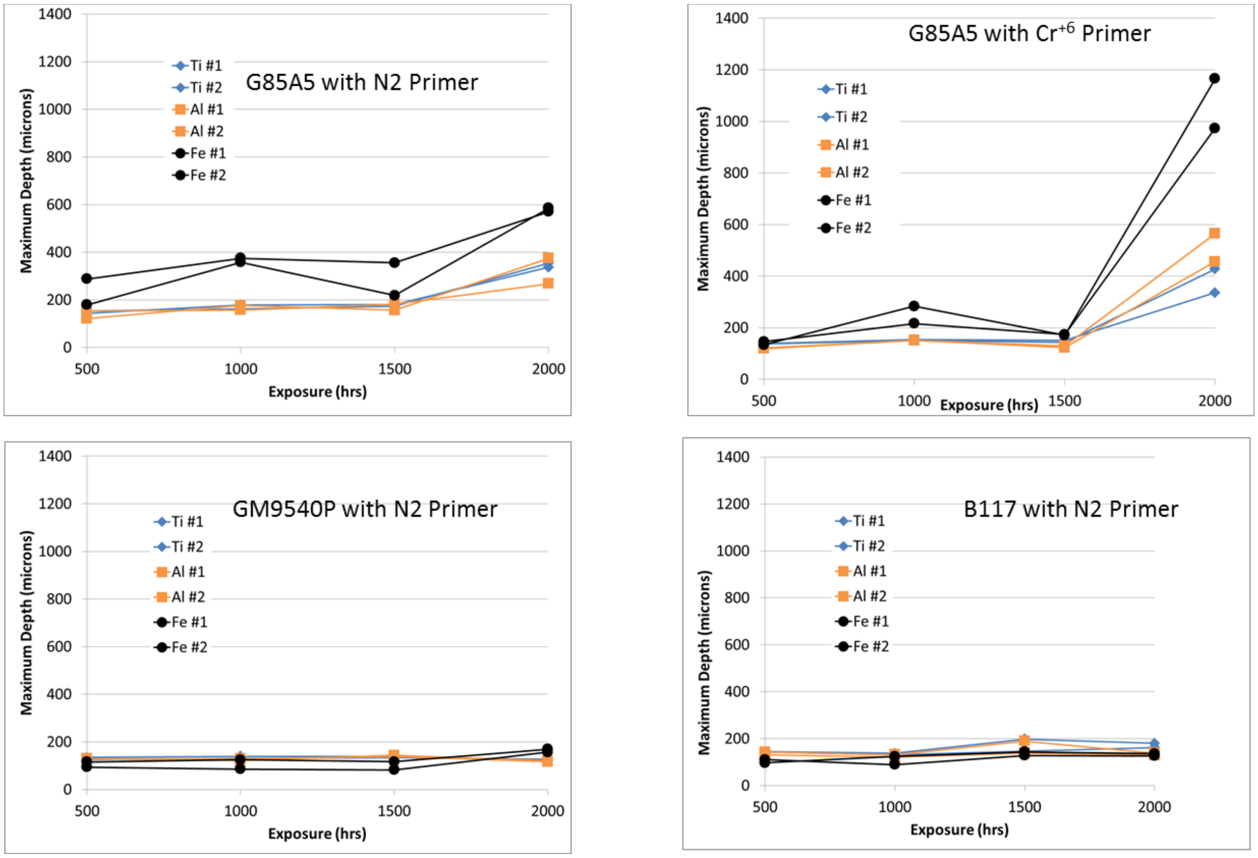

Figure 52. Maximum corrosion depth for different rivet materials measured in different laboratory exposure tests on assemblies B (Cr^{+6} primer) and G (N2 primer) (Table 2).

As shown in Figure 53, the volume loss and average corrosion depth show the same trend as the maximum corrosion depth.

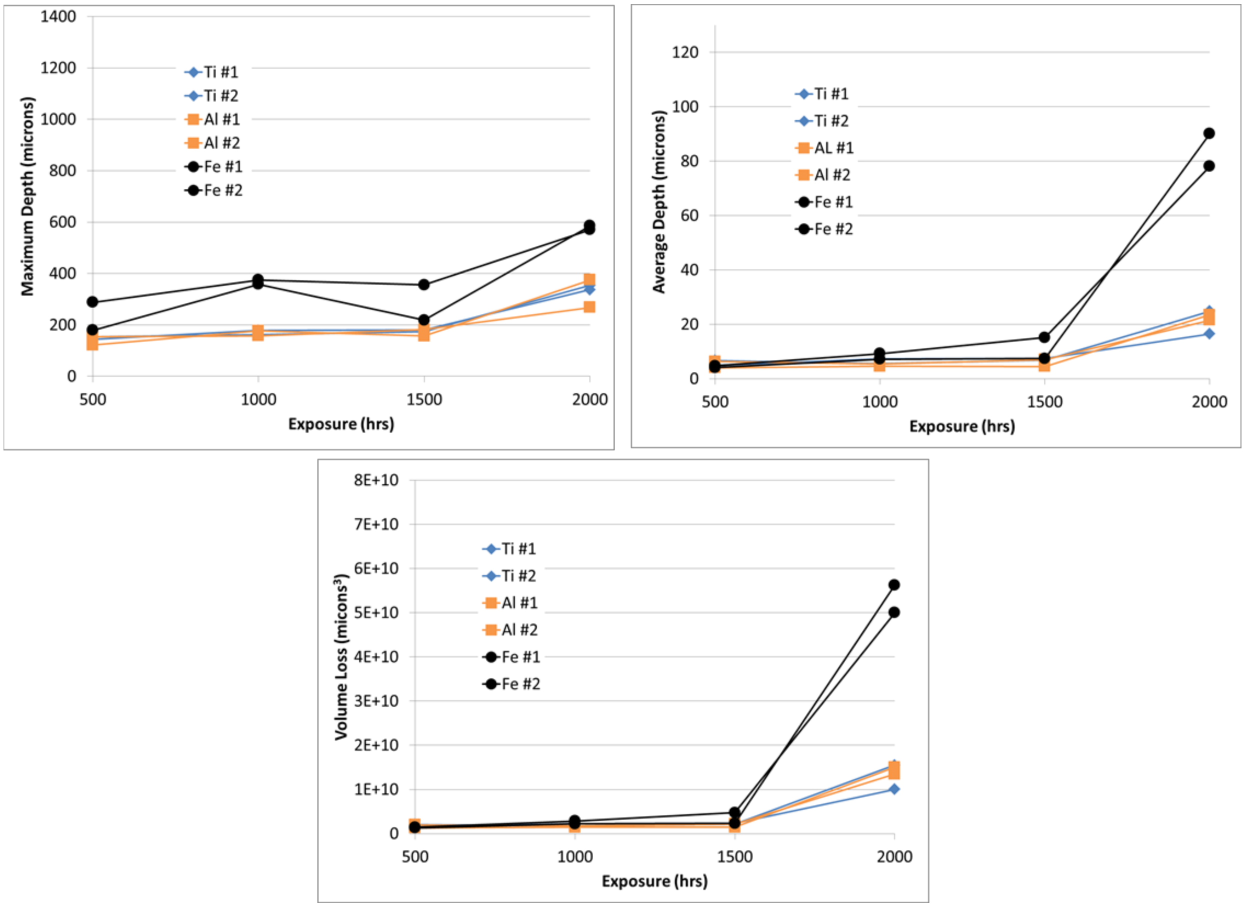

Figure 53. Maximum and average corrosion depth and volume loss as a function of exposure time for different rivet materials in G85A5 tests. The plate was coated with N2 primer (assembly G, Table 2).

The degraded surface area was also largest in the ASTM G85A5 exposure test, regardless of rivet material. Steel rivet material showed the greatest amount of degradation at 40% after 2000 hrs of exposure, while approximately 20% of the surface was corroded in the case of the aluminum and titanium rivets (Figure 54).

In the ASTM G85A5 environment, the steel rivets showed most significant dependence on the primer chemistry. The hexavalent chrome free N2 primer was found to suppress the depth of the corrosion damage most successfully (Figure 55), while the hexavalent chrome containing primer decreased the degraded surface area to a greater degree than the hexavalent chrome free primers (Figure 56).

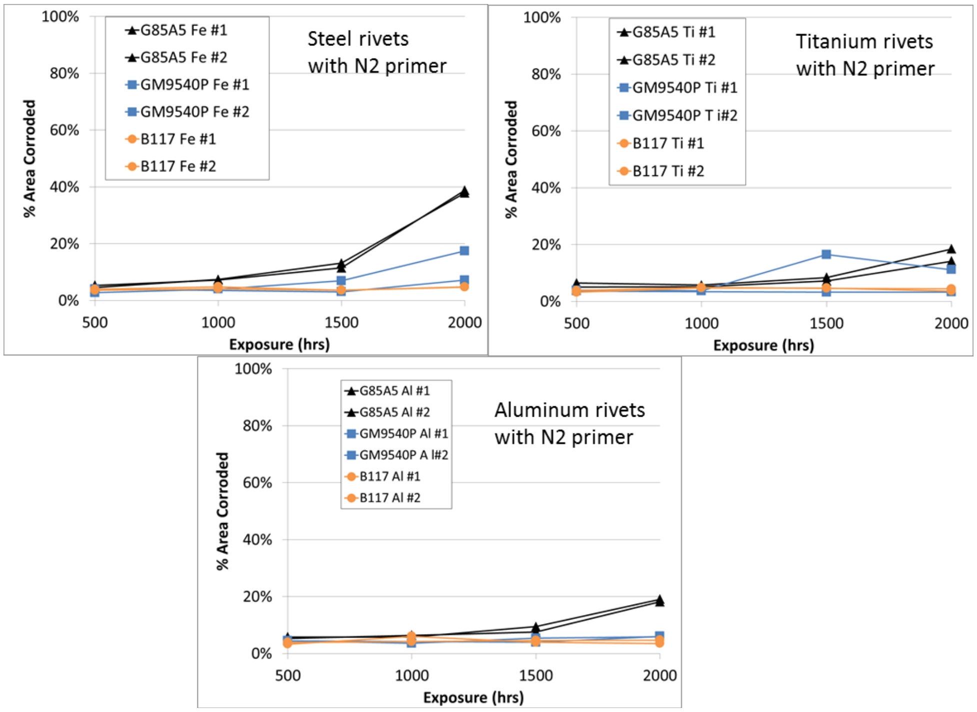

Figure 54. Surface area degraded as a function of exposure time for different rivet materials under different exposure conditions on assembly G (Table 2).

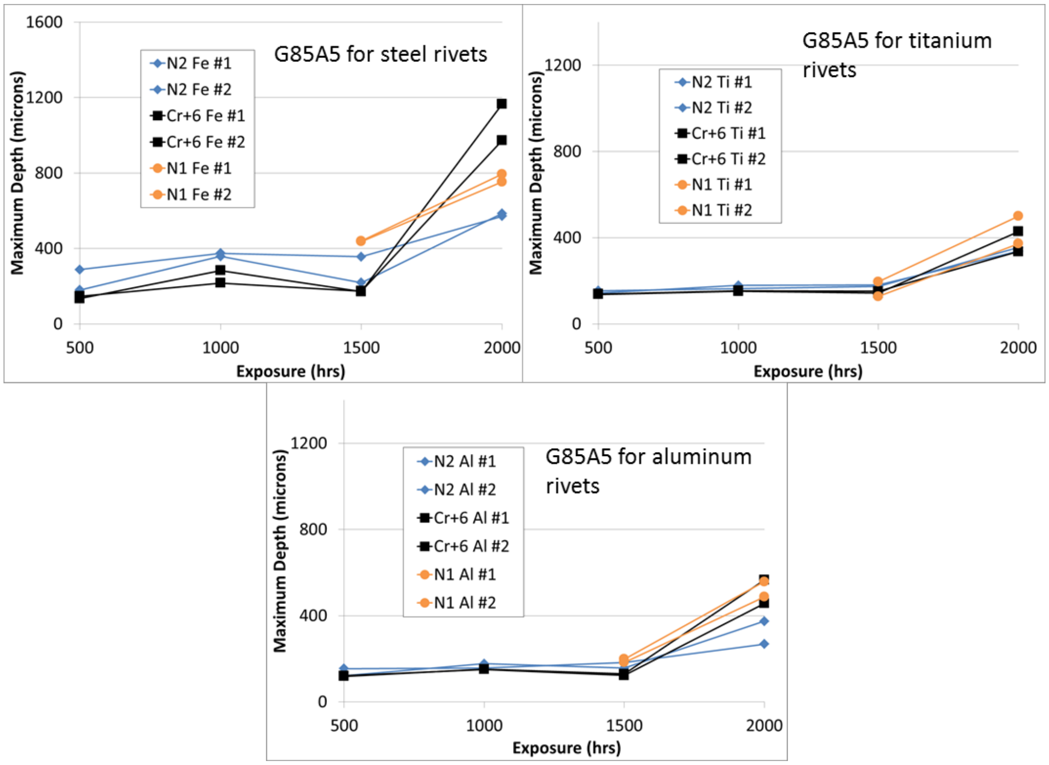

Figure 55. Maximum corrosion depth as a function of exposure time in G85A5 for different rivet materials and primers on assemblies B (Cr^{+6}), F (N1) and G (N2) (Table 2).

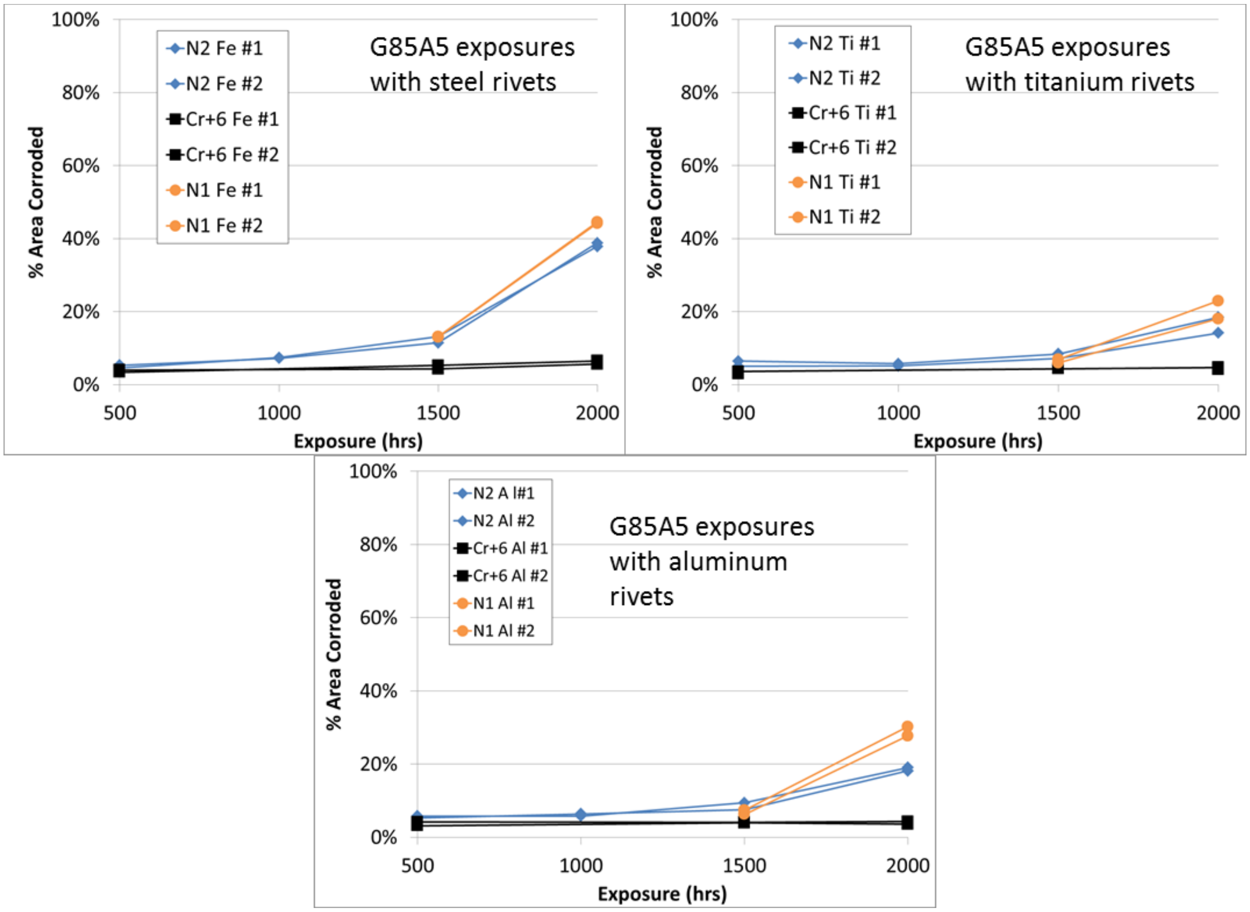

Figure 56. Degraded surface area as a function of exposure time in ASTM G85A5 for different rivet materials and primers on assemblies B (Cr^{+6}), F (N1) and G (N2) (Table 2).

4.2.5 *RH controlled coating evaluations*

The sensor data and witness coupon results on the effects of drying are detailed below along with a discussion of the significance of the exposure test cycles on the corrosion and coating performance.

4.2.5.1 Effects of RH cycling on coating impedance

The impedances of the coating systems with solvent borne primer (SBP) and water borne primer (WBP) were measured with the Au IDE. The Au IDE coatings were not scribed so that the impedance is dominated by the barrier properties of the intact coating. The impedance was initially high and dominated by capacitance as expected for a pristine, dry coating system (Figure 57). Impedance characterization of the barrier properties for a coating with solvent borne primer at the beginning of Cycle B using the Au IDE.). An ohmic resistance developed at low frequencies over the first few hours as the coating on the salt-dipped panel equilibrated at high humidity. The inverse of the impedance at 1 Hz was determined to be a useful representative parameter for quantifying the ionic conductance (1/R) of the coating. A small, but significant, amount of noise centered around 60 Hz was observed despite protection of the samples and instrumentation with grounded Faraday cages.

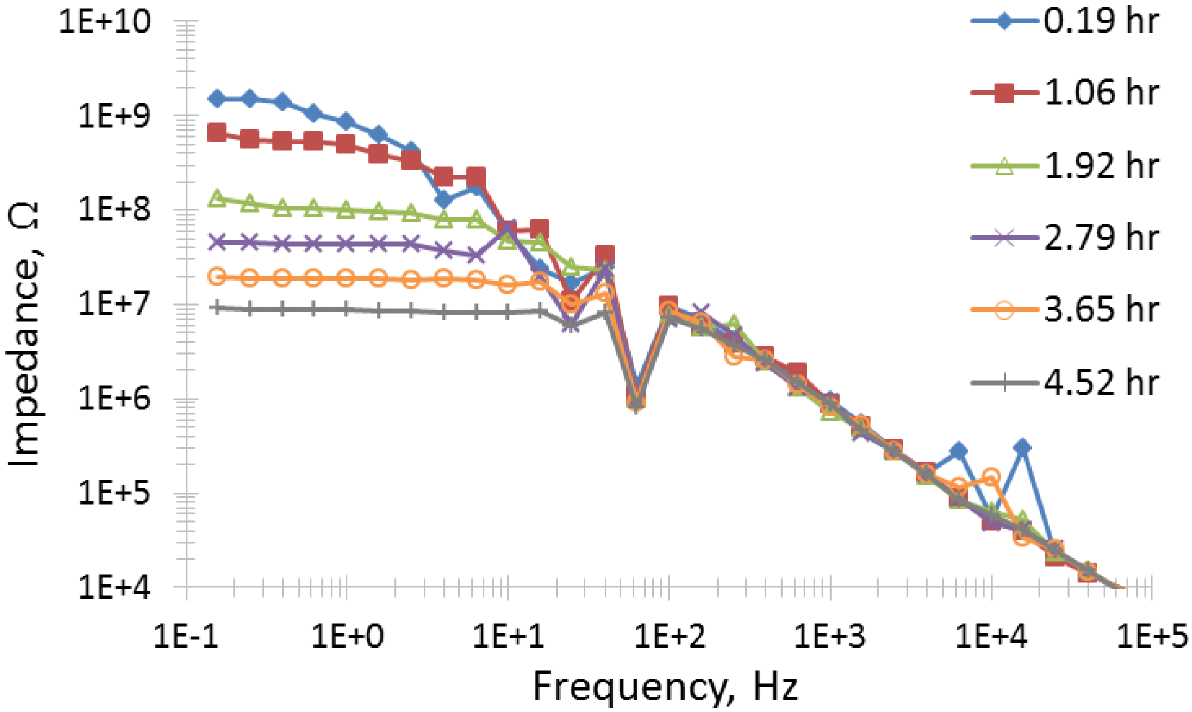

Figure 57. Impedance characterization of the barrier properties for a coating with solvent borne primer at the beginning of Cycle B using the Au IDE.

The changes of the coating ionic conductances in response to the RH cycling were observable in real time using the Au IDE sensor. Both the solvent borne primer and water borne primer coating systems had conductance that varied with RH (Figure 58). Periods of high coating conductance corresponded with periods of high humidity and periods of low conductance corresponded with periods of low humidity. The periodicity of the coating systems remained apparent but became less clearly resolved after 50 – 100 hours for Cycles A and B or 500 – 600 hours for Cycle C. The water borne primer had a larger change in conductance with RH as compared to the solvent borne primer for each of the three Cycles. The coating systems did not reach steady state conductivities for the short RH steps of Cycles A and B, however, both coating systems reached steady state conductivities in Cycle C. If thorough drying or wetting of the coating system is required to initiate or accelerate coating failure modes observed in the field, the test cycle should include dry or wet steps that are long enough for the conductivity of the coating to approach steady state values.

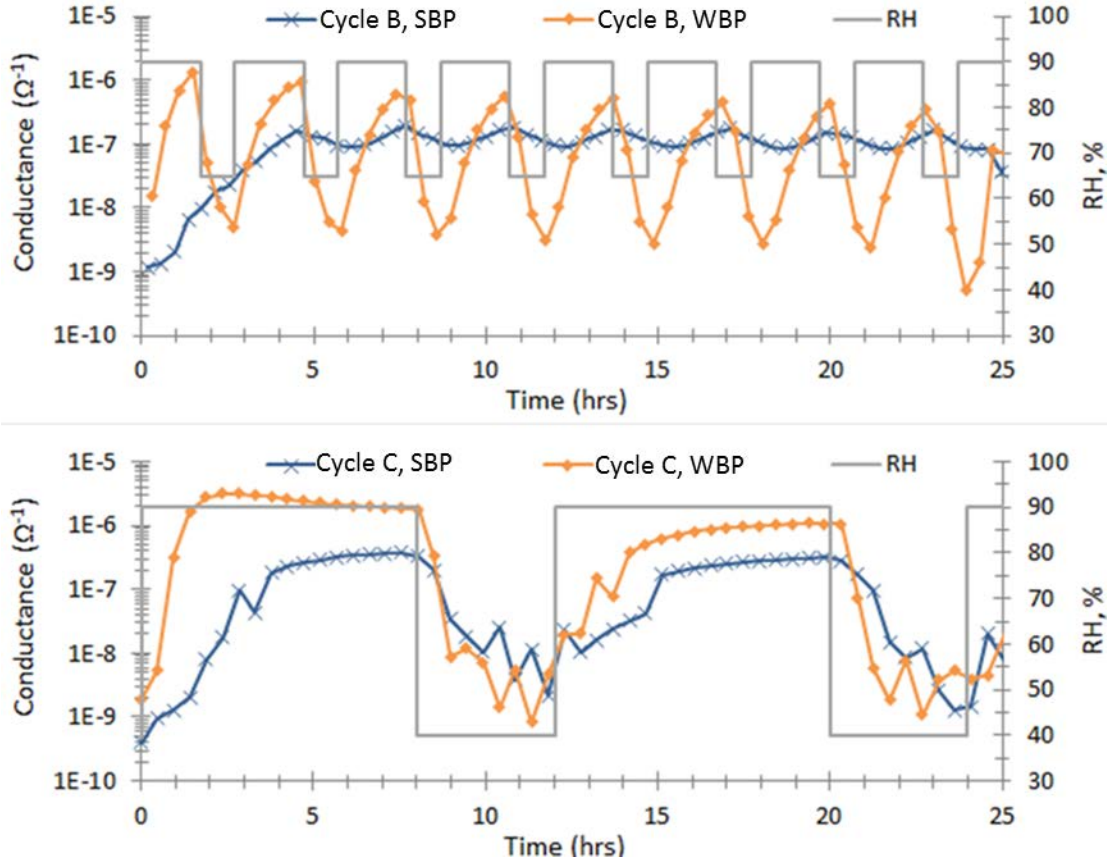

Figure 58. Conductance of the coating systems with solvent borne and water borne primers on the Au IDE at the beginning of Cycle B.

The conductance can be integrated with time to obtain a cumulative measure of coating barrier properties. The water borne primers had a greater cumulative conductance (lower barrier properties) than the solvent born primers for all three cycles (Figure 59). The larger range of conductances with humidity cycling indicates that the water borne primer has much greater moisture sensitivity than the solvent borne primer. The variation in conductance was higher Cycle A testing as compared to Cycle B, for both coatings, due to the higher minimum RH of Cycle B. The greatest conductivities occurred for Cycle C because the longer times of wetness at high humidity allowed the conductivities to approach maximum steady state values in. The sharp increases in conductivity observed around 1,300 hours in Cycle C may indicate adhesion loss of the solvent borne primer over the Au IDE conductivity sensor (Figure 59c). Note that the loss of adhesion on the Au IDE conductivity sensor, which is based upon vapor deposited gold electrodes on alumina substrates with a nominal surface roughness of 35 microinches, may not directly correlate to loss of adhesion on AA7075-T6 surfaces.

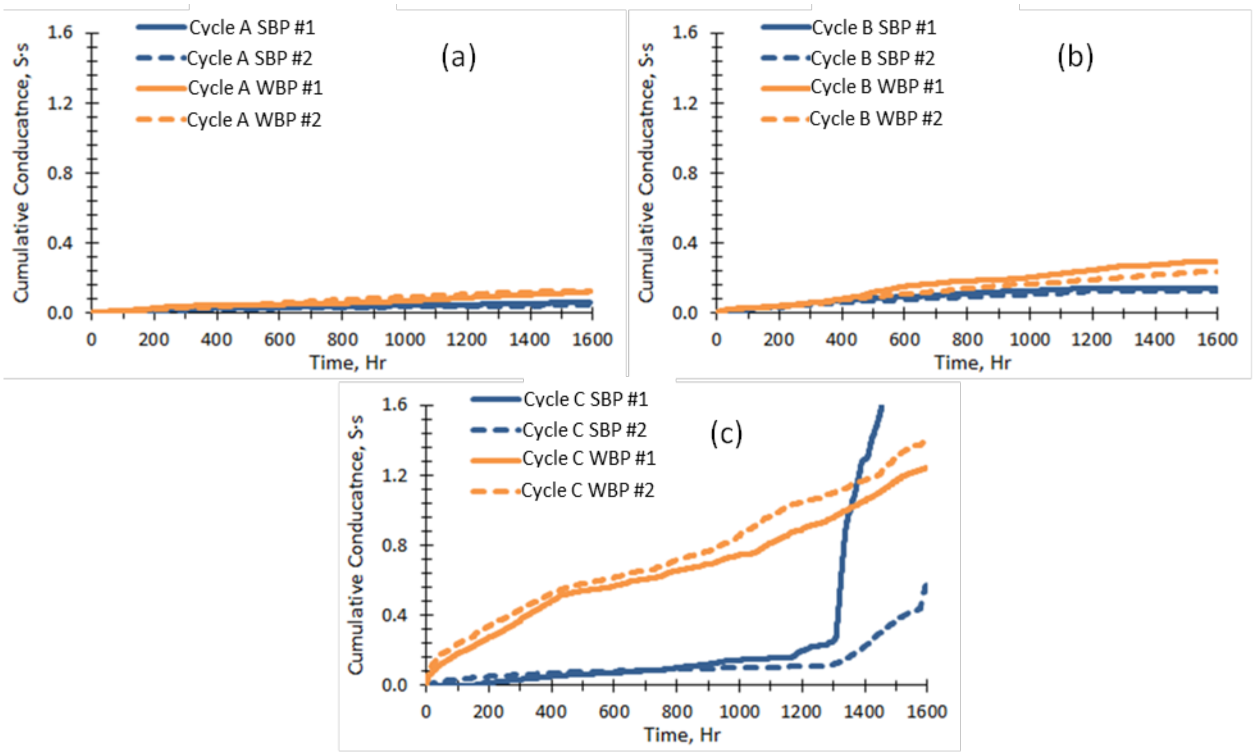

Figure 59. Cumulative conductance of the solvent borne primer (SBP) and water borne primer (WBP) in duplicate (#1 and #2) on the Au IDE sensor during (a) Cycle A, (b) Cycle B, and (c) Cycle C.

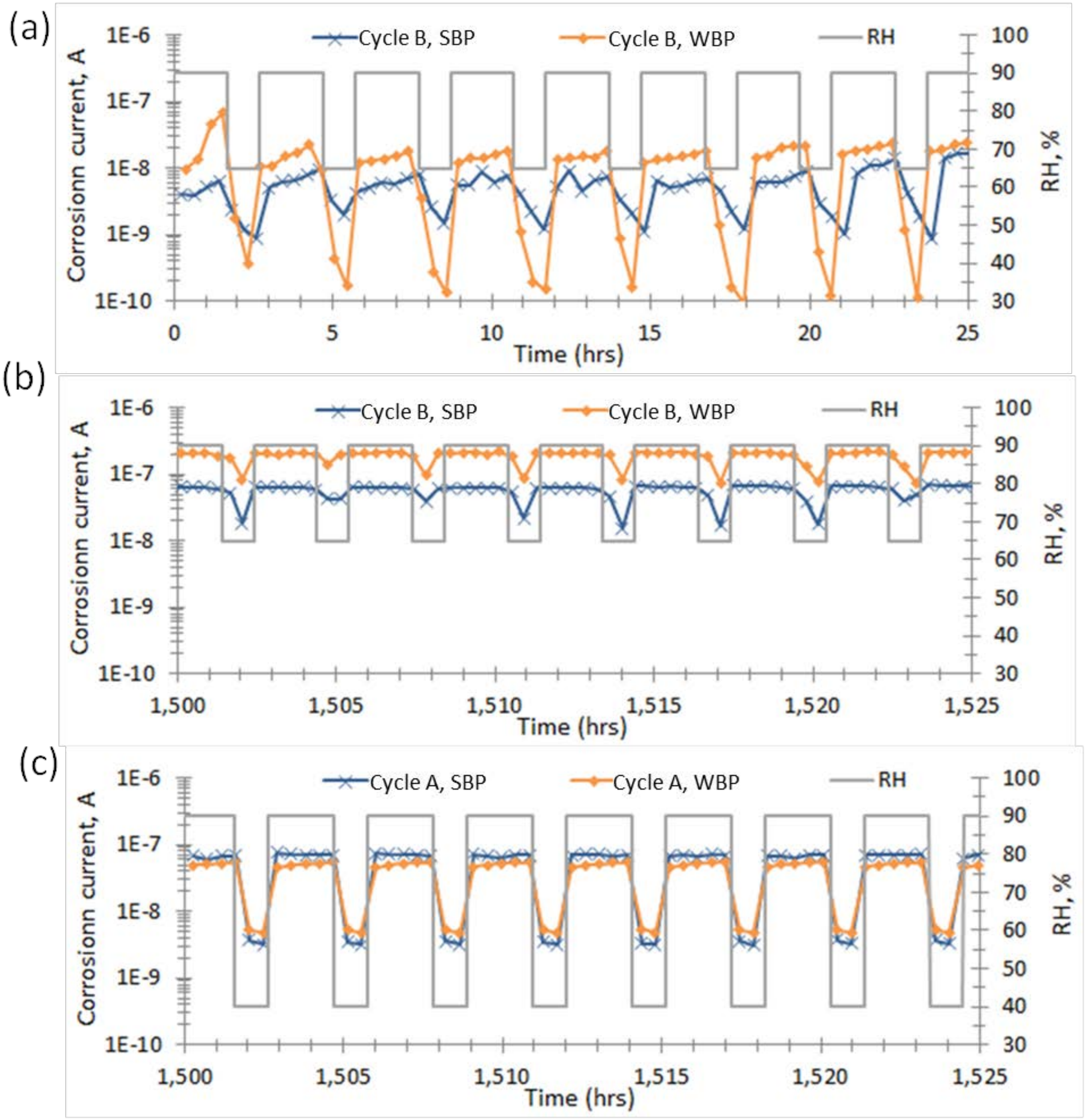

Figure 60. Corrosion current of the scribed coating systems with solvent borne primer and water borne primer on the Al IDE free corrosion sensor at the beginning of Cycle B (a), after 1,500 hours of Cycle B (b), and 1,500 hours of Cycle A (c).

4.2.5.2 Effects of RH cycling on AA7075-T6 free corrosion

The changes in AA7075-T6 free corrosion rates for the coated and scribed Al IDE sensors in response to the RH cycling was measured throughout the test. The impedance at 1 Hz was selected to represent the R_p of equation (1) because the impedance typically became constant for frequencies less than 1 Hz. The corrosion of the scribed Al IDE sensors with both solvent borne and water borne coating were dependent on RH (Figure 60). For Cycle B, the AA7075-T6 free corrosion currents during dry conditions were relatively low at the beginning of the test cycle while only small decreases in current were observed during the dry conditions after 1,500 hours. In comparison, the relatively large decreases in current density were still observed for the dry conditions in Cycle A after 1,500 hours. The AA7075-T6 underneath regions of coatings that have lost adhesion near the scribe may take longer to dry than at the scribe itself. Also, aluminum oxide and hydroxide corrosion byproducts are hygroscopic and are expected to accumulate in the Al IDE sensor scribes during the course of the test cycles. The development through time of either coating adhesion loss or hygroscopic aluminum corrosion byproducts may enable the relatively high corrosion rates during the Cycle B dry conditions by suppressing the drying of the sensor exposed around the scribe at 65% RH in comparison with 40% RH.

The cumulative corrosion rates of the water borne and solvent borne primers were lower for Cycle A than for Cycle B and Cycle C (Figure 61). The corrosion rates accelerated with exposure time for Cycle B and Cycle C yet remained relatively constant for Cycle A.

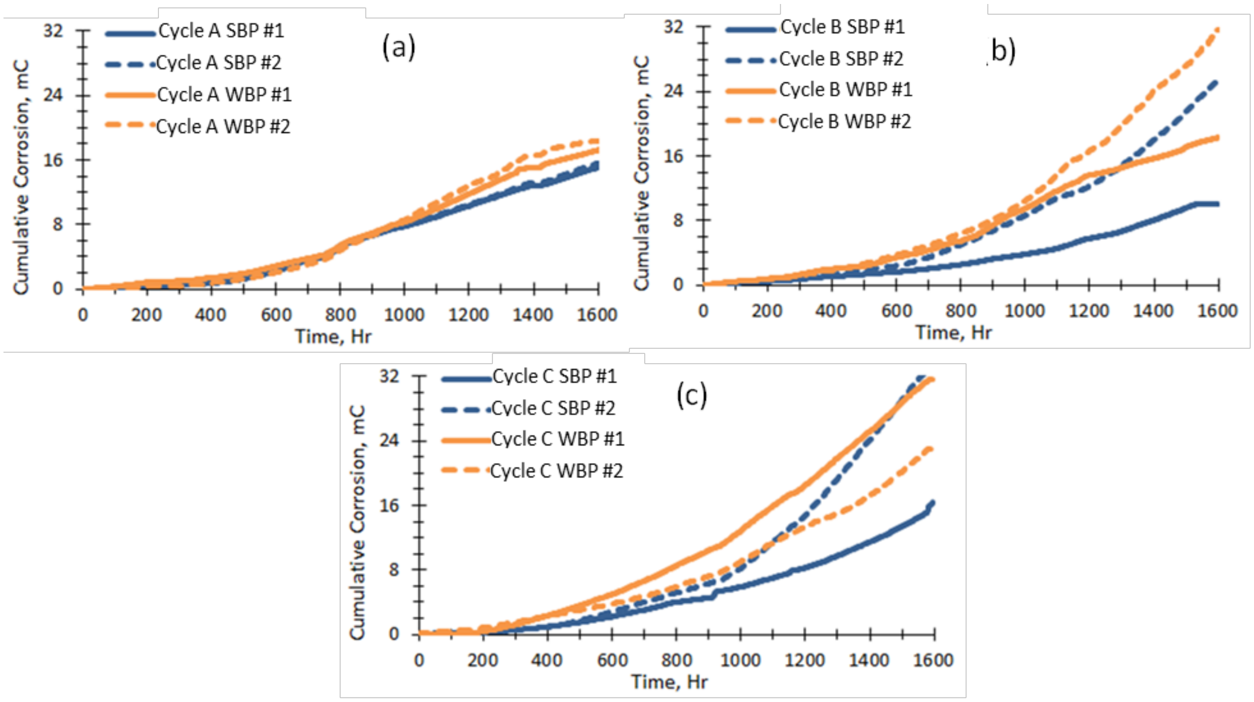

Figure 61. Cumulative corrosion of Al IDE sensor with scribed solvent borne primer (SBP) and water borne primer (WBP) in duplicate (#1 and #2) on the Au IDE sensor during (a) Cycle A, (b) Cycle B, and (c) Cycle C.

4.2.6 *Effects of RH cycling on galvanic corrosion*

The Al/SS IDE sensor measured galvanic corrosion between AA7075-T6 and SS316 throughout the tests. The 30 second interval between ZRA measurements provided a greater resolution in time than the multiplexed impedance sensors. The greater time resolution is more useful for determining environmental interactions that occur during the RH cycling. For example, the early galvanic corrosion rates cycle track the RH conditions (Figure 62). This simple dependency changes at longer exposure times where high current transients develop during humidity transitions or drying and wetting (Figure 63). These high galvanic current transients at RH transitions occurred on both coating systems. The development of the larger currents during the drying step is thought to be associated with adhesion loss and creep back at the scribe. The high galvanic current transients during drying began between 900 and 1,100 hours for Cycle A, between 150 and 250 hours for Cycle B, and between 550 and 650 hours for Cycle C. Even though the Cycle A conditions resulted in the longest times for coating adhesion loss to initiate, the greatest galvanic corrosion rates in any of the test cycles occurred in Cycle A after the initiation of coating adhesion loss around 900 and 1,100 hours. The cumulative galvanic corrosion rates were significantly greater for Cycle A than for Cycle B and Cycle C because of the high galvanic corrosion rates that occurred after the initiation of coating adhesion loss.

There was no statistically significant difference between the performance of the water borne and solvent borne primers for the three different cycles when comparing the cumulative corrosion of the galvanic sensors (Figure 64).

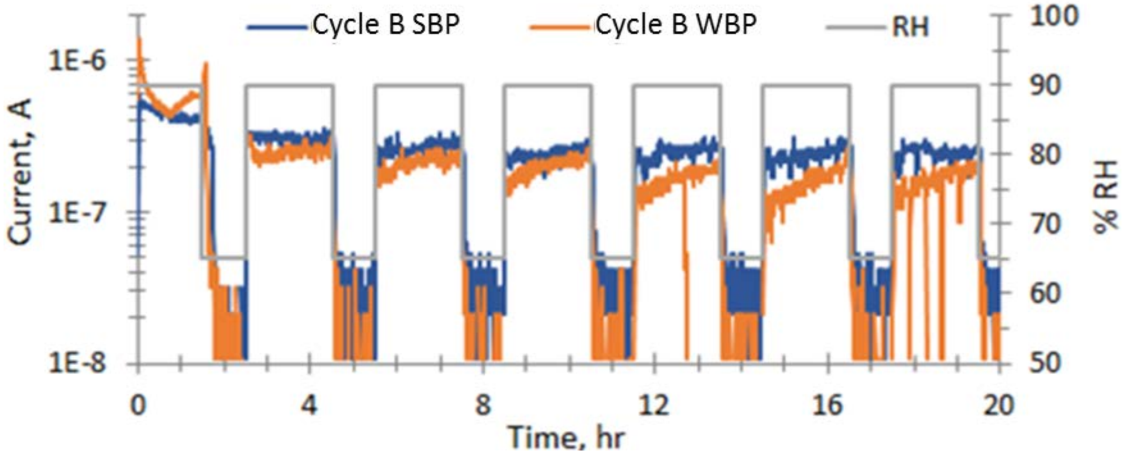

Figure 62. Galvanic corrosion of Al/SS IDE sensor with scribed solvent borne primer and water borne primer coating systems during Cycle B.

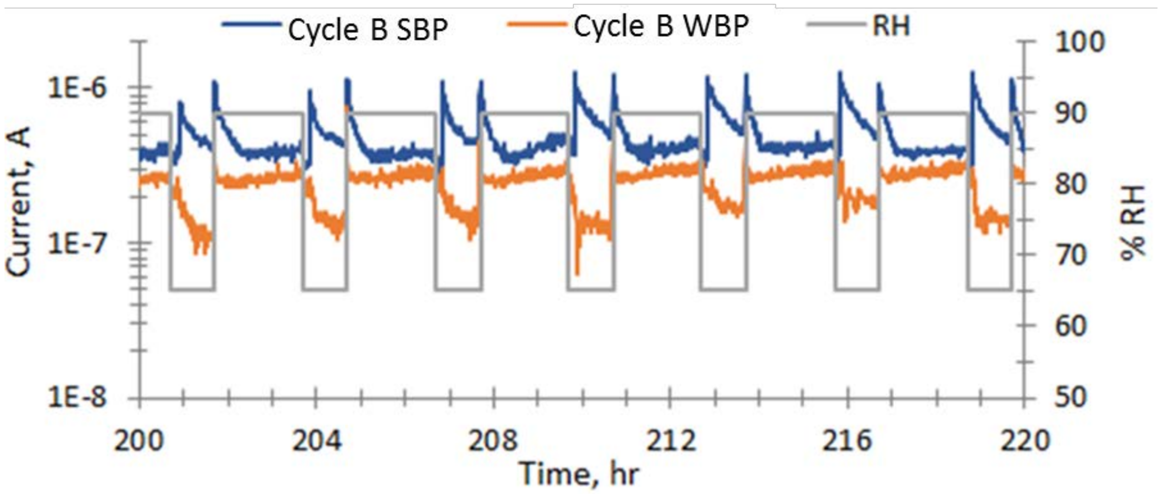

Figure 63. High galvanic corrosion rate transients develop during the drying steps after about 150 – 250 hours in Cycle B testing. The Al/SS IDE sensors with scribed solvent borne primer and water borne primer coating systems developed relatively high galvanic currents at the low humidity step around during Cycle B.

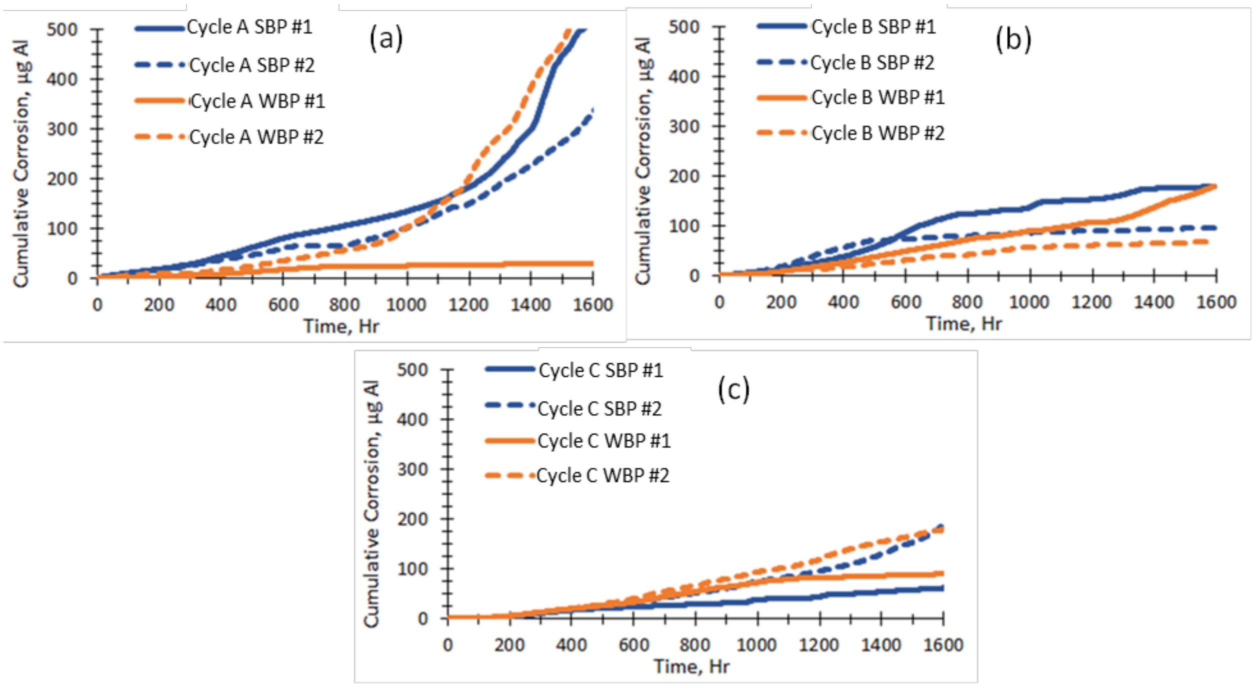

Figure 64. Cumulative corrosion of the galvanic Al/SS IDE sensors with scribed solvent borne primer (SBP) and water borne primer (WBP) in duplicate (#1 and #2) on the Au IDE sensor during (a) Cycle A, (b) Cycle B, and (c) Cycle C.

Together, the results of the three corrosion sensors throughout the three atmospheric test cycles indicate that some conditions are more severe for initiation coating adhesion loss while other conditions are more severe for further accelerating corrosion after the initiation of adhesion loss. The sensors indicated that Cycle B did not fully reach dry conditions because the minimum RH was 65% RH instead of the 40% RH minimum of Cycles A and C. The sensors also indicated that the 8 hour period at 90% RH was long enough to fully wet the coating systems during Cycle C but the 2 hour period at 90% RH was not long enough to fully wet the coating systems in Cycle A and Cycle B. Cycle A therefore represented relatively dry conditions while Cycle B and Cycle C were relatively wet. The initiation of coating adhesion loss was relatively faster for Cycle B and Cycle C than for Cycle A according to the Al/SS IDE galvanic corrosion sensor. Coating adhesion loss could increase corrosion rates by increasing the surface area of metal exposed to the electrolyte. The persistence of wet regions underneath unadhered coatings during dry periods could also increase corrosion rates. The Al IDE free corrosion sensor responses were consistent with these two effects of coating adhesion loss for both Cycle B and Cycle C. The Al IDE and SS/Al IDE corrosion rates may have been generally the higher for the first 1,000 hours of Cycle B and Cycle C than for Cycle A due to the early initiation of adhesion loss for these two wetter cycles. The greatest galvanic corrosion rates occurred for Cycle A after the initiation of coating adhesion loss at around 1,000 hours on the SS/Al IDE. It was not apparent that coating adhesion was ever lost for the Al IDE for Cycle A. These results indicate that the most aggressive conditions for both initiating coating adhesion loss <u>*and*</u> accelerating corrosion would be to integrate Cycle A with either Cycle B or C.

4.2.7 *Witness coupon analysis*

4.2.7.1 <u>Mass loss and scribe creep</u>

Mass loss coupons and standard test panels were included in the RH cycle experiments to provide more conventional measures of damage state. The three sets of six mass loss coupons and three sets of standard test panels were pulled from the environmental chamber at 450, 905, and 1,320 hours (Figure 65). The mass loss corrosion rate effects were qualitatively similar to the Al/SS IDE galvanic sensor measurements with regards to coating system performance as well as the relative corrosion rates for the three test cycles. The corrosion rates were typically greater for the water borne primer coating system than for the solvent borne primer coating system except for Cycle C (Figure 66). The corrosion rates for the AA7075-T6 mass loss coupons with stainless steel fasteners were typically greater for Cycle A than for Cycle B and Cycle C, particularly towards the ends of the cycles. The aluminum corrosion rates of the mass loss coupons with stainless steel 316 fasteners were about 1,000 times greater than the Al/SS IDE galvanic sensor. In part, this is due to the uncoated area of the stainless steel fastener creating a much larger cathode to anode ratio on the coupons, relative to the galvanic sensors. The scribe creep in the standard test panels was characterized with ASTM D1654 and was typically greater for the solvent borne primer system (Figure 67, Table 6). Scribe creep was observed on the multisensor panels (MSPs) with more creep back on the Al/SS sensor than the Al IDE (Figure 68).

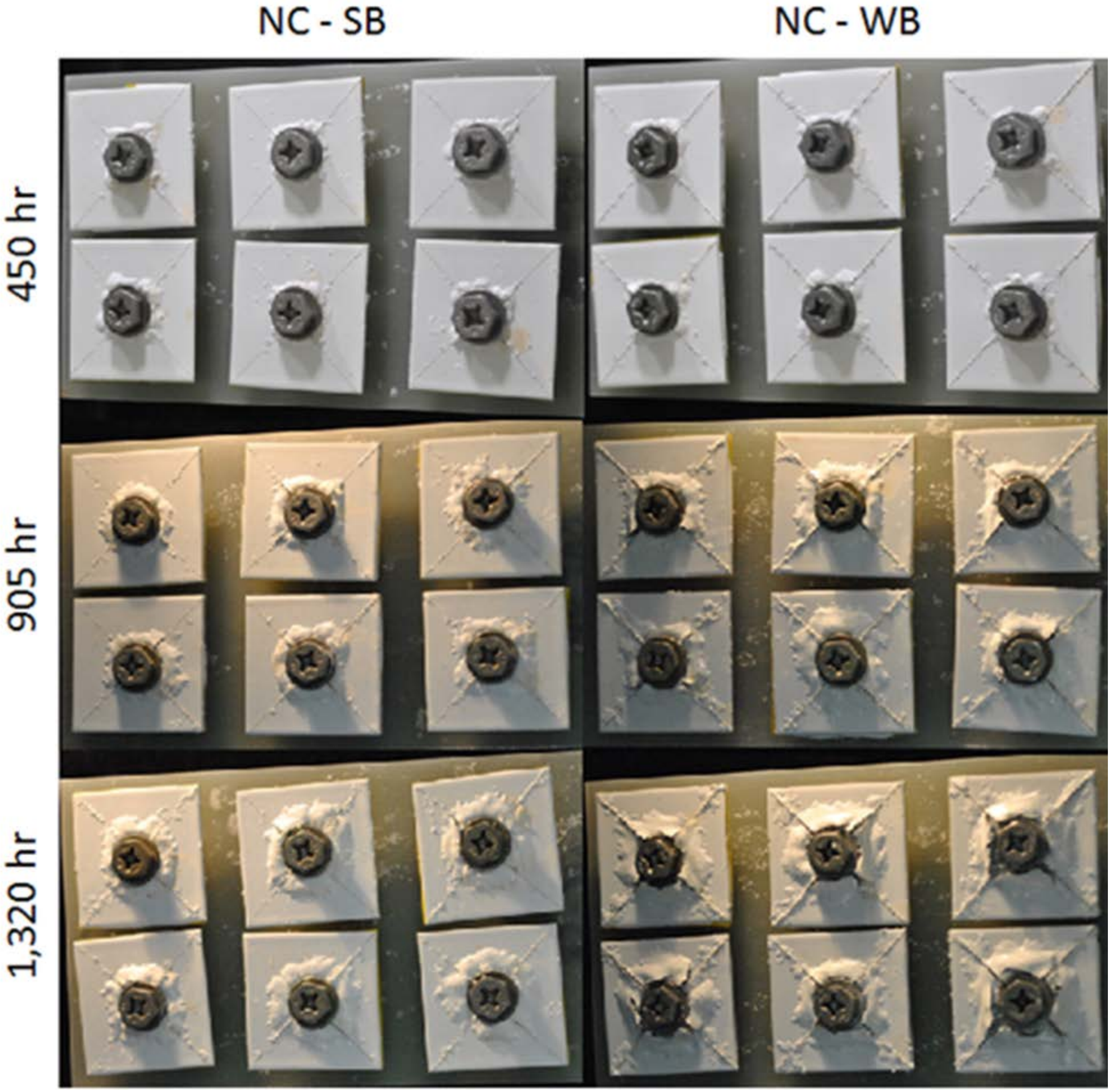

Figure 65. Photographs of the AA7075-T6 mass loss coupons with boldly exposed SS316 fasteners. The three sets of six mass loss coupons for both the non-chrome solvent borne (NC-SB) and non-chrome water borne (NC-WB) primer were pulled at the indicated times during cycle A.

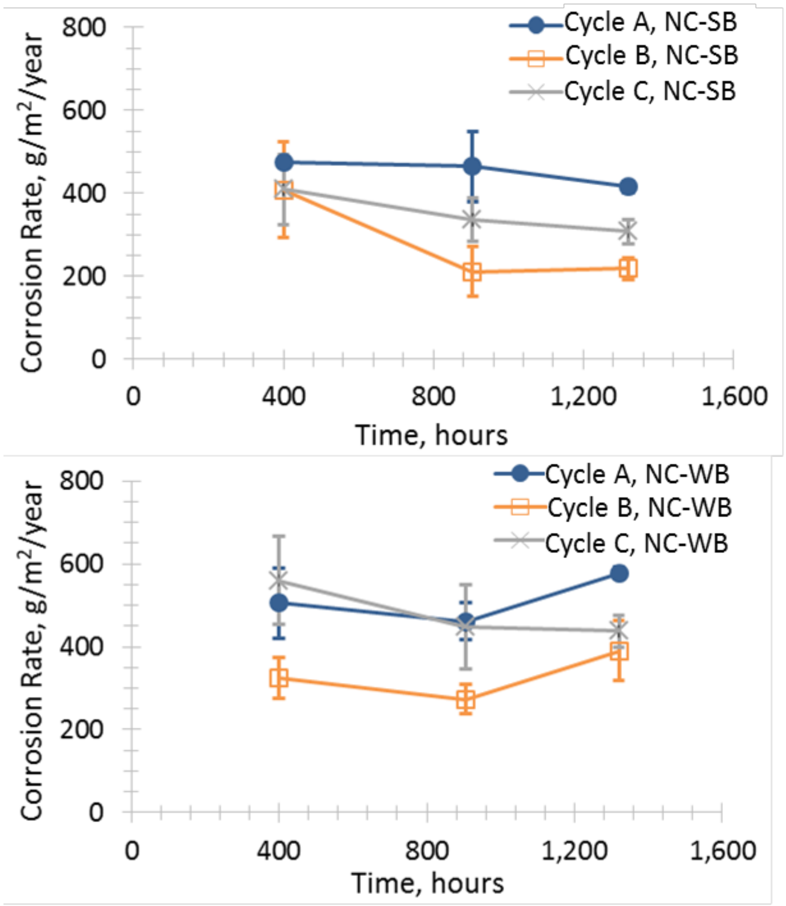

Figure 66. Aluminum corrosion rates determined from the AA7075-T6 mass loss coupons with boldly exposed SS316 fasteners. The mass loss measurements were performed in triplicate for both the non-chrome solvent borne (NC-SB) and non-chrome water borne (NC-WB) primer pulled at the indicated times during three cycles.

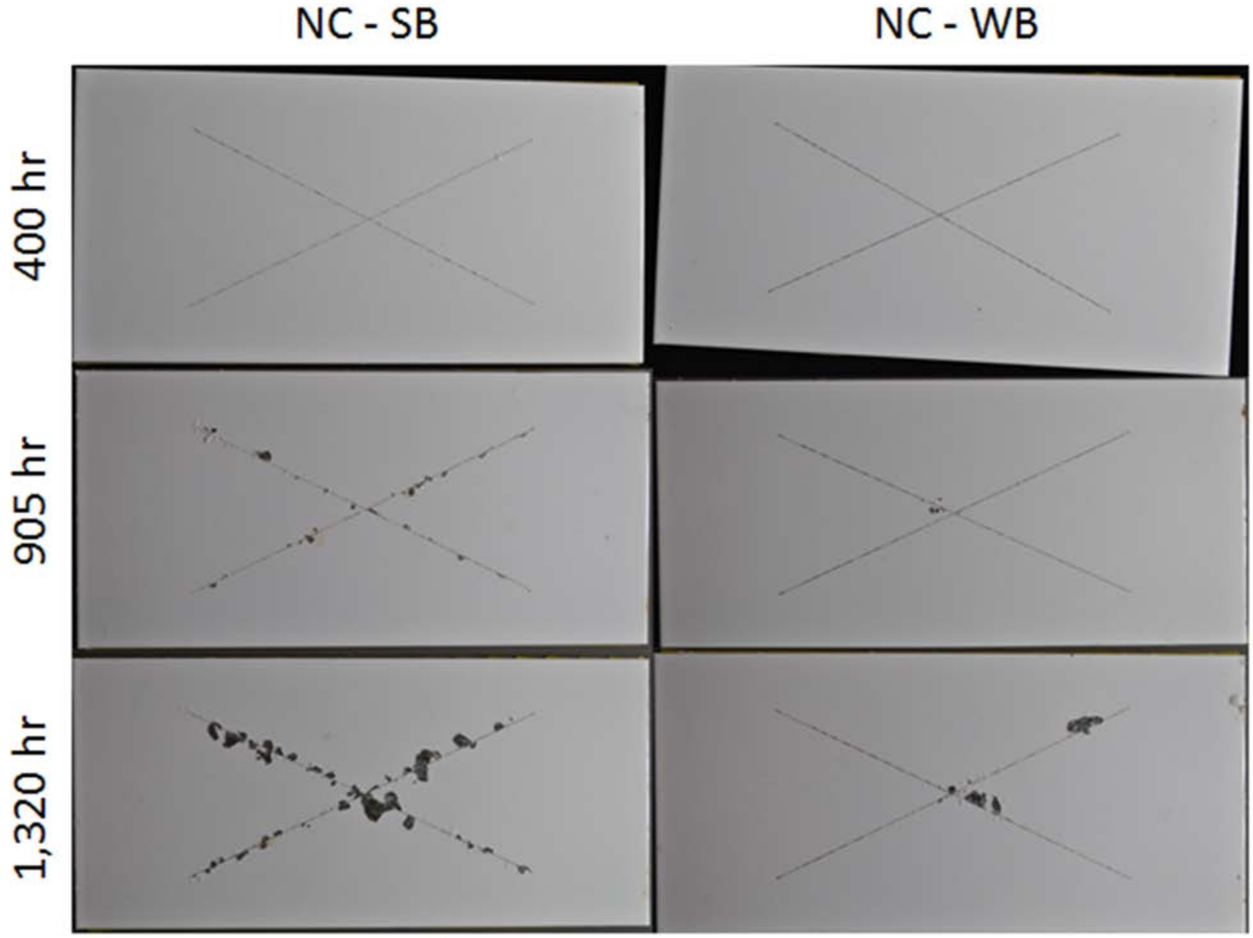

Figure 67. Photographs of AA7075-T6 standard test panels with the non-chrome solvent borne (NC-SB) and non-chrome water borne (NC-WB) primer pulled during cycle A after scribed creep analysis.

Table 6. Scribe Creep Analysis of the Standard Test Coupons (ASTM D1654).

Test Time	Coating	Min (mm)	Max (mm)	Ave (mm)	Rating	Blistering
400 hr	NC-SB	0	0.25	0.125	9	None
	NC-WB	0	0	0	10	None
905 hr	NC-SB	0	3	1.5	7	None
	NC-WB	0	1	0.5	9	None
1,320 hr	NC-SB	0	6.5	3.25	5	None
	NC-WB	0	4	2	7	Few, size 6

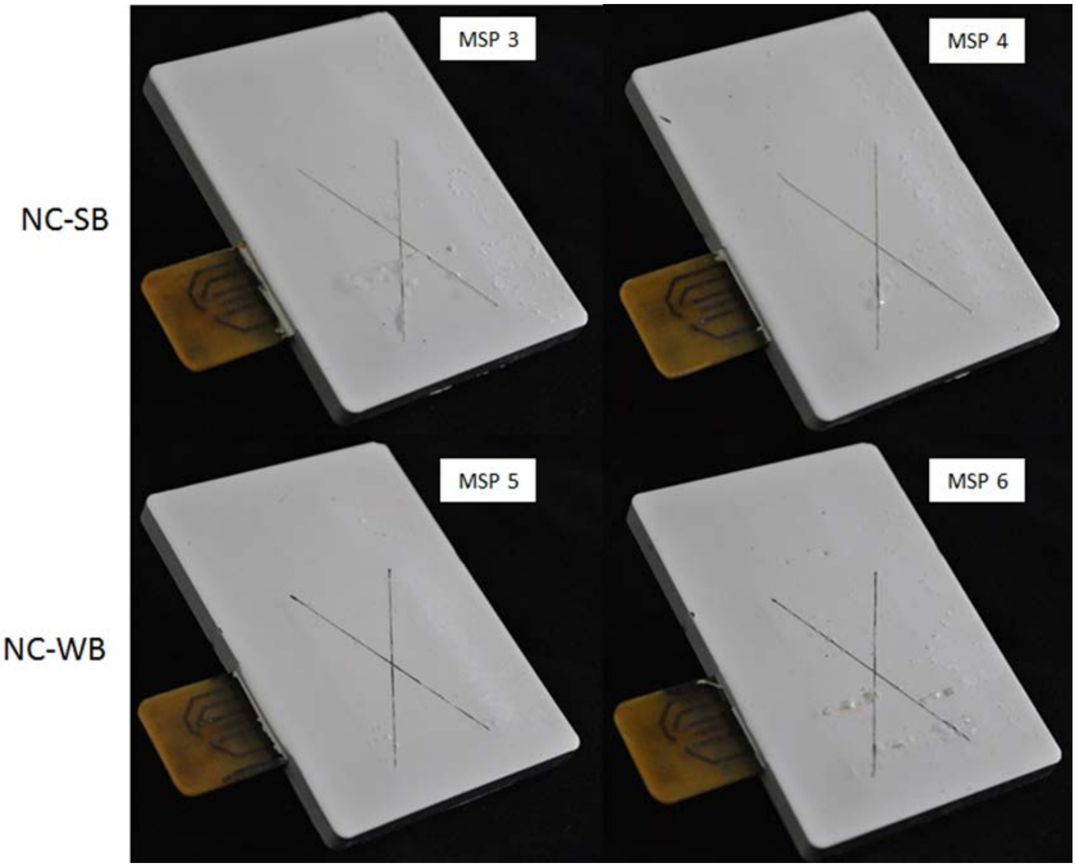

Figure 68. The multisensor panels with the non-chrome solvent borne (NC-SB) and non-chrome water borne (NC-WB) primer after 1,320 hours in Cycle A conditions.

4.2.7.2 Image analysis

The effect of the frequency of test cycles at constant total time of wetness was also evaluated using image analysis of the mass loss coupons. A subset of the mass loss coupons exposed to Cycles 1, 2 and 3 were sent to SwRI for image analysis using a Keyence macroscope. The analysis protocol was the same as for the lap joint samples described in Section 4.1.4.

The Keyence macroscope images of samples exposed in Cycles A, B and C for 450 hrs, 905 hrs, and 1320 hrs, respectively are shown in Figure 69 and Figure 70. The test coupons shown in Figure 69 were coated with water-borne primer, while the coupons in Figure 70 were coated with solvent-borne primer. Visual inspection of the test coupons revealed that the extent of corrosion increased for both the solvent-borne and water-borne primers as a function of exposure time. The test coupons coated with solvent-borne primer showed less damage than those coated with water-borne primer. The extent of drying and the frequency of the cycles both had a significant effect of the corrosion damage. Cycle A with higher cycle frequency and lower minimum RH caused shallower damage (less deep blue areas, which are indicative of deep corrosion damage) than either cycle B or C. Cycle C showed the deepest damage, indicated by deep blue areas in the WLI images.

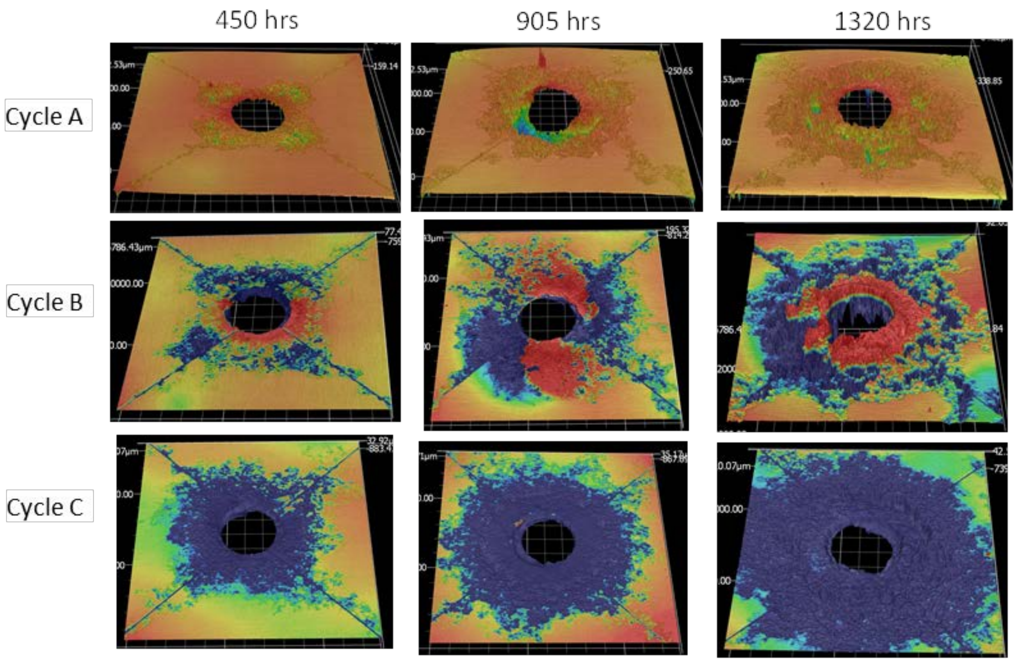

Figure 69. Representative images of test panels coated with water-borne primer exposed to three different test cycles. Samples were pulled for imaging at three different time intervals.

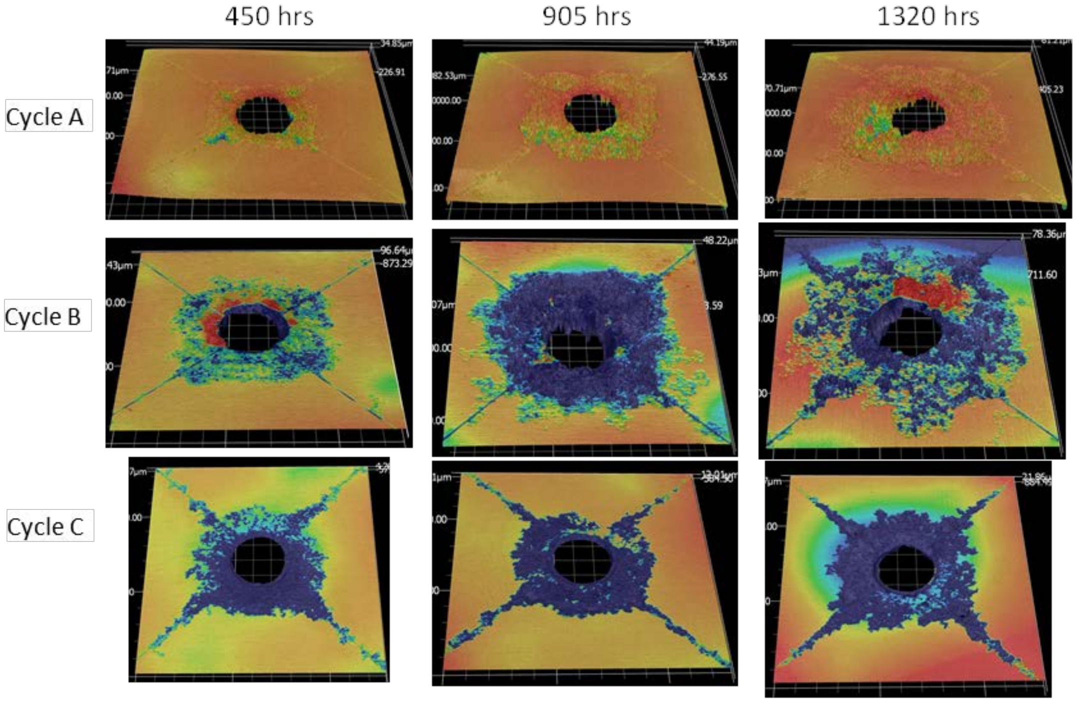

Figure 70. Representative images of test panels coated with solvent-borne primer exposed to three different test cycles. Samples were pulled for imaging at three different time intervals.

When comparing the images with photographs of the sample surfaces (Figure 71), several important features are discovered. The coupons exposed to cycle A show a very shallow damage that is restricted to the uppermost surface layer of the metal. In the case of Cycle B, exfoliation corrosion was found after 1320 hrs of exposure, which presents on the images as red areas, thus, areas above the reference plane. The exfoliation is believed to be due to heavy intergranular corrosion caused by the extended exposure to intermediate RH values (65%) and lack of drying below 50% RH. Extensive coating delamination and material volume loss are also observed in the Cycle B exposure. Under these conditions, creviced areas form under the coated surface in areas where the primer had delaminated. This leads to the development of aggressive chemistry and rapid corrosion in these areas. In Cycle C, the samples are exposed to high humidity for a longer time during each cycle, which allows for more sustainable corrosion process, leading to significant corrosion damage. Upon inspection of the samples exposed to Cycle C, deep corrosion trenches were found along the location of the fastener, as well as significant pitting. In some cases, pitting led to the formation of through-thickness holes as shown in Figure 72. No exfoliation was observed during Cycle C.

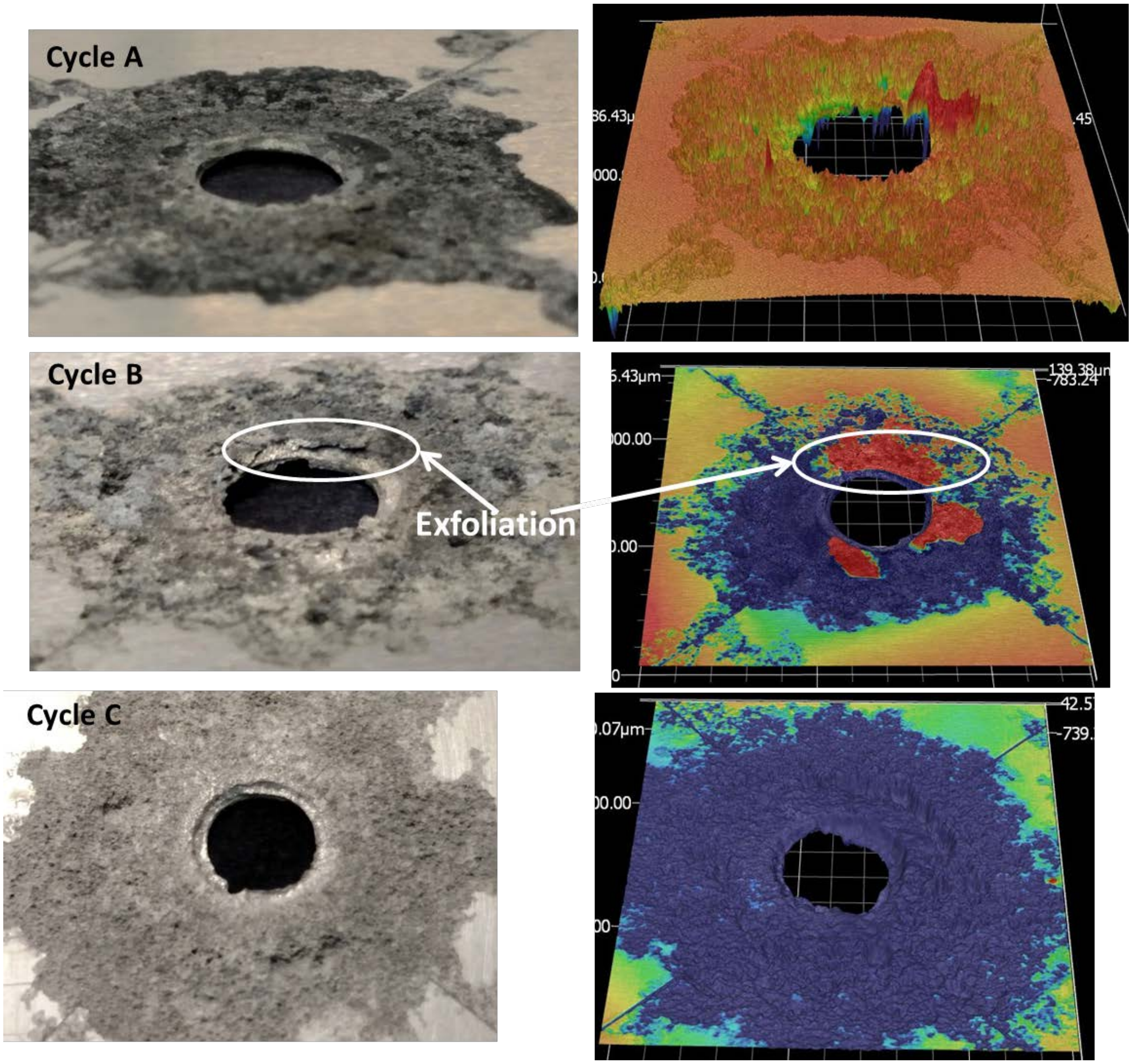

Figure 71. Photographs and 3D images of representative samples from each exposure cycle. The samples were coated with water-borne primer and exposed to the different cycles for 1320 hrs.

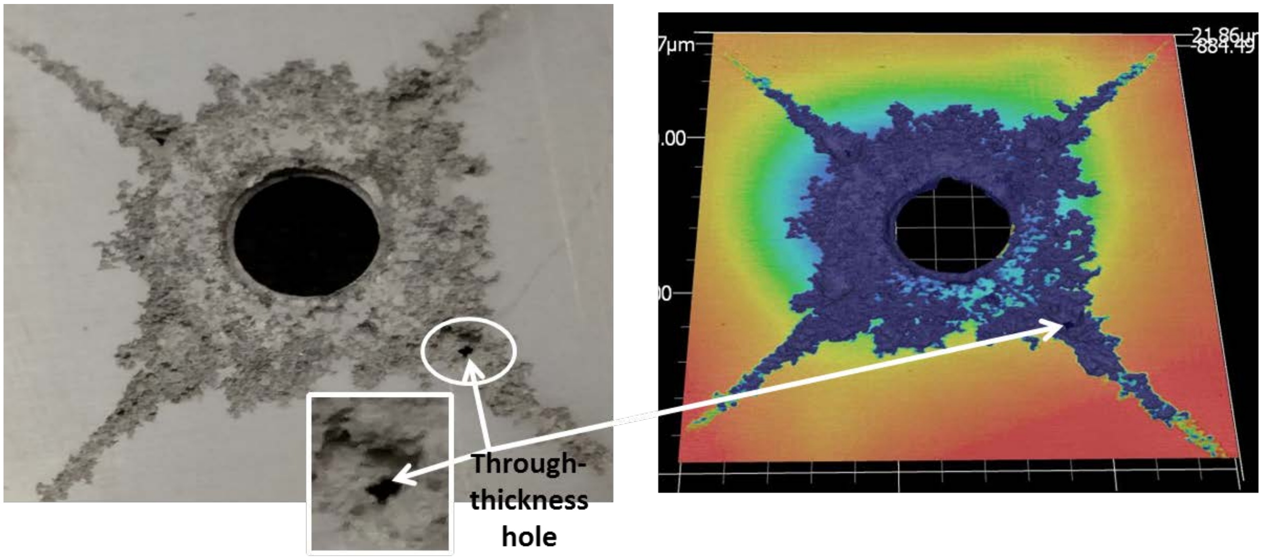

Figure 72. Photograph and 3D image of test coupon showing severe corrosion damage, including a through-thickness hole. The coupon was coated with solvent-borne primer and exposed to Cycle C for 1320 hrs.

In order to quantify the visual observations, several parameters were calculated from the Keyence macroscope images, including: (i) the percent of surface area corroded, (ii) the total volume loss, (iii) the maximum damage depth, and (iv) the average damage depth. These parameters were compared between the different exposure cycles and different types of coatings. The percent surface area corroded and volume loss and a function of exposure time for the different cycles in the case of water-borne and solvent-borne primers are shown in Figure 73. While the scatter between the datapoints is relatively large, as expected in the case of environmental chamber exposures, several trends can be observed. In agreement with the visual observations, cycle C is the most aggressive for both primers. While the percent area corroded appears to be lower in the case of cycle C, the depth of damage is significantly greater than in the case of cycles A and B. Cycle A is the mildest, especially when considering the volume loss, thus depth of damage. These parameters do not adequately capture the exfoliation observed in the case of cycle B (Figure 71), and the percent area corroded parameter does not account for the significant depth of damage in the case of cycle C. For example, for the solvent-borne primer, the percent area corroded is similar after 1320 hrs of exposure in the case of cycles A and C, while the volume loss is more than three times greater, due to the deep damage in the case of the solvent-borne primer in Cycle C.

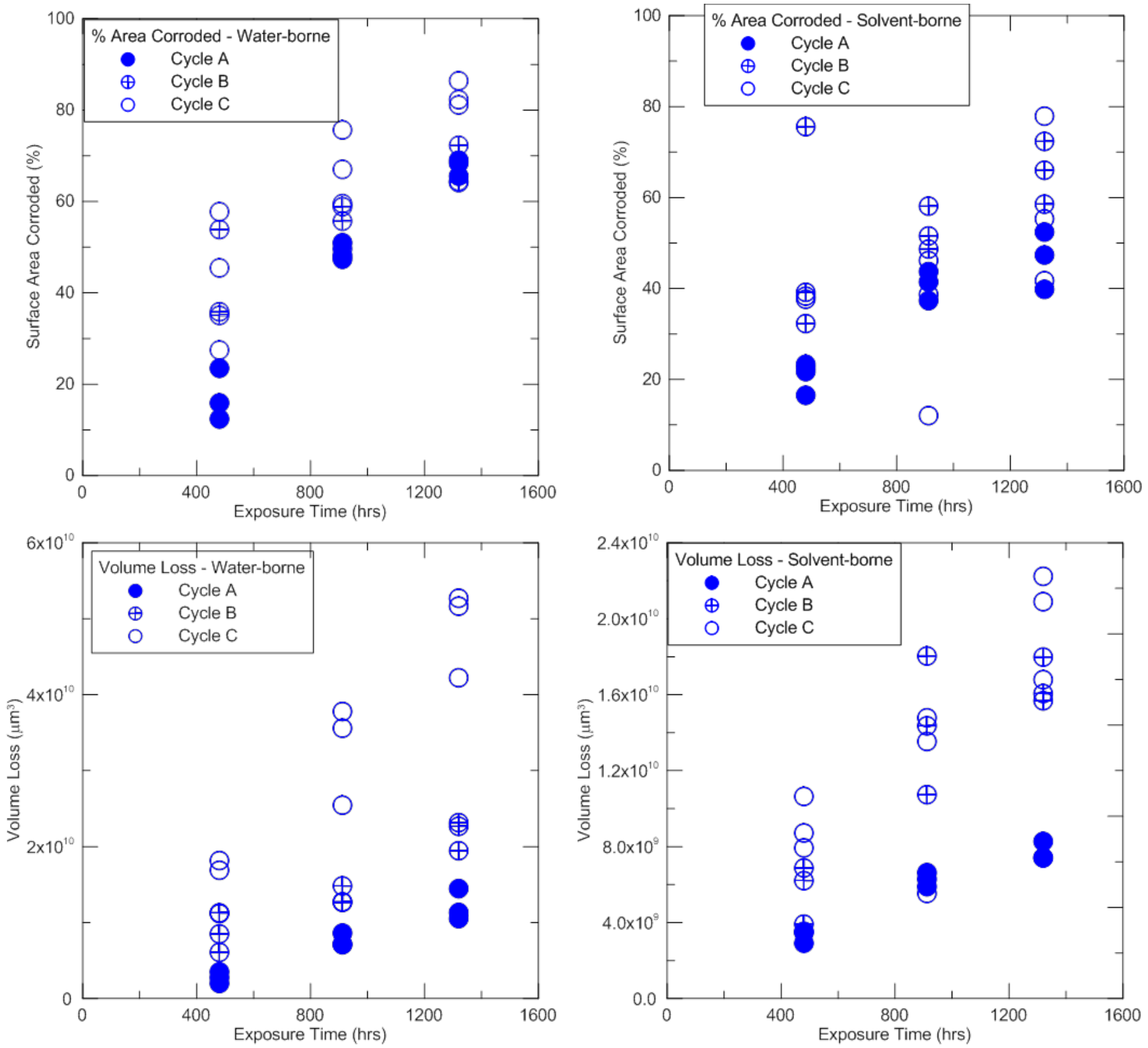

Figure 73. Percent surface area corroded and volume loss and a function of exposure time for the different cycles in the case of water-borne and solvent-borne primers.

The calculated maximum and average depths as a function of exposure time and exposure cycle for the different coating types are shown in Figure 74. The maximum depth was found to be constant as a function of exposure time and it did not distinguish between the performances of the coating types in the different cycles. The average depth, however, increased with exposure time for both coatings. Based on the average depth of attack, Cycle C was the most aggressive for both coatings, followed by Cycle B.

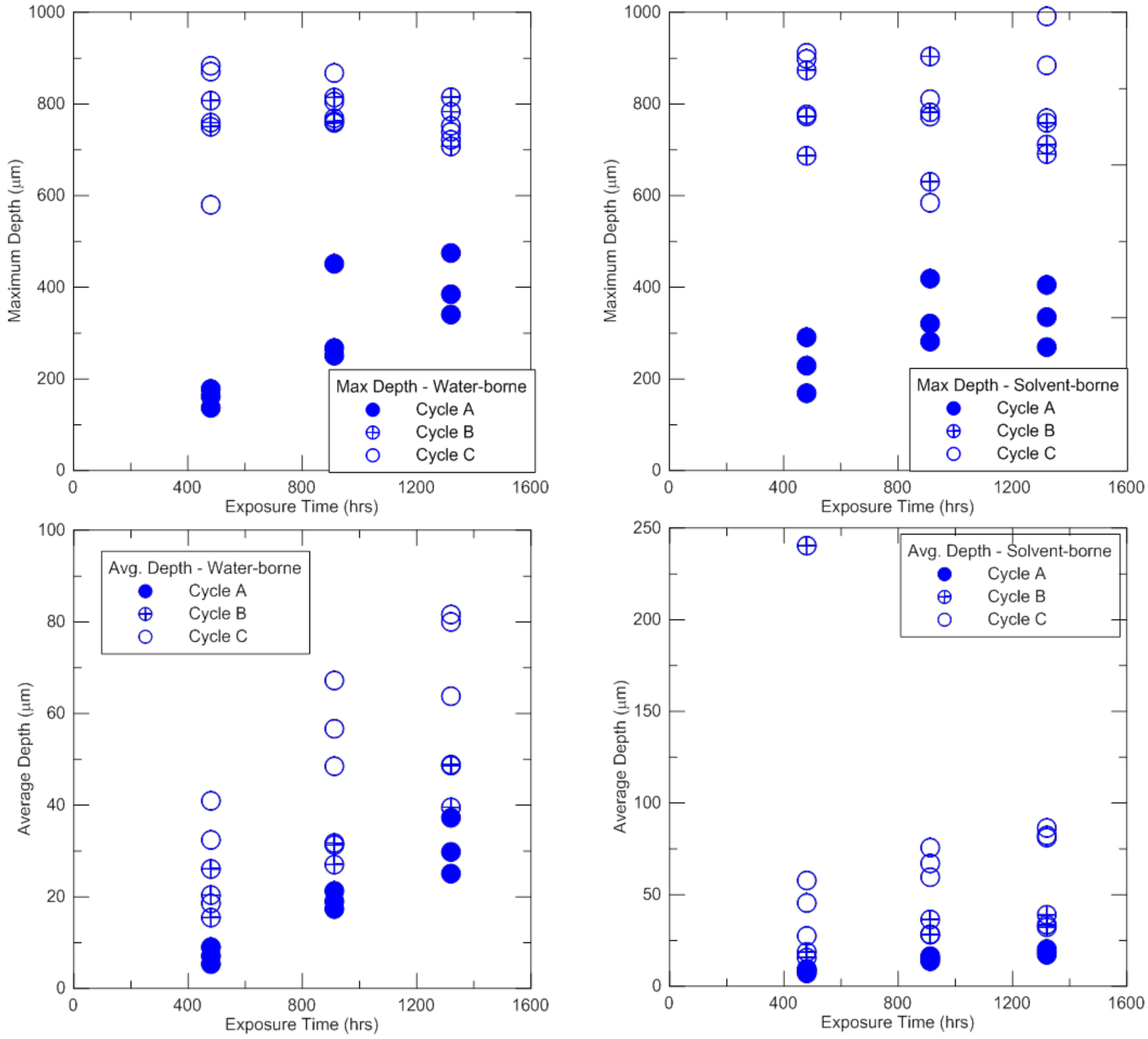

Figure 74. Maximum and average damage depths and a function of exposure time for the different cycles in the case of water-borne and solvent-borne primers.

The goal of the new accelerated exposure test is twofold: it must (i) identify coating degradation as performance function of time and (ii) differentiate various coating systems in performance evaluation tests. When the two primers are compared in the three investigated cycles as a function of corroded surface area and volume loss as the two investigated parameters, Cycles A and C appear to meet both goals (Figure 75), while the performance of the two primers could not be distinguished in the case of Cycle B. Note, however, that the failure modes observed in Cycle A and Cycle C are different (exfoliation vs. bulk metal attack, respectively).

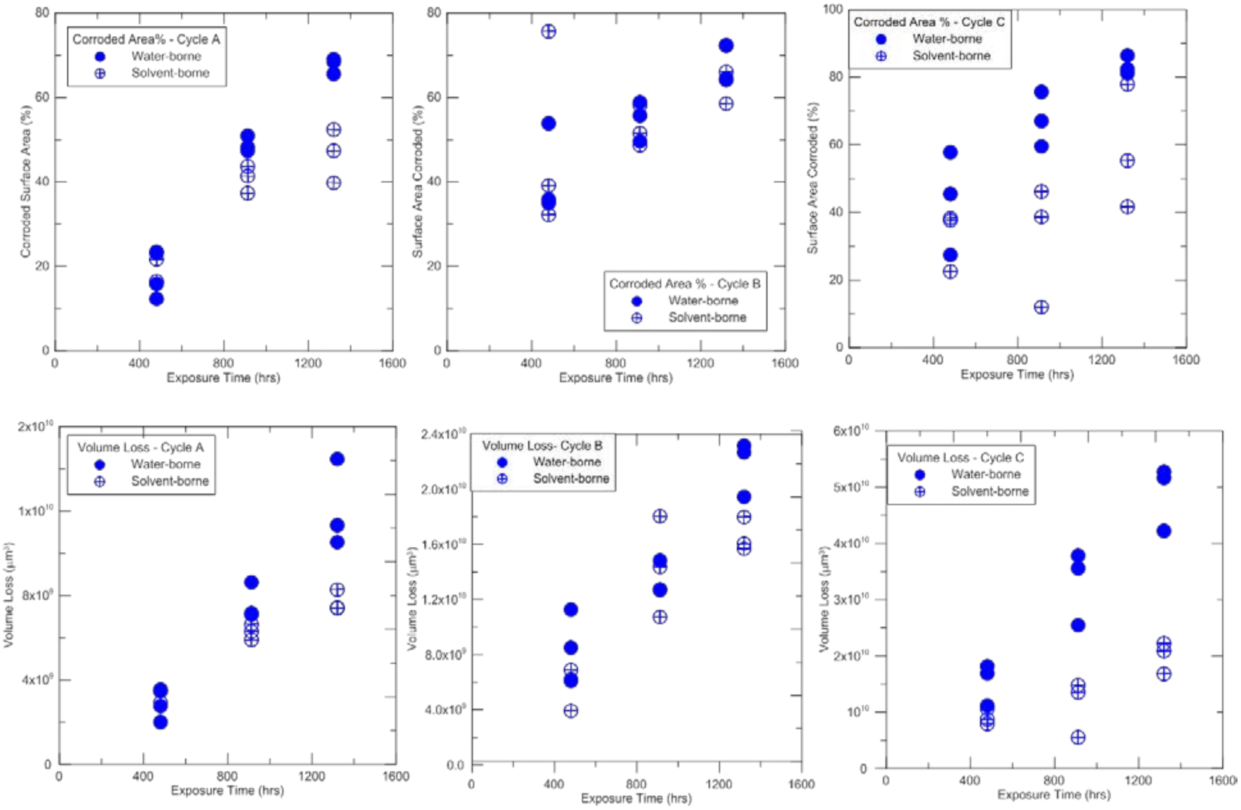

Figure 75. Corroded area and volume loss as a function of exposure time for samples coated with water-borne and solvent-borne primers and exposed to Cycle A, B, and C.

CHAPTER 5
EFFECT OF RH ON CORROSION AT COATING DEFECTS

The effect of RH on the release of corrosion inhibitors from the primers at coating defects is investigated in this chapter. The inhibitor release is an important feature of primers that prevent corrosion along coating defects, and the new accelerated test method needs to be able to capture this phenomenon. In this Chapter, multi-electrodes array studies are performed to demonstrate the effect of RH on corrosion in galvanic couples during exposure. Key RH regimes are identified that are critical to induce relevantnt failure modes during laboratory testing.

5.1 Materials and Methods

The MEA described in Section 3.1.2.1 was coated with MIL-DTL-23377 Class C primer which was allowed to cure for four days. After the coating was cured, NaCl solution equivalent to 10 mg/m^2 loading was deposited on the surface and dried. The salt-loaded MEA was exposed to the RH ramps described in Section 3.1.2.2, while the currents of the individual electrodes were measured using the Scribner MMA multi-electrode array system.

In addition, an AA7075/316SS multielectrode array (MEA) probe was fabricated with 100 electrodes, each measuring 250 µm in diameter. The electrodes were placed in a 5 by 20 grid, with the first 5 columns (5 by 5 grid) made out of 316 stainless steel wires, and the other 15 columns (5 by 15 grid) made out of AA7075-T6 wires. The layout of these electrodes is shown in Figure 76a. In some cases, the MEA surface around the electrode was coated with MIL-DTL-23377 Class C or Class N primer and allowed to cure for four days (Figure 76b).

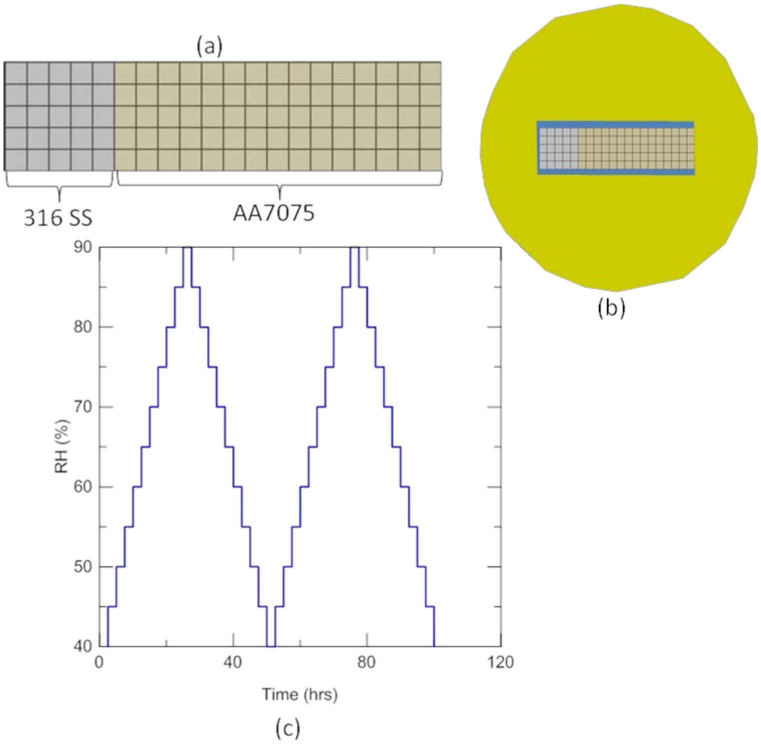

Figure 76. (a) Schematic of 316SS/AA7075 MEA; (b) MEA coated with MIL-STD-23377 primer; (c) RH profile of double ramp used in MEA work.

In order to investigate the behavior of the steel electrodes, the aluminum electrodes were masked with electroplaters tape. Similarly, to investigate the behavior of AA7075, the 316 stainless steel columns were masked. To investigate the coating properties on the galvanic couple, both the aluminum and steel electrodes were exposed. After masking and/or application and curing of the coating, NaCl solution was pipetted on the electrode surface and dried to achieve an even coating with approximately 100 mg/m^2 salt loading. The prepared electrodes were placed in a controlled RH chamber (Espec), supported face down. The RH was ramped from 40% to 90 %, then down to 40%, back to 90% and finally down to 40% in 5% increments, as shown in Figure 76c. Each step lasted 2.5 hours. The current on each electrode was measured and recorded using a Scribner MMA multi-electrode array system. These currents were then analyzed as a function of relative humidity.

5.2 Results and Discussion

5.2.1 *Single RH ramp of Al/Cu/Steel MEA*

First, the effect of the coatings on the MEAs was examined using the aluminum/copper/steel MEA in the single RH ramp exposure. To examine the effect of chromate corrosion inhibitors leached out of primers on the aluminum alloys, the steel-containing rows of the aluminum/copper/steel MEA were masked with the coating being examined, leaving only aluminum and copper electrodes (which simulate copper intermetallic particles). All anodic currents on the 50 exposed electrodes of the MEA were summed to generate the total anodic current passed by the MEA during testing. Additionally, the anodic charge passed during each humidity step was calculated from the anodic current. Due to its high reversible potential, the copper acted as a cathode throughout all MEA exposures. Thus copper current is not included in the anodic current totals.

Results from the aluminum exposures are shown in Figure 77 and demonstrate that the majority of anodic charge is passed during transitions between wet and dry conditions, particularly for the uninhibited case (labeled tape in the figures). The presence of chromate decreases the total current and total charge passed, particularly during the wetting and drying.

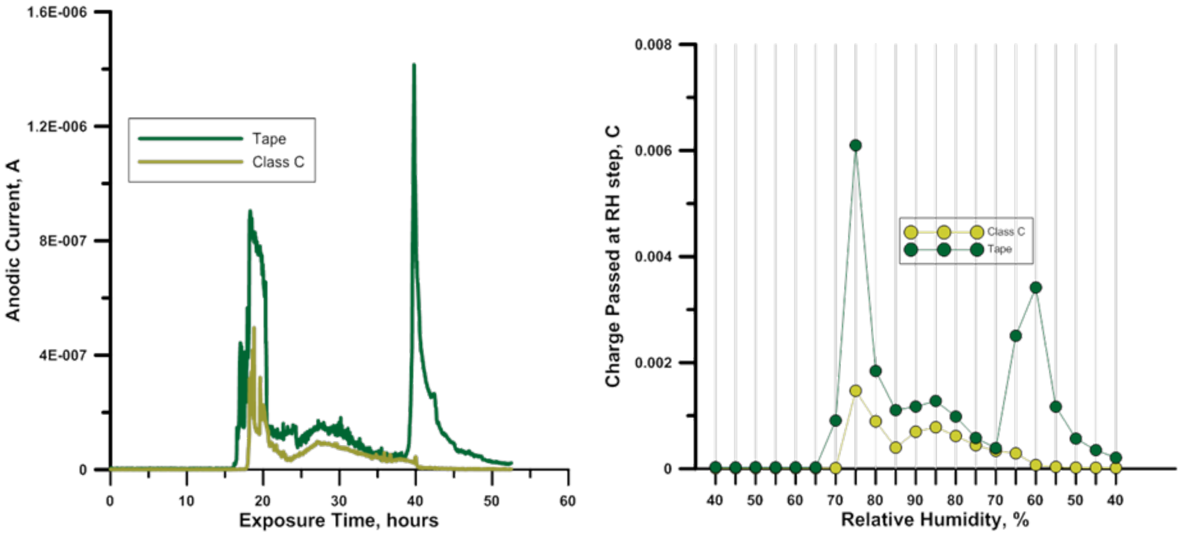

Figure 77. Anodic currents passed by aluminum electrodes during humidity cycle (left). Summed charges passed at each humidity step (right). The top five rows of the aluminum/copper/steel MEA were used during this testing.

Next, the effect of chromate inhibitors on steel was investigated using an all-steel MEA. In this case, a burst of current activity is observed near the deliquescence RH of NaCl on the upward ramp and near drying on the downward ramp, shown in Figure 78. However, unlike aluminum, more sustained corrosion is observed at high relative humidities. The presence of the chromate-containing primer decreases the charge passed during the initial wetting peak and the sustained corrosion at higher RH, but the effect of chromate is not as significant for steel as it appears to be for aluminum.

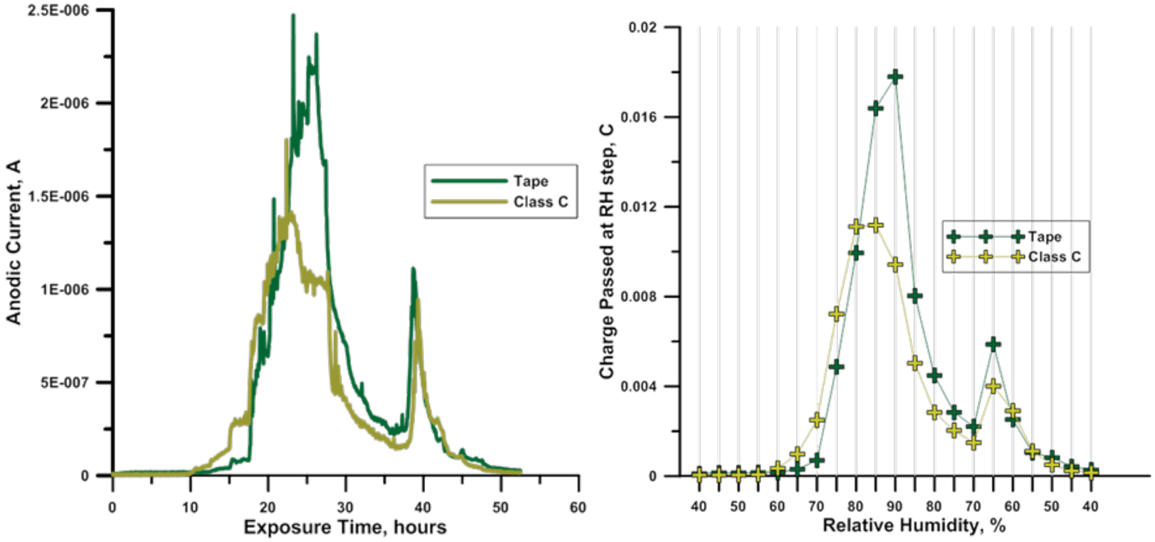

Figure 78. Anodic currents passed by steel electrodes during the humidity cycle (left). Summed charges passed at each humidity step (right). The all-steel MEA was used during this testing.

The behavior of the uninhibited galvanic electrode was discussed above in Section 3.2.2.2. Similar patterns of coupling and decoupling between the steel and aluminum electrode were observed for the inhibited multi-electrode array. As can be seen in Figure 79, which shows anodic currents on aluminum on the left and anodic currents on steel on the right, the steel is primarily cathodic (i.e. its anodic current goes to zero) during the high-humidity conditions where the aluminum anodic current is strongest. However, the comparison of the inhibited and uninhibited currents shows that the chromate does not appear to inhibit aluminum corrosion in the presence of steel. In this experiment, chromate appears to enhance the steel anodic current when steel and aluminum are coupled.

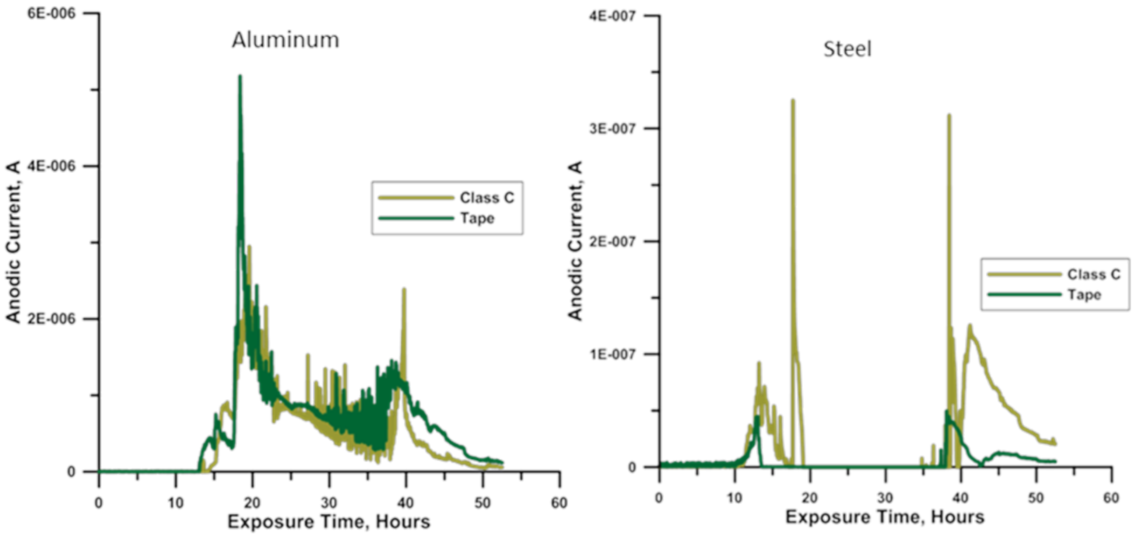

Figure 79. Anodic currents measured on the galvanic MEA during an RH ramp for aluminum (left) and steel (right).

One way in which chromate inhibitors are believed to inhibit corrosion in the case of AA2024 alloy is by preventing the cathodic reaction on the copper intermetallic particles that form during heat treating. By preventing the cathodic reaction from occurring, the galvanic interaction between the noble copper and the susceptible aluminum is disrupted, protecting the aluminum. The reduced effectiveness of chromate to reduce corrosion current on the steel electrodes provides evidence that the chromate is less effective at reducing cathodic currents on the steel compared with copper. Examination of the MEA diagrams in Figure 80 shows that the number of corroding electrodes is greater on the uninhibited array. In the presence of chromate, the number of overall corroding aluminum electrodes is reduced at distances far from the steel cathode consistent with the ability of chromate to slow cathodic currents on aluminum and copper. However, in the vicinity of the steel cathode, the reduced effectiveness of chromate to inhibit cathodic reactions on steel results in corrosion of aluminum electrodes.

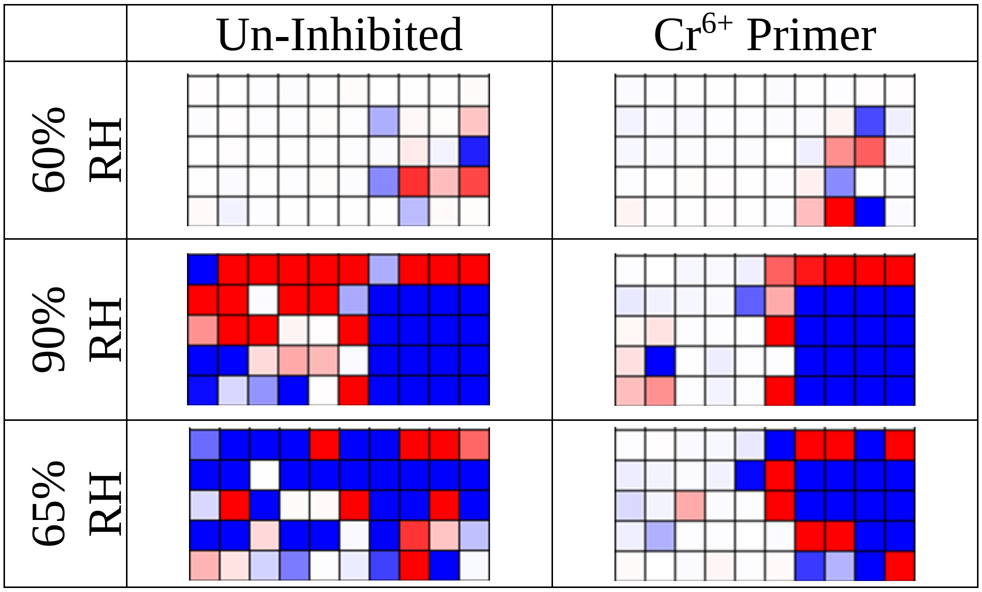

Figure 80. Comparison of the inhibited and uninhibited galvanic MEA at select values of RH during the humidity ramps. The sixteen steel electrodes are in the bottom right of the array. The top 5 rows were masked and are not shown here.

Above the deliquescence RH (DRH), chromate leaching from a coating was shown to significantly reduce the corrosion current on aluminum but was less effective at reducing the corrosion current on steel. In the case of a galvanic couple, corrosion of aluminum away from the couple interface was reduced. However, the leached chromate could not protect the aluminum in close proximity to the steel. Below the DRH, the corrosion current of aluminum decreases and the corrosion current of steel are observed to increase.

5.2.2 *Double RH ramp of AA7075/316SS MEA*

In order to further investigate the effect of RH cycling on the coated galvanic couples, a 100-pin AA7075/316SS MEA was studied without coating, with Class N and with Class C coating in a double RH ramp environment as described in Section 5.1. The total currents measured for the different coatings and bare galvanic MEA on the AA7075 and 316SS electrodes as a function of exposure time are shown in Figure 81. As expected, the AA7075 electrodes were anodic, while the 316SS electrodes were cathodic during the exposure. The Class C coating significantly reduced both the anodic and cathodic current densities of this galvanic couple compared to the uninhibited case. The Class N coating did not significantly affect the measured current densities compared to the uninhibited case. Current maps shown in Figure 82-Figure 84 indicate the same observations. In the uninhibited case, there was considerable galvanic activity at the AA7075/316SS interface. The measured current values were very low in the case of the Class C (Cr^{6+}) coating. The Class N coating provided some protection, as the current values were lower than the uninhibited case, however, galvanic activity was still observed, especially at the high RH values (90%).

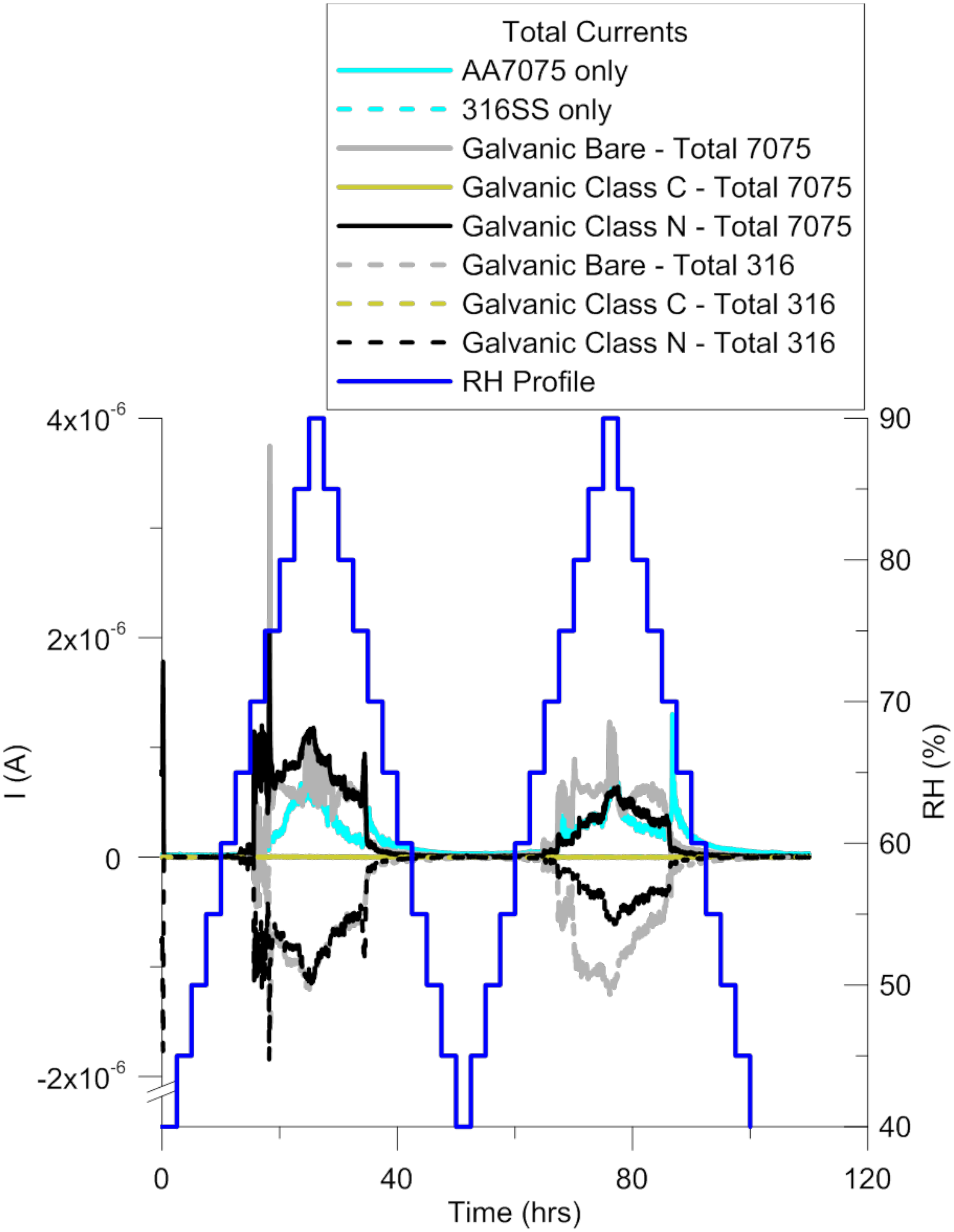

Figure 81. Total measured currents as a function of exposure time for bare and coated AA7075/316SS MEA in the double RH ramp environment.

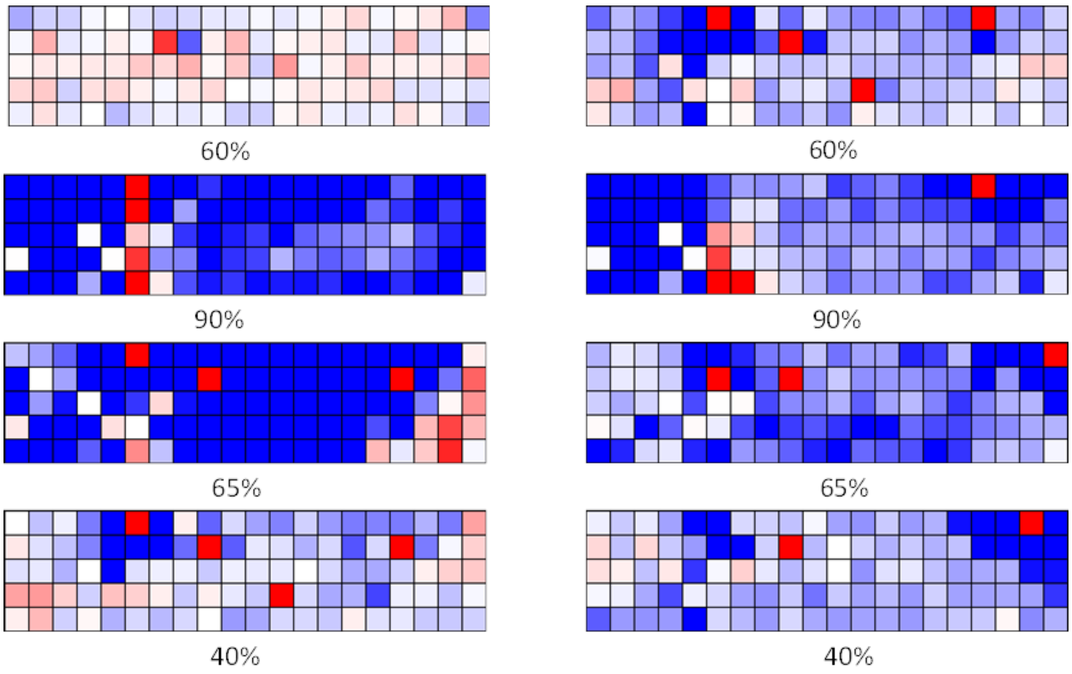

Figure 82. Current maps measured at different RH levels during the double RH ramp on uncoated AA7075/316SS MEA.

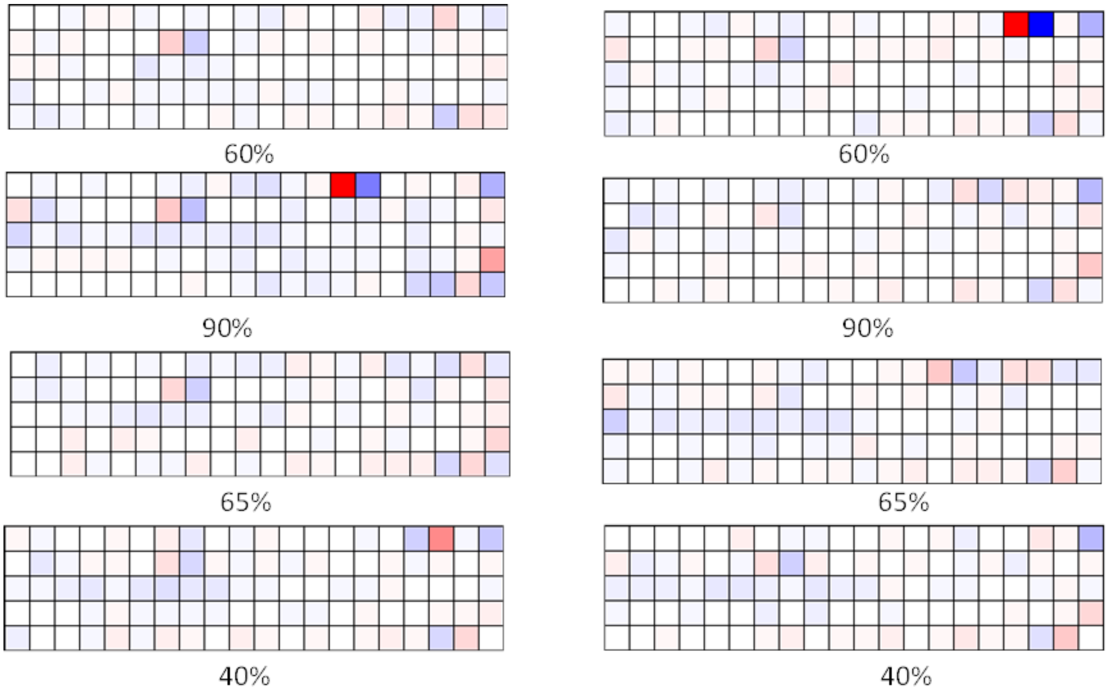

Figure 83. Current maps measured at different RH levels during the double RH ramp on AA7075/316SS MEA coated with MIL-DTL-23377 Class C.

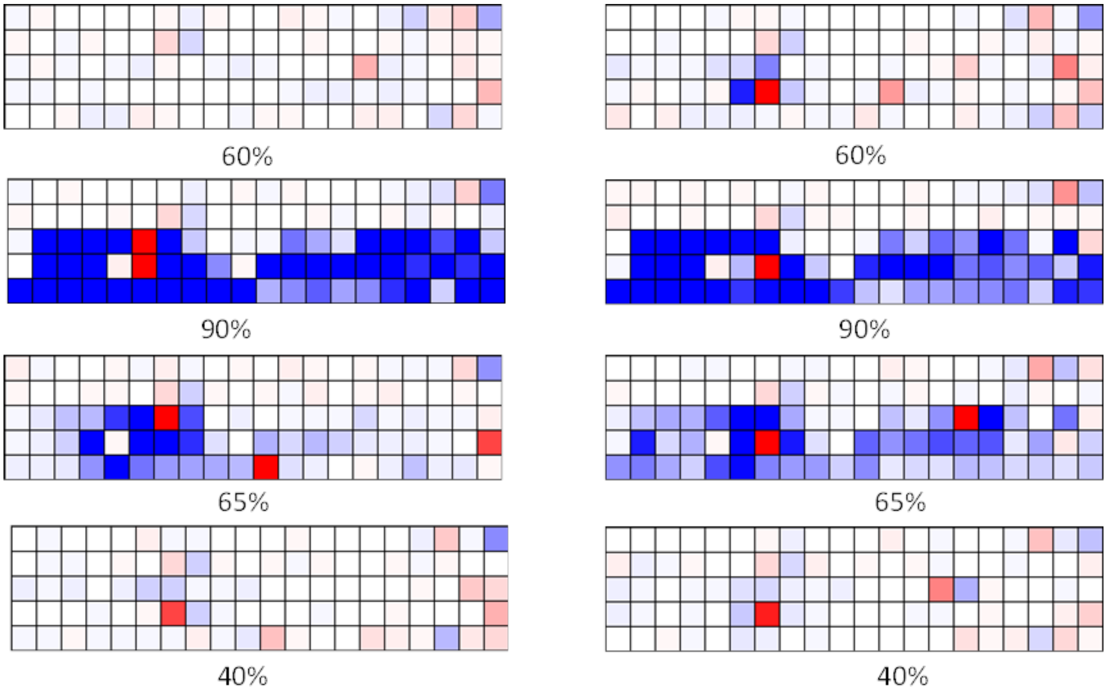

Figure 84. Current maps measured at different RH levels during the double RH ramp on AA7075/316SS MEA coated with MIL-DTL-23377 Class N.

The cumulative anodic currents as a function of exposure time are summarized in Figure 85. The 316SS electrodes show very low anodic activity throughout the exposure in both the uninhibited and inhibited cases. The AA7075 electrodes, on the other hand, show significant anodic activity in the uninhibited case due to the galvanic coupling between the aluminum and stainless steel at the interface of the galvanic couple in the deliquesced salt solution at high RH. As the surface dries, the galvanic activity disappears and the cumulative current value reaches a plateau. As the RH is increased again in the second ramp, the anodic current is again increasing on the AA7075 electrodes, leading to a jump in the cumulative current values. During the second drying period, the current again decreases, and the cumulative current reaches a second plateau. The cumulative anodic current is significantly lower, if the 316SS electrodes are masked and only the AA7075 electrodes are exposed, due to the lack of the galvanic coupling. In the presence of the Class C coating, the cumulative current is very low, while the values are only slightly lower than the uninhibited case when the surface is coated with the Class N coating.

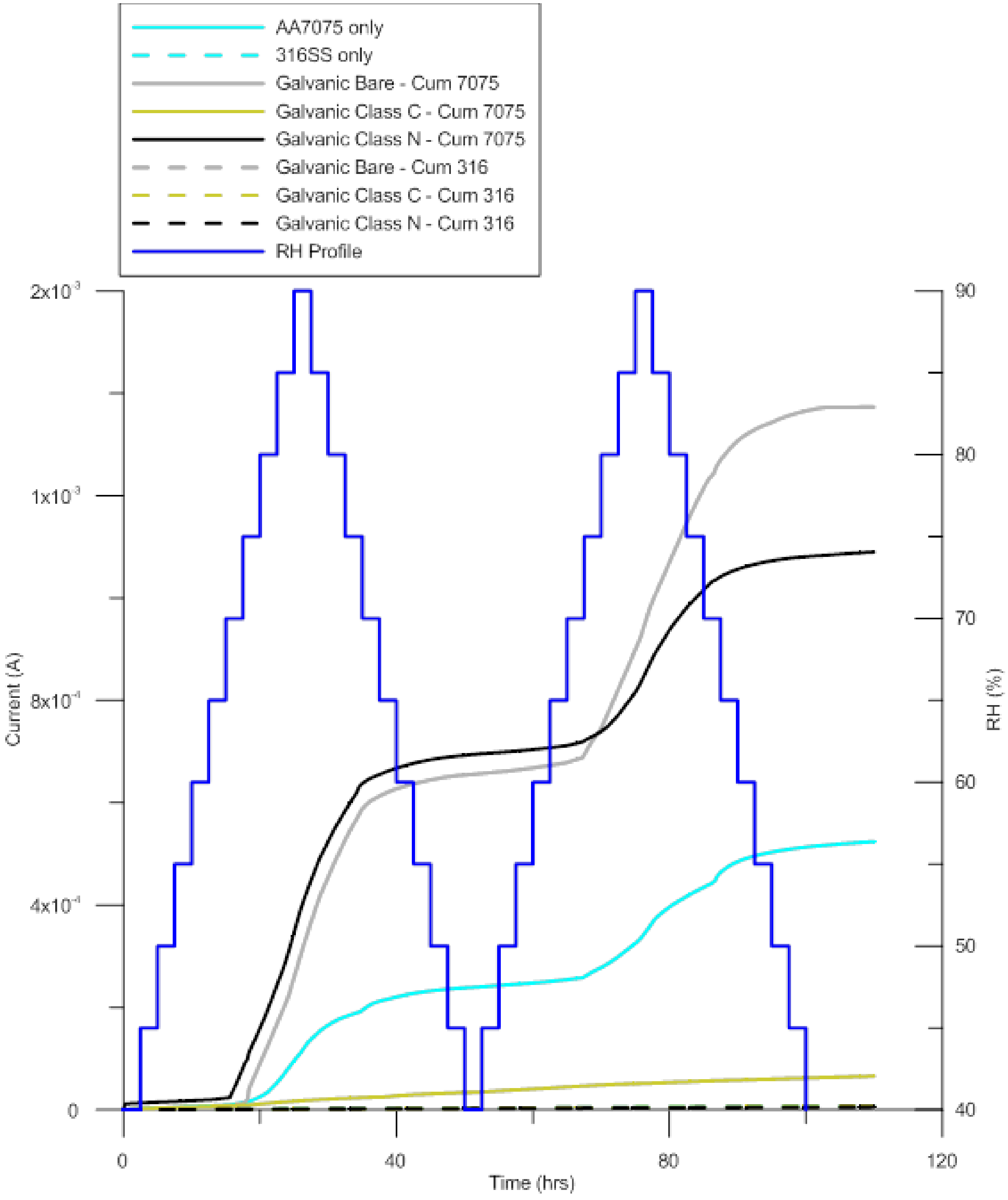

Figure 85. Cumulative anodic currents measured on AA7075/316SS as a function exposure time for bare and coated AA7075/316SS MEA in the double RH ramp environment.

CHAPTER 6
EFFECT OF RH ON CRACKING

Environment-assisted cracking (EAC) is a complex, unpredictable failure mode of a material that occurs through interaction with the environment, usually in the presence of tensile stresses. EAC is characterized by brittle fracture of otherwise ductile materials (Cramer, 2003). Stress corrosion cracking (SCC) is a form of EAC associated with metals that is characterized by unpredictable brittle crack formation and growth of susceptible alloying, heat treatment, and microstructure combinations when exposed to specific corrosive conditions and residual or applied tensile stresses (Sprowls, 1984). Aluminum, in its pure form, is corrosion resistant and does not suffer from SCC (Davis, 2002). To achieve high strength for demanding applications such as structural elements in military aircraft, naval vessels, and vehicles, aluminum is alloyed with small additions of elements such as magnesium (Mg), zinc (Zn), and copper (Cu) (Davis, 2002). Additionally, the alloys are subject to specific processing regimens that include heat treatment (annealing and aging) and/or cold working to further increase strength.

While allowing aluminum to meet strength requirements, the anisotropic microstructure developed by alloying and processing in alloys such as the 5XXX and 7XXX series can be highly susceptible to SCC when exposed to chloride environments (Davis, 1999). For the 5XXX series with greater than 3 wt.% Mg, exposure to slightly elevated temperatures for extended periods of time causes precipitation of an Mg-rich phase (Beta phase) in continuous films at grain boundaries in a process called sensitization (Dix, Anderson, & Shumaker, 1959). Sensitized 5XXX aluminum is known to fail rapidly by intergranular corrosion (IGC) and intergranular SCC (IGSCC) when exposed to chloride (Sprowls & Brown, 1967). In the peak aged condition (T6), many 7XXX series alloys are most susceptible to SCC in the S-L orientation (Speidel, 1984).

The SCC mechanism of aluminum alloys is not yet fully understood, particularly under atmospheric conditions, where deposited hygroscopic contaminants create thin electrolyte films on aluminum surfaces. These thin films, strongly influenced by relative humidity (RH), are known to be the most aggressive in terms of corrosion, as compared to full immersion conditions for aluminum. The majority of SCC work conducted on aluminum alloys has been under immersion and may not be representative of real failure modes due to increased concentrations of chlorides, free radicals, and oxygen in thin films causing more severe corrosion (Zhao & Frankel, 2006; Vera Cruz, Nishikata, & Tsuru, 1998; Maier & Frankel, 2011). It is understood that cyclic wetting and drying accelerates corrosion and EAC of metals (Buchheit, Wall, Stoner, & Moran, 1995; Bovard et al., 2011), however SCC measurement methods such as direct-current potential drop (DCPD) are not well suited to deployment in accelerated testing or outdoor exposure testing conditions. In this chapter, the development of new, robust, easily deployable EAC sensors for *in situ* cracking characterization during cyclic accelerated atmospheric corrosion testing, is described and detailed. Additionally, results obtained in accelerated tests conducted on 5XXX and 7XXX series aluminum are presented. The correlation of cyclic conditions and SCC measurements will impact the design of accelerated test regimes by informing the most aggressive conditions where a material is most at risk for SCC.

6.1 Materials and Methods

Details of the EAC sensors including their design and development are given in the following sections. Additionally, experimental procedures for accelerated cyclic corrosion tests used to induce SCC are presented.

6.1.1 *Constant displacement crack sensor and fixture*

The first crack sensor developed for accelerated corrosion testing to assess material SCC resistance was a constant displacement crack sensor. The design considerations for the sensor were that it needed to measure the SCC crack growth rates in real time when exposed to realistic conditions, including both outdoor exposure but more importantly accelerated atmospheric corrosion tests. A previous design, to assess hydrogen embrittlement of high strength steel in immersion conditions subject to cathodic protection, was leveraged along with commercially available commercial off-the-shelf (COTS) electrical enclosures to minimize design and fabrication costs.

The constant displacement crack sensor components included a circumferentially V-notched fracture mechanics sample, load frame, load cell, temperature sensor (potted in the frame), sealed cap, embedded electronics and sealed enclosure (Figure 86). Further details on each component of the overall sensor are given below.

The sensor exposes a 1.016 cm (0.4 inch) diameter V-notched (1.429 cm major diameter) cylindrical fracture mechanics sample under tensile load to the environmental conditions of interest (Figure 88a). The fracture sample is fabricated to produce cracking on a plane oriented parallel to the S-L and S-T orientations according to ASTM E399 nomenclature (ASTM, 2005) (Figure 87). This orientation was selected as it is the most susceptible to IGC, IGSCC, and SCC in 5XXX and 7XXX rolled products. To achieve S-L/S-T with the constant displacement crack sensor design, four inch thick plates of rolled material were required. The 9.779 cm (3.85 inch) long fracture sample is placed inside the load frame with a Transducer Techniques LWO-25 through-hole compression, strain gauge based, load cell between the bolt hub of the fracture sample and one side of the load frame (Figure 88b). A hydraulic press is used to strain the sample in tension. The load nut is advanced to lock in the desired load/displacement creating compressive stresses on the load frame and strain gauge.

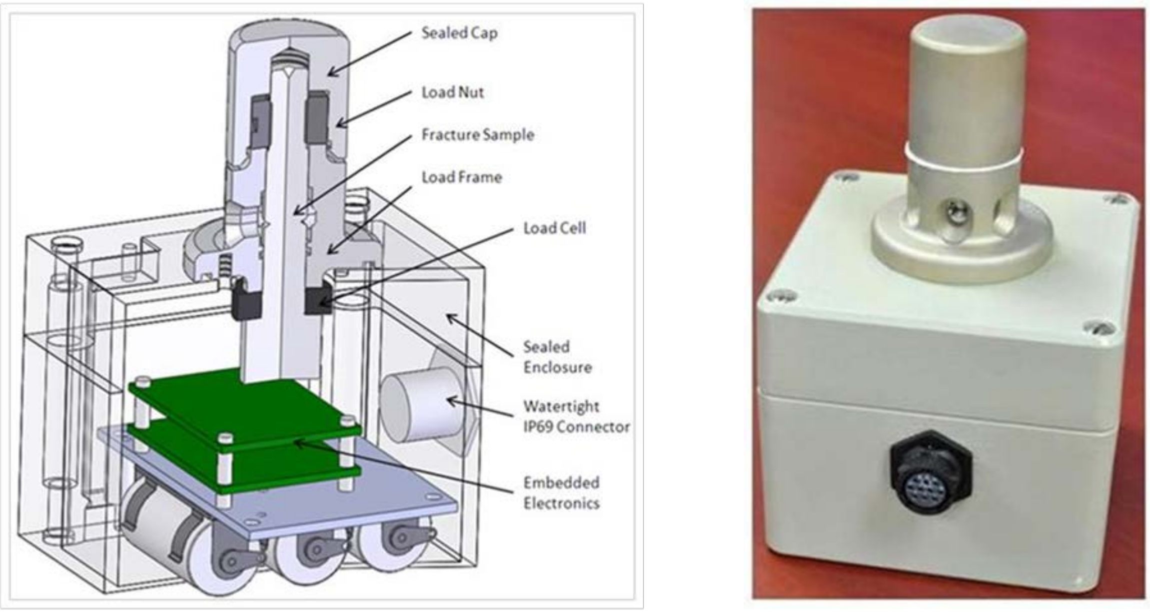

(a) (b)

Figure 86. (a) Constant displacement crack sensor cutaway schematic and (b) assembly image.

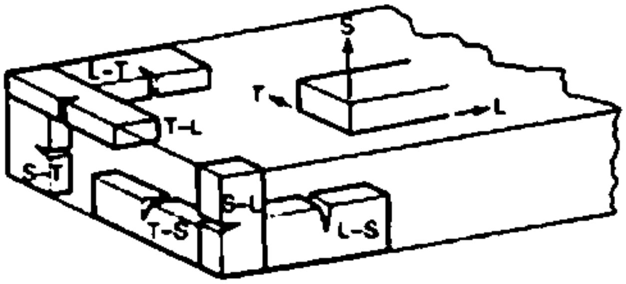

Figure 87. ASTM E399 crack plane orientations (ASTM, 2005).

The load frame was fabricated from 6.604 cm (2.6 inch) diameter blanks that were water-jet machined from a 30.48 by 30.48 by 5.715 cm (12.0 by 12.0 by 2.25 inch) AA5083-H131 plate provided by Alcoa. Finite element analysis (FEA) was used to design the load frame to ensure mating faces remain flat and parallel under load for increased measurement confidence. The load frame's radial vent holes allow for atmospheric exposure to the fracture sample, and the flange is used to mate with the electrical enclosure. AA5083 was selected for all wetted sensor load frame components to minimize galvanic interactions.

A sealed cap machined from AA5083-H116 was used to prevent environment exposure of the fracture sample outside the V-notched region or the load nut, which could potentially alter the tensile load on the fracture sample. The sealed cap was designed to thread onto the fracture sample, but "floated" on the sensor assembly to avoid load cell errors from overtightening or thermal expansion. Sealant around the circumference of the interface between the sealed cap and the load frame secured the sealed cap to the sensor assembly. Sealant was also used between the fracture sample and the load frame above and below the V-notched region.

A suitable sealant with low enough viscosity to flow into the 0.127 cm (0.050 inch) radial gap between the frame and fracture sample, while maintaining flexibility to not inhibit load cell readings or component disassembly was selected. A 3M Marine Adhesive/Sealant 5200 Fast Cure was used because of its flexibility, robustness towards salt water, and relatively short cure time of 24 hours (for full curing). Xylene was mixed in at ten weight percent to lower the mixture's viscosity for assembly. The xylene was then able to evaporate out of the mixture, and did not negatively affect curing time or material performance during preliminary testing.

The constant displacement cracking sensor was designed to be configured for wired or wireless operation. All testing to date was performed using a wired sensor incorporating a Mantracourt DSCH4ASC digitizing strain converter (DSC). The use of a DSC allows for higher resolution measurements but requires integration with a PC, RS485 communications module, and 12 V power. Wireless sensors are able to utilize a modular baseboard, EAC analog board, and three C-cell alkaline batteries rigidly mounted inside a Nema 4X electrical enclosure. The specified enclosure has mounting holes which can be used to mount to an adapter or straight to an exposure rack. Overall sensor dimensions are 17.78 by 12.77 by 12.77 cm (7.0 by 5.0 by 5.0 inch).

(a) (b)

Figure 88. Circumferentially V-notched aluminum fracture mechanics sample and load nut (a) and assembled sensor without electronics box (b).

6.1.1.1 Constant displacement sensor crack depth measurement

Calibration curves were developed for the constant displacement crack sensor by measuring the sample and assembly stiffness during a preload operation, before cracking. Sample stiffness was inferred from the load cell output and the measured extension of the sample. Assembly stiffness was estimated by the advance angle of the nut at each preload (i.e., the total assembly deflection) and load cell output. The sample stiffness vs. crack depth curve generated by numerical FEA was refined using the actual stiffness values to generate the calibration curve for the sensor (Figure 89). Using this curve, the load cell measurement was converted to a crack depth indication. The calibration curve was implemented in the data acquisition software as a simple lookup table with k/k0 as the input and the non-dimensional crack depth (2a/d) as the output, where d is the non-cracked ligament diameter.

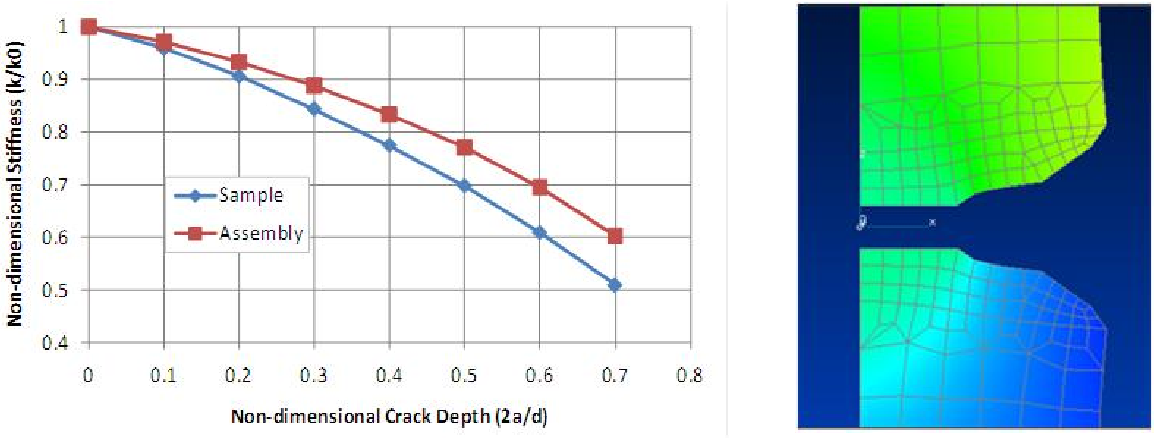

(a) (b)

Figure 89. (a) Calibration curve for crack depth and sensor stiffness. (b) Fracture sample FEA.

6.1.1.2 Constant displacement crack sensor calibration

Prior to testing a new fracture sample using the constant displacement cracking sensor at each initial load, a temperature calibration was performed to obtain a temperature correction coefficient to minimize the effect of temperature on crack depth measurements. For this calibration, the sensor was placed in an environmental chamber where it was cycled for three days from 20 °C to 40 °C in increments of 5 °C while holding relative humidity (RH) constant at 40%.

Significant hysteresis was observed in the sensor force data over the first half of the first temperature cycle (Figure 90a). The second half of the first cycle and the last two cycles had no hysteresis (Figure 90b). This phenomenon was most likely due to load settling of the sensor to a steady-state value as the components expanded and compressed due to changing temperature. Because of the hysteresis in load response to temperature during the first half of cycle one, the temperature sensitivity over the full three cycles was very non-linear (Figure 90c). However, with the removal of the data that exhibited hysteresis, the temperature sensitivity was found to be extremely linear, with an R^2 value of 0.9998 (Figure 90d). The force-temperature relationship was then applied within the LabView data acquisition program as a correction coefficient for temperature fluctuations.

The observed load settling indicates that the fracture samples are prone to relaxation to a lower stress intensity value than the original target preload value. In one case after preloading, the sensor measured a load of 3290 lbf (stress intensity of 10.8 MPa-$m^{1/2}$), but decreased by 14% to 2820 lbf (stress intensity of 9.1 MPa-$m^{1/2}$) after thermal cycling. Because of this load settling effect, fracture samples were iteratively loaded to achieve and maintain higher initial stress intensity values that were thought to be above the material's K_{ISCC} threshold.

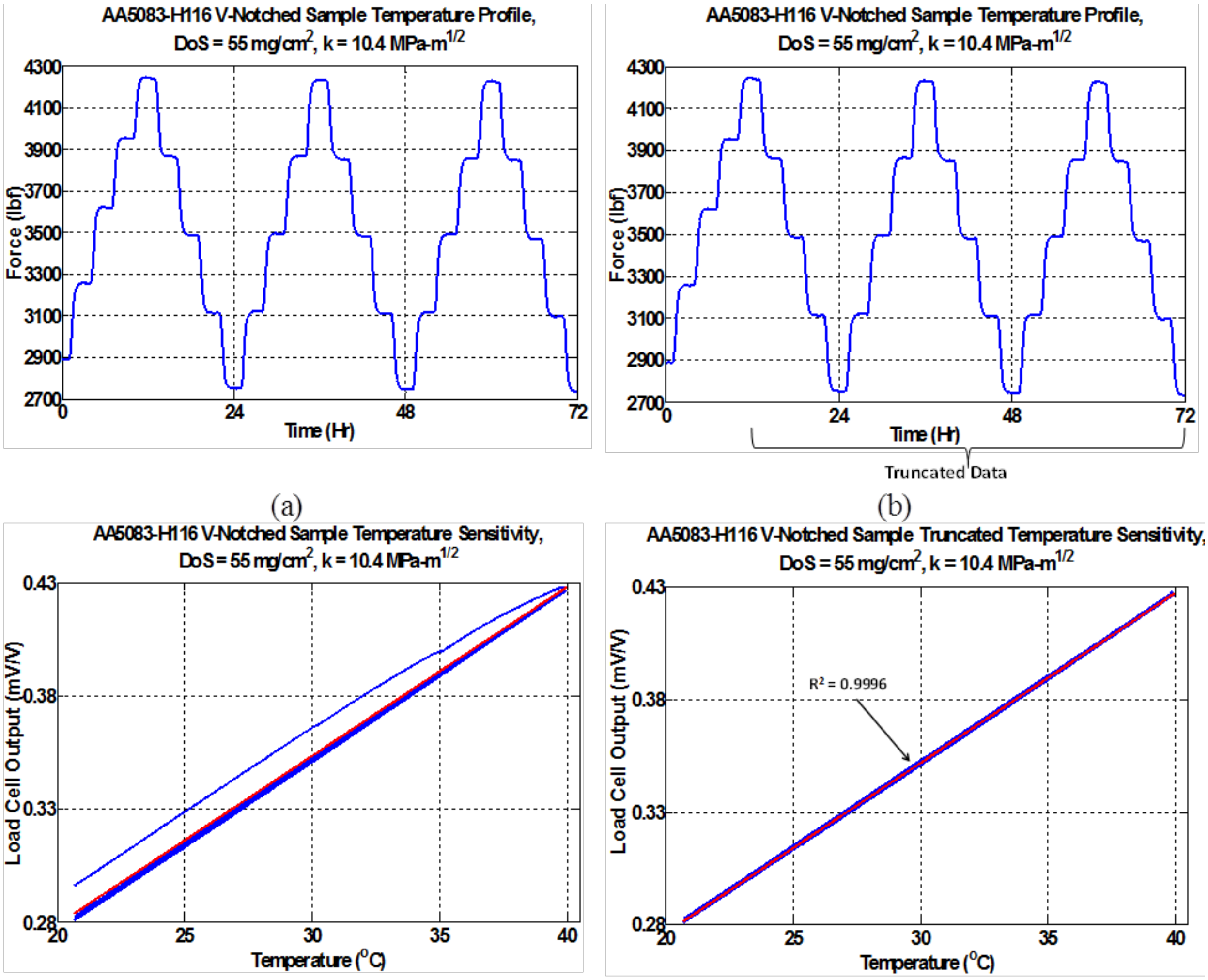

(a) (b)

(c) (d)

Figure 90. Plots of AA5083-H116 (a) temperature profile, (b) truncated temperature profile, (c) temperature sensitivity and (d) truncated temperature sensitivity.

6.1.1.3 AA5083-H116 specimen sensitization

A four inch thick (10.16 cm) rolled AA5083-H116 plate was sourced from Alcoa, with tensile specimens extracted to allow SCC growth on the S-L/S-T plane. Due to the 5XXX series alloy's increased susceptibility to SCC following sensitization (prolonged exposure at slightly elevated temperatures leading to precipitation of continuous films of Mg-rich beta phase at grain boundaries), the AA5083 specimens were sensitized to facilitate more aggressive SCC. A range of conditions were obtained by heat treating the fracture samples at 150 °C for up to 60 days. Nitric acid mass loss testing (NAMLT) according to ASTM G67 (ASTM, 1999) was used to characterize the degree of sensitization (DoS) of each heat treatment duration (Figure 91). New fracture samples were utilized for each test performed. Fracture sample V-notch tips were polished with 0.3 µm alumina suspension, and all sensor components were thoroughly cleaned prior to testing.

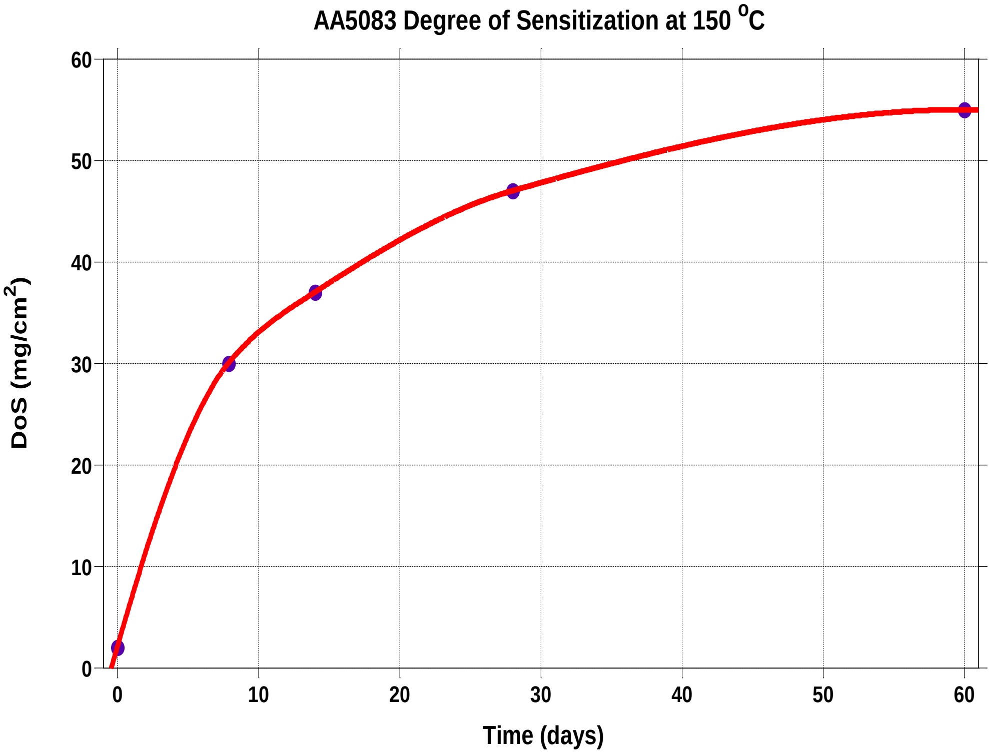

Figure 91. AA5083-H116 degree of sensitization at 150ºC as a function of time. The red trace represents an interpolant – shape preserving fit of NAMLT lab test data (blue dots).

6.1.1.4 AA7075-T651 specimen preparation and calibration

In addition to the AA5083-H116 fracture specimens, AA7075-T651 samples were also prepared. It was of interest to study the EAC behavior of an alloy not susceptible to sensitization using the constant displacement crack sensor. The four inch thick plate for specimen extraction was also sourced from Alcoa for SCC crack growth in the S-L/S-T plane. AA7075-T651, being a higher strength and non-sensitizable alloy, required a higher applied stress intensity to ensure SCC initiation and growth. The EAC-ATM sensor was temperature calibrated by first preloading the fracture sample with an assumed temperature correction coefficient implemented in the LabView data acquisition program. Next, the sensor was thermal cycled ten times in a Thermotron 8200 accelerated environmental test chamber from 20 °C to 60 °C to 20 °C to elucidate load settling. The sensor was then removed from thermal cycling, and the fracture sample preload was increased to an estimated stress intensity of 15 MPa-m$^{1/2}$. Higher stress intensity relative to previous AA5083-H116 testing was chosen to maximize chances of cracking AA7075-T651.

As for the AA5083-H116 specimens, the EAC-ATM sensor with AA7075-T651 fracture specimen installed was cycled for five days from 20 °C to 60 °C to 20 °C to obtain a temperature correction coefficient. Increments of 10 °C were held for 150 minutes, and RH was held constant at 35%. After thermal cycling, the EAC atmospheric crack sensor preload was approximately 5343 lbf correlating to a stress intensity of 17.3 MPa-m$^{1/2}$.

6.1.2 *Constant load crack sensor and fixture*

Gaps for improvement in EAC sensing were identified during development and testing of the constant displacement crack sensor. Namely, these were related to (1) the extremely thick source material needed for S-L/S-T cracking, (2) relatively short effective crack growth range before ductile overload in the cylindrical specimen (~5 mm), (3) rising, non-constant stress intensity with crack growth, and (4) relatively complex temperature correction procedures necessary for each test. To address these gaps, a new SCC crack sensor was designed. The new design was based upon a four point bend fixture subject to a constant applied load. The bend fracture specimen was 10.16 cm (4 inches) in length, 1.27 cm (0.5 inch) in height, and 1.59 cm (0.625 inch) in width. Two relief notches, machined into the top side of the specimen, allowed for S-L cracking along the mid-plane of the specimen (Figure 92).

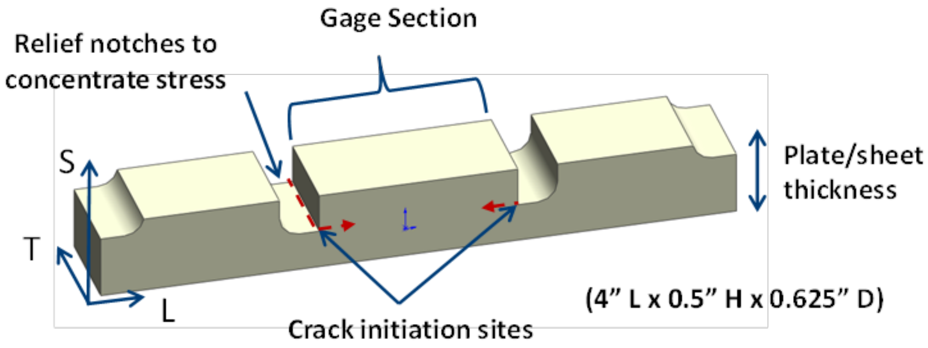

Figure 92. Constant load crack sensor fracture specimen.

The fracture specimen was designed to be loaded into a four point bend fixture (Figure 93). The top and bottom loading plates were compressed together using an ADMET load frame with an applied force of 980 lbf. In doing so, two high strengths, precipitate hardened stainless steel springs, each able to sustain a compressive force of up to 1000 lbf, were compressed. Locking nuts were tightened down around each spring to lock in the compressive force for constant loading during testing and the ADMET applied load was removed. The loading springs and fixture plates were fabricated from stainless steel to minimize corrosion during testing. Ceramic rollers were used for the four-point loading contacts to prevent direct electrical contact between the aluminum specimens and the steel load frame.

Assuming cracking along the mid-plane of the specimen with uniform inward crack growth from both notches, FEA was carried out for the four-point bend specimen at initial loading conditions and at increments of mid-plane crack extension (Figure 94). The FEA results were used to calculate the center deflection of the specimen as well as the crack tip stress intensity as a function of crack length (Figure 95). The FEA analysis was carried out for two purposes. First, the deflection of the gauge section as a function of crack length was needed as a metric for measuring crack length and velocity during EAC testing (described below). The FEA also informed the stress intensity at the crack tip. It was found that a mixed mode (Mode I and Mode II) stress state existed at the crack tip. The stress intensity was found to be nearly constant for a relatively wide range of crack lengths allowing for many crack velocity measurements at the same stress intensity during cyclic environmental testing. Another feature elucidated by the FEA was that the Mode I stress intensity decreases after a given crack length. This observation was useful in that a threshold K_{ISCC} could be observed with dead weight loading.

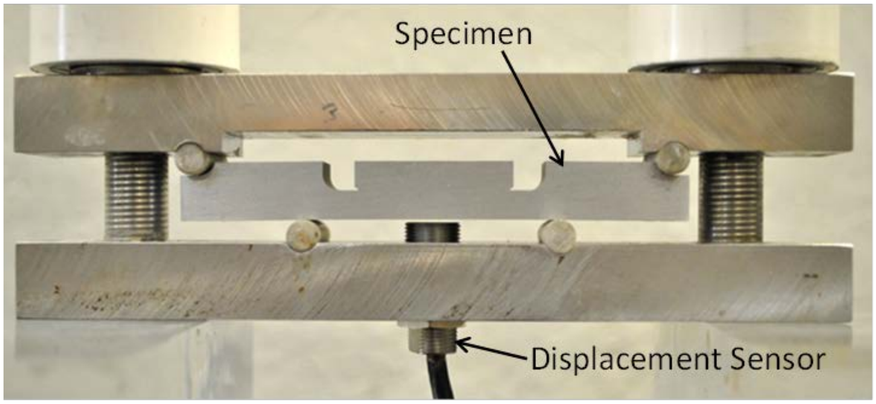

Figure 93. Constant load crack sensor fixture with specimen and displacement sensor installed.

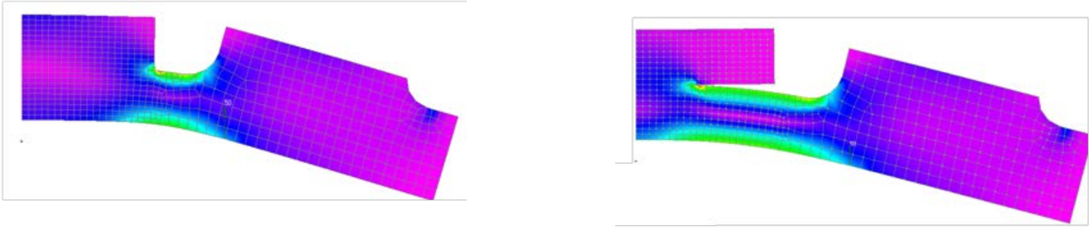
(a)
(b)

Figure 94. FEA of four point loading specimen (a) initial conditions and (b) after crack growth along mid-plane (S-L).

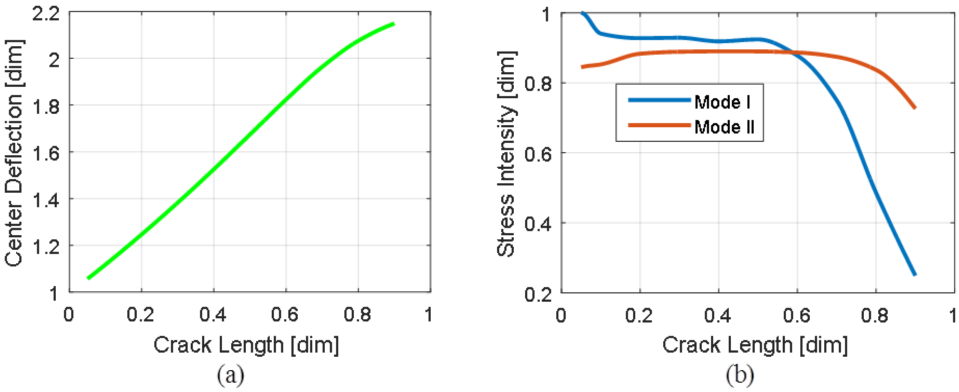

(a) (b)

Figure 95. FEA results for four point bending specimen, (a) center deflection as a function of crack length and (b) mixed mode stress intensity as a function of crack length.

The deflection of the four-point bend constant load crack fixture was monitored using an inductive air gap sensor (observable in bottom loading plate of Figure 93). Note that the design was recently revised, placing the air gap sensor on the top loading plate. The air gap measured, *in situ*, by the inductive sensor during cyclic corrosion testing or in outdoor exposures, was correlated with the center deflection versus crack length calibration curve (Figure 95a) calculated by FEA to estimate instantaneous crack length. The calibration curve assumes mid-plane cracking of the four point bend specimen. Preliminary testing confirmed that SCC propagates along the mid-plane of both sensitized AA5083-H116 and AA7075-T651 when crack growth occurs in the S-L orientation (Figure 96). The inductive air gap sensor is temperature sensitive, however the constant displacement crack sensor does not experience the same interfacial stress relaxation during thermal cycling that necessitates pre-testing thermal cycling for temperature correction in the constant displacement sensor.

The constant load cracking sensor was able to address the gaps identified for the constant displacement sensor. The cracking specimen could be machined from source material plate that is 1.27 cm thick (0.5 inch) opening up material sourcing options to many suppliers as opposed to the 100 mm (4 inch) thick plate that had to be specialty ordered from Alcoa for the constant displacement fracture mechanics specimens. The constant displacement fixture only had an effective crack length of about 5 mm before ductile overload, limiting the amount of data that could be collected from a single specimen. The constant load crack sensor cracking range was up to approximately 15 mm. Additionally, the constant load fixture cracks were exposed to nearly constant stress intensity allowing for not only more measurements during testing but also, the ability to compare crack velocities cycle to cycle as the SCC crack grows. The temperature response of the constant load crack sensor was relatively more straightforward and could be accounted for in crack length measurements without complicated and time consuming pre-test temperature cycling.

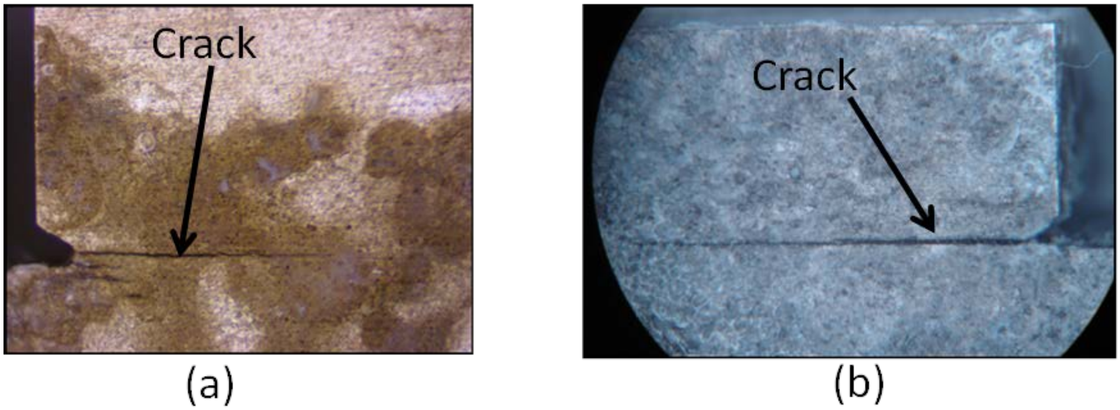

Figure 96. Mid-plane cracking observed in (a) sensitized AA5083-H116 and (b) AA7075-T651.

6.1.3 *Accelerated testing procedures and techniques*

Four accelerated test environments were selected for study using the constant displacement and constant load crack sensors. These environments included: (1) cyclic relative humidity (RH) testing with salt loading, (2) ASTM B117 salt fog testing (ASTM, 2011a), (3) ASTM G85-A5 (ASTM, 2011b) and (4) GM 9540P (1997). The parameters within each test are given below.

6.1.3.1 Cyclic relative humidity

Testing was performed in a Thermotron 8200 environmental test chamber. Each 24-hour RH cycle began with a three-hour initial hold at 40% RH. RH was increased from 40% to 90% over the next three hours and then held at 90% for six hours. The RH was decreased to 40% over the next nine hours and held for an additional three hours at 40%. Temperature was held constant at 30 °C. A 0.5 M sodium chloride salt solution was sprayed on the crack tip at the beginning of an RH cycle, approximately every 75 hours of testing. Cyclic RH testing was performed on both AA5083 and AA7075 specimens.

A second cyclic relative humidity trial was conducted using the AA7075-T651 constant load crack sensor to more clearly observe the effects of intermediate RH holds during wetting and drying. These tests were also performed in a Thermotron 8200 environmental chamber. The sensors were pre-cracked using cathodic polarization to -1.3V versus SCE in 3.5 wt% sodium chloride solution for approximately eight hours. The pre-cracking procedure was employed to ensure running SCC cracks considering the short duration of the second round of tests. Each test was 48 hours in length with RH steps from 90% to 80% to 70% to 60% to 40% to 60% to 70% to 80% to 90% (one cycle) with each step lasting two hours. Three cycles were conducted for each test. The tests were held at a constant 35 °C throughout the test. The pre-cracked four point bend specimen notches were doped with saturated sodium chloride solution prior to each test.

6.1.3.2 ASTM B117

EAC cracking sensors were exposed continuously in an Auto Technology cyclic corrosion chamber to ASTM B117 salt fog (5% sodium chloride). Temperature was held constant at 35 °C. Crack velocity remained low and relatively constant during ASTM B117, so RH was then ramped down until fracture of the sample occurred.

6.1.3.3 ASTM G85-A5

EAC cracking sensors were exposed to an ASTM G85-A5 environment in the Auto Technology accelerated corrosion testing chamber. This testing included cyclic exposure of sensors during one hour of drying at room temperature and one hour of fogging at 35 C, with a solution containing 0.05% sodium chloride and 0.35% ammonium sulfate by mass. A modified ASTM G85-A5 experiment was also performed by changing the steps to two hours of drying at room temperature and two hours of fogging at 35 °C in order to provide more time for sensor thermal stabilization. The same solutions were utilized during the standard and modified tests.

6.1.3.4 GM 9540P

Sensors were exposed to a GM 9540P environment in the accelerated corrosion testing chamber. This test included a cyclic exposure of alternating wet and dry cycles with varying temperature of the sensor with a solution containing 0.9% sodium chloride, 0.1% calcium chloride, and 0.25% sodium bicarbonate by mass. An iso-temperature GM 9540P experiment was also performed at a constant temperature of 35 °C to reduce thermal influences on the crack depth measurement. The same solutions were utilized for both sets of experiments.

6.1.4 *Outdoor exposures of crack sensor design*

Two constant displacement crack sensors were redesigned to be deployable in outdoor environmental exposure trials. The sensors were designed to track crack depth and temperature while deployed at outdoor corrosion racks at the Daytona Beach, FL and LAX. The primary differences between the outdoor exposure constant displacement sensors and those developed for accelerated chamber testing was size of the overall sensor and electronics box, extended battery life, and extended data storage.

A COTS Fibox UV-resistant, polycarbonate enclosure with exterior dimensions of 11.94 x 7.87 x 8.89 cm (4.7 x 3.1 x 3.5 inch) and a NEMA 4X (watertight and corrosion resistant) rating was used for the sensor housing (Figure 97a). The COTS enclosure facilitated lower acquisition costs and quicker deployment. The selected enclosure also significantly reduced the overall package volume compared to the existing enclosure used for the lab-based system (Figure 88). A 3.7 V Li-ion battery with a 7.8 A-h capacity was used to power the embedded sensing system. Preliminary system power usage estimated up to a three year system battery lifetime, assuming low duty cycle measurement. The battery was placed on the bottom of the enclosure, and a foam backed aluminum plate provided a location for mounting embedded electronics, signal conditioning circuitry, and on-board flash memory. An aluminum plate was mounted to the enclosure internal bosses. A Souriau Industrial 10 pin through-hole connector, with an IP68/IP69 rating, allowed for periodic data downloading (Figure 97b). RS-485 communications protocol facilitated a LabVIEW GUI to process raw transducer outputs into temperature compensated crack depth and velocity values.

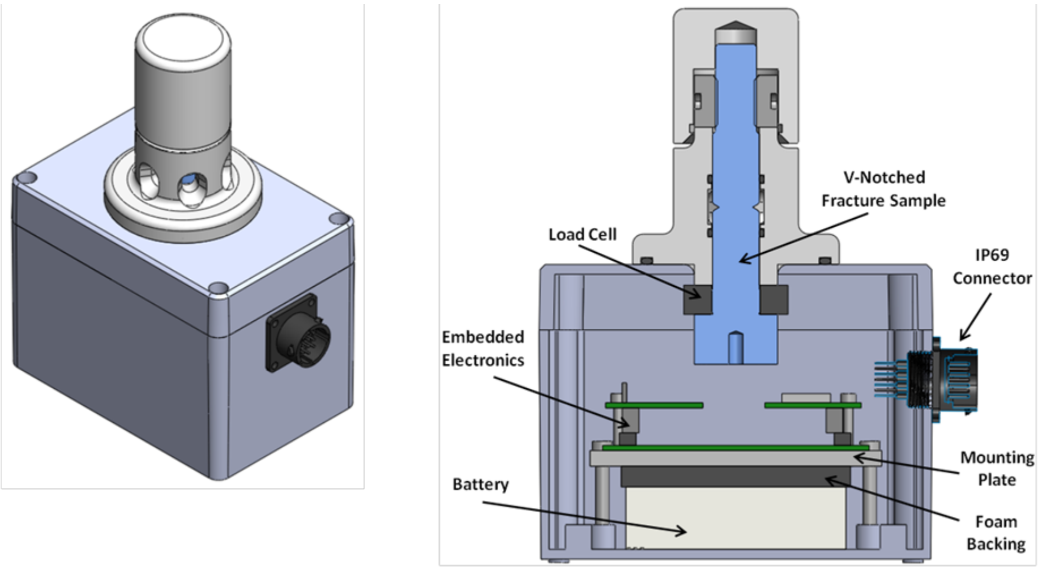

(a) (b)

Figure 97. (a) Outdoor constant displacement crack sensor and (b) internal cutaway view.

6.2 Results and Discussion

This section presents results from atmospheric and outdoor exposure tests using the constant displacement and constant load crack sensors for both AA5083-H116 and AA7075-T651 fracture specimens. First, the results using the constant displacement crack sensor will be presented broken down into results for each test type and each material. Next the results using the constant load displacement crack sensor will be presented, also with results broken down by test exposure type and material. Finally, a brief summary of experience and results with the constant displacement sensors for outdoor exposure testing will be presented.

6.2.1 *Constant displacement crack sensor testing results*

Experimental results and discussion for the constant displacement crack sensor is presented below, partitioned between the specific tests conducted. For the cyclic relative humidity test, both AA5083 (sensitized) and AA7075 alloys were evaluated as a comparative study. The remainder of the testing focused on sensitized AA5083 as the primary material of interest.

6.2.1.1 Cyclic relative humidity (AA5083-H116)

Crack depth and RH are plotted as a function of time for the last five RH cycles of the test where most of the cracking occurred (Figure 98 a). The crack depth data were filtered with a moving average method and differentiated with respect to time to produce crack velocity as a function of time (Figure 98 b). The crack velocity plot is separated into five 24-hour RH cycles. Each cycle showed a peak in the crack velocity, representative of the increase in crack rate during the dry-off portion of the RH cycle. The peaks increased in magnitude with each subsequent RH cycle and increasing crack depth. This increase most likely occurred because the stress intensity at the crack tip in the circumferentially V-notched specimen increased as the crack propagated.

Lower crack velocity values were associated with the high humidity portion of the RH cycle.

Crack velocity as a function of RH is plotted for the last five RH cycles of the test Figure 99). Little crack growth occurred during the ramp-up portion of the RH cycle. RH cycle number four is the only cycle that displayed increasing crack velocity as the RH increased towards 90%. However, there was a sharp decrease in crack velocity immediately before reaching 90% RH. During the transition from wet to dry, all five cycles show an increase in crack velocity that occurred between 78% and 85% RH. The crack velocities continued to increase to a maximum around 55% to 68% RH. Each cycle's crack velocity then decreased as the RH decreased to 40%. It should be noted that the crack velocities remained above zero for the entirety of the cycle, including at low RH equal to or slightly below the efflorescence relative humidity of sodium chloride (43% ± 3% RH) (Seinfeld & Pandis, 2012). The fracture surface of the failed specimens were inspected post testing and were found to have characteristics of SCC in aluminum alloys, that is flat crack paths with no evidence of ductile fracture (Figure 100).

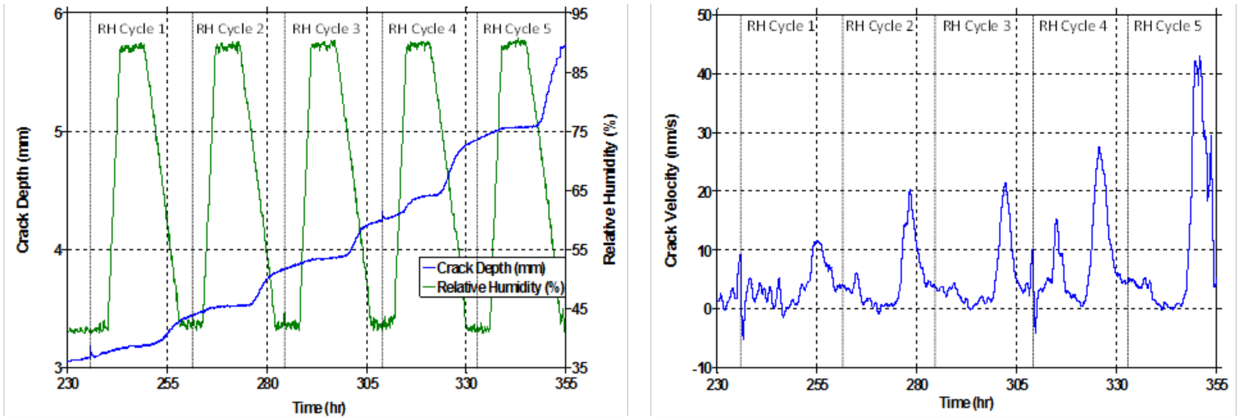

(a) (b)

Figure 98. Cyclic RH results for AA5083-H116 constant displacement crack sensor (a) crack length and (b) crack velocity.

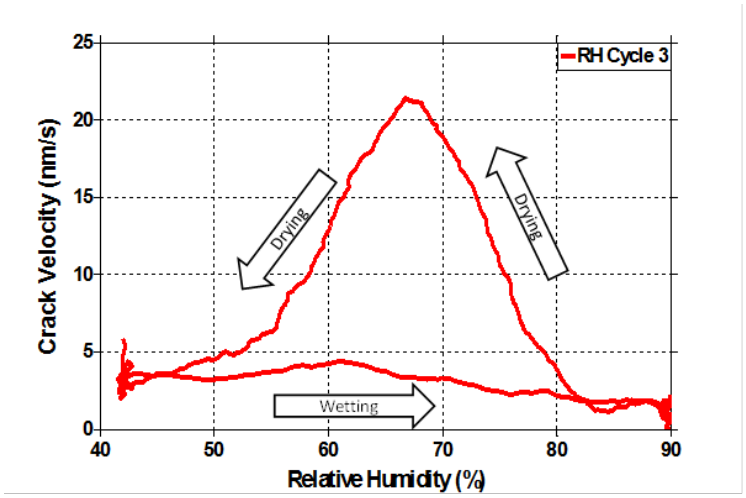

Figure 99. Cyclic RH results for AA5083-H116 showing crack velocity for the third RH cycle of Figure 98b as a function of RH.

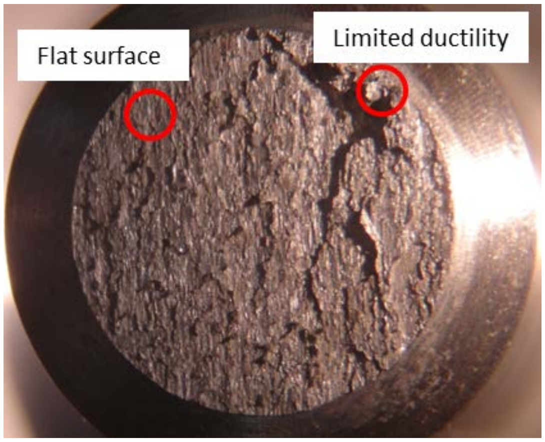

Figure 100. Fracture surface of circumferentially V-notched 5083-H116 constant displacement crack sensor specimen failed following cyclic RH exposure. Flat fracture surface with little evidence of ductile fracture is characteristic of aluminum SCC.

6.2.1.2 Cyclic relative humidity (AA7075-T651)

Crack depth and RH are plotted as a function of time, where the last five RH cycles of the test are plotted to more easily show the crack depth response as it relates to changes in RH (Figure 101 a). The crack depth data was differentiated with respect to time to produce crack velocity. Each cycle showed a peak in the crack velocity representative of the increase in crack growth rate during the dry-off portion of the RH cycle (Figure 101 b). The peaks increased in magnitude with each subsequent RH cycle and increasing crack depth. This increase most likely occurred because the stress intensity at the crack tip increased as the crack propagated. Lower crack velocity values were associated with the high humidity portion of the RH cycle. Slightly negative crack velocity values are an artifact of temperature variation effects on the sensor instrumentation.

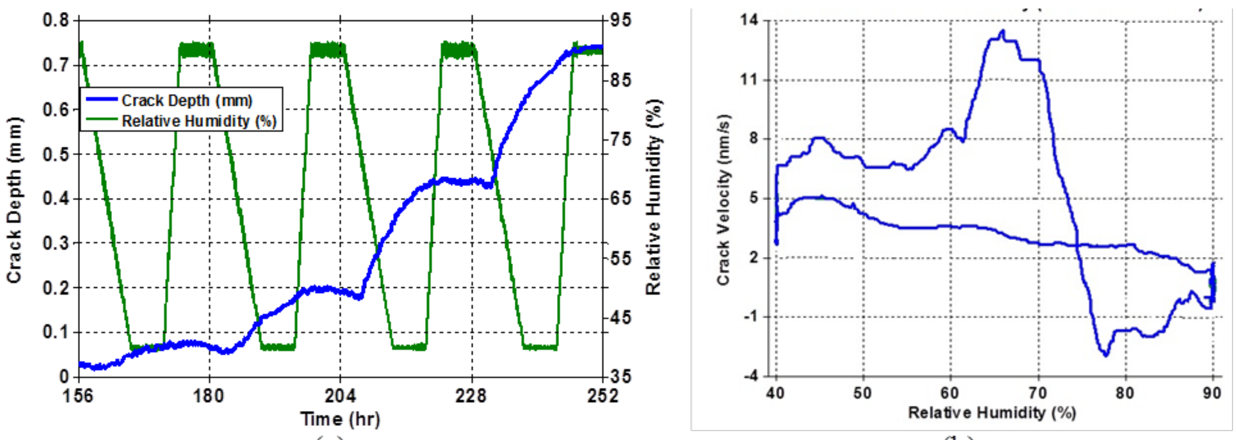

(a) (b)

Figure 101. Cyclic RH results for AA7075-T651 constant displacement crack sensor (a) crack length and (b) crack velocity versus RH representing 228 – 252 hours in (a).

Minimal crack growth occurred during the ramp-up portion of the RH cycle. During the transition from wet to dry, all cycles showed an increase in crack velocity that occurred between 76% and 78% RH, similar to AA5083-H116 measurement results. Crack velocities continued to increase to a maximum crack velocity around 65% RH. Each cycle's crack velocity then decreased as the RH decreased to 40%. It should be noted that the crack velocities remained above zero during the entirety of the cycle, including at low RH equal to or slightly below the efflorescence relative humidity of sodium chloride.

6.2.1.3 ASTM B117

There was no significant crack depth increase during 330 hours of B117 salt fog exposure (Figure 102a). At 330 hours, a power interruption disabled the salt fog and the RH dropped accordingly, but with no appreciable change in cracking response. However, the crack depth (and velocity) increased dramatically after the salt fog was restarted and shut down a second time causing the chamber RH to decrease below 80% (~410 hours). The cracking continued until final fracture occurred even as the RH decreased and was held constant at 35% for 15 hours.

Minimal crack depth increase was also observed during the replicate B117 salt fog experiment. Again after salt fog ceased and the RH was decreased, crack depth increased dramatically and the sample fractured after 120 hours of testing (Figure 102b). B117 salt fog was initiated just prior to final fracture to determine if rewetting the sensor would arrest crack growth, visualized by the sharp rise in humidity at 119 hours. By the time the humidity ramped up, the sample had already entered into ductile overload and was not able to be arrested.

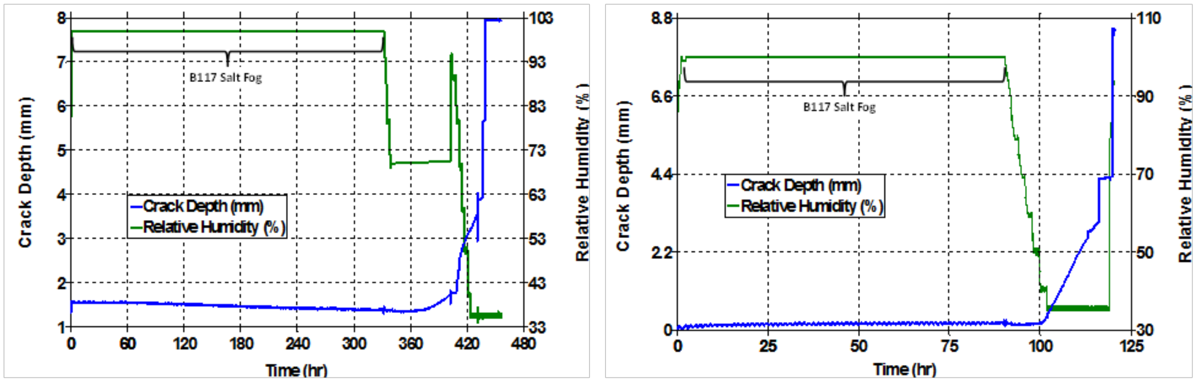

(a) (b)

Figure 102. Cyclic RH crack depth results for sensitized AA5083-H116 constant displacement crack sensor in two different ASTM B117 salt fogging tests.

6.2.1.4 ASTM G85-A5

The first ASTM G85-A5 test cycle was comprised of a one hour fog at room temperature and a one-hour dry-off at 35 °C (a). During the first 13 hours of the first ASTM G85-A5 test, minimal change in crack growth was observed. The cyclic response during this period was correlated with the change in chamber air temperature. The effectiveness of the temperature compensation algorithm in the LabView data acquisition software was limited due to the rapidly changing cycles relative to the long thermal time constant of the sensor assembly.

After 13 hours of testing, the crack depth began to increase at a decreasing rate until a slight inflection point was observed at approximately 37 hours. After 37 hours of testing, crack depth continued to increase but at an accelerating pace. After 51 hours of testing, four small step changes of 0.06 mm to 0.16 mm were observed prior to final fracture occurring after 54 hours of testing. The small step changes prior to final fracture are assumed to be representative of ductile overload of remaining AA5083-H116 ligaments.

As mentioned, the temperature compensation strategy implemented in the sensor's data acquisition for the first ASTM G85 experiment is only capable of correcting for longer-term transients, typical of natural outdoor atmospheric temperature changes. Extremely quick transients or step changes in temperature that occurred during the one-hour drying and fogging cycles resulted in a peak in the crack depth data, convoluting crack velocity values calculated as the derivative of the crack depth with respect to time. Therefore, longer two-hour holds were used in the replicate experiment and both the dry-off and fog portions of the modified ASTM G85-A5 test were performed at 35 °C. Despite changes to the ASTM G85-A5 test, the accelerated corrosion testing chamber's temperature varied several degrees when switching between dry-off and fog portions of the test cycle, resulting in a cyclical, systematic response clearly evident in the first 54 hours of testing (Figure 103b). After 54.5 hours, the crack depth began steadily increasing to 0.57 mm at an average rate of 19.6 nm/s. After 62.6 hours of testing, a sharp increase of 0.51 mm was observed and followed by a flatter region, representative of lower crack velocities. This cycle of a steep increase in crack depth followed by a flatter region occurred two more times, beginning after 63.9 and 66.2 hours of testing and correlates to an increase in crack depth of 0.79 and 0.86 mm, respectively. The small step changes prior to final fracture are assumed to be representative of ductile overload of remaining AA5083-H116 ligaments. After 69 hours of testing and only approximately 15 hours of cracking, the AA5083-H116 V-notched sample fully fractured.

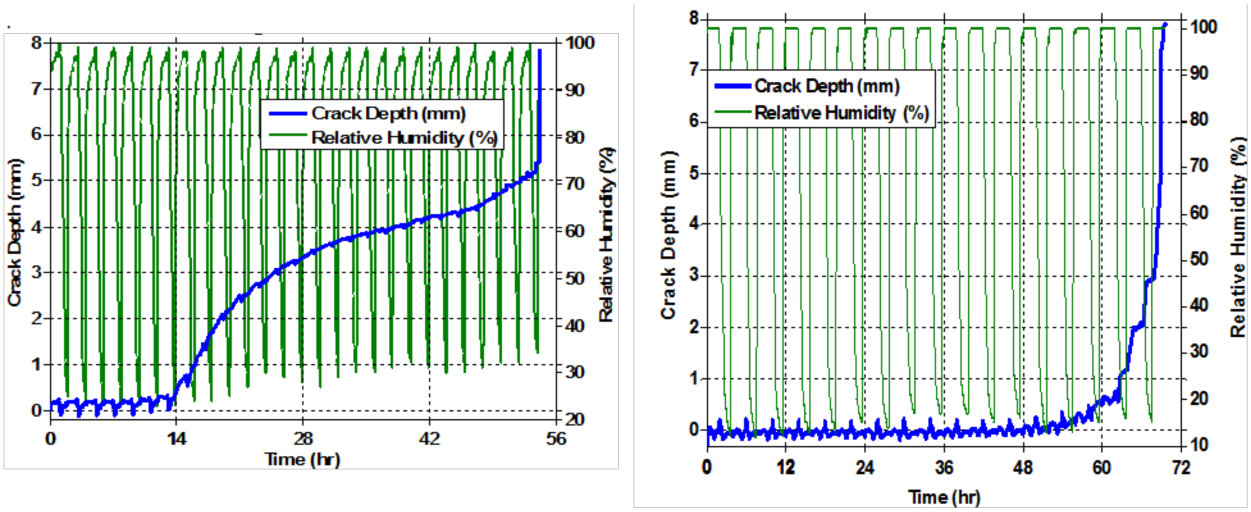

(a) (b)

Figure 103. ASTM G85-A5 test results for constant displacement crack sensor with AA5083-H116 material, (a) standard test and (b) modified procedure with two hour holds.

Crack velocity values were calculated by differentiating crack depth with respect to time. The resulting crack velocity was plotted as a function of relative humidity to study the dependence of crack velocity on cyclic humidity (Figure 104). Three (four-hour) cycles are shown, representing 12 hours of data beginning after 57 hours of testing. The negative crack velocity values and peaks at 100% RH are again due to temperature variation occurring when switching between dry-off and fog portions of the test cycle. Minimal cracking occurred during the wetting cycle as RH was increasing. During the drying cycle, crack velocity increased to a single maximum that shifted from 31% to 37% to 48% RH as crack depth increased. The highest crack velocity of 610 nm/s occurred during the drying portion of the final RH cycle at 48%. The peaks increased in magnitude with each subsequent RH cycle and increasing crack depth. This increase most likely occurred because the stress intensity at the crack tip increased as the crack propagated (Figure 105) (Rihan, Singh Raman, & Ibrahim, 2005). For all three cycles, crack velocity was halted once RH dropped below 22% RH.

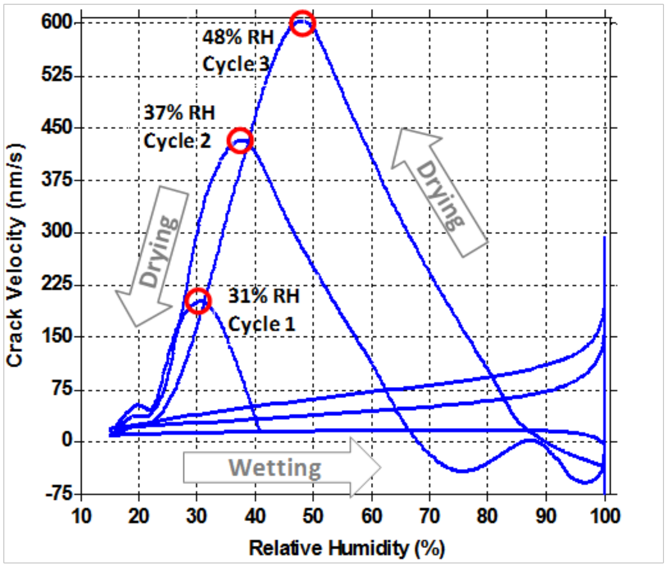

Figure 104. AA5083-H116 crack velocity versus relative humidity during modified ASTM G85-A5 testing.

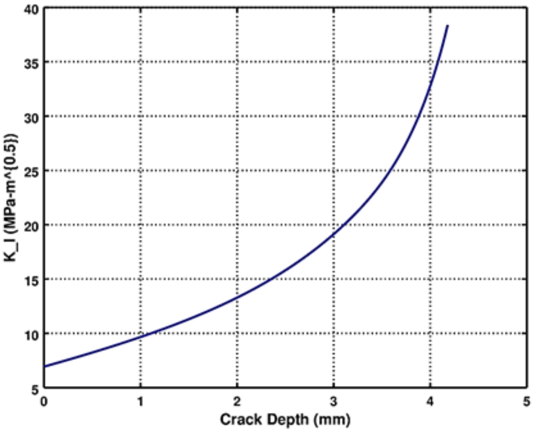

Figure 105. Calculation of Mode I stress intensity as a function of crack depth in circumferentially V-notched specimen (Rihan, Singh Raman, & Ibrahim, 2005).

6.2.1.5 GM 9540P

During the initial 24 hours of the first GM 9540P test, minimal change in crack growth was observed (Figure 106). Crack depth deviations observed during this time were assumed to be related to temperature change effects on the sensor. After 24 hours of testing, a large step change correlating to 0.48 mm of crack growth was observed during the transition from dry to wet in the test cycle. This result was not consistent with previously observed cracking during the drying cycle. Minimal change in crack growth was observed during sustained wetting and drying portions of the test cycle. This trend of minimal crack growth followed by a large step change in crack growth (ranging from 0.35 to 1.10 mm) during the transition from drying to wetting was observed on all eight 24-hour GM 9540P test cycles until final fracture occurred after 192 hours of testing. During the transition from dry to wet, crack velocity increased to a maximum value at very low RH, approximately 30-40%. All cycles demonstrated that cracking was predominately shut down at 50% RH and higher.

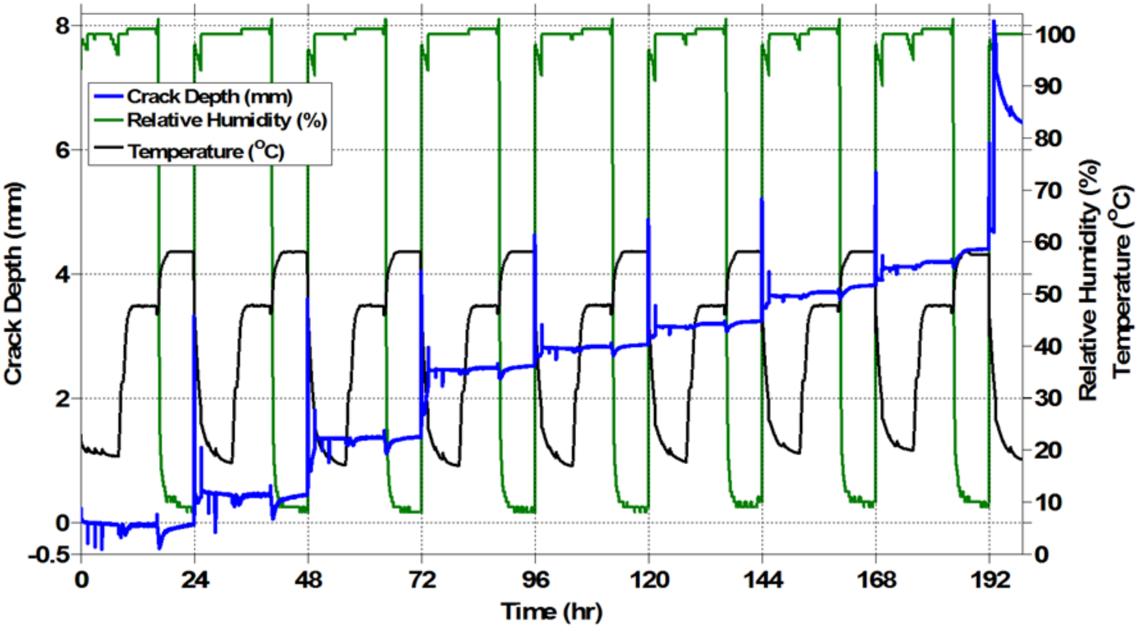

Figure 106. AA5083-H116 crack propagation measured by constant displacement cracking sensor in GM 9540P test.

A modified GM 9540P test was conducted next, where temperature set-point was constant at 35 °C, although chamber temperatures still fluctuated by 1-2 °C during RH transients. Temperature was maintained to isolate crack response as a function of RH. During the first 94 hours of testing, minimal change in crack growth was observed. Slight deviations observed during this time were related to the inherent temperature changes as the sample was wetted and dried. After 94 hours of testing, a pattern of cracking was observed for each 24-hour cycle of the GM 9540P iso-temperature test (Figure 107). This pattern remained consistent until final fracture occurred after 384 hours of testing. During the transitions from wet to dry, a large increase in crack growth (up to 0.56 mm) was observed. Crack growth rates decreased as the drying period continued before a small step change increase in crack depth (~0.08 mm) occurred during the transition from dry to wet. Cracking was then observed to rapidly arrest when transitioning to periods of high RH.

The resulting crack velocity was plotted as a function of relative humidity to study the dependence of crack velocity on cyclic humidity (Figure 108). Four 24-hour cycles are shown, representing test hour 234 to test hour 331 of the previously discussed GM 9540P iso-temperature testing. Test cycles were labeled in chronological order such that ‘Cycle 1’ and ‘Cycle 4’ correlate to the first and last 24 hours of the test window, respectively. Negative crack velocity values are assumed to be a result of temperature variation effects. Because the test was run under ambient temperature conditions, some variation occurred as a result of HVAC system switching and test cycle period switching (e.g., wetting to drying).

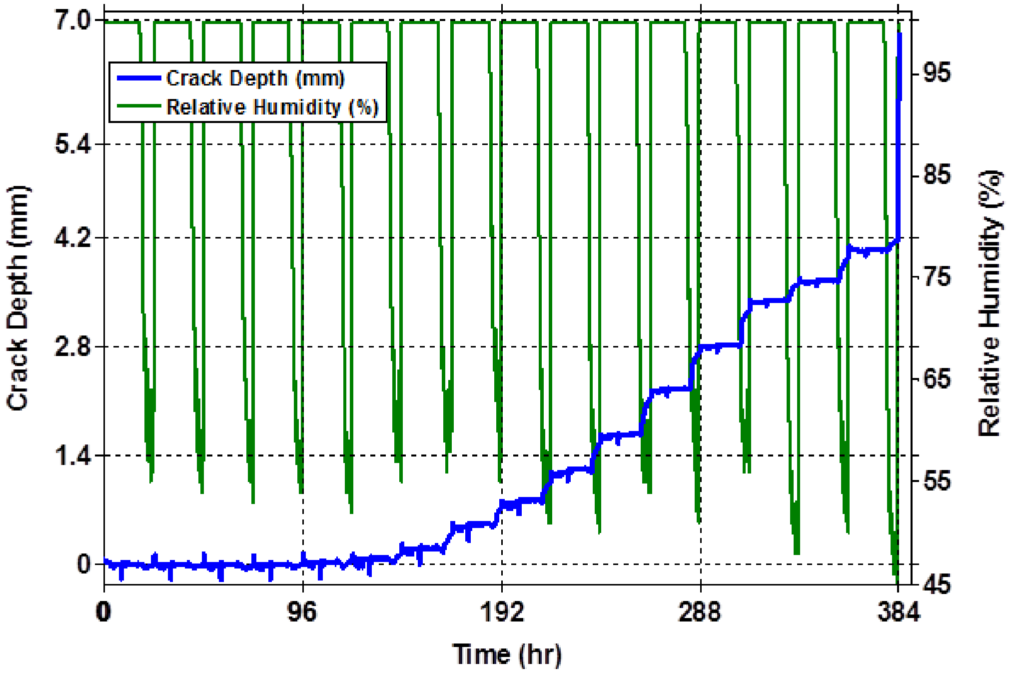

Figure 107. **AA5083-H116 crack propagation measured by constant displacement cracking sensor in modified, isothermal GM 9540P test.**

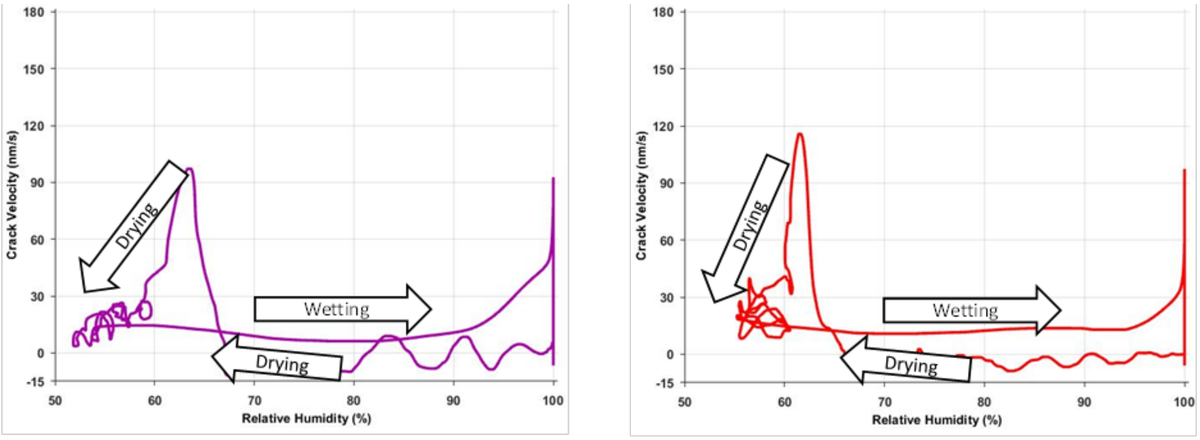

Cycle 1 Cycle 2

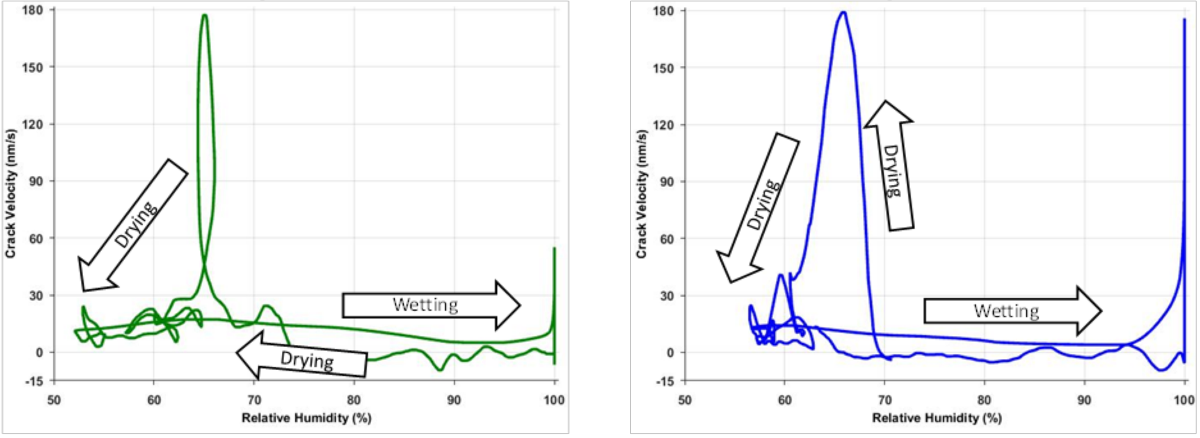

Cycle 3 Cycle 4

Figure 108. AA5083-H116 crack velocity measured by constant displacement sensor during modified, isothermal GM 9540P test as a function of RH for 4 cycles.

Crack velocity values increased during the transition from wet to dry, and reached a maximum value at 61-66% RH. The magnitude of the crack velocity peaks increased as the fracture sample's crack depth increased, as observed with the other tests. Cracking rates then decreased as the drying cycle progressed. Because the drying cycle was also run at ambient temperatures, RH was only controlled to mid-50% levels. No increase in crack rate was observed during the transition from dry to wet until > 90% RH when a small step change in crack growth occurred. Cracking was then quickly arrested during the remaining wetting period.

6.2.2 *Constant load crack sensor testing results*

The preliminary demonstration of the constant load crack sensor was carried out using AA7075-T651. A four point bend specimen was spring loaded into the test fixture to create an applied Mode I stress intensity of 10 MPa-m$^{1/2}$. The fixture was salted by exposing it to cyclic ASTM G85-A5 conditions for 300 hours. Following this exposure, the constant load crack sensor was exposed to cyclic RH treatments in a Thermotron chamber. RH was cycled between 30% and 90% RH at 35 °C. Hold time at the maximum and minimum RH was one hour with a two hour ramp time between RH steps. As with the constant displacement crack sensor, maximum crack velocity was measured during the drying ramps of the cyclic test (Figure 109 and Figure 110). The maximum velocity measured during the drying step occurred at approximately 40% RH with maximum values in the range of 13 to 21 nm/s. A "double" spike in crack velocity was observed in two of the cycles.

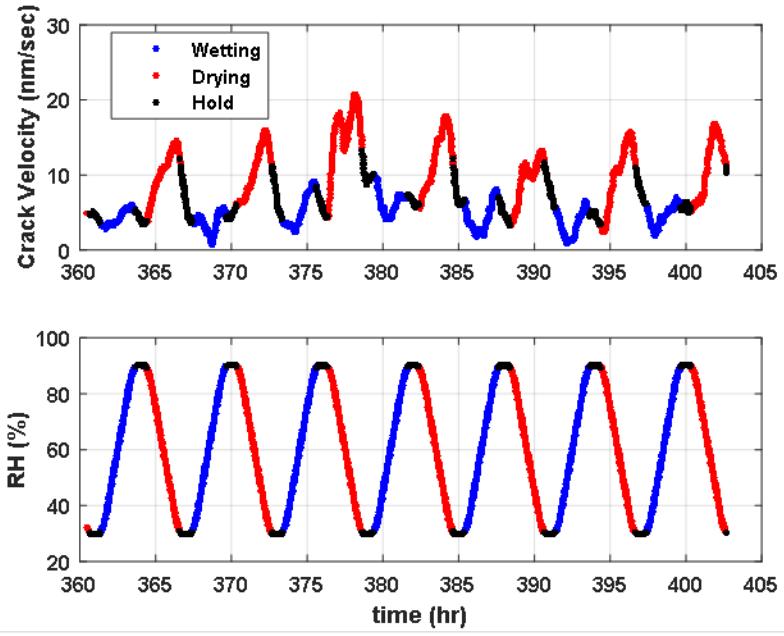

Figure 109. AA7075-T651 constant load crack sensor SCC velocity measurements (top) during RH cycling (bottom).

The next round of testing conducted with the constant load crack sensors on AA7075-T651 focused on intermediate RH holds both during wetting and drying. Crack growth versus RH and average crack velocity versus RH is plotted in Figure 111. Similar SCC velocity-RH relationships were observed in the pre-cracked specimens doped with saturated NaCl. Crack velocity was observed to be maximum at the 60% RH hold. The velocity stayed low but, non-zero for the entirety of the drying steps and re-wetting steps up until the transition from 70% to 80% RH where a second, mall spike in velocity occurred. The 70% to 80% transition brought the salted specimen through the deliquescence point of 76% RH. Following this spike, crack velocity decreased to nearly zero during fully wetted conditions.

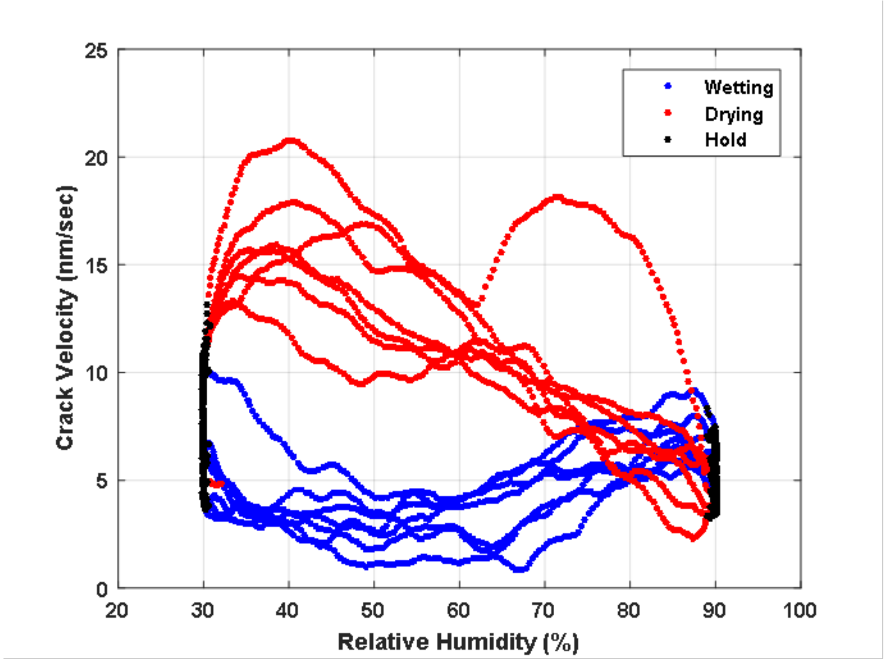

Figure 110. AA7075-T651 constant load crack sensor SCC velocity as a function of RH.

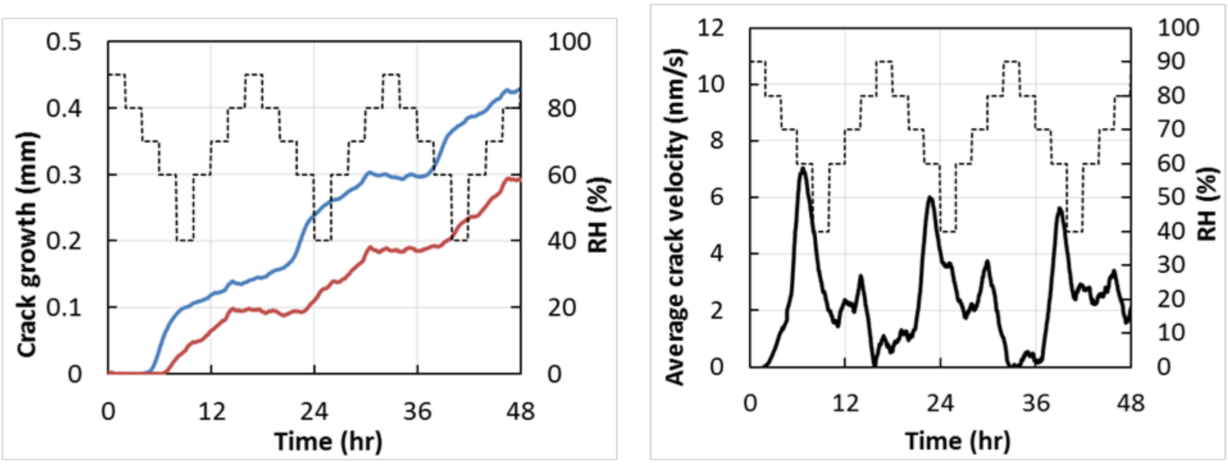

(a) (b)

Figure 111. AA7075-T651 constant load crack sensor results during cyclic RH testing with intermediate RH step holds. (a) Crack length for two sensors and (b) average velocity versus time/RH.

6.2.3 *Outdoor exposure of cracking sensor testing results*

Two EAC constant displacement sensors were deployed at corrosion racks in Battelle Ponce Inlet facility (FL) and at Alcoa LAX to collect crack depth and temperature measurements.

The outdoor EAC constant displacement sensor deployed to Battelle Ponce Inlet facility, FL was returned after inconsistent communication issues were reported. It was determined that the polycarbonate NEMA 4X enclosure had several small cracks, allowing moisture ingress to the sensor's printed circuit boards. Despite the circuit boards' damage due to corrosion, the sensor's data was safely stored on the embedded flash memory. Crack depth as a function of time is presented in the below figure (Figure 112a). Crack depth appears to fluctuate, which may be a result of the circuit board issues. However, temperature effects on the sensor electronics as well as physical changes in load due to differing material coefficients of thermal expansion also may have caused some fluctuation in sensor output. The AA5083-H116 sample was visually fractured upon return.

A second outdoor EAC constant displacement deployable sensor installed at Alcoa LAX was returned after it appeared that minimal cracking was occurring (Figure 112b). The sensor's preload was increased and it was redeployed at Alcoa LAX. Crack depth as a function of time for the initial exposure is presented below. The new data had not yet been collected from the second deployment during preparation of this report.

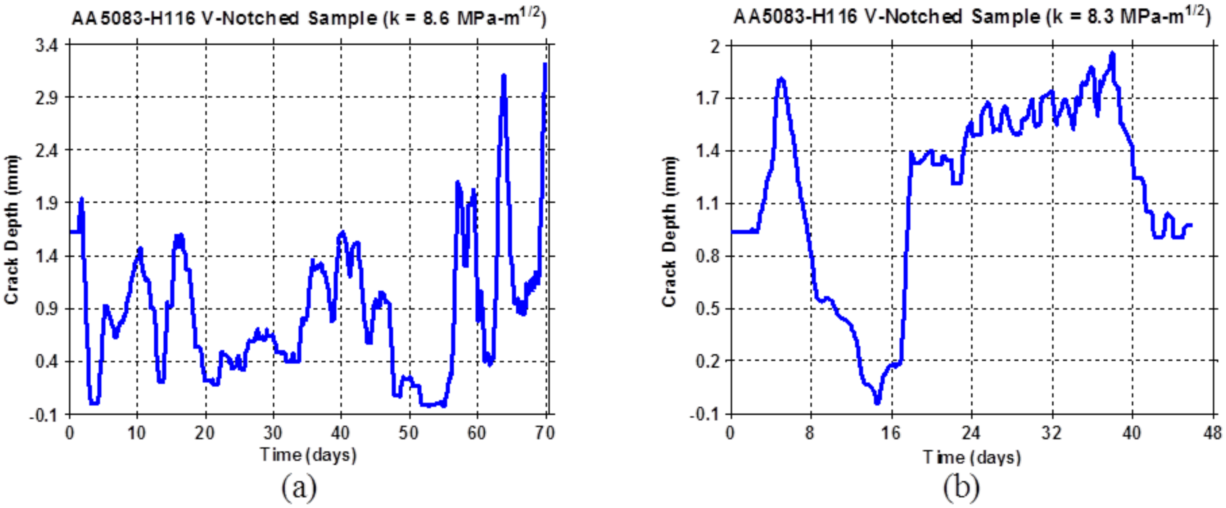

Figure 112. AA5083-H116 constant displacement crack sensor results from outdoor exposure at (a) Daytona Beach, FL (b) LAX.

6.2.4 *SCC crack velocity and cyclic RH discussion*

Many authors have conducted EAC studies of sensitized 5XXX series alloys using double-cantilever beam (DCB) specimens with intermittent salt solution applied to the crack tip using a dropper (Bovard et al., 2011; Cormack, 2012; Gao, 2011). This effectively creates a cyclic wet-dry condition. Crack velocities are recorded manually throughout testing. Bovard measured crack growth in AA5083 sensitized to 44 mg/cm^2 on the order of 1000 nm/s with applied stress intensities (K_I) ranging from 10-18 MPa-m$^{1/2}$. At a stress intensity of 8 MPa-m$^{1/2}$, crack velocities were an order of magnitude lower at approximately 100 nm/s (Bovard et al., 2011). Cormack observed EAC velocities in AA5456-H116 sensitized to approximately 60 mg/cm^2 on the order of 3-30 nm/s for applied K_I of 10-14 MPa-m$^{1/2}$ (Cormack, 2012). Gao recorded crack growth rates in 5083 DCB specimens using ultrasonic techniques ranging from 300-700 nm/s in 1.0 M NaCl at an applied K_I of ~11 MPa-m$^{1/2}$ (Gao, 2011). The velocity measurements for AA5083 in the ASTM G85-A5 conditions in this work (200-600 nm/s) correspond well to these literature values. EAC of sensitized AA5083 is typically attributed to electrochemical interactions of the Mg-rich β-phase (anodic) precipitated in a more-or-less continuous distribution along grain boundaries with the surrounding matrix (Searles, Gouma, & Buchheit, 2001), although the role of hydrogen (embrittlement) has been suggested (Pickens, Gordon, & Green, 1983), with sources of hydrogen including reduction reactions supporting anodic corrosion of the β-phase and absorption from a humid environment.

EAC studies with AA7075-T651 have been conducted using both immersion and humid atmosphere exposures with crack velocity measurements similar to those obtained in this work (10-13 nm/s). Nguyen et al. conducted immersion tests in NaCl solutions using DCB specimens and measured crack velocities ranging from 10-20 nm/s. The authors did not quantify the applied stress intensity magnitude. They measured alterations in crack solution chemistry and found that local changes in concentration of dissolved metal ions and pH within the occluded crack contributed to EAC. Nguyen concluded that anodic dissolution was the primary contributory mechanism (Nguyen, Brown, & Foley, 1982). Shastry et al., using DCB specimens, measured crack velocity of AA7075-T651 to be 7-10 nm/s at an applied K_I of about 5.5 MPa-m$^{1/2}$, under immersion conditions. Their study was focused on the metallurgical aspects of AA7075 and found that increased grain boundary solute concentration of Mg, Zn, and Cu due to changes in solution heat treatment, were likely responsible for increased EAC susceptibility (Shastry, Levy, & Joshi, 1981). Cooper and Kelly measured EAC velocities ranging from 10 to 90 nm/s in under-aged material of AA7050 and roughly 4 nm/s in peak aged material using wedge-open loaded specimens, in immersion conditions. Applied stress intensities were reported as 14-15 MPa-m$^{1/2}$ at the start of the test and 9-12 MPa-m$^{1/2}$ at the conclusion. Cooper and Kelly concluded that anodic dissolution contributed significantly to stage II crack growth in aqueous chloride solution by generating a critical crack tip solution chemistry, but its effect on EAC was on the same order of magnitude as hydrogen embrittlement (Cooper & Kelly, 2001). Scully reported plateau EAC crack velocity for AA7075-T651 at 15-20 MPa-m$^{1/2}$ in humid air environments to be approximately 10 nm/s (Scully, Young, & Smith, 2012).

The increased cracking rates during drying steps measured in this work is thought to be due to increased electrochemical activity during drying. High corrosion rates in metals during transients from wet to dry conditions under atmospheric exposure have long been known (Stratmann & Strenkel, 1990). This observation has been rationalized on the basis of accelerated oxygen reduction, as the electrolyte thickness is reduced in the drying phase. Mansfeld and Kenkel found maximum corrosion current in a galvanic couple under atmospheric conditions to occur at a point just before complete drying, again attributed to increased oxygen reduction with decreasing solution layer thickness (Mansfeld & Kenkel, 1976). Development of critical chloride concentrations leading to onset of pitting has also been attributed to the wet to dry transient (Vera Cruz, Nishikata, & Tsuru, 1996). It is therefore feasible that anodic dissolution and corresponding cathodic reactions (namely hydrogen generation and uptake leading to hydrogen embrittlement) are accelerated under the thin film developed during drying and may be responsible for the observed increase in EAC rates for AA5083 and AA7075 (Gangloff, 2003). The occluded geometry of the crack and capillary effects may also allow electrolyte to exist at RH below where the rest of the boldly exposed surface has fully dried.

CHAPTER 7
COMPARISON OF CORROSION RATE AND MORPHOLOGY BETWEEN LABORATORY AND OUTDOOR EXPOSURE TESTING

Next generation treatments and coating systems need to better protect against the mechanisms of corrosion-related failure most commonly observed in practice. Accelerated corrosion tests ideally increase corrosion rates while producing the same failures modes observed in outdoor conditions. Corrosion rates can be accelerated with the application of greater amounts (loading) of corrosive contaminants, elevated temperatures, and cyclic environmental conditions. Accelerated corrosion tests that cycle between wet and dry conditions have been developed to produce better correlations with actual atmospheric corrosion. In comparison with corrosion contaminants and temperature effects, the acceleration of corrosion by cycling environmental conditions is less understood. For example, both stress corrosion cracking and corrosion of sensors with damaged coatings are greatest during the drying process. These results indicate that the frequency of drying events may be an important parameter for accelerating corrosion. It is not yet clear whether the greatest acceleration in cracking or corrosion is dependent upon achieving a fully dry condition, or if only a highly concentrated thin film electrolyte due to drying is required.

In this chapter, the parameters that effect corrosion in outdoor exposure and indoor accelerated test conditions are evaluated. The corrosion morphology and electrolyte chemistry were analyzed and compared for indoor and outdoor exposures. In addition, the corrosion rates and damage modes were characterized with a combination of environmental sensors, corrosion sensors, crack sensors, and witness coupons. The corrosion and crack sensors are useful for evaluating the temporal effects of environmental conditions. The continuous measurements enable direct comparisons between corrosion rates and environmental conditions. The stress corrosion crack sensor results for outdoor exposure were previously described in Section 6.2.3. The comparison of indoor and outdoor exposure conditions that affect corrosion will facilitate the development of accelerated test methods that are more representative of damage modes observed in service.

7.1 Outdoor Sensor Measurements

The outdoor and indoor exposure conditions, corrosion rates, and damage modes are described. The AA7075-T6 Al IDE sensors provide continuous corrosion measurements that respond in real time to the environmental exposure conditions. The mass loss, witness coupons support verification of trends measured with the corrosion sensors.

7.1.1 *Environmental conditions and measurements*

Corrosion sensors, crack sensors, and witness coupons were evaluated in outdoor exposures and accelerated test conditions. Outdoor exposure conditions and corrosion damage were measured at four locations. The outdoor locations include the Battelle laboratory near Dayton Beach, FL, the Alcoa facility near LAX, CA, the Alcoa facility near Point Judith, RI, and

Wright-Patterson Air Force Base, OH. The outdoor exposure conditions were measured with the LS2A sensor suite for aircraft corrosion monitoring. The LS2A system includes temperature and relative humidity sensors. The system collected measurements in 30 minute increments. LS2A includes the Au IDE sensor described in Section 0 for measuring the conductance of the thin film electrolytes that are dependent on contaminant deposition and moisture. The outdoor exposure measurements were compared with the cyclic accelerated tests described in Table 4 in Section 4.1.5.1. The laboratory test temperature and relative humidity conditions were measured with the sensors built into the environmental chamber (Figure 39 in Section 4.1.5.1). The LS2A makes measurements and records data every two minutes in laboratory accelerated test cycles.

7.1.2 *Corrosion measurements and materials*

The severity of the environmental conditions was evaluated with respect to corrosion of AA7075-T6 using corrosion sensors and witness coupons. The LS2A systems measured corrosion with the same Al IDE impedance sensor described in Section 0, except that the sensors were bare (no coatings). Uncoated mass loss coupons of AA7075-T6 with stainless steel fasteners were included in both the outdoor and indoor exposures. The mass loss of the coupons was measured according to ASTM G1.

The outdoor exposure conditions of the four locations were relatively similar with regards to relative humidity and temperature from March to May 2014 (Figure 113). Similar to the indoor RH cycle of Cycle A in 4.1.5.1, the outdoor RH typically cycled daily between 45% and 85% RH. The overnight low temperature minimums almost always corresponded with overnight humidity peaks greater than 85% for all of the locations. Point Judith was the least likely to not dry out during the day, and RH did not go below 45% in almost one out of five days.

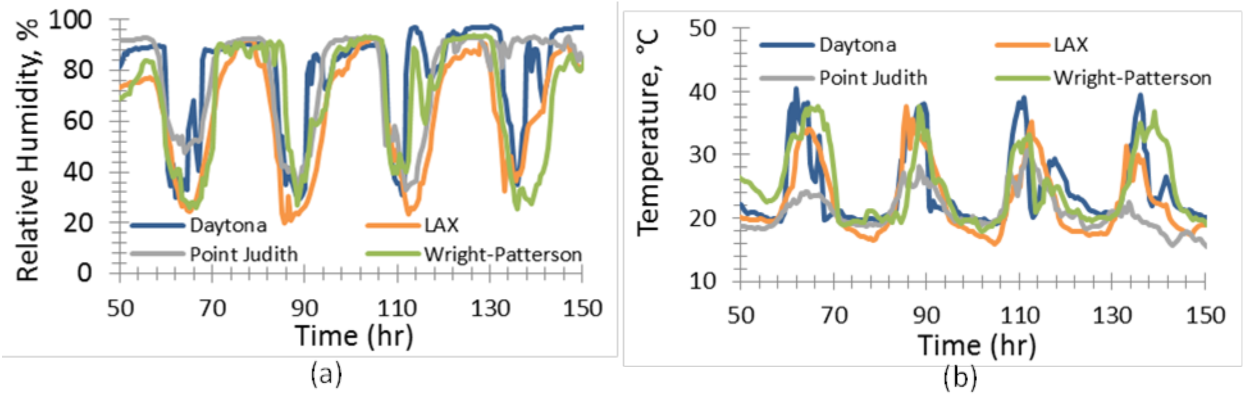

Figure 113. Example outdoor exposure conditions of (a) relative humidity and (b) temperature measured with LS2A corrosion monitoring systems in March of 2014.

7.1.3 *Outdoor corrosion measurements using corrosion sensors*

The most severe corrosion occurred overnight. The peak free corrosion rates of AA7075-T6, measured with the LS2A, corresponded with the time periods of highest humidity (Figure 114). The highest humidities surpass the deliquescence of sodium chloride, a predominant constituent of sea aerosols, so that these surfaces would be expected to be hydrated. Salt contaminants that accumulate on the panel surfaces absorb water from the atmosphere at humidities above NaCl deliquescence. The formation of aqueous electrolytes on the panel facilitates ionic transport required for corrosion and supports coupling of anodic and cathodic sites over the surface. The highest corrosion rates occurred when the conductances were greatest. High conductance measurements are related to high humidity and contaminant loading to produce thin film electrolytes. The cumulative corrosion measured with the Al IDE sensor were similar for Daytona, LAX, and Wright-Patterson Air Force Base; while, the cumulative corrosion for Point Judith was about fives time greater than these other locations (Figure 115). Corrosion measurements based upon the mass loss coupons were comparable to the LS2A measurements, where mass losses for Daytona, LAX, and Wright-Patterson Air Force Base were similar, and those of Point Judith were about five times greater (Figure 116).

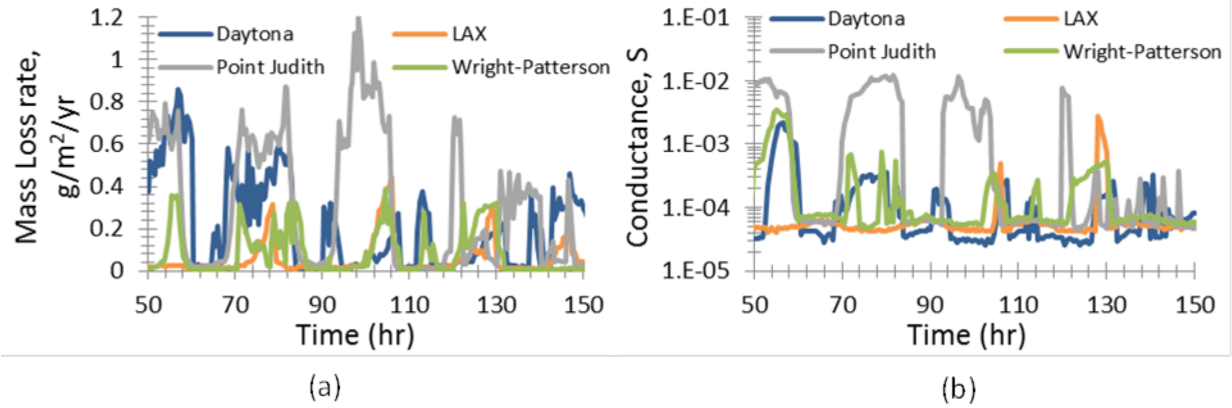

Figure 114. (a) Free corrosion and (b) atmospheric thin film conductance measured on AA7075-T6 outdoors with LS2A corrosion monitoring systems in March of 2014.

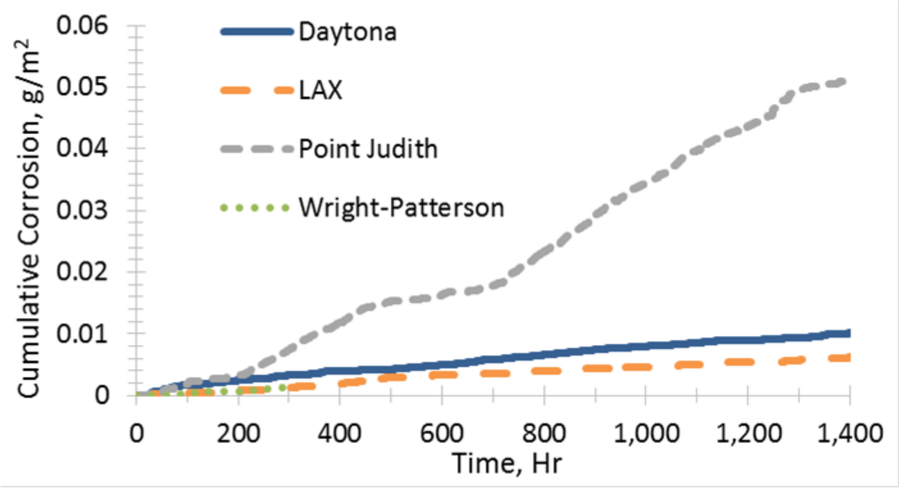

Figure 115. The cumulative corrosion of AA7075-T6 measured with the Al IDE sensor starting in March of 2014.

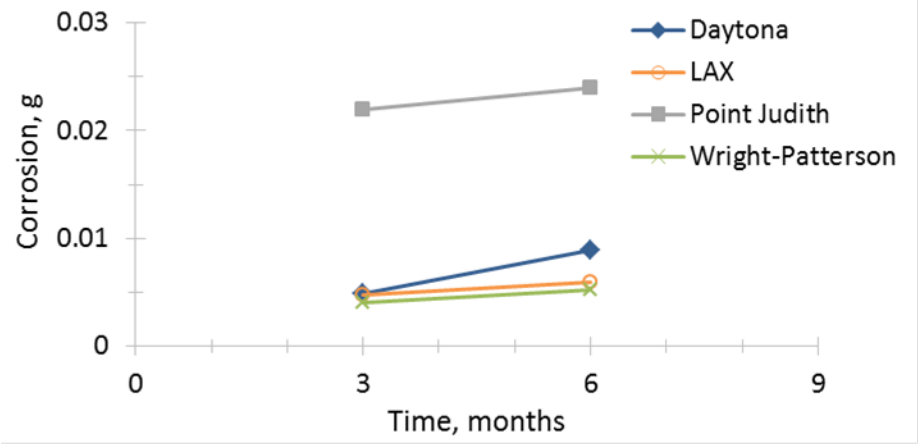

Figure 116. Mass loss measurements of corrosion with bare mass loss coupons.

The greater corrosion rates of Point Judith may be associated with the high minimum RH (less drying) or high amounts of salt deposition. The time of wetness at Point Judith, defined by the hours exposed to relative humidity greater than 76%, was about 50% greater than those of the other locations (Figure 117). Times of increased corrosion rates, at 200 and 700 hours, corresponded with periods of increased conductance (Figure 115). By integrating the conductance with respect to time, a cumulative severity parameter associated with contaminant loading and RH can be calculated. The cumulative conductance measured at Point Judith was about ten times greater than the other locations (Figure 118). The five times greater corrosion rate of Point Judith, relative to the other exposure sites, may be the most indicative of higher salt loading although a greater time of wetness would also be a contributing factor.

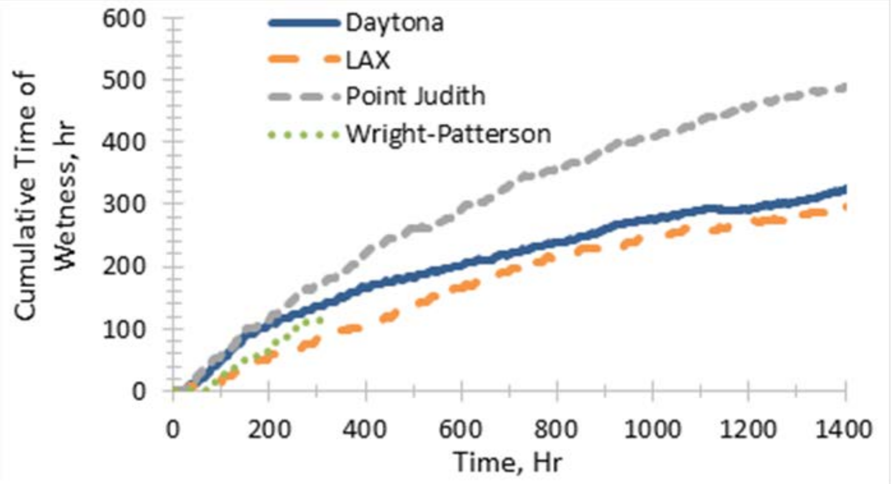

Figure 117. The cumulative time of wetness determined by the RH measurements by the LS2A corrosion monitoring systems starting in March of 2014.

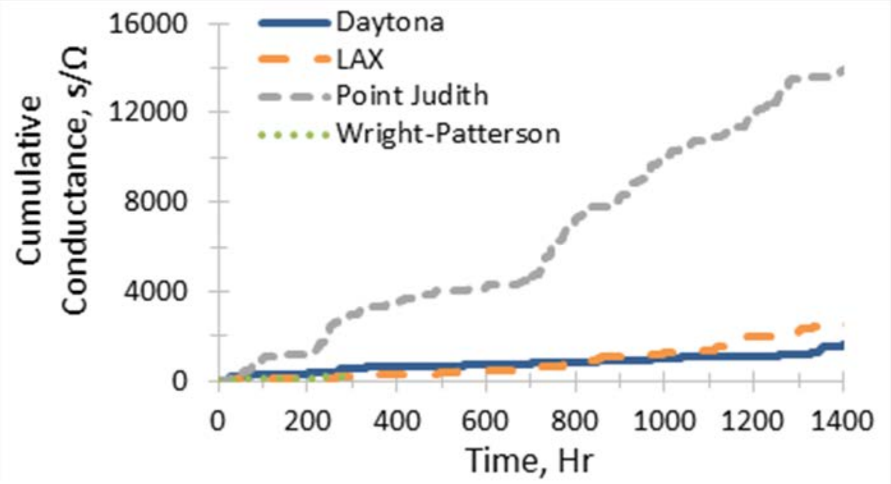

Figure 118. The cumulative conductance of the thin film electrolytes that form on the bare Au IDE due to the deposition of environmental contaminants, such as sea aerosol, and exposure to high humidity by the LS2A corrosion monitoring systems starting in March of 2014.

7.1.4 *Comparison of sensor measurements during outdoor exposures and accelerated laboratory tests*

The indoor exposure conditions of the accelerated test cycles of Table 4 were more severe than the outdoor exposures at the four locations identified i n Section 7.1.1. Note that the following results regard measurements with bare, uncoated Al IDE and Au IDE sensors while those presented in Section 4.2.5 were for coated and scribed sensors. The AA7075-T6 free corrosion rates on bare Al IDE sensors in the accelerated laboratory tests were about four to twenty times greater than those measured for the outdoor exposures (Figure 119). These increased corrosion rates correlated with cumulative conductance measurements of bare Au IDE sensors that were four to twenty times greater for the laboratory accelerated tests than for the outdoor exposure conditions (Figure 120).

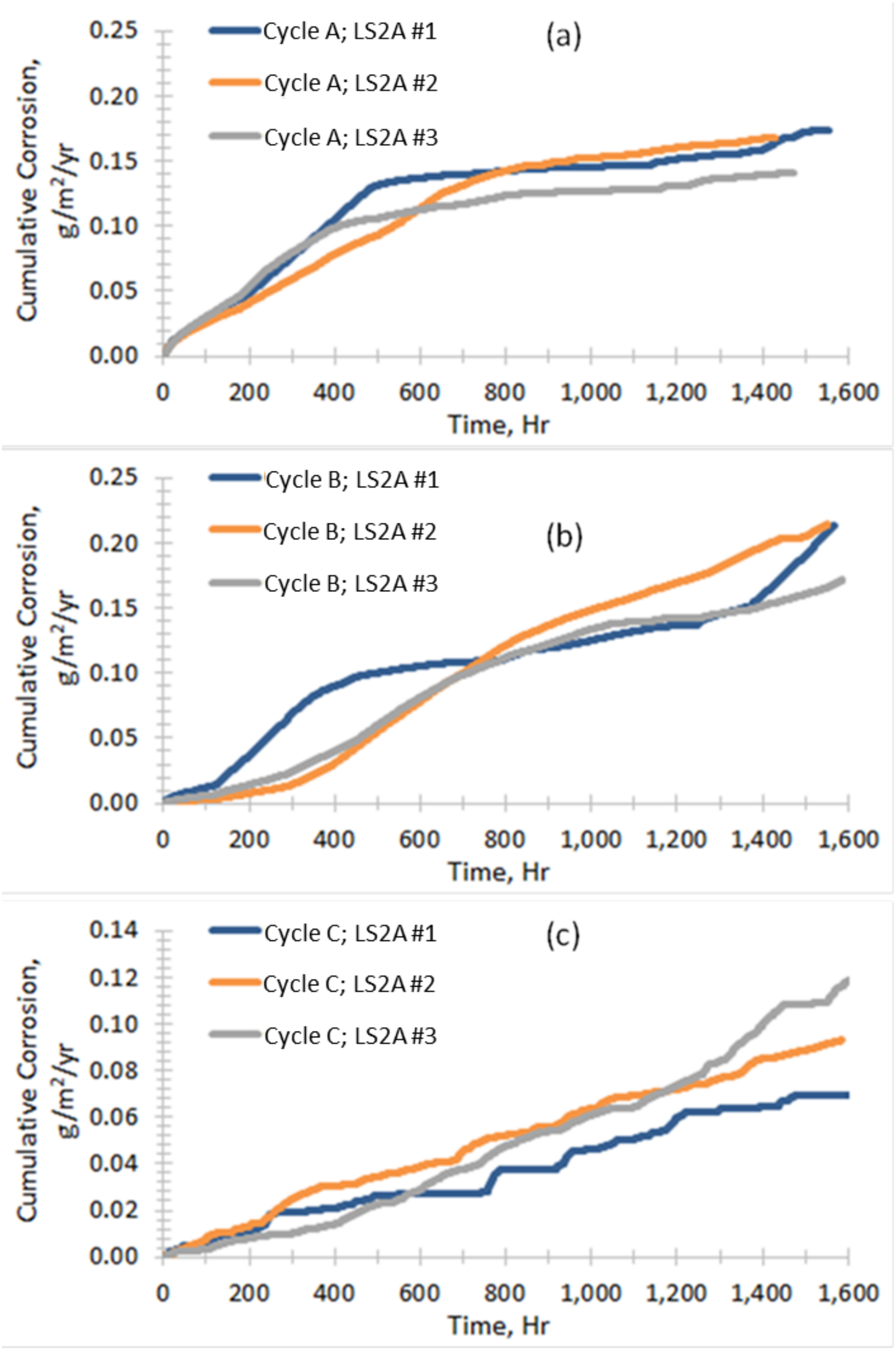

Figure 119. Cumulative corrosion of bare Al IDE sensors in triplicate (#1, #2, and #3) during the indoor accelerated test cycles of (a) Cycle A, (b) Cycle B, and (c) Cycle C from Table 4.

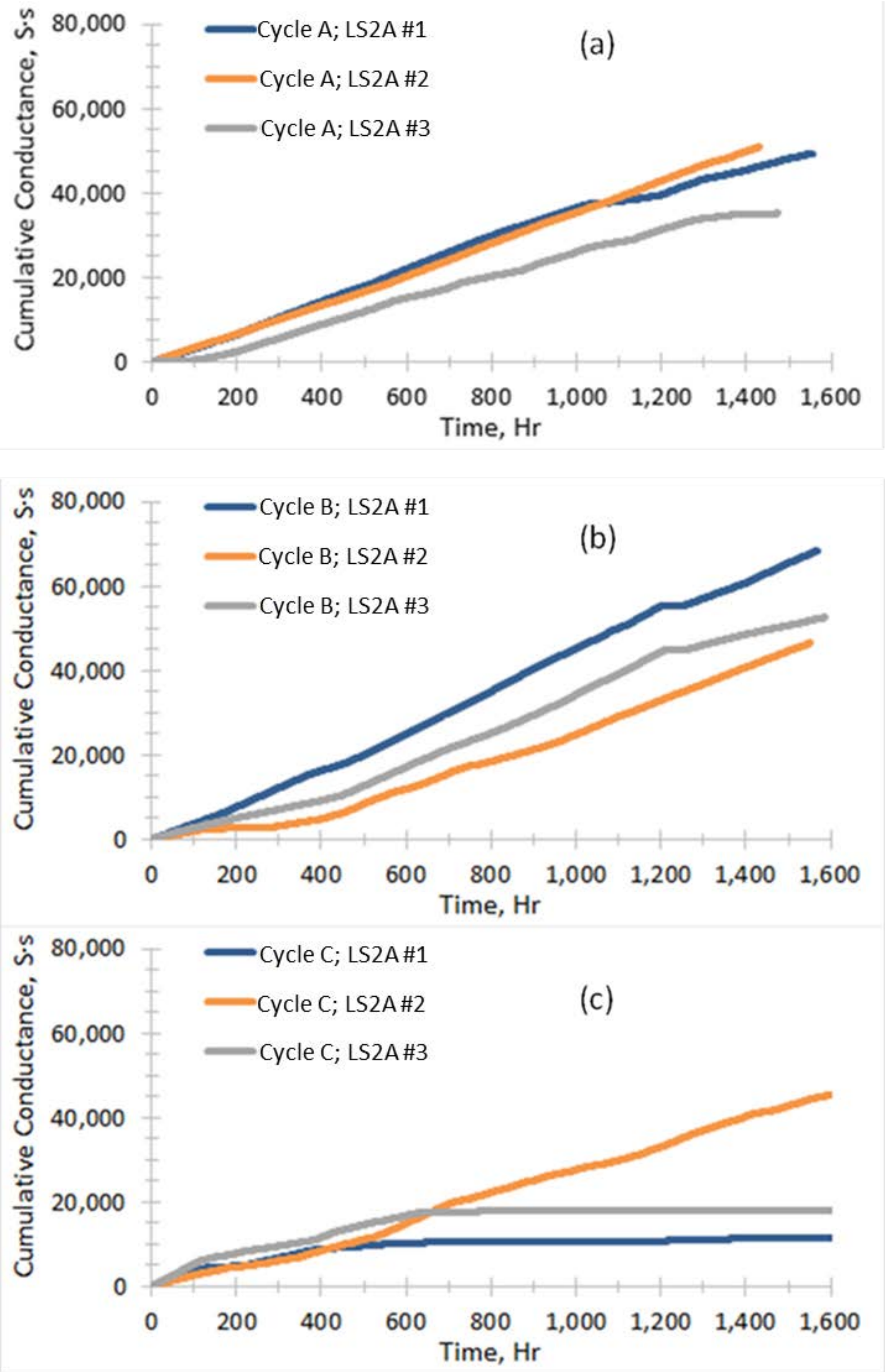

Figure 120. Cumulative conductance of bare Au IDE sensors in triplicate (#1, #2, and #3) during the indoor accelerated test cycles of (a) Cycle A, (b) Cycle B, and (c) Cycle C from Table 4.

7.2 Visual Observations of Outdoor Exposures

This chapter presents results on the effects of exposure environment on galvanic coupling between dissimilar substrates, as well as galvanic interactions due to different fasteners. Given the prevalence of mixed metal assemblies within the DoD systems, it is important to understand the effect of environmental exposure on the behavior of these galvanic couples. The environments of interest included four existing accelerated chamber tests: ASTM B117, ASTM G85-A4, ASTM G85-A5, and GM9540, as well as several outdoor exposure sites: Daytona Beach, FL, Wright Patterson Air Force Base (WPAFB), Point Judith, RI, and LAX airport. These exposure sites were chosen to represent a variety of environmental severities. The Pt. Judith and Los Angeles (LAX) sites have heavy industrial atmospheres, but with different average exposure temperature. Additionally, the Pt. Judith site is directly on the coast. Daytona Beach, FL provides one of the most aggressive exposure sites in the world with a high Environmental Severity Index (ESI). The WPAFB site in Dayton, OH has a low ESI. The range of atmospheric environments provided a range of chemical and morphology differences that allowed for making conclusions regarding environmental effects on corrosion.

7.2.1 *Materials and methods*

7.2.1.1 Effect of exposure environment on coating performance

The effects of exposure environment on coating degradation and performance were investigated using laboratory and outdoor exposure tests. The environments of interest included four accelerated chamber tests: ASTM B117, ASTM G85 A4, ASTM G85 A5, and GM9540. In addition to accelerated laboratory testing, coupons were placed at four different outdoor exposure sites: Daytona Beach, FL, Wright Patterson Air Force Base (WPAFB), Point Judith, RI, and LAX airport.

A detailed description of the test coupons, coating systems, surface imaging and analysis methods used in this portion of the work is documented in Section 4.1.

7.2.1.2 Fastener cross-sectioning procedures

The extent of the corrosion attack produced by ASTM B117, ASTM G85A4, ASTM G85A5 and GM9540P standard tests and the Pt Judith environment was assessed with optical microscopy. The panels were first cleaned according to the procedure described in Section 4.1 to remove the corrosion products, then cross-sectioned such that the damage inside occluded region and in the rivet holes could be imaged. The panels were cut with a high-speed wet saw and cold-mounted in epoxy resin to preserve the surface. The mounted samples were then polished to a 1 μm surface finish.

After images were collected from the optical microscope, they were analyzed ImageJ software and a Matlab code developed in-house. This software analysis yielded quantitative corrosion depth data.

7.2.2 *Results and discussion*

7.2.2.1 Effect of exposure environment on coating performance

A series of photographs documenting the extent of corrosion in lap coupons exposed at different outdoor sites for 12 months —both before and after disassembly—is shown in Figure 121 and Figure 122. Several general observations were made from visual inspection of the test coupons:

- Point Judith and Daytona Beach outdoor coupons showed minor effects at the fastener scribes. The lap surfaces more closely resembled GM9540P and ASTM G85 A5 than either ASTM G85 A4 or ASTM B117.
- ASTM B117 and WPAFB were the most benign environments for laboratory testing and outdoor exposure, respectively.
- Al fasteners did not survive on the C22 bare coupons, except in the case of the LAX and WPAFB outdoor exposures.

Another series of photographs documenting the extent of corrosion in lap coupons exposed at different outdoor sites for three years—both before and after disassembly—is shown in Figure 123 and Figure 124. Observations on the severity of each exposure site and the performance of different galvanic assembly types were made from visual inspection of the test coupons:

- Assembly type A showed the greatest resistance to environmental degradation at all exposure sites. The Al fasteners were the worst of the set, with corrosion product being visible around the fasteners at both the Daytona (DAY) and Point Judith (PTJ) sites. There was not extensive corrosion product formed in the lap. Some of the fasteners were difficult to remove from the PTJ set. Both the LAX and DAY sets only required mild force during disassembly.
- Assembly type B showed little corrosion around the scribes. Some of the fasteners were difficult to remove from the PTJ set, but overall, there was only minor corrosion in the lap.
- Assembly type C only performed well at LAX. The DAY panels had large amounts of bubbling under the coating on the back panel. The PTJ panels experienced excessive degradation, and the composite substrate failed (see Figure 125). The fastener heads were pulled through the composite panel, and the back panels could be crushed barehanded. The composite panel itself did not have much corrosion product on it.
- Assembly type D had a large amount of corrosion product on the steel substrates, and there was some coating flaking on the aluminum panels. The lap area showed a large amount of corrosion.
- Assembly type E performed better than D. Due to extensive rusting, fasteners could not be completely removed to take photographs of the lap areas.
- Assembly type F only performed well at LAX. The Ti and A286 fasteners both showed more corrosion than the Al. The fasteners could not be removed on the PTJ panels due to the large amount of corrosion product and metal exfoliation around the Ti fasteners.
- Assembly type G had large amounts of corrosion product on the PTJ panels, and the overall corrosion morphology at each site seemed to be similar to that observed on assembly type F panels.

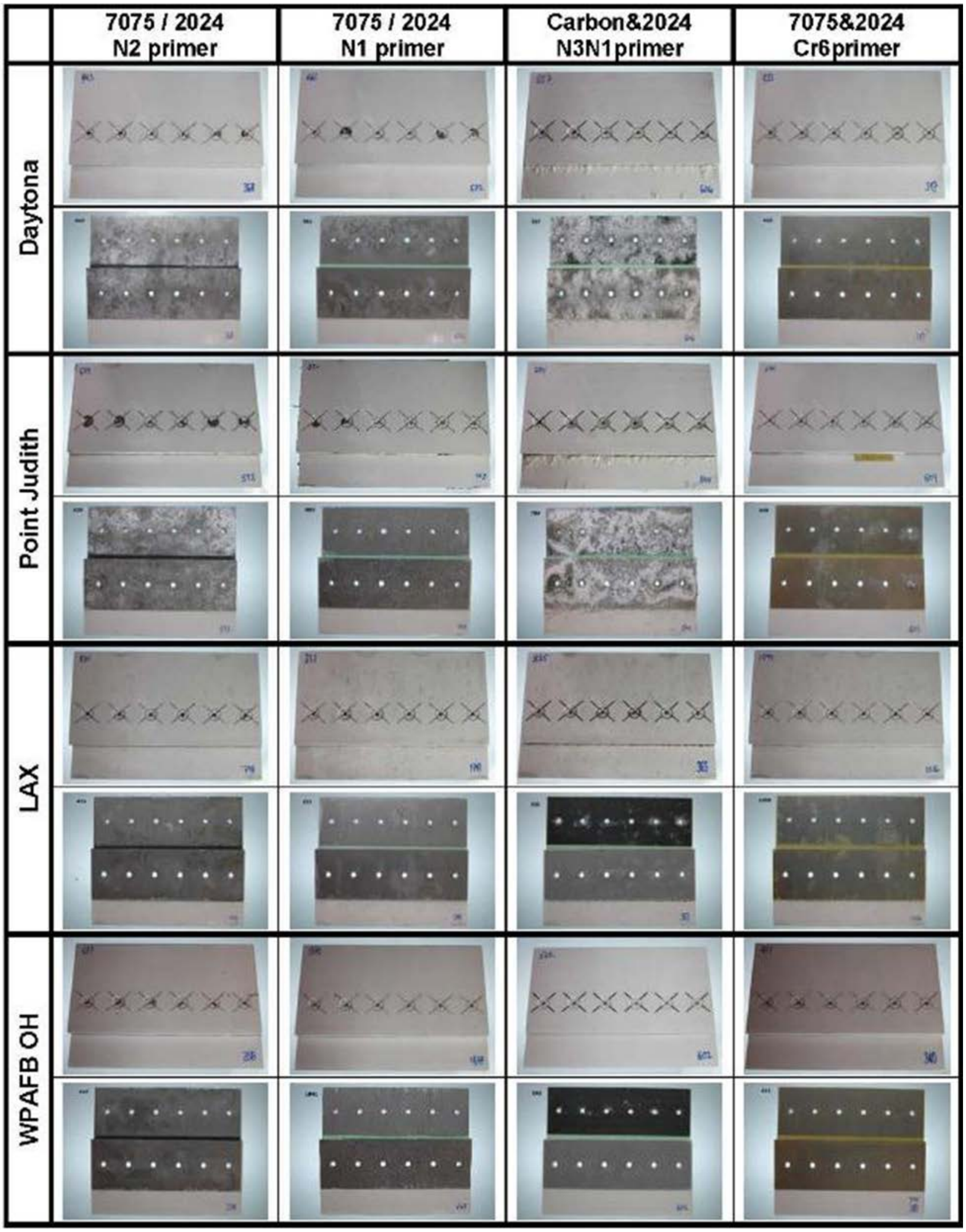

Figure 121. Lap coupons consisting of primarily Al alloy panels after 12 months of outdoor exposure.

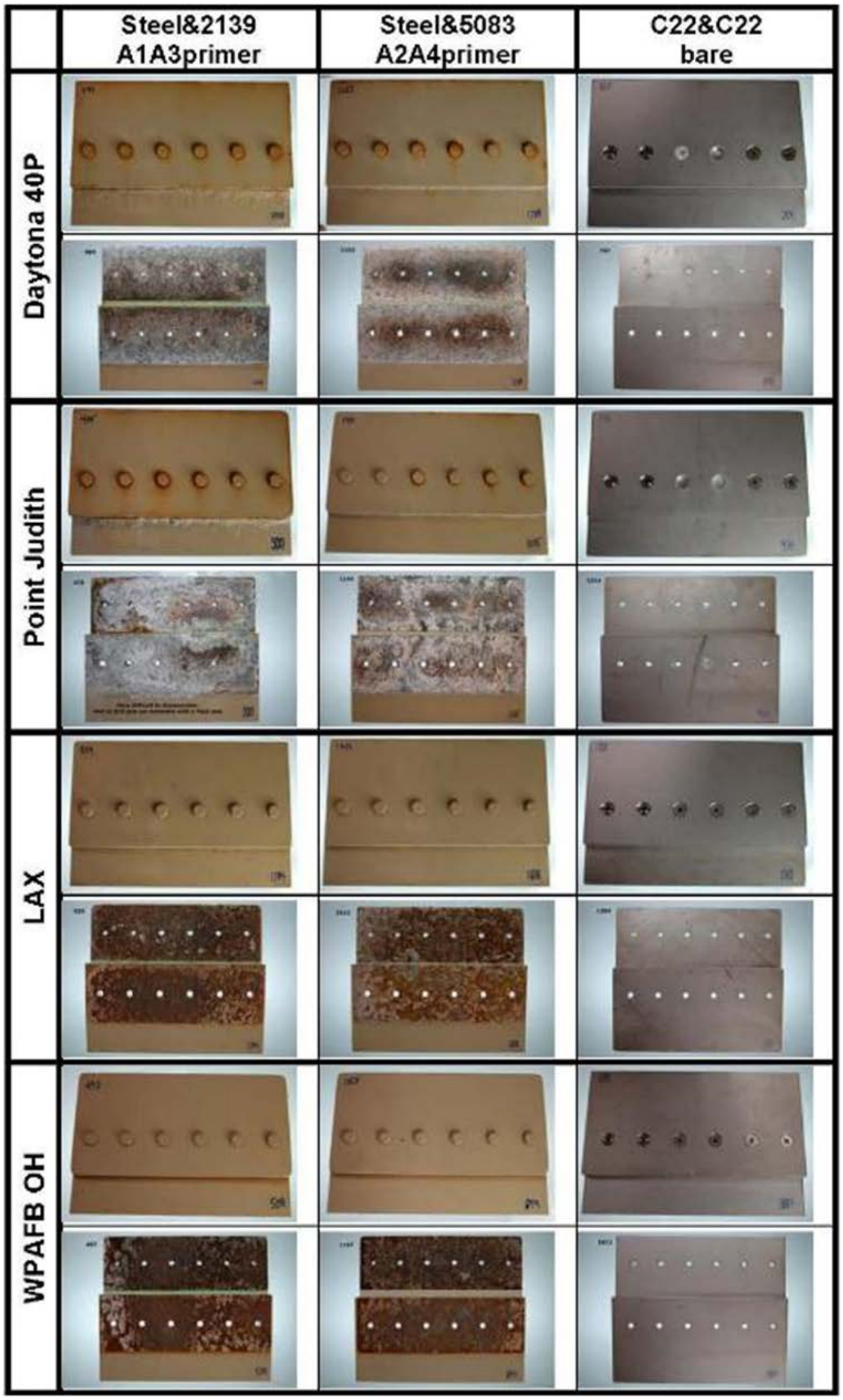

Figure 122. Lap coupons consisting of either steel or C22 panels after 12 months of outdoor exposure.

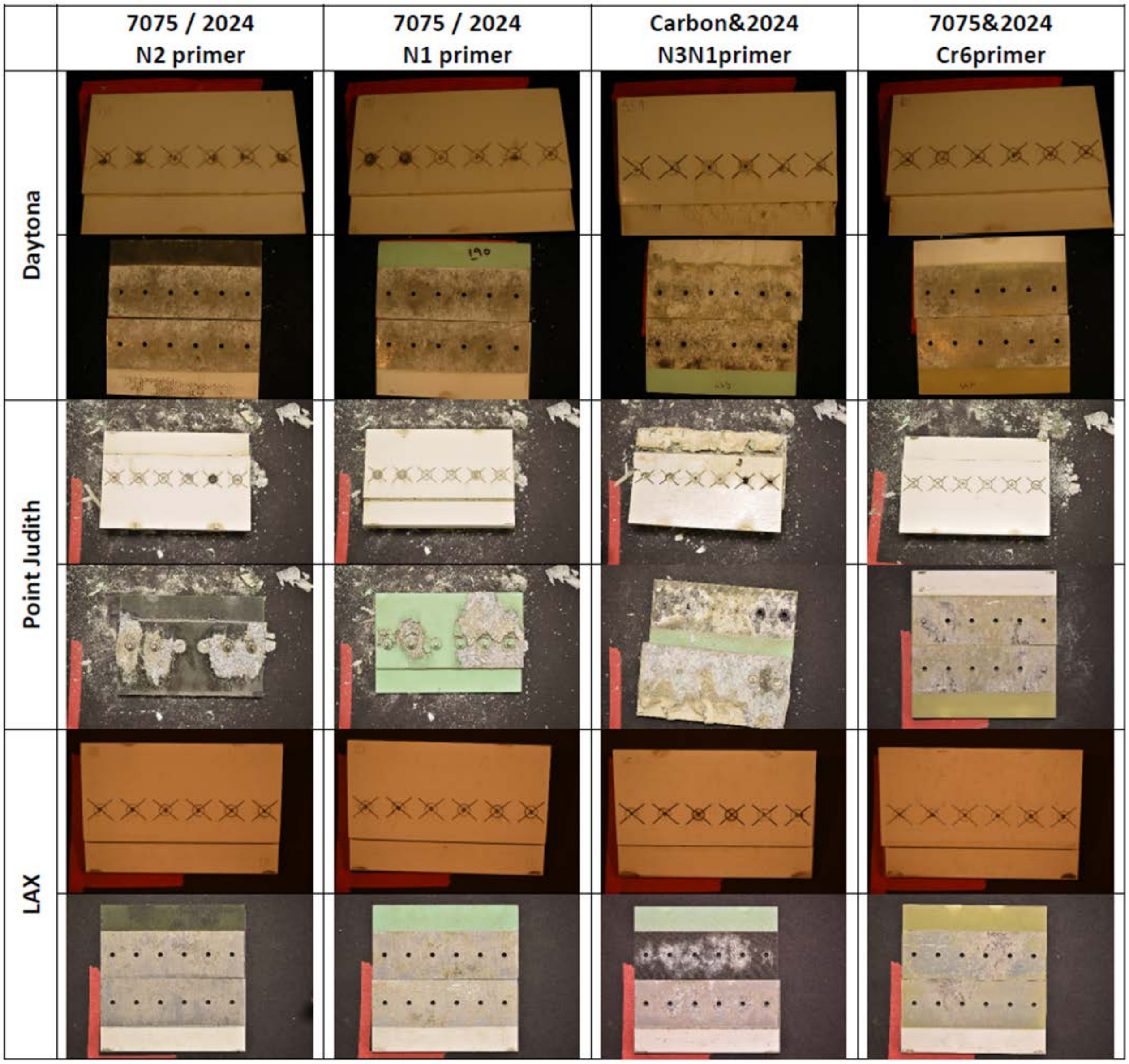

Figure 123. Lap coupons consisting of primarily Al alloy panels after three years of outdoor exposure.

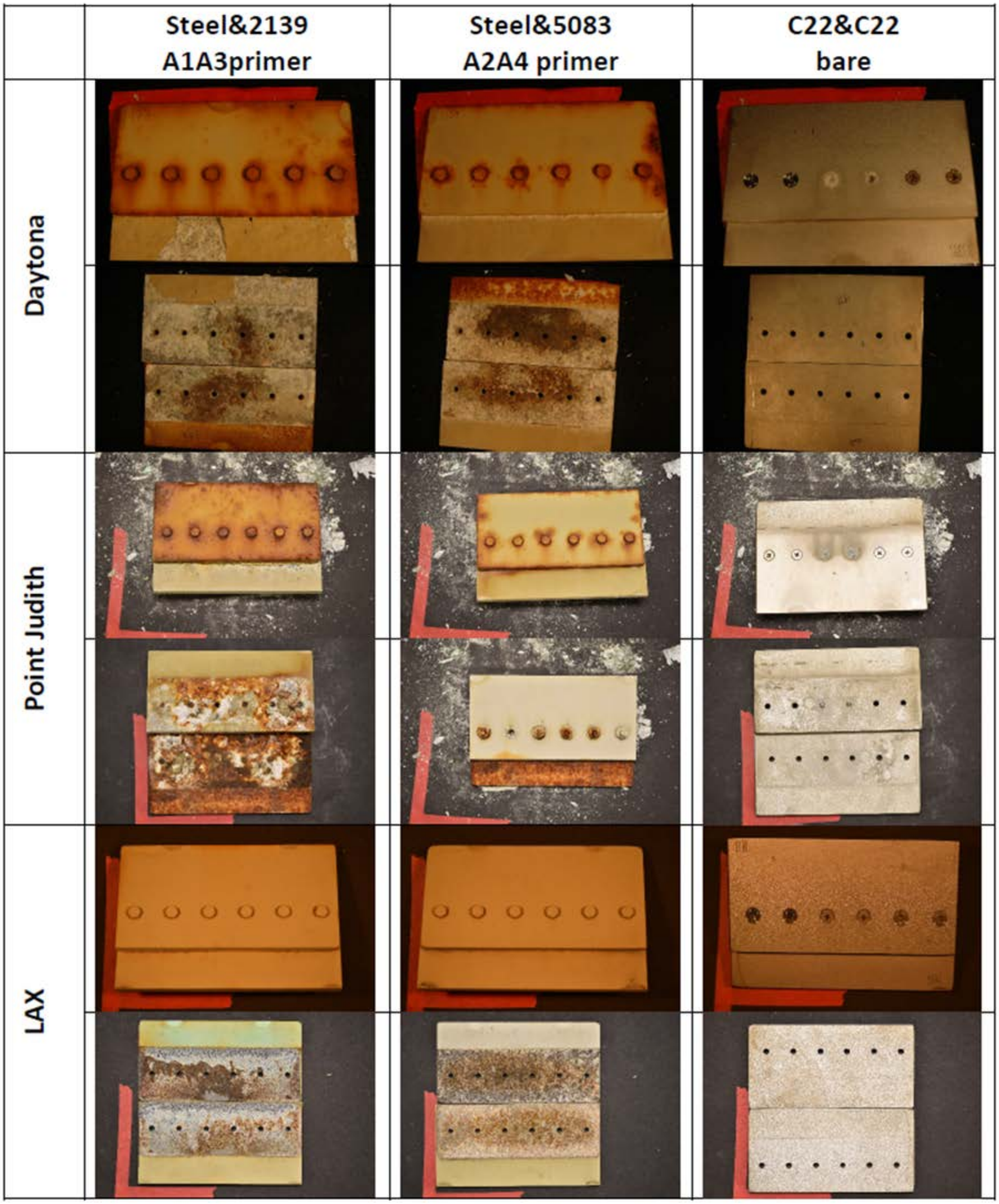

Figure 124. Lap coupons consisting of either steel or C22 panels after three years of outdoor exposure.

Figure 125. Extensive degradation of a composite substrate in assembly type C after three years of outdoor exposure at Point Judith.

7.2.2.2 Coating degradation and scribe creep in outdoor exposure environments

Lap coupons that were exposed at two outdoor test sites (Daytona Beach, FL and LAX airport) were analyzed to determine the extent of coating degradation and corrosion damage incurred after 6 months of outdoor exposure. Figure 126 shows photographic images of the coupons before and after disassembly, but prior to coating removal. The test panel that was coated with a hexavalent chromium coating (i.e. the control coating system) and exposed at Daytona Beach for 6 months, appeared mostly bright in the scribes around the Ti and Al fasteners, while the scribes around the CRES fasteners had darkened. In contrast, all scribes on the panel that was finished with a non-chrome coating system—appeared dark gray. Other than color changes in the scribe, there was no other discernable coating degradation in outdoor test panels exposed at Daytona Beach for 6 months.

The test panel coated with the hexavalent chromium coating and exposed at LAX for 6 months, had extensively more damage than its counterpart exposed at Daytona Beach. Namely, there was darkening in every scribe and coating degradation in both the countersink areas and across the entire test panel. In the case of the test panel finished with the non-chrome coating system, after 6 months of outdoor exposure at LAX, there was extensive coating degradation in the countersink areas and coating delamination on the Al fastener heads. Uniform coating degradation was observed across the test panel and it was more extensive than that of the chromate coating.

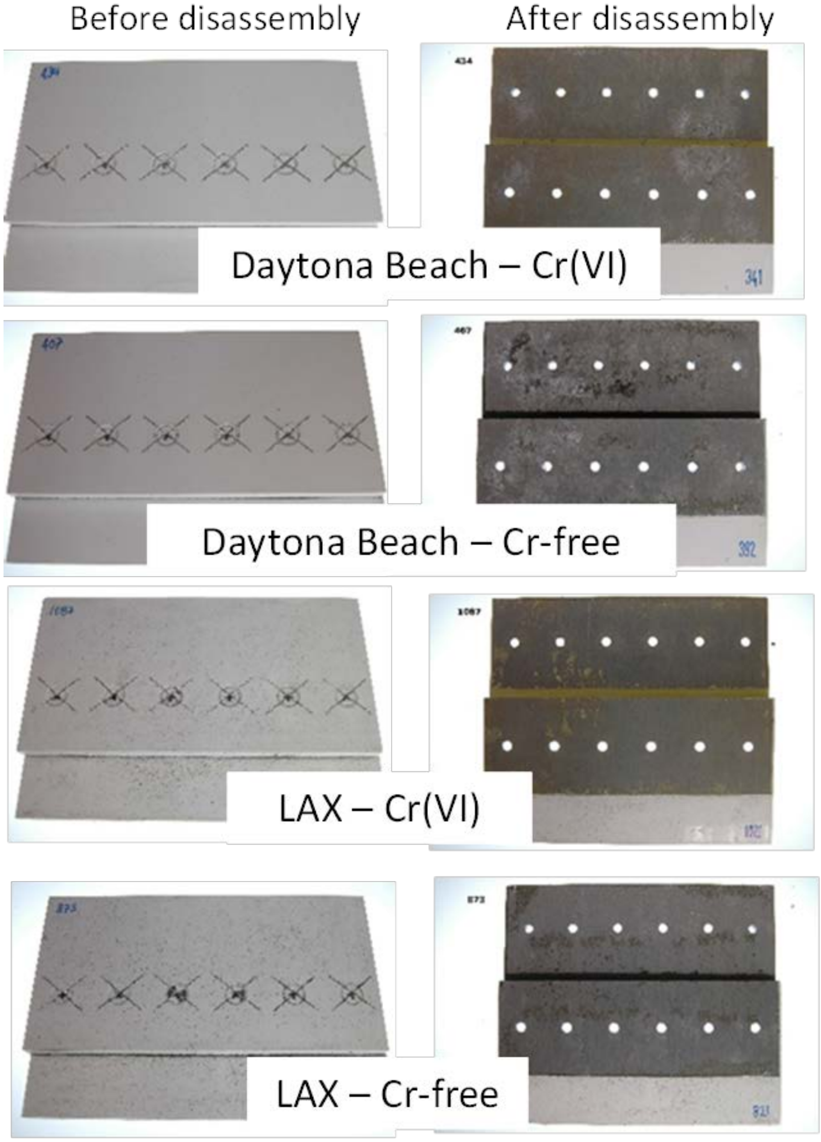

Figure 126. Test coupons after exposure in outdoor environments in Daytona Beach and LAX for 6 months.

In addition to visual inspection, a set of test panels were imaged and analyzed with optical profilometry to determine surface parameters that quantify the extent of corrosion damage. The coatings and corrosion products were first removed through a chemical cleaning procedure, which is described in Section 4.1.3.

After coating removal, the test panels were imaged using a Bruker NPFLEX optical profilometer. An example of a 2D surface profile for a test panel coated with non-chromated coating system exposed at Daytona Beach for 6 months is shown in Figure 127. The scan area around the scribe was 1.16 mm wide and 8.5 mm long, which was sufficiently large enough to capture all features of the scribe and the surrounding “uncorroded” surface. The scan area was subsequently increased based on the extent of scribe creep so that the entire scribe volume could be well characterized. The extent of corrosion in the scribes on this coupon is so minimal that the tooling marks from the scribe machine are still distinctly visible with both an optical microscope and WLI. There was also no destruction of the scribe “boundary;” namely, the ridges on the edge of the scribe that were created when small amounts of metal are pushed up during the machining process were still intact.

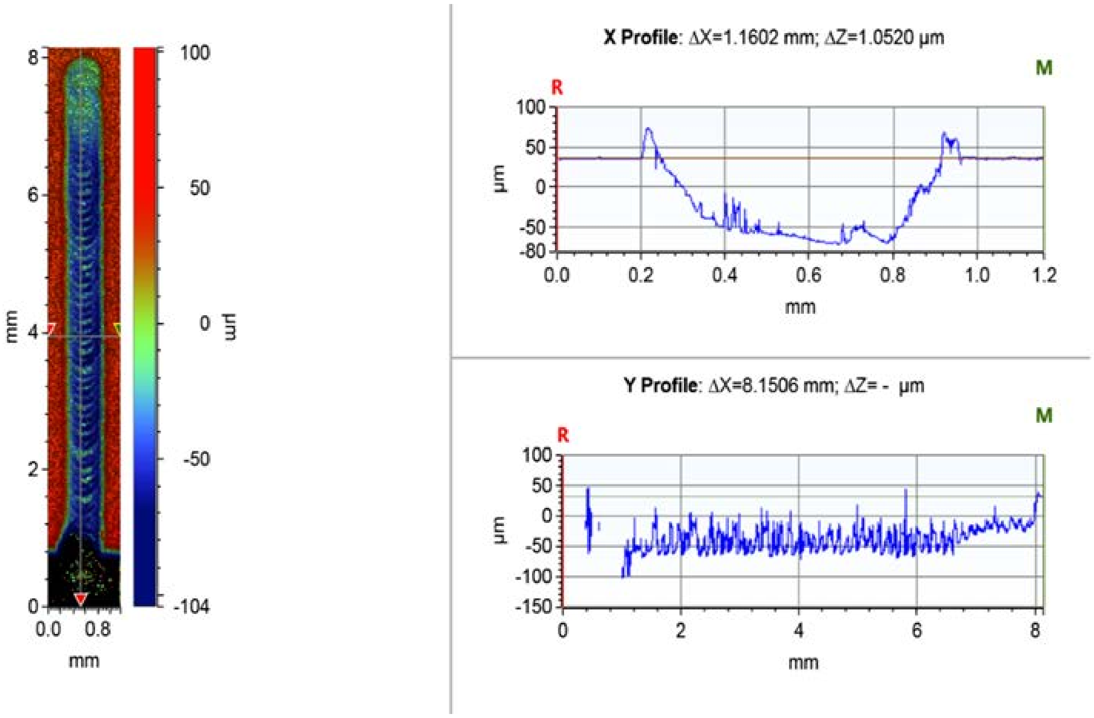

Figure 127. 2D surface profile of scribe adjacent to rivet #1, coupon 407 after coating removal. The test panel was coated with the chromate-free coating system and exposed at Daytona Beach for 6 months.

Scribe characteristics were also analyzed for coupons exposed at different sites for 12 months, as well as at Daytona Beach for ~3 years. Figure 128 shows WLI images of the localized initiation of metal loss around fastener scribes after 12 months of exposure at Daytona Beach (left) and Point Judith (right). After this exposure period, small areas of corrosion began to initiate at selected sites along the scribe line, but damage was not yet emanating from every edge of the scribe. The machining marks, however, were still clearly visible, as in the 6-month exposure coupons.

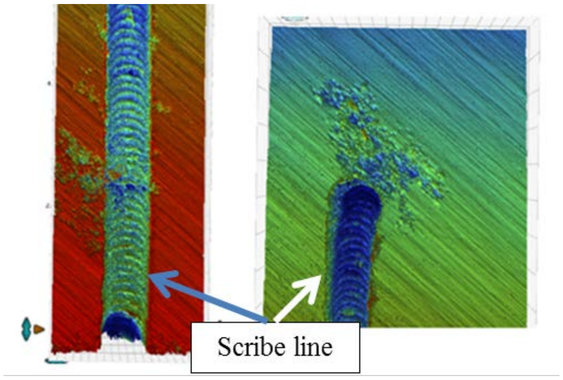

Figure 128. WLI images of localized corrosion along the scribe line in non-chromated coatings exposed from 12 months at Daytona Beach (left) and Pt. Judith (right).

Figure 129 shows a comparison of the surface area index between chromated and non-chromated coatings exposed at Daytona Beach. Data was averaged over three different exposure periods—6, 12, and 36 months—to assess general coating performance in this outdoor environment. The graph shows that surface area index, which is a measure of the relative flatness of the scribe, is generally higher for coupons coated with non-hexavalent chromium coatings. An increase in surface area index can be attributed to scribe widening (from increased 2D lateral surface area) or scribe roughening. Across all exposure sites, the hexavalent chromium coating consistently performed better indicated by its lower surface area index. This was consistent with the visual inspection of the coupons, as well.

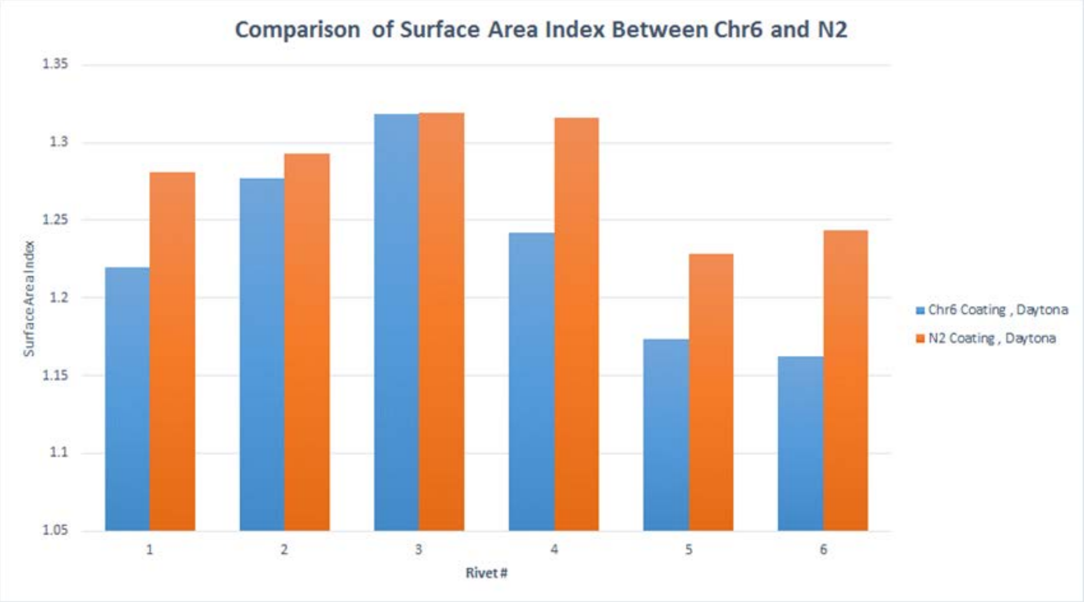

Figure 129 Comparison of surface area index for chromated (Chr6) and non-chromated (N2) coating systems exposed at Daytona Beach. Data was averaged over all exposure times (6, 12, and 36 months).

Figure 130 compares the lateral surface area (i.e. corroded area) around each rivet in a top panel from assembly type G (non-chromate coating system) that was exposed at Daytona Beach for 3 years. Lateral surface area is higher for scribes around the CRES fasteners, which is consistent with the visual observation that CRES fasteners cause the most extensive galvanic attack in Al substrates. With the exception of ASTM G85 A5, galvanic interactions between the fasteners and substrates caused more lateral scribe growth, i.e. scribe creep, as opposed to scribe deepening.

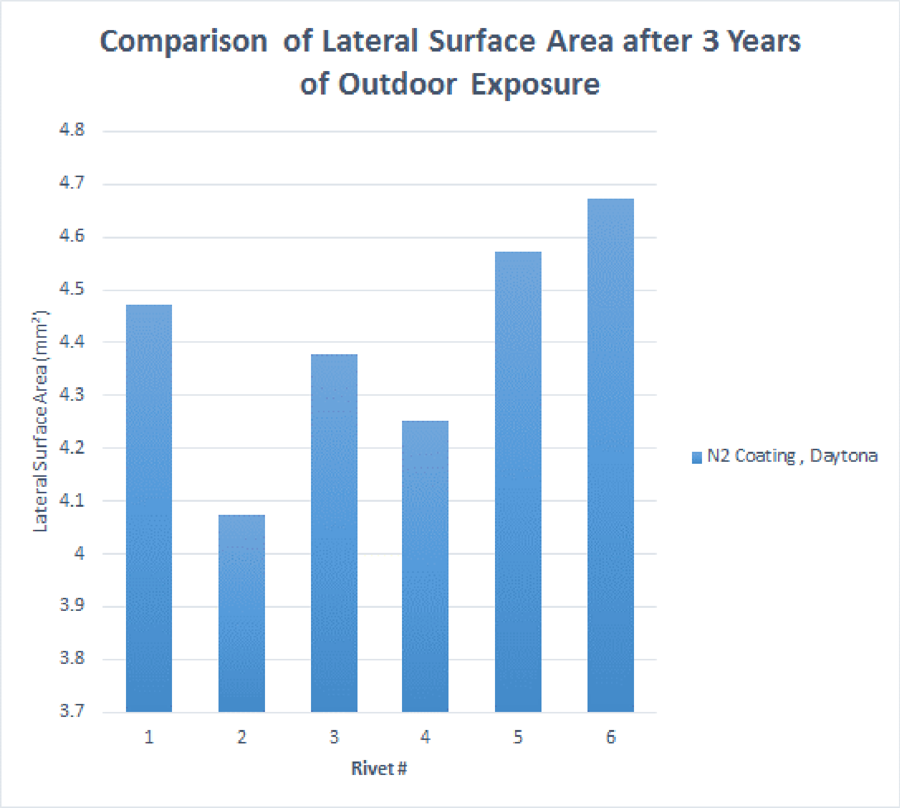

Figure 130. Comparison of lateral surface area around fastener scribes on a type G panel exposed at Daytona Beach for 3 years.

7.2.2.3 Comparison of fastener scribe characteristics for outdoor exposure sites and accelerated chamber tests

Figure 131 shows a comparison of maximum scribe depth between two coating systems: chromated and non-chromated. The panels were compared after either 6 months of outdoor exposure (Daytona Beach and LAX) or 1500 hours of accelerated chamber testing (ASTM B117 and ASTM G85 A5). The first observation is that the scribes were generally deeper for the non-chromated coating (N2) than those of the chromated coating (Chr6), in both outdoor exposures and laboratory tests. After only 6 months of the outdoor exposure, there was no discernable difference between the aggressiveness of the two exposure sites. Thus, the coating degradation and delamination that was observed on the LAX coupons did not necessarily translate to excessive metal loss in the scribe. Another trend observed was that maximum scribe depth decreased moving from left to right across the panel. Since the tooling marks were still visible in the bottom of the scribes, and the scribe boundaries were still intact after 6 months of exposure, it can be concluded that the variation in scribe depth from rivet 1 to 6 was generated during the manufacturing process.

For the two coating systems exposed to accelerated test conditions, the maximum scribe depth increased. With the exception of the CRES Rivet #6, which showed excessive deepening of the scribe, the cyclic ASTM G85 A5 test and the static ASTM B117 test caused similar deepening of the scribe on non-chromated test panels. The chromated coating showed the smallest scribe depth penetration.

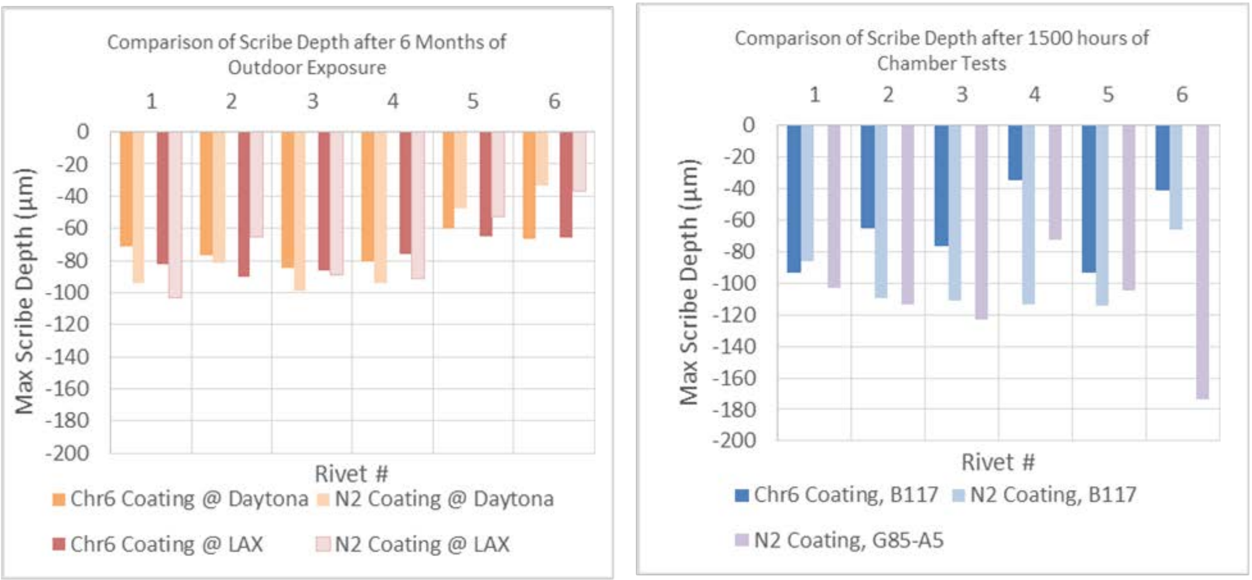

Figure 131. Comparison of maximum scribe depth for outdoor exposures and chamber tests.

Figure 132 shows a comparison of scribe volume between the two coating systems after either 6 months of outdoor exposure (Daytona Beach and LAX) or 1500 hours of accelerated chamber testing (ASTM B117 and ASTM G85 A5). Once again, a trend is observed from left to right across the panels that were exposed outdoors for 6 months. This indicates that at low levels of corrosion, when scribe creep was minimal or non-existent, scribe volume tracked with scribe depth. The small scribe volumes measured for the outdoor exposure panels was consistent with the visual observations and microscopic evidence of original tooling marks – all of which indicate that 6 months of outdoor exposure did not cause significant corrosion damage.

Scribe volumes for the ASTM B117 test articles were fairly low compared to ASTM G85 A5, especially for the CRES fasteners. The non-chromated coating did not protect the scribe as well as the chromated coating did in the ASTM B117 test.

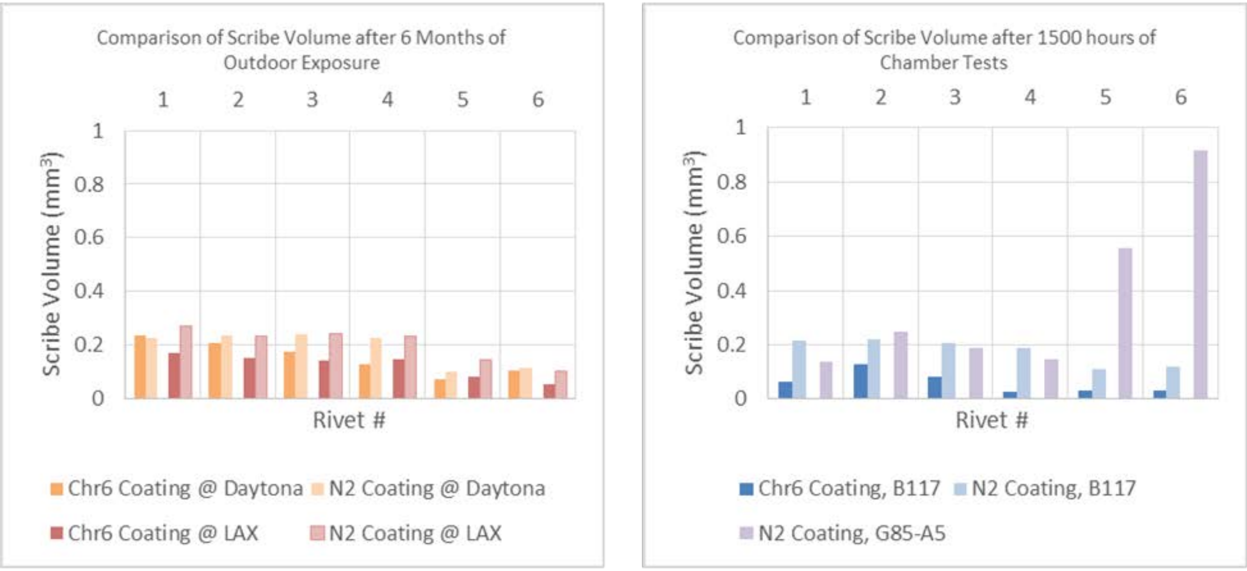

Figure 132. Comparison of scribe volume for outdoor exposures and chamber tests.

Figure 133 shows a comparison of lateral surface area between the two coating systems after either 6 months of outdoor exposure (Daytona Beach and LAX) or 1500 hours of accelerated chamber testing (ASTM B117 and ASTM G85 A5). The magnitude of lateral surface area was nearly identical for coupons exposed outdoors for 6 months, regardless of the coating system. This was another indicator that 6 months of exposure was not enough time to initiate substantial corrosion in these lap specimens and that the extent of damage at 6 months was not distinguishable enough to rank coating performance.

After 1500 hours of accelerated tests, however, the lateral surface area showed definite trends that could be used to assess coating performance. For example, the “area corroded” during ASTM B117 testing of the chromated coating was uniform across the panel, regardless of rivet type. The area corroded increased for the non-chromated coating, but the damage was still somewhat uniform across the length of the panel. This was consistent with visual observations, which indicated that coating failure after 1500 hours of ASTM B117 testing was similar around each rivet. The ASTM G85 A5 chamber test, however, caused preferential attack around the CRES fasteners.

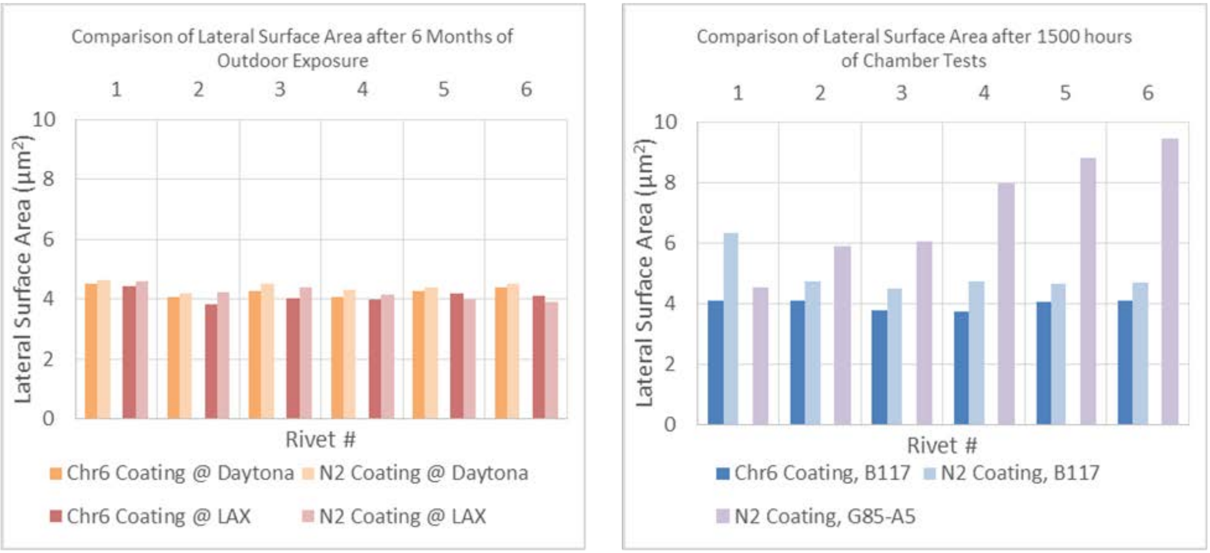

Figure 133. Comparison of lateral surface area for outdoor exposures and chamber tests.

The ultimate objective was to compare corrosion damage at outdoor exposure sites with that induced during accelerated chamber testing. The surface parameters for coupons after 6 months of outdoor exposure are more indicative of the panels in their as-machined condition (i.e. the damage at t=6 months is roughly equal to t=0). Figure 134 shows a comparison of average lateral surface area for coupons exposed outdoors for 6, 12 or 36 months vs. coupons subjected to 2000 hours of accelerated testing in ASTM B117 or ASTM G85 A5. As expected, ASTM G85 A5 is significantly more aggressive than ASTM B117. Moreover, 2000 hours of exposure in the ASTM B117 environment produced a similar magnitude of scribe widening as 3 years of outdoor exposure at Daytona Beach.

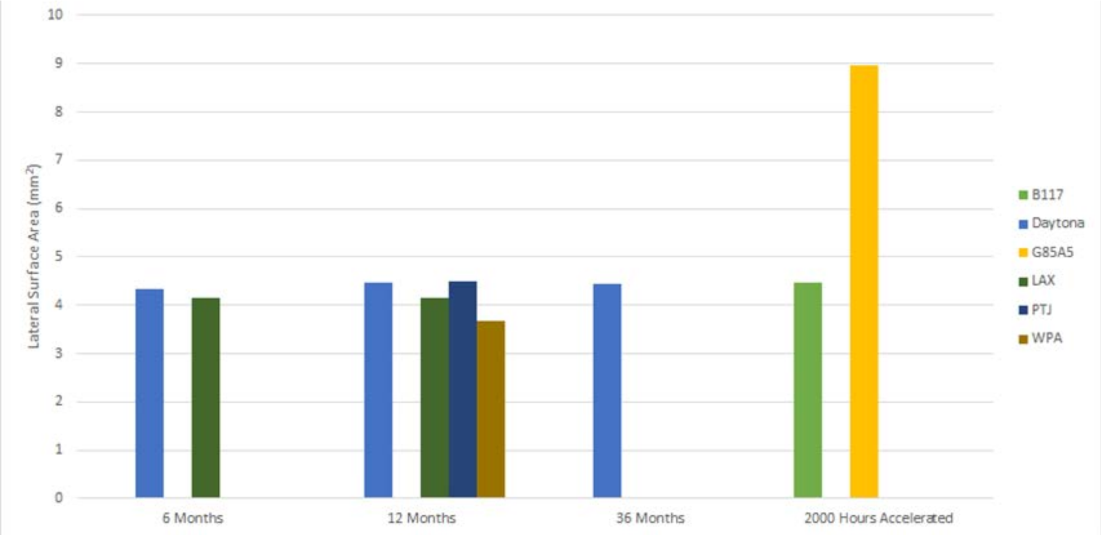

Figure 134. Comparison of lateral surface area for different outdoor exposure environments, exposure times, and chamber tests.

7.2.2.4 IGC morphology in cross section

The comparison of the corrosion morphology, more specifically, extent of intergranular corrosion (IGC) at the faying surfaces and the cross sections of the rivet holes, after the accelerated laboratory corrosion tests and outdoor exposures were used as one way of defining the test parameters for the new accelerated test method. During this work, it was found that ASTM G85 A5 produced general corrosion of the lap joints that was somewhat similar to the damage observed on the panels exposed at the Pt Judith site, while the other existing accelerated tests were either too mild or too aggressive to produce damage similar to that observed during the outdoor exposures. Based on this qualitative assessment, the G85A5 protocol was used as the basis for the first iteration of the test development.

Based on the results of the chemistry sampling that will be described in Figure 135, a new test solution, containing sodium, magnesium, calcium, potassium chlorides in addition to sodium sulfate, sodium nitrate, sodium oxalate, and potassium bromide, was designed. The composition of this solution is shown in Figure 135, which also describes the cycle as a first iteration of the new accelerated test. The damage inside the rivet holes produced by this cycle was compared to Pt Judith environment. The results are summarized in Figure 136. It was found that the proposed cycle and/or solution chemistry did not closely mimic the damage observed in Pt Judith. Moreover, no IGC attack was found on AA7075 after exposure to the new accelerated test environment, while extensive IGC was detected on the sample received from Pt Judith.

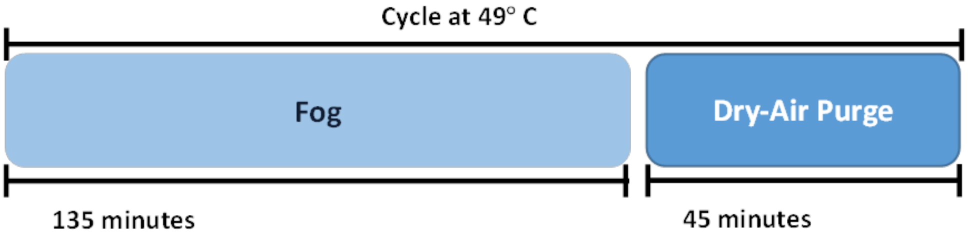

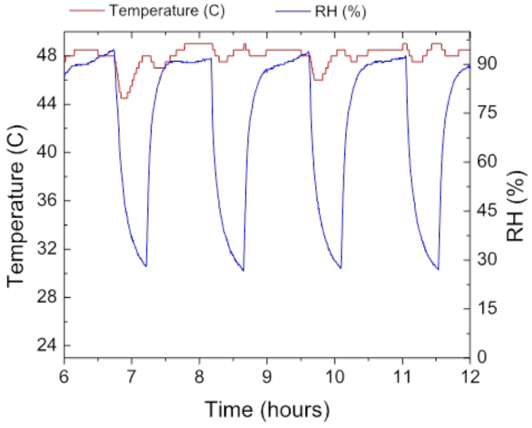

NaCl	0.023 M
$MgCl_2 \cdot H_2O$	7 mM
Na_2SO_4	1.7 mM
$CaCl_2$	0.65 mM
KCl	0.58 mM
KBr	53 µM
$NaNO_3$	2.4 mM
$Na_2(COO)_2$	0.189 mM
HCl	0.75 mM

Figure 135. Representative RH and temperature profiles and the solution chemistry used in the first iteration of the new accelerated test cycle.

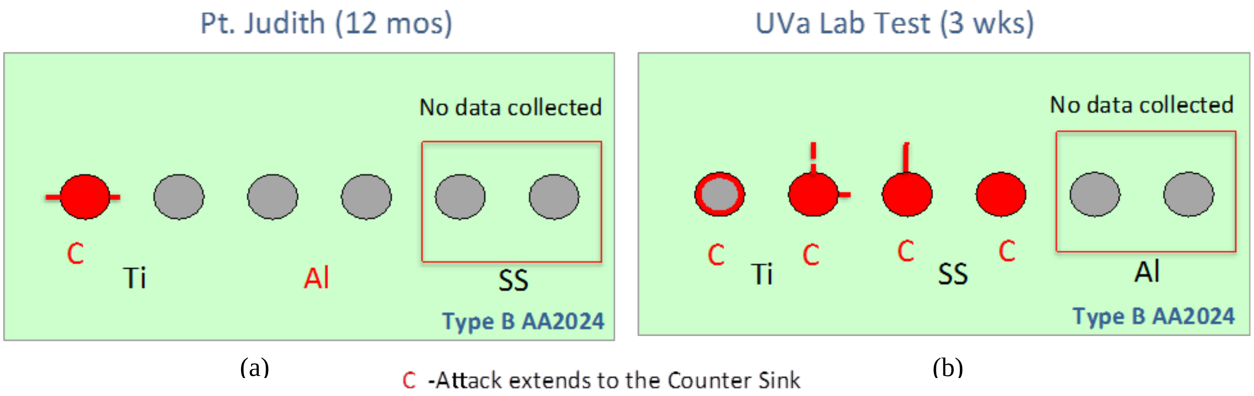

(a) (b)

Figure 136. Comparison of the IGC attack found on a AA2024 test panel exposed (a) at the Pt Judith site for 12 months and (b) in the first iteration of the new accelerated test for 500 hours.

After further refinement of the proposed cycle based on the results from the first iteration, two cycles were designed as shown in Figure 137.

The choice of a spray solution was based on the finding that natural atmospheric aerosols are acidic and have relatively high chloride concentrations (see Chapter 8 below). Preliminary testing of solution chemistries containing other ions measured in lap joints indicated that the presence of the other sea salt aerosols and oxalates in the simulant solution is not critical, therefore, those additional ions were omitted from the final solution chemistry.

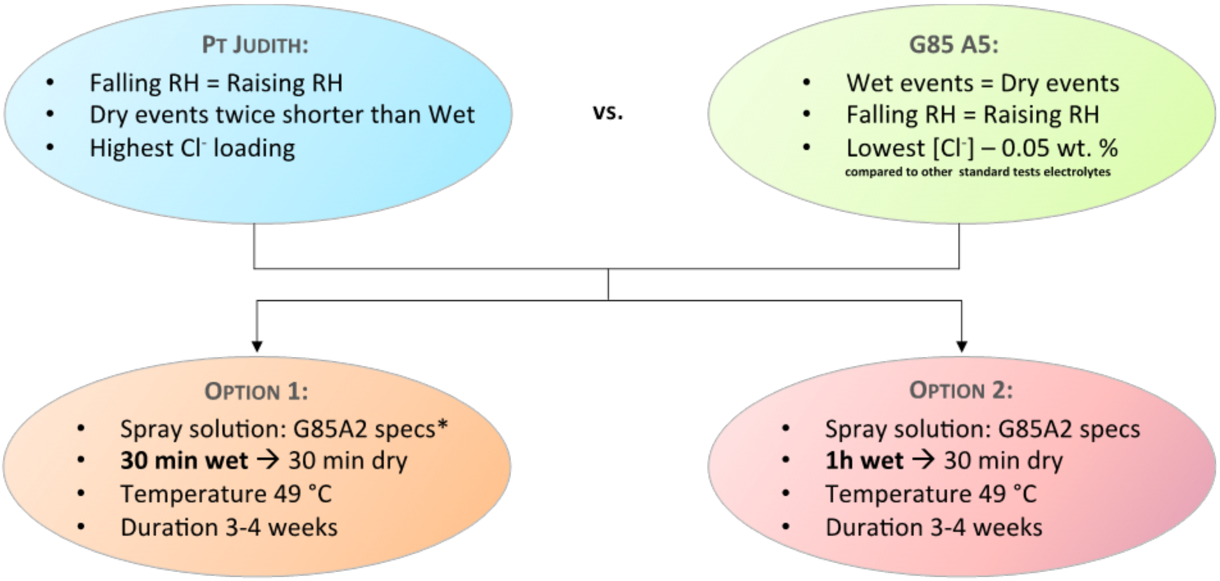

Figure 137. A graphical representation of the proposed cycles. *Spray solution: 5 wt. % NaCl & acetic acid to yield pH 3.

After preliminary testing, option 2 was chosen as the second iteration of the test cycle (UVa Trial 1). The cycle was run for 500 and 1000 hours and the resulting corrosion damage inside the rivet holes was compared to the damage observed at Pt Judith (12 months), as well as the ASTM G85 A5 test (500 and 1000 hour exposures). Figure 138 summarizes the extent of the intergranular corrosion attack (IGC) seen on AA2139 test panels. Extensive IGC was found inside the rivet holes after 500 hours of exposure to the UVa Trial 1 cycle. After 1000 hours of exposure, the attack further extended inside and in-between the rivet holes. Similar attack was observed on the Pt Judith samples. No IGC initiated on the panels exposed to 500 hours of the G85A5 environment, and little IGC attack developed after 1000 hours. These results suggest that the second iteration of the new test cycle produces the damage and corrosion morphology on AA2139 panel observed after 12 months of field exposure at Pt. Judith.

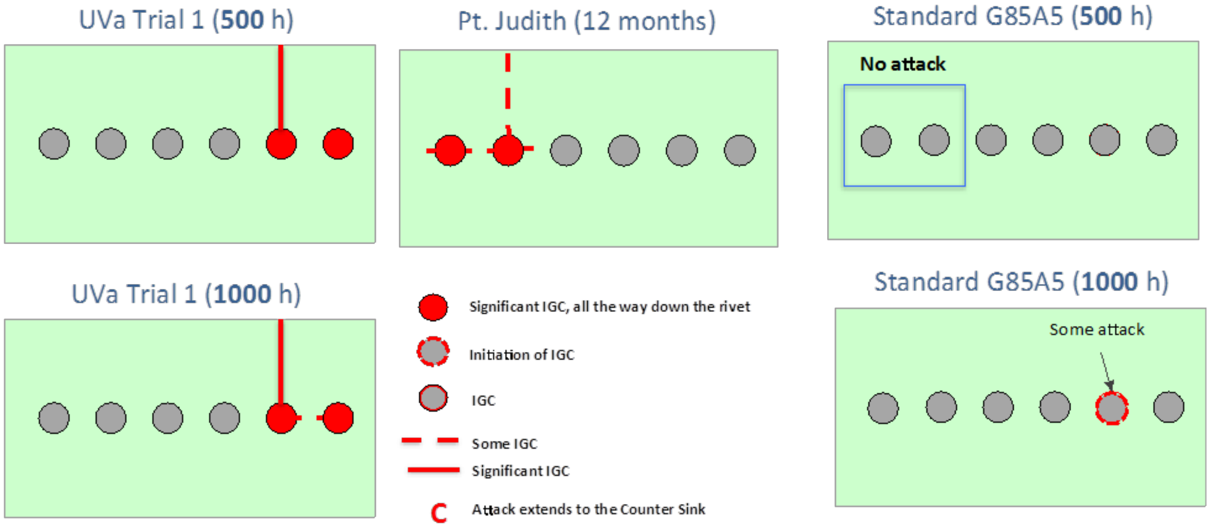

Figure 138. Comparison of the IGC attack found on AA2139 test panels exposed to Pt Judith and second iteration of the new accelerated test (UVa trial 1) and ASTM G85 A5.

Figure 139 schematically illustrates the corrosion attack found on AA7075 samples galvanically coupled to AA2024 panels with Ti, Al and stainless steel rivets after 500 and 1000 hours of exposure to the second iteration of the proposed accelerated test, ASTM G85 A5, and 12 months of field exposure at the Pt. Judith site. These panels were coated with hexavalent-chromium coating. The results indicate that significantly more substantial IGC developed on the AA2024 plate after 12 months in Pt Judith inside all the rivet holes extending all the way down to the countersink. This attack was not replicated by the second iteration of the new accelerated test. The latter did not show any attack inside the Ti rivet holes, but had extensive IGC inside one of the stainless steel rivet holes with the corrosion attack present at the mouth of the crevice. Minimal damage was observed on the AA7075 panel showing some IGC fissures after 500 hours of the second iteration of the new cycle. Pt. Judith, on the other hand, was found to be more aggressive for the AA7075 leading to extensive IGC inside one of the Ti rivet holes with lateral propagation towards both the edge of the plate and towards the rivet hole next to it. The 500 hours of exposure in the ASTM G85A5 environment produced no damage on either plates inside the Ti rivet holes.

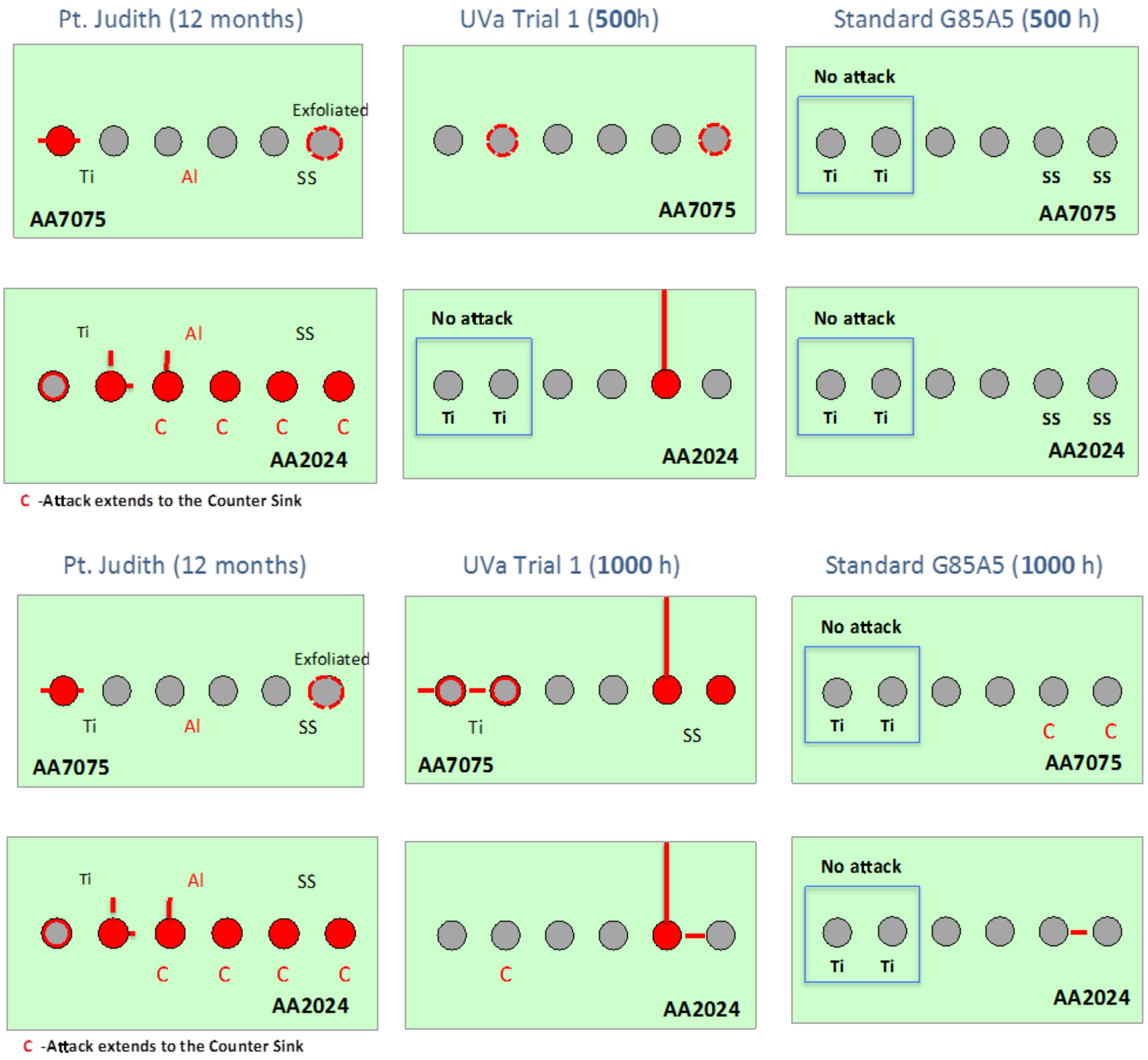

Figure 139. Comparison of the IGC attack found on hexavalent-chrome-coated AA2024/AA7075 test panels exposed at the Pt. Judith site, the second iteration of the new accelerated test (UVa trial 1 cycle) and ASTM G85 A5.

After 1000 hours of exposure in the UVa trial 1 cycle environment, corrosion attack at the mouth of the crevice on both aluminum panels was found. This type of attack was not present on the samples exposed to Pt Judith. After 1000 hours of exposure to the UVa trial 1 cycle, the corrosion developed inside the Ti rivet holes with lateral propagation in-between the holes, which was similar to the corrosion damage seen on the samples exposed at the Pt Judith site. However, the IGC inside the Ti rivet holes was not as significant as in the case of the Pt. Judith exposures. The 1000 hours in the ASTM G85 A5 environment did not reproduce the damage observed in the field. In this case, no attack occurred inside the Ti rivet holes, some attack was found in between and at the countersink of the stainless steel rivet holes on the AA2024 and AA7075 plates, respectively.

Figure 140 compares the corrosion damage observed on AA7075 samples galvanically coupled to AA2024 panels with Ti, Al and stainless steel rivets, coated with non-chrome coating, after field and laboratory exposures. The analysis of the cross-sectioned samples indicated relatively severe IGC inside the stainless steel rivet holes after 500 hours and even more so after 1000 hours of exposure to the UVa trial 1 cycle. Interestingly, neither 500, nor 1000 hours of the ASTM G85 A5 environment initiated IGC inside the Ti and stainless steel rivet holes on the AA2024 plate. These results are in contrast with the extensive pitting and IGC observed after 500 hours of UVa trial 1 cycle on both aluminum panels inside the stainless steel rivet holes with the IGC attack extending along the mouth of the crevice. In contrast with the IGC attack produced by the UVa trial 1 cycle, little or no damage was found inside the Ti rivet holes on the AA2024 panel exposed in Pt Judith. However, the quantitative analysis of the maximum length of the ICG fissures (see below) indicates that the Pt Judith environment produced more damage on the AA2024 than either the UVa Trial 1 cycle or ASTM G85A5. The severe IGC and exfoliation corrosion of this sample configuration are associated with the absence of the chromate primer, which led to the coating failure and disbondment, thus exposing the bare alloy surface.

As mentioned above, the ICG attack was also analyzed quantitatively by measuring the maximum length of the ICG fissures on microscopic images, as shown in Figure 141. The optical micrographs were taken inside the rivet holes and in-between the holes, shown as side cut and horizontal cut. The measurements were carried out using a Matlab code developed in-house. The resulting maximum ICG fissure lengths for the different samples and exposure environments are summarized in Table 7 and Table 8. Figure 142 shows optical images of the cross section of the stainless steel rivets through the AA7075-T6 panel after exposure to 12 months at Pt. Judith, 1,000 hours in ASTM G85-A5 and 1,000 hours in the UVA Trial 1 cycle. The micrographs used for the analysis are compiled in the following the link: Optical analysis of corrosion damage inside the rivet holes.

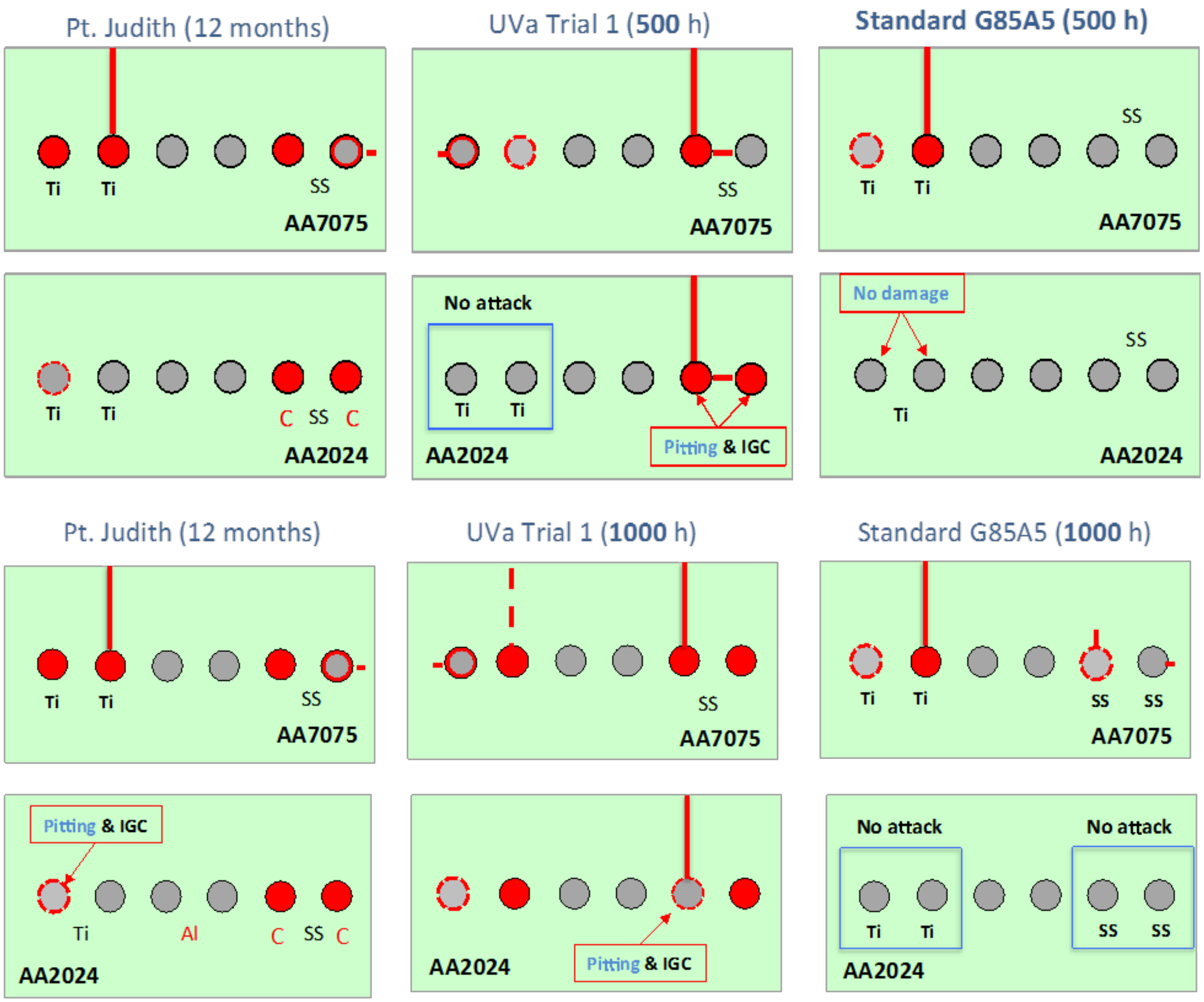

Figure 140. Comparison of the IGC attack found on non-chrome-coated AA2024/AA7075 test panels exposed at the Pt. Judith site, the second iteration of the new accelerated test (UVa trial 1 cycle) and ASTM G85 A5.

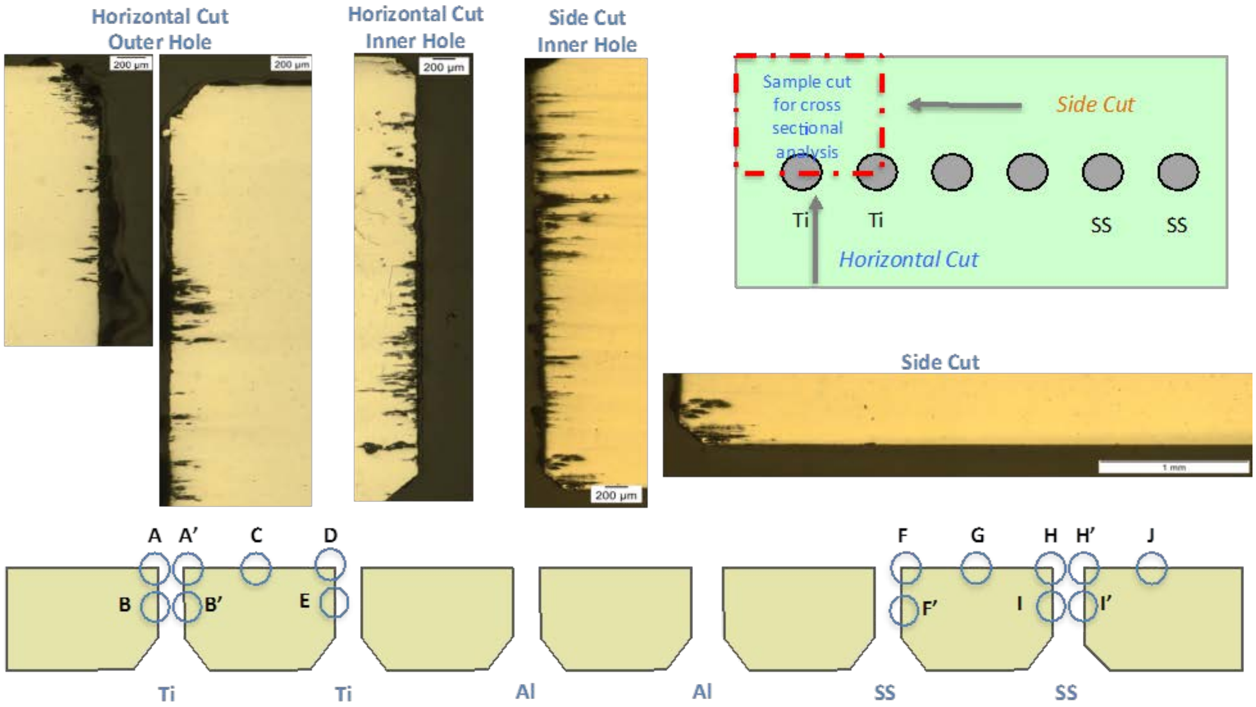

Figure 141. The top right schematic shows the area of the panel where optical analysis of IGC was performed. The micrographs depicting IGC inside the Ti rivet holes on chromate coated AA7075/AA2024 test panel exposed to 12 months at the Pt. Judith site. The schematic at the bottom shows the areas where IGC was quantitatively assessed.

Table 7. Maximum Lengths of IGC Fissures Observed Inside the Ti and Stainless Steel Rivet Holes in Chromate-Coated AA2024/AA7075 Samples (the values are given in micrometers).

Area	Pt Judith	UVa Trial 1		G85A5
	12 months	500 hours	1000 hours	1000 hours
Plate – AA7075				
A	0	<5	268	0
A’	193	<5	261	0
B	0	134	246	0
B’	541	17.2	204	0
C	20	8	50	0
D	<5	<5	99	0
E	0	22	132	0
F	20	0	164	0
F’	0	0	203	0
G	14	0	0	0
H	1200	0	156	0
H’	350	166	0	0
I	250	41.4	246	0
I’	207	0	0	0
J	10.4	0	0	0
Plate – AA2024				
A	0	0	<5	0
A’	58	11	<5	0
B	0	0	16	0
B’	260	14	24	0
C	0	15	0	0
D	0	0	0	0
E	<6	0	0	0
F	7	0	114	<5
F’	359	380	286	10.4
G	0	0	Exfoliation	78
H	62	0	0	<5
H’	10	0	0	6.5
I	731	0	0	15
I’	593	0	0	18
J	0	0	0	0

Table 8. Maximum IGC Observed Inside the Ti and Stainless Steel Rivet Holes in AA2024/AA7075 Samples Coated with Chrome-Free Coating (the values are given in micrometers).

Plate – AA7075				
Area	Pt Judith	UVa Trial 1		G85A5
	12 months	500 hours	1000 hours	1000 hours
A	217	11	8.5	0
A’	93	6	353	<5
B	206	260	195	0
B’	338	255	155	220
C	0	24	30	0
D	262	<5	152	212
E	543	308	210	226
F	326	58	88	12.2
F’	62	153	147	67
G	43	0	0	0
H	59	Exfoliation	79	11
H’	297	250	259	8.5
I	102	Exfoliation	0	33.7
I’	252	148	0	11.4
J	49	0	0	47
Plate – AA2024				
A	0	9	17.4	0
A’	167	<5	10	0
B	0	12.5	115	0
B’	158	21.4	99	0
C	0	16	0	0
D	0	<5	25.4	0
E	0	13	249	0
F	89	0	0	11
F’	964	0	0	0
G	30.5	0	0	0
H	120	0	0	4
H’	365	0	0	6.6
I	575	0	0	6.4
I’	748	0	0	26
J	42	0	0	35

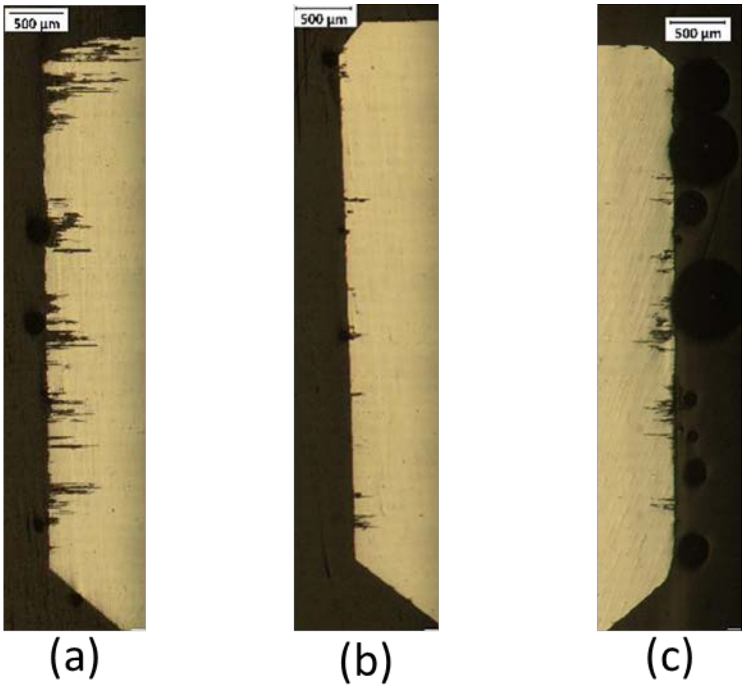

Figure 142. Cross-sectional images of AA7075-T6 coated with non-chromate primer system, where a stainless steel rivet was removed after exposure to (a) Pt. Judith for 12 months, (b) ASTM G85 A5, and (c) UVA Trial 1 cycle for 1,000 hours.

CHAPTER 8
COMPARISON OF IONIC SURFACE CHEMISTRY BETWEEN LABORATORY AND OUTDOOR EXPOSURE TESTING

Salt deposition plays a critical role in corrosion processes. Surface wetting and drying are defined by the deliquescence of the deposited salt films and the slat loading density may have an effect on the amount of corrosion observed. However, little detail is known about the evolution of deposited salt during accelerated testing compared with outdoor testing. In this Chapter, the ionic salt content found during accelerated testing and on exposed coupons is quantified. Differences in salt content observed between outdoor and accelerated testing will be used to define appropriate salt constituents and loading levels for improved corrosion testing.

8.1 Materials and Methods

8.1.1 *Surface chemistry of indoor and outdoor exposure samples*

The chemistry of the surfaces of the top and bottom plates of the lap joint assemblies (Table 2) and the crevice of the lap joint was analyzed. In order to perform these analyses, the surfaces and crevice were washed with deionized water to remove (extract) the salt from the samples. These extracted solutions were then analyzed for several different cations and anions. Detailed experimental procedures and results are discussed below.

8.1.1.1 Preliminary testing

Prototype sample assemblies were fabricated, exposed to accelerated corrosion testing in the laboratory and to ambient environments near Charlottesville, VA, and at Daytona Beach, FL. The solution from the assemblies was extracted after exposure, and chemically characterized. Based on results from these preliminary test exposures, the methodology described below was developed and optimized. Detailed operator’s manuals were prepared and distributed to technical staff at exposure sites to ensure that accurate sample collection and preservation procedures were followed.

8.1.1.2 Sample types

Seven different sample types were designed, fabricated, exposed to corrosive environments, and analyzed as part of this component of the effort. Each sample assembly consisted of two separate plates (top and base) joined with six fasteners each through a lapped section. Table 9 details the composition, fastener types, and coatings used for each assembly.

Table 9. Sample Assembly Composition.

Sample Type	Base Plate	Top Plate	Coating System	Fasteners
A	Inert metal (C-22)	Inert metal (C-22)	None	Ti, Cres, Al
B	AA2024	AA7075-T6	1200S+PPG CA7233+PPG CA8201	Ti, Cres, Al
C	AA2024	Carbon fiber composite	TCP+Deft02GN084+PPG CA8201	Ti, Cres, Al
D	AA2139	High hard steel	TCP+23377-N(Deft)+53039-Type 4	Grad 8, Rc = 35, Zn plated
E	AA5083	High hard steel	TCP+53022-Type 3+53039-Type 4	Grad 8, Rc = 35, Zn plated
F	AA2024	AA7075-T6	TCP+Deft02GN084+PPG CA8201	Ti, Cres, Al
G	AA2024	AA7075-T6	TCP+PPG EWAE118A+PPG CA8201	Ti, Cres, Al

8.1.1.3 Cleaning, handling, shipping, exposure, and storage procedures

To maximize resolution in deconvoluting influences of environmental parameters on the nature and rates of corrosion processes, variability introduced by factors other than the environment of interest must be minimized. Other controllable factors of this nature include variability in the amounts and types of contaminant substances on sample surfaces at the onset of exposure. The following cleaning, handling, and storage protocols were developed to minimize artifact variability introduced by surface contaminants.

Standard clean-room procedures were employed to clean, dry, assemble, mount, and pack samples. Operators wore clean nitrile gloves when handling samples. Following fabrication, sample plates and fasteners were cleaned with acetone and dried. Plates, fasteners, mounting hardware, and storage boxes where then washed with detergent, rinsed copiously with deionized water (DIW), and dried in a class 100 clean bench configured with an active charcoal scrubber on the inlet to remove soluble reactive trace gases from the air stream. Samples were assembled in the clean bench. Following assembly, coatings were applied to samples as appropriate. Coatings at the joints between the two plates were scribed. In the clean bench, sample assemblies for analysis by UVA-ES were mounted on Plexiglas panels (two identical assemblies per panel), transferred to precleaned airtight polyethylene storage boxes containing a desiccant (to minimize corrosion prior to exposure), and sealed (Figure 143). Boxes were then transferred to insulated containers and shipped to the exposure test sites.

Figure 143. Sample plate (upper left), duplicate sample assemblies mounted on Plexiglas panel (right), and mounted assemblies in air-tight container for shipping (lower left).

Operators at each test site unpacked and deployed clean sample assemblies and recovered and packed exposed assemblies wearing clean nitrile gloves following explicit written protocols. As described in more detail below, sixteen identical samples of each of the 7 different sample types (total of 112 individual samples) were deployed simultaneously at each of four accelerated corrosion and four ambient test sites. Accelerated tests employed freshly prepared simulant solutions. At specified exposure times following the initial deployment at each test site, two identical sample assemblies of each type (mounted on a single Plexiglas panel) were recovered for analysis by UVA-ES and a paired set of two identical samples were recovered for analysis by Boeing. The original plan specified exposure durations to the accelerated test environments of 1, 3, 6, and 12 weeks and to the ambient environments of 6, 12, 18, and 24 months. As described in more detail below, to accommodate more intensive characterization of loadings following each time increment, the numbers of durations over which sample assemblies were exposed to the laboratory and ambient environments were reduced from 4 to 3 and from 4 to 2, respectively. Using the same procedures as those for the normal exposure samples, dynamic handling blanks of each sample type were briefly (~10 seconds) mounted and promptly recovered at each test site and subsequently processed and analyzed. Table 10 summarizes the accelerated test and ambient exposure locations. Immediately after recovery, exposed samples and blanks were frozen temporarily on site, shipped frozen to UVA, and stored frozen prior to analysis. Freezing minimized physicochemical evolution of sample and blank surfaces between recovery and analysis.

Table 10. Exposure Locations and Types.

Abbreviation	Agency / Exposure Location	Exposure Type
NAVAIR	US Naval Air Systems Command, Petuxant, MD	ASTM G85, Annex 4
ARL	US Army Research Laboratory, Aberdeen Proving Ground, MD	GM9540
AMCOM	US Army Aviation and Missile Command, Redstone Arsenal, AL	ASTM G85, Annex 5
ALCOA	Aluminum Company of America	ASTM B117
LAX	Los Angeles Airport, CA	Ambient
PTJ	Point Judith, RI	Ambient
DAY	Daytona Beach, FL	Ambient
WPA	Wright Patterson Air Force Base, OH	Ambient

8.2 Results and Discussion

8.2.1 *Surface Chemistry of Sample Assemblies Exposed to Accelerated-Corrosion and Ambient Environments*

8.2.1.1 Spatial Variability in Surface Loadings Across the Same Sample Types Exposed to the Same Conditions

Spatial variability in analyte loadings across given surfaces exposed to the same conditions is illustrated with an example in Figure 144.

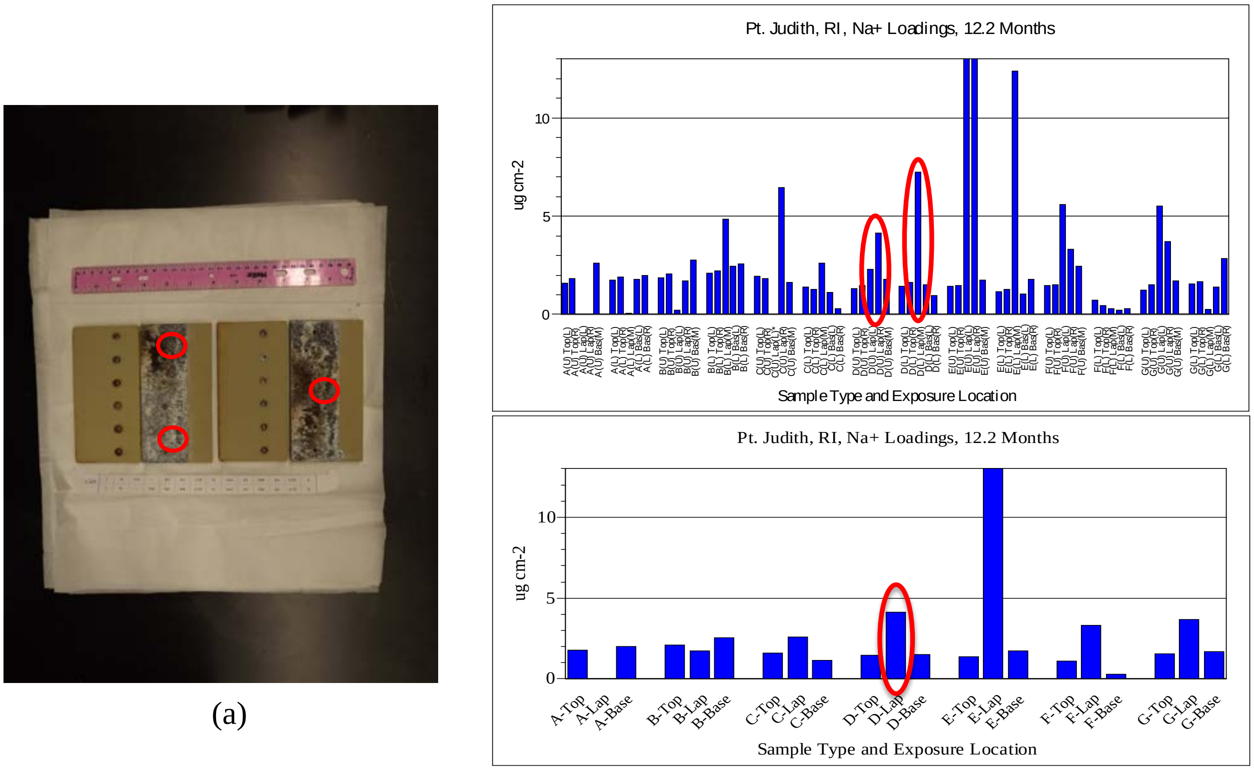

(a)

(b)

Figure 144. (a) Extraction locations for the lapped portion of a representative sample following exposure at Point Judith for 12.2 months. (b) Ion concentrations (loadings) measured across the lap joint panel. The locations marked on (a) are circled on the concentration map in (b).

Figure 144a depicts the extraction locations for the lapped portion of sample type D following exposure at Point Judith for a period of 12.2 months. Figure 144b shows the corresponding loadings measured at individual locations across all samples types and surfaces. Those for the lapped surfaces of sample type D are circled. In that panel, data for duplicate extractions at different locations on the same exposed surface of each sample assembly are plotted side-by-side. For each assembly, results for the top plate are plotted first followed by those for corresponding lap and finally those for the base plate. Data for duplicate sample assemblies mounted on individual Plexiglas panels and exposed in parallel are depicted in the following sequence: “A” upper, “A” lower, “B” upper, “B” lower, “C” upper, “C” lower, etc. Significant spatial variability across surfaces of the same type is evident. Factors such as spatial differences in fastener types, variability in the plane or texture of plate surfaces, and/or variability in the scribe between plates probably contributed to spatial variability in surface loadings and associated rates of corrosion within laps. Variability in fastener types, the texture and degree of degradation of surface coatings, and chemical coupling with lapped areas probably also contributed to spatial variability across exposed portions of top and base plates. Relative to average values, median values are less sensitive to outliers and, consequently, are considered to be more representative sample statistics for sets of replicate measurements such as these. Subsequent data analysis focuses on median values for replicate sets of measurements.

8.2.1.2 Variability in surface loadings among different sample types exposed to the same conditions

In each panel of subsequent figures, median loadings on top plates are grouped to the left, those on exposed portions of base plates in the center, and those on lapped portions of base plates to the right. Median mass loadings of Na^+ on sample surfaces exposed to accelerated corrosion environments for nominal periods of 3 weeks (Figure 145) and to ambient environments for nominal periods of 12 months (Figure 146) reveal substantial variability in loadings among (1) different surfaces (top, base, lapped) of a given sample assembly type A through G exposed to the same conditions, (2) the same surfaces of different sample assembly types exposed to the same conditions, (3) and surfaces of different sample types exposed to different conditions.

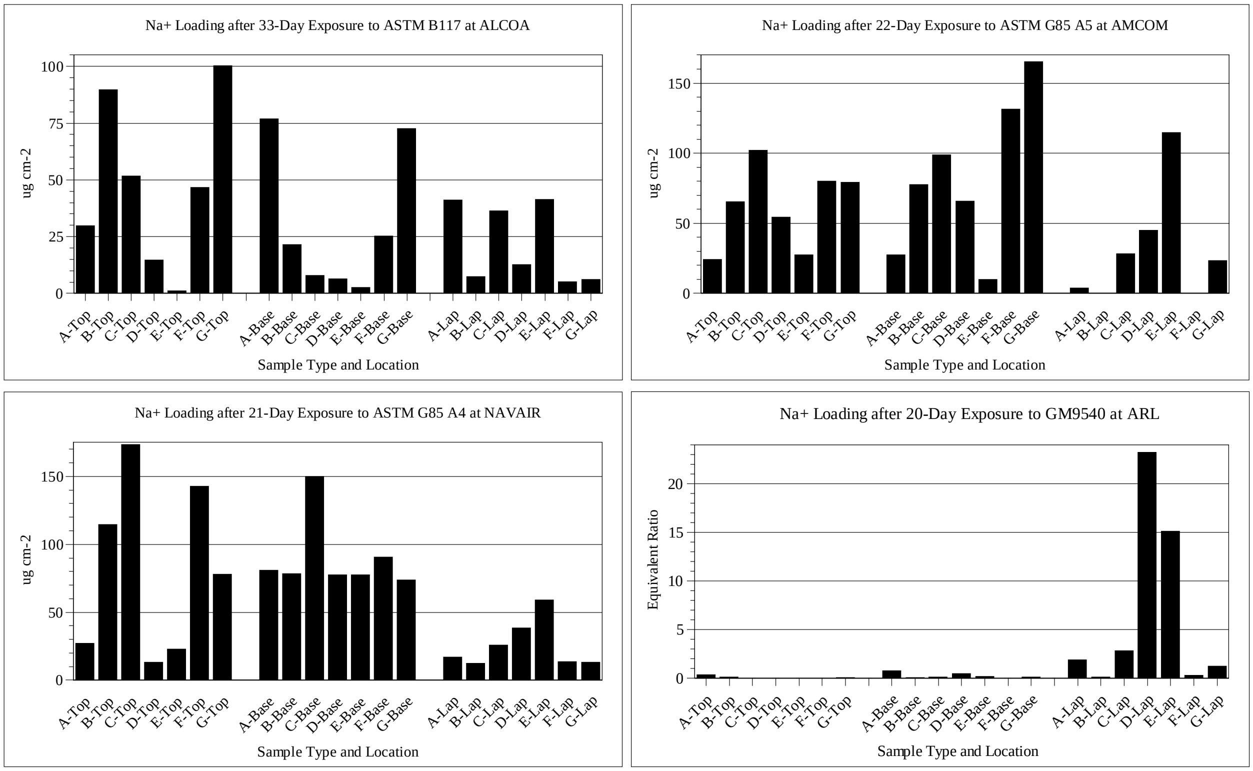
Na+ Loading after 33-Day Exposure to ASTM B117 at ALCOA

Na+ Loading after 22-Day Exposure to ASTM G85 A5 at AMCOM

Na+ Loading after 21-Day Exposure to ASTM G85 A4 at NAVAIR

Na+ Loading after 20-Day Exposure to GM9540 at ARL

Figure 145. Median surface loadings of Na^+ following nominal three-week exposures to four different accelerated corrosion environments. Note that scales on Y axes differ.

Several specific relationships are evident:

1. In general, loadings on assemblies exposed to accelerated corrosion environments are much greater than those exposed to ambient environments. This reflects the fact that dry deposition rates to surfaces from ambient air are relatively lower than loading rates in laboratory chambers. In addition, periodic precipitation events remove material that accumulates on surfaces via dry deposition (and subsequent chemical reactions) exposed to ambient environments whereas, with the exception of GM9540 at ARL, simulant solutions and associated reaction production in laboratory tests are removed only by drainage. The lower loadings on surfaces of assemblies exposed to GM9540 at ARL

Figure 145, upper right panel) reflect removal of simulate from surfaces via DIW misting as part of that test protocol.

It is important to recognize that loadings on sample assemblies exposed to ambient environments correspond to point in time conditions that vary as a function of meteorological conditions that preceded recovery.

2. Absolute loadings on top plates of field samples varied substantially among sites (Figure 146). On average, those at Point Judith were approximately 4 times greater than those at LAX and approximately 70 times greater than those at Daytona Beach. These differences reflect influences of both upwind source strengths for marine aerosol and other deposited material as well as the timing and size of precipitation events that flushed off deposited material prior to recovery. The absence of upwind marine sources accounted for the much lower loadings of Na^+ on samples exposed at WPAFB.

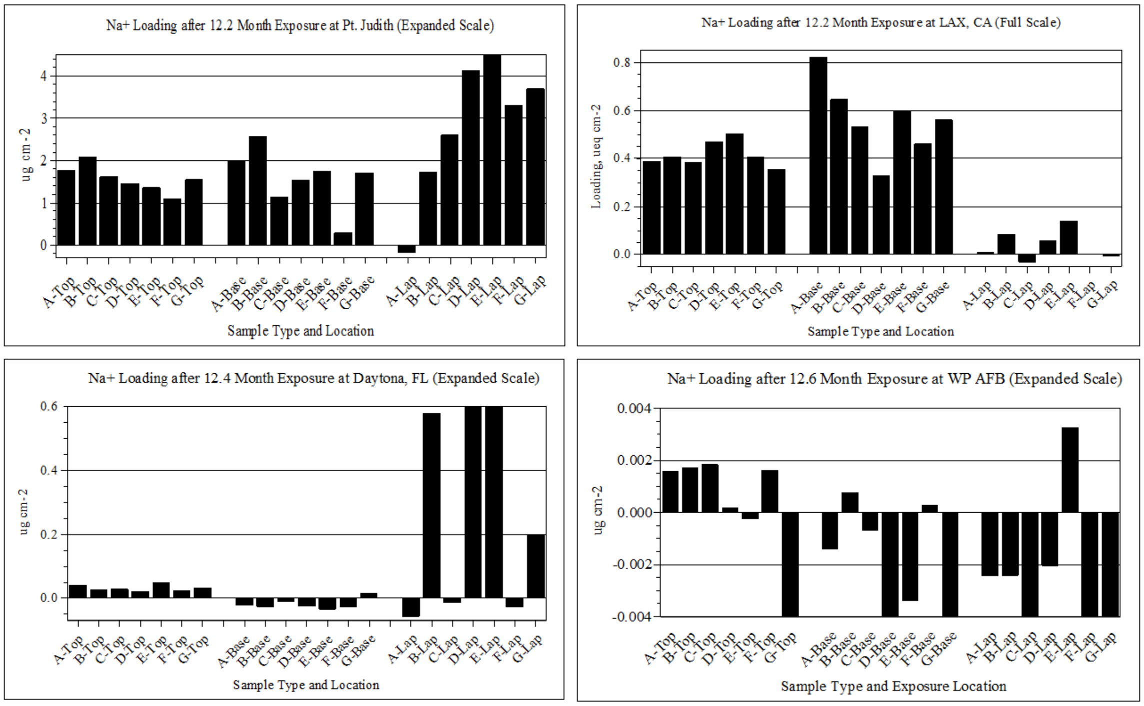

Figure 146. Median surface loadings of Na^+ following nominal twelve-month exposures to ambient corrosion environments at four different locations. Note that one loading at PTJ, two at DAY, and four at WPA are off scale and that scales on Y axes differ.

Variability in Na^+ loadings on top plates of assemblies exposed to marine-influenced environments (Figure 146) is relatively low compared to those on top plates of assemblies exposed to laboratory environments (Figure 145). As discussed below, available evidence suggests that Na^+ deposited on top plates is reasonably conservative with respect to corrosion chemistry. As such, we infer that the much greater variability in Na^+ loadings on top plates of assemblies exposed in chambers is caused primarily by differential rates of loading within the chambers due to physical factors such as variable proximity to simulant deliver nozzles and shadowing by adjacent assemblies. If so, variability in corrosion rates within chambers may be driven in part by spatial variability in simulant loadings onto sample assemblies within chambers.

The substantial variability in mass loadings on surfaces of different sample types exposed to the same conditions confounds evaluation of the influences of corrosion processes on the chemical evolution of those loadings. To normalize for variable loadings, we evaluated chemical evolution based on relative variability of analytes. Because some species were relatively more conservative than others with respect to chemical evolution, ratios also provide insight regarding interactions among ionic composition and corrosion processes. Because Na^+ is relatively conservative, ratios of major analytes to Na^+ were evaluated based on (1) For laboratory loadings, the original composition of the simulant solutions use in the laboratory exposures; (2) for ambient loading, ratios of sea-salt constituents in marine aerosol (Keene, Pszenny, Galloway, & Hawley, 1986); and (3) for both laboratory and ambient loadings, the composition of loadings on top plates, which were minimally impacted by corrosion.

8.2.1.3 Variability in relative loadings

General Considerations

Uncertainties associated with ratios of two constituents are greater than those associated with either of the individual constituents. In addition, relative uncertainties increase as absolute loadings decrease. At low loadings such as many of those on samples from Daytona Beach, ratios are inherently noisy and should be interpreted with caution. Very low loadings coupled with the lack of information on the chemical composition of the parent material preclude credible interpretation of constituent ratios at WPAFB.

Available evidence suggests that all chemical constituents are reactive to some degree and, consequently, variability in ratios of two constituents are driven in part by changes in both individual constituents. Although Na^+ appears to be relatively less reactive than other constituents, it is not completely inert.

Finally, the net effect of corrosion processes on ionic loadings on sample surfaces reflects the combined influences of interactions involving (1) The composition of plates in different sample assembles, (2) the coatings on those assemblies, (3) the composition of fasteners, (4) the ionic concentrations and compositions of solutions to which the samples were exposed, (5) the durations of exposures, and (6) for ambient exposures, meteorological conditions. In the following, we describe and interpret results based on the types of sample assemblies, measured loadings on different surfaces of those sample assemblies, and the corresponding ionic compositions of parent solutions. However, it is important to recognize that the plates themselves are not the only reactive material in sample assemblies. In addition to plates, corrosion of fasteners as well as degradation of coating materials contributes to the observed variability in ionic loadings.

General Observations

Ratios of selected species in loadings following selected exposure periods at ambient field sites and in chamber are depicted in Figure 147 - Figure 153. In general, the relative compositions of loadings on the top plates were similar to those of the parent aerosol at field sites or to test solutions in lab exposures whereas those for the base plates diverged to variable degrees and those for the lapped areas diverged to the greatest degrees. These results suggest that, relative to the top plates, the exposed base-plate surfaces were more chemically active and coupled with the lapped areas to a substantially greater degree, which is not unexpected given the deployment angles and influence of both gravity and capillary action.

As noted above, relative loadings on top plates of paired samples exposed to lab tests varied to a much greater degree than those exposed to ambient environments. The large differences in median loadings on sample assemblies exposed in laboratory chambers may contribute to variable corrosion rates among lab samples exposed to the same test for the same duration to time.

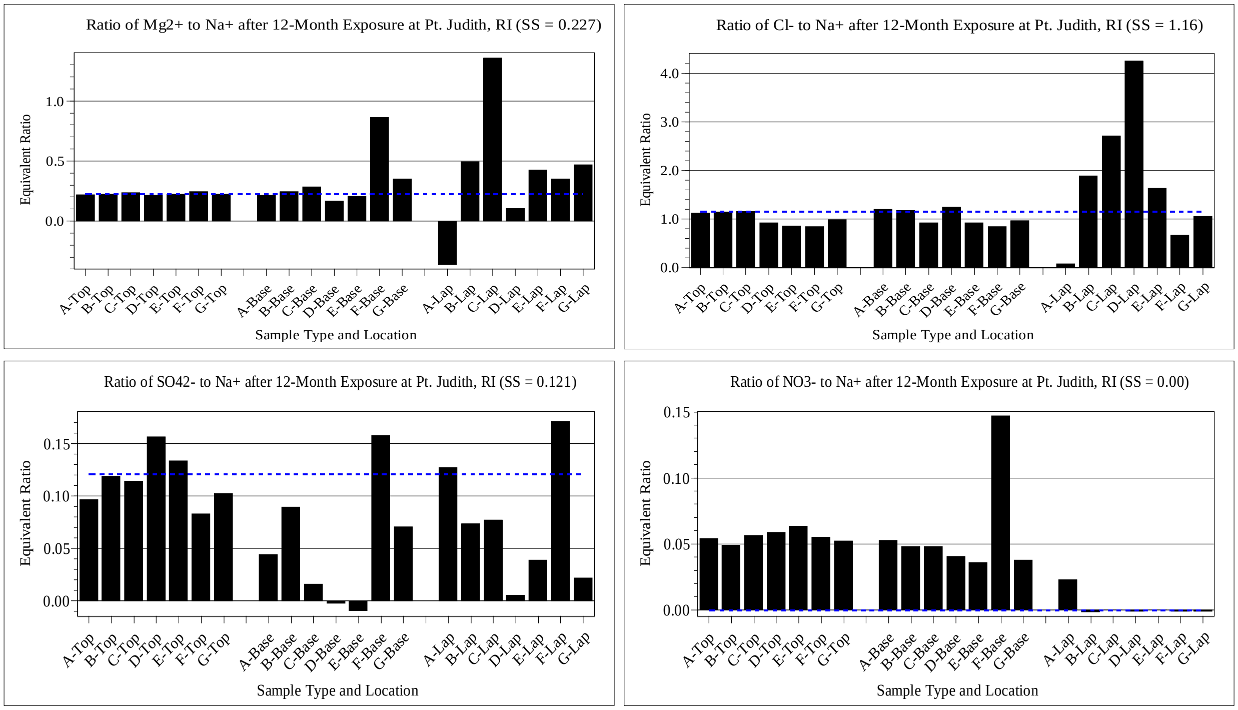

Figure 147. Ratios of Mg^{2+}, Cl^-, SO_4^{2-}, and NO_3^- to Na^+ on surfaces of sample assemblies exposed at Pt. Judith for 12.2 months. The dashed horizontal lines depict the corresponding sea-salt (SS) ratios in freshly produced marine aerosol.

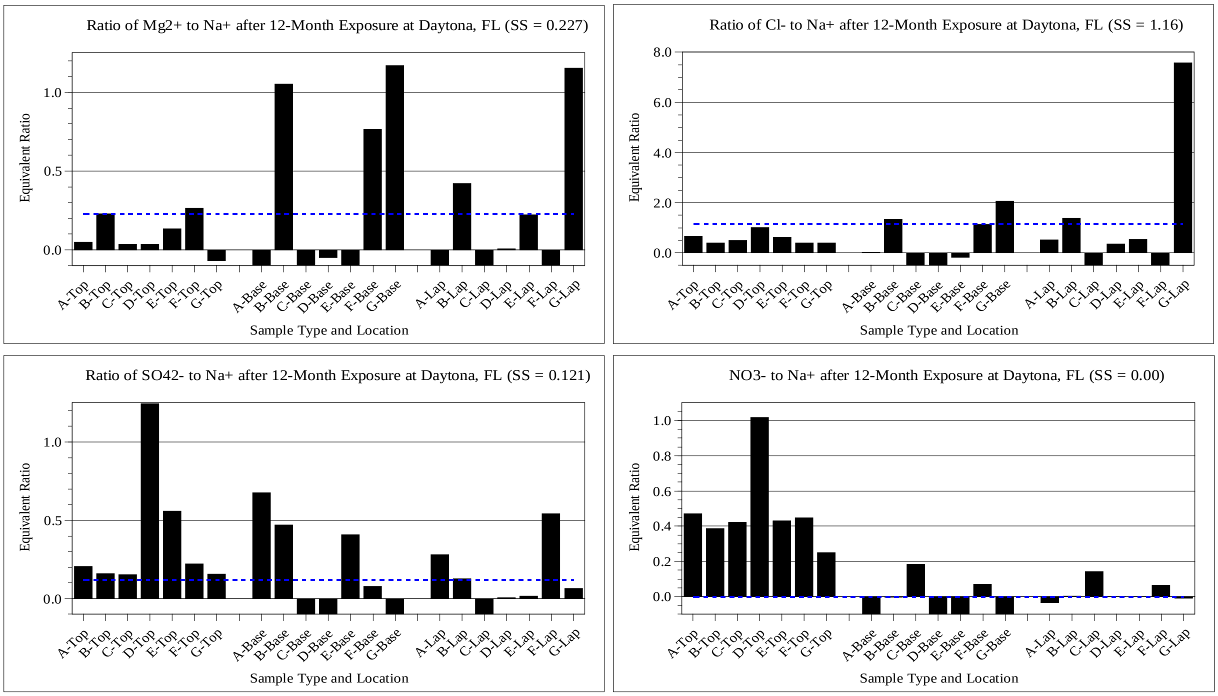

Figure 148. Ratios of Mg^{2+}, Cl^-, SO_4^{2-}, NO_3^- and $(COO)_2^{2-}$ to Na^+ on surfaces of sample assemblies exposed at LAX for 12.5 months. The dashed horizontal lines depict the corresponding sea-salt (SS) ratios in freshly produced marine aerosol.

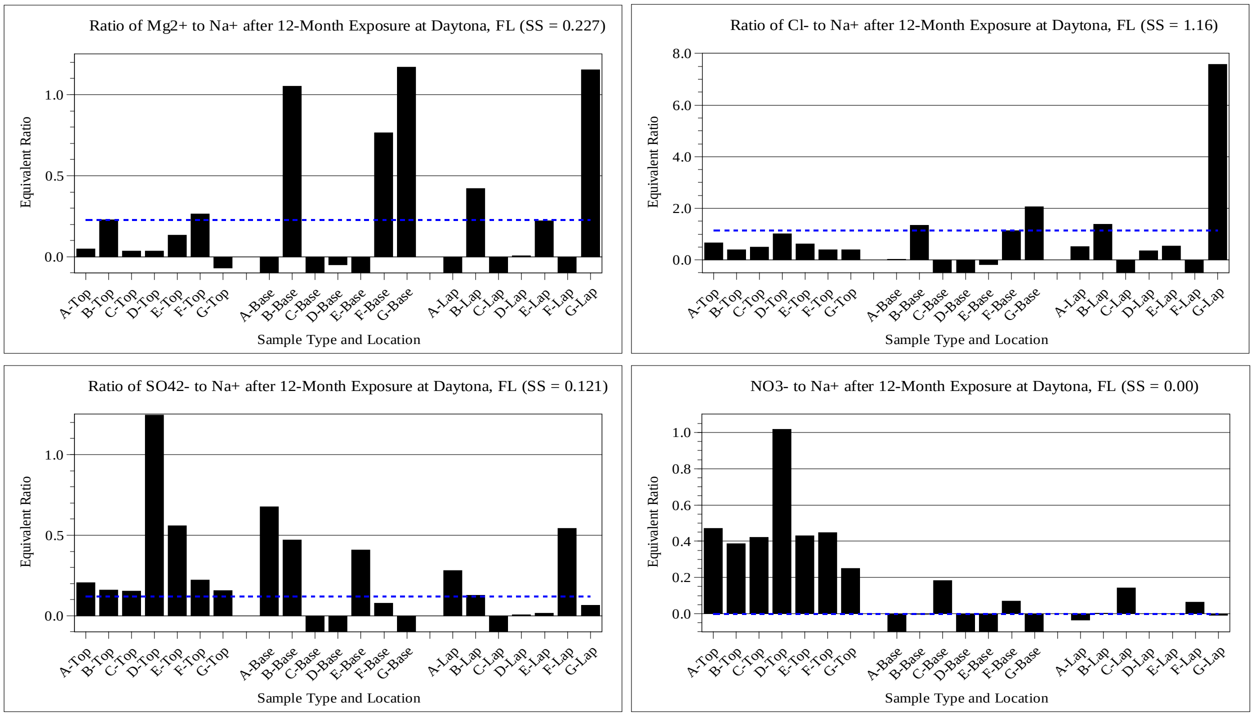

Figure 149. Ratios of Mg^{2+}, Cl^-, SO_4^{2-} and NO_3^- to Na^+ on on surfaces of sample assemblies exposed at Daytona Beach for 12.4 months. The dashed horizontal lines depict the corresponding sea-salt (SS) ratios in freshly produced marine aerosol.

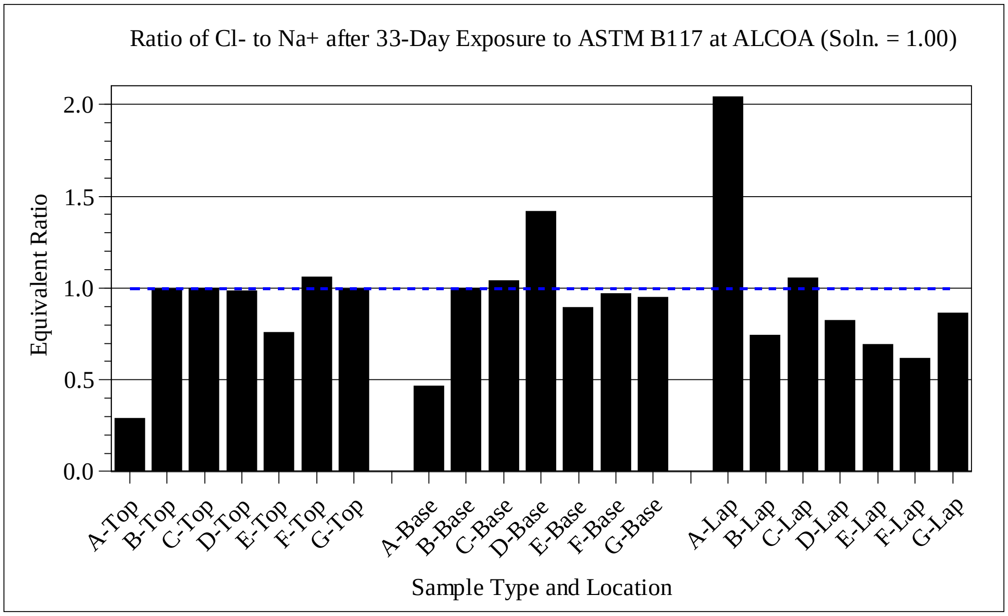

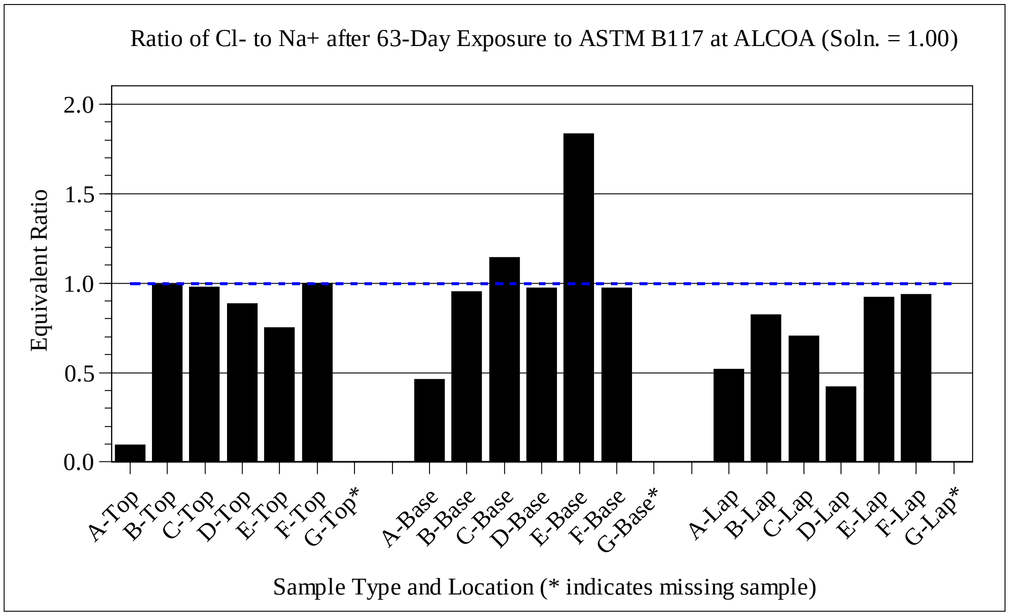

Figure 150. Ratios of Cl^- to Na^+ on surfaces of sample assemblies exposed to ASTM B117 for 33 and 63 days. The dashed horizontal lines depict the corresponding ratio in the simulate solution.

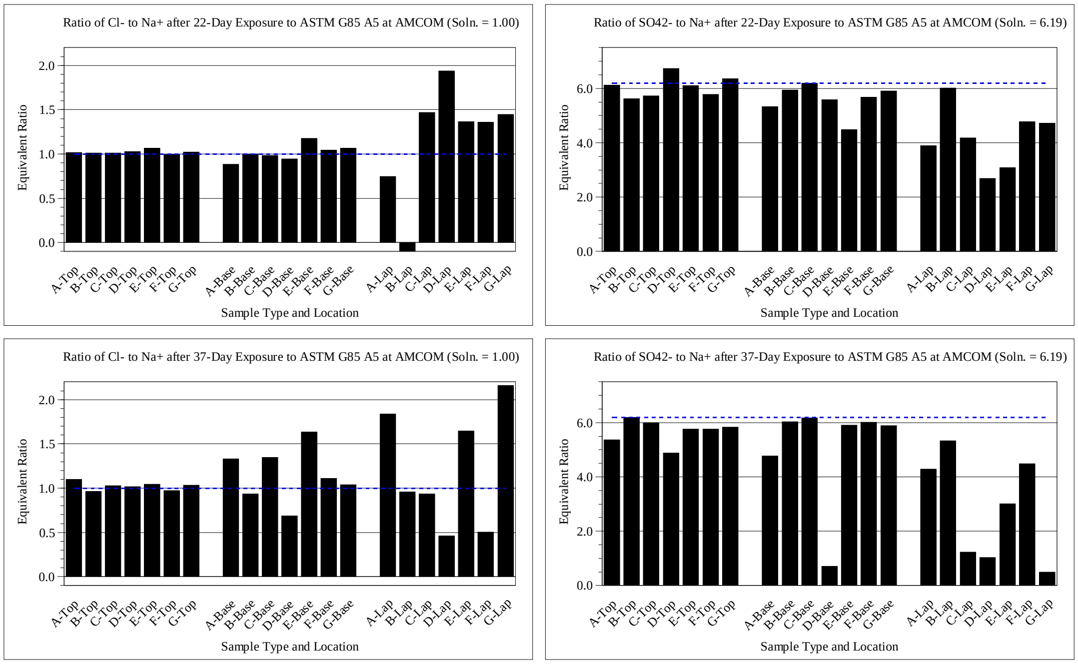

Figure 151. Ratios of Cl$^-$ and SO$_4^{2-}$ to Na$^+$ on surfaces of sample assemblies exposed to ASTM G85 A5 for 22 and 37 days. The dashed horizontal lines depict the corresponding ratios in the simulate solution.

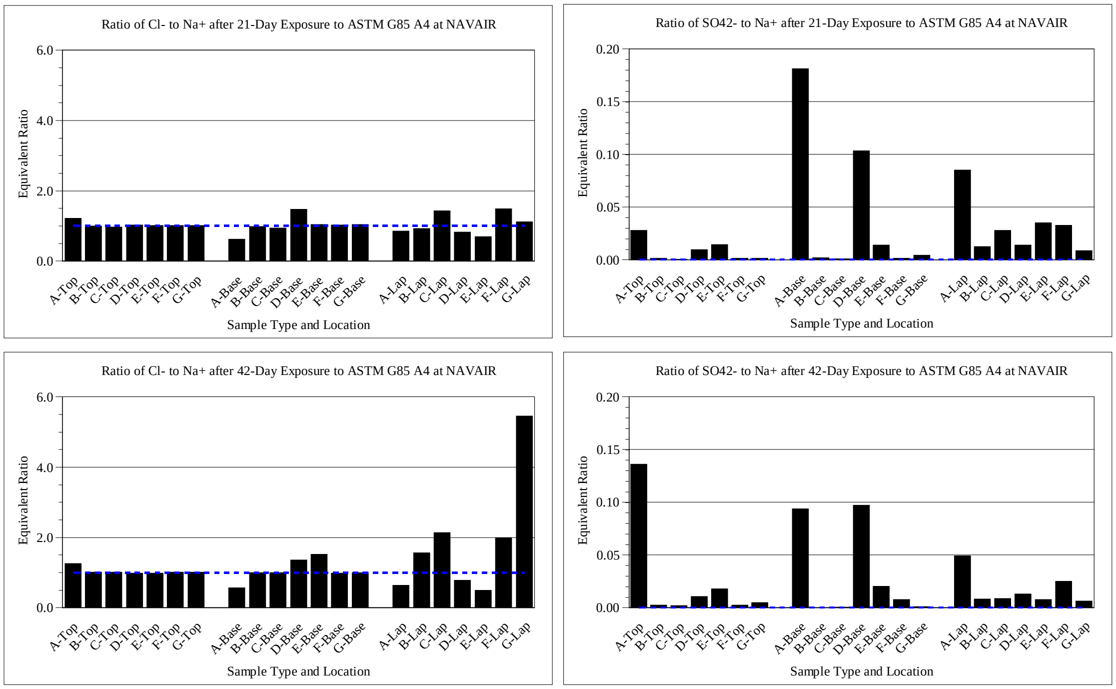

Figure 152. Ratios of Cl$^-$ and SO$_4^{2-}$ to Na$^+$ on surfaces of sample assemblies exposed to ASTM G85 A4 for 21 and 42 days. Horizontal lines depict the corresponding ratios in the simulant solution.

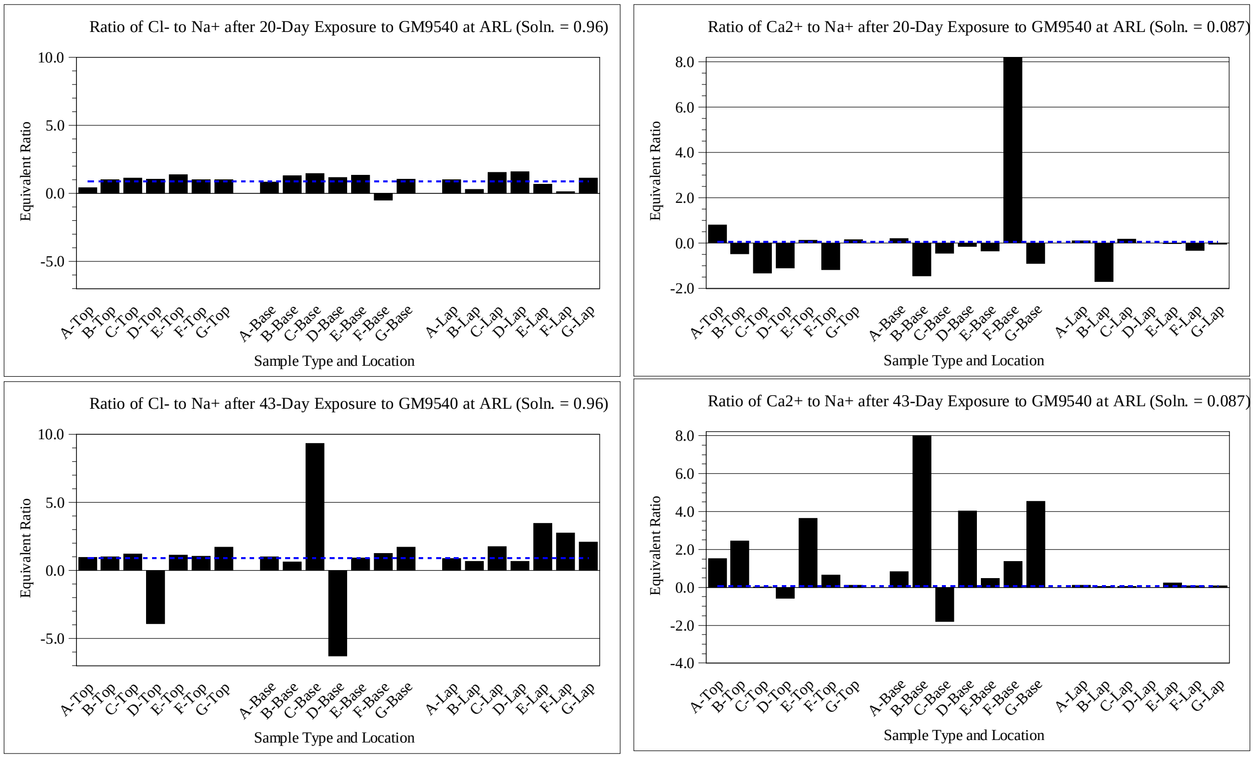

Figure 153. Ratios of Cl^- and Ca^{2+} to Na^+ on surfaces of sample assemblies exposed to GM9540P for 20 and 43 days. The ratio of Ca^{2+} to Na^+ on the exposed base plate of sample type F following the 20-day exposure is off scale. Horizontal lines depict the corresponding ratios in the simulant solution.

The relative composition of material deposited on top plates of field samples also varied substantially among sites. For example, ratios of K^+ and Ca^{2+} relative to Na^+ at Point Judith (not shown) were similar to those in seawater indicating that most of these species originated from the surface ocean in association with marine aerosol. In contrast, ratios of these constituents at both Daytona Beach and LAX were much higher than sea-salt ratios suggesting that crustal dust and/or calcareous shell fragments contributed significantly to loadings of these constituents at these latter sites. In addition, top plates at LAX exhibited high concentrations of $(COO)_2^{2-}$ (Figure 148) whereas samples exposed at the other field sites (not shown) did not. The above results suggest that the importance of different corrosion pathways may vary substantially among field exposure sites.

8.2.1.3.1 Point Judith (Figure 147)

Ratios of Mg^{2+} to Na^+ were generally similar to those for both seawater and marine aerosols suggesting that, following deposition, corrosion on the top plate caused minimal compositional change in either of these species.

Ratios of Cl^- to Na^+ on most top plates were lower than those in seawater. Similar depletions relative to sea-salt ratios are typically observed in marine aerosols (e.g., Keene et al., 2007; 2009). Dechlorination of marine aerosol is driven primarily by acidification and subsequent volatilization of HCl following the incorporation of more soluble acids (primarily HNO_3 and to a lesser extent H_2SO_4). The Cl^- deficits relative to Na^+ on the top plates may reflect those of the parent aerosol. However, relative to ratios of Mg^{2+} to Na^+, ratios of Cl^- to Na^+ exhibited greater variability among plates suggesting that Cl^- varied somewhat in response to post-deposition modification involving corrosion processes via either differential volatilization or scavenging of HCl vapor to/from the gas phase, in situ chemical production of Cl^- from the corroding surface, and/or in situ chemical loss of Cl^- via incorporation into non-soluble corrosion products.

The similarity in Cl^- to Na^+ ratios in loadings on the top and base plates suggests similar chemical processing on both surfaces. These relationships coupled with the relatively greater variability in Cl^- to Mg^{2+} ratios between the top versus base plates implies that differences in the corresponding ratios of Mg^{2+} to Na^+ between the top and base plates were driven primarily by the accumulation or loss of Mg^{2+} on/from the base plates. Accumulation may reflect selective retention of Mg^{2+} from previous loadings that were subsequently flushed off by precipitation and/or in situ chemical production from the corroding surface itself. Loss would likely reflect incorporation into non-soluble corrosion products.

Behavior of Na^+, Mg^{2+}, and Cl^- in the lapped area is more complex but, compared to those on the top-plate surfaces and to sea-salt composition, the generally higher ratios and enrichments of Mg^{2+} to Na^+ and of Cl^- to Na^+ and relatively lower ratios of Cl^- to Mg^{2+} indicates that, in most sample laps, Cl^- is enriched relative to Na^+ and Mg^{2+} is enriched relative to both Cl^- and Na^+.

Ratios of SO_4^{2-} to Na^+ on the top plate were considerably more variable that those for other species and, in most cases, were less than those in seawater. In addition, SO_4^{2-} in most samples is depleted relative to Na^+ to greater degrees on both the base plates and the lapped areas. Sea-salt SO_4^{2-} is chemically conserved when primary marine aerosols are produced at the ocean surface and S compounds in aerosol solutions are highly soluble. In the atmosphere, H_2SO_4 accumulates in marine aerosol via condensation from the gas phase and in-situ chemical production from the scavenging and oxidation of SO_2 in aerosol solutions (Keene et al., 1998). Consequently, over their atmospheric lifetimes, marine aerosols become enriched to variable degrees in SO_4^{2-} relative to sea salt. The generally low ratios of SO_4^{2-} to Na^+ on the top plates relative to aerosols and particularly depletions relative to sea salt on several (which are never observed in the atmosphere) coupled with the generally lower ratios of SO_4^{2-} to Na^+ on the base plates and in laps strongly suggests that SO_4^{2-} was converted to another form (presumably an insoluble product) via corrosion processes on most samples (type F being the notable exception). If anaerobic conditions existed within laps, S reduction pathways many have contributed to the apparent losses of deposited SO_4^{2-} within laps.

Equivalent ratios of NO_3^- relative to Na^+ for loadings on the top plates (median of 0.06) were at the lower end of the range for super-μm-diameter aerosols in polluted marine air at Bermuda (median 0.08 (Keene, Pszenny, Maben, & Sander, 2002)) and along the east coast (median 0.42 (Keene, Pszenny, Maben, Stevenson, & Wall, 2004)]). However, these regional differences in median ratios for aerosols were driven primarily by variability in the amount of sea salt rather than the amount of NO_3^-. The median concentration of particulate NO_3^- at Bermuda during spring was only 25% lower than that along the east coast during summer (9.1 versus 12.1 nmol m^{-3}). Ratios of NO_3^- to Na^+ on base plates were generally lower than those on top plates and, NO_3^- was undetectable within most laps. These results suggest that significant amounts of NO_3^- on most sample surfaces (the base plate of type F being the notable exception) may have converted to another form (presumably either an insoluble corrosion product or microbial biomass). If anaerobic conditions existed within laps, N reduction could have also contributed to corresponding losses of NO_3^-. Finally, volatilization of HNO_3 from loadings in which acidity increased via corrosion could have also contributed to the apparent losses. Since results indicate that some SO_4^{2-} was almost certainly lost from the top plates, it seems reasonable to assume that some NO_3^- may have also been lost suggesting that ratios on the top plate represent lower limits for the original ratios in the parent aerosol. In addition, larger sea-salt size fractions are typically undersaturated with respect to HNO_3 vapor due to kinetics (small surface-to-volume ratios and corresponding long thermodynamic equilibration times coupled with relatively short atmospheric lifetimes against depositions of hours to a couple days) (e.g., Keene & Savoie, 1998; Erickson, Seuzaret, Keene, & Gong, 1999). Consequently, assuming that corrosion did not produce acidity, marine aerosol deposited on surfaces should have continued to scavenge HNO_3 from the gas phase until phase partitioning reached thermodynamic equilibrium, which would have increased NO_3^- to Na^+ ratios on surfaces relative to the parent aerosols. Finally, if corrosion produced alkalinity, additional HNO_3 would have been scavenged from the gas phase, which would have also increased ratios.

As in marine aerosols, ratios of K^+ and Ca^{2+} to Na^+ on the top plates (no shown) were close to those for sea salt. Of the analytes evaluated, K^+ exhibits the least overall variability among different locations on samples (top, base, lap). In contrast Ca^{2+} was considerably more variable among surfaces of different sample types.

$(COO)_2^{2-}$ is an important secondary organic reaction product in marine aerosol (e.g., Turekian, Macko, & Keene, 2003) but was undetectable on all sample surfaces (not shown). We infer that $(COO)_2^{2-}$ deposited onto sample surfaces at Point Judith was either oxidized to form unmeasured perhaps volatile reaction products (e.g., CO or CO_2) or incorporated into insoluble corrosion products.

8.2.1.3.2 LAX (Figure 148)

Although not quantified as part of this program, visible inspection revealed substantial loadings of graphitic carbon (from combustion sources) on top and base plates of samples exposed at LAX. Like activated charcoal, graphitic carbon is reactive and, thus, may influence corrosion processes.

Loadings of Na^+ and other species within laps exposed at LAX were low relative to those on exposed top and base plates. Because associated uncertainties are relatively high, caution is warranted in interpretation of ratios within laps. Lower amounts and frequencies of precipitation and lower relative humidities and associated water contents of deposited material at LAX relative to other field sites may be responsible for the lower loadings within laps at this site.

Loadings of Na^+ on exposed base plates were generally higher than those on top plates. However, the similarity of ratios of most constituents to Na^+ on base and top plates indicates that these differences were driven primarily by differences on absolute loadings rather than differential chemical evolution of ionic constituents.

Ratios of Mg^{2+} (as well as those of K^+, and Ca^{2+}, not shown) versus Na^+ on top plates were much higher than sea-salt ratios indicating substantial contributions from non-sea-salt (presumably crustal) sources at this site. The similarity in ratios of Mg^{2+} and K^+ versus Na^+ on top and base plates of samples suggests that these three constituents on these surfaces were reasonably conservative with respect to corrosion. On average, ratios of Mg^{2+} to Na^+ on base plates were slightly higher than those on top plate (and corresponding ratios of Cl^- to Mg^{2+} were slightly lower) suggesting the possibility of modest accumulation of Mg^{2+} on base plates. In contrast, ratios of Ca^{2+} versus Na^+ on base plates varied substantially from those on top plates suggesting differential loss or accumulation of Ca^{2+} associated with corrosion processes on base plates.

Ratios of Cl^- to Na^+ on top and base plates were similar, which suggests that, like Na^+, Cl^- was probably also reasonably conservative with respect to corrosion. The higher ratios relative to seawater suggests that the dry deposition of HCl vapor may have contributed to Cl^- loadings on samples. The atmospheric lifetime against deposition for HCl produced from marine aerosol is longer than that of the mass-weighted lifetime against deposition of the parent aerosol. Consequently, concentrations of HCl in near-surface air over the open ocean are generally higher than the corresponding Cl^- deficit relative to sea salt in the parent aerosol (Keene et al., 2009). It follows that ratios Cl^- (contributed by both HCl and particulate Cl^-) to Na^+ in atmospheric deposition cannot be interpreted unambiguously with respect to sea-salt versus non-sea-salt sources. The enrichment of Cl^- relative to sea salt in loadings on samples exposed at LAX probably reflects contributions of HCl that originated from both marine and combustion sources upwind.

Ratios of SO_4^{2-} to Na^+ indicate that SO_4^{2-} is highly enriched relative to sea salt on both the top and base plates. Although loadings of SO_4^{2-} on base plates were somewhat more variable, loadings on top and base plates fell within a similar range. The non-sea-salt SO_4^{2-} almost certainly originated from combustion sources of precursor SO_2 upwind. Both the deposition of particulate SO_4^{2-}, the primary atmospheric oxidation product of SO_2, as well as the condensation and subsequent in situ oxidation of SO_2 in surface deposits may be important incorporation pathways.

NO_3^- to Na^+ ratios were similar on the top and base plates. Given the low absolute loadings within laps, the generally low ratios within laps are difficult to interpret unambiguously with respect to corrosion processes.

Ratios of NH_4^+ to Na^+ (not shown) were low on virtually all surfaces. In light of the fact that the atmosphere over LAX contains substantial concentrations of particulate NH_4^+ and gaseous NH_3, we infer that these results represent losses of NH_4^+ following deposition (and/or solubility limitations on deposition). Loss pathways include volatilization of NH_3 from (or limitation of its deposition into) alkaline deposits in which the solubility of NH_3 is low, incorporation into microbial biomass, and/or incorporation into insoluble corrosion products.

The systematically higher ratios of $(COO)_2^{2-}$ to Na^+ on top relative to base plates indicates enhanced in-situ production of $(COO)_2^{2-}$ from precursors on top relative to base plates and/or enhanced chemical loss $(COO)_2^{2-}$ on base relative to top plates. These results indicate that, despite light loadings within laps, chemical coupling between the lapped and exposed areas of base plates modified the chemical evolution of exposed surfaces of base plates to some extent.

8.2.1.3.3 Daytona Beach (Figure 149)

As noted above, the low loadings on most sample surfaces at Daytona limit resolution in interpreting processes.

The negative loadings of Na^+ on most base plates and on lapped section of three sample types (A, C, and F) suggest that the corresponding blank corrections were too high. The most probable explanation for these results is that an equivalent amount of background Na^+ present on most base plates prior to exposure plus some fraction of Na^+ deposited onto base plates during exposure were incorporated into insoluble reaction products. Consequently, interpretation of ratios on base plates and on lapped sections of sample types A, C, and F is problematic.

Ratios of Mg^{2+} to Na^+ on top plates of 5 of the 7 sample types (A, C, D, E, and G) were less than the sea-salt ratio suggesting that disproportionately larger amounts of Mg^{2+} were incorporated into insoluble reaction products. Ratios of Mg^{2+} to Na^+ varied differentially relative to the sea-salt ratio within laps of sample types with significant loadings of Na^+ (B, D, E, and G).

Cl^- to Na^+ ratios on top plates were systematically lower than that of sea salt by a mean factor of ~2. These results suggest significant losses of Cl^- relative to Na^+ from exposed samples via either volatilization of HCl or incorporation of Cl^- into insoluble reaction products. Like those for Mg^{2+} versus Na^+, ratios of Cl^- versus Na^+ within laps that contained significant Na^+ varied differentially relative to sea salt.

Ratios of SO_4^{2-} to Na^+ on top plates were variable and systematically higher than that of sea salt indicating variable contributions of SO_4^{2-} from non-sea-salt (presumably combustion) sources. Relatively lower ratios of SO_4^{2-} to Na^+ within laps that contained significant Na^+ suggest losses of SO_4^{2-} via either incorporation into insoluble reaction products or S reduction.

The fairly consistent equivalent ratios of NO_3^- to Na^+ on top plates (median value of ~0.4) coupled with undetectable NO_3^- (i.e., ratios of NO_3^- to Na^+ of ~0.0) within laps that contained significant Na^+ indicate that, as observed at Pt. Judith, NO_3^- originally present was lost within laps. Presumably, these losses reflect some combination NO_3- incorporation into insoluble corrosion products or microbial biomass, N reduction if anaerobic conditions existed, and/or HNO_3 volatilization if highly acidic conditions existed.

Like NO_3^-, results indicate that NH_4^+ originally present was also lost within laps. Presumably, these losses reflect some combination NH_4^+ incorporation into insoluble corrosion products or microbial biomass and/or NH_3 volatilization if alkaline conditions existed.

Ratios of K^+ and Ca^{2+} to Na^+ on top plates were systematically higher than those of sea salt indicating significant contributions of K^+ and Ca^{2+} from non-sea-salt sources (presumable crustal dust or calcareous shell fragments). In addition, the systematically lower ratios of K^+ and Ca^{2+} to Na^+ within laps that contained Na^+ relative to those on top plates indicate that significant amounts of K^+ and Ca^{2+} originally present was lost via incorporation into insoluble corrosion products within laps.

8.2.1.3.4 ASTM B117 (Figure 150)

Relative to the test solution composition, systematically lower ratios of Cl^- to Na^+ on the top and base plates of sample type A indicate that either (1) Na^+ was produced via corrosion of the top and base plates or (2) Cl^- was lost via incorporated into insoluble reaction products or HCl volatilization. If Na^+ was produced or Cl^- was incorporated into insoluble corrosion products, an equivalent amount of unmeasured anion (or anions) must have also been produced to maintain charge neutrality of the surface loading.

Ratios of Cl^- to Na^+ on top and base plates of other sample types (B through G) were generally similar to those in the test solution suggesting the both analytes on these surfaces were reasonably conservative with respect to corrosion processes.

After 33 days of exposure, Cl^- to Na^+ ratios within laps of 5 of 7 sample types were less than that of the test solution and after 63 days, ratios within laps of all sample types were less than that of the test solution. These results indicate that either (1) Na^+ was produced via corrosion within laps or (2) Cl^- was lost via incorporated into insoluble reaction products or, if corrosion produced acidity, HCl volatilization. If Na^+ was produced or Cl^- was incorporated into insoluble corrosion products, an equivalent amount of unmeasured anion (or anions) must have also been produced to maintain charge neutrality of the surface loading.

8.2.1.3.5 ASTM G85 A5 (Figure 151)

Despite large (greater than a factor of 10) variability in absolute loadings on top plates, Cl^- to Na^+ ratios on top plates following both exposure periods were close to that of the test solution. Although ratios on the base plates following the 22-day expose were also similar to that of the test solution, ratios following the 37-day exposure varied to a greater degree among sample types; some were higher than that of the test solution and some were lower.

With one exception (type A), after the 22-day exposure period, Cl^- to Na^+ ratios within laps of samples with significant Na^+ loadings (A, C, D, E, and G) were higher than that of the test solution whereas greater variability was evident after the 37-day exposure. For samples with significant Na^+ loadings within laps, sample types B, C, D, and F exhibited Cl^- to Na^+ ratios within laps that were less than that of the text solution and sample types E and G exhibited ratios that were greater than that of the text solution.

The deviations from ratios in the test solution mentioned above indicate differential production and/or loss of Na^+ and/or Cl^- via corrosion processes.

With the exception of sample type D following the 37-day exposure period, ratios of SO_4^{2-} to Na^+ on top and base plates of most samples were marginally less than that in the test solution. However, ratios within laps of all samples were significantly lower than that of the test solution and, for most samples, the magnitude of deviations from the test solution increased between the 22- and 37-day exposures. These results indicate that, most notably within laps, SO_4^{2-} was incorporated into insoluble corrosion products and/or, if anaerobic conditions existed, lost via S reduction.

Again with the exception of sample type D following the 37-day exposure period, ratios of NH_4^+ to Na^+ on top and base plates of most samples (not shown) were generally similar to that of the test solution. Like those for SO_4^{2-}, ratios of NH_4^+ to Na^+ within laps were lower than those of the test solution and the magnitude of divergence for most sample types increased from the 22- to 37-day exposure period.

Ratios of NH_4^+ to SO_4^{2-} (not shown) indicate that, on most sample surfaces following both exposure periods, the two species were present in ratios similar to that of the test solution, which implies similar chemical processing of both species. However, relatively greater variability within laps of several sample types (A, D, and G) following the 37-days exposure suggest differential processing. Lower ratios of NH_4^+ to SO_4^{2-} may reflect preferential incorporation of NH_4^+ into microbial biomass and/or, if alkalinity were produced via corrosion, loss via NH_3 volatilization whereas higher ratios may reflect preferential incorporation of SO_4^{2-} into insoluble corrosion products and/or, if anaerobic conditions were present, loss via S reduction. Regardless, preferential loss of either species implies production of equivalent concentrations of unmeasured ions to maintain charge balance of the residual loadings on surfaces.

8.2.1.3.6 ASTM G85 A4 (Figure 152)

Despite large (greater than a factor of 10) variability in absolute loadings on top plates (Figure 152), Cl^- to Na^+ ratios on top plates following both exposure periods were close to that of the test solution. Although somewhat more variable that those for the top plates, ratios on the base plates were also similar to that of the test solution. Ratios within laps varied to a greater degree among sample types and the degree of variability increased with duration of exposure; some were higher than that of the test solution and others were lower.

Although loadings of SO_4^{2-} were detectable on virtually all surfaces, absolute amounts varied greatly among samples. A few patterns are evident. For both exposure durations, loadings on the top, base, and lapped surfaces of sample type A were higher than or comparable to the highest loading on the same surfaces of other sample types. In addition, for both exposure periods, SO_4^{2-} loadings on exposed portions of the base plates of sample type D were also relatively high. Causes for this variability are not known but may be driven in part by differential exposures to SO_2 within chambers.

8.2.1.3.7 GM9540P (Figure 153)

The low loadings on exposed surfaces preclude reliable interpretation of corresponding constituent ratios (Figure 153) but, in general, Cl^- to Na^+ ratios on those surfaces are similar to those in the simulant solutions. Cl^- to Na^+ ratios within laps were more variable with some greater than and some less than that in the simulant.

For sample types D and E, which exhibited Na^+ loadings within laps that were 5 to 10 times higher than the next highest loadings (Figure 153), ratios of Ca^{2+} to Na^+ were lower than that in the simulant solution suggesting that Ca^{2+} had been incorporated into insoluble corrosion products.

8.2.1.4 Implications for Development of New Accelerated Test

The much greater degree of variability in loadings on top plates of samples exposed within chambers (Figure 145) relative to those exposed to ambient conditions (Figure 146) is problematic. Variability in loadings may contribute to corresponding variability in corrosion processes within test chambers under otherwise identical test conditions. Accelerated test chambers should be designed to minimize spatial variability in the delivery of simulant solutions to test samples.

Variability in absolute and relative loadings of ionic constituents exposed to ambient conditions implies that a single accelerated test may not adequately simulate corrosion processes at all locations.

The following interpretations focus primarily on exposure results for which loadings provided reasonable signal to noise. These include ambient exposures at Point Judith and Los Angeles and accelerated test exposures to ASTM B117, ASTM G85 A5, and ASTM G85 A4.

For ambient exposures (Figure 147 and Figure 148) and for lab exposures (Figure 151 and Figure 152) in which SO_4^{2-} was present, Cl_- to Na^+ ratios within laps varied differentially among sample types. For ASTM B117 in which only Na^+ and Cl^- were present, Cl^- within laps was depleted relative to Na^+ in all sample types following 63 days of exposure. In addition, relative to ratios in sea salt in the simulant solution as well as loadings on top plates, SO_4^{2-} was generally depleted within laps of samples exposed to ambient conditions and to ASTM G85 A5. These results suggest that SO_4^{2-} is an important reactant in corrosion chemistry and that its chemical processing is coupled with that of Cl^-.

Ambient exposures reveal systematic depletions of NO_3^- within laps, which suggest that NO_3^- is an important reactant in corrosion chemistry.

Ambient exposures reveal systematic depletions of $(COO)_2^{2-}$ relative to the composition of ambient aerosols and within laps, which suggests that $(COO)_2^{2-}$ is an important reactant in corrosion chemistry.

Although not evaluated directly as part of this study, in most regions, fresh marine aerosol are rapidly (seconds to tens of minutes) acidified following production via the condensation of acids (primarily HNO_3, HCl, H_2SO_4, HCOOH, and CH_3COOH) and acid precursors (primarily SO_2) (e.g., Chameides & Stelson, 1992; Keene & Savoie, 1998; Keene et al, 1998; Keene et al., 2004; Keene et al., 2007; Keene et al., 2009; Erickson et al., 1999; Pszenny et al., 2004). Because many chemical pathways are strongly pH dependent, H^+ is considered to be an important ionic component of a representative simulant solution.

In situ photochemical reactions and the condensation of gas-phase oxidants (e.g., Zhou et al., 2008) as well as the condensation of gas-phase acids and acid precursors into aqueous films on corroding surfaces are potentially important pathways that were not evaluated explicitly as part of this investigation.

CHAPTER 9
TEST METHOD DEVELOPMENT

In this chapter, the steps taken to define the test method are outlined. A systematic approach is taken, where each of the controlling factors defined in the previous chapters is discussed such that a clear understanding of the parameters that define the exposure cycle are justified. Based on this discussion, the effect of varying these parameters will be explored in order to provide insight into means by which the test can be varied to suit particular environmental conditions or to initiate specific failure modes. Further, two initial recommendations for a test protocol are defined. Finally, surface ionic chemistry and corrosion morphology are measured after exposure to the new test protocols. Comparison of chemistry and morphology with samples after exposure to existing test protocols and outdoor environments provides the basis for recommendations to improve the test protocol.

9.1 Summary of Key Environmental Factors to be Considered in Test Method Development

In this section, a summary of the key environmental factors is provided.

9.1.1 *Relative humidity*

The single most relevant factor in governing atmospheric corrosion is the RH. Significant work has been invested throughout the course of this effort with the goal of defining how RH and cyclic RH affect corrosion rates and corrosion modes.

9.1.1.1 Effect of RH on single alloy bare surfaces

Under iso-humidity conditions, the effect of RH value and salt composition was elucidated for steel. Relative humidity governs surface wetness in two ways. First, adsorbed electrolyte layers on the surface can provide enough moisture for corrosion to occur. In this work, significant effort was focused on the interaction between RH and salt content. It was shown in Figure 20 that depending on the salt composition, corrosion can continue at RH values as low as 10%. In the case of sea salt, deliquescence is controlled by the Mg_2Cl content which has a DRH value around 35%. The presence of hydrates, however, allows the formation of a salt crust on a droplet preventing evaporation of moisture beneath. However, it should be noted that below 50% RH, the corrosion rate is considered to be “very low” according to the ISO standard 9223. While corrosion rate is low below 50% RH, certain corrosion modes are not manifested without a dry-out period as will be discussed below.

MEA studies of steel under cyclic RH conditions were also carried out. MEA data taken under iso-humidity conditions revealed similar behavior to what is observed in Figure 20. Real time MEA data revealed that under cyclic RH conditions, spikes in corrosion rate occurred during wetting and drying cycles. These spikes were not only observed for steel systems but also aluminum systems, indicating the importance of cyclic RH. MEA data was also used to verify that corrosion rates below 50% RH were negligible. While corrosion rates between 50% and 76% RH under a NaCl film were lower than those under fully deliquesced conditions, they were not negligible. Further, measurements were made over an 8 hour period showing constant corrosion current behavior over long time periods at 50% < RH < 76%. Lastly, as time above DRH increases, the corrosion currents for steel were observed to increase with time. Although the limiting current was not measured in this study, it was observed that corrosion currents for steel have been observed to increase for periods of 10 hours. Thus, for equivalent total time of wetness, more cumulative charge is passed for conditions where each wet period is longer. In other words, for longer exposure times to wet conditions, not only is the time of wetness increased, but additionally, absolute corrosion currents are higher.

Based on this information, several key elements of the corrosion method can be identified:

1) There are at least two critical RH ranges needed. RH < 50% for drying to occur and RH > DRG for complete wetting to occur,
2) Total time of wetness (TOW) is a major factor governing corrosion, and
3) For given cyclic wet/dry conditions, the amount of time spent in each wet period is important.

9.1.1.2 Effect of RH on crevice corrosion and galvanic corrosion

The effect of cyclic RH conditions on a creviced steel MEA was examined. Corrosion currents were observed to initiate on both the outside of the crevice as well as the inside. However, during drying, while the outside of the crevice dried and corrosion currents ceases, the inside remained wet and significant corrosion currents were observed. Further, after the corrosion currents within the crevice were stabilized, a coupling between the inside and outside of the crevice was observed. Under conditions of high RH, the surface outside of the crevice became totally cathodic such that all anodic currents were within the occluded crevice. Upon drying, the internal and external portions of the crevice decoupled, and corrosion current was observed external to the crevice mouth.

This coupling and decoupling effect was also observed for galvanic couples between steel and aluminum (Figure 32). Specifically, coupling was seen above the DRH point. Steel corrodes at RH values greater than 60% while Aluminum does not corrode until a chloride rich environment is present. Above the DRH, the NaCl deliquesces and aluminum begins to corrode. At the same time, the steel electrodes become entirely cathodic and enhance the corrosion rate of the aluminum. Upon reducing RH, the steel electrodes can decouple from the aluminum as the electrolyte film begins to break apart and corrosion currents are observed to occur on the steel electrodes.

These findings suggest that for values of RH above 50%, there are at least two regions of RH that are important. The regions are divided at the DRH. Below the DRH, it is likely that as drying begins, the thin electrolyte film begins to degrade, breaking into smaller islands. While corrosion can still occur under these electrolyte islands, long-range electrochemical coupling forces can no longer effect corrosion. To validate this understanding, MEA electrodes were placed into accelerated corrosion chambers undergoing various cycles. A comparison between the time when galvanic coupling is observed with periods of time that chamber RH > DRH yields a relatively good correlation (Table 1).

This phenomenon is important for two reasons. First, corrosion of steel fasteners in aluminum panels is not observed under continuous fog conditions (as in ASTM B117). By lowering RH values below the DRH, decoupling of the steel and aluminum allows corrosion of the steel fastener to occur. Second, many metal-rich primers are either in use or being considered for use in DoD systems. These primers act to protect the substrate material by galvanic interactions where the coating serves as the anode. As RH falls below DRH, the galvanic protection scheme will be much less effective.

Metallographic analysis showed that IGC, pitting and fissure formation within the bolt hole of a galvanic fastener only occurred under conditions only where RH was cycled. For example, IGC was not observed along the inner side of a fastener hole with a steel bolt for samples exposed to ASTM B117. Some attack was shown for samples exposed to ASTM G85-A5 where cyclic wetting and drying occurred. The attack was minimal presumably because of the low salt content. Under the UVA Trial 1 environment, concentrated NaCl was used and the pH was adjusted to 3. In this case, a greater degree of IGC and fissure formation was observed (although none as severe as found in Pt. Judith samples as seen in Figure 141).

Based on this information, additional constraints for the improved accelerated corrosion test method can be identified:

1) There are three regions of RH that are critical: RH < 50%, 50% < RH < DRH and RH > DRH,
2) Exposure conditions that fall in the middle RH range will reveal potential failure locations on samples with crevices and galvanic couples, and
3) The formation of corrosion within occluded sites was observed in the rivet holes for Ti and steel fasteners when exposed to cyclic conditions with high concentrations of salt and reduced pH suggesting the importance of these variables.

9.1.1.3 Effect of RH on coating adhesion

In a comparison between ASTM B117, GM9540P, ASTM G85 A4 and ASTM G85 A5, the loss of coating adhesion primarily occurs for samples exposed to ASTM G85 A5 and to a lesser extent in GM9540P (Figure 54). Two distinguishing factors for this test are that there is cyclic, wetting and drying, and the pH is reduced to pH = 5. The GM9540P test also is cyclic in nature. However, during the high RH DI fog step, the surface solution is diluted resulting in a reduction in corrosion current (Figure 35). Therefore, as with bare metal, the cyclic RH plays a key role in driving degradation. Additionally, corrosion rate of the bare metal has a role in adhesion loss.

In an attempt to better understand the role of the number of cycles and time of wetness on adhesion, further testing was performed using cycles identified in Table 4. Image analysis indicates that short periods of wetting and drying (cycle A) result in significant surface area exposed but limited volume of attack and average depth. Cycle B (low RH = 65%) does not completely dry and cycle C (long times of wet and dry) results in significant surface exposure to long periods of corrosion. In both cases, significant coating delamination is observed. Image analysis reveals that the most attack (surface area, volume and average depth) is observed for cycle C (Figure 73 and Figure 74) which is consistent with the observation that corrosion rate increases with time during a wet cycle. Sensor data reveals the onset of delamination is shortest for cycle B (no drying period below 50% RH) at 150 hours to 250 hours, between 550 hours and 650 hours for cycle C and longest for cycle A (between 900 hours and 1100 hours). This suggests that adhesion loss is a dual function of the number of cycles and corrosion rate. For example, cycles A and B have four times more cycles per day than cycle C yet cycle C creates the most damage (Figure 75). The drying step is still required to solidify corrosion product and lift the coating from the surface. This dual relationship between damage and number of cycles and corrosion rate is in agreement with observations from ASTM and GM cyclic testing.

It is important to note that cycle A and cycle C are able to distinguish the difference in corrosion performance between two non-chrome coating systems and show increased degradation as a function of time for each coating. However, the mode of corrosion for these environments is quite different. In cycle A and cycle C, significant surface delamination occurs. In cycle C, however, the attack depth is much deeper. In cycle C, the extended periods above DRH result in extensive corrosion (volume loss). Coating delamination occurs as the result of drying when the solidifying corrosion products lift the coating. In cycle A, superficial corrosion damage is observed but the corrosion products that form under the coating are able to solidify and lift the coating. As mentioned before, the time above the DRH is important. For longer times, higher corrosion rates are achieved, leading to increased coating delamination and corrosion damage despite the much lower cycle frequency in cycle C.

It is also informative to compare cycle A and cycle B. These cycles both have the same cycle frequency yet distinct corrosion modes. Of all cycles, cycle B results in exfoliation. Both cycle A and cycle B have the same time above the DRH. In cycle B, however, the RH does not fall below 50% RH. This results in more corrosion damage compared with cycle A. However, unlike cycle C, bulk metal loss occurs at a slower rate. This suggests that extended periods between DRH and 50% RH allow exfoliation and likely intergranular attack.

From Figure 34 and Figure 35, MEA data taken during exposure testing in accelerated laboratory testing is shown. Of particular note is corrosion current measured in ASTM G85 A5. During the short drying steps, there is an increase in the aluminum current that remains higher than the corrosion rate during the wet cycle. This transient is seen when cycling between wet and dry conditions as mentioned previously. For tests with short drying durations, the overall corrosion damage would be expected to be higher than for conditions where the drying time is long, allowing the transient to decline to corrosion current values near zero (as is the case for cycle C).

Based on these observations, the accelerated corrosion test method can be further refined by noting:

1) Coating delamination is a strong function of the time of wetness within a given cycle.
2) For cyclic corrosion testing, short drying times result in higher corrosion rates.
3) Exfoliation attack can be induced by holding the RH between DRH and 50% RH, even for a relatively short 2 hour period. Above DRH, an aggressive environment can cause delamination that is extremely accelerated compared with normal operational exposures. To control coating delamination, adjust aggressiveness and time (i.e. dilute solution spray for long periods or concentrated spray for short periods).
4) Minimize time below 50% RH.

9.1.1.4 Effect of RH on corrosion at a coating defect

From the preceding section, it was seen that RH duty cycle plays a strong role in both coating adhesion and corrosion rate in a defect site. MEA data (Section 3.2.2) indicates the effect of coating inhibitors on the corrosion current distribution. For the double RH ramps, the galvanic couple consisted of stainless steel and aluminum. The addition of Class N primer resulted in the localization the galvanic attack to the vicinity of the steel electrodes at high RH values. Aluminum attack was more distributed at RH values below DRH. For the system with a Class C primer, corrosion currents were stifled. For the MEA with carbon steel/aluminum electrodes, galvanic currents were much higher and more distributed for uncoated samples. Unlike the case with the stainless elements, the Class C coating could not stifle aluminum corrosion, but corrosion was localized to the interface of the galvanic couple. The stainless steel electrodes were more resistant to corrosion than the carbon steel as would be expected. The stainless electrodes are also weaker cathodes limiting the aluminum corrosion.

The implications from these observations on an improved cyclic test are as follows:

1) As before, decoupling of a galvanic couple occurs below the DRH within the intermediate RH range.
2) While not specifically tested here, coating failure will be accelerated upon depletion of inhibitors within a coating (or consumption of a galvanic primer metal). Conditions favoring high corrosion rates and high time of wetness (i.e. long exposure times with RH > DRH) would result in rapid depletion of coating protection systems. However, under conditions where high delamination rates occur, the exposure of more surface primer may increase depletion time.

9.1.1.5 Effect of RH on cracking

Examination of Figure 142 reveals that both the ASTM G85-A5 and UVA Trial 1 can induce IGC fissures similar to those observed in outdoor exposures at Pt. Judith for 12 months. It is likely that the cycle B environment also caused this type of attack based on the appearance of exfoliation on the surface. Cross sectional analysis would be required to verify this statement fully. In each case, the environments were cyclic in nature and had pH values of 5 or less. The formation of IGC fissures would result in crack nucleation sites as a result of high K values at the sharp defects formed. Therefore, cyclic exposures that directly affect localized corrosion morphology would also affect cracking.

As with coating delamination and galvanic decoupling, cracking is enhanced under conditions of cyclic RH. This is in agreement with observations of localized corrosion morphology described above. An increase in crack growth is only observed under conditions where the RH is falling. Crack growth rates for AA7075-T6 appear to be around 10 – 15 nm/s in the different cyclic environments. AA5083-H116 was testing in 3 different environments. The cracking always occurred during drying but it appears that exposure chemistry has an effect on crack growth rates. Under conditions of 0.5M NaCl, the crack growth rate reached values of 20 nm/s at RH values between 60% and 70% (Figure 99). In a modified ASTM G85-A5 environment, however, values reached as high as 600 nm/s at RH values range from 30% to 50% (Figure 104). Under exposure to GM9540P, values were maximized between 60% and 70% RH with values reaching 180 nm/s (Figure 108).

For testing in ASTM G85-A5, the sulfate chemistry has potentially two roles. First, since sulfate is a reactive species, it is likely that some sulfur species evolve creating DRH values in the 50% range. Thus, drying does not occur until low RH values. Additionally, based on unpublished data, it is known that sulfate directly affects the morphology of pit surfaces and promotes intergranular attack. Both of these phenomena would result in a significant increase in crack growth rate that is observed (Figure 104).

Interestingly, each of the cyclic environments resulted in cracking. While the pH = 5 sulfate containing environment induced the highest crack growth rate, sulfate and low pH are not critical for cracking to occur. For example, the GM9540P environment is buffered with bicarbonate resulting in a slightly alkaline environment with no sulfate present. Even in the case of ASTM B117, cracking could be induced by removing the loaded sample from the exposure. If morphology is related to crack growth, it would be expected that the UVA Trial 1 would result in cracking despite the lack of sulfate in the environment. It is also possible that this environment would result in significantly higher crack growth rates since localized fissure depths are even higher than those of ASTM G85-A5 (Figure 142).

Considerations for the improved test, therefore, should also consider:

1) Other corrosion failure modes discussed previously indicate that testing in the range between 50% RH and 76% RH is important. For cracking to occur, however, it is of prime importance that a cyclic testing is required with focus placed on the time for RH to decrease within this RH range.
2) Chemistry of the solution is already known to strongly influence corrosion mode. Observations of stress corrosion cracking indicate the potential importance specifically for sulfate species. pH below 5 may also be important for cracking.

Measure of outdoor RH conditions

Thus far, it has been demonstrated that RH control is important in governing corrosion modes. Based on this information, a means to define appropriate time intervals within each RH range must be defined. To achieve this goal, sensors were used to continuously measure RH at the outdoor exposure sights over a period extend several months. Based on the discussions above, the RH was analyzed for each environment and binned in four regions: (RH < 50%, rising RH with 50% < RH < DRH, falling RH with 50% < RH < DRH, and RH > DRH. In this case, it was assumed that NaCl dominated chemistry and so 76% RH was used as the DRH value. Figure 153 shows the analysis method used for binning the RH values. From this data, the percentage of time spent in each bin can be calculated and normalized to the total exposure time (Figure 154).

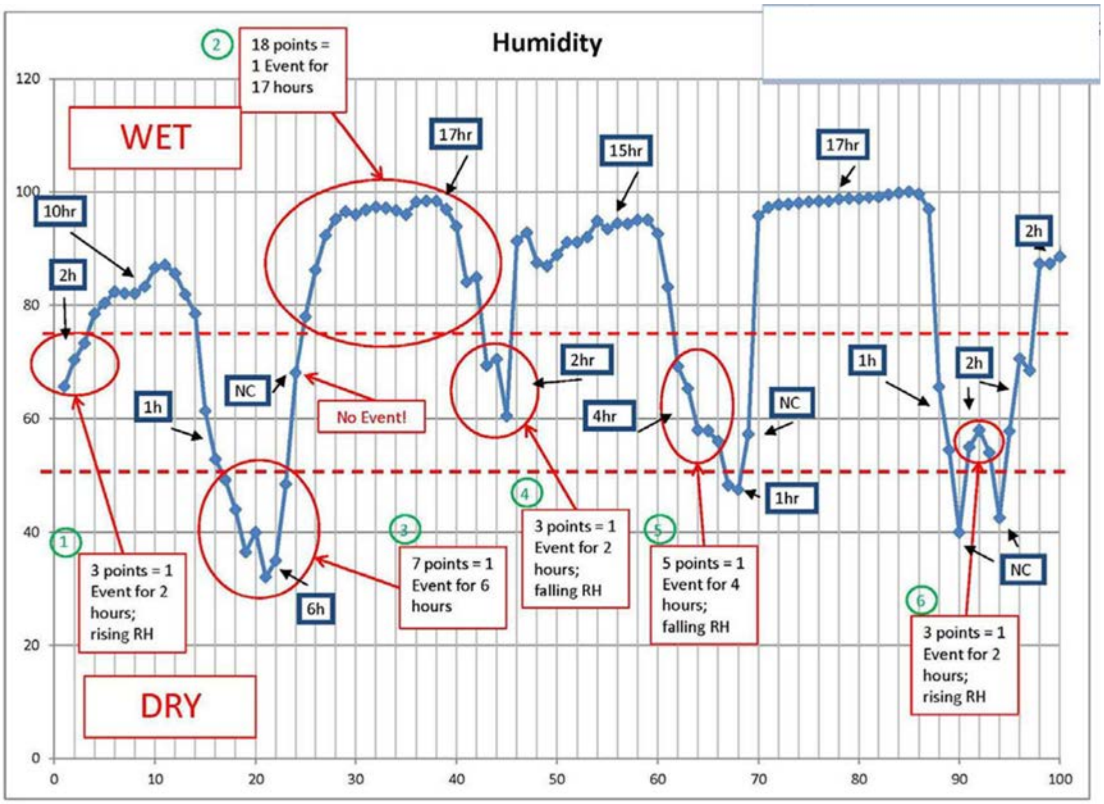

Figure 154. Span of RH data showing how representative RH bins were selected. Events must be greater than 1 hour to be counted as an event. Note that this analysis method does not capture all data points.

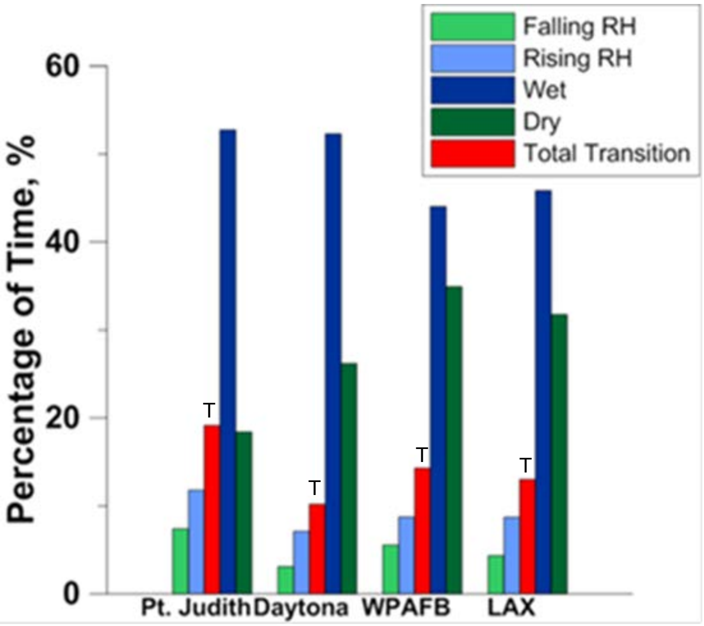

Figure 155. Time spent within each RH range normalized to the total exposure time. Data is presented for the four outdoor environments from this effort.

At first glance, it is obvious that both Pt. Judith and Daytona Beach have the highest percentage of time under high RH conditions. Exposures in these two environments have been the most aggressive after 3 years of test (Figure 123 - Figure 125). Al/IDE sensor data also indicates that these two environments are most aggressive. The higher cumulative time of wetness observed for the Pt. Judith compared with the Daytona Beach exposure is associated with the increased percentages of time in the within the intermediate RH range for Pt. Judith (total transition - red bar marked with "**T**" in Figure 155). While Daytona Beach and Pt. Judith have similar percentage of time at RH values above 76%, sample assemblies exposed at Daytona Beach spend much more time at very low RH values. As noted in the adhesion studies, coating delamination is more prevalent in environments with extended times at high RH and minimum time below 50% RH. Thus, it is expected that the relative damage observed at Pt. Judith compared with the samples at Daytona Beach would be greater. This is not the case in that both exposures result in coating delamination from the fastener heads after 3 years. There is a small amount of coating delamination around one scribe in the Pt. Judith exposure near a stainless steel fastener. However, in considering a one year exposure period, coating delamination was observed at Pt. Judith but not at Daytona Beach, which is consistent with the relative time spent in the middle RH ranges.

A major difference in corrosion damage between Pt. Judith and Daytona Beach is the corrosion observed in the fastener holes. The Pt. Judith samples were so corroded after three years that they could not be separated. Thus, it is expected that even more extensive IGC fissures are observed compared with the one year data. No such damage is observed at Daytona Beach. This suggests that factors governing exfoliation and IGC near a fastener are different. As discussed earlier, exfoliation and IGC are observed under conditions of low pH and cyclic RH. Further, based on results from cycle B, it is likely that extended times at RH values between DRH and 50% RH with minimal drying enhance exfoliation and IGC. This is consistent with conditions at Pt. Judith compared with those at Daytona Beach.

A comparison of the percent time of wetness in each of the three RH ranges for a number of environments is tabulated in Table 11 for comparison with the outdoor data. Exposures that resulted in delamination of coatings include Pt. Judith within 12 months, Daytona Beach within 36 months, ASTM G85-A5,GM9540P, Adhesion Test Cycles A – C and UVA Trial 1. Items in green represent environments where delamination is mild, while environments in red indicate extensive coating delamination. While cycle frequency is important, the Adhesion Cycle C only has 2 cycles per day yet significant delamination was observed; particularly when comparing with ASTM G85-A5. The time below 50% RH in cycle C is sufficient to cause coating delamination despite the limited cycle frequency.

In ASTM G85-A5 and UVA Trial 1, the amount of time above 76% RH is much lower than observed at Pt. Judith yet coating delamination is observed. There are several reasons for this. For the ASTM G85-A5 exposure, a steady state salt film builds on the samples. The salt loading is more than is found in external environments. During the spray period, the concentration is kept low and controlled by the spray composition. As discussed earlier, while the exposure enters a low RH state, corrosion rate transients exist and the overall corrosion rate is accelerated at RH below 50% because of the short drying time (although the rate is still lower than observed in ASTM B117). The transients are at least partly a function of increasing concentration during drying. Similar affects are also at play for the UVA Trial 1 exposure. In both exposure environments, the drying time is one hour or less. It should be noted that corrosion transients are on the order of 30 minutes to one hour. Secondly, as is the case for Adhesion Cycle B (see discussion below), there is a significant amount of time at the intermediate RH range. Lastly, during the spray cycle for UVA Trial 1, concentration of the solution is very high (compared with that of ASTM G85-A5) allowing corrosion to occur at an accelerated pace.

ASTM G85-A5 and Adhesion Cycle A have the lowest amount of coating delamination occurring (for the most aggressive delamination environments) with ASTM G85-A5 having the least. Note that the Adhesion Cycle A test has very high percentage of time above 76% RH suggesting that corrosion attack can occur. As with the ASTM G85-A5 test, the drying time is only one hour suggesting that high corrosion rates can occur during that portion of the exposure as a result of corrosion transients yet delamination is slow. It may be concluded, then that time in the intermediate RH region will act to significantly enhance delamination. Part of the reason for the lower delamination rates after exposure to ASTM G85-A5 is that there is an incubation period prior to delamination. This is because it has a lower time above 76% RH. For longer times above this value, inhibitors are leached from the coating system at a higher rate resulting in exhaustion of the inhibitor leading to enhanced delamination.

A potentially confounding result is that the Adhesion Cycle B cause very severe coating delamination and exfoliation. Additionally, differences in coating system performance are very hard to detect. Yet for this environment, there is no time spent below 50% RH. The exact reason for this observation is not clear since for ASTM B117 and ASTM G85-A1 (nor shown here), there is no adhesion loss. ASTM G85-A1 is a continuous acidic fog. Therefore, the adhesion observed in Adhesion Cycle B cannot be accounted for by pH effects. One explanation may be that while complete drying is not observed, some drying does occur promoting delamination yet the corrosion rate remains high throughout the entire exposure resulting in severe attack. As noted earlier, this environment causes exfoliation attack. It may be that as exfoliation occurs the mechanical force of the grain-lifting damages both coatings equally, resulting in the inability to distinguish performance. In other words, damage is not dependent on the coating system.

Table 11. Percentage of Time in Each RH Range for a Number of Exposure Environments.

	RH > DRH	50% < RH < DRH	RH < 50%	Comment
Point Judith* (3 years)	53	29	18	Sea salt exposure, saturated
Daytona* (3 years)	52	23	25	Sea salt exposure, saturated
WPAFB* (3 years)	45	20	35	Very low chloride
LAX (3 years)	46	21	33	Low chloride, industrial
ASTM G85-A5* (2000 hrs)	39.5	26.7	34	Dilute NaCl fog, 12 cycles/day
GM9540P (2000 hrs)	56.3	18.3	25.4	High NaCl brief spray, 1 cycle/day, diluting fog
ASTM B117 (2000 hrs)	100	0	0	High NaCl, no cycles
Adhesion Testing (Cycle 1) (1400 hrs)	66	0	34	High NaCl, low pH dip applied 1/week, 8 cycles/day, high temp, RH controlled
Adhesion Testing (Cycle 2) 1400 hrs)	66	34	0	High NaCl, low pH dip applied 1/week, 8 cycles/day, high temp, RH controlled
Adhesion Testing (Cycle 3) (1400 hrs)	66	0	34	High NaCl, low pH dip applied 1/week, 2 cycles/day, high temp, RH controlled, long cycles
UVA Trial 1 (1000 hrs)	33	34	33	High NaCl fog, low pH, 16 cycles/day, high temp

Another potentially confounding finding exists for the GM9540P chamber. In this environment, the RH is above 76% for 54% of the time and it is above 50% for 74% of the time. Yet minimal delamination is observed. Close examination of Figure 35 reveals that during the DI fog cycle, corrosion rate is observed result to decrease because of dilution effects. Thus, while the surface remains wet enough, the dilution of the electrolyte film results in a reduction of the corrosion rate, thus slowing delamination.

Outdoor exposure data at Pt. Judith is consistent with lab cycles. Pt. Judith has a minimum drying time with significant time in the intermediate RH range leading to coating delamination. As with the GM9540P cycle and as noted when comparing outdoor and accelerated laboratory chemistry, there is a relatively low loading of corrosive species. Thus while the RH factors governing corrosion and coating delamination are favorable for corrosion, the dilute surface film results in slowed delamination. Interestingly, severe IGC fissuring is still observed. This is likely the result of trapped corrosion species in the occluded regions of the sample increasing localized corrosion.

There is one other item to note regarding the cycling frequency and stress corrosion cracking testing. The most rapid humidity cycling was performed with one hour wet/one hour dry and two hours wet/two hours dry. In both cases, accelerated cracking was observed within the time frame of the drying step. As noted in Chapter 6 (Figure 111), crack growth rate is observed to increase at two RH values with the greatest increase occurring during the drying cycle. The RH values of these rate increases are consistent with values where increases in anodic kinetics are observed, suggesting a link between corrosion reactions and the onset/sustainment of cracking. For experiments where cycling is much quicker (compare Figure 111 with Figure 109), crack growth rates are increased by a factor of 2 to 3. As with corrosion rates, it appears that stress corrosion cracking rates also increase with decreasing drying times. These makes sense if crack growth rate is linked with active corrosion rates.

Several considerations for the accelerated test are obtained from the analysis of RH:

1) Severity of attack is not simply a function of percentage of time in each RH range but also the absolute amount of time in each range in each cycle.
2) RH should be above 76% for 50% of a given cycle, regardless of its duration.
3) Corrosion is highest in cases where the percent of time above 76% RH + the percent of time of 50% < RH < 76% is greater than 65%.
4) The degree of coating delamination, exfoliation and cracking can be controlled by the amount of time in the intermediate RH range.
5) The percentage of time below 50% RH can be controlled to reduce the overall corrosion rate but only if the drying interval per cycle is greater than 3 hours (this is a conservative estimate). Reducing drying time per cycle to one hour or less will result in an increase in corrosion rate over simply holding the RH above 76%.
6) Salt loading plays a critical role in the amount of degradation. Lower loads or dilution affects reduce the amount of delamination.

9.1.2 *Atmospheric chemistry*

Atmospheric chemistry is a major factor in governing corrosion rates. Salt speciation will determine the value of DRH. For coastal environments, DRH is governed by NaCl since it has the highest content in sea salt. Inland, sulfate species may dominate the DRH although the values are close. Reaction products will reduce the DRH, but these values are consistent with values of efflorescence and thus have little effect on the time of wetness.

Salt composition will have an effect on specific corrosion rates. Likewise, salt loading density will directly affect electrolyte formation geometry and overall material coverage. Both factors directly affect corrosion rate. Based on work in this effort (Section 8.2.1.3.7), it was observed that the composition of salts that are found on sample assemblies (both in laboratory environments and outdoors) mimic the exposure conditions. In other words, in coastal environments, deposit composition closely resembles that of seawater while in accelerated lab tests, the composition closely resembles that of the spray solution. Nevertheless, slight differences in composition are observed. For example, samples exposed at Pt. Judith and Daytona Beach have slightly reduced amounts of chloride, sulfate and nitrate indicating their reactiveness to the exposed surfaces. Thus, these ionic constituents are important in the corrosion reactions observed. Also, based on charge imbalances observed and knowledge that atmospheric acid gasses interact directly with sea salt aerosols, pH is considered an important factor in controlling corrosion rate. pH in sea salt aerosols is typically on the order of pH = 3 while in industrial areas it can be between pH = 4 and 5.

Despite the extreme variability in the measured amount of species from surface to surface, it can been seen that after three weeks of exposure to laboratory environments (Figure 145), the maximum amount of salt loading is fairly similar for ASTM B117, ASTM G85-A5 and ASTM G85-A4. In contrast, loading levels for the GM9540P test are nearly a factor of 10 or more lower. This latter effect is a result of the dilution of the salts during the 8 hour DI fog. The chemical dilution is consistent with the observed reduction in corrosion rate (see Figure 35).

Measurements were also made on samples exposed to external environments for a period of one year (Figure 145). It was observed that Pt. Judith had the highest salt content by a factor of four over LAX and a factor of 70 over Daytona Beach. Salt loads are about three orders of magnitude higher than those observed at WPAFB. Examination of in-situ corrosion rate data (Figure 115) and short term mass loss data (Figure 116) reveal that the highest rates were observed at Pt. Judith, which is consistent with visual observations. Further examination of sensor data reveals that the increase in cumulative corrosion coincides with increases in time of wetness (Figure 117) and conductance (Figure 118). Conductance data relates directly to the salt loading observed, revealing that the chemical environment at Pt. Judith is more aggressive than the other ambient locations.

Of particular interest is that the salt load loads for LAX are high yet the damage observed after long term exposure is mild. Examination of the data reveals, however, that the cumulative time of wetness is relatively low at LAX (Figure 117). Thus despite the relatively high salt loading, the conductance remains low (Figure 118). Since conductance is directly relatable to corrosion rate, it is no surprise that the observed corrosion at LAX is low.

The relationship between conductance and cumulative corrosion is further verified by examining sensor data taken during the Adhesion Cycles 1 – 3 (Figure 119). Comparison with ambient environments reveals an increase in corrosion rate by a factor of 4 to 20 for AA7075. This increase in rate is of the same order of magnitude observed in the conductance data (comparison of Figure 120 with Figure 118). Additionally, comparison of the measured values of lateral surface damage between the ambient sites after one year to that of ASTM B117 (Figure 134) reveals that 3 months of exposure to ASTM B117 is nearly equivalent to the damage observed after 12 months in ambient exposures. This results in an acceleration factor of four which is consistent with other accelerated laboratory tests. It should be noted that, consistent with visual observations, the lateral surface area parameter is greatest for the Pt. Judith location even after one year exposure. Finally, the lateral surface area damage measured after the ASTM G85-A5 exposure results in an acceleration factor of nine.

9.2 Accelerated Test Protocol

This section presents the SERDP accelerated test protocol developed based on the findings described in the previous chapters and summarized above. The test protocol provides detailed information regarding the testing apparatus, sample preparation, solution preparation, testing procedure, as well as post-test inspections and reporting. The test protocol was written in the format of the standard ASTM tests.

SERDP Accelerated Test Protocol

1. Scope

1.1. This practice describes conditions and methodology for performing cyclic salt spray testing with monitored Relative Humidity (RH) for specification purposes.

1.2. This practice prescribes a test cycle and a test specimen to be used. It does not prescribe the exposure periods to be used, nor the interpretation to be given to the results.

1.3. *This standard does not claim to address all of the safety concerns, if any, associated with its use. It is the responsibility of the user of this standard to consult and establish appropriate safety and health practices and determine the applicability of regulatory limitations prior to use.*

2. Significance and Use

2.1. This practice is applicable to ferrous and nonferrous metals; as well as organic and inorganic coatings. The practice described herein is useful when a more realistic environment than the salt fog described in Specification ASTM B 117 is desired.

3. Apparatus

3.1. *Cabinet*:

3.1.1. The apparatus required for salt spray (fog) testing consists of a fog chamber, a salt solution reservoir, a supply of suitably conditioned compressed air, one or more atomizing nozzles, specimen supports, provision for heating the chamber, and necessary means of control. The size and detailed construction of the cabinet are optional, provided the conditions obtained meet the requirements of this practice. The material of construction shall be such that it will not affect the corrosiveness of the fog. Suitable apparatus that may be used to obtain these conditions is described in Appendix A1 of Specification ASTM B 117 with necessary modifications described herein.

3.1.2. The cabinet shall be designed so that drops of solution that accumulate on the ceiling or cover of the chamber do not fall on the specimens being testedDdrops of solution that fall from the specimens shall not be returned to the solution reservoir for respraying.

3.1.3. The cabinet shall be equipped with one or more timing devices to provide for intermittent spraying.

3.2. *Air Supply*:

3.2.1. The compressed air supply to the nozzle or nozzles for atomizing the salt solution shall be free of oil and dirt[1] and maintain the air supply between 69 and 172 kPa (10 and 25 psi).

3.2.2. Temperature in the saturator tower (bubble tower) shall be set to 47^o C.

3.3. *Conditions in Salt-Spray Chamber*:

3.3.1. *Temperature*—The temperature in the exposure zone shall be set to 40^o C +/- 3^{o}C. Tolerance represents an operational control point for equilibrium conditions at a single location in the cabinet which may not necessarily represent the uniformity of conditions throughout the cabinet. The temperature shall be recorded continuously throughout the test[2].

---

[1] Note that the air supply may be cleaned of oil and dirt by passing it through a water scrubber or at least 2 ft (610 mm) of activated alumina.

[2] Note that the recorded temperature must be obtained with the salt spray chamber closed to avoid a false low reading.

3.3.2. *Atomization and Quantity of Fog*—At least two clean fog collectors shall be placed within the exposure zone so that no drops of solution from the test specimens or any other source can be collected. The collectors shall be positioned in the proximity of the test specimens, one nearest to any nozzle and the other farthest from all nozzles. For each 80 cm^2 of horizontal collecting area, the collection rate for the fog accumulation in each collector shall be from 1.0 to 2.0 mL of solution per hour based on an average run of at least 16 h continuous spray[3].

3.3.3. The nozzle or nozzles shall be directed or baffled so that none of the spray impinges directly on the test specimens.

4. Test Specimens

4.1. The type and number of test specimens to be used, as well as the criteria for the evaluation of the test results shall be defined in the specifications of the material or product being tested or upon mutual agreement between the purchaser and the seller. However, the test specimen shown in Figure 156 is recommended. This specimen provides multiple locations for differing failure modes to occur including galvanic corrosion, crevice corrosion and corrosion at a coating defect.

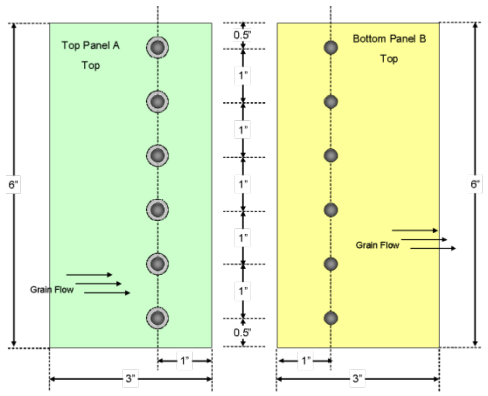

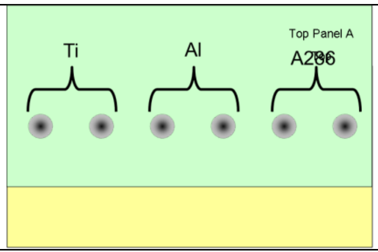

Figure 156. Lap joint configuration recommended for this practice. High Lock fasteners are recommended for aerospace applications and should be dry installed. An "x" scribe should be placed through the center of the fasteners that extends 0.25" from the scribe edge (edge of fastener) on each side.

4.2. *Preparation of Test Specimens*:

4.2.1. The test specimens shall be cleaned according to applicable specification(s) for the material(s) being tested, or as agreed upon between the test lab and the customer.

4.2.2. Specimens for evaluation of paints and other organic coatings shall be prepared in accordance with applicable specification(s) for the material(s) being tested, or as agreed upon between the test lab and the customer.

4.2.3. Test panels shall be scribed across each fastener such that 0.25" of scribe protrudes from the edge of the fastener. Scribes should be cut after installation of the countersunk fasteners.

Any continuous temperature device or thermometer which can be read from the outside can be used.

[3] Glass funnels with the stems inserted through stoppers into graduated cylinders or crystallizing dishes can be used. Funnels and dishes with diameters of 100 mm have an area of about $80cm^2$.

4.2.4. The cut edges of the sample assemblies and areas that contain identification marks or that are in contact with the racks or supports shall be protected with electro-plater's tape.

5. **Salt Solutions**

5.1. The salt solution shall be prepared in accordance with one of the two modified sea salt solutions shown in Table 12. Make-up water shall be deionized water conforming to Type IV water in Specification ASTM D 1193. All chemicals shall be reagent grade.

Table 12. Salt Solution Compositions.

Test Solution #1 – Modified Sea Salt Solution with Nitrate Ions	
NaCl	46.81 g/L
$MgCl_2.6H_2O$	23.31 g/L
Na_2SO_4	8.40 g/L
$NaNO_3$	6.86 g/L
HCl (1N)	(1 mL)
Test Solution #2 – Modified Sea Salt Solution without Nitrate Ions	
NaCl	51.53 g/L
$MgCl_2.6H_2O$	23.31 g/L
Na_2SO_4	8.40 g/L
HCl (1N)	(1 mL)

5.2. The pH of the salt solution shall be pH = 3 and shall be measured daily to ensure it is maintained at that value.

6. **Procedure**

6.1. Position of Specimens During Test:

6.1.1. Unless otherwise specified, the specimen shall be supported at 15° from the vertical, and preferably parallel to the principal direction of horizontal flow of fog through the chamber, based upon the dominant surface being tested.

6.1.2. Contact of the specimens between each other, between any metallic material or between any material capable of acting as a wick shall not be permitted.

6.1.3. Each specimen shall be placed so as to permit free settling of fog on all specimens. A minimum spacing between specimens of 30 mm is recommended.

6.1.4. Dripping of the salt solution from one specimen on any other specimen shall not be permitted.

6.1.5. It is recommended that placement of replicate specimens be randomized to avoid possible bias caused by difference in spray patterns. Individual specimens may also be rotated daily for the same reason.

6.1.6. Suitable materials for the construction or coating of racks and supports are glass, rubber, plastic, or suitably coated wood. Do not use bare metal. Support specimens preferably from the bottom or the side. Slotted wooden, laminated plastic, or inert plastic strips are suitable for the support of flat panels.

6.2. Exposure Cycle

6.2.1. The cycle test consists of a 1-hour high humidity wet period and a 1-hour dry-off period. During the wet period, the test solution will be fogged into the chamber for 15 minutes followed by 45 minutes under high RH wet bottom conditions.

6.2.2. The relative humidity during the wet cycle must be above 80% RH for at least 50 minutes.

    - 6.2.3. In the dry-off portion of the cycle, the relative humidity must fall to at least 40% RH for at least 35 minutes
    - 6.2.4. Ramp rates must be set such that 80% RH is reached within 10 minutes after the dry-off phase is completed. Ramp rates must be set such that the relative humidity falls from 80% RH to 40% RH in 25 minutes (but not shorter).
  - 6.3. *Continuity of Test*:
    - 6.3.1. Unless otherwise specified, in the specifications covering the material or product being tested, the test shall be continuous for the duration of the entire test period. Continuous operation implies that the chamber be closed except for the short daily interruptions necessary to inspect, rearrange, or remove test specimens, and to check and replenish the solution in the reservoir. Operations shall be so scheduled that the maximum time for these interrupting is held to 60 min or less per day. It is recommended to have only one interruption per day if possible.
  - 6.4. *Period of Test*:
    - 6.4.1. The period of test shall be designated in accordance with the specifications covering the material or product being tested or as mutually agreed upon between the purchaser and the seller. An exposure period of multiples of 1000 hours is suggested.
  - 6.5. *Cleaning of Tested Specimens*:
    - 6.5.1. Unless otherwise specified in the specifications covering the material or product being tested, at the end of the test, specimens may be gently washed or dipped in clean running water no warmer than 38°C (100°F) to remove salt deposits from their surface, and then immediately dried. Dry with a stream of clean, compressed air.

7. Evaluation of Results
  - 7.1. A careful and immediate examination shall be made for the extent of corrosion of the dry test specimens or for other failure as required by the specifications covering the material or product being tested or by agreement between the testing lab and the client.
  - 7.2. For the recommended test specimen, the following evaluations shall be made:
    - 7.2.1. Corrosion in the scribes, scribe creep back, coating appearance and extent of corrosion within the lap joint.
    - 7.2.2. As optional analyses, quantitative image analysis of the corrosion damage is recommended. Additionally, metallographic cross sections of the faster hole region can be made.

8. Report
  - 8.1. The following information shall be recorded, unless otherwise prescribed in the specifications covering the material or product being tested:
    - 8.1.1. Continuous readings of temperature and relative humidity within the exposure zone of the chamber,
    - 8.1.2. Data obtained from each fog-collecting device for volume of salt solution collected in milliliters per hour of operation per 80 cm^2 of horizontal collection area. Data should be collect for 16 hours prior to exposure of the samples.
    - 8.1.3. Records of data obtained from fog-collecting devices for pH of collected solution. Sample to be measured may be a composite sample from multiple fog-collecting devices (within one test chamber), if necessary to obtain sufficient solution volume for the measurement.
    - 8.1.4. Type of specimen and its dimensions, or number or description of part, method of cleaning specimens before and after testing,

8.1.5. Exposure period,
8.1.6. Interruptions in test, cause and length of time, and
8.1.7. Results of all inspections.

9.3 Results of Accelerated Test Protocol

9.3.1 *Materials and methods*

Based on the combined analysis from corrosion damage, chemistry experienced during outdoor exposure, and basic scientific studies performed by the SERDP team, the final year of the project focused on the development of a next-generation accelerated corrosion test methodology that can be used to assess novel corrosion prevention technologies and quantify the performance of material systems. To support this effort, Boeing and NAVAIR each performed slightly different modified test cycles using sets of lap coupon assemblies that were fabricated at NAVAIR in Patuxent River, MD. Figure 157 shows panel movement throughout the test. As indicated in the figure, Boeing was shipped seven sets of lap coupons consisting of assembly types A-G (8 assemblies per set for a total of 56 lap coupons). A second set of duplicate panels was exposed at NAVAIR. All Boeing coupons were tested in a Q-fog Controlled Relative Humidity (CRH) cyclic corrosion test chamber while NAVAIR samples were testing in an AutoTechnology Cyclic Corrosion chamber.

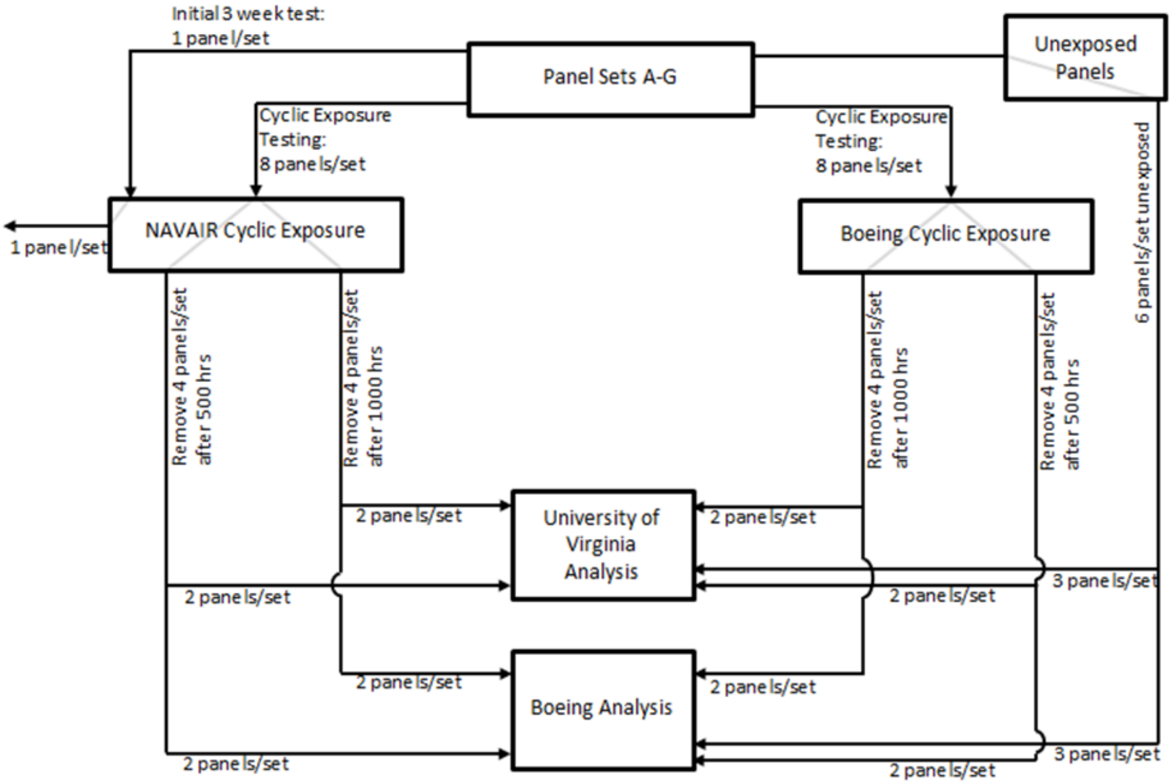

Figure 157. Panel movement throughout the test.

A detailed test protocol was provided from UVA which included instructions for coupon handling, electrolyte chemistry to use during testing, and shipping information for post exposure. The electrolyte formulation was developed by Bill Keene and John Maben at UVA. The electrolyte is a modification of ASTM artificial seawater, with small amounts of hydrochloric acid added to make the solution acidic (target pH = 3). The composition of the electrolyte solution is typical of ambient marine aerosols over the western North Atlantic Ocean, with ionic strength about twice that of ambient seawater (1M). The solution compositions are detailed in Table 13 for both Boeing and NAVAIR. NE#1 solution contained no nitrate (Boeing testing) while NE#2 contained nitrate. The tests were designed to determine if nitrate had an effect on the observed corrosion rate. There were concerns about potential contamination of the chamber's reservoir that could influence solution pH. Therefore the pH of the electrolyte was measured both before and after adding the solution to the reservoir, verifying that the pH remained at 3 throughout testing.

Table 13. Exposure Environments for NE#1 and NE#2.

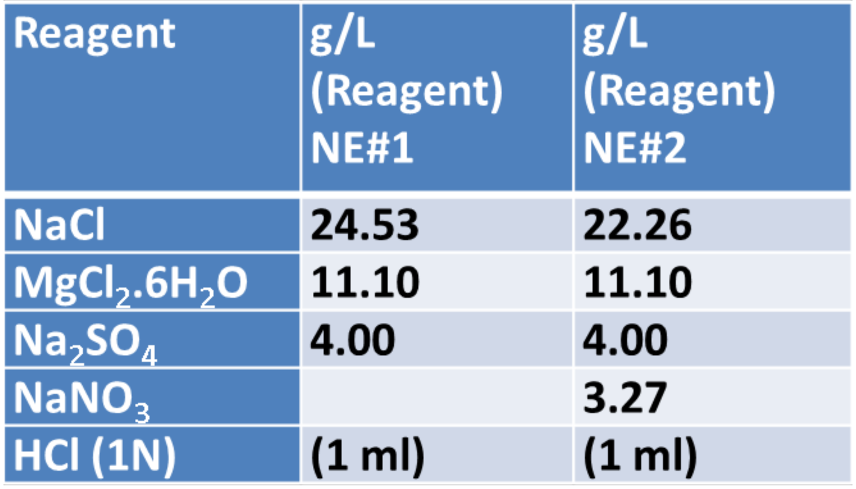

Reagent	g/L (Reagent) NE#1	g/L (Reagent) NE#2
NaCl	24.53	22.26
$MgCl_2.6H_2O$	11.10	11.10
Na_2SO_4	4.00	4.00
$NaNO_3$		3.27
HCl (1N)	(1 ml)	(1 ml)

Note that the AutoTechnology chamber could not specifically control RH values. Time under conditions of RH < DRH and below 50% were designed based on knowledge from previous exposure at other team member locations. For the Q-Panel CRH chamber, specific values of RH and ramp times were programmed. For the CRH chamber (NE#1 environment), an asymmetric cycle was programmed into the CRH consisting of a 15-minute fog to reach high humidity and a 25-minute ramp down from 80% to 40% RH. The temperature was held at 40°C for the entire test. Figure 158 shows the temperature and RH profiles of the test cycle. For the AutoTechnology chamber (NE#2 environment), a 15 minute fog was followed by a high RH wet bottom humidity hold for 45 minutes. This wet cycle was followed by a 1 hour dry period.

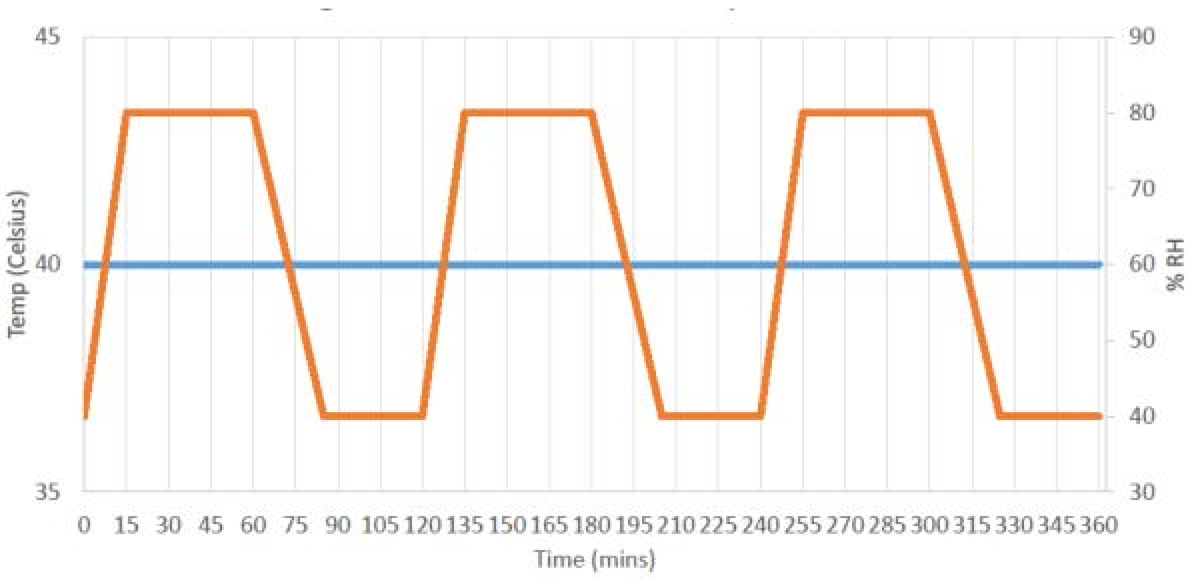

Figure 158. Asymmetric test cycle used in accelerated test.

Unfortunately, operators at both test sites deviated from planned exposure protocols.

- At Boeing, sample assemblies were removed from mounting panels prior to exposure and remounted following exposure. The protocol specified that samples be exposed while mounted on the panels.
- At Boeing, samples were exposed to a test solution with the correct ratios of constituents but at an ionic strength of 0.48 M Na^+ (or about the same as that of seawater) rather than 1.0 M Na^+ as specified in the protocol.
- At NAVAIR, fog was sprayed for 30 minutes during each cycle (rather than 15 minutes as specified in the protocol).
- The corresponding RHs within chambers differed substantially over wet-dry cycles at the two sites.

In addition, the chamber used at NAVAIR produced fog by bubbling air through the test solution whereas the chamber used at Boeing produced fog by atomizing the test solution. Available evidence suggests that, relative to atomization, bursting bubbles produce a distribution of smaller droplets with lower deposition velocities. Although not quantified at either test site, we infer that, for a given liquid water content of fog in chamber air, deposition rates of fog to sample surfaces within the chamber at NAVAIR were lower (and probably much lower) than those at Boeing.

Because exposure protocols followed at the two sites differed in several important respects, results cannot be interpreted unambiguously to test the hypothesized influence of NO_3^- in corrosion processes.

After recovery, samples were stored frozen at the exposure site, shipped frozen, and, upon receipt, stored frozen in the laboratory prior to extraction and analysis. Each location extracted was analyzed for surface loadings of a suite of 13 ionic species including: $HCOO^-$, CH_3COO^-, $(COO)_2^{-2}$, $CH_3SO_3^-$, SO_4^{2-}, Cl^-, Br^-, NO_3^-, NH_4^+, Na^+, K^+, Mg^{2+}, and Ca^{2+}.

All sample assemblies were photographed prior to extraction. Samples were disassembled while wearing clean gloves and without touching surfaces to be extracted. However, for some heavily corroded samples, extreme measures were required to remove fasteners to separate plates. Pre-cleaned tools used for this purpose included: Clamps, impact wrench, bolt cutter, manual arbor press, hammer, and chisel. Because of the associated handling, some surfaces may have been altered during the disassembly process. Following extraction, samples and blanks were archived for possible future use.

Finally, large salt crystals visible on the outer surfaces of samples from the second pull (1000-hour exposure) at Boeing clearly indicated surface loadings that were far greater than those from the first pull at Boeing (or from either pull at NAVAIR). To provide context, samples the first pull at Boeing were far more heavily loaded than any other samples analyzed as part of this project. In addition, many loose individual crystals were also observed on the mounting panels (which, as indicated above, were not deployed in the test chamber) and in the bottoms of the shipping boxes from the second pull at Boeing. It was evident that significant but variable amounts of loadings on exposed sample surfaces had fallen off during shipping. Due to these unquantifiable losses coupled with the difficulty of extracting and analyzing such heavy loadings, the second pull from Boeing was not analyzed as the resulting data would be largely uninterpretable.

9.3.2 *Results and discussion*

9.3.2.1 Characterization of CRH chamber response

Prior to beginning the test, various cyclic profiles were programmed in the Q-fog CRH, and the chamber response was characterized with Luna's LS2A Environmental Monitoring Sensor Suite. The asymmetric cycle shown in Figure 158 was run in the Q-fog CRH for about 10 days, and poor performance was observed in the drying portion of the cycle. Figure 159 shows the relative humidity as a function of time measured with the LS2A. The chamber was able to reach a very high RH (~90-100%) during the 15-min fog, and then held at 80% RH for 45 minutes, as programmed. But the chamber could not dry below ~60% RH and struggled to maintain the low humidity. It was considered that the data could be representative of issues with the Q-fog internal RH sensor, issues with the LS2A humidity sensor, or both.

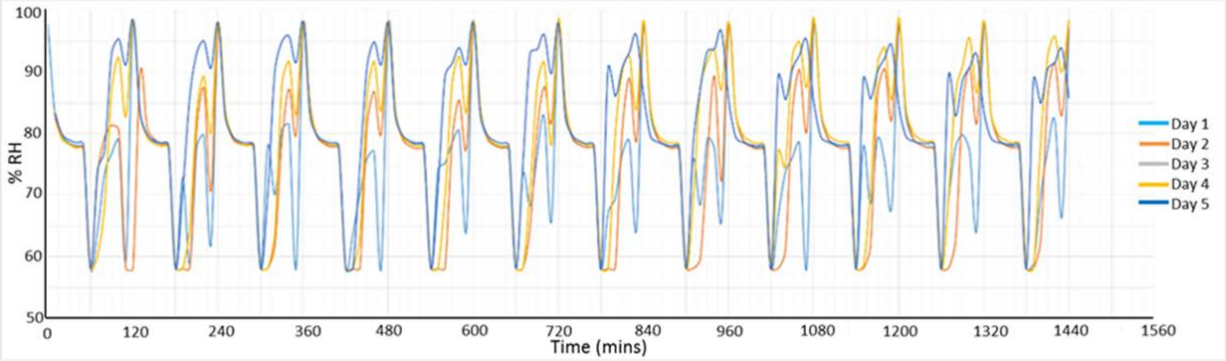

Figure 159. RH profile measured with LS2A during the initial characterization run.

In response to the initial characterization run, some problems were corrected with the CRH chamber and sensors, and the CRH was re-programmed for a second characterization run using the same asymmetric test cycle. Humidity data from the LS2A sensor node was validated with a third, independent RH sensor (Omega wireless probe). Figure 4 shows a graph of RH vs. time for the second characterization run, in which both the LS2A and Omega wireless probe were used to monitor chamber humidity levels. Interestingly, both the LS2A and Omega sensors showed that the RH during the drying cycle actually goes much lower 40%, down to ~20-30%. This could be happening because the built-in RH probe in the Q-fog is situated in the bubble tower, and there is a discrepancy between the RH level in the bubble tower and that in the exposure area of the chamber. However, this has not been a barrier to successfully running the modified test cycle.

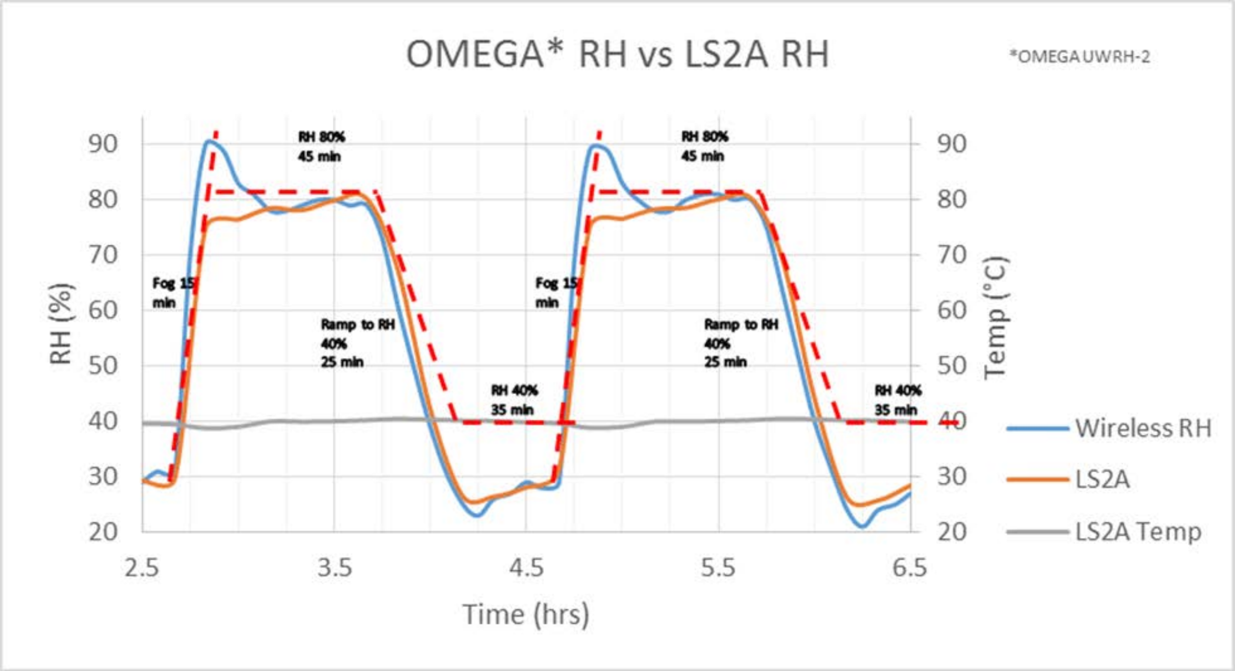

Figure 160. Temperature and RH profiles measured with LS2A and an Omega probe during the second characterization run in a Q-Panel CRH accelerated corrosion chamber.

The following is a summary of the modified test cycle, which was programmed in a Q-fog CRH chamber:

1. The first step of the cycle is a 15-minute fog. During this time, the RH rises sharply to ~90%.
2. The next step of the cycle is to hold the chamber at 80% RH for 45 minutes.
3. The chamber then begins a 25-minute ramp down to 40% RH and holds dry for another 35 minutes (1 hour total). At this ramp rate, it takes ~20 minutes to drop below 50% (similar to results obtained with wet-bottom chambers at UVA and SwRI).
4. After 35 minutes at low RH, fogging begins, and the cycle repeats.

9.3.2.2 Characterization of AutoTechnology chamber response

Significant difficulties were encountered with the NAVAIR AutoTechnology cyclic corrosion chamber. Several modifications were made to the chamber, but it did not perform as expected based on other results. Note that rather than a 15 minute fog, NE#2 used a 30 minute fog in an attempt to keep RH > DRH. The RH and temperature profile are shown in Figure 161 over a 4 hour period in the NE#2 environment. It is clear from the figure that the humidity remains above 76% RH for only 30 minutes.

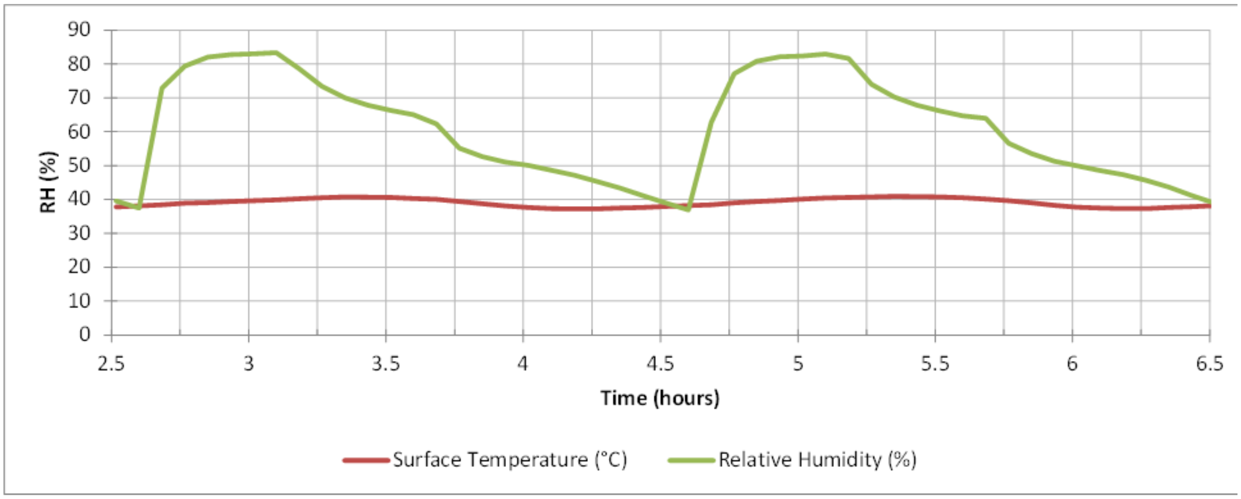

Figure 161. RH and temperature profile acquired using an LS2A sensor (Luna Innovations) over a 4 hour period of exposure to NE#2 in an AutoTechnologies accelerated exposure chamber.

The percentage of time in NE#1 and NE#2 are shown in Table 14. A number of important facts should be pointed out based on examination of the table. First, the amount of time spent with RH < DRH is relatively low compared to all test environments where severe corrosion and coating delamination is visible. This is especially true for NE#2. As noted previously, at least 50% of the exposure time must be above DRH. Further, coating delamination and corrosion increase with absolute time under conditions of RH > DRH. In environment NE#2, high RH conditions only lasted for 30 minutes compared to 50 – 60 minute exposures found in other cyclic test environments.

Table 14. Percentage of time the samples were exposed to the three RH regions for the new NE#1 and NE#2 exposures.

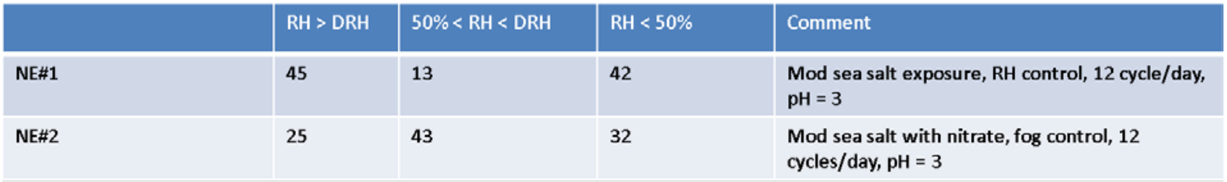

	RH > DRH	50% < RH < DRH	RH < 50%	Comment
NE#1	45	13	42	Mod sea salt exposure, RH control, 12 cycle/day, pH = 3
NE#2	25	43	32	Mod sea salt with nitrate, fog control, 12 cycles/day, pH = 3

Based on these observations, it is found that the RH profile NE#1 most closely resembles the environment experienced at LAX and Dayton (Table 11). Since the environment has much higher salt deposition than what is found in Dayton, it would be expected that exposure to NE#1 resemble results observed in LAX. NE#2 has the lowest percentage of time above DRH and thus would be expected to have very little corrosion despite the high salt loading.

As noted, the NE#1 profile mimics the percent of time of wet/dry cycles observed at LAX. Examination of panel G (non-chromate waterborne N2 primer) (Figure 162) after 1000 hours exposure to NE#1 reveals very little corrosion. Comparison with Figure 123 reveals very similar lap joint corrosion compared with damage observed in the LAX environment as expected based on the cycling data. Similarly, no coating degradation is observed around the fasteners in the accelerated and LAX environment. Corrosion was observed within the lap joint for the aluminum/steel couple and red rust was observed coming from the scribes around the fasteners. Comparison with Figure 124 for the steel/AA2039 panels reveals similar damage in the lap joint at LAX and 1000 hours of exposure to NE#1. These observations support the idea that we have accurately replicated field behavior at LAX. While we are working to develop a more aggressive environment, we have shown that we can control laboratory environments to mimic operational exposures.

Images from the NAVAIR environment are not included. Almost no corrosion was observed on any panels. This is primarily the result of the short duration exposure to RH > DRH and the very low percentage of exposure time to those conditions.

Figure 162. (left) Photographs of assembly type G after 1000 hrs of exposure to NE#1. (right) Photograph of assembly D after 1000 hours of exposure to NE#1.

It has been extensively shown that RH in different regions plays a critical role in replicating failure modes observed in operational environments. It should be pointed out that in both test chambers, the resulting environment was not expected, particularly for the AutoTechnology chamber. Throughout this effort, team members have needed to modify test chambers to control the environment to desired settings. Even then, exact duplication between laboratories was not possible. For example, the NAVAIR cyclic chamber could not maintain RH > DRH. The importance of RH control cannot be overstated. In many accelerated cyclic test chambers, there is no specific control over RH. It is strongly believed that to ensure lab-to-lab reproducibility and to ensure higher control over failure modes, RH must be specifically controlled and called out in the specification. Additionally, RH and temp must be reported as part of the qualification procedure.

9.3.2.3 Results of chemical analysis

Figure 163 through Figure 167 show mass loadings of major analytes (Na^+, Mg^{2+}, Cl^-, SO_4^{2-}, and NO_3^-) corresponding to individual extractions at different locations on surfaces of duplicate sample assemblies of each type (A through G) that had been exposed in parallel for 500 and 1000 hours at NAVAIR. Elements of the 4-component sample ID numbers are as follows:

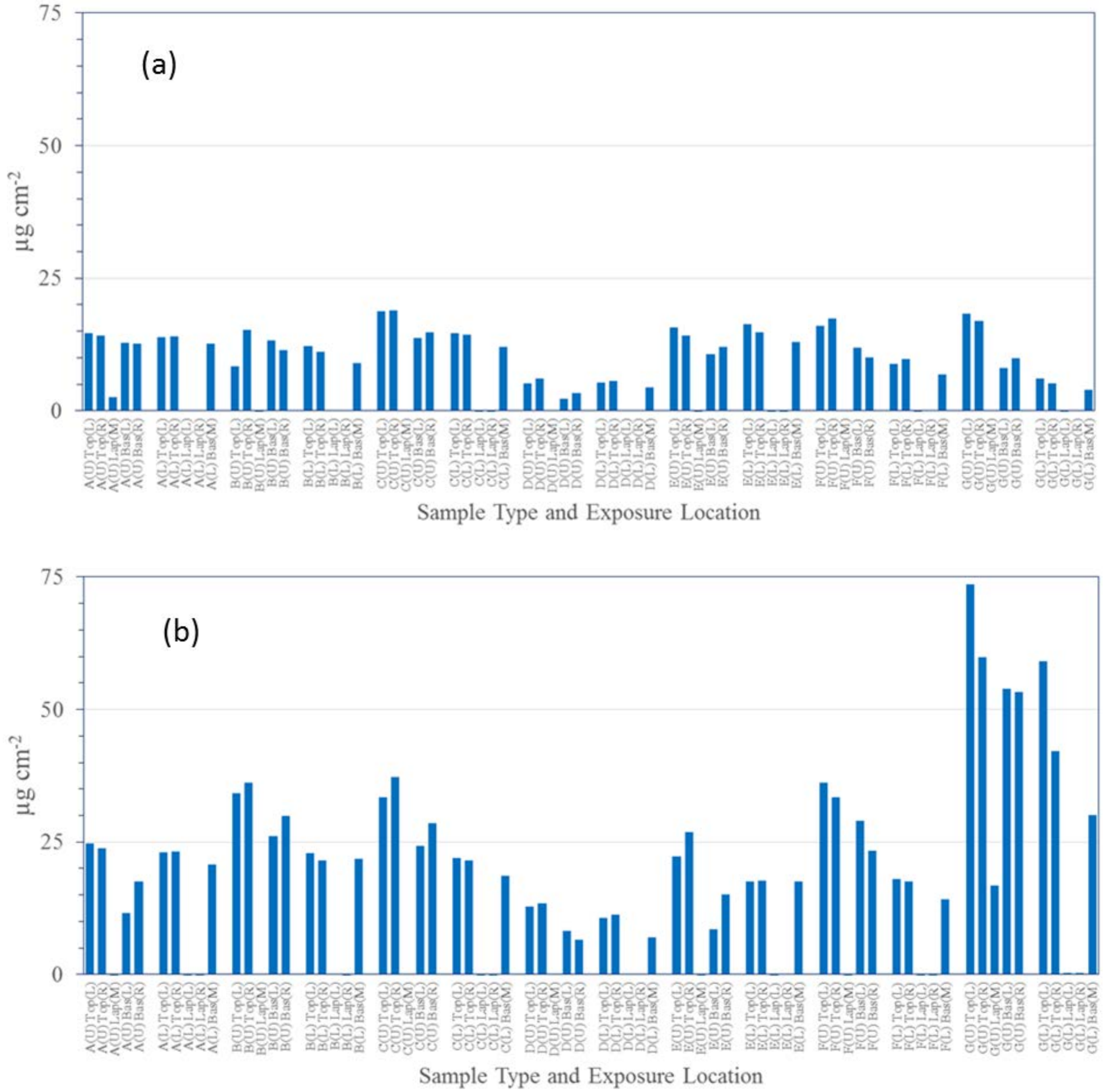

Figure 163. Na^+ loadings measured after (a) 500 hrs and (b) 1,000 hrs of exposure to the new accelerated test environment (NE#2) in the presence of nitrate ions.

(1) Sample assembly type (‘A’ through ‘G’).

(2) Location on mounting panel when shipped to exposure site (‘U’ for upper and ‘L’ for lower). Note that samples were erroneously removed from panels before exposure at Boeing.

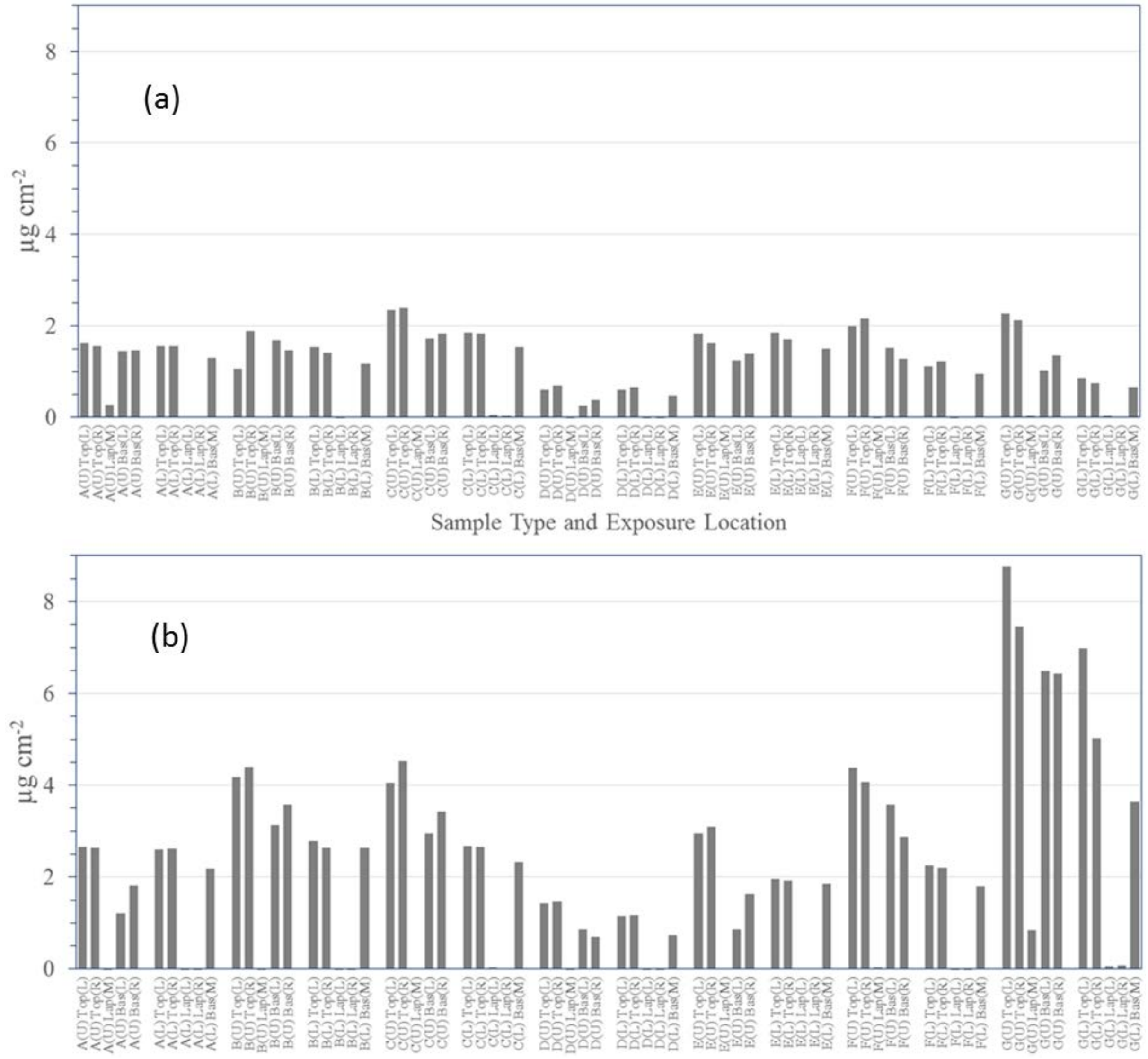

Figure 164. Mg^{2+} loadings measured after (a) 500 hrs and (b) 1,000 hrs of exposure to the new accelerated test environment (NE#2) in the presence of nitrate ions.

(3) Area of sample assembly extracted (‘Top’ refers to the exposed upper surface of the top plate, ‘Lap’ refers to the lapped upper surface of base plate, and ‘Bas’ refers to the exposed upper surface of the base plate).

(4) Relative location of extraction site on a given plate (‘L’ for left, ‘R’ for right, ‘M’ for middle).

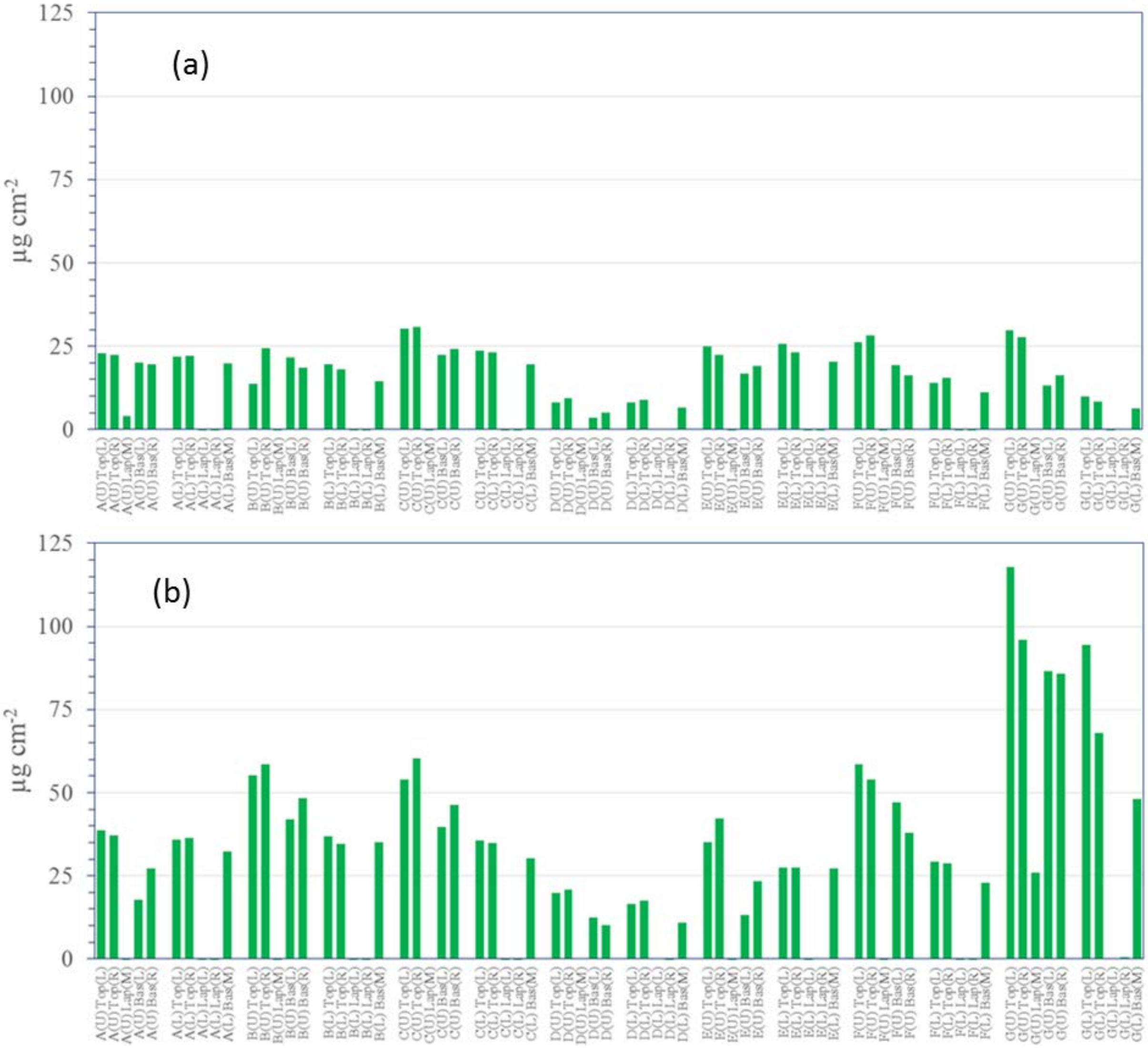

Figure 165. Cl$^-$ concentrations measured on the surface after (a) 500 hrs and (b) 1,000 hrs of exposure to the new accelerated test environment (NE#2) in the presence of nitrate ions.

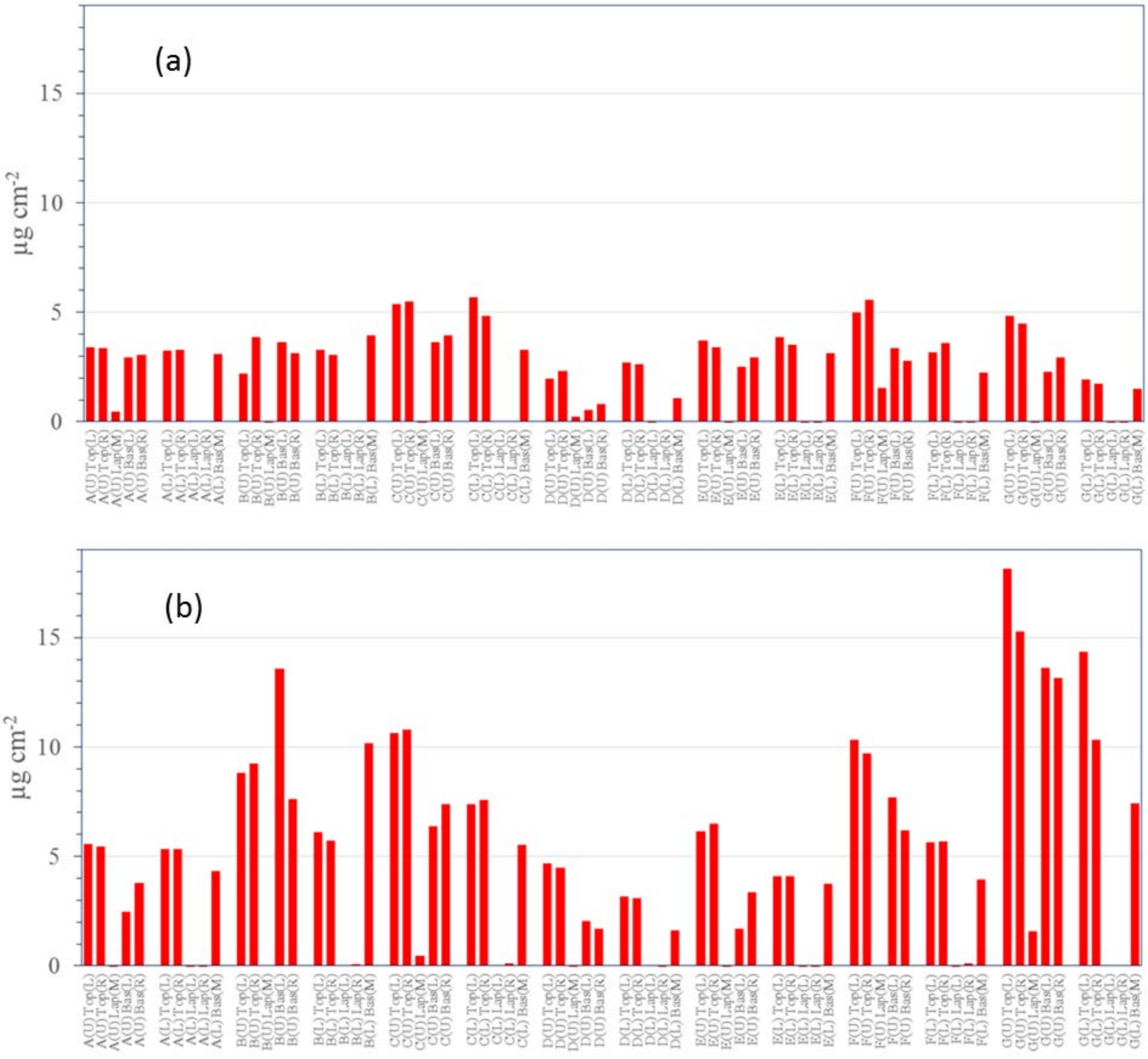

Figure 166. SO_4^{2-}concentrations measured on the surface of the lap joint samples after (a) 500 hrs and (b) 1,000 hrs of exposure to the new accelerated test environment (NE#2) in the presence of nitrate ions.

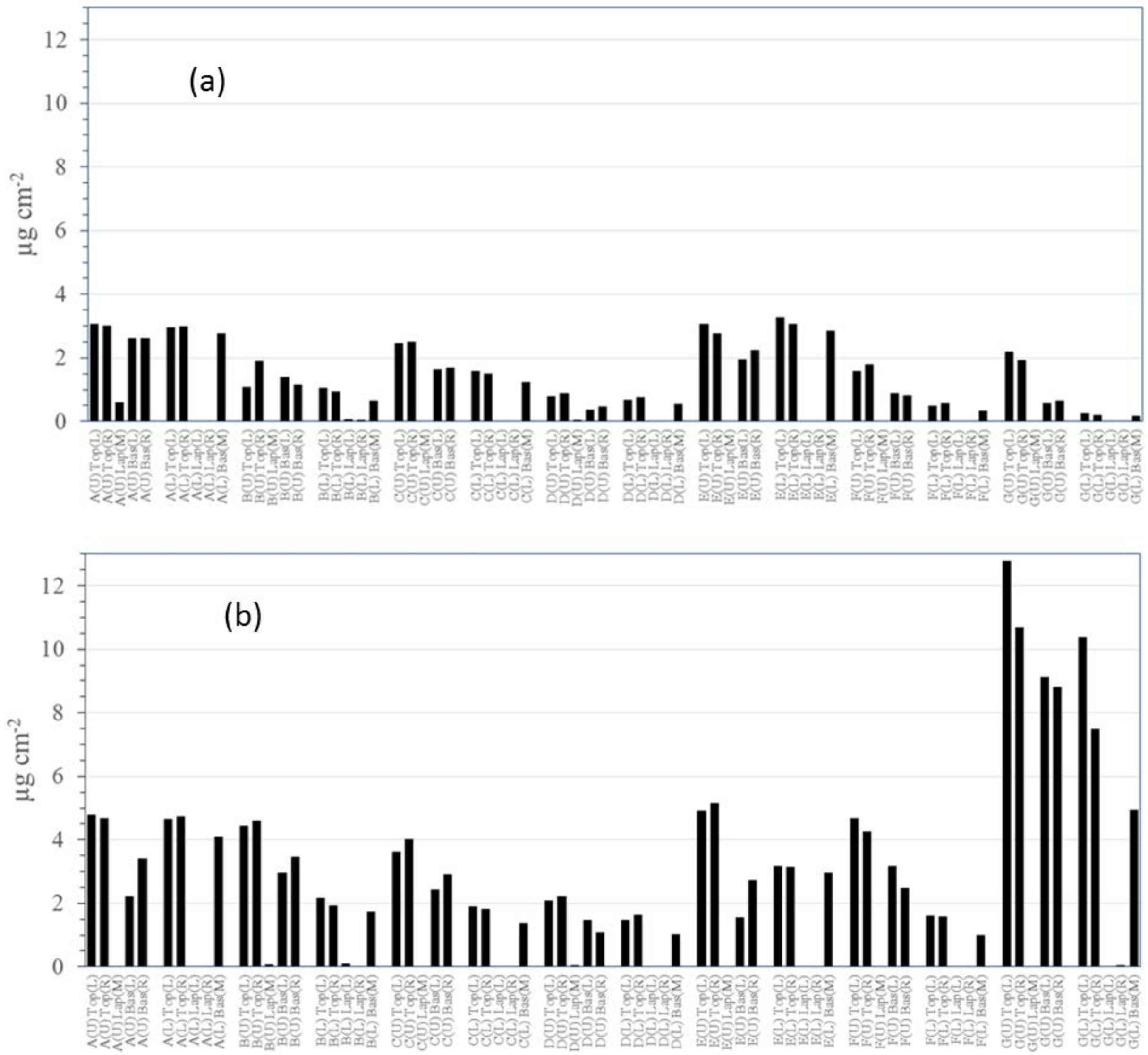

Figure 167. NO_3^- concentrations measured on the surface after (a) 500 hrs and (b) 1,000 hrs of exposure to the new accelerated test environment (NE#2) in the presence of nitrate ions.

Figure 168 through Figure 171 show mass loadings of major analytes (Na^+, Mg^{2+}, Cl^-, and SO_4^{2-}) corresponding to individual extractions at different locations of duplicate sample assemblies of each type (A through G) that were exposed in parallel for 500 hours at Boeing without the presence of nitrate ions in the test solution.

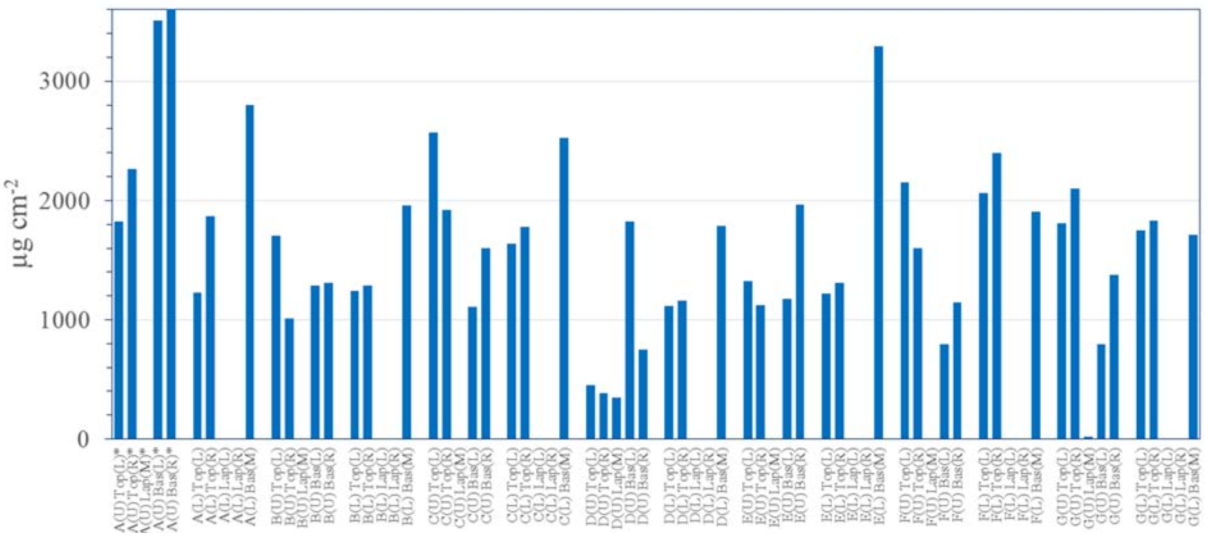

Figure 168. Na^+ loadings on the surface of lap joint samples after 500 hrs of exposure to the new accelerated environmental test (NE#1) without the presence of nitrate ions.

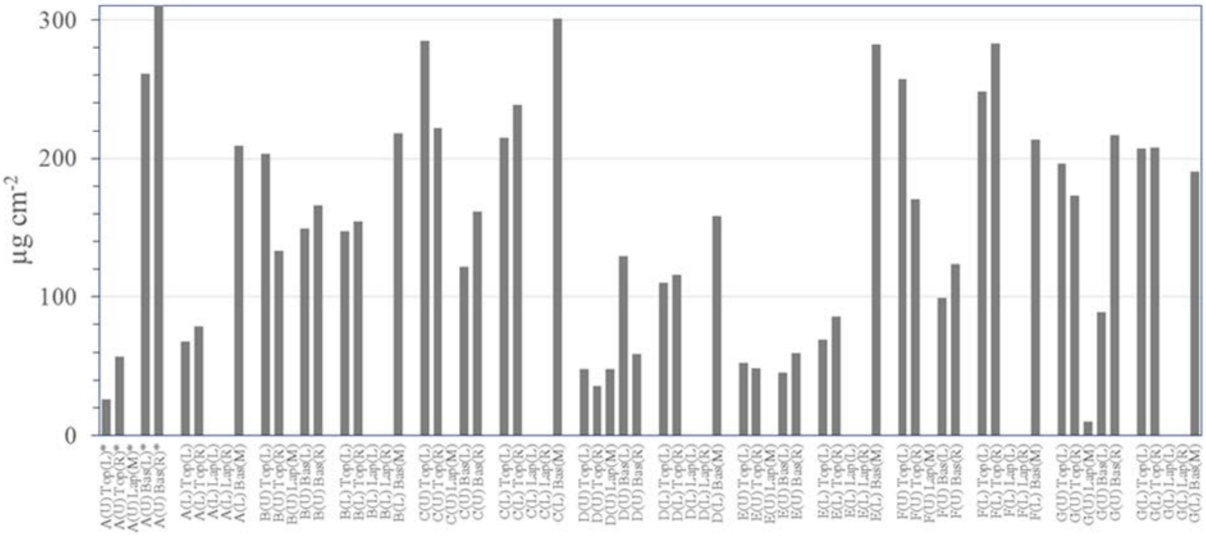

Figure 169. Mg^{2+} loadings measured on the surface of the lap joint samples after 500 hrs of exposure to the new accelerated test environment (NE#1) without the presence of nitrate ions.

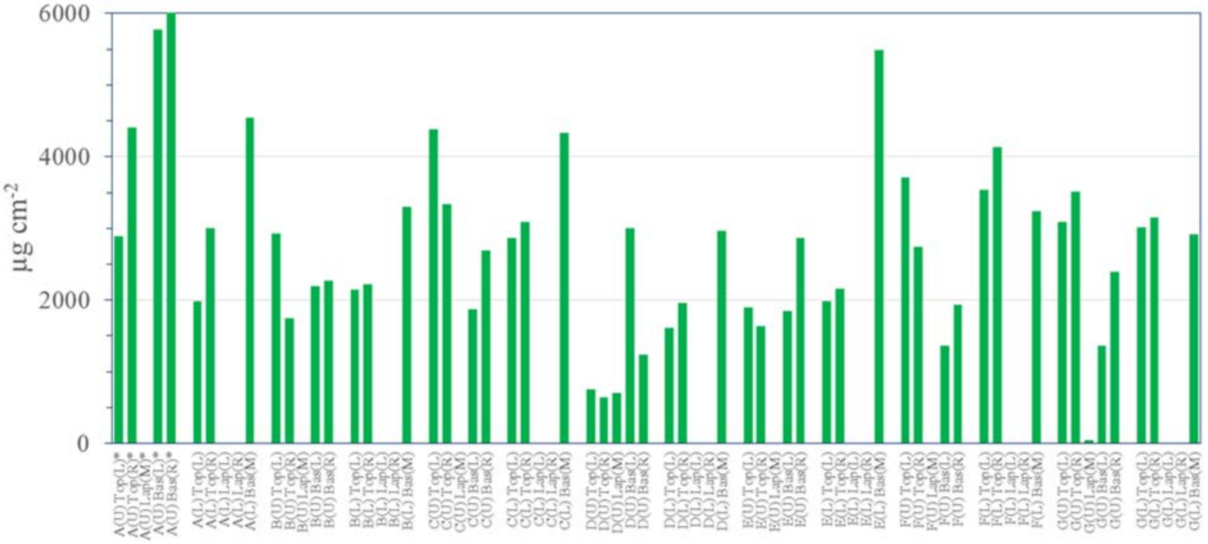

Figure 170. Cl^{-} concentrations measured on the surface of the lap joint samples after 500 hrs of exposure to the new accelerated test environment (NE#1) without nitrate ions.

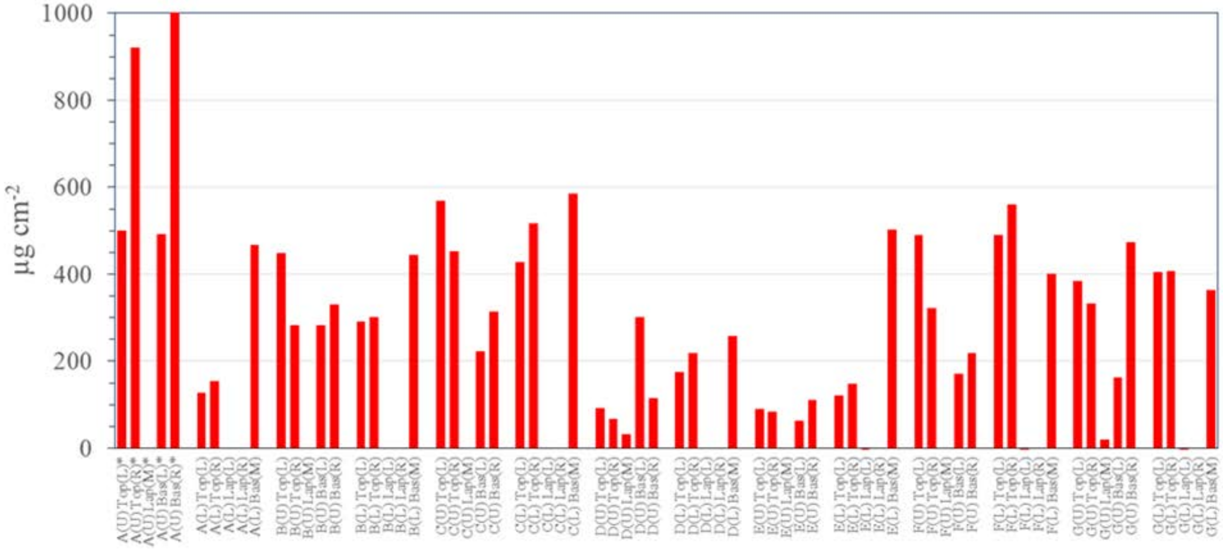

Figure 171. SO$_4^{2-}$ concentrations measured on the surface of the lap joint samples after 500 hrs of exposure to the new accelerated test environment (NE#1) without nitrate ions,

Figure 172 through Figure 180 summarize the median values for each of the above sets of replicate loadings (N = 4 for exposed upper surface of top plates, N = 3 for exposed upper surface of base plates, and N = 3 for lapped upper surface of base plates). Note that in these and subsequent plots, results for top plates are grouped on the left, base plates in the middle, and laps on the right.

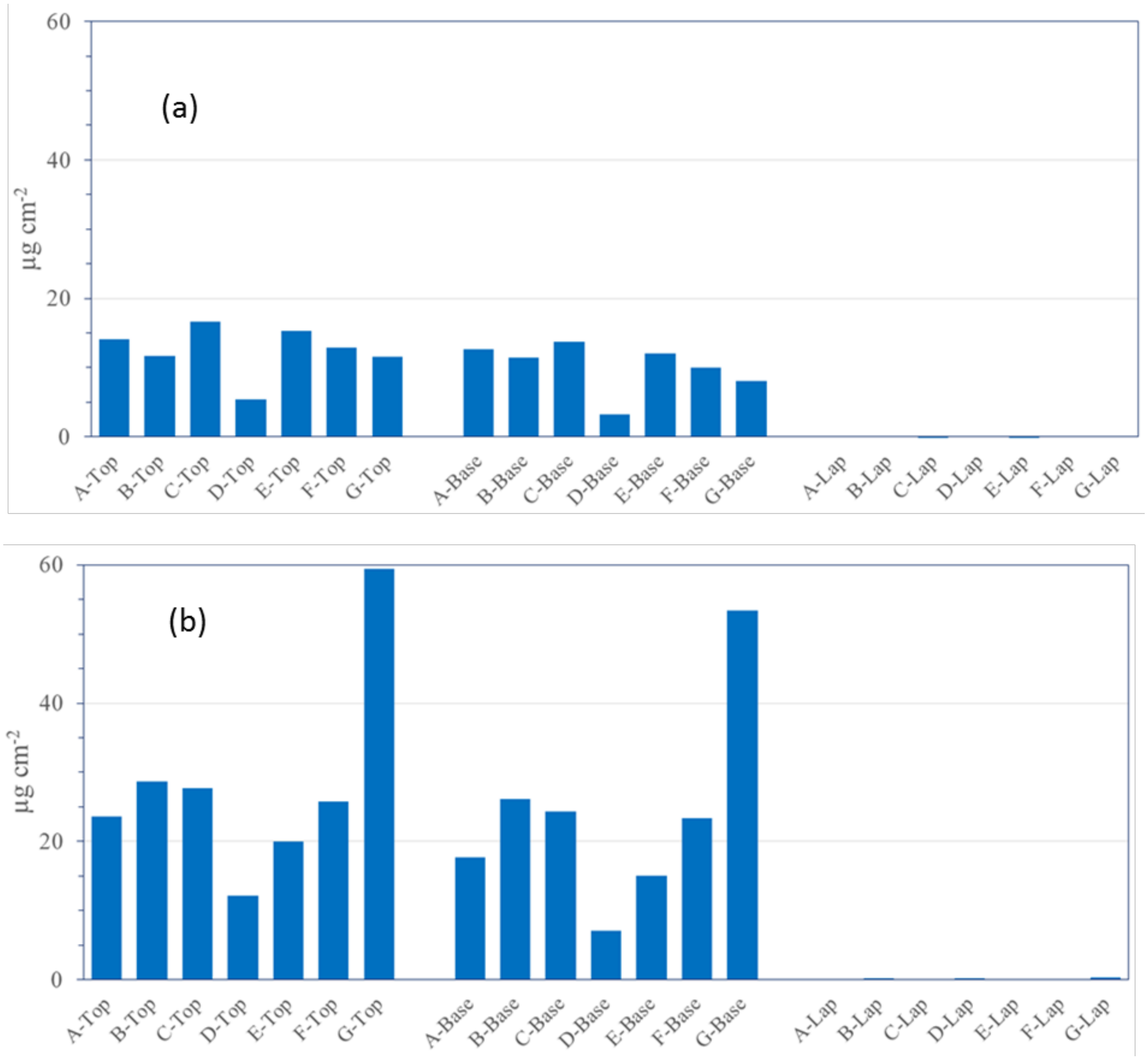

Figure 172. Median Na^+ loadings measured on the surface of the lap joint samples after (a) 500 hrs and (b) 1,000 hrs of exposure to the new accelerated test environment (NE#2) in the presence of nitrate ions.

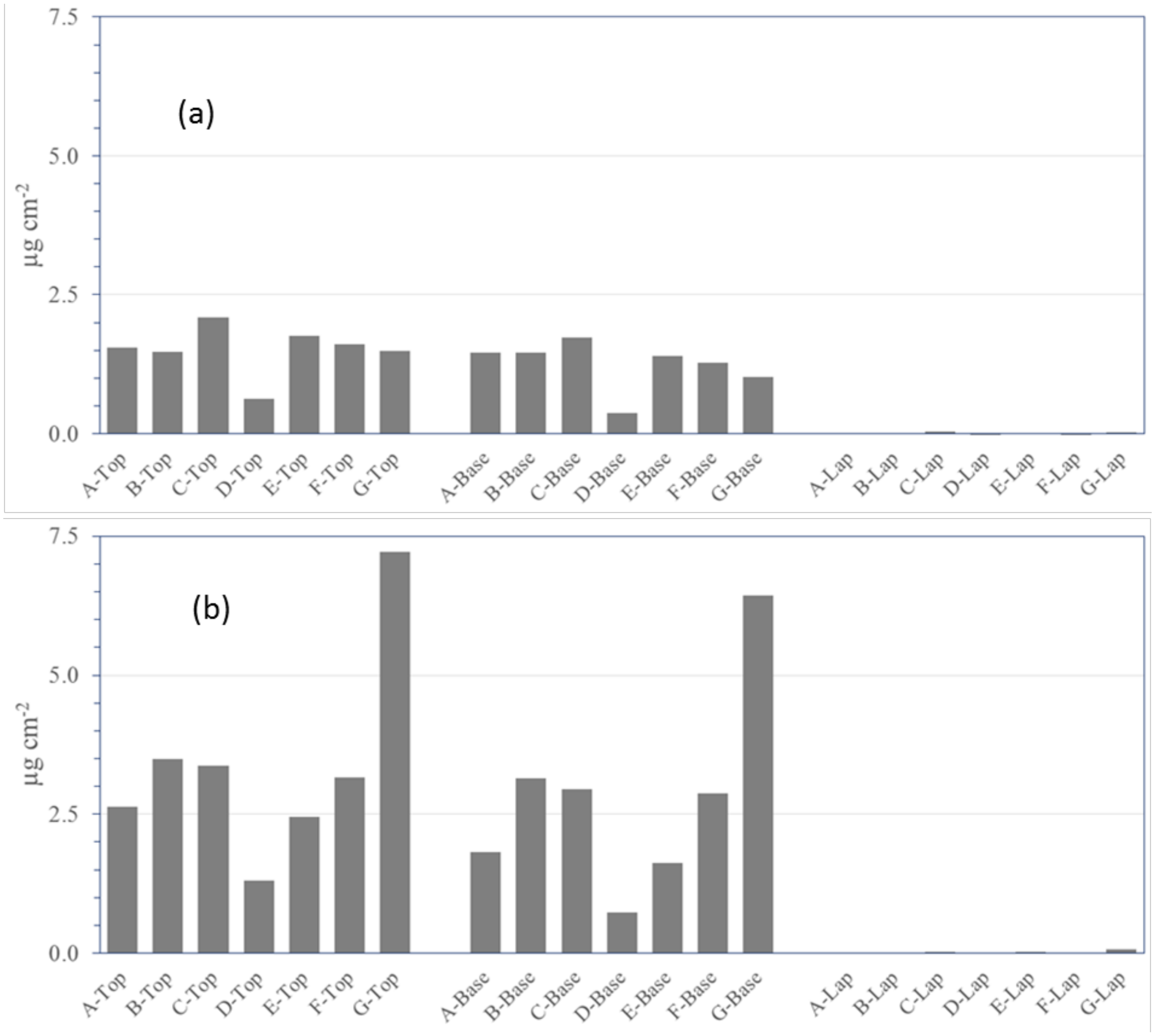

Figure 173. Median Mg^{2+} loadings measured on the surface of the lap joint samples after (a) 500 hrs and (b) 1,000 hrs of exposure to the new accelerated test environments (NE#2) in the presence of nitrate ions.

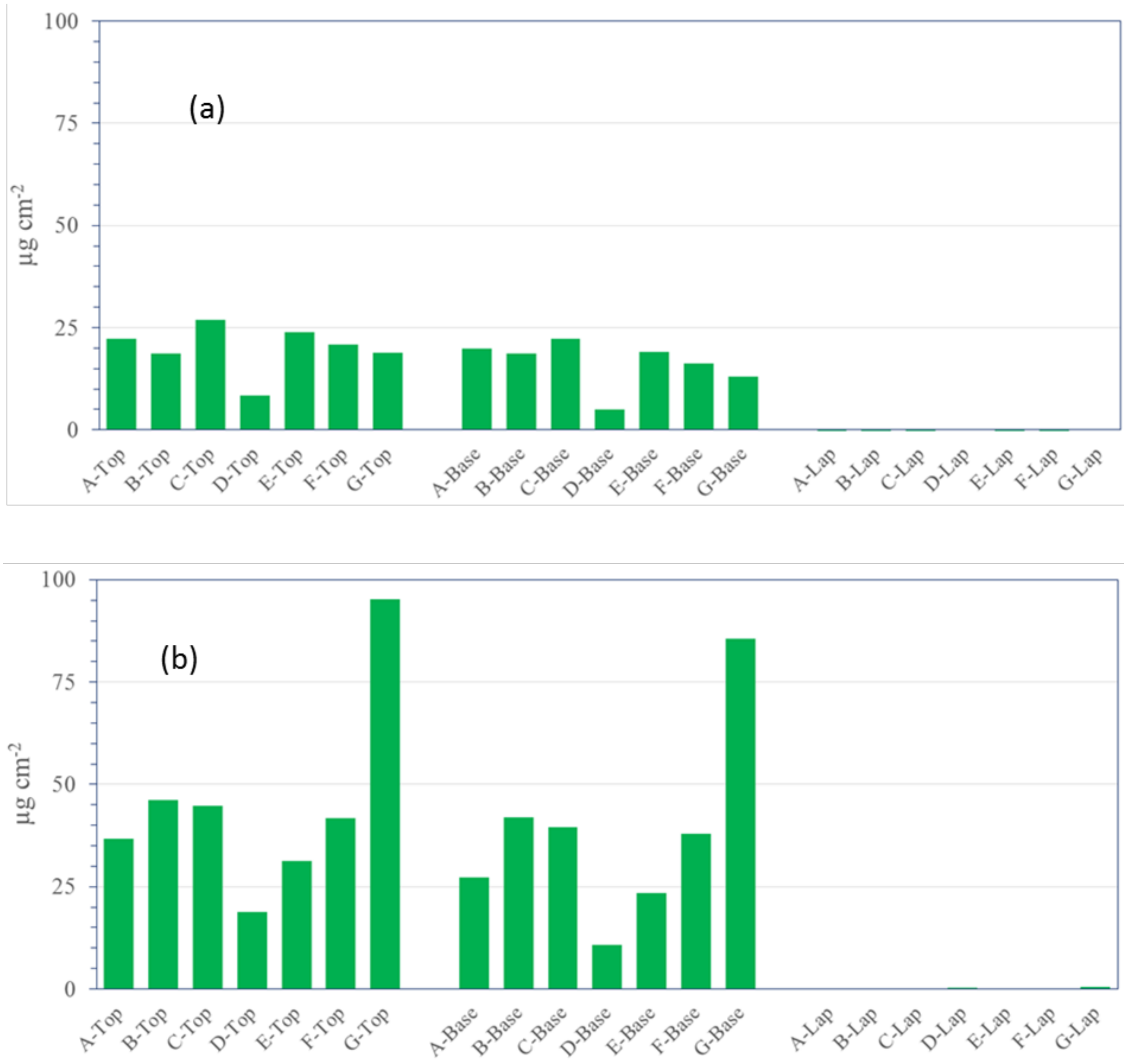

Figure 174. Median Cl^- loadings measured on the surface of the lap joint samples after (a) 500 hrs and (b) 1,000 hrs of exposure to the new accelerated test environment (NE#2) in the presence of nitrate ions.

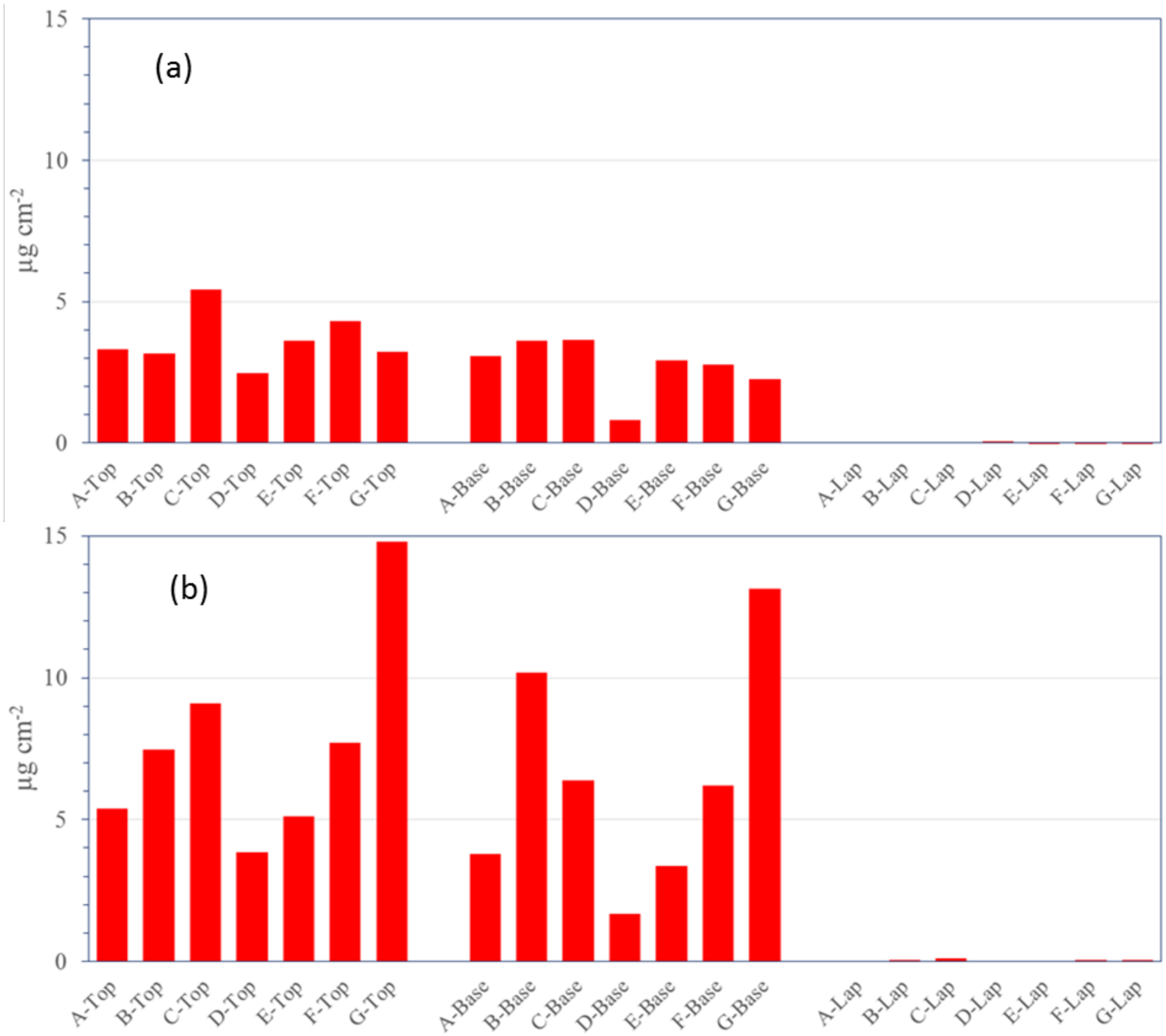

Figure 175. Median SO_4^{2-} loadings on the surface of the lap joint samples after (a) 500 hrs and (b) 1,000 hrs of exposure to the new accelerated test environment (NE#2) in the presence of nitrate ions.

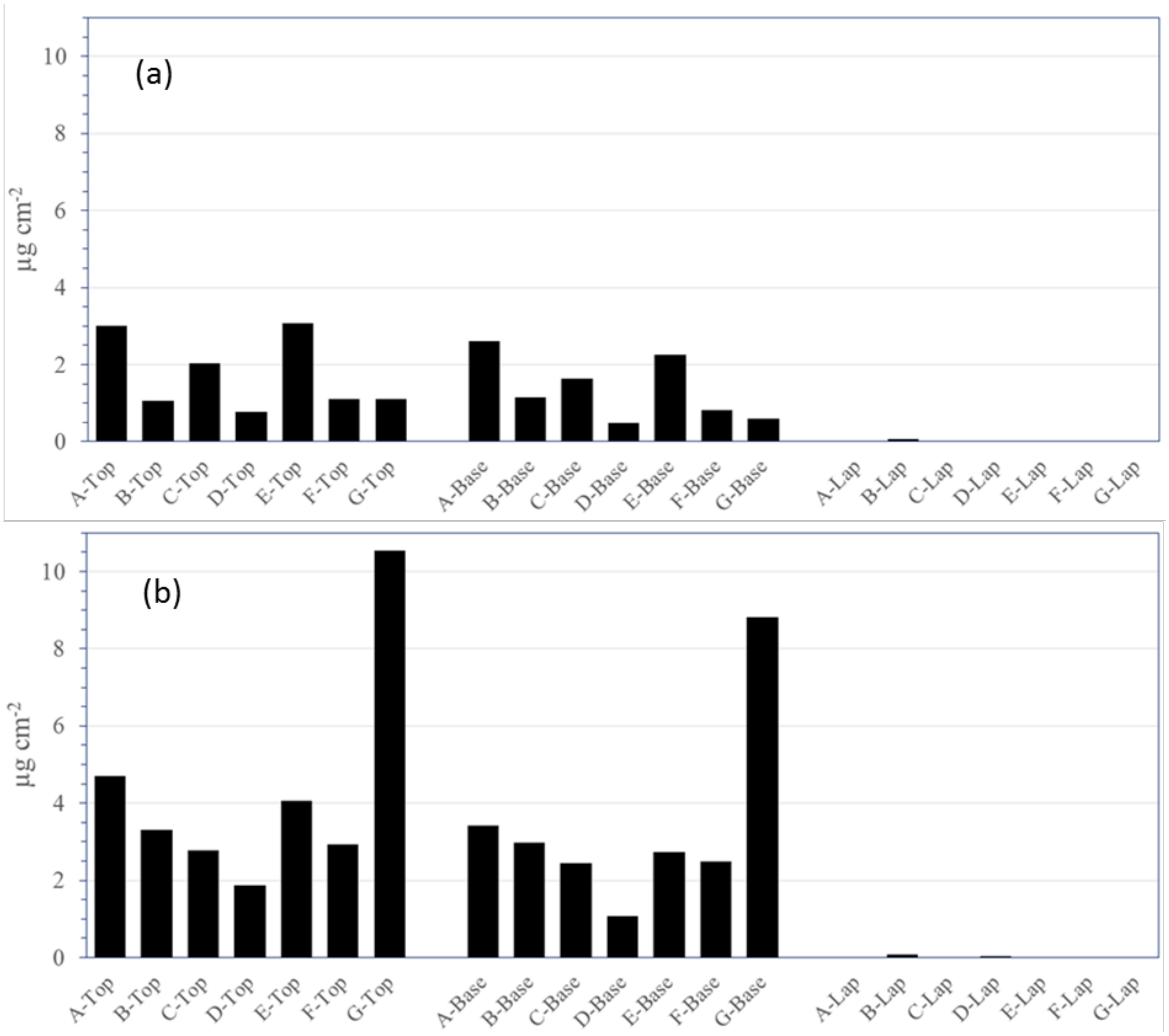

Figure 176. Median NO_3^- concentration measured on the surface of the lap joint samples after (a) 500 hrs and (b) 1,000 hrs of exposure to the new accelerated test environment (NE#2) in the presence of nitrate ions.

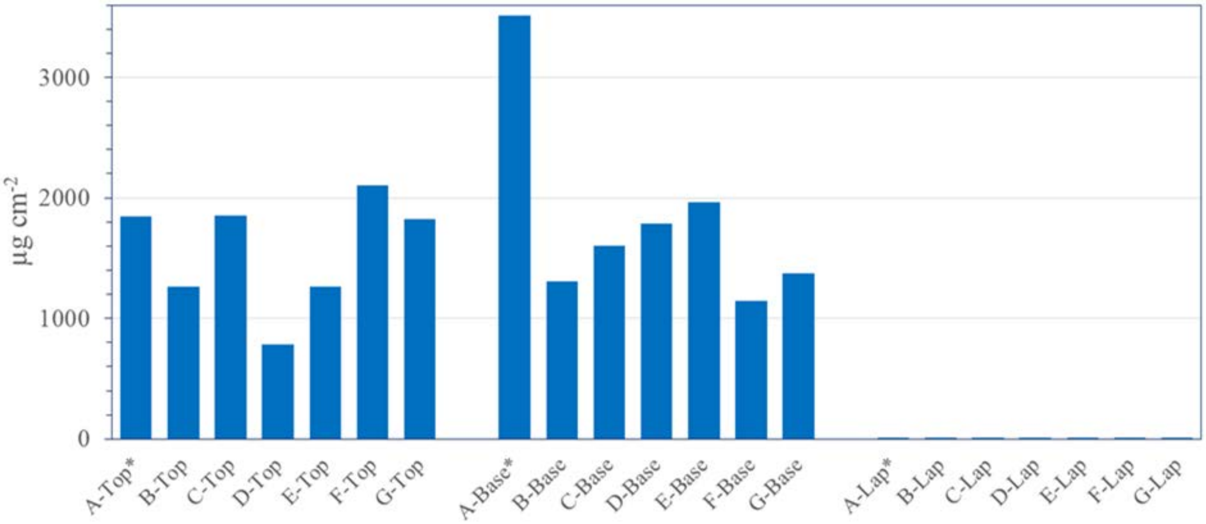

Figure 177. Median Na$^+$ loadings measured on the surface of the lap joint samples after 500 hrs of exposure to the new accelerated test environment (NE#1) without nitrate ions.

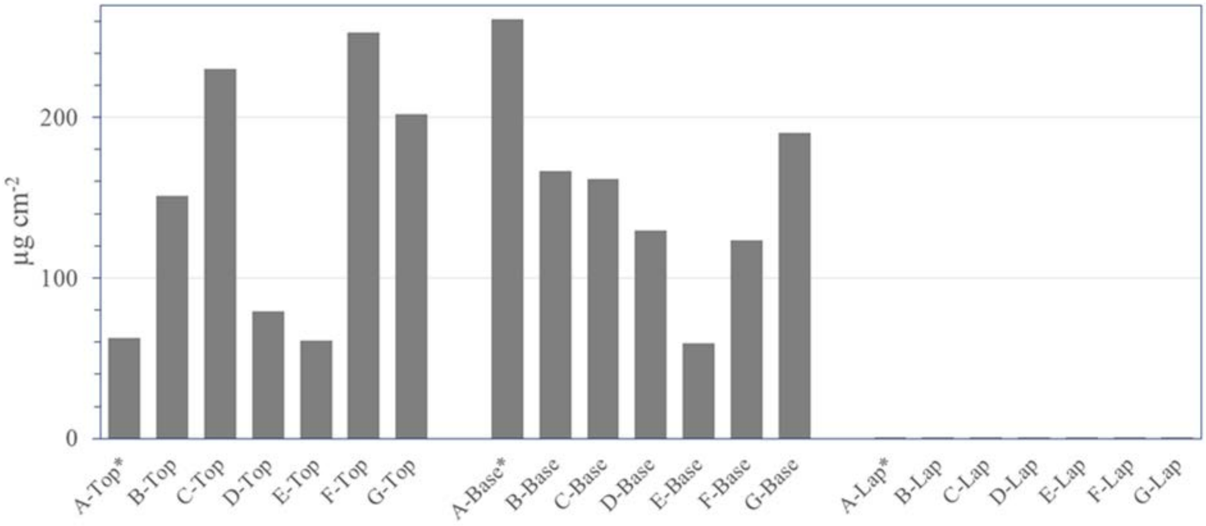

Figure 178. Median Mg^{2+} loadings on the surface of the lap joint samples after 500 hrs of exposure to the new accelerated test environment (NE#1) without nitrate ions.

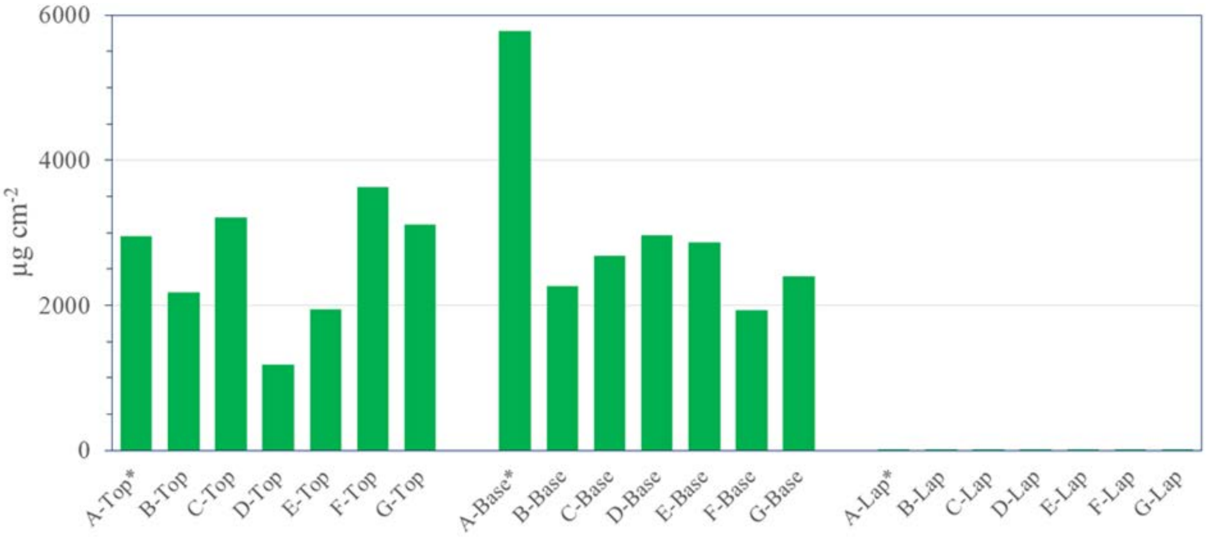

Figure 179. Median Cl^- loadings measured on the surface of the lap joint samples after 500 hrs of exposure to the new accelerated test environment (NE#1) without nitrate ions.

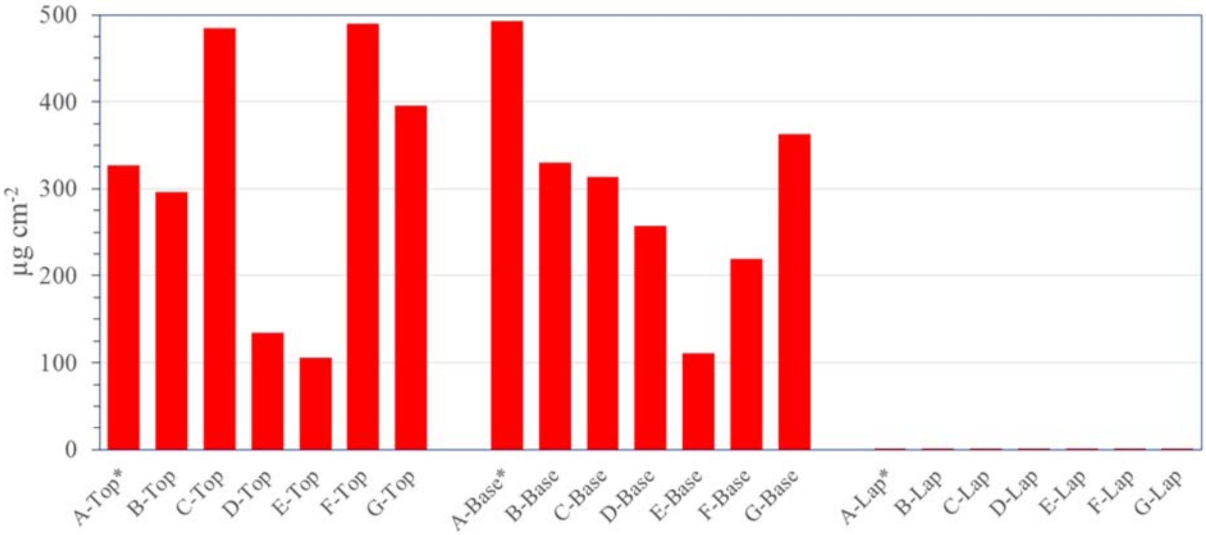

Figure 180. Median SO_4^{2-} loadings measured on the surface of the lap joint samples after 500 hrs of exposure to the new accelerated test environment (NE#1) without nitrate ions.

Figure 181 through Figure 187 show equivalent ratios of median constituent loadings relative to corresponding ratios of those constituents in test solutions.

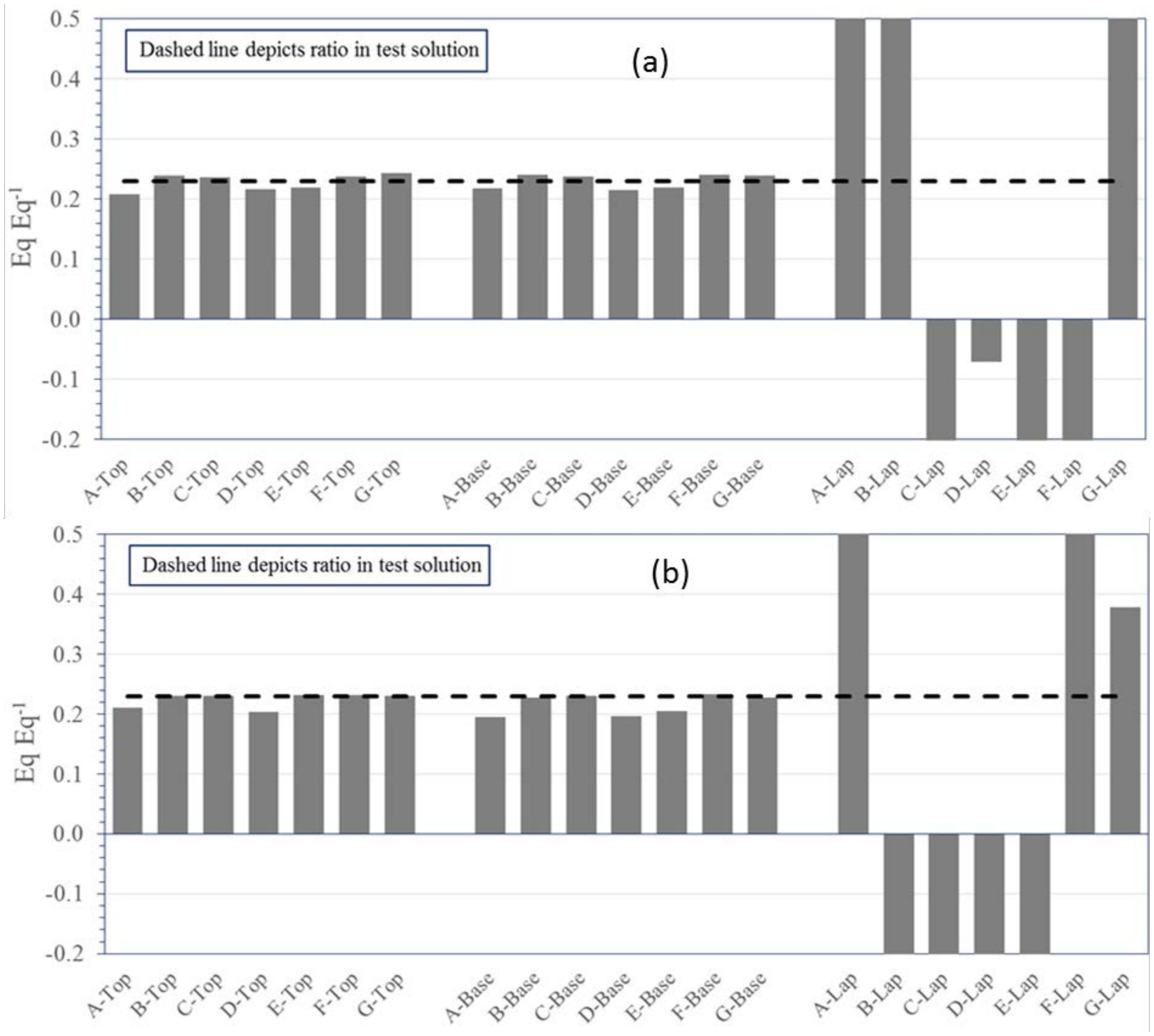

Figure 181. Equivalent ratios of median loadings of Mg^{2+} and Na^+ ions measured on lap joint samples after (a) 500 hrs and (b) 1,000 hrs of exposure to the new accelerated test environment (NE#2) in the presence of nitrate ions.

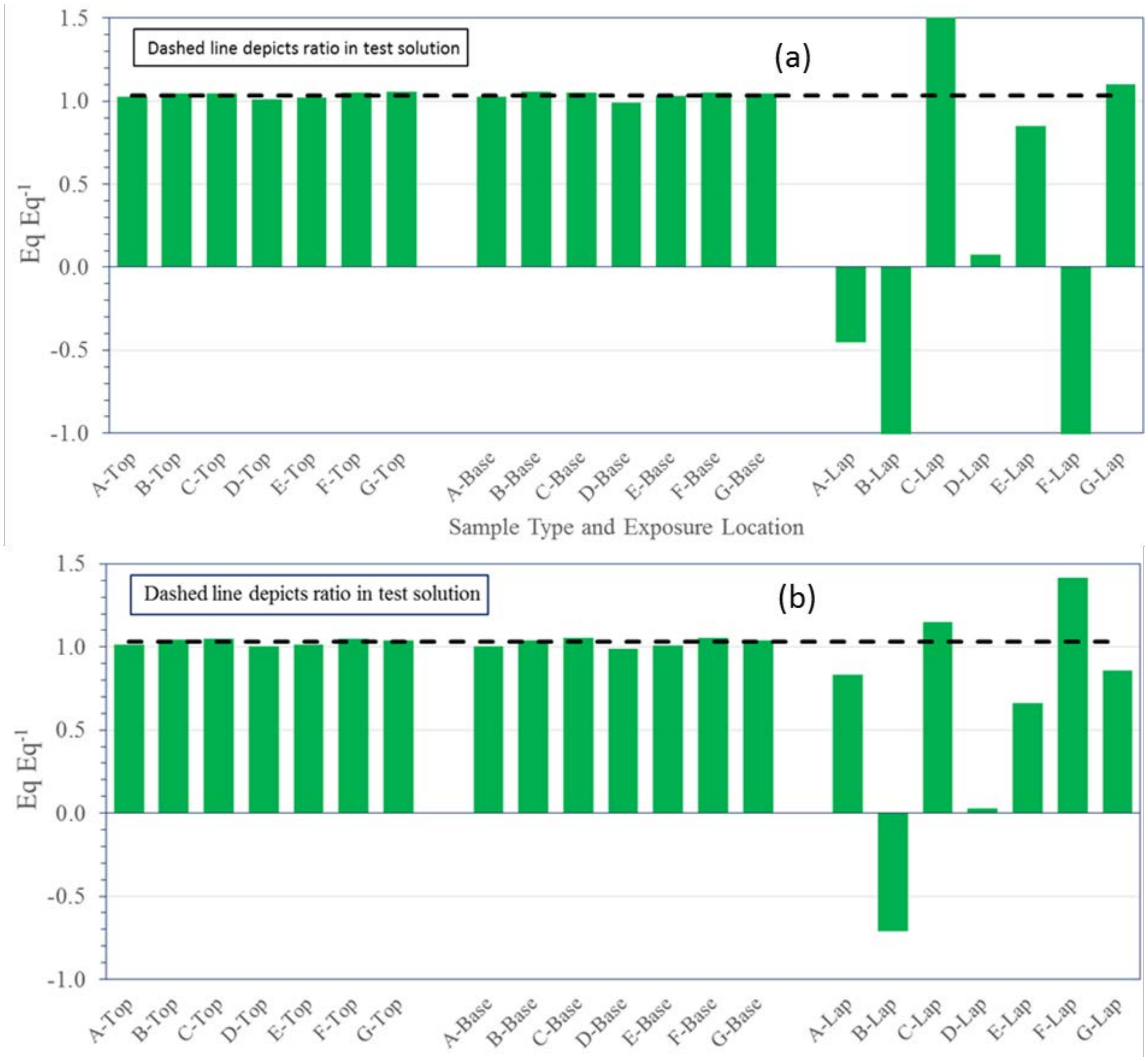

Figure 182. Equivalent ratios of median loadings of Cl$^-$ and Na$^+$ ions measured on lap joint specimens after (a) 500 hrs and (b) 1,000 hrs of exposure to the new accelerated environmental test (NE#2) in the presence of nitrate ions.

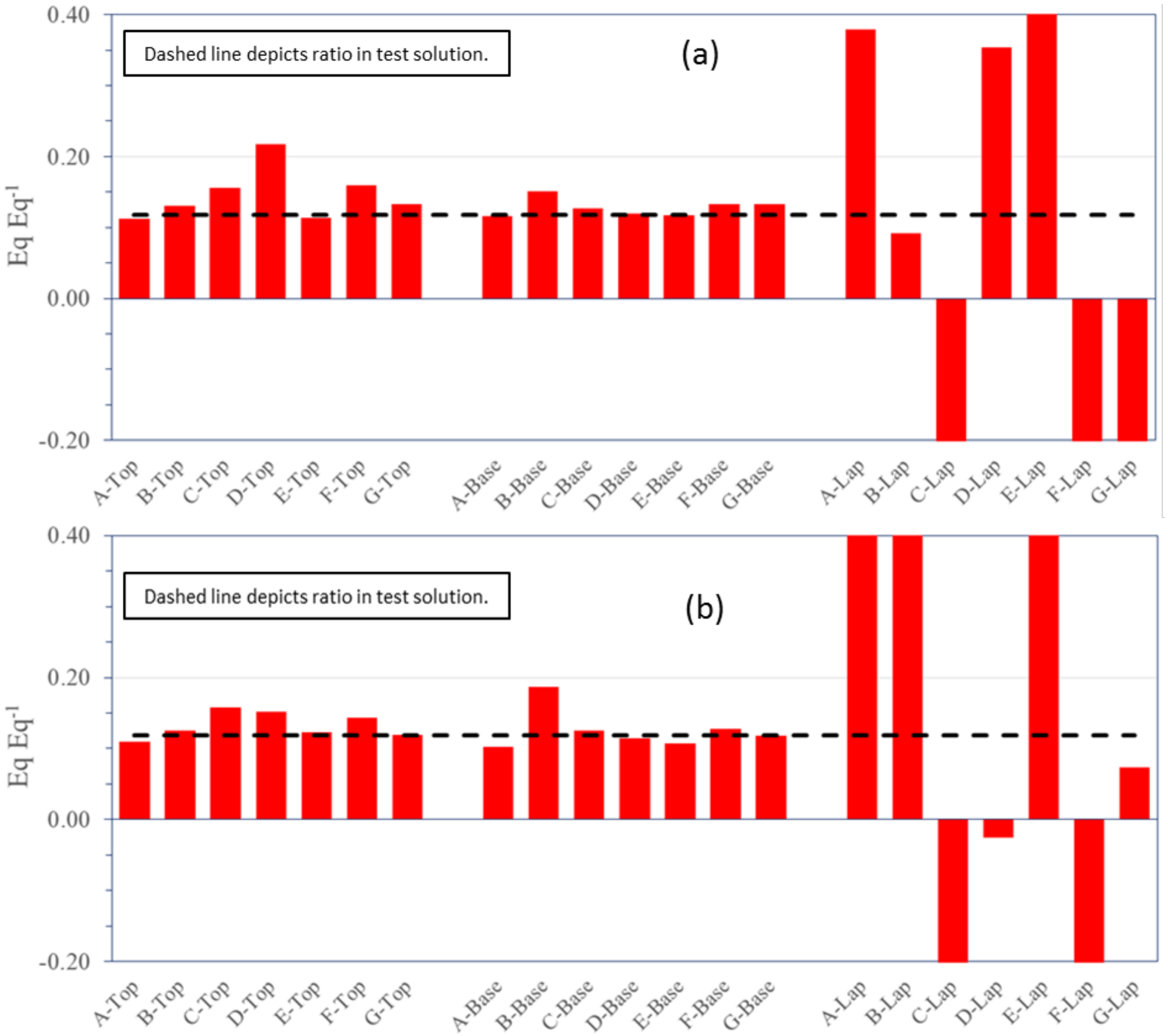

Figure 183. Equivalent ratios of median loadings of SO_4^{2-} and Na^+ ions measured on lap joint specimens after (a) 500 hrs and (b) 1,000 hrs of exposure to the new accelerated environmental test (NE#2) in the presence of nitrate ions.

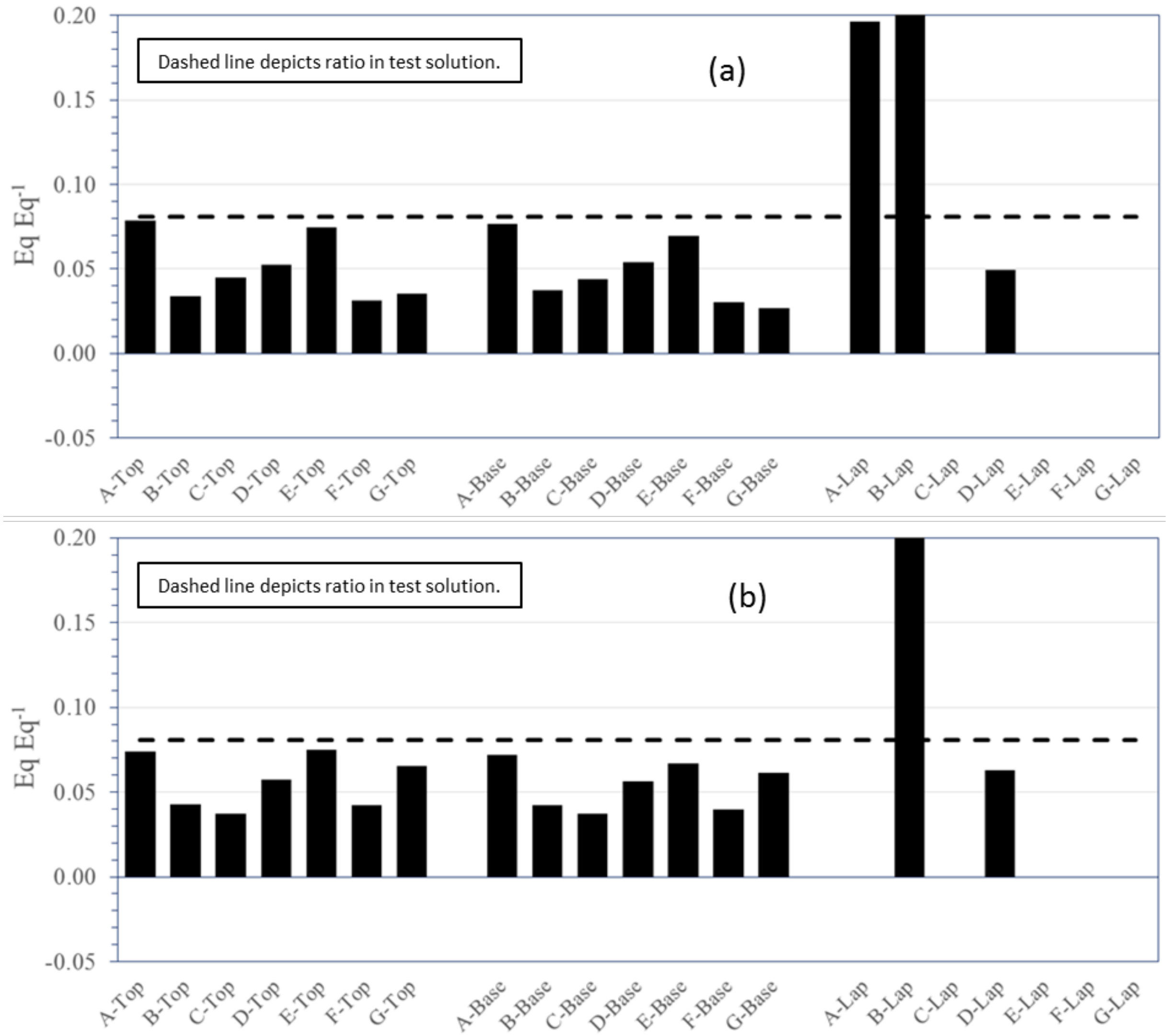

Figure 184. Equivalent ratios of median loadings of NO_3^- and Na^+ ions measured on lap joint specimens after (a) 500 hrs and (b) 1,000 hrs of exposure to the new accelerated environmental test (NE#2) in the presence of nitrate ions.

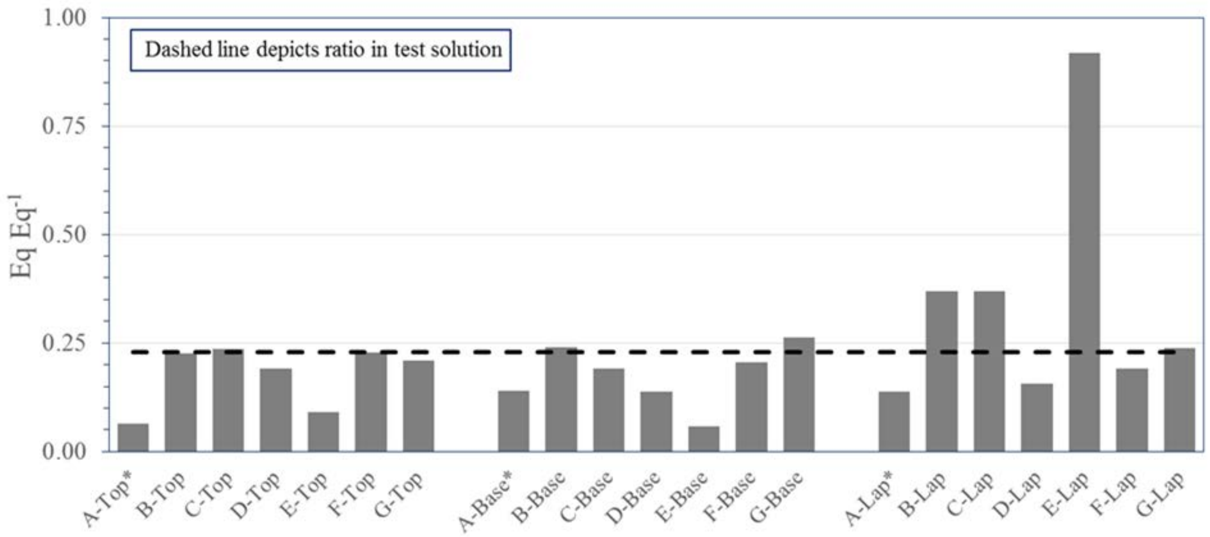

Figure 185. Equivalent ratios of median loadings of Mg^{2+} and Na^{+} ions measured on lap joint samples after 500 hrs of exposure to the new accelerated test environment (NE#1) without nitrate ions.

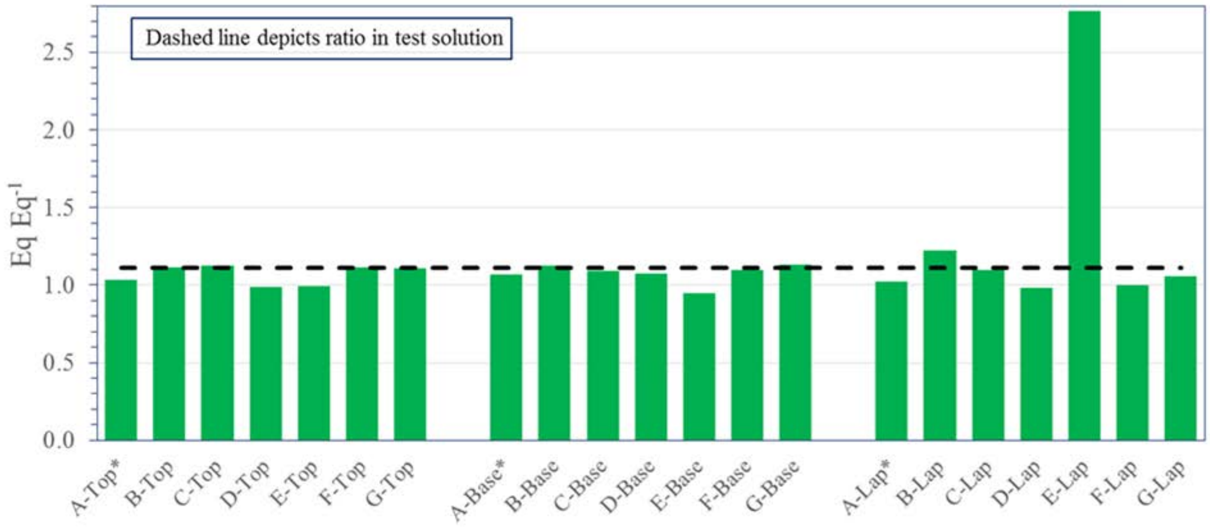

Figure 186. Equivalent ratios of median loadings of Cl^{-} and Na^{+} ions measured on lap joint samples after 500 hrs of exposure to the new accelerated test environment (NE#1) without nitrate ions.

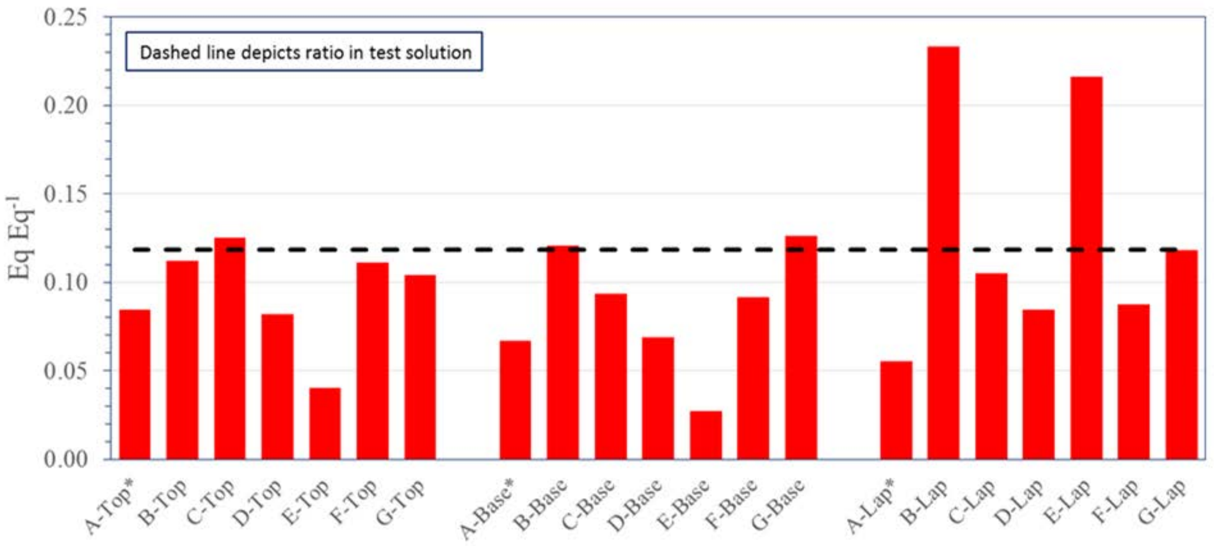

Figure 187. Equivalent ratios of median loadings of SO_4^{2-} and Na^+ ions measured on lap joint samples after 500 hrs of exposure to the new accelerated test environment (NE#1) without nitrate ions.

Results for sample assemble number A(U) that was exposed at Boeing (designated with a '*' on the plots) are more uncertain that those for other assembles. Extracts of that sample were analyzed before we noted the much higher concentration range at Boeing relative to NAVAIR. The very low remaining volumes of extracts for that sample had to be diluted into the analytical range before rerunning, which resulted in lower analytical resolution relative to other samples.

NAVAIR processed handling blanks but Boeing did not. The NAVAIR results are blank corrected whereas those for Boeing are not.

Despite the lower ionic strength of the test solution (0.48 M Na^+ instead of 1.0 M Na^+) and the shorter fogging time during each wet-dry cycle (15 minutes instead of 30 minutes) at Boeing relative to NAVAIR, median ionic loadings on exposed upper surfaces of top and base plates after 500-hour exposures were about 2 orders of magnitude greater at Boeing (Figure 172a and Figure 177). Causes for these very large differences are not known, but possible contributing factors include (1) differences in droplet size distributions and associated deposition velocities corresponding to the method by which fog was produced (bursting bubbles vs. atomization) and/or (2) differences in the relative periods of wetting and drying at the two sites.

Loadings within laps of samples exposed at NAVAIR were near analytical detection limits and consequently the corresponding ratios of constituents measured within laps (Figure 181 through Figure 184) are highly uncertain and, from our perspective, uninterpretable.

Loadings of all analytes on outer top and base plates of sample assemblies exposed at NAVAIR increased with duration of exposure and also varied systematically among sample types.

Ratios of median Na^+, Mg^{2+}, Cl^-, and SO_4^{2-} loadings on the top and base plates of samples exposed at NAVAIR (Figure 181 through Figure 183) were generally similar to those in the test solution whereas surface loadings of NO_3^- decreased by variable amounts relative to the other constituents (Figure 184). Relative to top plates, NO_3^- on base plates and within laps of samples exposed at Pt. Judith also decreased. These results support the hypothesis that NO_3^- was lost from solution via reaction during the corrosion process and that the relative amounts lost varied among sample types.

Ratios of median Cl^- to Na^+ loadings on samples exposed at Boeing were similar to those in the test solution but ratios of Mg^{2+} and SO_4^{2-} to Na^+ were lower (Figure 185 through Figure 187). In addition, the apparent decreases in both Mg^{2+} and SO_4^{2-} relative to Na^+ and Cl^- exhibited similar variability among sample types. The results suggest that similar relative amounts Mg^{2+} and SO_4^{2-} were incorporated into insoluble corrosion products on all sample types but that the absolute amounts incorporated varied among sample types.

Clearly, relative variability among loadings of ionic species differed between the two tests. However, it is unclear whether the lack of NO_3^- in the test solution at Boeing, the much higher ionic loading on samples exposed at Boeing, differences in the exposure protocols at the two sites (wet-dry cycles, RH), or some combination of these factors was (were) the primary driver(s) of these differences.

While specific comparisons cannot be made between NE#1 and NE#2, several general comments can be made. As stated earlier, the salt loading in NE#1 is two orders of magnitude greater than in NE#2. The salt loadings in NE#2 are generally of the same order of magnitude as those from ASTM B117, ASTM G85-A5 and ASTM G85-A4. Notably, however, very little corrosion is observed even for the high salt loads of NE#1. This may be a result of slow wetting of the salt film but it may also indicate that corrosion rate is governed more by RH than by salt loading density for high salt loads.The GM9540P environment has lower salt loads primarily because of dilution effects and lower corrosion rates as well. Thus, “high” salt loads would be considered those above the levels found in ASTM B117 and ASTM G85.

ASTM B117 provides a continuous salt spray and thus the salt loading is a function of the fixed concentration and fluid dynamics that result in a flow of the thin film (dripping of the samples). In the case of ASTM G85-A5, a cyclic spray is used with a concentration of salt spray that is 2 orders of magnitude lower than that of ASTM B117. It is hypothesized that if the solution concentration were equivalent to the ASTM B117, significantly more salt build-up would occur. For a continuous fog, the film concentration will come to a fixed equilibrium value. For alternative wet and dry conditions, surface salt loading with increase during each cycle. The implication is that for the improved test, the ionic strength of the solution should be significantly reduced from that of seawater to prevent heavy salt film build-up that may unexpectly affect corrosion rates.

CHAPTER 10
FUTURE EFFORTS AND RECOMMENDATIONS

The work performed within the project was successful at showing key relationships between environmental parameters and corrosion rate. Results observed from current accelerated laboratory testing and ambient outdoor exposure have been shown to be consistent with the knowledge gained from the experimental testing. Efforts towards establishing a test method (rather than a practice) as a NACE International test method are underway. However, the acceptance of Test Methods and Standards into standards organizations is dependent on reproducibility of the test between laboratories. The next logical progression for this work would be to fund inter-laboratory Round Robin testing under an ESTCP program. Other future efforts may also be facilitated based on the success of this effort. These are described below.

10.1 ESTCP Effort

The ESTCP effort will be divided into several tasks.

10.1.1 *Task 1: Optimization of cycle period*

The completed SERDP effort provided much needed information on what is required within a test cycle. One of the major findings was that duration of each step in the method is critical to driving different corrosion modes. A systematic design of experiments approach needs to be taken to fully understand the optimal values for producing the expected failures (coating delamination and galvanic decoupling for example).

Additionally, work will be leveraged with the newly funded ESTCP effort related to corrosion sensor technology. Data from each of the 9 base locations will be analyzed for specific times in each RH condition. This analysis will provide an improved understanding of RH cycling factors that control environmental aggressiveness. This, in turn, will provide a critical ability to dial in specific severity conditions and expand the usefulness of the developed test method.

10.1.2 *Task 2: Round Robin testing*

It is proposed that a mix of multiple service government and industry laboratories participate in this activity. The hope is to have a minimum of eight participating laboratories. The goal of this task is to ensure that results from each of the test laboratories are consistent. A number of material and coating systems will be chosen. As such, damage on one sample type can be compared between laboratories and relative performance can be ranked among laboratories.

To facilitate the testing, proven statistical methods for performing round robin testing will be used. Testing will also be supplemented by the use of corrosion sensors (again leveraged from the newly funded ESTCP effort). Sensor data as well as quantified damage will be used to compare laboratory results. Corrosion damage will be quantified using methods developed within WP-1673.

NAVAIR is developing Risk Based assessment tools based on sensor data. Therefore, sensor data acquired in the laboratory exposures can be used to inform these models.

10.1.3 *Task 3: Standard development and acceptance*

In parallel with the technical efforts, representatives from the various labs will support the writing and ballotting process for the standard in NACE International. This will require participation in NACE Working Group meetings and phone calls throughout the program.

10.2 In-Situ Measurements of Coating Performance

Many SERDP efforts have focused on the understanding the mechanisms of non-chromate inhibitors. Additionally, ESTCP efforts have focused on field testing of the "best" performing systems. Performance testing in the SERDP funded efforts was primarily done in aqueous environments. The transition from these exposure conditions to on-asset testing under ESTCP requires the fundamental mechanisms of corrosion processes to be the same. This is not necessarily the case (e.g. Mg rich primers). Techniques developed in WP-1673 have the potential to streamline the performance testing of these new coating systems. Specifically, the improved environmental tests provide a more realistic exposure condition for candidate coatings. Also, MEA techniques and sensored panels provide the opportunity to measure corrosion real time in actual environments.

10.2.1 *Task 1: Laboratory exposure testing of non-chrome coatings in the SERDP test environment*

Several non-chrome systems will be chosen for testing. These systems will be exposed to the newly developed SERDP accelerated corrosion environment. Performance of the various systems will be quantified using image analysis techniques developed in SERDP WP-1673. Data will be compared to the performance of panels exposed in other accelerated exposure environments. These latter samples will be provided from past SERDP/ESTCP funded efforts. Corrosion sensors will also be exposed within the corrosion environment and a rank order of coatings systems will be obtained. Algorithms developed under the newly funded ESTCP program related to corrosion sensors will be used to quantify coating performance based on sensor data.

10.2.2 *Task 2: Outdoor exposures of non-chrome coating systems*

Duplicate samples will be exposed to a select outdoor exposure environment. Additionally, sensors will also be deployed with the same coating systems applied. As in the previous task, ESTCP-developed corrosion algorithms will be used to quantify performance of the coated panels and compared with actual observed damage.

10.2.3 *Task 3: Comparison of sensor data from accelerated laboratory corrosion testing and outdoor exposure*

In this final task, sensor data collected from accelerated testing and ambient outdoor testing will be compared. The main goal is to determine if the rank order of coating performance is the same between laboratory and outdoor exposures. If this is true, then the use of sensors to characterize fielded samples is justified, providing performance data in actual environments in a rapid manner. The advantage of such an approach is that sensor panels can be placed in various environments to provide information in the variation of new coating system performance in a variety of conditions.

Aside from rank order of performance, the relative improvement factor between various coating systems can be provided. Of interest, for example, would be the time at which coating inhibitors are depleted and the corrosion rate after depletion of the inhibitor. By directly comparing initiation times and corrosion rates, the relative performance can be quantified more accurately under actual service conditions.

Lastly, a comparison between lab based and fielded sensors will provide useful data regarding the acceleration factor for the environmental testing. This would be particularly useful during the early phase of coating system development where quick testing needs to be performed to evaluate the ability of the non-chromate coating to protect a surface and a measure of the relative improvement from existing coatings.

CHAPTER 11
REFERENCES

ASTM (1999). *ASTM G67-99, Standard test method for determining the susceptibility to intergranular corrosion of 5XXX series aluminum alloys by mass loss after exposure to nitric acid (NAMLT Test)*. West Conshohocken, PA: ASTM International.

ASTM (2005). *ASTM E399-05, Standard test method for linear-elastic plane-strain fracture toughness KIC of metallic materials*. West Conshohocken, PA: ASTM International.

ASTM (2011a). *ASTM B117-11, Standard practice for operating salt spray (fog) apparatus*. West Conshohocken, PA: ASTM International.

ASTM (2011b). *ASTM G85-11, Standard practice for modified salt spray (fog) testing*. West Conshohocken, PA: ASTM International.

Bovard, F., Tardiff, J., Jafolla, T., McCune, D., Courval, G., Smith, K. A., Lee, F., Repp, J., Ramamurthy, S., Shaffer, R. J., & Vartolas, F. M. (2007). *Development of an improved cosmetic corrosion test for finished aluminum autobody panels*. SAE Paper No. 2007-01-0417.

Bovard, F., Smith, K. A., Repp, J., Tardiff, J., Jafolla, T., McQuiston, L., McCune, D., Ramamurthy, S. & Courval, G.(2006). *Development of an improved cosmetic corrosion test by the automotive and aluminum industries for finished aluminum autobody panels: Correlation of laboratory and OEM test track results*, Paper presented at the SAE World Congress, Warrendale, PA.

Buchheit, R., Wall, F., Stoner, G., & Moran, J. (1995). Anodic dissolution-based mechanisms for the rapid cracking, pre-exposure phenomenon demonstrated by Al-Li-Cu alloys. *Corrosion, 51*(6), 417-428.

Chameides, W. L., & Stelson, A. W. (1992). Aqueous-phase chemical processes in deliquescent sea-salt aerosols: A mechanism that couples the atmospheric cycles of S and sea salt, *Journal of Geophysical Research*, *97*(20), 565-580.

Cleveland Society for Coatings Technology Technical Committee. (1994). *Journal of Coatings Technology, 66*(837), 49-67.

Cooper, K. R. & Kelly, R. G. (2001). *Measurement and modeling of crack conditions during the environment-assisted cracking of an Al-Zn-Mg-Cu Alloy*. Paper presented at the TMS Annual Meeting, Warrendale , PA.

Cooper, K. R., Ma, Y., Wikswo, J. P. & Kelly, R. G. (2004). Simultaneous monitoring of the corrosion activity and moisture inside aircraft lap joints. *Corrosion Engineering Science and Technology, 39*(4), 339-345.

Cormack, E. (2012). *The effect of sensitization on the stress corrosion cracking of aluminum alloy*

5456. (Master's thesis). Naval Post Graduate School, Monterery, CA, p. 81.

Cramer, S. (2003). Forms of corrosion, in S. Cramer & B. Covino (Eds.), *ASM Handbook Volume 13A - Corrosion: fundamentals, testing, and protection* (187-248). Materials Park, OH: ASM International.

Dante, J. F., & Petry, L. (1999). *G-8 comparison of laboratory corrosion test methods and outdoor corrosion tests for air force coating systems.* SAE G-8 Round Robin Evaluation Report.

Dante, J. F., Price, K., Sabata, A., & Sabata, B. (2007). *Embedded coating degradation sensors for monitoring performance of temporary coatings*, in *CORROSION/2007*, Paper no. 07387, NACE International, Houston, Texas.

Davidson, D., Thompson, L., Lutz, F., Tiburcio, B., Smith, K., Meade, C., Mackle, T., McCune, D., Townsend, H., & Tuszynski, R. (2003). Perforation corrosion performance of autobody steel sheet in on-vehicle and accelerated tests. In *SP-1770: Advances in coatings & corrosion prevention*. 2003.

Davis, J. (1999). *Corrosion of aluminum and aluminum alloys*. J. Davis (Ed.). Materials Park, OH: ASM International, p. 313.

Davis, J. (2002). Aluminum and aluminum alloys. In J. Davis (Ed.). *ASM specialty handbook* Materials Park, PH: ASM International, p.784.

Dean, S.W., Reiser, D. B. (2002). Analysis of long-term atmospheric corrosion results from ISO CORRAG program. In *Outdoor atmospheric corrosion, ASTM STP 1421.* West Conshohocken, PA: ASTM.

De La Fuente, D., Chico B., & Morcillo, M. (2006). Laboratory simulation of formation of steel corrosion products with soluble salt contents. *Corrosion Engineering, Science and Technology, 41*(2), 130-134.

Dix, E., Anderson, W. & Shumaker, M. (1959). Influence of service temperature on the resistance of wrought aluminum-magnesium alloys to corrosion," *Corrosion, 15*(2), 55t-62t.

Erickson, D. J., Seuzaret, C., Keene, W. C. & Gong, S.-L. (1999). A general circulation model calculation of HCl and $ClNO_2$ production from sea-salt dechlorination: Reactive chlorine emissions inventory, *Journal of Geophysical Research*, 104, 8347-8372.

Feliu, S., Morcillo, M,. & Feliu, S., Jr (1993). The prediction of atmospheric corrosion from meteorological and pollution parameters - I. Annual corrosion. *Corrosion Science*, 34, 403-414.

Ferrer, K.S., & Kelly R.G. (2002). Development of an aircraft lap joint simulant environment. *Corrosion*, *58*(5), 452-459.

Gangloff, R. (2003). Hydrogen assisted cracking of high strength alloys. In I. Milne, R. Ritchie, B. Karihaloo (Eds.), *Comprehensive structural integrity,* (113-194). New York, NY: Elsevier Science.

Gao, J. (2011). *Experiments to explore the mechanism of stress corrosion cracking*. (Dissertation) University of Rochester, Rochester, NY, p. 147.

GM (1997). *GM 9540P, Accelerated corrosion testing*. Detroit, MI: General Motors Corporation.

Goldie, B. (1996). Cyclic corrosion testing: A comparison of current methods. *Protective Coatings Europe*, p. 23-24.

Howard, R.L., Lyon, S. B., & Scantlebury, J. D. (1999). Accelerated tests for the prediction of cut-edge corrosion of coil-coated architectural cladding: Part I: cyclic cabinet salt spray. *Progress in Organic Coatings 37*(1-2), 91-98.

Howard, R.L., Lyon, S. B., & Scantlebury, J. D., (1999). Accelerated tests for prediction of cut edge corrosion of coil-coated architectural cladding. Part II: cyclic immersion. *Progress in Organic Coatings*, *37*(1-2), 91-98.

Keene, W. C., Long, M. S., Pszenny, A. A. P., Sander, R., Maben, J. R.,Wall, A. J., O'Halloran, T. L., Kerkweg, A., Fischer, E. V. & Schrems, O. (2009). Latitudinal variation in the multiphase chemical processing of inorganic halogens and related species over the eastern North and South Atlantic Oceans. *Atmospheric Chemistry and Physics*, *9*, 7361-7385.

Keene, W. C., Pszenny, A. A. P., Maben, J. R. & Sander, R. (2002). Variation of marine aerosol acidity with particle size. *Geophysical Research Letters*, *29*(7), 1101, doi:10.1029/2001GL013881.

Keene, W. C., Pszenny, A. A. P., Galloway, J. N. & Hawley, M. E. (1986). Sea-salt corrections and interpretation of constituent ratios in marine precipitation. *Journal of Geophysical Research,91*(D6), 6647-6658.

Keene, W. C., Pszenny, A. A. P., Maben, J. R., Stevenson, E. & Wall, A. (2004). Closure evaluation of size-resolved aerosol pH in the New England coastal atmosphere during summer. *Journal of Geophysical. Research*, *109*(D23), 307, doi:10.1029/2004JD004801.

Keene, W. C., Sander, R., Pszenny, A. A. P., Vogt, R., Crutzen, P. J. & Galloway, J. N. (1998). Aerosol pH in the marine boundary layer: A review and model evaluation. *Journal of Aerosol Science*, *29*, 339-356.

Keene, W. C., & Savoie, D. L. (1998). The pH of deliquesced sea-salt aerosol in polluted marine air. *Geophysical Research Letter, 25*, 2181-2194.

Keene, W. C., Stutz, J., Pszenny, A. A. P., Maben, J. R., Fischer, E., Smith, A. M., von Glasow, R, Pechtl, S., Sive, B. C. & Varner, R. K. (2007). Inorganic chlorine and bromine in coastal New England air during summer. *Journal of Geophysical Research*, *112*, d10S12, doi:10.1029/2006JD007689.

Knotkova, D., Boschek, P., & Kreislova, K. (2005). Results of ISO CORRAG program: Processing of one-year data in respect to corrosivity classification. In W.W. Kirk, H. H. Lawson (Eds.) *Atmospheric Corrosion, ASTM STP 1239* (pp. 38-55). Philadelphia, PA: ASTM.

Leard, R., & Dante, J. F. (2003). in *Air Force Structural Integrity Program Conference*. 2003: Savannah GA.

LeBozec, N., Jonsson, M. & Thierry, D. (2004). Atmospheric corrosion of magnesium alloys: Influence of temperature, RH and chloride deposition. *Corrosion, 60*, 356-361.

Li, S. X. & Hihara, L. H. (2010). Atmospheric corrosion initiation on steel from predeposited NaCl salt particles in high humidity atmospheres. *Corrosion Engineering, Science and Technology 45*(1), 49-56.

Lyon, S.B., Thompson, G. E., & Johnson, J. B., (1992). Materials evaluation using wet-dry mixed salt-spray tests. In V.S. Agarwala, G. M. Ugiansky (Eds.), *New Methods for Corrosion Testing Aluminum Alloys*. (pp. 20-31). San Francisco, CA:ASTM.

Maier, B. & Frankel, G. (2011). Pitting corrosion of silica-coated type 304 stainless steel under thin electrolyte layers, *Corrosion, 67*(3), 035004-1 – 035004-10.

Mansfeld, F. & J. Kenkel, J. (1976). Electrochemical monitoring of atmospheric corrosion phenomena. *Corrosion Science, 16*(3), 113-122.

Pickens, R., Gordon, J. & Green, J. (1983). The effect of loading mode on the stress-corrosion cracking of aluminum alloy 5083. *Metallurgical Transactions A., 14*(4), 925-930.

Placzankis, B., Miller, C., & Mullis, B. (2001). *Examination of nonchromate conversion coatings for aluminum armor from three final candidates using accelerated corrosion and adhesion test methods.*, DTIC Document.

Price, K., Dante, J. F., Buckingham, J. P (2007)., *CPC performance in occluded sites*, in *CORROSION/2007*, Paper No. 07226, NACE International, Houston, TX.

Pszenny, A. A. P., Moldanová, J., Keene, W. C., Sander, R., Maben, J. R., Martinez, M., Crutzen, P. J., Perner, D. & Prinn, R. G. (2004), Halogen cycling and aerosol pH in the Hawaiian marine boundary layer, *Atmospheric Chemistry and Physics*, *4*, 147-168 (www.atmos-chem-phys.org/acp/4/147).

Rihan, R., Raman, R. K. S., Ibrahim, R. N. (2005). Circumferential notched tensile testing of cast iron for determination of threshold KISCC for caustic crack propagation. *Materials Science and Engineering 407*(1), 207-212.

SAE (2003). *SAE J2334 laboratory cyclic corrosion test*. SAE International, Automotive Corrosion And Prevention Committee: Warrendale, PA.

Schneider, O. & Kelly, R. (2007). Localized coating failure of epoxy-coated aluminum alloy 2024-T3 in 0.5 M NaCl solutions: Correlation between coating degradation, blister formation and local chemistry within blisters. *Corrosion Science 49*(2), 594-619.

Scully, J.R., (2000). Polarization resistance method for determination of instantaneous corrosion rates. *Corrosion, 56*(2), 199-218.

Scully, J., Young,, G. & Smith, S. (2012). Hydrogen embrittlement of aluminum and aluminum-based alloys. In R. Gangloff & B. Somerday (Eds.), *Gaseous hydrogen embrittlement of materials in energy technologies* (p. 864), Sawston, Cambridge: Woodhead Publishing.

Seinfeld, J. & Pandis, S. (2012). *Atmosheric chemistry and physics: From air pollution to climate change*, (pp. 1232) New York, NY: Wiley.

Searles, J., Gouma, P. & Buchheit, R. (2001). Stress corrosion cracking of sensitized AA5083. *Metallurgical and Materials Transactions A, 32A*, 2859-2867.

Shastry, C., Levy, M. & Joshi, A. (1981). The effect of solution treatment temperature on stress corrosion susceptibility of 7075 aluminum alloy. *Corrosion Science, 21*, 673-688.

Sheetz, A.D. (2000). *Comparison of accelerated corrosion test results on aluminum substrates for U.S. Marine Corps applications*, in *NSWCCD-61-TR-2000/18*.

Speidel, M. (1984). Hydrogen embrittlement and stress corrosion cracking of aluminum alloys. In M. Speidel (Ed.), *Hydrogen embrittlement and stress corrosion cracking* (pp. 271-295). Materials Park, OH: ASM International.

Sprowls, D. (1984). *A study of environmental characterization of conventional and advance aluminum alloys for selection and design: Phase I literature review*, Alcoa, NASA Contract Report No. 172387, August 31, 1984, p. 1-100.

Sprowls D. & Brown, R. (1967, September). *Stress corrosion mechanisms for aluminum alloys*. Paper presented at the International Conference on Fundamental Aspects of Stress Corrosion Cracking, Columbus, Ohio.

Stratmann, M. & Streckel, H. (1990). On the atmospheric corrosion of metals which are covered with thin electrolyte layers : I. Verification of the experimental technique. *Corrosion Science, 30*(6-7), 681-696.

Turekian, V. C., Macko, S. A. & Keene, W. C. (2003). Concentrations, isotopic compositions, and sources of size-resolved, particulate organic carbon and oxalate in near-surface marine air at Bermuda during spring, *Journal of Geophysical Research, 108*(D5), 4157, doi:10.1029/2002JD002053.

Vera Cruz, R., Nishikata, A. & Tsuru, T. (1996). AC impedance monitoring of pitting corrosion of stainless steel under a wet-dry cyclic confition in chloride-containing environment. *Corrosion Science, 38,*(8), 1397-1406.

Vera Cruz, R., Nishikata, A. & Tsuru, T. (1998) Pitting corrosion mechanism of stainless steels under wet-dry exposure in chloride-containing environments. *Corrosion Science*, 40,(1), 125-139.

Weissenrieder, J. & Leygraf, C. (2004). In-situ studies of filiform corrosion of iron. *Journal of the Electrochemical Society, 151*(3), B165-B171.

Zhao, X. & Frankel, G. (2006). Effects of relative humidity, temper, and stress on exfoliation corrosion kinetics of AA7178. *Corrosion*, *62*(11), 956-966.

Zhou, X., Davis, A. J., Kieber, D. J. , Keene, W. C., Maben, J. R., Maring, H., Dahl, E. E., M.A. Izaguirre, M. A., Sander, R. & Smoydzyn, L. (2008). Photochemical production of hydroxyl radical and hydroperoxides in water extracts of nascent marine aerosols produced by bursting bubbles from Sargasso seawater. *Geophysical Research. Letter*, 35, L20803, doi:10.1029/2008GL035418.

APPENDIX A
FULL-SIZED PICTURES AND GRAPHS

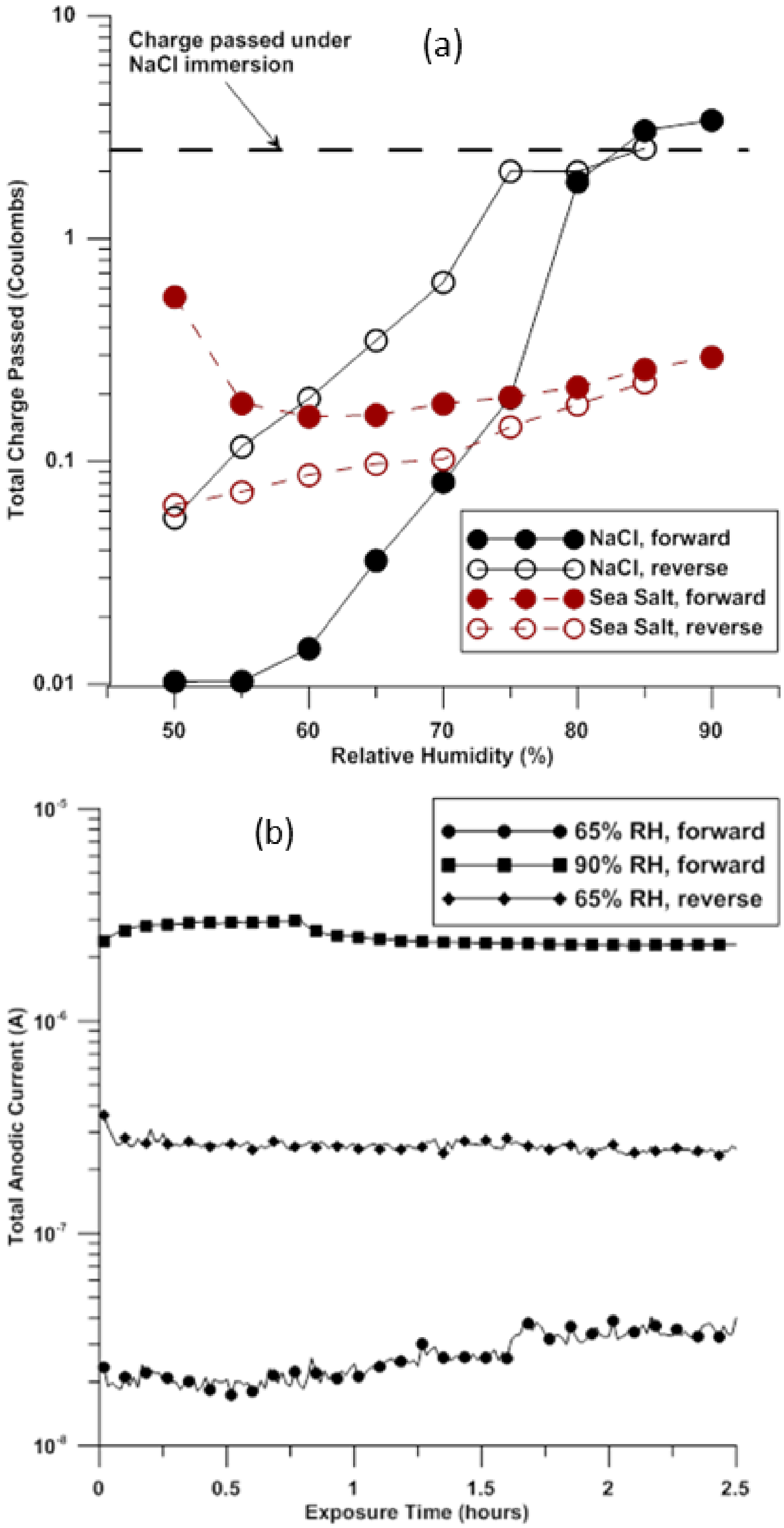

Figure 21. (a) Total charge passed at various values of RH under a 2.7 mg deposit of NaCl or Sea Salt. Each RH values was held for 2.5 hours. Open circles represent stepping from higher RH values down. (b) Total anodic current passed under a NaCl deposit at select values of RH during the stepped RH experiment.

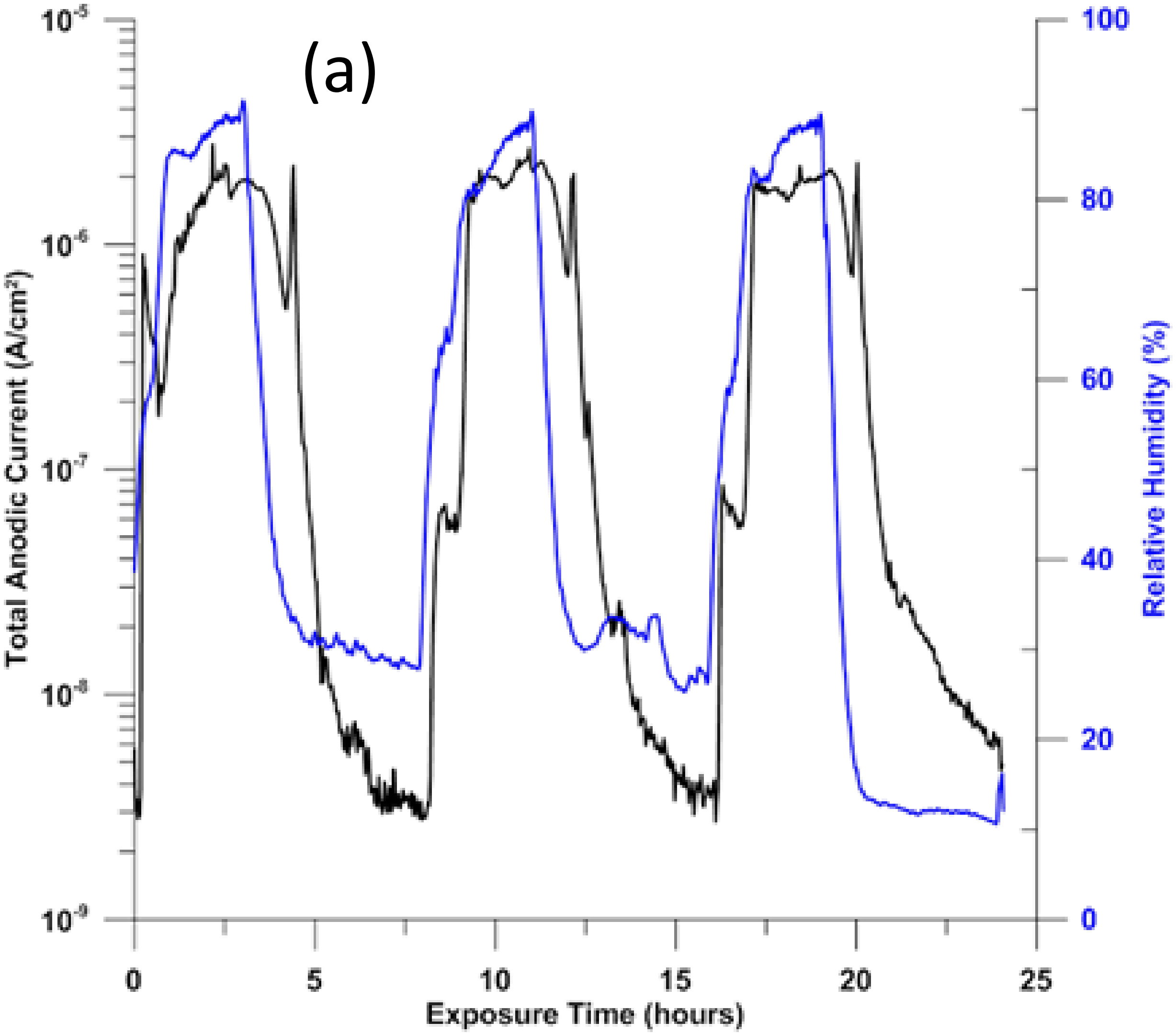
(a)
Total Anodic Current (A/cm²)
10^{-5}
10^{-6}
10^{-7}
10^{-8}
10^{-9}
Relative Humidity (%)
100
80
60
40
20
0
0
5
10
15
20
25
Exposure Time (hours)

Figure 25a.

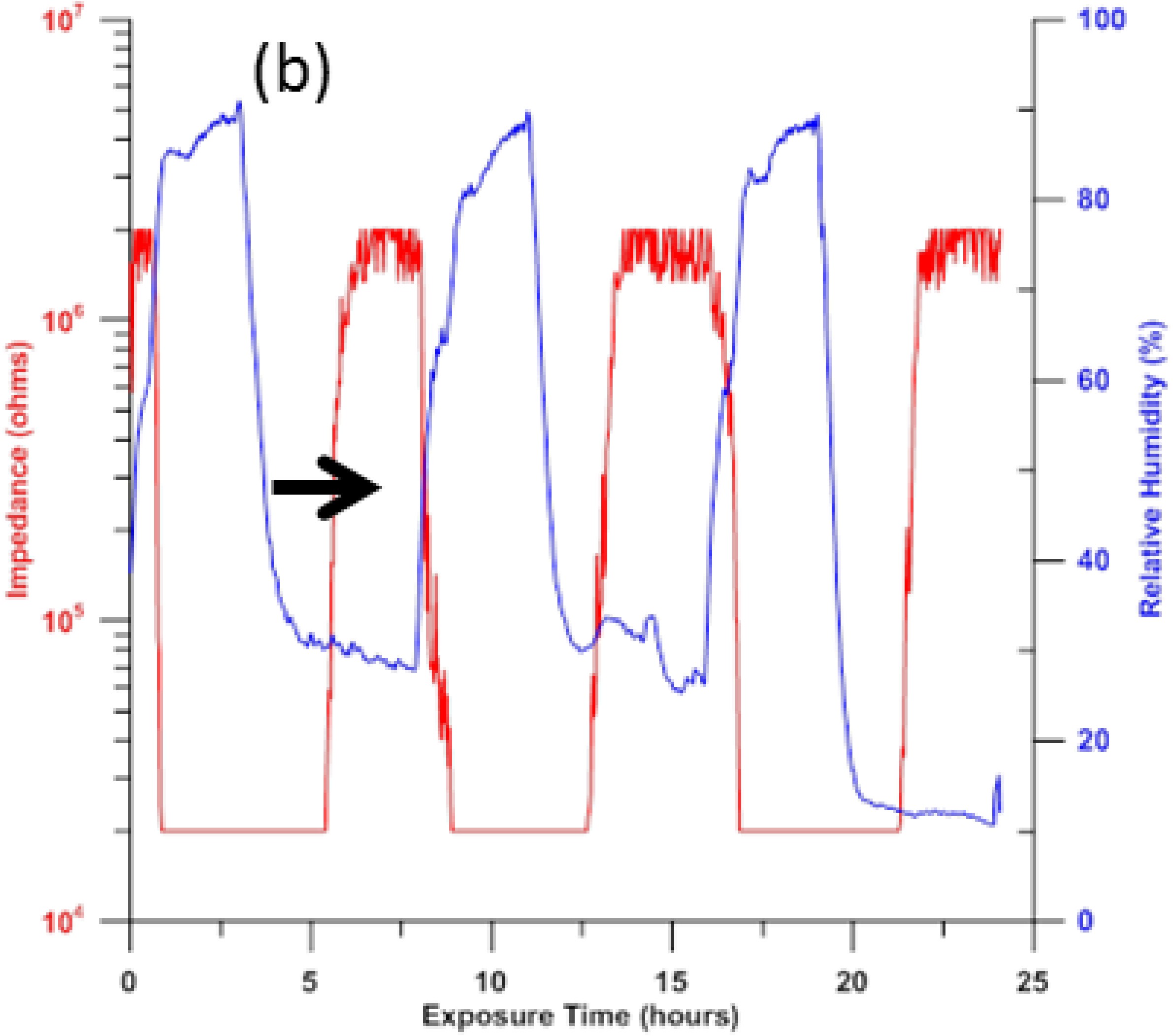
(b)
10⁷
10⁶
10⁵
10⁴
Impedance (ohms)
100
80
60
40
20
0
Relative Humidity (%)
0
5
10
15
20
25
Exposure Time (hours)

Figure 25b.

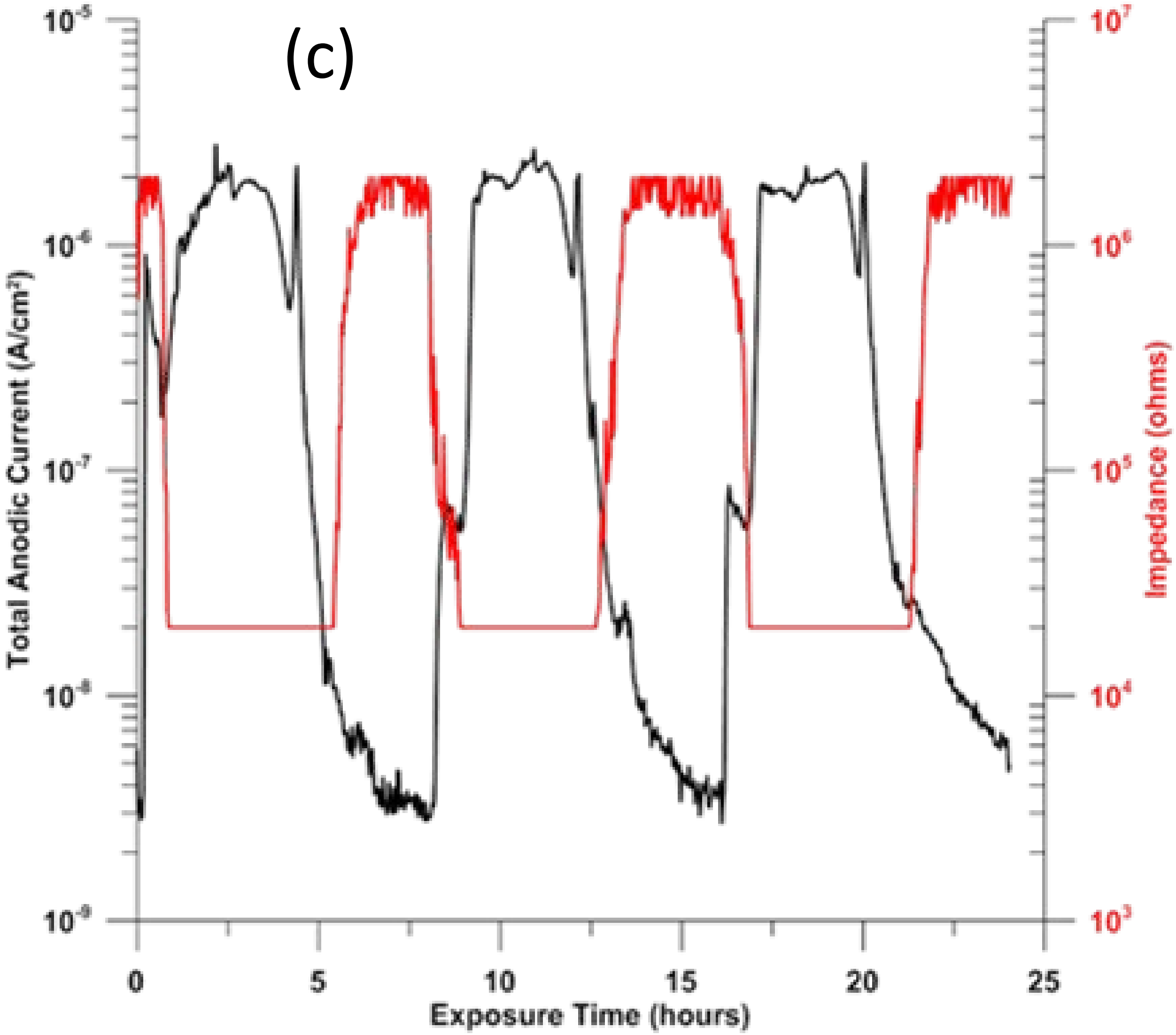
(c)
Total Anodic Current (A/cm²)
Impedance (ohms)
Exposure Time (hours)
10⁻⁵
10⁻⁶
10⁻⁷
10⁻⁸
10⁻⁹
10⁷
10⁶
10⁵
10⁴
10³
0
5
10
15
20
25

Figure 25c.

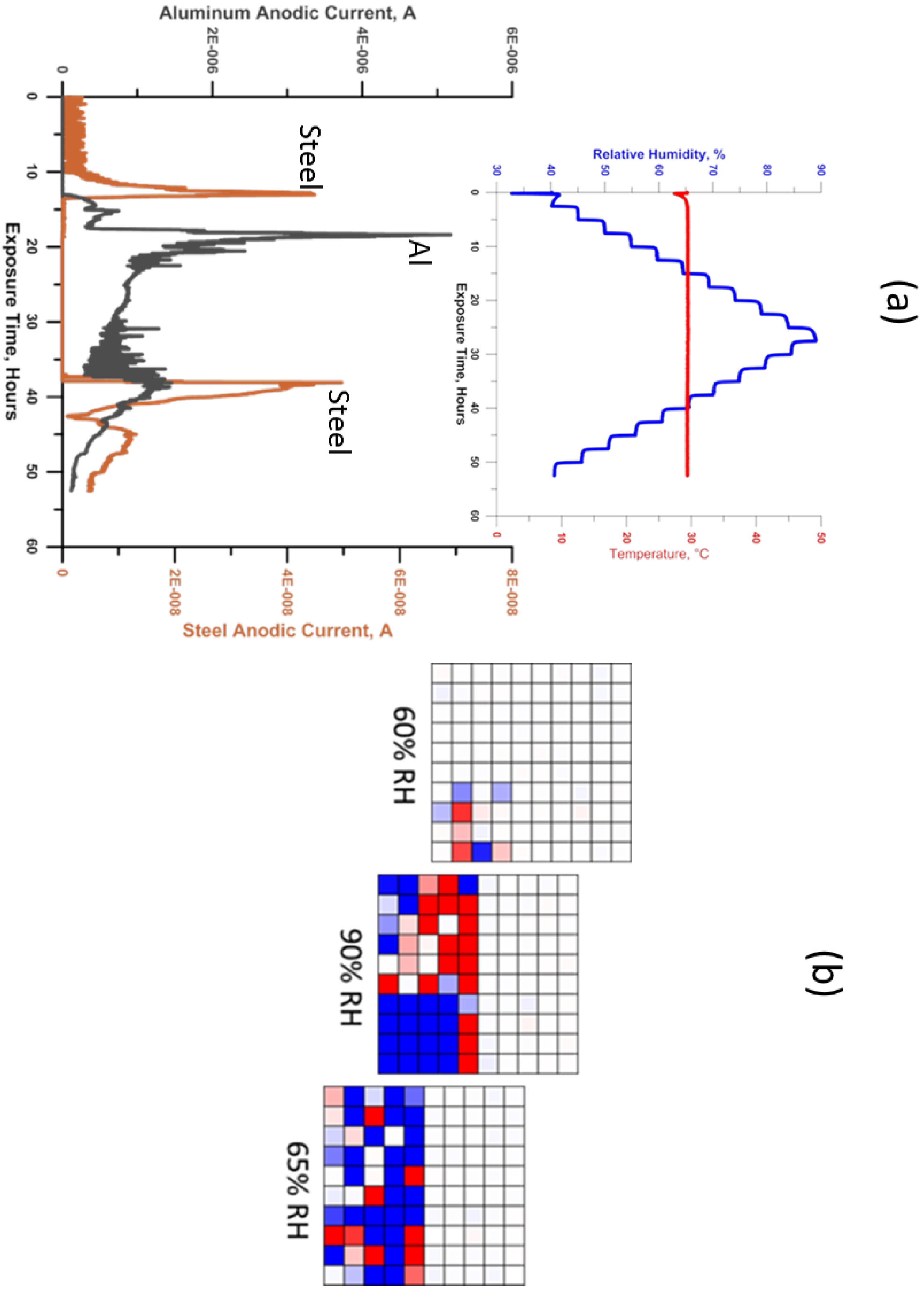
(a)
Relative Humidity, %
30
40
50
60
70
80
90
Exposure Time, Hours
0
10
20
30
40
50
60
Temperature, °C
0
10
20
30
40
50
Aluminum Anodic Current, A
0
2E-006
4E-006
6E-006
Steel
Al
Steel
Exposure Time, Hours
0
10
20
30
40
50
60
Steel Anodic Current, A
0
2E-008
4E-008
6E-008
8E-008
(b)
60% RH
90% RH
65% RH

Figure 32.

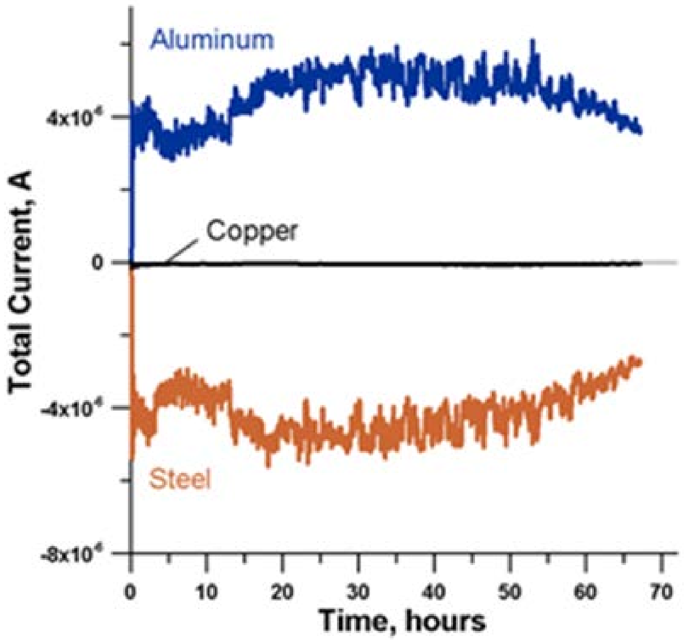

ASTM B117

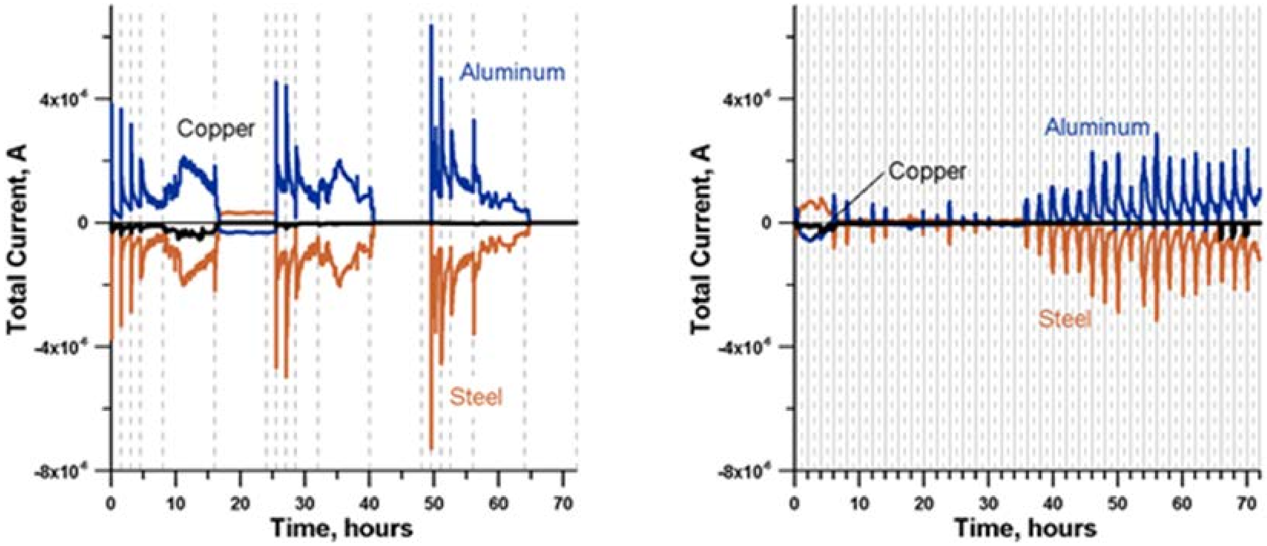

GM 9540P

ASTM G85-A5

Figure 33.

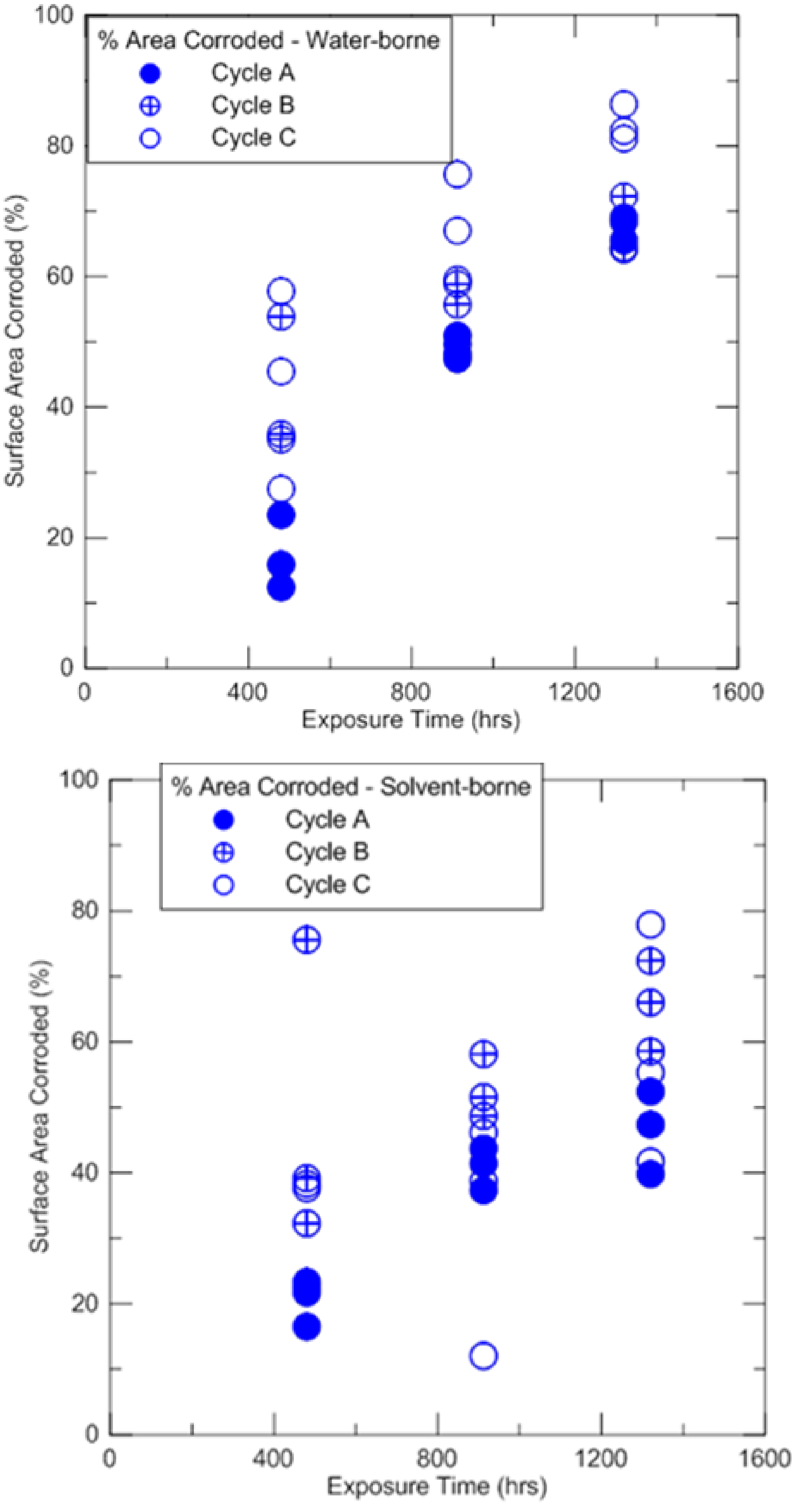

Figure 73. Surface area corroded.

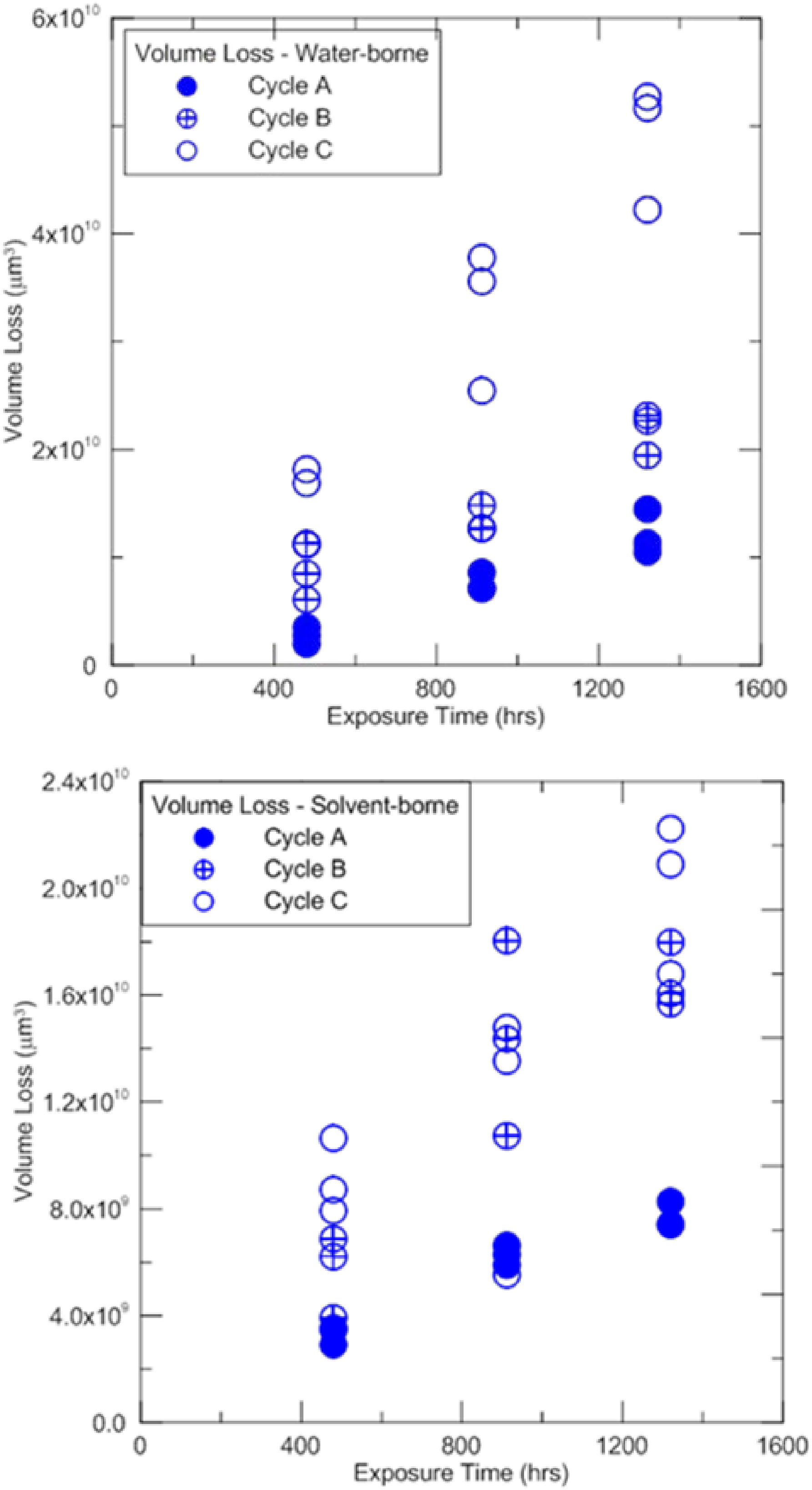

Figure 73. Volume loss.

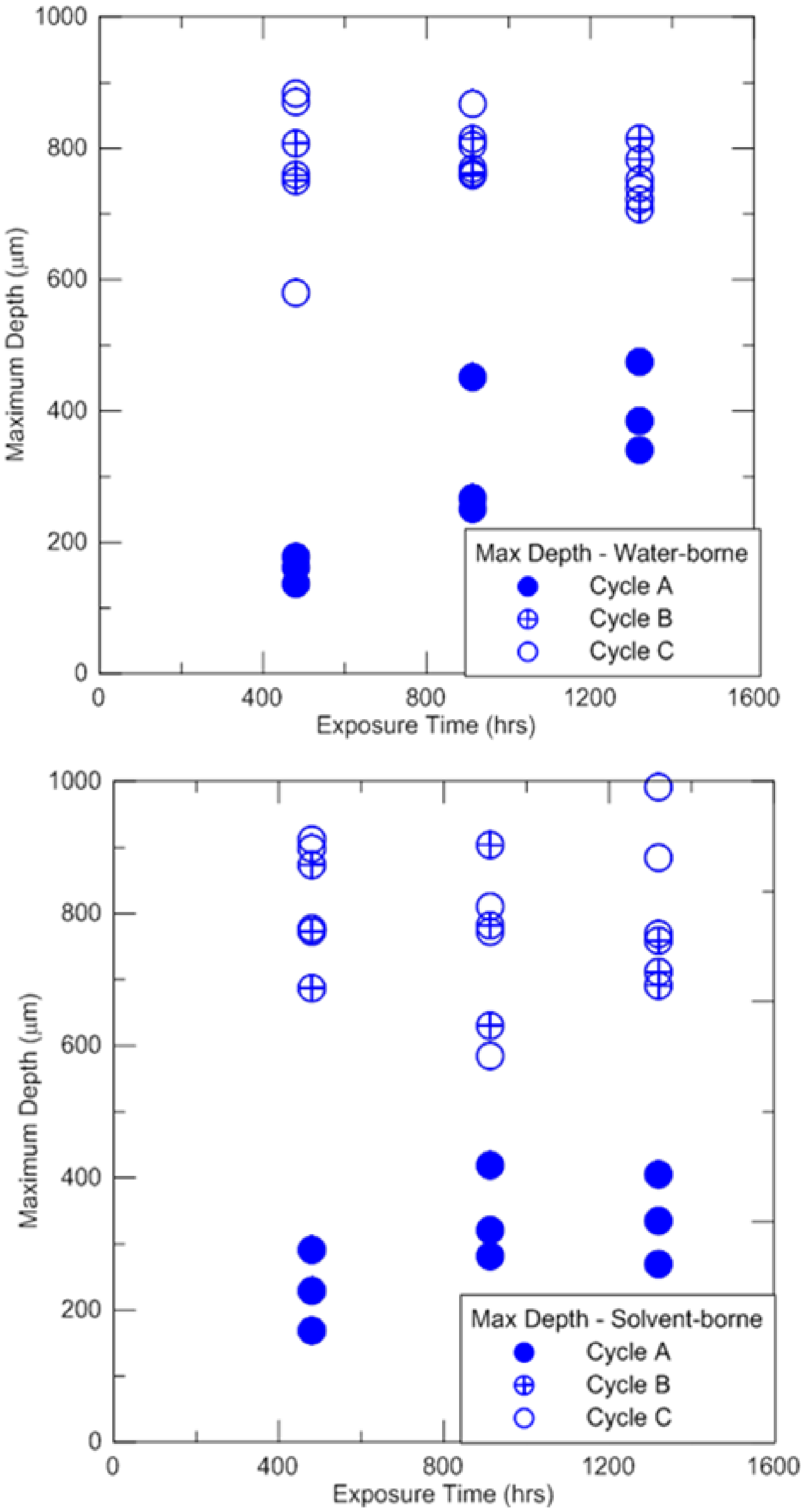

Figure 74. Maximum depth.

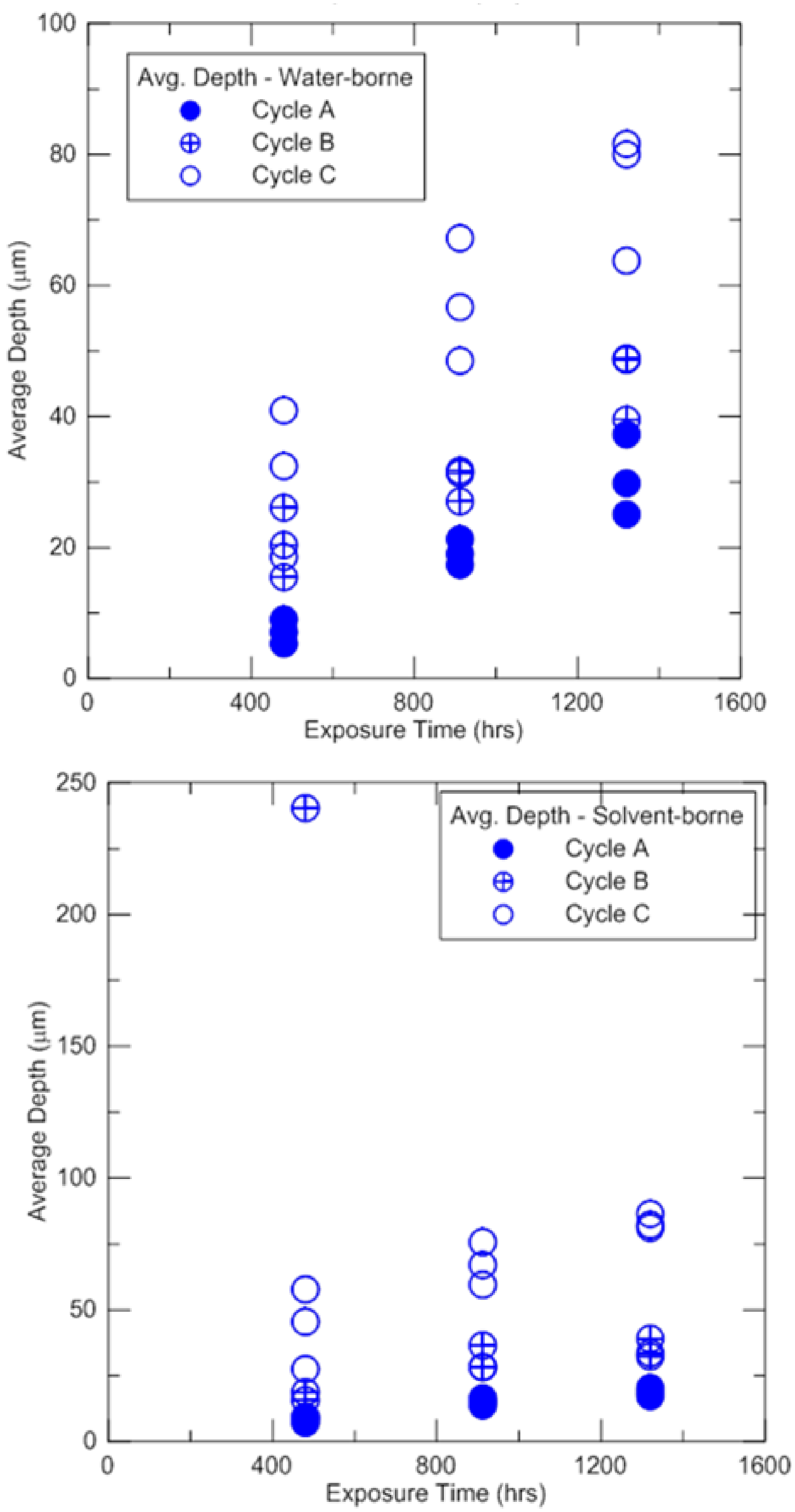

Figure 74. Average depth.

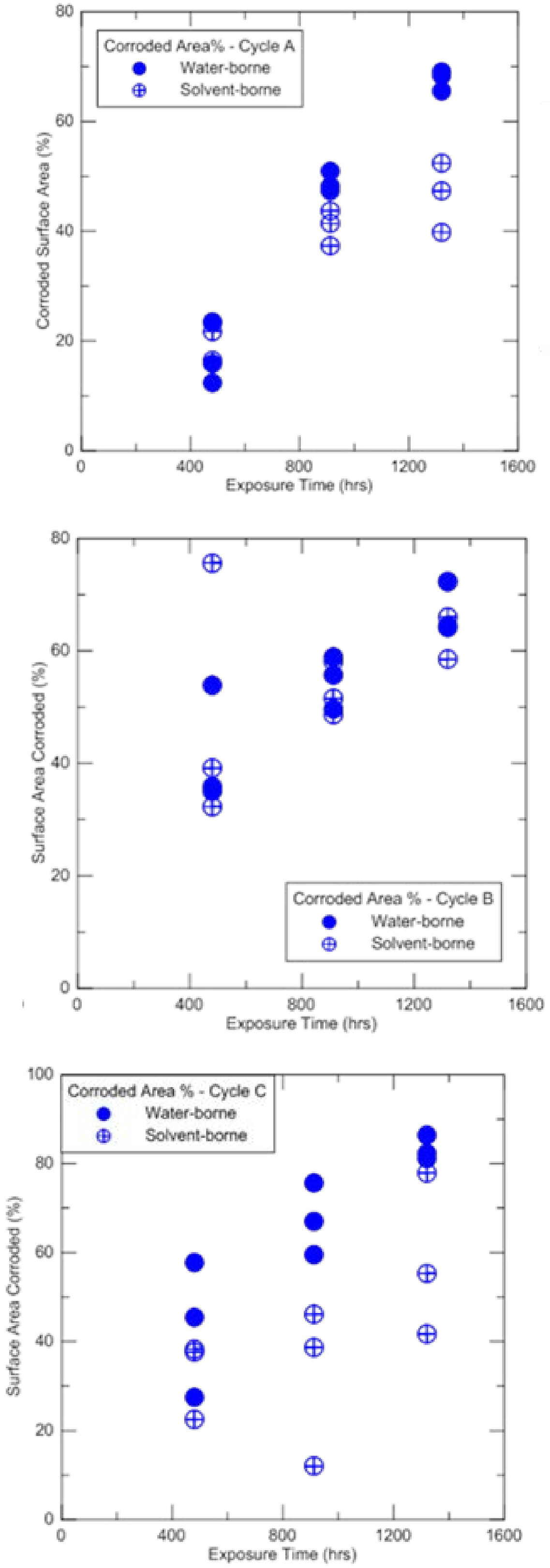

Figure 75. Corroded area %.

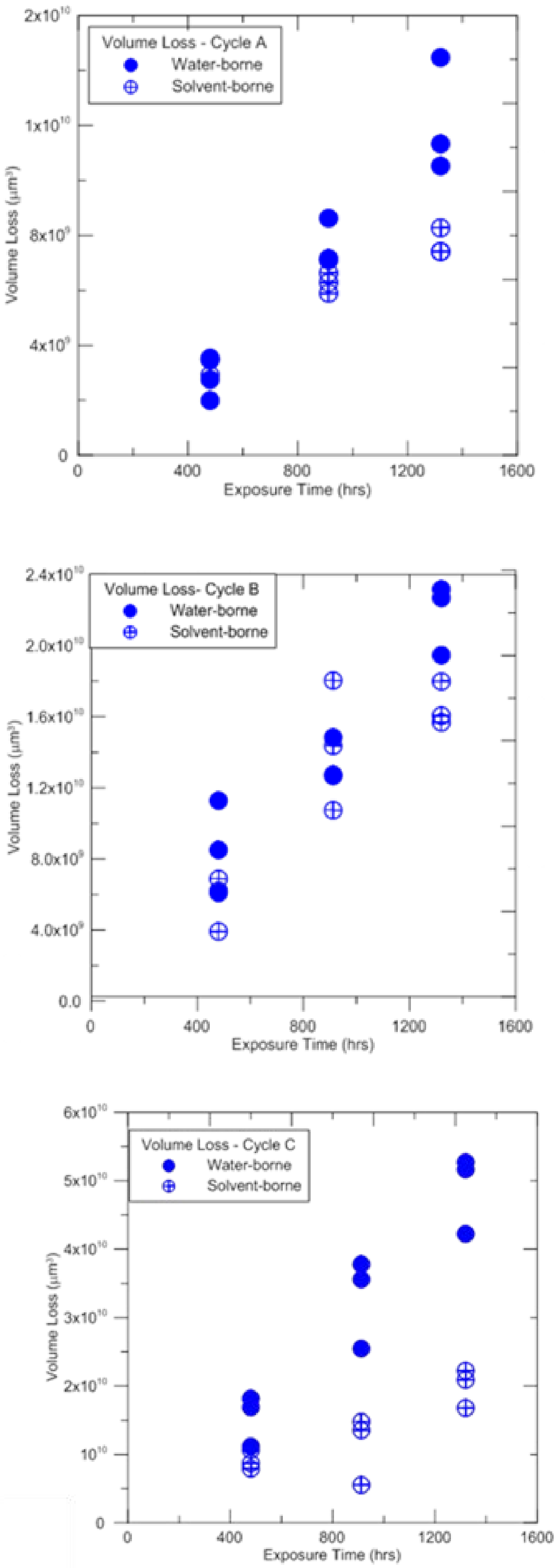

Figure 75. Volume loss.

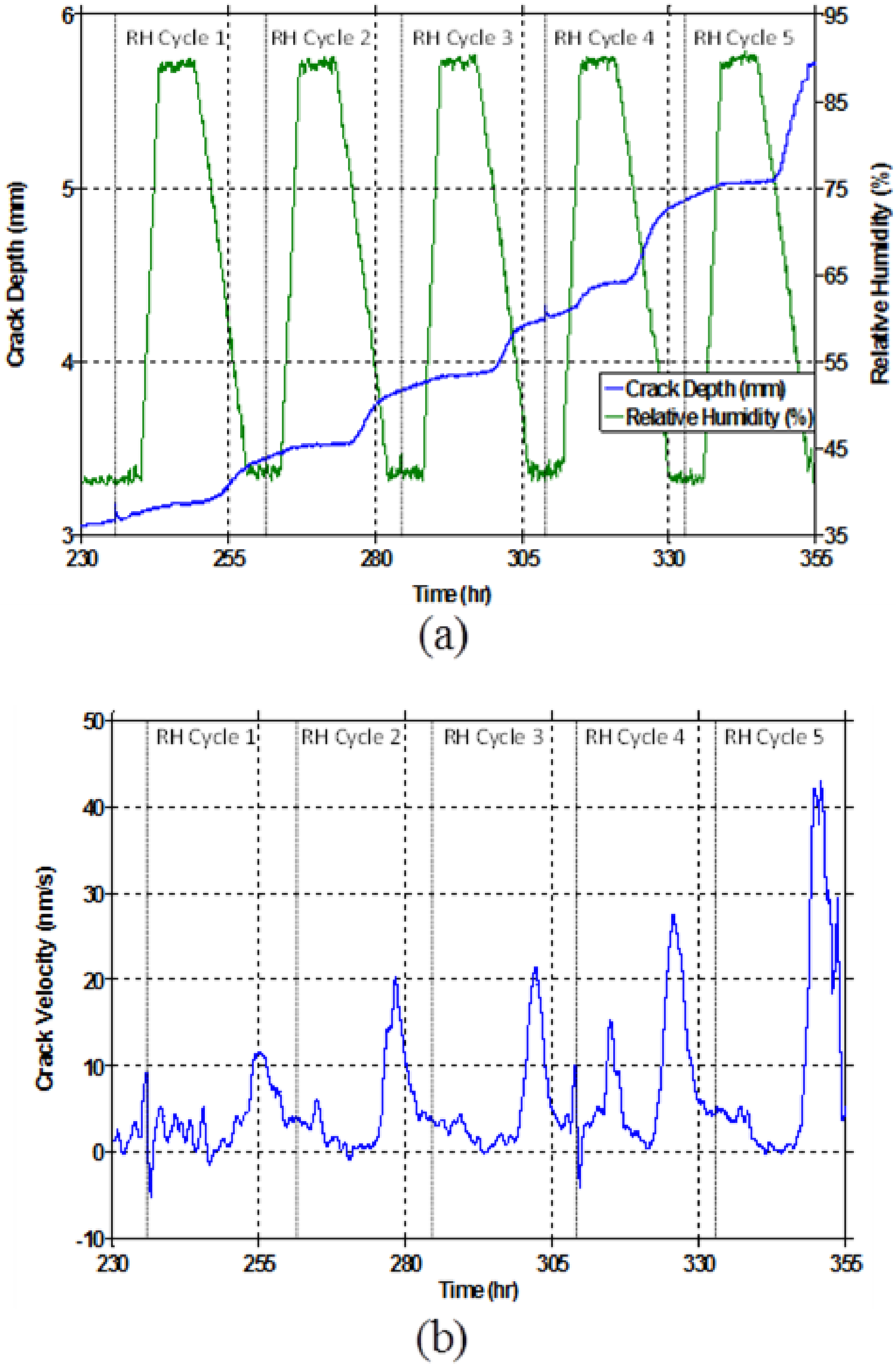
RH Cycle 1
RH Cycle 2
RH Cycle 3
RH Cycle 4
RH Cycle 5
Crack Depth (mm)
Relative Humidity (%)
6
5
4
3
95
85
75
65
55
45
35
230
255
280
305
330
355
Time (hr)
Crack Depth (mm)
Relative Humidity (%)
RH Cycle 1
RH Cycle 2
RH Cycle 3
RH Cycle 4
RH Cycle 5
Crack Velocity (nm/s)
50
40
30
20
10
0
-10
230
255
280
305
330
355
Time (hr)

(a)

(b)

Figure 98.

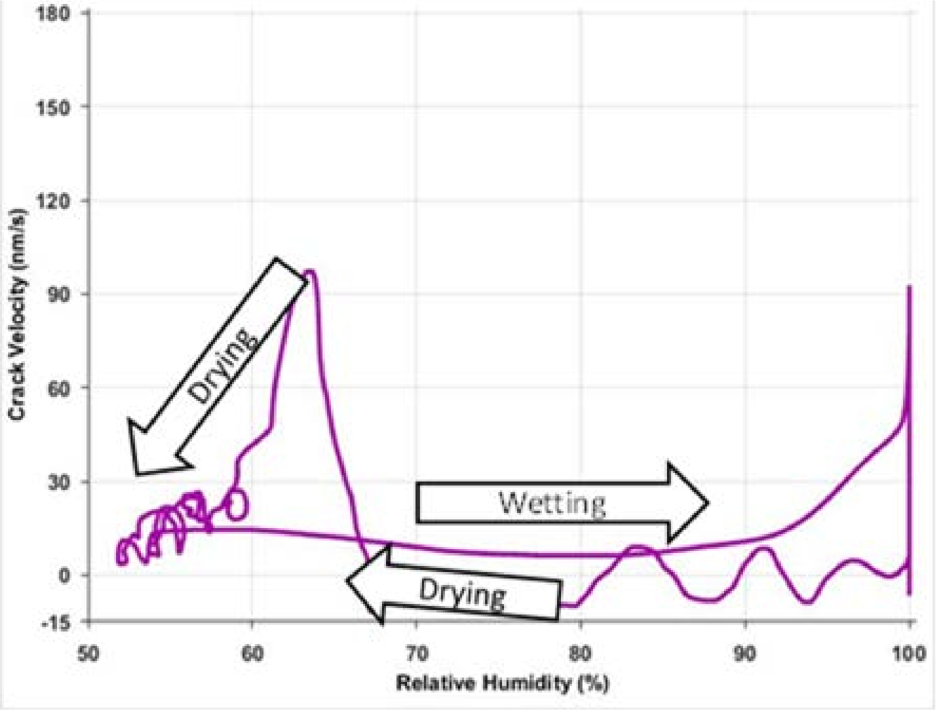

Cycle 1

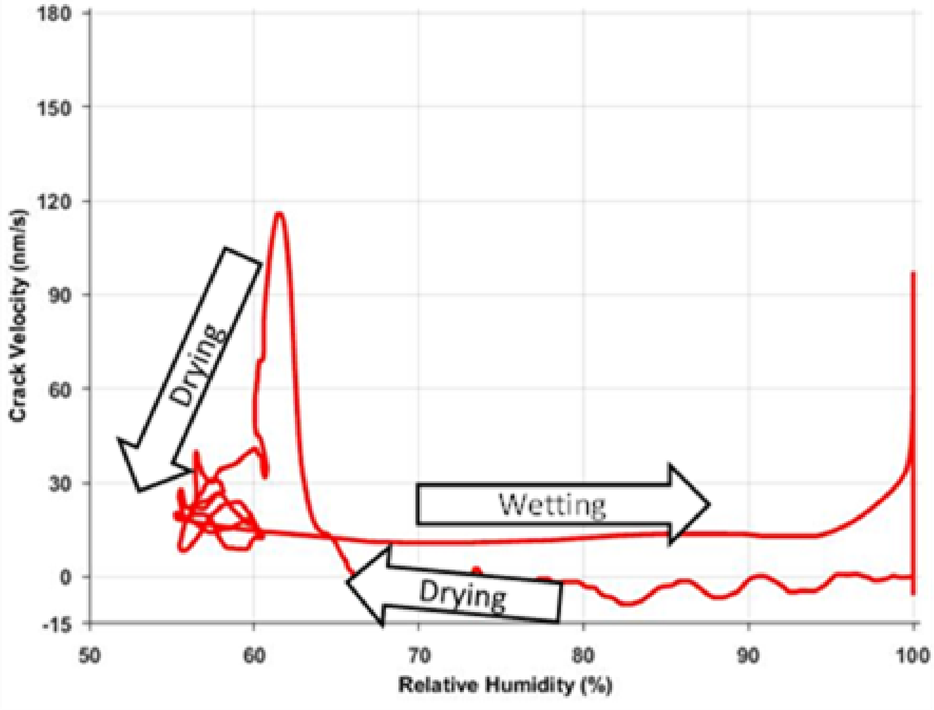

Cycle 2

Figure 108. Cycles 1 and 2.

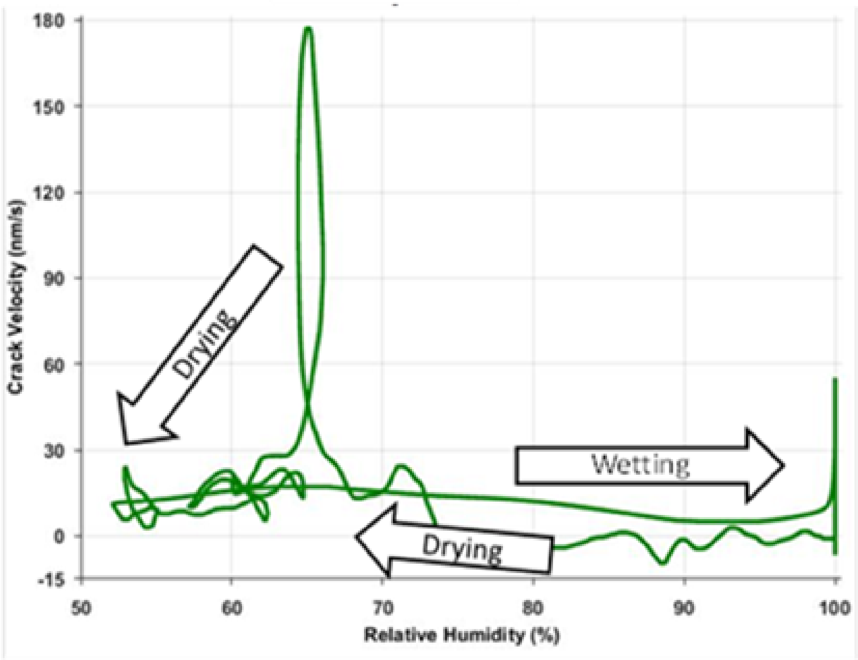

Cycle 3

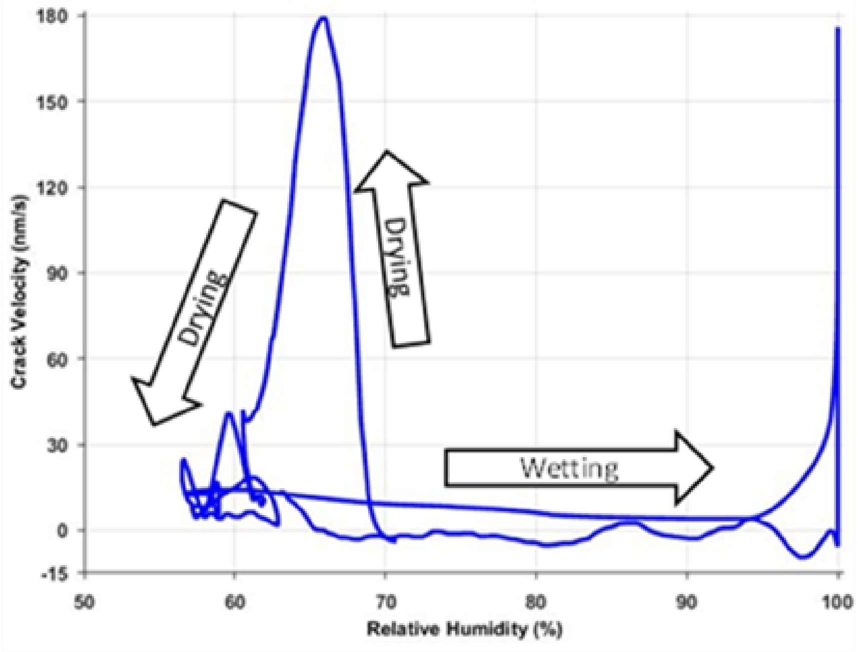

Cycle 4

Figure 108. Cycles 3 and 4.

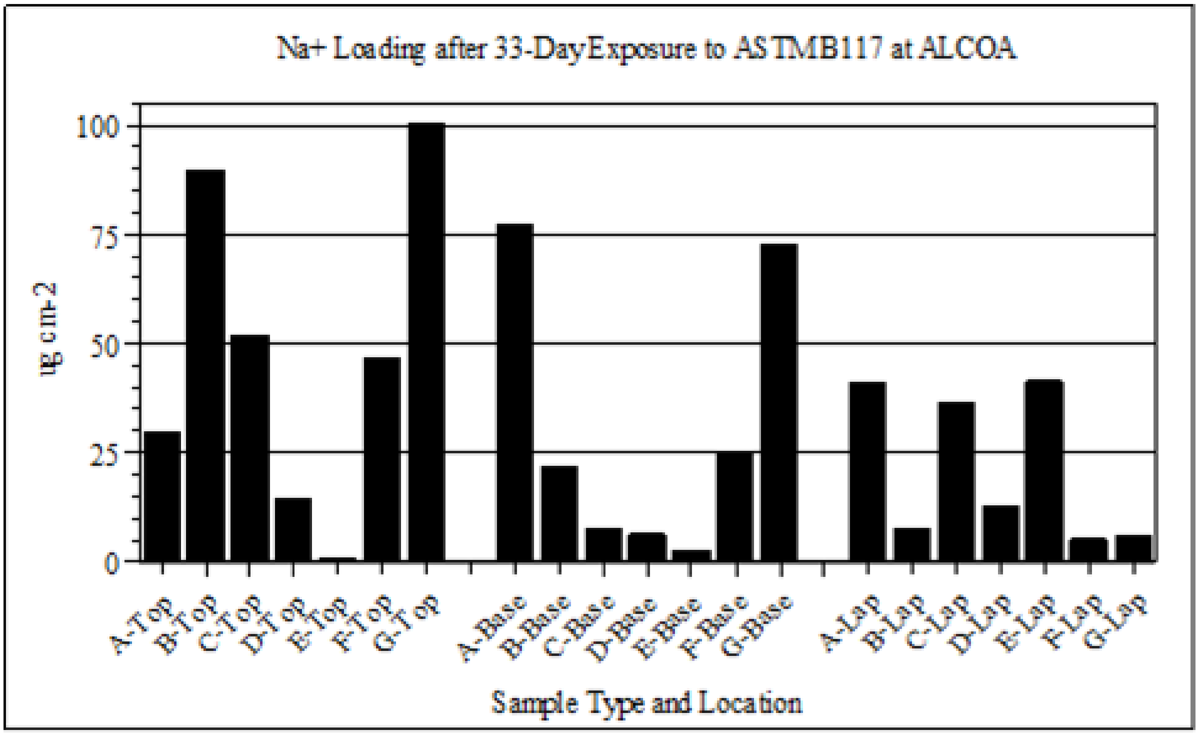

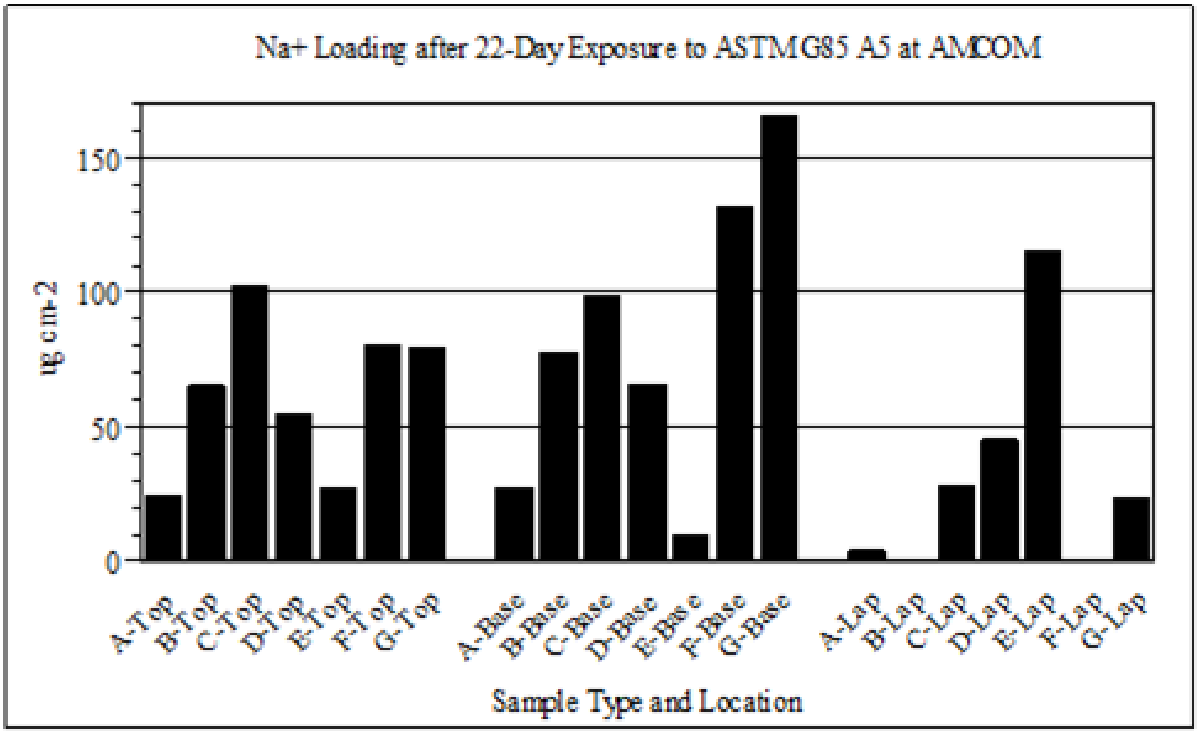

Figure 145. ALCOA and AMCOM sites.

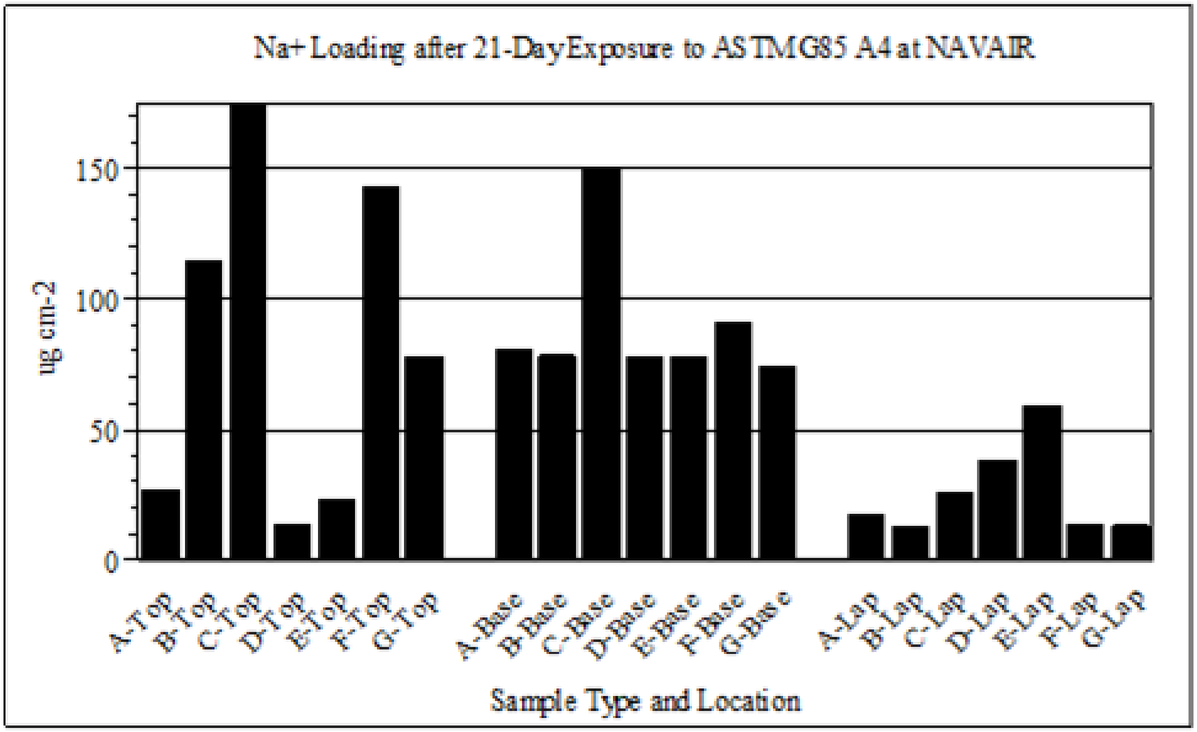

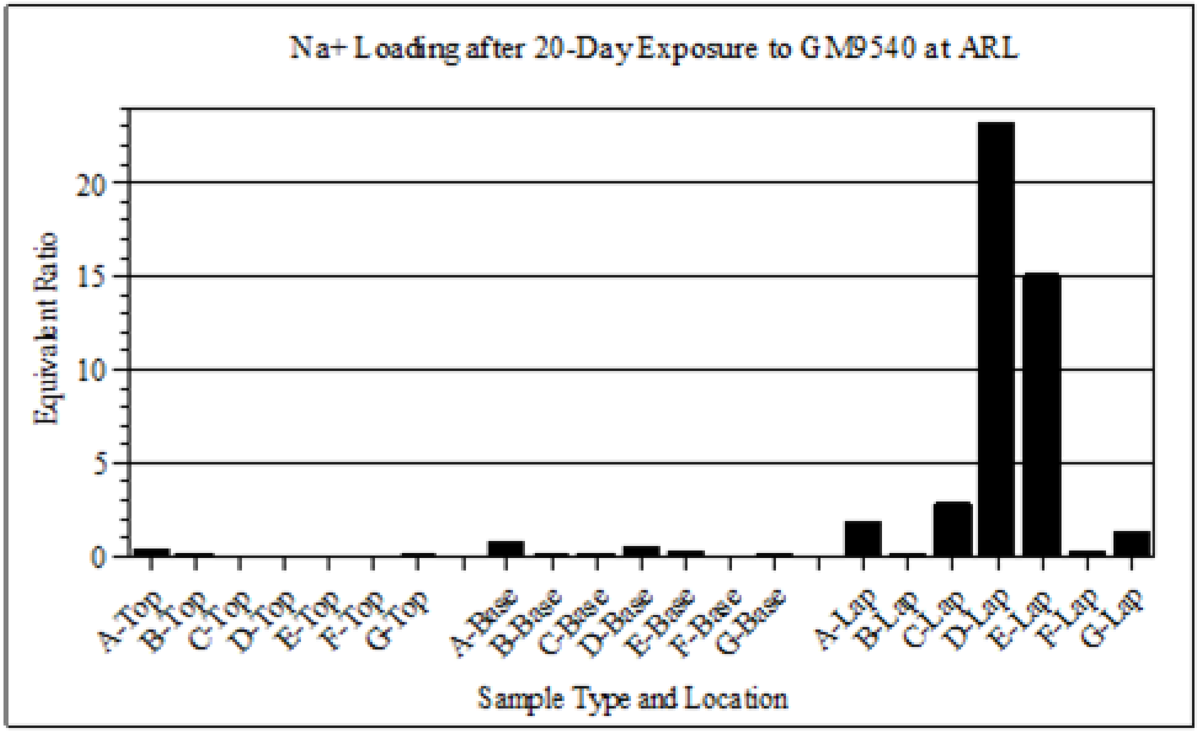

Figure 145. NAVAIR and ARL sites.

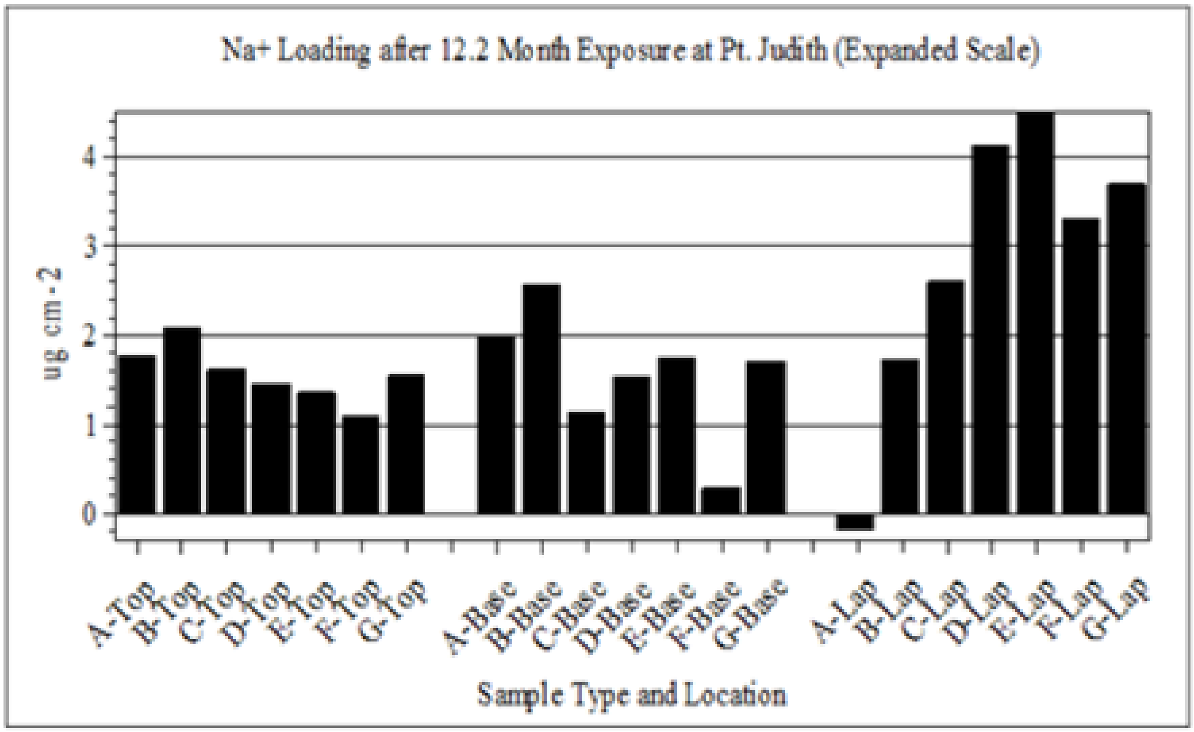

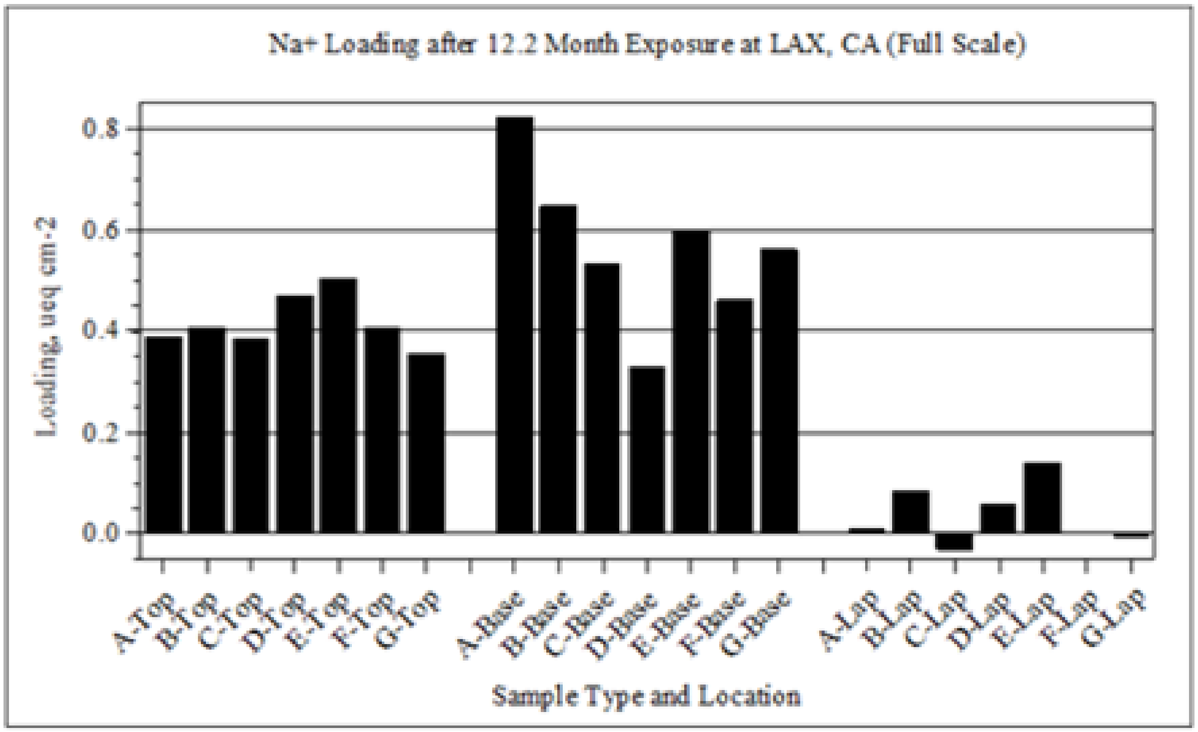

Figure 146. Pt. Judith and LAX, CA sites.

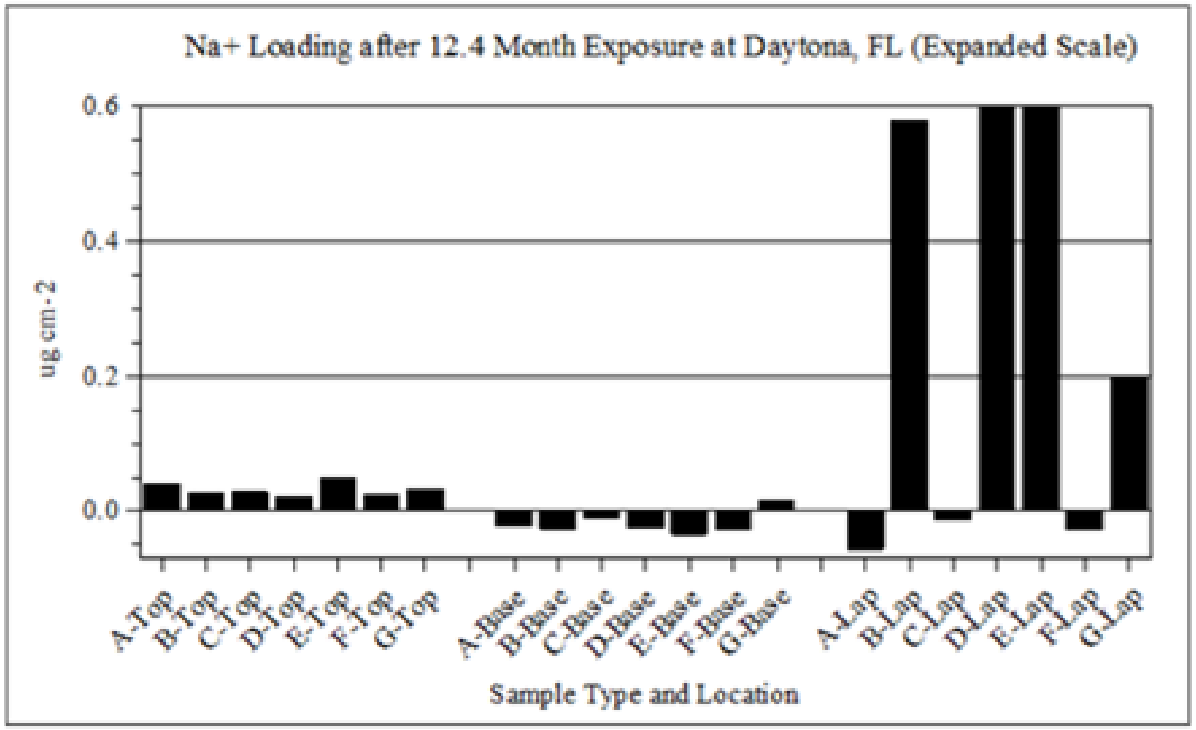

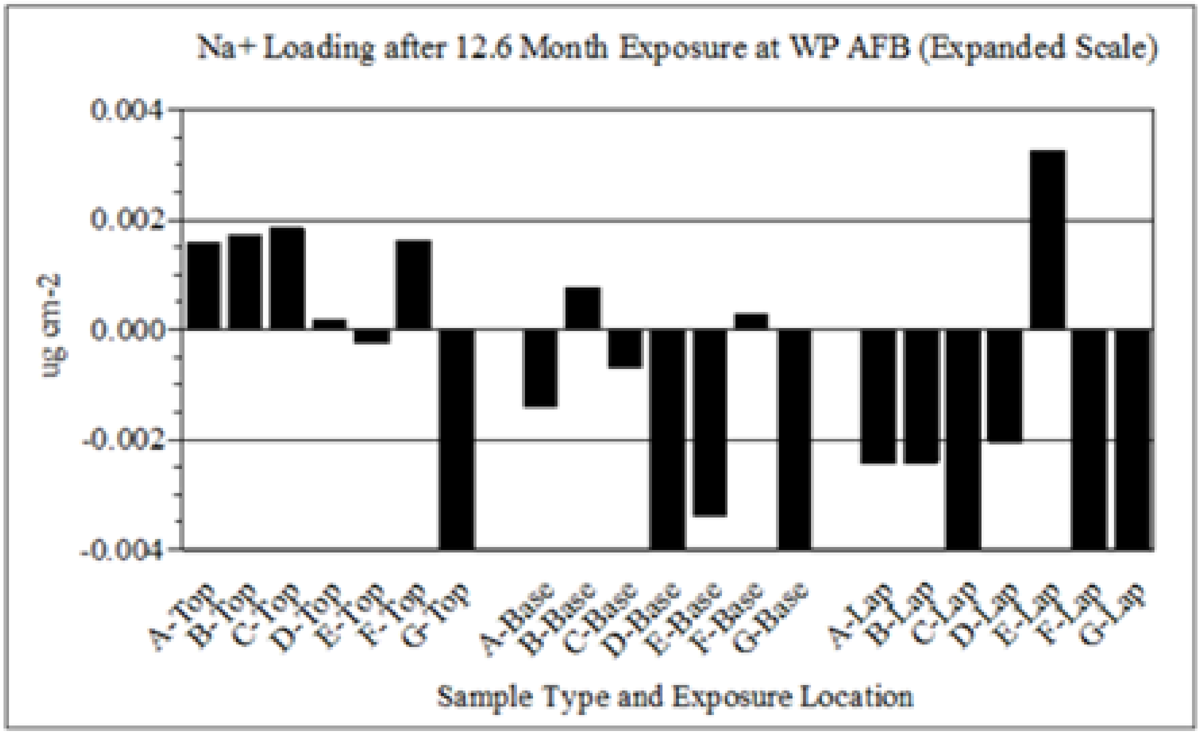

Figure 146. Daytona, FL and WPAFB sites.

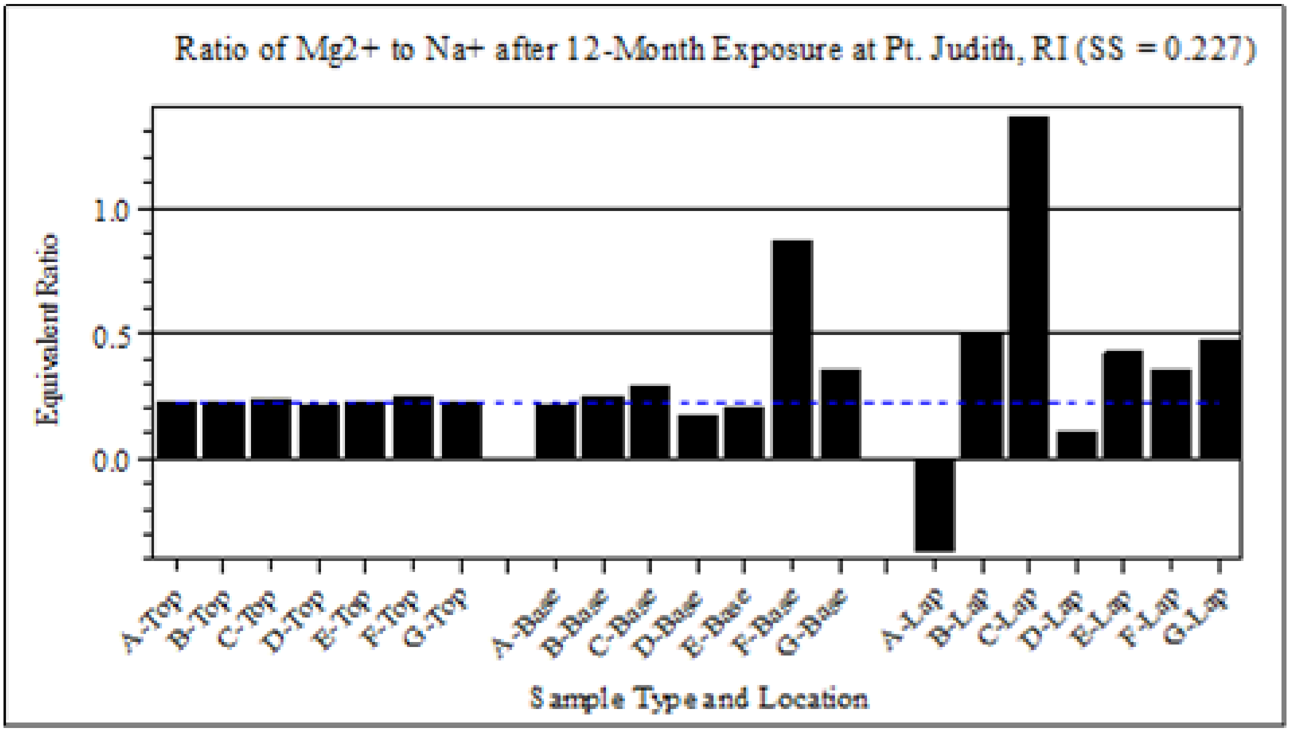

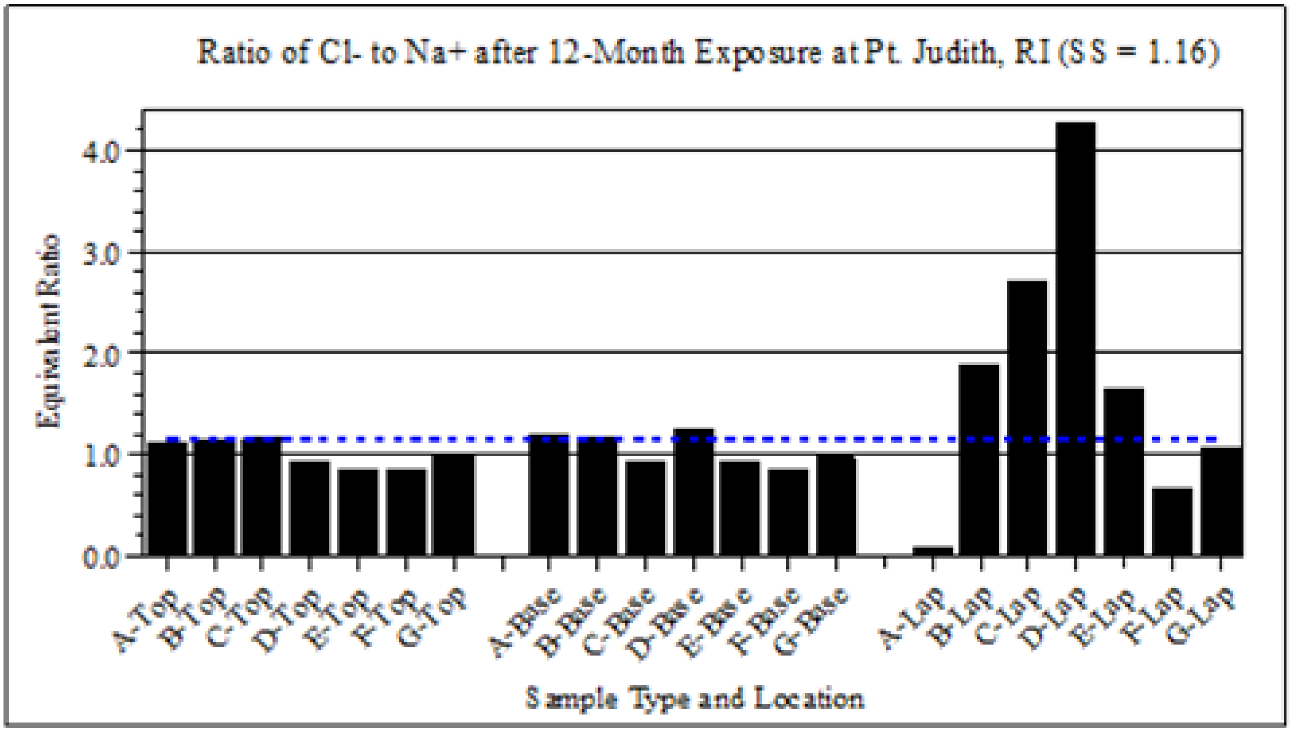

Figure 147. Ratio of Mg^{2+} to Na^{+} and ratio of Cl^{-} to Na^{+}.

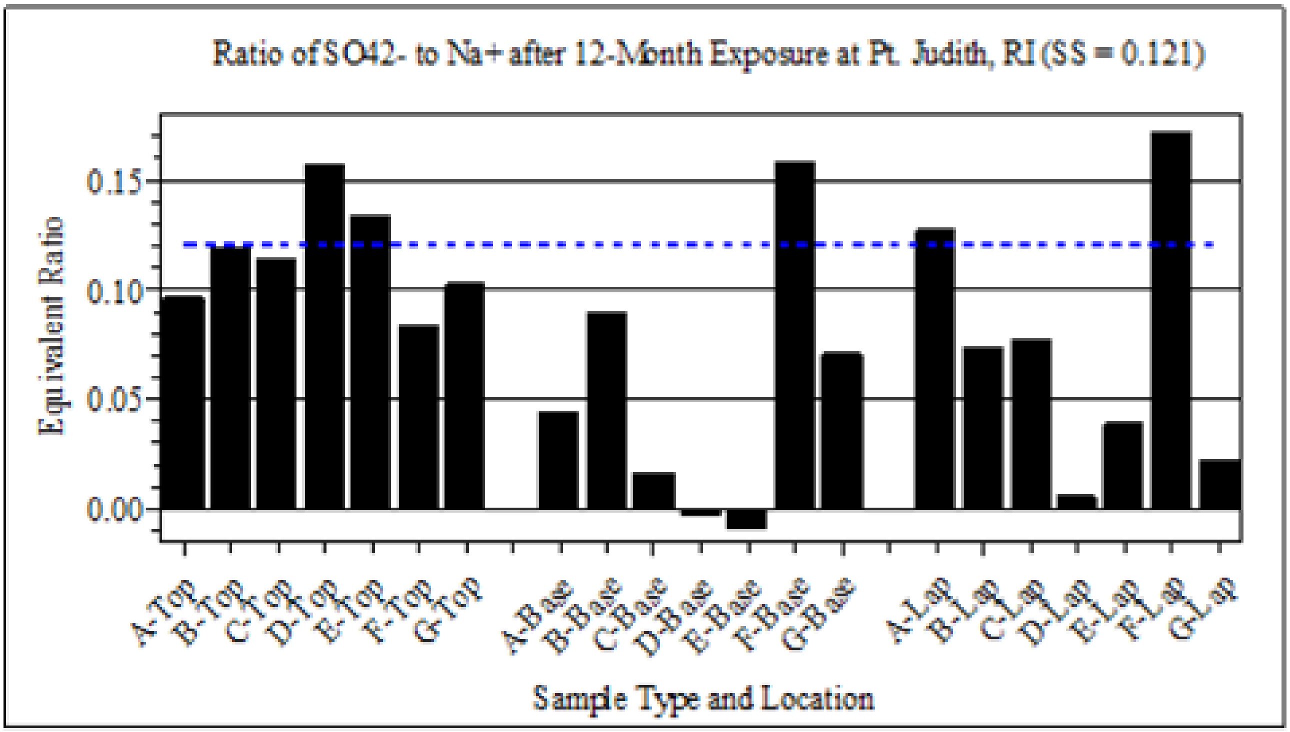

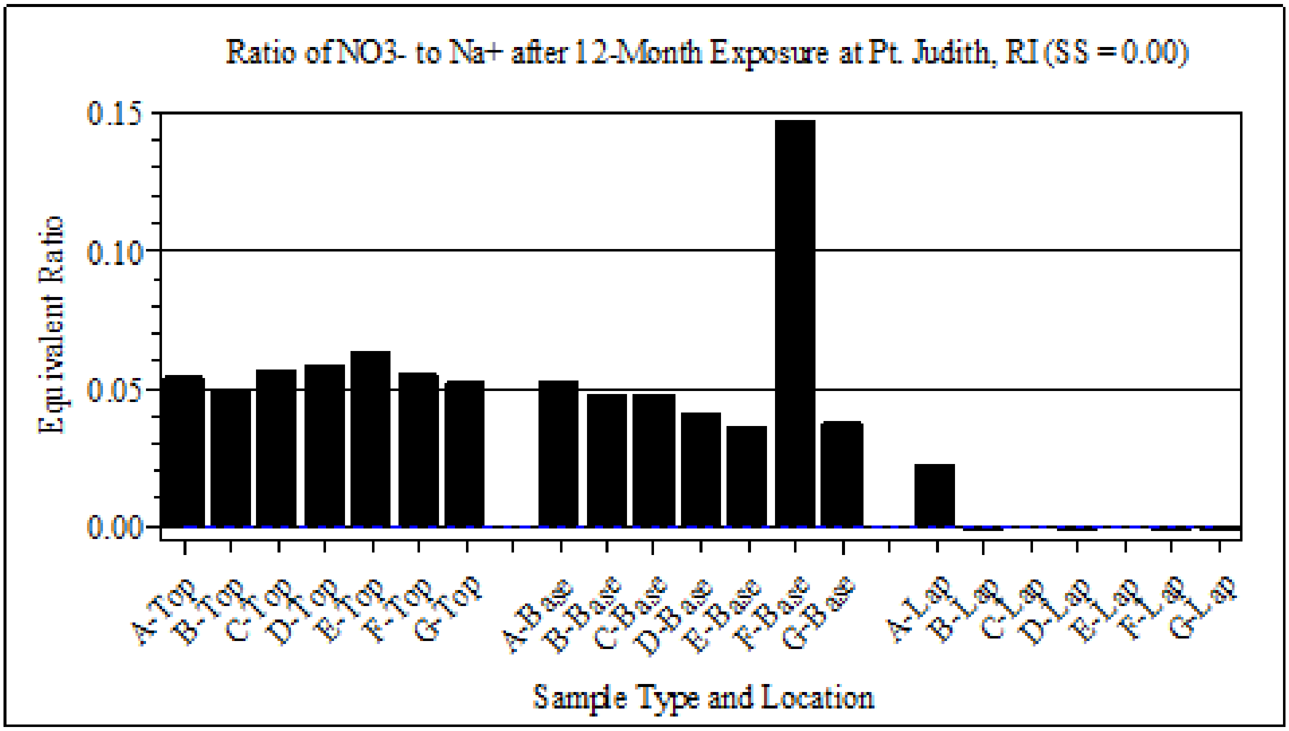

Figure 147. Ratio of SO_4^{2-} to Na^+ and ratio of NO_3^- to Na^+.

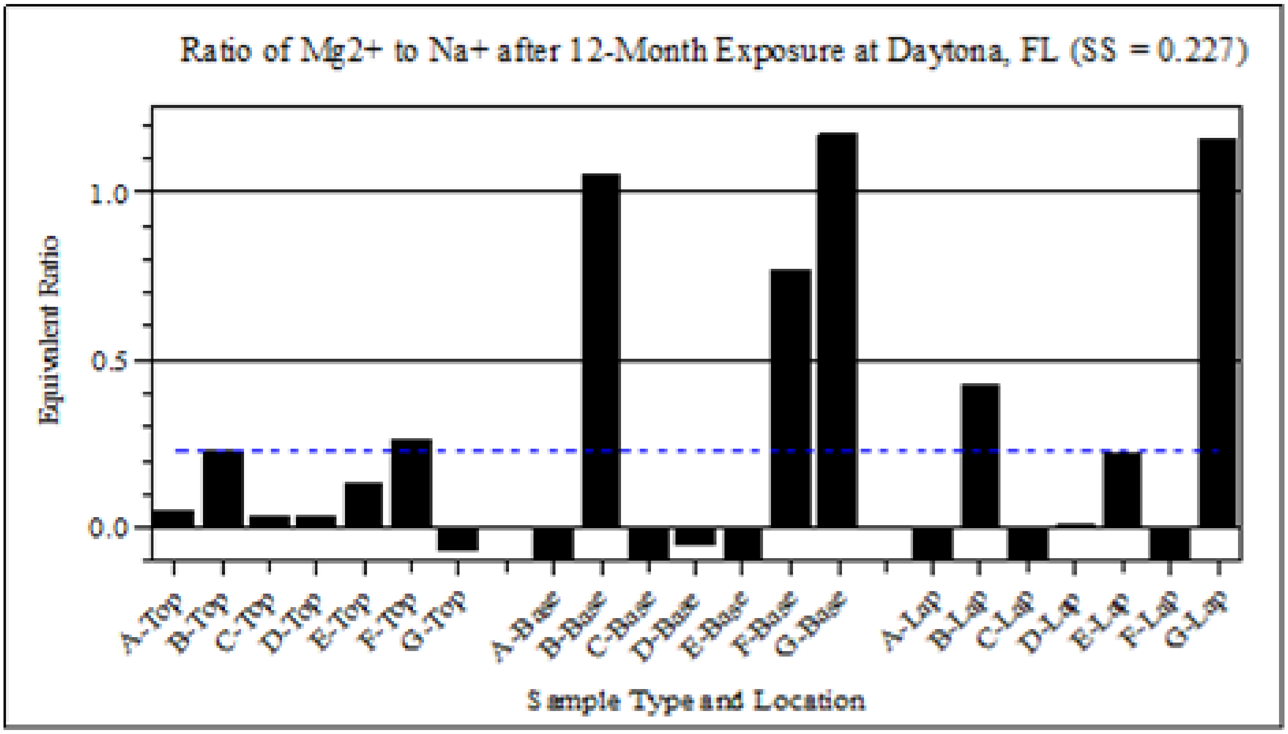

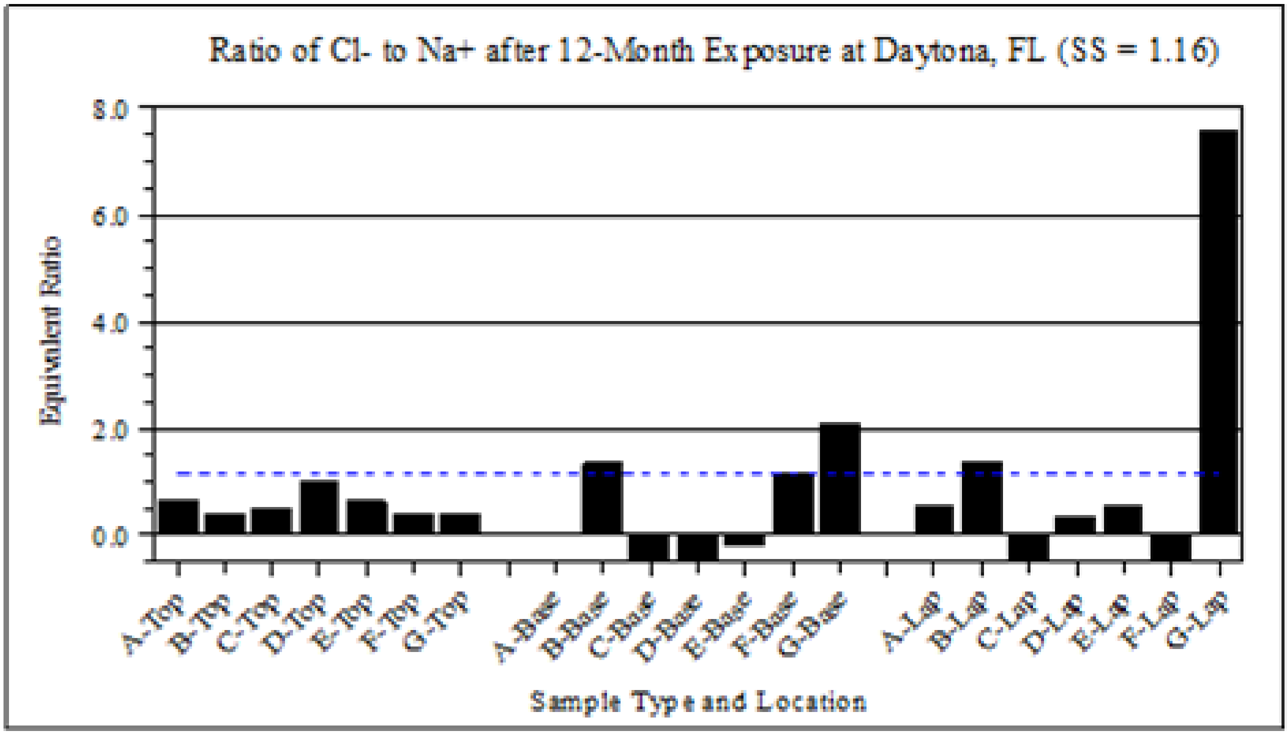

Figure 148. Ratio of Mg^{2+} to Na^{+} and ratio of Cl^{-} to Na^{+}.

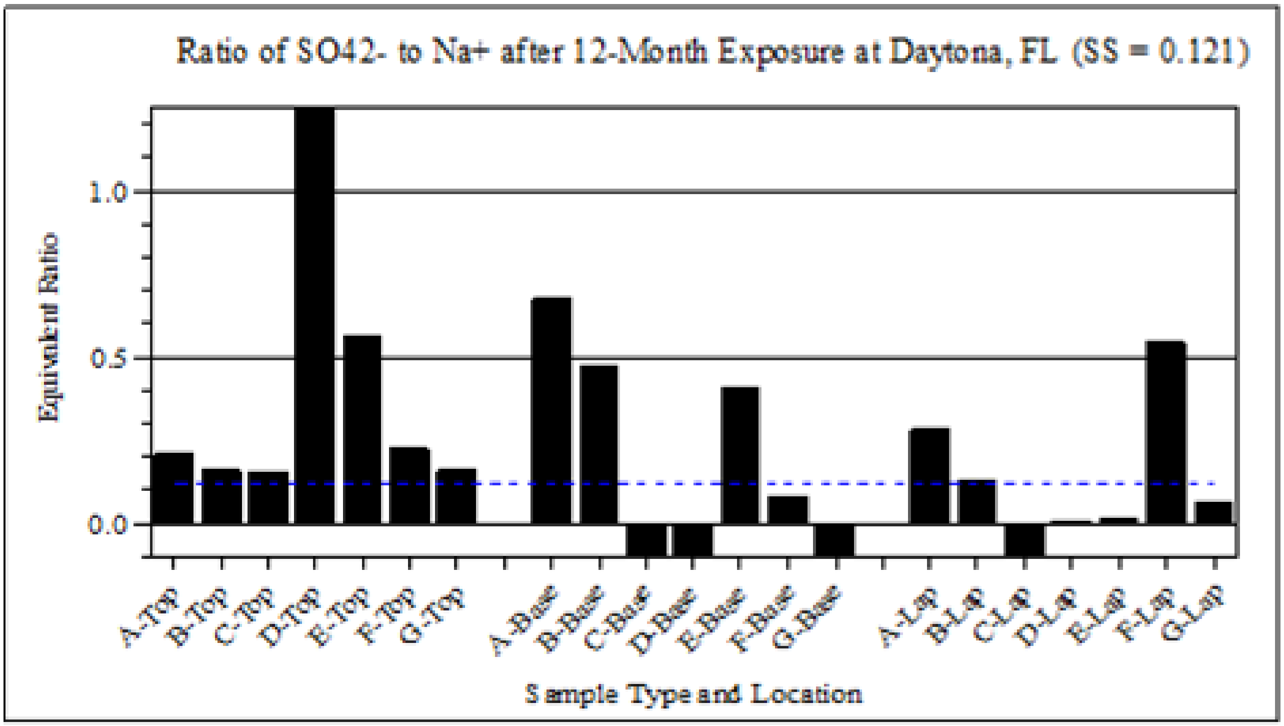

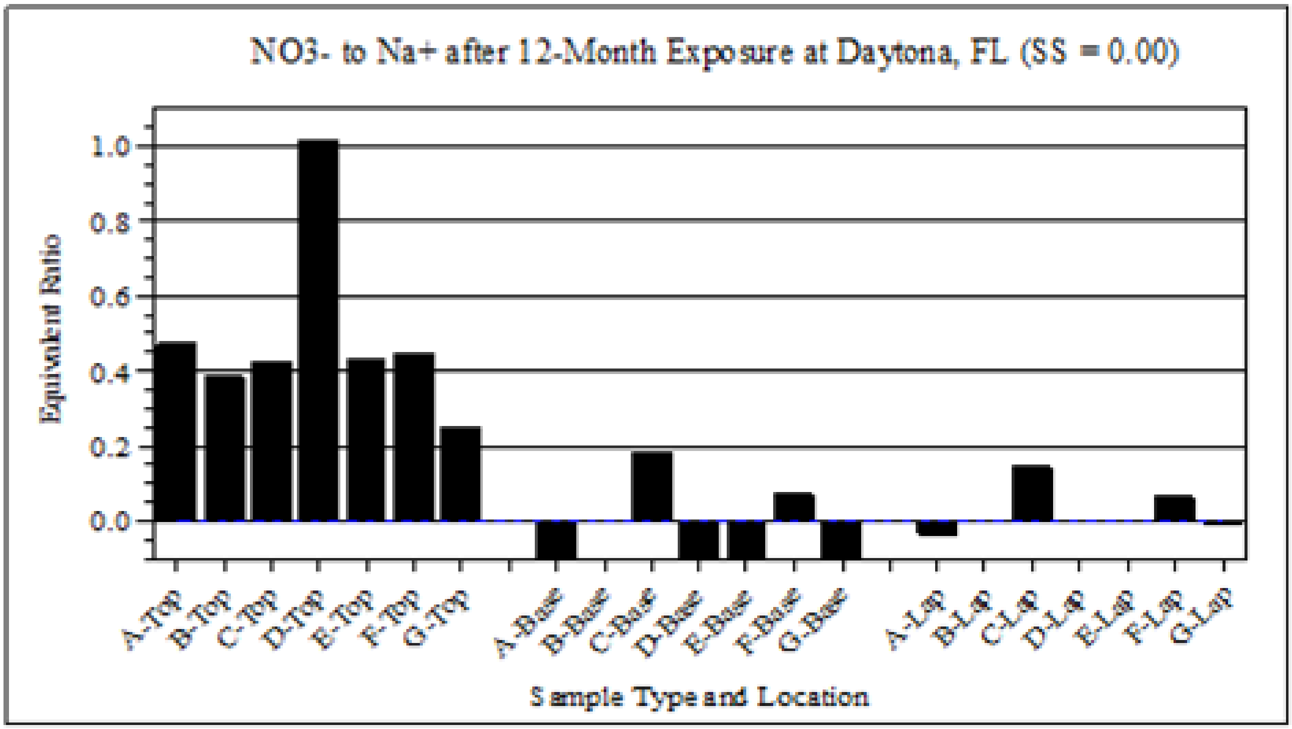

Figure 148. Ratio of SO_4^{2-} to Na^+ and ratio of NO_3^- to Na^+.

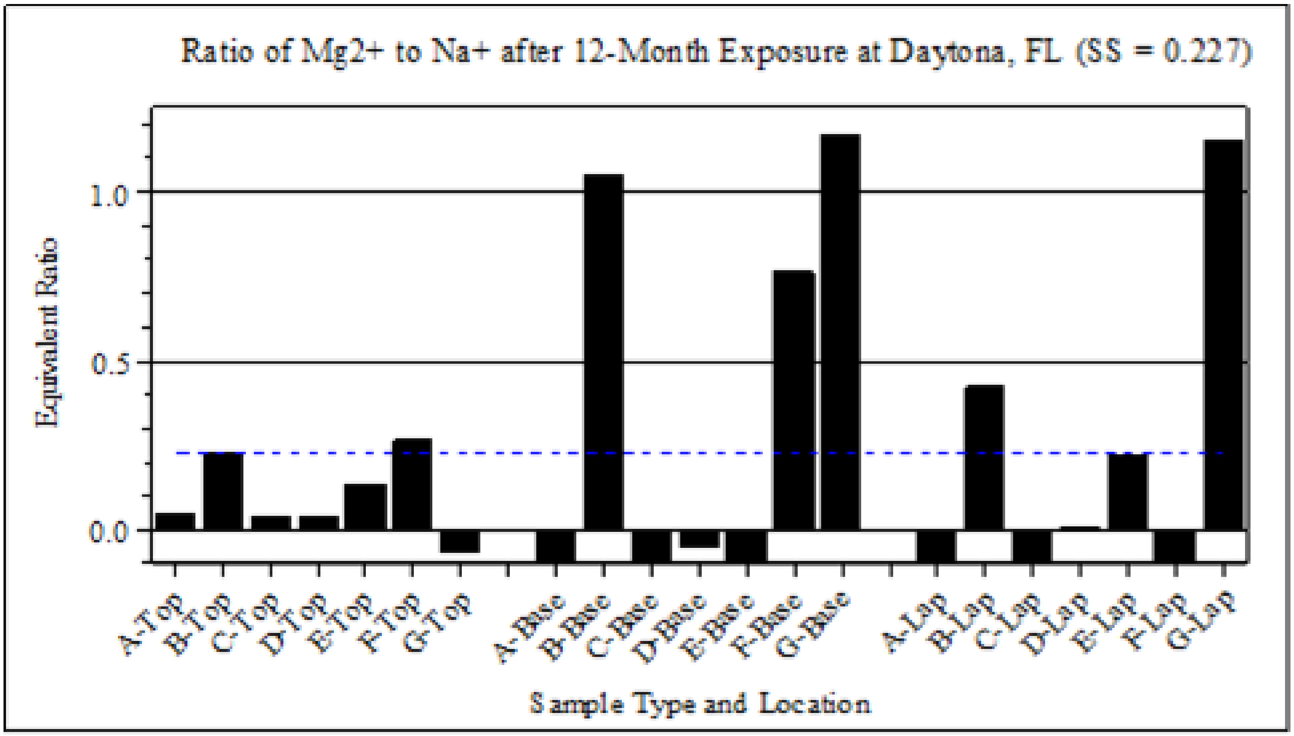

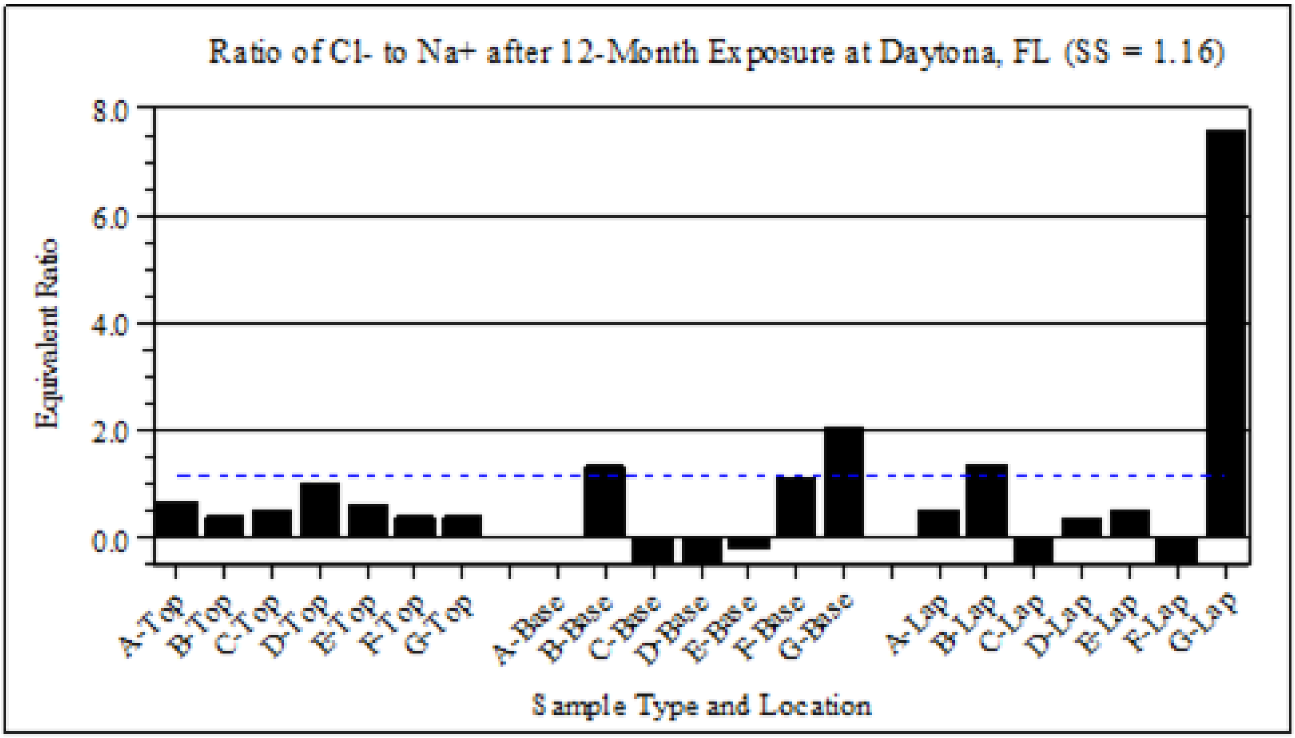

Figure 149. Ratio of Mg^{2+} to Na^+ and ratio of Cl^- to Na^+.

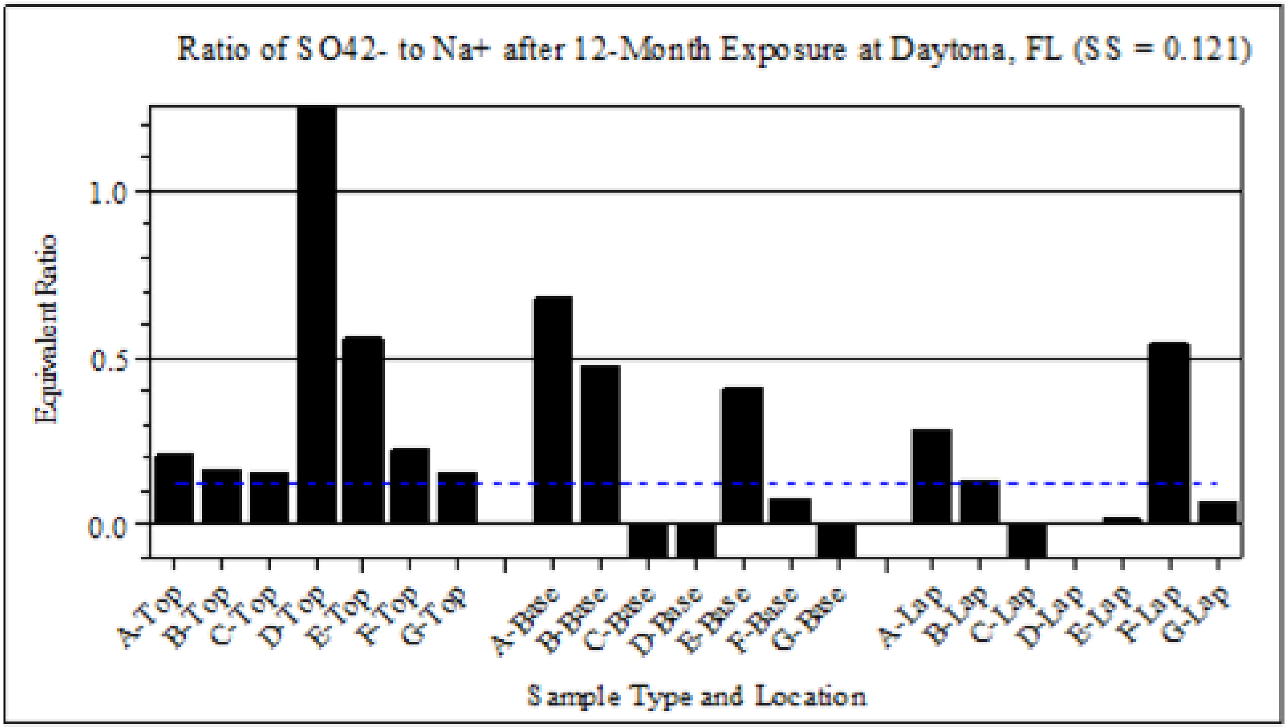

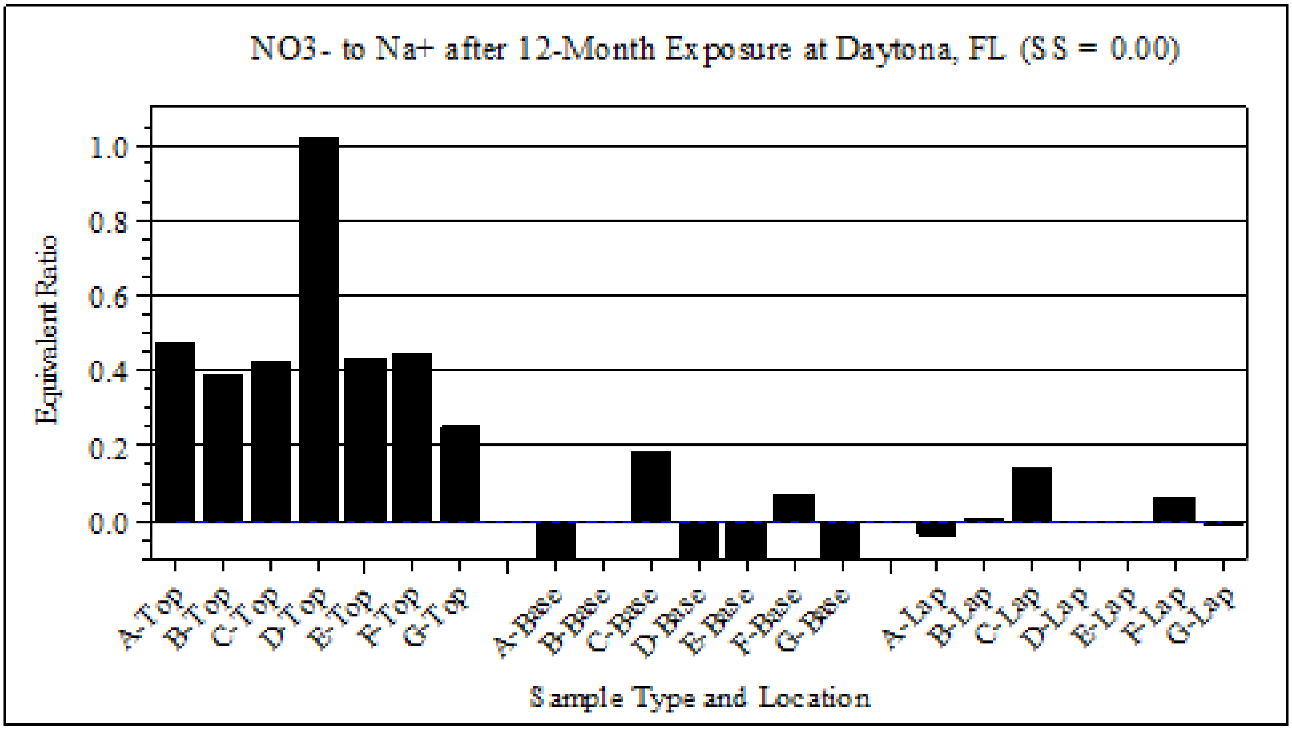

Figure 149. Ratio of SO_4^{2-} to Na^+ and ratio of NO_3^- to Na^+.

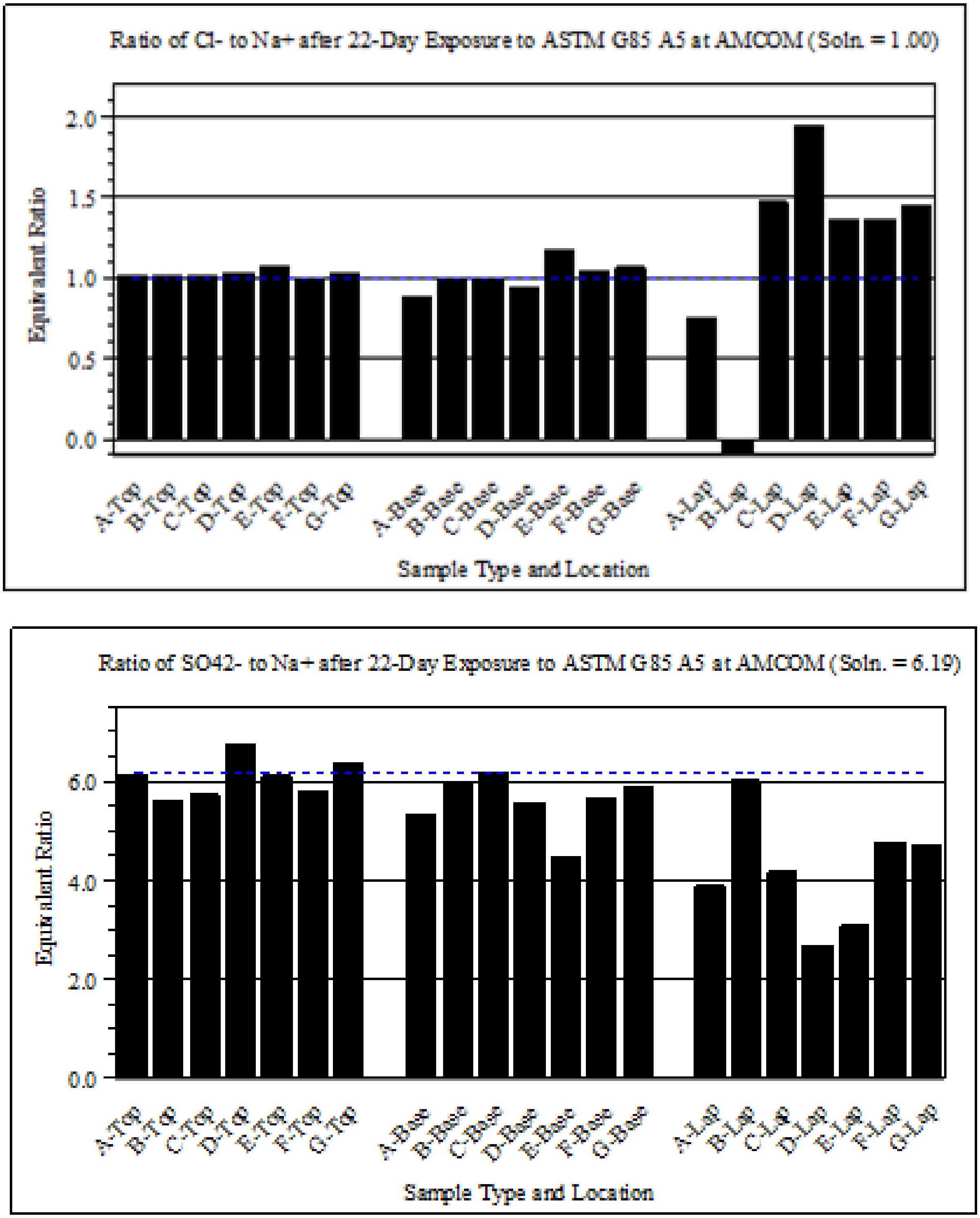

Figure 151. Ratio of Cl^- to Na^+ and ratio of SO_4^{2-} to Na^+.

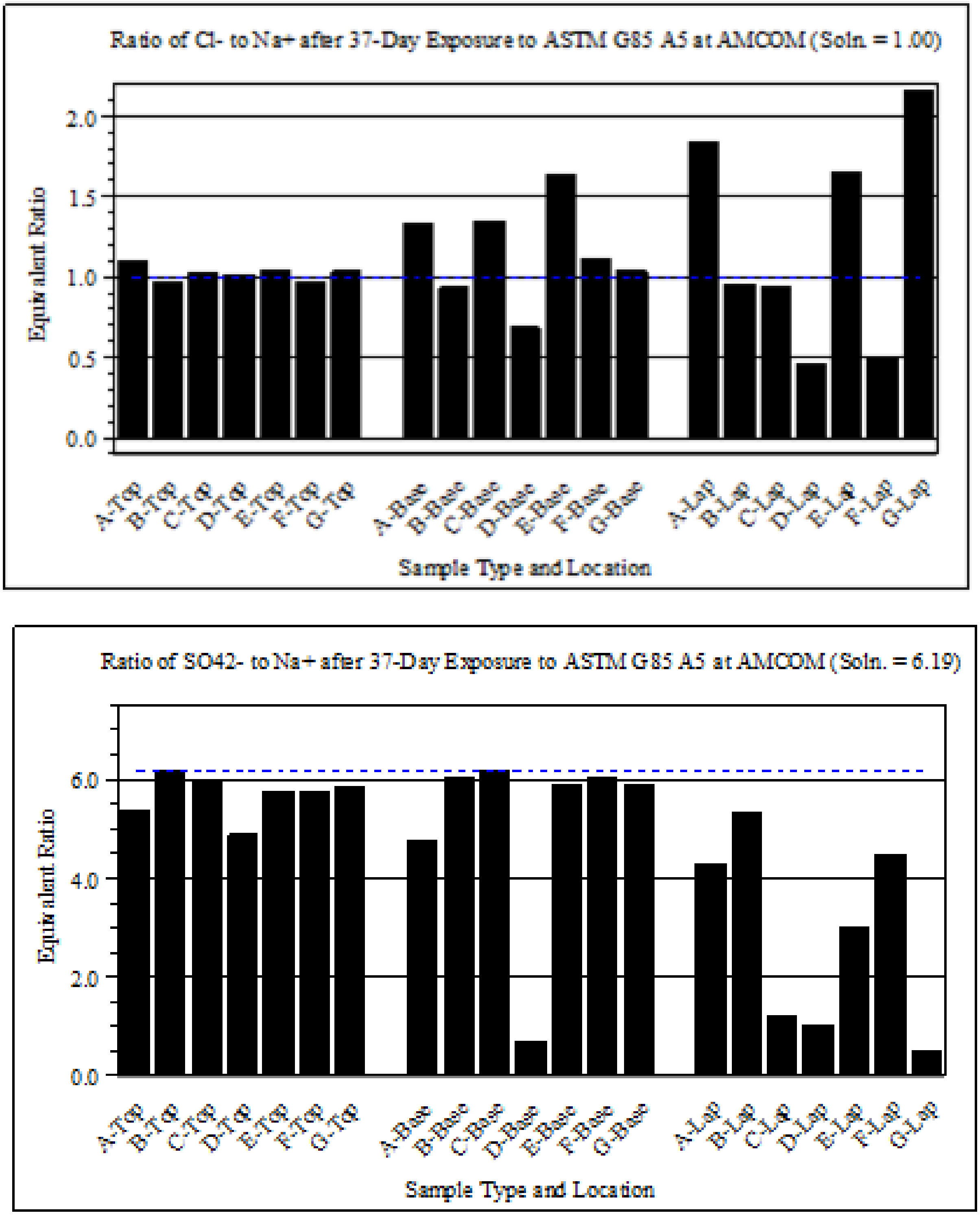

Figure 151. Ratio of Cl^- to Na^+ and ratio of SO_4^{2-} to Na^+.

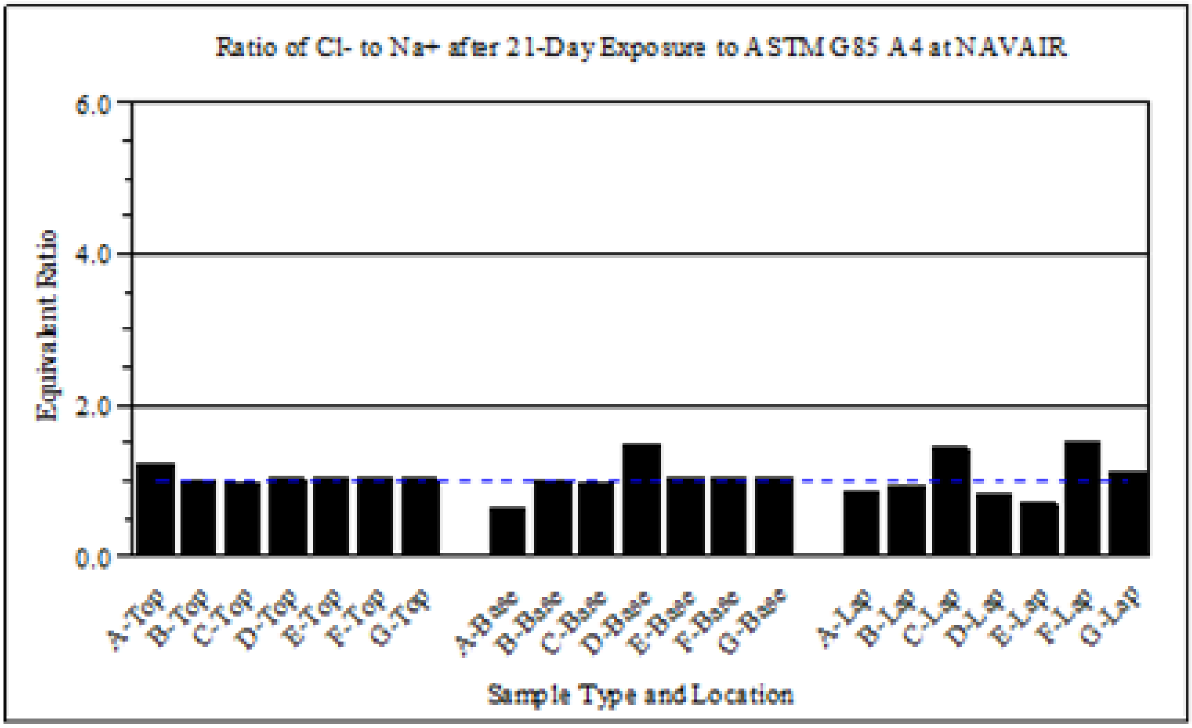

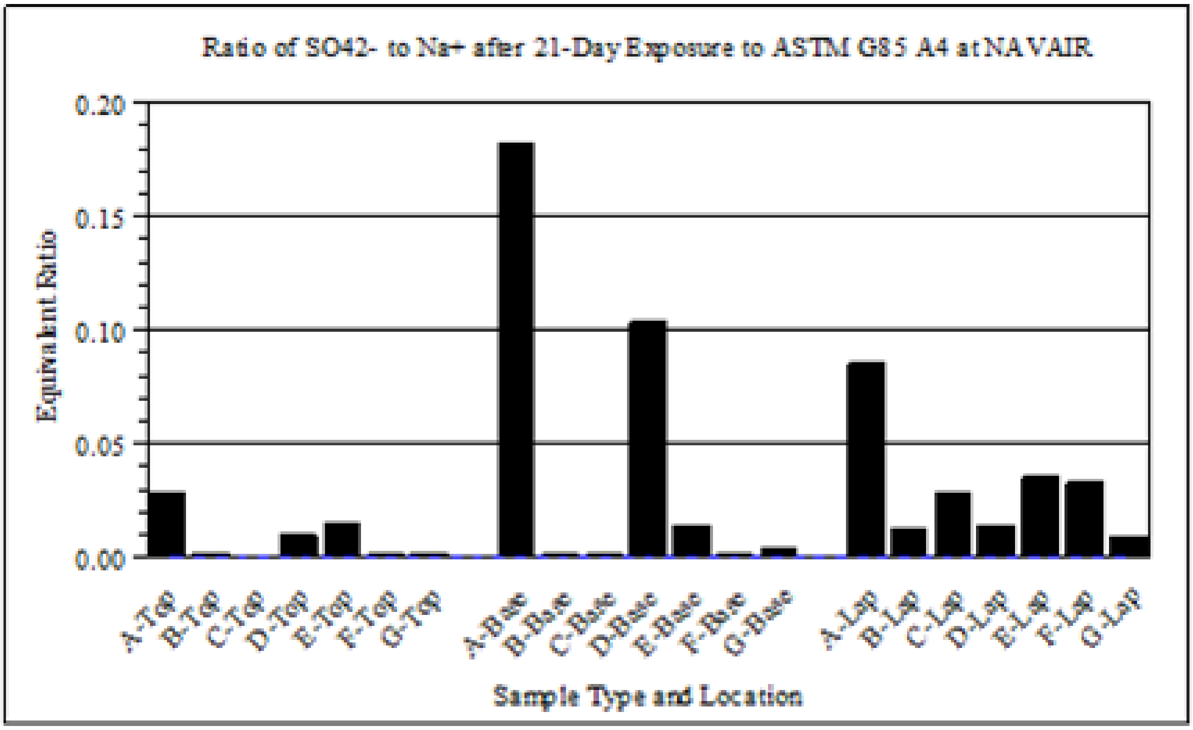

Figure 152. Ratio of Cl^- to Na^+ and ratio of SO_4^{2-} to Na^+.

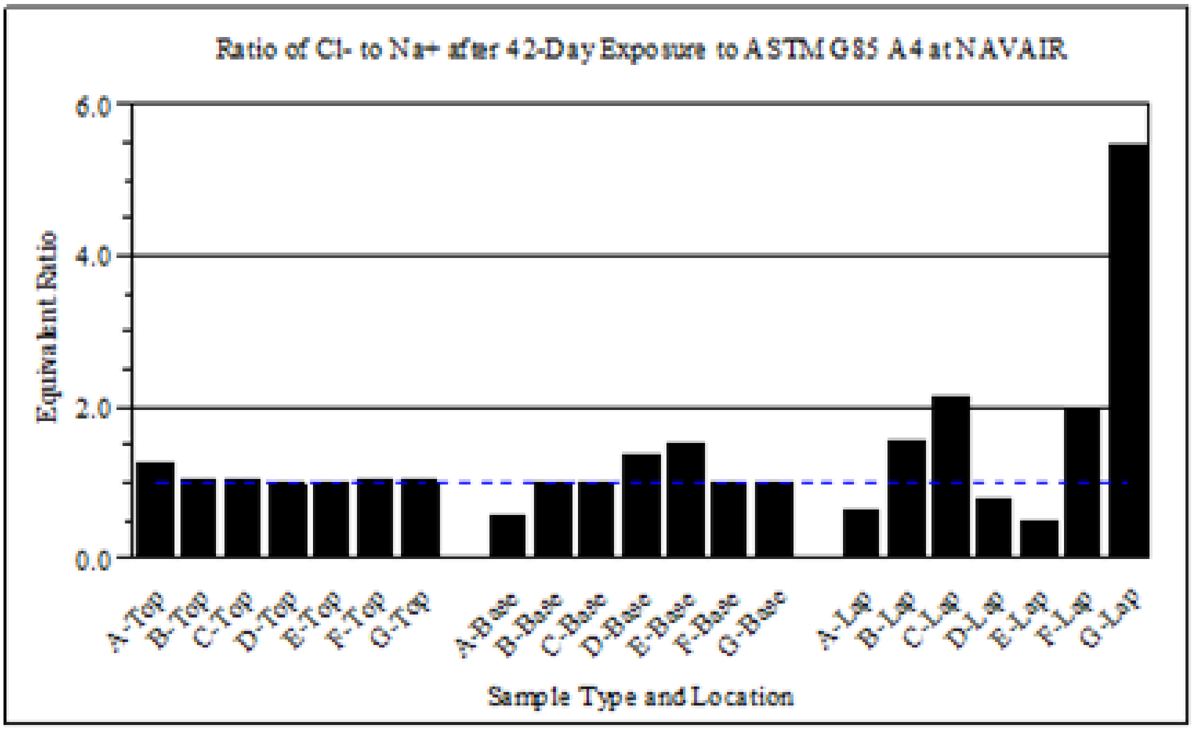

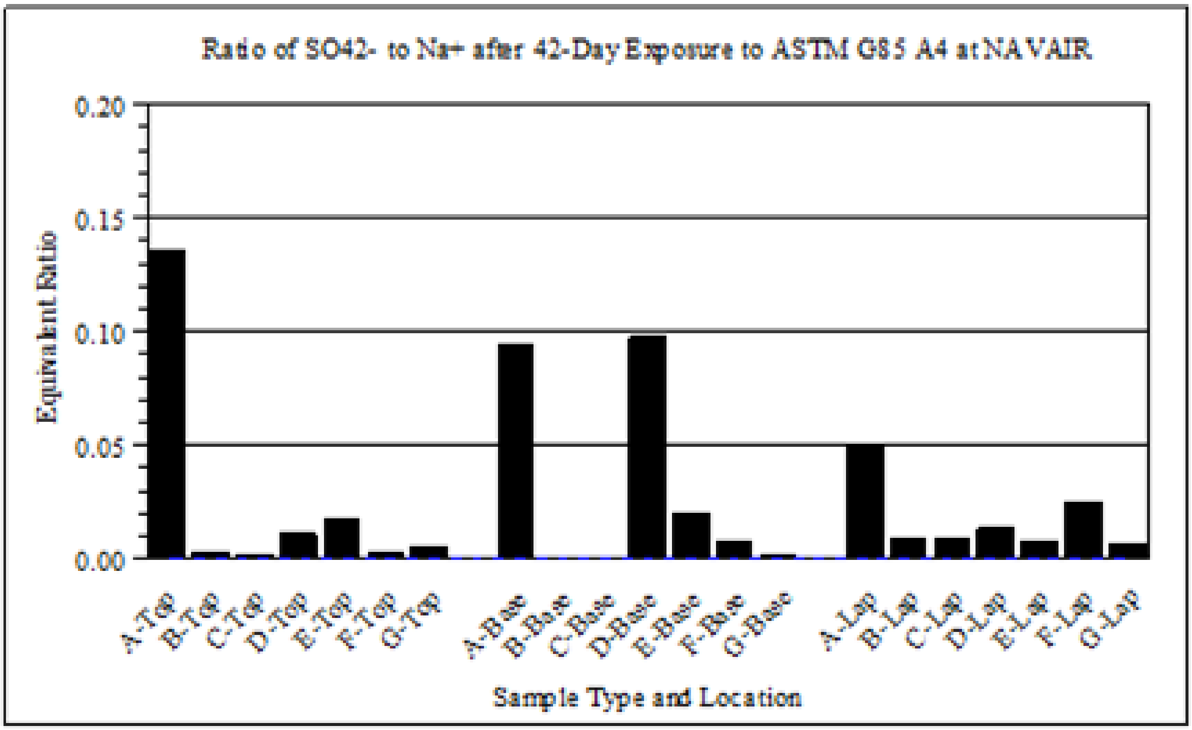

Figure 152. Ratio of Cl^- to Na^+ and ratio of SO_4^{2-} to Na^+.

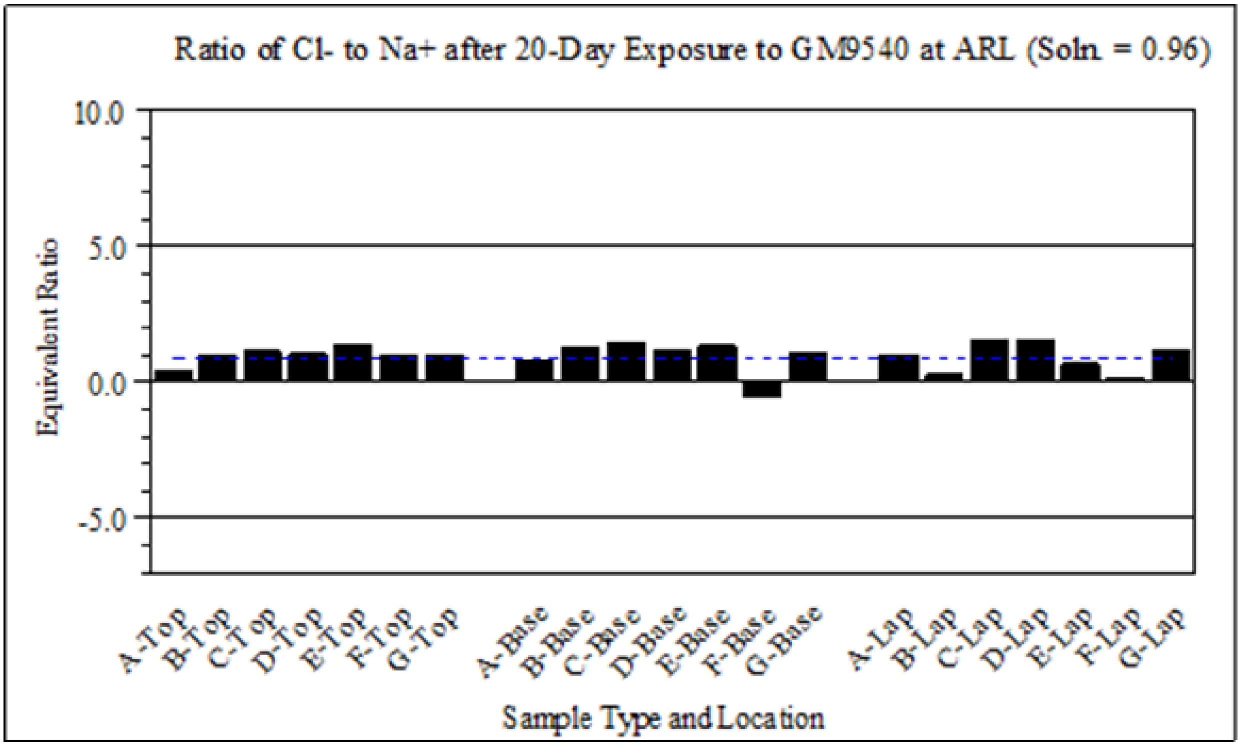

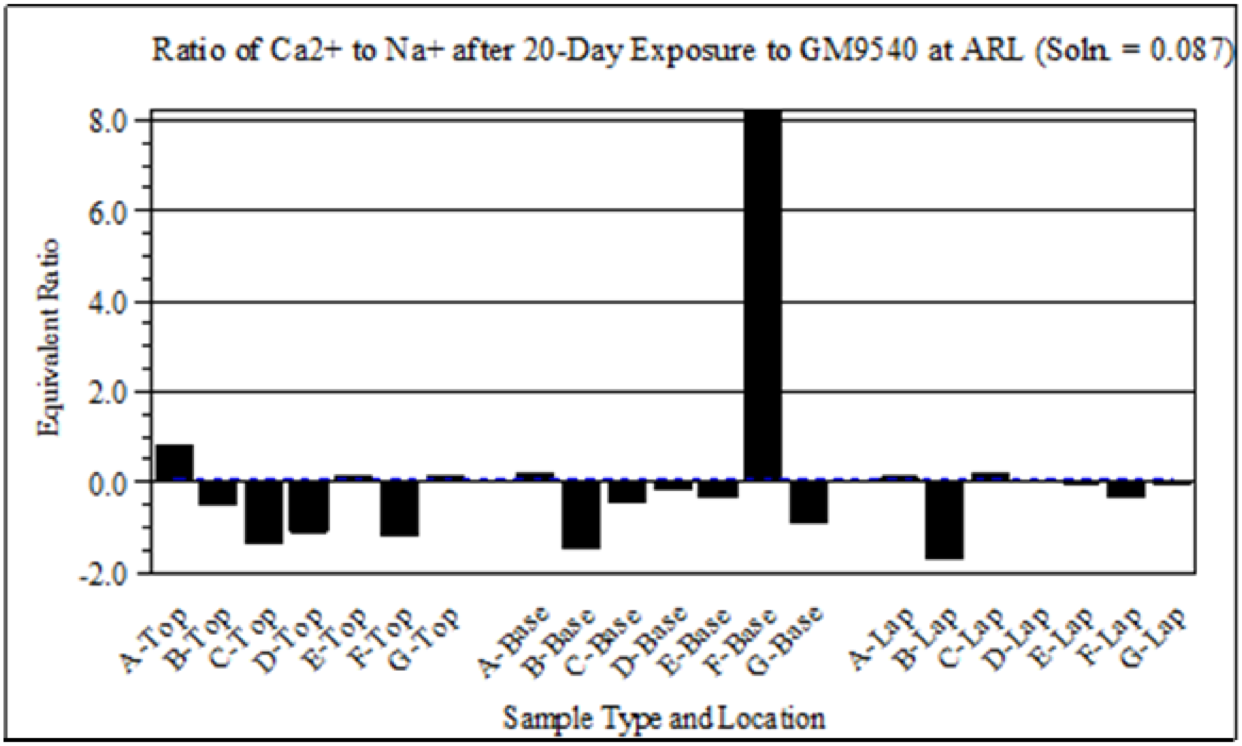

Figure 153. 20 days of exposure.

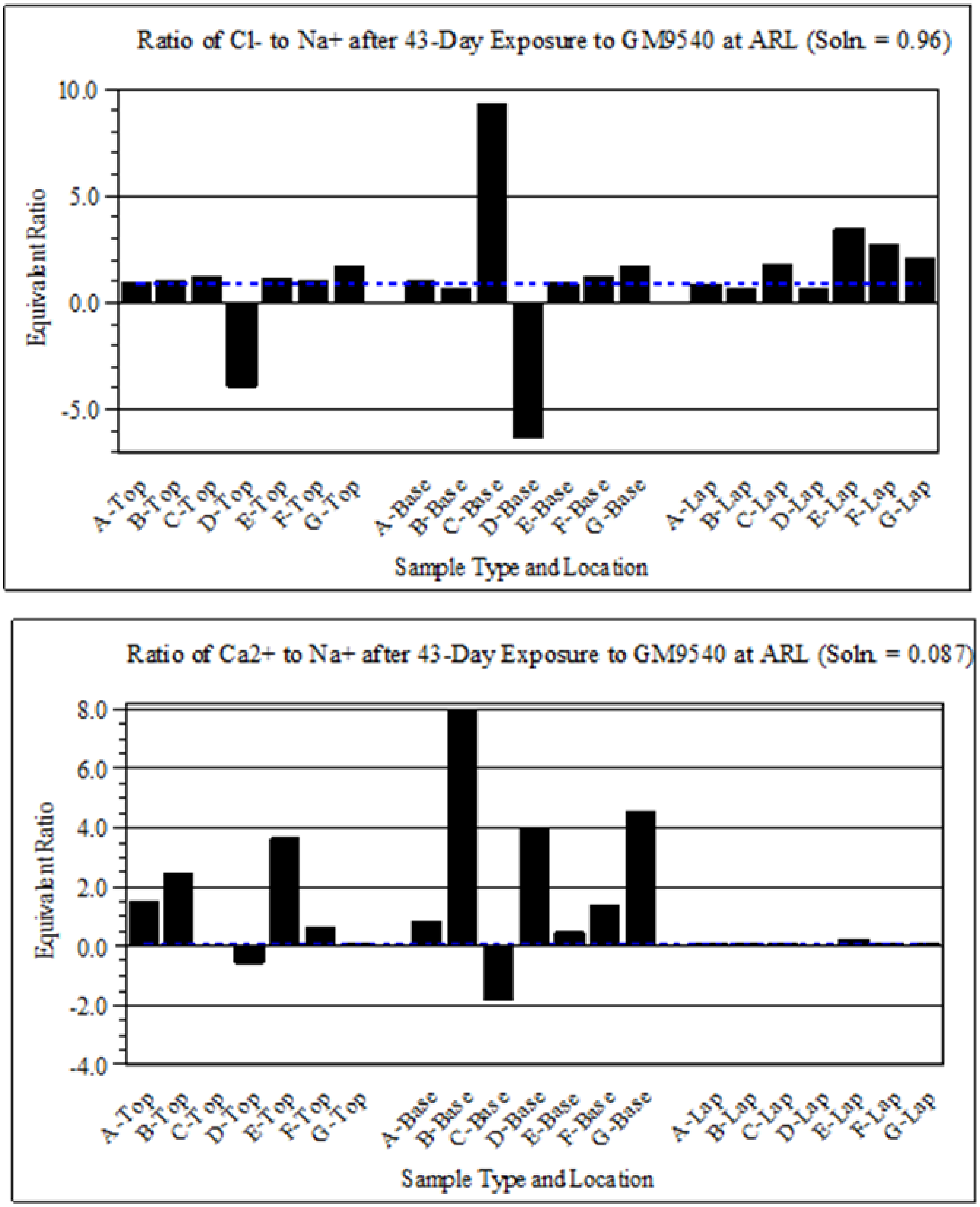

Figure 153. 43 days of exposure.

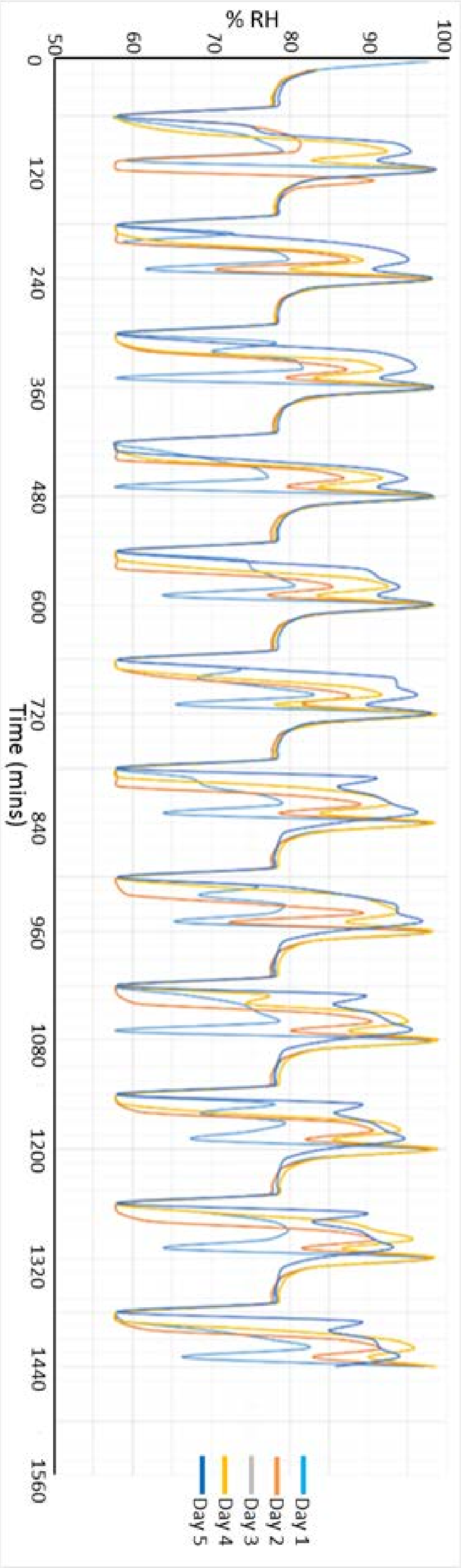
% RH
100
90
80
70
60
50
0
120
240
360
480
600
720
840
960
1080
1200
1320
1440
1560
Time (mins)
Day 1
Day 2
Day 3
Day 4
Day 5

Figure 159.

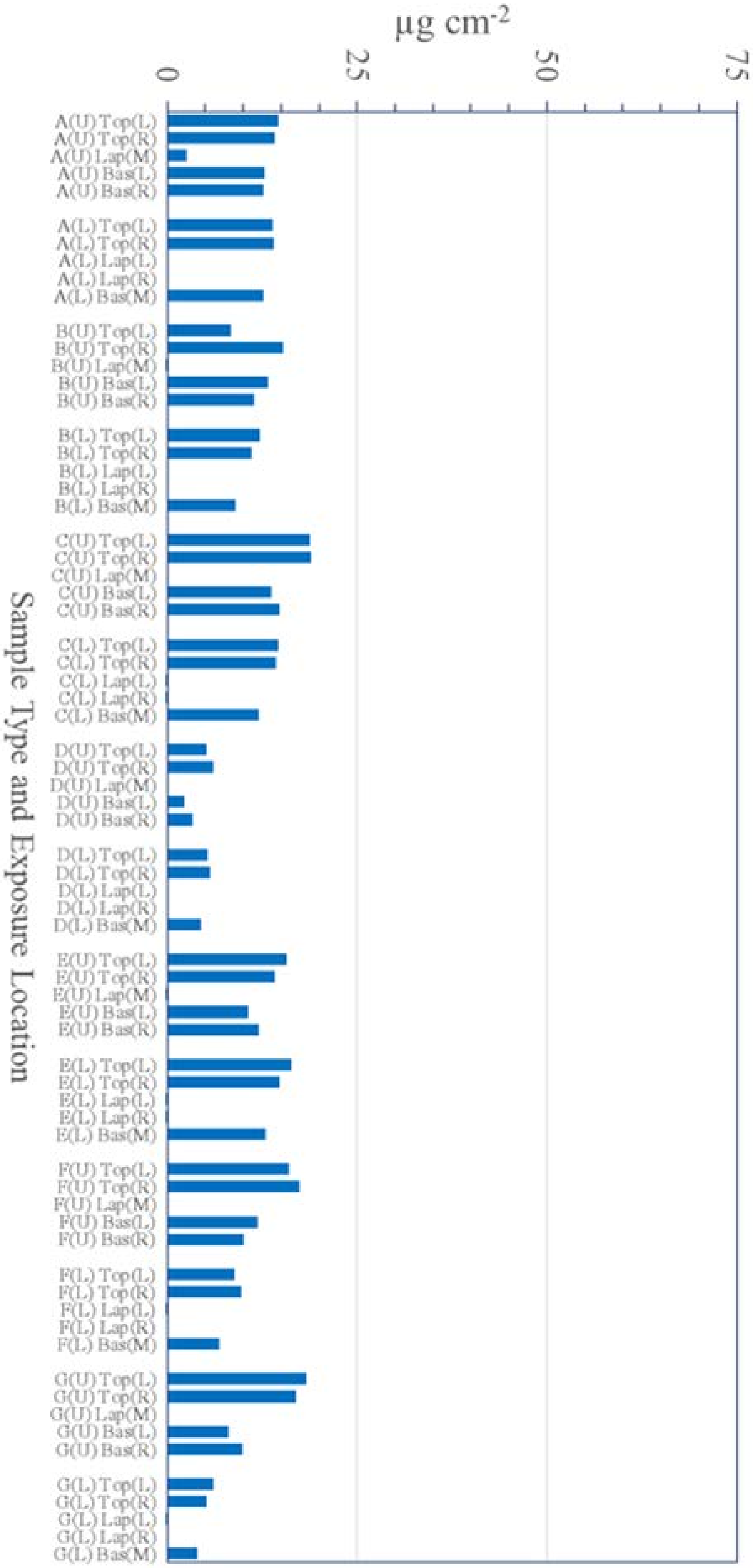
µg cm^{-2}
0
25
50
75
Sample Type and Exposure Location
A(U) Top(L)
A(U) Top(R)
A(U) Lap(M)
A(U) Bas(L)
A(U) Bas(R)
A(L) Top(L)
A(L) Top(R)
A(L) Lap(L)
A(L) Lap(R)
A(L) Bas(M)
B(U) Top(L)
B(U) Top(R)
B(U) Lap(M)
B(U) Bas(L)
B(U) Bas(R)
B(L) Top(L)
B(L) Top(R)
B(L) Lap(L)
B(L) Lap(R)
B(L) Bas(M)
C(U) Top(L)
C(U) Top(R)
C(U) Lap(M)
C(U) Bas(L)
C(U) Bas(R)
C(L) Top(L)
C(L) Top(R)
C(L) Lap(L)
C(L) Lap(R)
C(L) Bas(M)
D(U) Top(L)
D(U) Top(R)
D(U) Lap(M)
D(U) Bas(L)
D(U) Bas(R)
D(L) Top(L)
D(L) Top(R)
D(L) Lap(L)
D(L) Lap(R)
D(L) Bas(M)
E(U) Top(L)
E(U) Top(R)
E(U) Lap(M)
E(U) Bas(L)
E(U) Bas(R)
E(L) Top(L)
E(L) Top(R)
E(L) Lap(L)
E(L) Lap(R)
E(L) Bas(M)
F(U) Top(L)
F(U) Top(R)
F(U) Lap(M)
F(U) Bas(L)
F(U) Bas(R)
F(L) Top(L)
F(L) Top(R)
F(L) Lap(L)
F(L) Lap(R)
F(L) Bas(M)
G(U) Top(L)
G(U) Top(R)
G(U) Lap(M)
G(U) Bas(L)
G(U) Bas(R)
G(L) Top(L)
G(L) Top(R)
G(L) Lap(L)
G(L) Lap(R)
G(L) Bas(M)

Figure 163a.

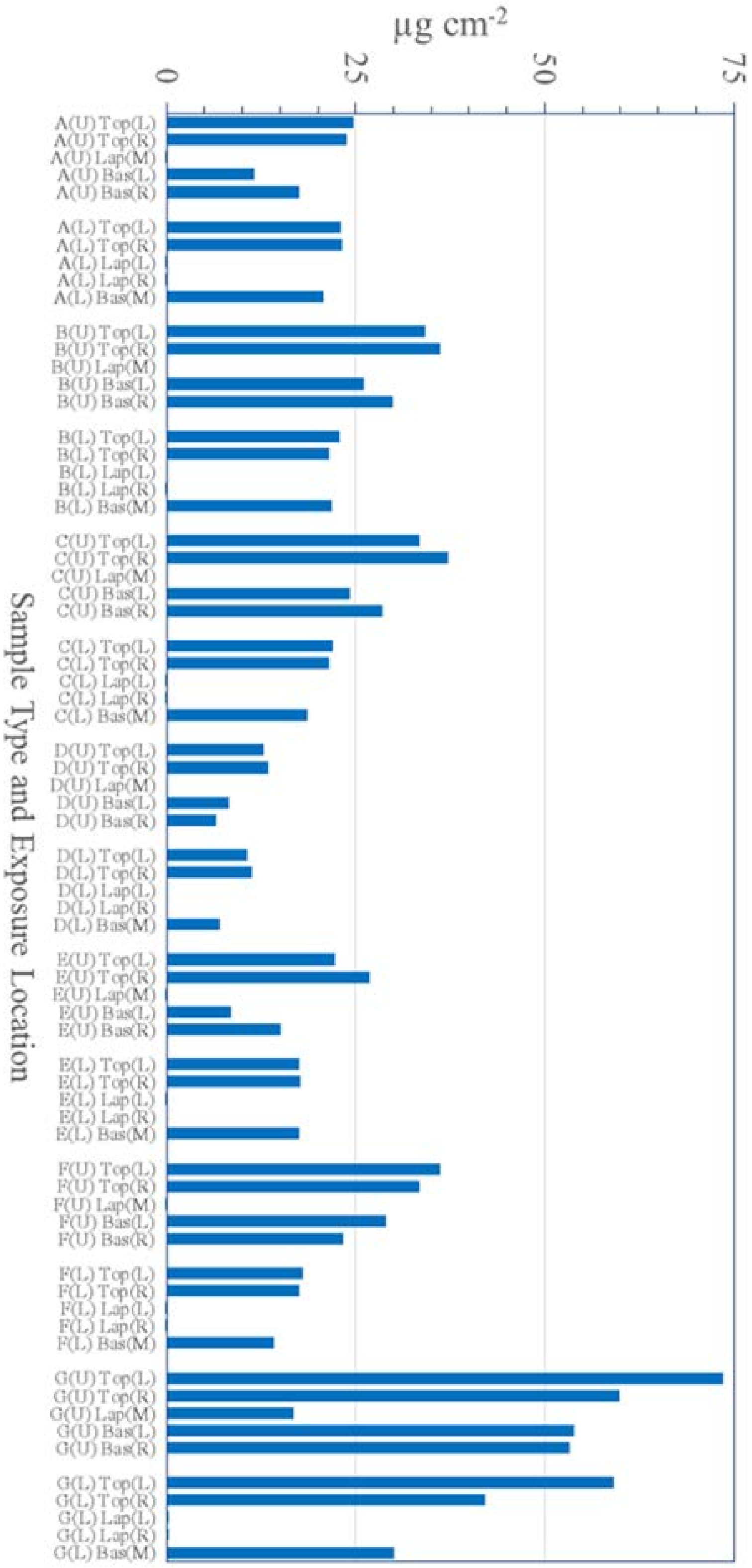
µg cm-2
0
25
50
75
Sample Type and Exposure Location
A(U) Top(L)
A(U) Top(R)
A(U) Lap(M)
A(U) Bas(L)
A(U) Bas(R)
A(L) Top(L)
A(L) Top(R)
A(L) Lap(L)
A(L) Lap(R)
A(L) Bas(M)
B(U) Top(L)
B(U) Top(R)
B(U) Lap(M)
B(U) Bas(L)
B(U) Bas(R)
B(L) Top(L)
B(L) Top(R)
B(L) Lap(L)
B(L) Lap(R)
B(L) Bas(M)
C(U) Top(L)
C(U) Top(R)
C(U) Lap(M)
C(U) Bas(L)
C(U) Bas(R)
C(L) Top(L)
C(L) Top(R)
C(L) Lap(L)
C(L) Lap(R)
C(L) Bas(M)
D(U) Top(L)
D(U) Top(R)
D(U) Lap(M)
D(U) Bas(L)
D(U) Bas(R)
D(L) Top(L)
D(L) Top(R)
D(L) Lap(L)
D(L) Lap(R)
D(L) Bas(M)
E(U) Top(L)
E(U) Top(R)
E(U) Lap(M)
E(U) Bas(L)
E(U) Bas(R)
E(L) Top(L)
E(L) Top(R)
E(L) Lap(L)
E(L) Lap(R)
E(L) Bas(M)
F(U) Top(L)
F(U) Top(R)
F(U) Lap(M)
F(U) Bas(L)
F(U) Bas(R)
F(L) Top(L)
F(L) Top(R)
F(L) Lap(L)
F(L) Lap(R)
F(L) Bas(M)
G(U) Top(L)
G(U) Top(R)
G(U) Lap(M)
G(U) Bas(L)
G(U) Bas(R)
G(L) Top(L)
G(L) Top(R)
G(L) Lap(L)
G(L) Lap(R)
G(L) Bas(M)

Figure 163b.

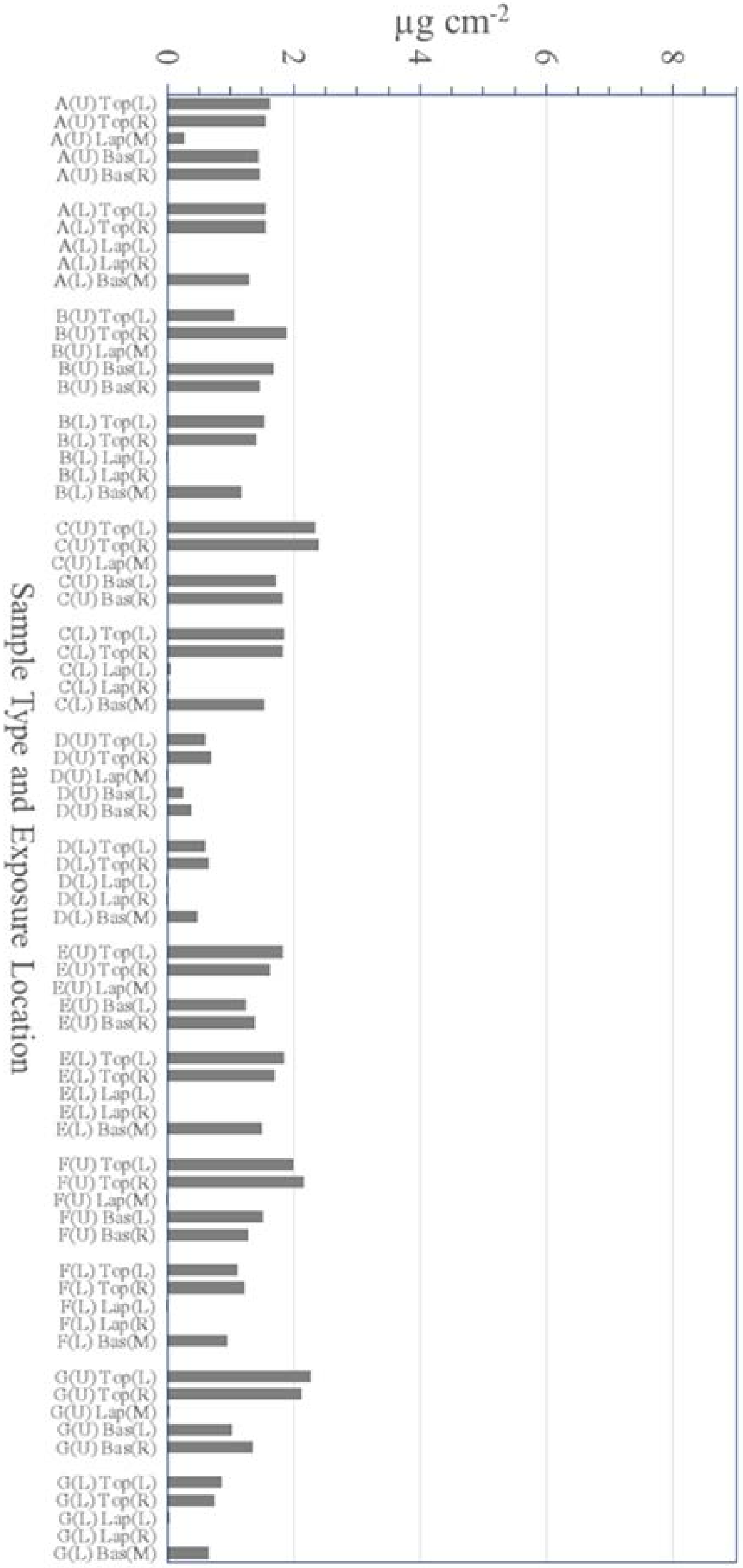
µg cm-2
0
2
4
6
8
Sample Type and Exposure Location
A(U) Top(L)
A(U) Top(R)
A(U) Lap(M)
A(U) Bas(L)
A(U) Bas(R)
A(L) Top(L)
A(L) Top(R)
A(L) Lap(L)
A(L) Lap(R)
A(L) Bas(M)
B(U) Top(L)
B(U) Top(R)
B(U) Lap(M)
B(U) Bas(L)
B(U) Bas(R)
B(L) Top(L)
B(L) Top(R)
B(L) Lap(L)
B(L) Lap(R)
B(L) Bas(M)
C(U) Top(L)
C(U) Top(R)
C(U) Lap(M)
C(U) Bas(L)
C(U) Bas(R)
C(L) Top(L)
C(L) Top(R)
C(L) Lap(L)
C(L) Lap(R)
C(L) Bas(M)
D(U) Top(L)
D(U) Top(R)
D(U) Lap(M)
D(U) Bas(L)
D(U) Bas(R)
D(L) Top(L)
D(L) Top(R)
D(L) Lap(L)
D(L) Lap(R)
D(L) Bas(M)
E(U) Top(L)
E(U) Top(R)
E(U) Lap(M)
E(U) Bas(L)
E(U) Bas(R)
E(L) Top(L)
E(L) Top(R)
E(L) Lap(L)
E(L) Lap(R)
E(L) Bas(M)
F(U) Top(L)
F(U) Top(R)
F(U) Lap(M)
F(U) Bas(L)
F(U) Bas(R)
F(L) Top(L)
F(L) Top(R)
F(L) Lap(L)
F(L) Lap(R)
F(L) Bas(M)
G(U) Top(L)
G(U) Top(R)
G(U) Lap(M)
G(U) Bas(L)
G(U) Bas(R)
G(L) Top(L)
G(L) Top(R)
G(L) Lap(L)
G(L) Lap(R)
G(L) Bas(M)

Figure 164a.

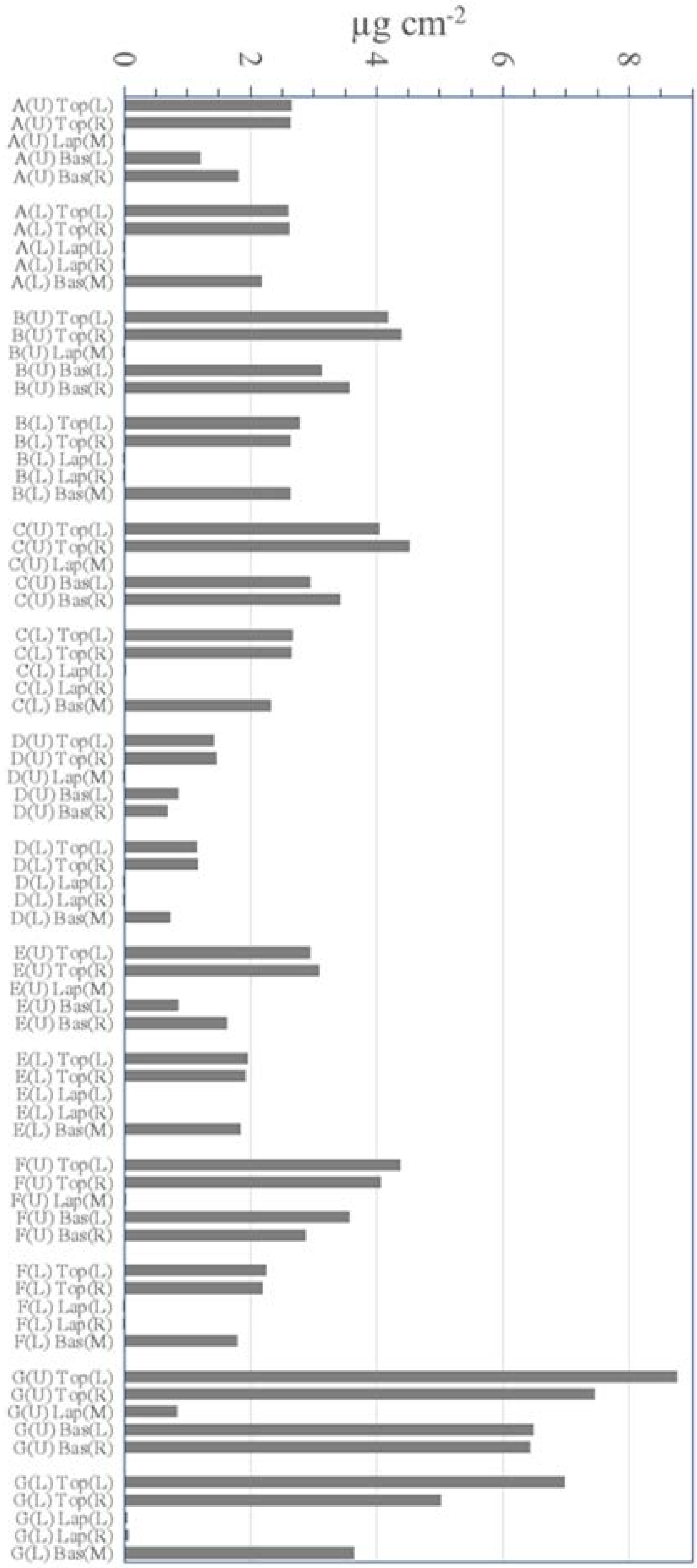
µg cm-2
0
2
4
6
8
A(U) Top(L)
A(U) Top(R)
A(U) Lap(M)
A(U) Bas(L)
A(U) Bas(R)
A(L) Top(L)
A(L) Top(R)
A(L) Lap(L)
A(L) Lap(R)
A(L) Bas(M)
B(U) Top(L)
B(U) Top(R)
B(U) Lap(M)
B(U) Bas(L)
B(U) Bas(R)
B(L) Top(L)
B(L) Top(R)
B(L) Lap(L)
B(L) Lap(R)
B(L) Bas(M)
C(U) Top(L)
C(U) Top(R)
C(U) Lap(M)
C(U) Bas(L)
C(U) Bas(R)
C(L) Top(L)
C(L) Top(R)
C(L) Lap(L)
C(L) Lap(R)
C(L) Bas(M)
D(U) Top(L)
D(U) Top(R)
D(U) Lap(M)
D(U) Bas(L)
D(U) Bas(R)
D(L) Top(L)
D(L) Top(R)
D(L) Lap(L)
D(L) Lap(R)
D(L) Bas(M)
E(U) Top(L)
E(U) Top(R)
E(U) Lap(M)
E(U) Bas(L)
E(U) Bas(R)
E(L) Top(L)
E(L) Top(R)
E(L) Lap(L)
E(L) Lap(R)
E(L) Bas(M)
F(U) Top(L)
F(U) Top(R)
F(U) Lap(M)
F(U) Bas(L)
F(U) Bas(R)
F(L) Top(L)
F(L) Top(R)
F(L) Lap(L)
F(L) Lap(R)
F(L) Bas(M)
G(U) Top(L)
G(U) Top(R)
G(U) Lap(M)
G(U) Bas(L)
G(U) Bas(R)
G(L) Top(L)
G(L) Top(R)
G(L) Lap(L)
G(L) Lap(R)
G(L) Bas(M)

Figure 164b.

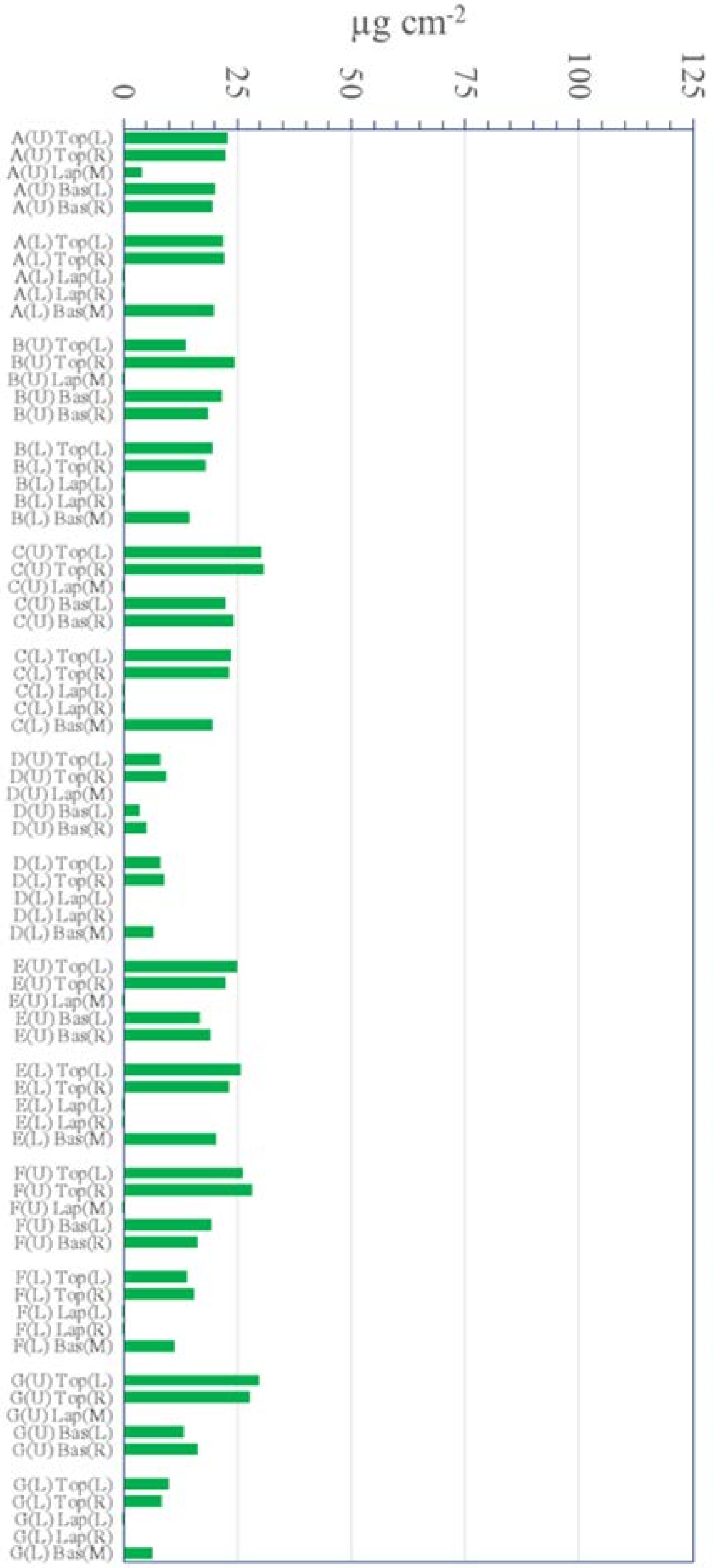
μg cm-2
0
25
50
75
100
125
A(U) Top(L)
A(U) Top(R)
A(U) Lap(M)
A(U) Bas(L)
A(U) Bas(R)
A(L) Top(L)
A(L) Top(R)
A(L) Lap(L)
A(L) Lap(R)
A(L) Bas(M)
B(U) Top(L)
B(U) Top(R)
B(U) Lap(M)
B(U) Bas(L)
B(U) Bas(R)
B(L) Top(L)
B(L) Top(R)
B(L) Lap(L)
B(L) Lap(R)
B(L) Bas(M)
C(U) Top(L)
C(U) Top(R)
C(U) Lap(M)
C(U) Bas(L)
C(U) Bas(R)
C(L) Top(L)
C(L) Top(R)
C(L) Lap(L)
C(L) Lap(R)
C(L) Bas(M)
D(U) Top(L)
D(U) Top(R)
D(U) Lap(M)
D(U) Bas(L)
D(U) Bas(R)
D(L) Top(L)
D(L) Top(R)
D(L) Lap(L)
D(L) Lap(R)
D(L) Bas(M)
E(U) Top(L)
E(U) Top(R)
E(U) Lap(M)
E(U) Bas(L)
E(U) Bas(R)
E(L) Top(L)
E(L) Top(R)
E(L) Lap(L)
E(L) Lap(R)
E(L) Bas(M)
F(U) Top(L)
F(U) Top(R)
F(U) Lap(M)
F(U) Bas(L)
F(U) Bas(R)
F(L) Top(L)
F(L) Top(R)
F(L) Lap(L)
F(L) Lap(R)
F(L) Bas(M)
G(U) Top(L)
G(U) Top(R)
G(U) Lap(M)
G(U) Bas(L)
G(U) Bas(R)
G(L) Top(L)
G(L) Top(R)
G(L) Lap(L)
G(L) Lap(R)
G(L) Bas(M)

Figure 165a.

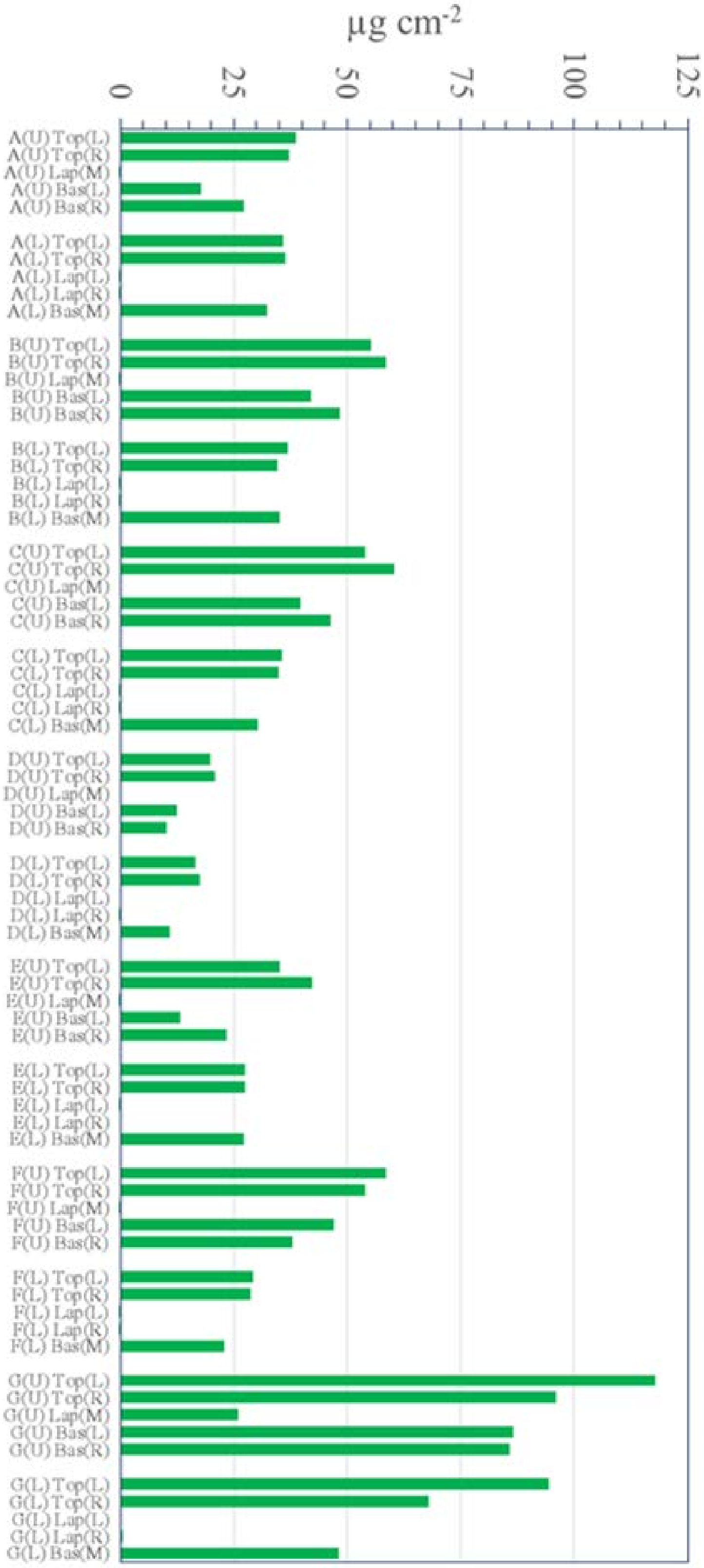
µg cm-2
0
25
50
75
100
125
A(U) Top(L)
A(U) Top(R)
A(U) Lap(M)
A(U) Bas(L)
A(U) Bas(R)
A(L) Top(L)
A(L) Top(R)
A(L) Lap(L)
A(L) Lap(R)
A(L) Bas(M)
B(U) Top(L)
B(U) Top(R)
B(U) Lap(M)
B(U) Bas(L)
B(U) Bas(R)
B(L) Top(L)
B(L) Top(R)
B(L) Lap(L)
B(L) Lap(R)
B(L) Bas(M)
C(U) Top(L)
C(U) Top(R)
C(U) Lap(M)
C(U) Bas(L)
C(U) Bas(R)
C(L) Top(L)
C(L) Top(R)
C(L) Lap(L)
C(L) Lap(R)
C(L) Bas(M)
D(U) Top(L)
D(U) Top(R)
D(U) Lap(M)
D(U) Bas(L)
D(U) Bas(R)
D(L) Top(L)
D(L) Top(R)
D(L) Lap(L)
D(L) Lap(R)
D(L) Bas(M)
E(U) Top(L)
E(U) Top(R)
E(U) Lap(M)
E(U) Bas(L)
E(U) Bas(R)
E(L) Top(L)
E(L) Top(R)
E(L) Lap(L)
E(L) Lap(R)
E(L) Bas(M)
F(U) Top(L)
F(U) Top(R)
F(U) Lap(M)
F(U) Bas(L)
F(U) Bas(R)
F(L) Top(L)
F(L) Top(R)
F(L) Lap(L)
F(L) Lap(R)
F(L) Bas(M)
G(U) Top(L)
G(U) Top(R)
G(U) Lap(M)
G(U) Bas(L)
G(U) Bas(R)
G(L) Top(L)
G(L) Top(R)
G(L) Lap(L)
G(L) Lap(R)
G(L) Bas(M)

Figure 165b.

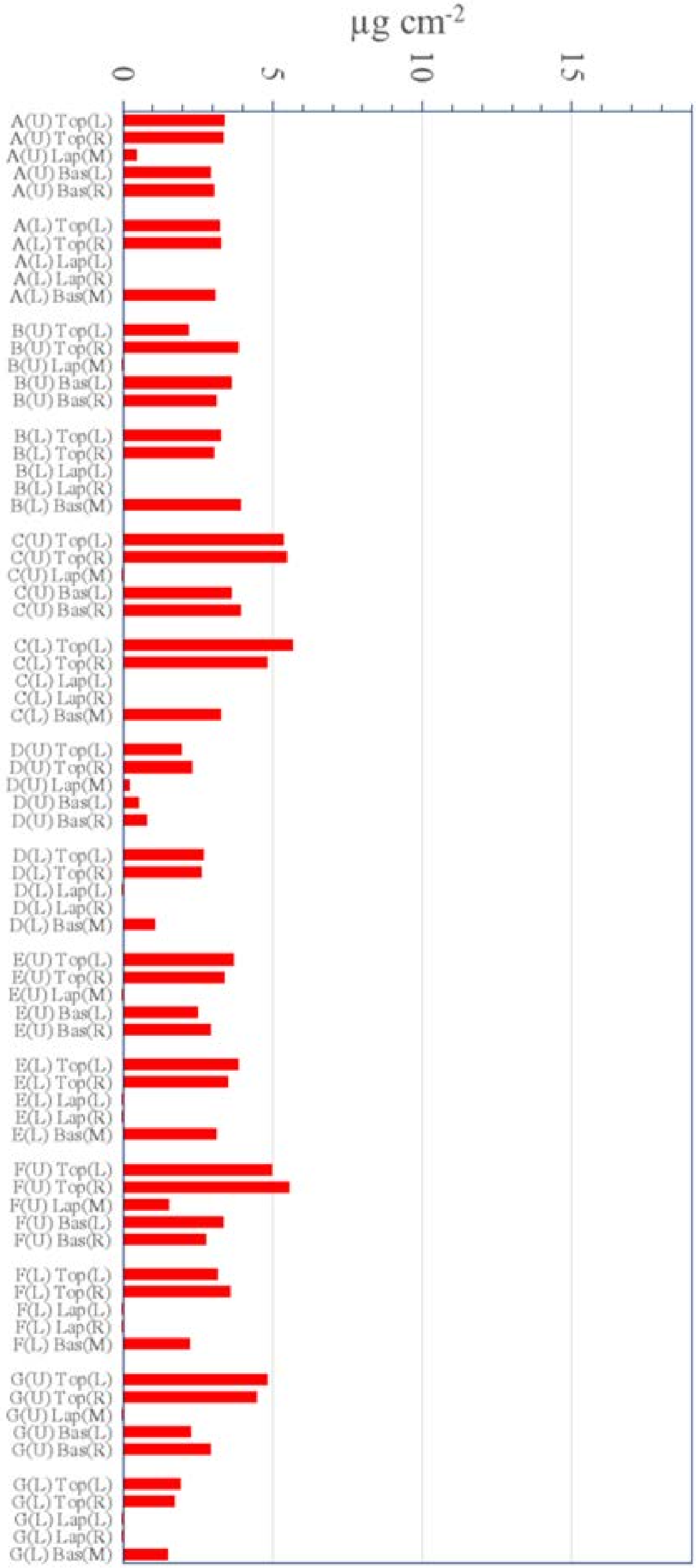
µg cm-2
0
5
10
15
A(U) Top(L)
A(U) Top(R)
A(U) Lap(M)
A(U) Bas(L)
A(U) Bas(R)
A(L) Top(L)
A(L) Top(R)
A(L) Lap(L)
A(L) Lap(R)
A(L) Bas(M)
B(U) Top(L)
B(U) Top(R)
B(U) Lap(M)
B(U) Bas(L)
B(U) Bas(R)
B(L) Top(L)
B(L) Top(R)
B(L) Lap(L)
B(L) Lap(R)
B(L) Bas(M)
C(U) Top(L)
C(U) Top(R)
C(U) Lap(M)
C(U) Bas(L)
C(U) Bas(R)
C(L) Top(L)
C(L) Top(R)
C(L) Lap(L)
C(L) Lap(R)
C(L) Bas(M)
D(U) Top(L)
D(U) Top(R)
D(U) Lap(M)
D(U) Bas(L)
D(U) Bas(R)
D(L) Top(L)
D(L) Top(R)
D(L) Lap(L)
D(L) Lap(R)
D(L) Bas(M)
E(U) Top(L)
E(U) Top(R)
E(U) Lap(M)
E(U) Bas(L)
E(U) Bas(R)
E(L) Top(L)
E(L) Top(R)
E(L) Lap(L)
E(L) Lap(R)
E(L) Bas(M)
F(U) Top(L)
F(U) Top(R)
F(U) Lap(M)
F(U) Bas(L)
F(U) Bas(R)
F(L) Top(L)
F(L) Top(R)
F(L) Lap(L)
F(L) Lap(R)
F(L) Bas(M)
G(U) Top(L)
G(U) Top(R)
G(U) Lap(M)
G(U) Bas(L)
G(U) Bas(R)
G(L) Top(L)
G(L) Top(R)
G(L) Lap(L)
G(L) Lap(R)
G(L) Bas(M)

Figure 166a.

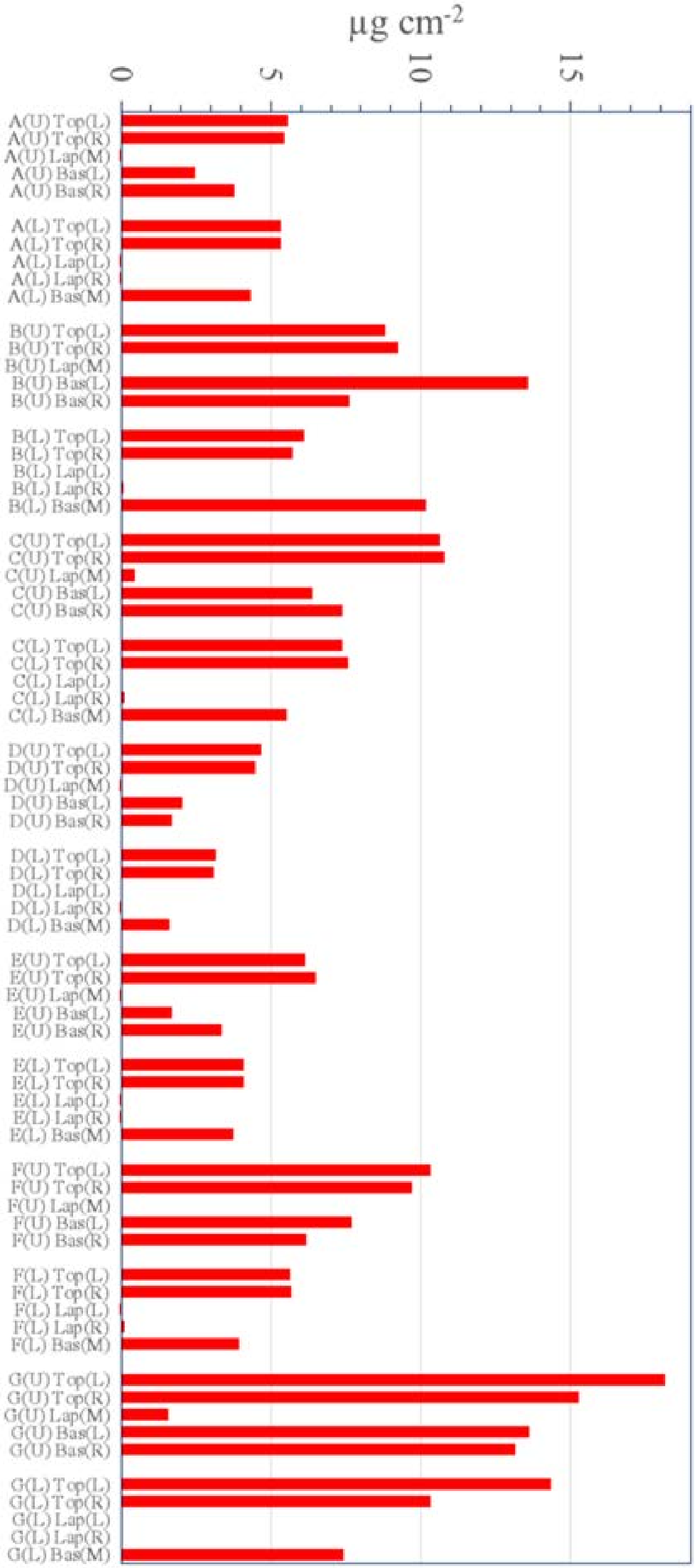
µg cm-2
0
5
10
15
A(U) Top(L)
A(U) Top(R)
A(U) Lap(M)
A(U) Bas(L)
A(U) Bas(R)
A(L) Top(L)
A(L) Top(R)
A(L) Lap(L)
A(L) Lap(R)
A(L) Bas(M)
B(U) Top(L)
B(U) Top(R)
B(U) Lap(M)
B(U) Bas(L)
B(U) Bas(R)
B(L) Top(L)
B(L) Top(R)
B(L) Lap(L)
B(L) Lap(R)
B(L) Bas(M)
C(U) Top(L)
C(U) Top(R)
C(U) Lap(M)
C(U) Bas(L)
C(U) Bas(R)
C(L) Top(L)
C(L) Top(R)
C(L) Lap(L)
C(L) Lap(R)
C(L) Bas(M)
D(U) Top(L)
D(U) Top(R)
D(U) Lap(M)
D(U) Bas(L)
D(U) Bas(R)
D(L) Top(L)
D(L) Top(R)
D(L) Lap(L)
D(L) Lap(R)
D(L) Bas(M)
E(U) Top(L)
E(U) Top(R)
E(U) Lap(M)
E(U) Bas(L)
E(U) Bas(R)
E(L) Top(L)
E(L) Top(R)
E(L) Lap(L)
E(L) Lap(R)
E(L) Bas(M)
F(U) Top(L)
F(U) Top(R)
F(U) Lap(M)
F(U) Bas(L)
F(U) Bas(R)
F(L) Top(L)
F(L) Top(R)
F(L) Lap(L)
F(L) Lap(R)
F(L) Bas(M)
G(U) Top(L)
G(U) Top(R)
G(U) Lap(M)
G(U) Bas(L)
G(U) Bas(R)
G(L) Top(L)
G(L) Top(R)
G(L) Lap(L)
G(L) Lap(R)
G(L) Bas(M)

Figure 166b.

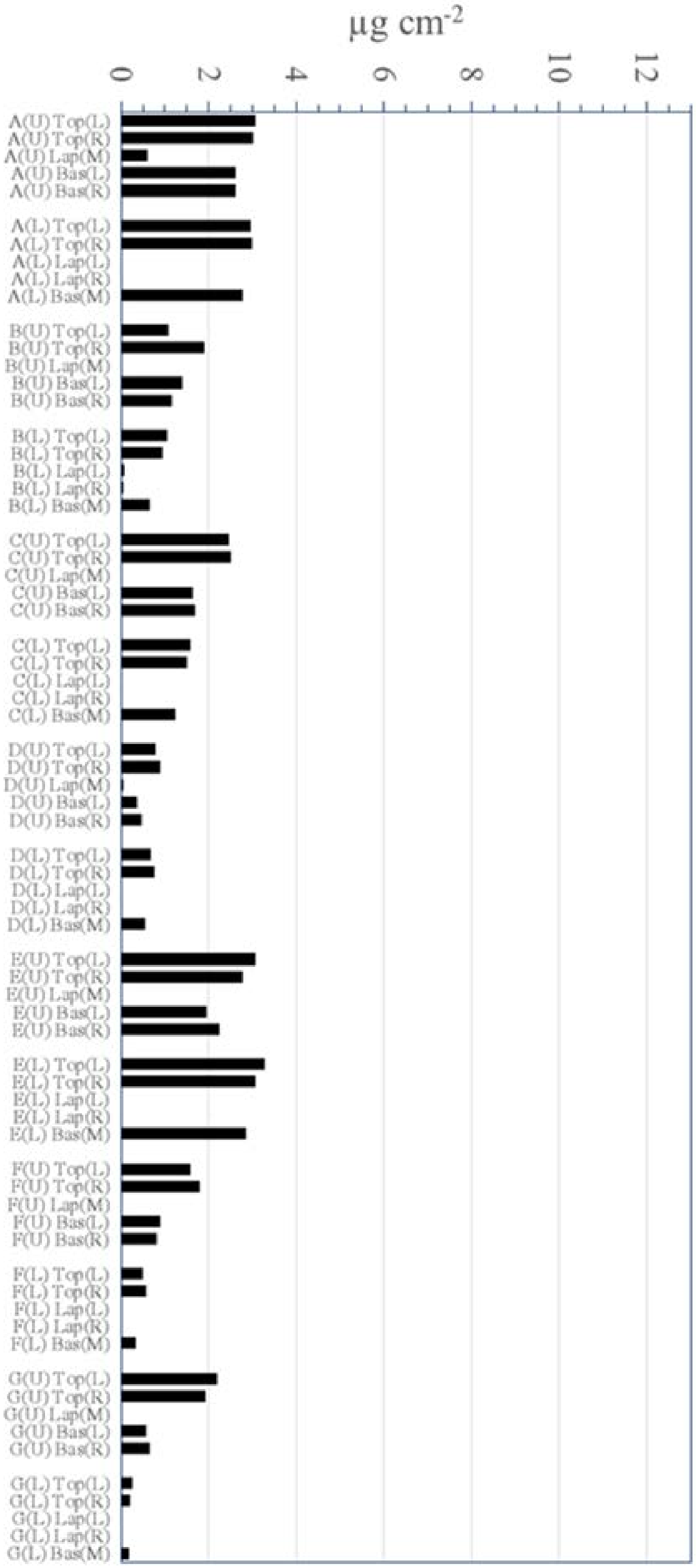
µg cm-2
0
2
4
6
8
10
12
A(U) Top(L)
A(U) Top(R)
A(U) Lap(M)
A(U) Bas(L)
A(U) Bas(R)
A(L) Top(L)
A(L) Top(R)
A(L) Lap(L)
A(L) Lap(R)
A(L) Bas(M)
B(U) Top(L)
B(U) Top(R)
B(U) Lap(M)
B(U) Bas(L)
B(U) Bas(R)
B(L) Top(L)
B(L) Top(R)
B(L) Lap(L)
B(L) Lap(R)
B(L) Bas(M)
C(U) Top(L)
C(U) Top(R)
C(U) Lap(M)
C(U) Bas(L)
C(U) Bas(R)
C(L) Top(L)
C(L) Top(R)
C(L) Lap(L)
C(L) Lap(R)
C(L) Bas(M)
D(U) Top(L)
D(U) Top(R)
D(U) Lap(M)
D(U) Bas(L)
D(U) Bas(R)
D(L) Top(L)
D(L) Top(R)
D(L) Lap(L)
D(L) Lap(R)
D(L) Bas(M)
E(U) Top(L)
E(U) Top(R)
E(U) Lap(M)
E(U) Bas(L)
E(U) Bas(R)
E(L) Top(L)
E(L) Top(R)
E(L) Lap(L)
E(L) Lap(R)
E(L) Bas(M)
F(U) Top(L)
F(U) Top(R)
F(U) Lap(M)
F(U) Bas(L)
F(U) Bas(R)
F(L) Top(L)
F(L) Top(R)
F(L) Lap(L)
F(L) Lap(R)
F(L) Bas(M)
G(U) Top(L)
G(U) Top(R)
G(U) Lap(M)
G(U) Bas(L)
G(U) Bas(R)
G(L) Top(L)
G(L) Top(R)
G(L) Lap(L)
G(L) Lap(R)
G(L) Bas(M)

Figure 167a.

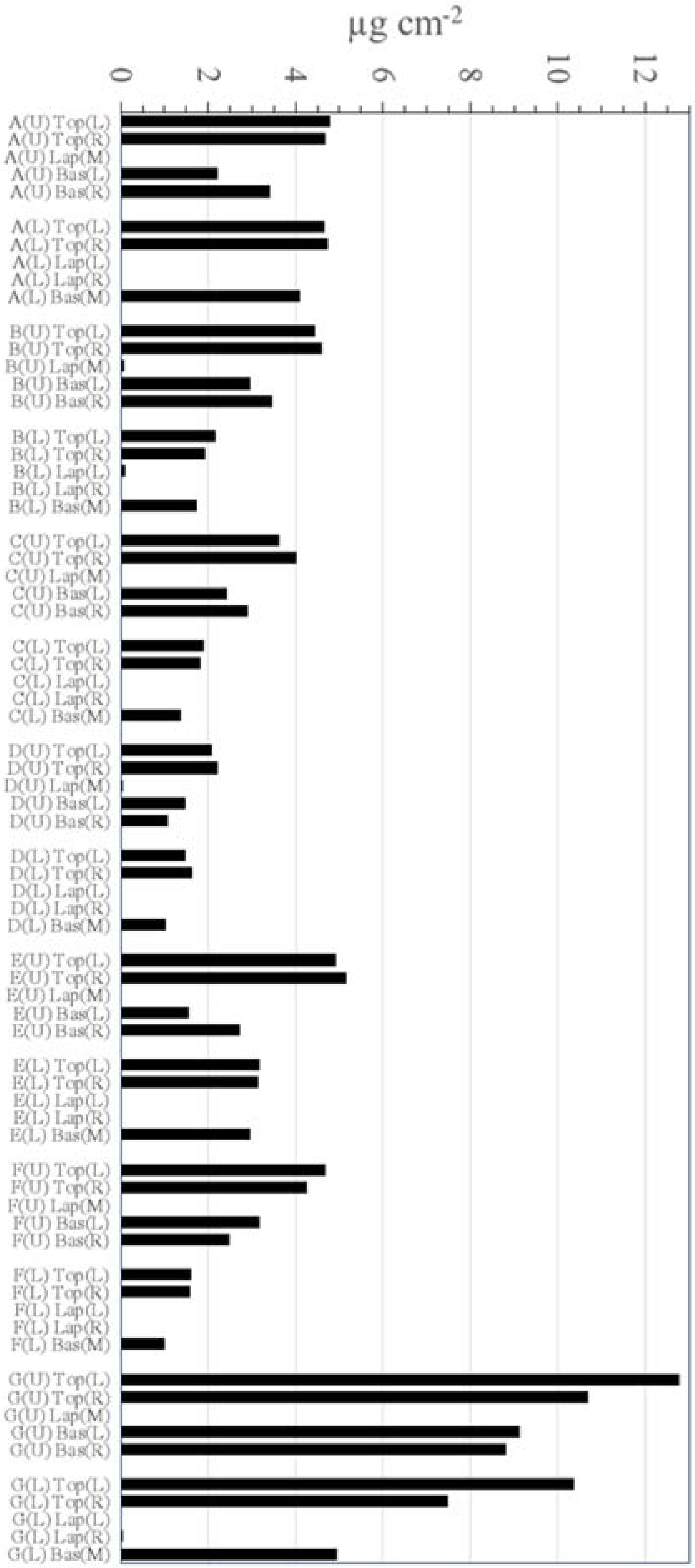
µg cm-2
0
2
4
6
8
10
12
A(U) Top(L)
A(U) Top(R)
A(U) Lap(M)
A(U) Bas(L)
A(U) Bas(R)
A(L) Top(L)
A(L) Top(R)
A(L) Lap(L)
A(L) Lap(R)
A(L) Bas(M)
B(U) Top(L)
B(U) Top(R)
B(U) Lap(M)
B(U) Bas(L)
B(U) Bas(R)
B(L) Top(L)
B(L) Top(R)
B(L) Lap(L)
B(L) Lap(R)
B(L) Bas(M)
C(U) Top(L)
C(U) Top(R)
C(U) Lap(M)
C(U) Bas(L)
C(U) Bas(R)
C(L) Top(L)
C(L) Top(R)
C(L) Lap(L)
C(L) Lap(R)
C(L) Bas(M)
D(U) Top(L)
D(U) Top(R)
D(U) Lap(M)
D(U) Bas(L)
D(U) Bas(R)
D(L) Top(L)
D(L) Top(R)
D(L) Lap(L)
D(L) Lap(R)
D(L) Bas(M)
E(U) Top(L)
E(U) Top(R)
E(U) Lap(M)
E(U) Bas(L)
E(U) Bas(R)
E(L) Top(L)
E(L) Top(R)
E(L) Lap(L)
E(L) Lap(R)
E(L) Bas(M)
F(U) Top(L)
F(U) Top(R)
F(U) Lap(M)
F(U) Bas(L)
F(U) Bas(R)
F(L) Top(L)
F(L) Top(R)
F(L) Lap(L)
F(L) Lap(R)
F(L) Bas(M)
G(U) Top(L)
G(U) Top(R)
G(U) Lap(M)
G(U) Bas(L)
G(U) Bas(R)
G(L) Top(L)
G(L) Top(R)
G(L) Lap(L)
G(L) Lap(R)
G(L) Bas(M)

Figure 167b.

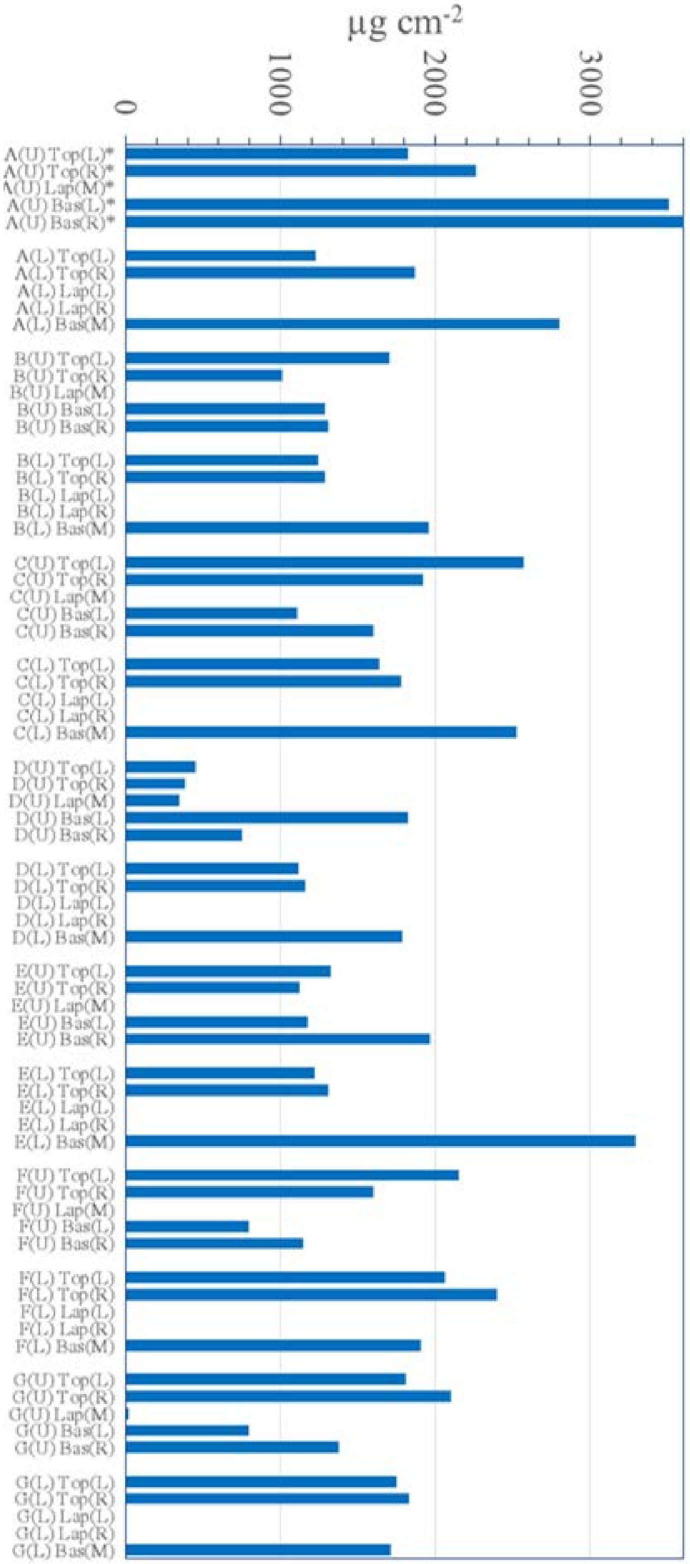
µg cm-2
0
1000
2000
3000
A(U) Top(L)*
A(U) Top(R)*
A(U) Lap(M)*
A(U) Bas(L)*
A(U) Bas(R)*
A(L) Top(L)
A(L) Top(R)
A(L) Lap(L)
A(L) Lap(R)
A(L) Bas(M)
B(U) Top(L)
B(U) Top(R)
B(U) Lap(M)
B(U) Bas(L)
B(U) Bas(R)
B(L) Top(L)
B(L) Top(R)
B(L) Lap(L)
B(L) Lap(R)
B(L) Bas(M)
C(U) Top(L)
C(U) Top(R)
C(U) Lap(M)
C(U) Bas(L)
C(U) Bas(R)
C(L) Top(L)
C(L) Top(R)
C(L) Lap(L)
C(L) Lap(R)
C(L) Bas(M)
D(U) Top(L)
D(U) Top(R)
D(U) Lap(M)
D(U) Bas(L)
D(U) Bas(R)
D(L) Top(L)
D(L) Top(R)
D(L) Lap(L)
D(L) Lap(R)
D(L) Bas(M)
E(U) Top(L)
E(U) Top(R)
E(U) Lap(M)
E(U) Bas(L)
E(U) Bas(R)
E(L) Top(L)
E(L) Top(R)
E(L) Lap(L)
E(L) Lap(R)
E(L) Bas(M)
F(U) Top(L)
F(U) Top(R)
F(U) Lap(M)
F(U) Bas(L)
F(U) Bas(R)
F(L) Top(L)
F(L) Top(R)
F(L) Lap(L)
F(L) Lap(R)
F(L) Bas(M)
G(U) Top(L)
G(U) Top(R)
G(U) Lap(M)
G(U) Bas(L)
G(U) Bas(R)
G(L) Top(L)
G(L) Top(R)
G(L) Lap(L)
G(L) Lap(R)
G(L) Bas(M)

Figure 168.

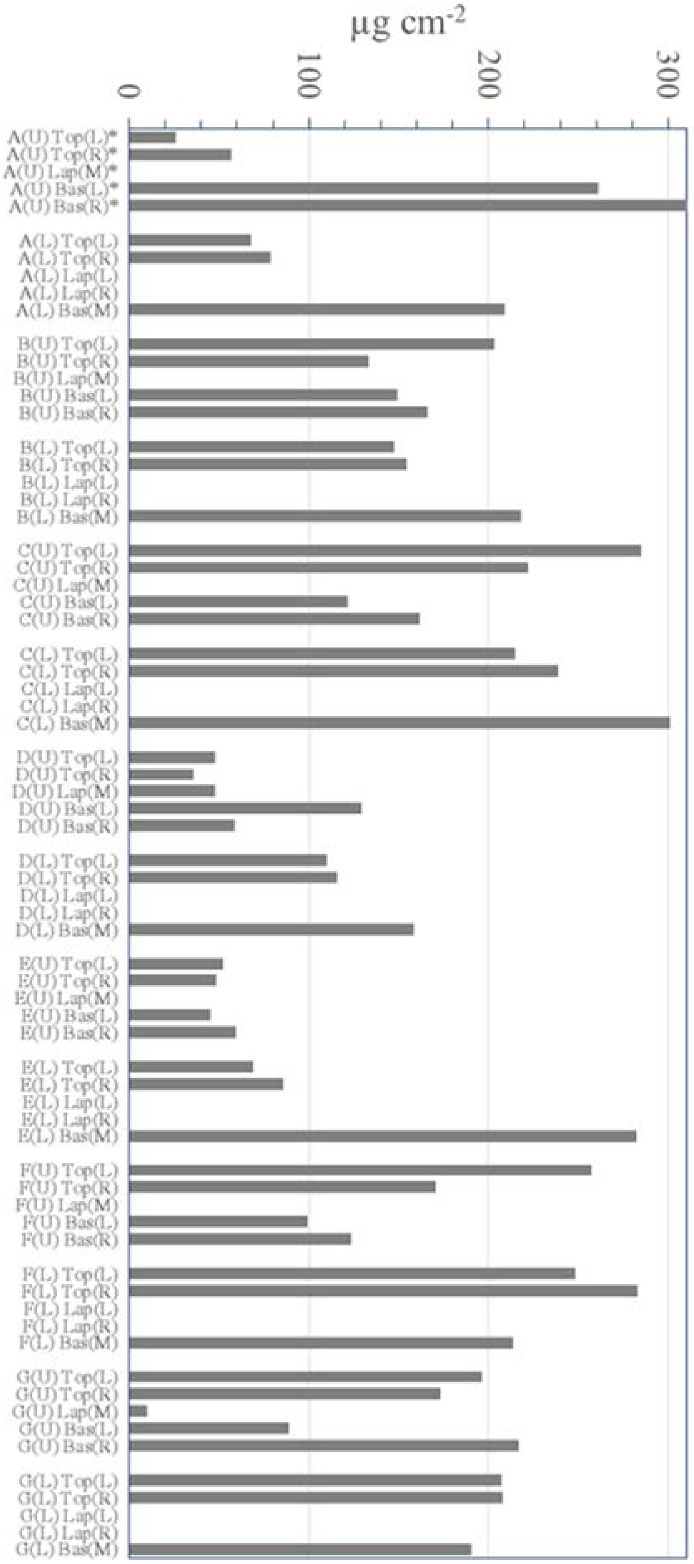
μg cm-2
0
100
200
300
A(U) Top(L)*
A(U) Top(R)*
A(U) Lap(M)*
A(U) Bas(L)*
A(U) Bas(R)*
A(L) Top(L)
A(L) Top(R)
A(L) Lap(L)
A(L) Lap(R)
A(L) Bas(M)
B(U) Top(L)
B(U) Top(R)
B(U) Lap(M)
B(U) Bas(L)
B(U) Bas(R)
B(L) Top(L)
B(L) Top(R)
B(L) Lap(L)
B(L) Lap(R)
B(L) Bas(M)
C(U) Top(L)
C(U) Top(R)
C(U) Lap(M)
C(U) Bas(L)
C(U) Bas(R)
C(L) Top(L)
C(L) Top(R)
C(L) Lap(L)
C(L) Lap(R)
C(L) Bas(M)
D(U) Top(L)
D(U) Top(R)
D(U) Lap(M)
D(U) Bas(L)
D(U) Bas(R)
D(L) Top(L)
D(L) Top(R)
D(L) Lap(L)
D(L) Lap(R)
D(L) Bas(M)
E(U) Top(L)
E(U) Top(R)
E(U) Lap(M)
E(U) Bas(L)
E(U) Bas(R)
E(L) Top(L)
E(L) Top(R)
E(L) Lap(L)
E(L) Lap(R)
E(L) Bas(M)
F(U) Top(L)
F(U) Top(R)
F(U) Lap(M)
F(U) Bas(L)
F(U) Bas(R)
F(L) Top(L)
F(L) Top(R)
F(L) Lap(L)
F(L) Lap(R)
F(L) Bas(M)
G(U) Top(L)
G(U) Top(R)
G(U) Lap(M)
G(U) Bas(L)
G(U) Bas(R)
G(L) Top(L)
G(L) Top(R)
G(L) Lap(L)
G(L) Lap(R)
G(L) Bas(M)

Figure 169.

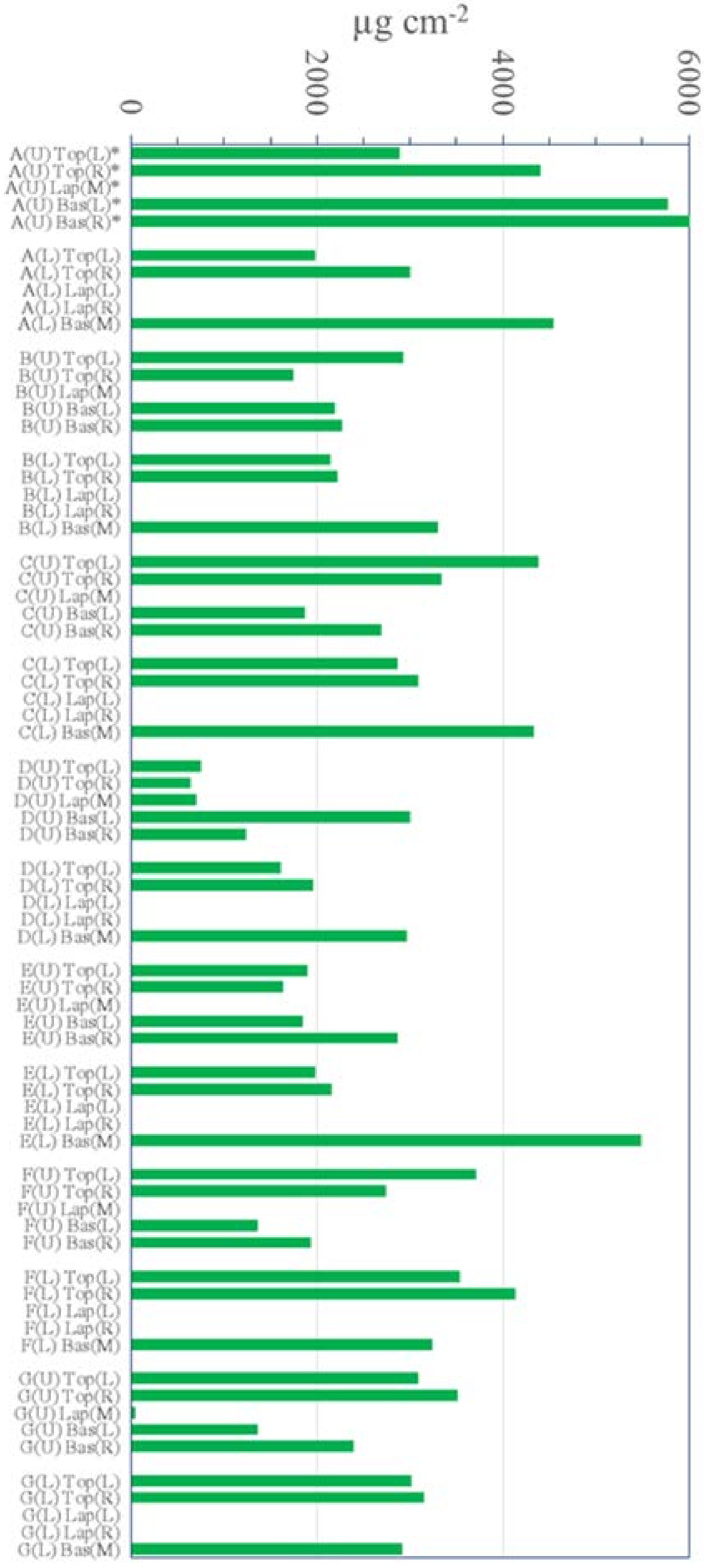
µg cm-2
0
2000
4000
6000
A(U) Top(L)*
A(U) Top(R)*
A(U) Lap(M)*
A(U) Bas(L)*
A(U) Bas(R)*
A(L) Top(L)
A(L) Top(R)
A(L) Lap(L)
A(L) Lap(R)
A(L) Bas(M)
B(U) Top(L)
B(U) Top(R)
B(U) Lap(M)
B(U) Bas(L)
B(U) Bas(R)
B(L) Top(L)
B(L) Top(R)
B(L) Lap(L)
B(L) Lap(R)
B(L) Bas(M)
C(U) Top(L)
C(U) Top(R)
C(U) Lap(M)
C(U) Bas(L)
C(U) Bas(R)
C(L) Top(L)
C(L) Top(R)
C(L) Lap(L)
C(L) Lap(R)
C(L) Bas(M)
D(U) Top(L)
D(U) Top(R)
D(U) Lap(M)
D(U) Bas(L)
D(U) Bas(R)
D(L) Top(L)
D(L) Top(R)
D(L) Lap(L)
D(L) Lap(R)
D(L) Bas(M)
E(U) Top(L)
E(U) Top(R)
E(U) Lap(M)
E(U) Bas(L)
E(U) Bas(R)
E(L) Top(L)
E(L) Top(R)
E(L) Lap(L)
E(L) Lap(R)
E(L) Bas(M)
F(U) Top(L)
F(U) Top(R)
F(U) Lap(M)
F(U) Bas(L)
F(U) Bas(R)
F(L) Top(L)
F(L) Top(R)
F(L) Lap(L)
F(L) Lap(R)
F(L) Bas(M)
G(U) Top(L)
G(U) Top(R)
G(U) Lap(M)
G(U) Bas(L)
G(U) Bas(R)
G(L) Top(L)
G(L) Top(R)
G(L) Lap(L)
G(L) Lap(R)
G(L) Bas(M)

Figure 170.

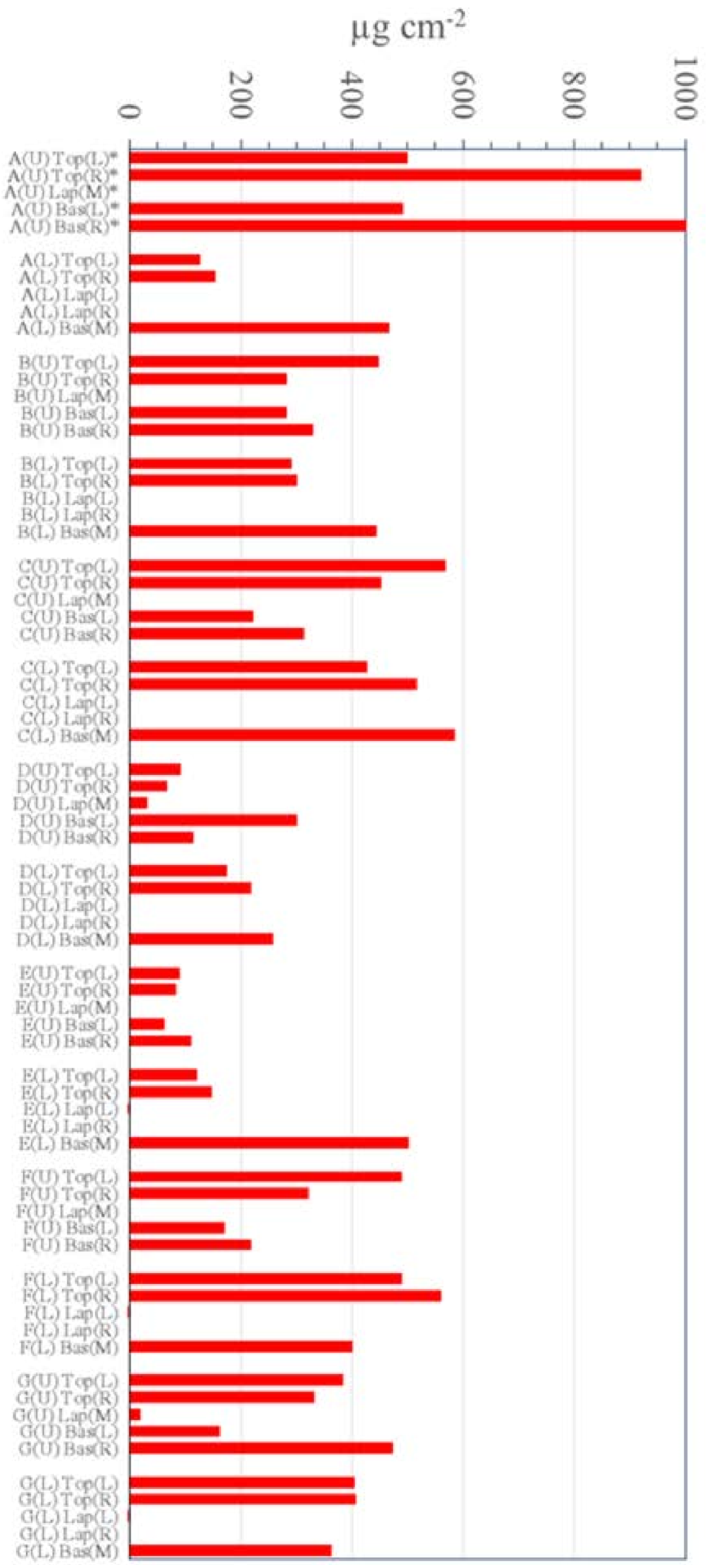
µg cm^{-2}
0
200
400
600
800
1000
A(U) Top(L)*
A(U) Top(R)*
A(U) Lap(M)*
A(U) Bas(L)*
A(U) Bas(R)*
A(L) Top(L)
A(L) Top(R)
A(L) Lap(L)
A(L) Lap(R)
A(L) Bas(M)
B(U) Top(L)
B(U) Top(R)
B(U) Lap(M)
B(U) Bas(L)
B(U) Bas(R)
B(L) Top(L)
B(L) Top(R)
B(L) Lap(L)
B(L) Lap(R)
B(L) Bas(M)
C(U) Top(L)
C(U) Top(R)
C(U) Lap(M)
C(U) Bas(L)
C(U) Bas(R)
C(L) Top(L)
C(L) Top(R)
C(L) Lap(L)
C(L) Lap(R)
C(L) Bas(M)
D(U) Top(L)
D(U) Top(R)
D(U) Lap(M)
D(U) Bas(L)
D(U) Bas(R)
D(L) Top(L)
D(L) Top(R)
D(L) Lap(L)
D(L) Lap(R)
D(L) Bas(M)
E(U) Top(L)
E(U) Top(R)
E(U) Lap(M)
E(U) Bas(L)
E(U) Bas(R)
E(L) Top(L)
E(L) Top(R)
E(L) Lap(L)
E(L) Lap(R)
E(L) Bas(M)
F(U) Top(L)
F(U) Top(R)
F(U) Lap(M)
F(U) Bas(L)
F(U) Bas(R)
F(L) Top(L)
F(L) Top(R)
F(L) Lap(L)
F(L) Lap(R)
F(L) Bas(M)
G(U) Top(L)
G(U) Top(R)
G(U) Lap(M)
G(U) Bas(L)
G(U) Bas(R)
G(L) Top(L)
G(L) Top(R)
G(L) Lap(L)
G(L) Lap(R)
G(L) Bas(M)

Figure 171.

APPENDIX B
PUBLICATIONS

1. Articles in Peer-reviewed journals:

   Schindelholz, E. & Kelly, R.G. (2010). Application of Inkjet Printing for Depositing Salt Prior to Atmospheric Corrosion Testing. *Electrochemical and Solid-State Letters,* 13(10): C29-C31.

   Schindelholz, E. & Kelly, R.G. (2012). Wetting phenomena and time of wetness in atmospheric corrosion: a review. *Corrosion Reviews*, 30(5-6): 135-170.

   Schindelholz, E., Kelly, R.G., Cole, I.S., Ganther, W.D. & Muster, T.H. (2013) Comparability and accuracy of time of wetness sensing methods relevant for atmospheric corrosion, *Corrosion Science,* 67: 233-241.

   Schindelholz, E., Risteen, B.E. & Kelly, R.G. (2014). Marine Aerosol Drop Size Effects on the Corrosion Behavior of Low Carbon Steel and High Purity Iron. *Journal of the Electrochemical Society,* 161 (14): C580-C586.

   Schindelholz, E., Risteen, B.E. & Kelly, R.G., (2014). Effect of Relative Humidity on Corrosion of Steel under Sea Salt Aerosol Proxies. I. NaCl. *Journal of the Electrochemical Society,* 161 (10): C450-C459.

   Schindelholz, E., Risteen, B.E. & Kelly, R.G. (2014). Effect of Relative Humidity on Corrosion of Steel under Sea Salt Aerosol Proxies. II. $MgCl_2$, Artificial Seawater. *Journal of the Electrochemical Society,* 161 (10): C460-C470.

   Schindelholz, E., Risteen, B.E., & Kelly, R.G. (2014). Effect of Relative Humidity on Corrosion of Steel under Sea Salt Aerosol Proxies. I. NaCl. *Journal of the Electrochemical Society,* 161 (10): C450-C459.

   Schindelholz, E., Tsui, L.K., & Kelly, R.G. (2014). Hygroscopic Particle Behavior Studied by Interdigitated Array Microelectrode Impedance Sensors. *J. Phys. Chem A* 118, 167-177

   Brown, N., Kramer, P., Friedersdorf, F., Schidelholz, M., & Siegel, J. (2016). Environmentally Assisted Cracking Measurements in Structural Aluminum Alloys Under Accelerated Test Conditions, *CORROSION,* 72(11):1351-1362.

   Macha, E. N., Zuflacht, M. A., & J. F. Dante. *Effects of Aerospace Primers on Galvanic MEASs in Controlled RH Environments. CORROSION* (in review)

2. Technical reports

3. Conference or symposium proceedings scientifically recognized and referenced

   Friedersdorf, F., Siegel, J., & Brown, N. (2015). *Environment Assisted Cracking Measurements in Accelerated and Outdoor Corrosion Tests.* Paper Presented at 2015 Department of Defense – Allied Nations Technical Corrosion Conference, Pittsburgh, PA, November 15-19, 2015.

Macha, E.N. & Dante, J.F. (2015). *Characterization of Accelerated Test Environments using Galvanically Coupled Multi-Electrode Arrays*, NACE Paper No. 2015-5982. Paper presented at CORROSION 2015, Dallas, TX.

Schindelholz, E., Kelly, R.G., & Risteen, B.E. (2015). *Effect of Relative Humidity on Corrosion of Steel under Acidified Artificial Seawater Particles.* NACE Paper No. 2015-5987. Paper Presented at CORROSION 2015, Dallas, TX.

Shedd, M., Siegel, J., & Friedersdorf, F. (2015). *Small Scale Crack Growth Sensor for Determination of AA5XXX Susceptibility to SCC.* NACE-2015-5530. Paper Presented at CORROSION 2015, Dallas, TX.

Jackson, D. & Williams, K.S. (2017). *Quantitative Comparison of Outdoor Sites and Accelerated Test Methods Using Optical Profilometry*. NACE Paper No. 2017-9730, Paper presented at CORROSION 2017, New Orleans, LA.

Macha, E. N., Zuflacht, M. A., & J. F. Dante. (2017). *Effects of Aerospace Primers on Galvanic MEASs in Controlled RH Environments.* Paper No 865014. Presented at the 2017 Department of Defense and Allied Nations Corrosion Conference, Birmingham, Al., August 2017.

4. Conference or symposium abstracts

Dante, J.F. (2011). *Understanding the Role of Relative Humidity Conditions in Accelerated Corrosion Testing*, ASETSDefense, New Orleans, LA, February, 2011

Dante, J.F. (2012) *Effect of Relative Humidity on Time of Wetness and Corrosion*. Research in Progress Symposium. Paper Presented at CORROSION 2012, Salt Lake City, UT.

Dante, J.F. (2012). *Implication of Atmospheric Wetness Levels on Corrosion at a Coating Defect during Accelerated Testing*, Paper presented at ASETSDefense 2012, San Diego, CA, August, 2012.

Dante, J.F., & Macha, E.N. (2014). *Effectiveness of Inhibitors on Aluminum and Aluminum/Steel Couples as a Function of Relative Humidity*, Research in Progress Symposium, Paper presented at CORROSION 2014, San Antonio, TX.

Dante, J.F. (2016) Development of Accelerated Corrosion Test Method, ASETSDefense Conference, Orlando, FL, December, 2016.

Dante, J.F., Macha, E.N., Zuflachat, M.A. *Accelerated Dynamic Corrosion Test Method Development*, Research in Progress Symposium invited speaker, CORROSION 2017, New Orleans, LA

5. Text books or book chapters

APPENDIX C
TEST PROTOCOL

SERDP Accelerated Test Protocol

9. Scope

9.1. This practice describes conditions and methodology for performing cyclic salt spray testing with monitored Relative Humidity (RH) for specification purposes.

9.2. This practice prescribes a test cycle and a test specimen to be used. It does not prescribe the exposure periods to be used, nor the interpretation to be given to the results.

9.3. *This standard does not claim to address all of the safety concerns, if any, associated with its use. It is the responsibility of the user of this standard to consult and establish appropriate safety and health practices and determine the applicability of regulatory limitations prior to use.*

10. Significance and Use

10.1. This practice is applicable to ferrous and nonferrous metals; as well as organic and inorganic coatings. The practice described herein is useful when a more realistic environment than the salt fog described in Specification ASTM B 117 is desired.

11. Apparatus

11.1. *Cabinet*:

11.1.1. The apparatus required for salt spray (fog) testing consists of a fog chamber, a salt solution reservoir, a supply of suitably conditioned compressed air, one or more atomizing nozzles, specimen supports, provision for heating the chamber, and necessary means of control. The size and detailed construction of the cabinet are optional, provided the conditions obtained meet the requirements of this practice. The material of construction shall be such that it will not affect the corrosiveness of the fog. Suitable apparatus that may be used to obtain these conditions is described in Appendix A1 of Specification ASTM B 117 with necessary modifications described herein.

11.1.2. The cabinet shall be designed so that drops of solution that accumulate on the ceiling or cover of the chamber do not fall on the specimens being tested Ddrops of solution that fall from the specimens shall not be returned to the solution reservoir for respraying.

11.1.3. The cabinet shall be equipped with one or more timing devices to provide for intermittent spraying.

11.2. *Air Supply*:

11.2.1. The compressed air supply to the nozzle or nozzles for atomizing the salt solution shall be free of oil and dirt[4] and maintain the air supply between 69 and 172 kPa (10 and 25 psi).

11.2.2. Temperature in the saturator tower (bubble tower) shall be set to 47^o C.

11.3. *Conditions in Salt-Spray Chamber*:

11.3.1. *Temperature*—The temperature in the exposure zone shall be set to 40^o C +/- 3^oC. Tolerance represents an operational control point for equilibrium conditions at a single location in the cabinet which may not necessarily represent the uniformity of conditions throughout the cabinet. The temperature shall be recorded continuously throughout the test[5].

---

[4] Note that the air supply may be cleaned of oil and dirt by passing it through a water scrubber or at least 2 ft (610 mm) of activated alumina.

[5] Note that the recorded temperature must be obtained with the salt spray chamber closed to avoid a false low reading.

11.3.2. *Atomization and Quantity of Fog*—At least two clean fog collectors shall be placed within the exposure zone so that no drops of solution from the test specimens or any other source can be collected. The collectors shall be positioned in the proximity of the test specimens, one nearest to any nozzle and the other farthest from all nozzles. For each 80 cm^2 of horizontal collecting area, the collection rate for the fog accumulation in each collector shall be from 1.0 to 2.0 mL of solution per hour based on an average run of at least 16 h continuous spray[6].

11.3.3. The nozzle or nozzles shall be directed or baffled so that none of the spray impinges directly on the test specimens.

12. **Test Specimens**

12.1. The type and number of test specimens to be used, as well as the criteria for the evaluation of the test results shall be defined in the specifications of the material or product being tested or upon mutual agreement between the purchaser and the seller. However, the test specimen shown in Figure 1 is recommended. This specimen provides multiple locations for differing failure modes to occur including galvanic corrosion, crevice corrosion and corrosion at a coating defect.

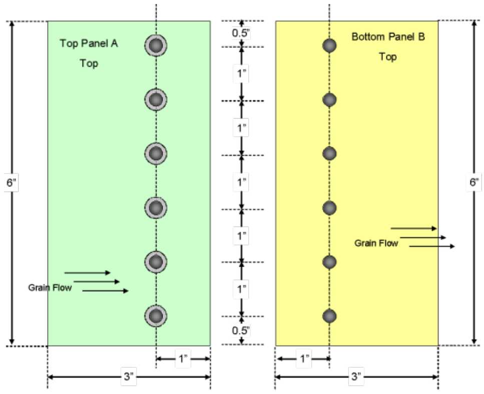

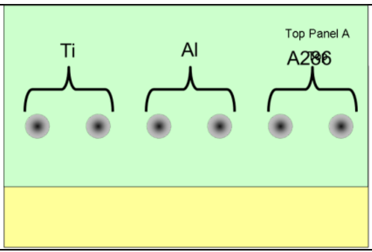

Figure 1. Lap joint configuration recommended for this practice. High Lock fasteners are recommended for aerospace applications and should be dry installed. An "x" scribe should be placed through the center of the fasteners that extends 0.25" from the scribe edge (edge of fasteners) on each side.

12.2. *Preparation of Test Specimens*:

12.2.1. The test specimens shall be cleaned according to applicable specification(s) for the material(s) being tested, or as agreed upon between the test lab and the customer.

12.2.2. Specimens for evaluation of paints and other organic coatings shall be prepared in accordance with applicable specification(s) for the material(s) being tested, or as agreed upon between the test lab and the customer.

12.2.3. Test panels shall be scribed across each fastener such that 0.25" of scribe protrudes from the edge of the fastener. Scribes should be cut after installation of the countersunk fasteners.

Any continuous temperature device or thermometer which can be read from the outside can be used.

[6] Glass funnels with the stems inserted through stoppers into graduated cylinders or crystallizing dishes can be used. Funnels and dishes with diameters of 100 mm have an area of about $80cm^2$.

12.2.4. The cut edges of the sample assemblies and areas that contain identification marks or that are in contact with the racks or supports shall be protected with electro-plater's tape.

13. **Salt Solutions**

13.1. The salt solution shall be prepared in accordance with one of the two modified sea salt solutions shown in Table 1. Make-up water shall be deionized water conforming to Type IV water in Specification ASTM D 1193. All chemicals shall be reagent grade.

Table 1. Salt Solution Compositions.

Test Solution #1 – Modified Sea Salt Solution with Nitrate Ions	
NaCl	46.81 g/L
$MgCl_2.6H_2O$	23.31 g/L
Na_2SO_4	8.40 g/L
$NaNO_3$	6.86 g/L
HCl (1N)	(1 mL)

13.2. The pH of the salt solution shall be pH = 3 and shall be measured daily to ensure it is maintained at that value.

14. **Procedure**

14.1. Position of Specimens During Test:

14.1.1. Unless otherwise specified, the specimen shall be supported at 15° from the vertical, and preferably parallel to the principal direction of horizontal flow of fog through the chamber, based upon the dominant surface being tested.

14.1.2. Contact of the specimens between each other, between any metallic material or between any material capable of acting as a wick shall not be permitted.

14.1.3. Each specimen shall be placed so as to permit free settling of fog on all specimens. A minimum spacing between specimens of 30 mm is recommended.

14.1.4. Dripping of the salt solution from one specimen on any other specimen shall not be permitted.

14.1.5. It is recommended that placement of replicate specimens be randomized to avoid possible bias caused by difference in spray patterns. Individual specimens may also be rotated daily for the same reason.

14.1.6. Suitable materials for the construction or coating of racks and supports are glass, rubber, plastic, or suitably coated wood. Do not use bare metal. Support specimens preferably from the bottom or the side. Slotted wooden, laminated plastic, or inert plastic strips are suitable for the support of flat panels.

14.2. Exposure Cycle

14.2.1. The cycle test consists of a 1-hour high humidity wet period and a 1-hour dry-off period. During the wet period, the test solution will be fogged into the chamber for 15 minutes followed by 45 minutes under high RH wet bottom conditions.

14.2.2. The relative humidity during the wet cycle must be above 80% RH for at least 50 minutes.

14.2.3. In the dry-off portion of the cycle, the relative humidity must fall to at least 40% RH for at least 35 minutes

14.2.4. Ramp rates must be set such that 80% RH is reached within 10 minutes after the dry-off phase is completed. Ramp rates must be set such that the relative humidity falls from 80% RH to 40% RH in 25 minutes (but not shorter).

14.3. *Continuity of Test*:

14.3.1. Unless otherwise specified, in the specifications covering the material or product being tested, the test shall be continuous for the duration of the entire test period. Continuous operation implies that the chamber be closed except for the short daily interruptions necessary to inspect, rearrange, or remove test specimens, and to check and replenish the solution in the reservoir. Operations shall be so scheduled that the maximum time for these interrupting is held to 60 min or less per day. It is recommended to have only one interruption per day if possible.

14.4. *Period of Test*:

14.4.1. The period of test shall be designated in accordance with the specifications covering the material or product being tested or as mutually agreed upon between the purchaser and the seller. An exposure period of multiples of 1000 hours is suggested.

14.5. *Cleaning of Tested Specimens*:

14.5.1. Unless otherwise specified in the specifications covering the material or product being tested, at the end of the test, specimens may be gently washed or dipped in clean running water no warmer than 38°C (100°F) to remove salt deposits from their surface, and then immediately dried. Dry with a stream of clean, compressed air.

15. Evaluation of Results

15.1. A careful and immediate examination shall be made for the extent of corrosion of the dry test specimens or for other failure as required by the specifications covering the material or product being tested or by agreement between the testing lab and the client.

15.2. For the recommended test specimen, the following evaluations shall be made:

15.2.1. Corrosion in the scribes, scribe creep back, coating appearance and extent of corrosion within the lap joint.

15.2.2. As optional analyses, quantitative image analysis of the corrosion damage is recommended. Additionally, metallographic cross sections of the faster hole region can be made.

16. Report

16.1. The following information shall be recorded, unless otherwise prescribed in the specifications covering the material or product being tested:

16.1.1. Continuous readings of temperature and relative humidity within the exposure zone of the chamber,

16.1.2. Data obtained from each fog-collecting device for volume of salt solution collected in milliliters per hour of operation per 80 cm^2 of horizontal collection area. Data should be collect for 16 hours prior to exposure of the samples.

16.1.3. Records of data obtained from fog-collecting devices for pH of collected solution. Sample to be measured may be a composite sample from multiple fog-collecting devices (within one test chamber), if necessary to obtain sufficient solution volume for the measurement.

16.1.4. Type of specimen and its dimensions, or number or description of part, method of cleaning specimens before and after testing,

16.1.5. Exposure period,

16.1.6. Interruptions in test, cause and length of time, and

16.1.7. Results of all inspections.